

Memory Circuit Elements: Complexity, Complex Systems, and Applications

Lead Guest Editor: Viet-Thanh Pham

Guest Editors: Sundarapandian Vaidyanathan, Esteban Tlelo-Cuautle,
and Tomasz Kapitaniak





Memory Circuit Elements: Complexity, Complex Systems, and Applications

Memory Circuit Elements: Complexity, Complex Systems, and Applications

Lead Guest Editor: Viet-Thanh Pham

Guest Editors: Sundarapandian Vaidyanathan,
Esteban Tlelo-Cuautle, and Tomasz Kapitaniak



Copyright © 2019 Hindawi. All rights reserved.

This is a special issue published in “Complexity.” All articles are open access articles distributed under the Creative Commons Attribution License, which permits unrestricted use, distribution, and reproduction in any medium, provided the original work is properly cited.

Editorial Board




José A. Acosta, Spain
C. F. Aguilar-Ibáñez, Mexico
Mojtaba Ahmadi Khanezar, UK
Tarek Ahmed-Ali, France
Alex Alexandridis, Greece
Basil M. Al-Hadithi, Spain
Juan A. Almendral, Spain
Diego R. Amancio, Brazil
David Arroyo, Spain
Mohamed Boutayeb, France
Átila Bueno, Brazil
Arturo Buscarino, Italy
Guido Caldarelli, Italy
Eric Campos-Canton, Mexico
Mohammed Chadli, France
É. J. L. Chappin, Netherlands
Diyi Chen, China
Yu-Wang Chen, UK
Giulio Cimini, Italy
Danilo Comminiello, Italy
Sara Dadras, USA
Sergey Dashkovskiy, Germany
Manlio De Domenico, Italy
Pietro De Lellis, Italy
Albert Diaz-Guilera, Spain
Thach Ngoc Dinh, France
Jordi Duch, Spain
Marcio Eisencraft, Brazil
Joshua Epstein, USA
Mondher Farza, France
Thierry Floquet, France
Mattia Frasca, Italy
J. Manuel Galán, Spain
Lucia Valentina Gambuzza, Italy
Bernhard C. Geiger, Austria

Carlos Gershenson, Mexico
Peter Giesl, UK
Sergio Gómez, Spain
Lingzhong Guo, UK
Xianggui Guo, China
Sigurdur F. Hafstein, Iceland
Chittaranjan Hens, Israel
Giacomo Innocenti, Italy
Sarangapani Jagannathan, USA
Mahdi Jalili, Australia
Jeffrey H. Johnson, UK
M. Hassan Khooban, Denmark
Abbas Khosravi, Australia
Toshikazu Kuniya, Japan
Vincent Labatut, France
Lucas Lacasa, UK
Guang Li, UK
Qingdu Li, Germany
Chongyang Liu, China
Xiaoping Liu, Canada
Xinzhi Liu, Canada
Rosa M. Lopez Gutierrez, Mexico
Vittorio Loreto, Italy
Noureddine Manamanni, France
Didier Maquin, France
Eulalia Martínez, Spain
Marcelo Messias, Brazil
Ana Meštrović, Croatia
Ludovico Minati, Japan
Ch. P. Monterola, Philippines
Marcin Mrugalski, Poland
Roberto Natella, Italy
Sing Kiong Ngung, New Zealand
Nam-Phong Nguyen, USA
B. M. Ombuki-Berman, Canada

Irene Otero-Muras, Spain
Yongping Pan, Singapore
Daniela Paolotti, Italy
C. Posadas-Castillo, Mexico
Mahardhika Pratama, Singapore
Luis M. Rocha, USA
Miguel Romance, Spain
Avimanyu Sahoo, USA
Matilde Santos, Spain
Josep Sardanyés Cayuela, Spain
Ramaswamy Savitha, Singapore
Hiroki Sayama, USA
Michele Scarpiniti, Italy
Enzo Pasquale Scilingo, Italy
Dan Selişteanu, Romania
Dehua Shen, China
Dimitrios Stamovlasis, Greece
Samuel Stanton, USA
Roberto Tonelli, Italy
Shahadat Uddin, Australia
Gaetano Valenza, Italy
Dimitri Volchenkov, USA
Christos Volos, Greece
Zidong Wang, UK
Yan-Ling Wei, Singapore
Honglei Xu, Australia
Yong Xu, China
Xinggang Yan, UK
Baris Yuce, UK
Massimiliano Zanin, Spain
Hassan Zargarzadeh, USA
Rongqing Zhang, USA
Xianming Zhang, Australia
Xiaopeng Zhao, USA
Quanmin Zhu, UK

Contents

Memory Circuit Elements: Complexity, Complex Systems, and Applications

Viet-Thanh Pham , Sundarapandian Vaidyanathan , Esteban Tlelo-Cuautle , and Tomasz Kapitaniak
Editorial (4 pages), Article ID 4936123, Volume 2019 (2019)

Fully Integrated Memristor and Its Application on the Scroll-Controllable Hyperchaotic System

Jie Jin  and Li Cui

Research Article (8 pages), Article ID 4106398, Volume 2019 (2019)

A Novel Memductor-Based Chaotic System and Its Applications in Circuit Design and Experimental Validation

Li Xiong , Yanjun Lu , Yongfang Zhang , and Xinguo Zhang

Research Article (17 pages), Article ID 3870327, Volume 2019 (2019)

A New Memristor-Based 5D Chaotic System and Circuit Implementation

Rui Wang , Mingjin Li , Zhaoling Gao , and Hui Sun 

Research Article (12 pages), Article ID 6069401, Volume 2018 (2019)

New Results on Fuzzy Synchronization for a Kind of Disturbed Memristive Chaotic System

Bo Wang  and L. L. Chen

Research Article (9 pages), Article ID 3079108, Volume 2018 (2019)

Exact Analysis and Physical Realization of the 6-Lobe Chua Corsage Memristor

Zubaer I. Mannan, Changju Yang, Shyam P. Adhikari, and Hyongsuk Kim 



Research Article (21 pages), Article ID 8405978, Volume 2018 (2019)

On Designing Feedback Controllers for Master-Slave Synchronization of Memristor-Based Chua's Circuits

Ke Ding 

Research Article (8 pages), Article ID 5431619, Volume 2018 (2019)

Family of Bistable Attractors Contained in an Unstable Dissipative Switching System Associated to a SNLF

J. L. Echenausía-Monroy , J. H. García-López, R. Jaimes-Reátegui, D. López-Mancilla,
and G. Huerta-Cuellar 

Research Article (9 pages), Article ID 6794791, Volume 2018 (2019)

Dynamical Behavior of a 3D Jerk System with a Generalized Memristive Device

Wei Feng , Yi-Gang He , Chun-Lai Li , Xun-Min Su, and Xiao-Qing Chen

Research Article (10 pages), Article ID 5620956, Volume 2018 (2019)

Chaos and Symbol Complexity in a Conformable Fractional-Order Memcapacitor System

Shaobo He, Santo Banerjee , and Bo Yan

Research Article (15 pages), Article ID 4140762, Volume 2018 (2019)

An Integer-Order Memristive System with Two- to Four-Scroll Chaotic Attractors and Its Fractional-Order Version with a Coexisting Chaotic Attractor

Ping Zhou  and Meihua Ke

Research Article (7 pages), Article ID 4970152, Volume 2018 (2019)

Dynamic Behaviors in Coupled Neuron System with the Excitatory and Inhibitory Autapse under Electromagnetic Induction

Ying Xu, Ya Jia , John Billy Kirunda, Jian Shen, Mengyan Ge, Lulu Lu, and Qiming Pei

Research Article (13 pages), Article ID 3012743, Volume 2018 (2019)

Evidence of Exponential Speed-Up in the Solution of Hard Optimization Problems

Fabio L. Traversa, Pietro Cicotti, Forrest Sheldon, and Massimiliano Di Ventra 

Research Article (13 pages), Article ID 7982851, Volume 2018 (2019)

Analysis and Implementation of a New Switching Memristor Scroll Hyperchaotic System and Application in Secure Communication

Ping Liu, Rui Xi, Pengbo Ren, Jialin Hou , and Xiang Li 

Research Article (15 pages), Article ID 3497640, Volume 2018 (2019)

Investigation of Cortical Signal Propagation and the Resulting Spatiotemporal Patterns in Memristor-Based Neuronal Network

Ke Ding , Zahra Rostami, Sajad Jafari, and Boshra Hatef 

Research Article (20 pages), Article ID 6427870, Volume 2018 (2019)

Fractional-Order Memristor Emulator Circuits

C. Sánchez-López , V. H. Carbajal-Gómez , M. A. Carrasco-Aguilar, and I. Carro-Pérez



Research Article (10 pages), Article ID 2806976, Volume 2018 (2019)

Memristor-Based Canonical Chua's Circuit: Extreme Multistability in Voltage-Current Domain and Its Controllability in Flux-Charge Domain

Han Bao, Tao Jiang, Kaibin Chu, Mo Chen, Quan Xu, and Bocheng Bao 

Research Article (13 pages), Article ID 5935637, Volume 2018 (2019)

Three-Dimensional Memristive Hindmarsh–Rose Neuron Model with Hidden Coexisting Asymmetric Behaviors

Bocheng Bao , Aihuang Hu, Han Bao, Quan Xu, Mo Chen, and Huagan Wu 

Research Article (11 pages), Article ID 3872573, Volume 2018 (2019)

Editorial

Memory Circuit Elements: Complexity, Complex Systems, and Applications

Viet-Thanh Pham ^{1,2} **Sundarapandian Vaidyanathan** ³,
Esteban Tlelo-Cuautle ⁴ and **Tomasz Kapitaniak**⁵

¹Faculty of Electrical and Electronic Engineering, Phenikaa Institute for Advanced Study (PIAS), Phenikaa University, Yen Nghia, Ha Dong district, Hanoi 100000, Vietnam

²Phenikaa Research and Technology Institute (PRATI), A&A Green Phoenix Group, 167 Hoang Ngan, Hanoi 100000, Vietnam

³Research and Development Centre, Vel Tech University, No. 42, Avadi-Vel Tech Road, Avadi, Chennai, Tamil Nadu 600062, India

⁴Department of Electronics, Instituto Nacional de Astrofísica, Óptica y Electrónica (INAOE), Puebla 72840, Mexico

⁵Division of Dynamics, Lodz University of Technology, Stefanowskiego 1/15, 90-924 Lodz, Poland

Correspondence should be addressed to Viet-Thanh Pham; thanh.phamviet@phenikaa-uni.edu.vn

Received 6 November 2018; Accepted 6 November 2018; Published 15 January 2019

Copyright © 2019 Viet-Thanh Pham et al. This is an open access article distributed under the Creative Commons Attribution License, which permits unrestricted use, distribution, and reproduction in any medium, provided the original work is properly cited.

Mem-systems, based on the Memory Circuit Elements (memristor, memcapacitor, and meminductor), have received significant attention after the realization of a solid-state memristor in the Hewlett-Packard laboratories in 2008. Various mem-systems have been reported in different fields, ranging from physics and biological models to engineering. In particular, mem-systems find potential applications in switching devices, bioinspired electronics, neural networks, memory elements, and so forth.

In the last few years, we have witnessed the rapid developments in investigating mem-systems such as theoretical models, complexity, chaos, fundamental fingerprints, numerical simulations, nonlinear properties, fabrication aspects, and experimentations. However, there are still different questions, which invite more discoveries in such systems. The special issue aims at presenting and discussing advanced topics of mem-systems with complex dynamic behavior. We had received a total of 38 submissions. After the review process, this special issue contains 17 articles, the contents of which are summarized as follows.

In the article “Fully Integrated Memristor and Its Application on Scroll-Controllable Hyperchaotic System” by J. Jin and C. Li, a fully integrated memristor emulator using operational amplifiers (OA) and analog multipliers is simulated.

Based on the fully integrated memristor, a scroll-controllable hyperchaotic system is presented. By controlling the nonlinear function with programmable switches, the memristor-based hyperchaotic system achieves scroll numbers controllably. Moreover, the memristor-based hyperchaotic system is fully integrated in one single chip, and it achieves lower supply voltage, lower power dissipation, and smaller chip area. The fully integrated memristor and memristor-based hyperchaotic system are verified with GlobalFoundries’ 0.18 μm CMOS process using Cadence IC Design Tools. The postlayout simulation results demonstrate that the memristor-based fully integrated hyperchaotic system consumes 90.5mW from $\pm 2.5\text{V}$ supply voltage, and it takes a compact chip area of 1.8mm².

In the article “A New Memristor-Based 5D Chaotic System and Circuit Implementation” by R. Wang et al., a 5D chaotic system with the flux-controlled memristor is proposed. The dynamics analysis of the new system can also demonstrate the hyperchaotic characteristics. The design and analysis of adaptive synchronization for the new memristor-based chaotic system and its slave system are carried out. Furthermore, the modularized circuit designs method is used in the new chaotic system circuit implementation. The Multisim simulation and the physical experiments are

conducted and compare and match with each other which can demonstrate the existence of the attractor for the new system.

In the article “A Novel Memductor-Based Chaotic System and its Applications in Circuit Design and Experimental Validation” by L. Xiong et al., a novel memductor-based chaotic system is introduced. The local dynamical entities, such as the basic dynamical behavior, the divergence, the stability of equilibrium set, and the Lyapunov exponent, are all investigated analytically and numerically to reveal the dynamic characteristics of the new memductor-based chaotic system as the system parameters and the initial state of memristor change. Subsequently, an active control method is derived to study the synchronous stability of the novel memductor-based chaotic system through making the synchronization error system asymptotically stable at the origin. Further to these, a memductor-based chaotic circuit is designed, realized, and applied to construct a new memductor-based secure communication circuit by employing the basic electronic components and memristor. Furthermore, the design principle of the memductor-based chaotic circuit is thoroughly analyzed and the concept of “the memductor-based chaotic circuit defect quantification index” is proposed for the first time to verify whether the chaotic output is consistent with the mathematical model. A good qualitative agreement is shown between the simulations and the experimental validation results.

In the article “New Results on Fuzzy Synchronization for a Kind of Disturbed Memristive Chaotic System” by B. Wang and L. L. Chen, the problem on the fuzzy synchronization for a kind of disturbed memristive chaotic system is studied. First, based on fuzzy theory, the fuzzy model for a memristive chaotic system is presented; next, based on H-infinity technique, a multidimensional fuzzy controller and a single-dimensional fuzzy controller are designed to realize the synchronization of master-slave chaotic systems with disturbances. Finally, some typical examples are included to illuminate the correctness of the given control method.

In the article “Exact Analysis and Physical Realization of the 6-Lobe Chua Corsage Memristor” by Z. I. Mannan et al., a novel generic memristor, dubbed the 6-lobe Chua corsage memristor, is proposed with its nonlinear dynamical analysis and physical realization. The proposed corsage memristor contains four asymptotically stable equilibrium points on its complex and diversified dynamic routes which reveals a 4-state nonlinear memory device. The higher degree of versatility of its dynamic routes reveals that the proposed memristor has a variety of dynamic paths in response to different initial conditions and exhibits a highly nonlinear contiguous DC V - I curve. The DC V - I curve of the proposed memristor is endowed with an explicit analytical parametric representation. Moreover, the derived three formulas, exponential trajectories of state $x_n(t)$, time period t_{fn} , and minimum pulse amplitude V_A , are required to analyze the movement of the state trajectories on the piecewise linear (PWL) dynamic route map (DRM) of the corsage memristor. These formulas are universal, that is, applicable to any PWL DRM curves for any DC or pulse input and with any number of segments. Nonlinear dynamics and circuit and system

theoretic approach are employed to explain the asymptotic quad-stable behavior of the proposed corsage memristor and to design a novel real memristor emulator using off-the-shelf circuit components.

In the article “On Designing Feedback Controllers for Master-Slave Synchronization of Memristor-Based Chua’s Circuits” by K. Ding, designing feedback controllers for master-slave synchronization of two chaotic memristor-based Chua’s circuits is investigated. The memductance function of memristor-based Chua’s circuits is a bounded function with a bounded derivative which is more generalized than those piecewise constant-valued functions or quadratic functions in some existing papers. The main contributions are that one master-slave synchronization criterion is established for two chaotic memristor-based Chua’s circuits, and the feedback controller gain is easily obtained by solving a set of linear matrix inequalities. One numerical example is given to illustrate the effectiveness of the design method.

In the article “Family of Bistable Attractors Contained in an Unstable Dissipative Switching System Associated to a SNLF” by J. L. Echenausia-Monroy et al., a multiscroll generator system is presented, which addresses the issue by the implementation of 9-level saturated nonlinear function, SNLF, being modified with a new control parameter that acts as a bifurcation parameter. By means of the modification of the newly introduced parameter, it is possible to control the number of scrolls to generate. The proposed system has richer dynamics than the original, not only presenting the generation of a global attractor; it is capable of generating monostable and bistable multiscrolls. The study of the basin of attraction for the natural attractor generation (9-scroll SNLF) shows the restrictions in the initial conditions space where the system is capable of presenting dynamical responses, limiting its possible electronic implementations.

In the article “Dynamical Behavior of a 3D Jerk System with a Generalized Memristive Device” by W. Feng et al., a 3D jerk system is proposed by introducing a generalized memristive device. It is found that the dynamical behavior of the system is sensitive to the initial conditions even the system parameters are fixed, which results in the coexistence of multiple attractors. And there exists different transition behavior depending on the selection of the parameters and initial values. Thereby, it is one important type of the candidate system for secure communication since the reconstruction of accurate state space becomes more difficult. Moreover, authors build a hardware circuit and the experimental results effectively confirm the theoretical analyses.

In the article “Chaos and Symbol Complexity in a Conformable Fractional-Order Memcapacitor System” by S. He et al., numerical solution of a conformable fractional nonlinear system is obtained based on the conformable differential transform method. Dynamics of a conformable fractional memcapacitor (CFM) system is analyzed by means of bifurcation diagram and Lyapunov characteristic exponents (LCEs). Rich dynamics is found, and coexisting attractors and transient state are observed. Symbol complexity of the CFM system is estimated by employing the symbolic entropy (SybEn) algorithm, symbolic spectral entropy (SybSEn) algorithm, and symbolic C_0 (Syb C_0) algorithm. It shows

that pseudorandom sequences generated by the system have high complexity and pass the rigorous NIST test. Results demonstrate that the conformable memcapacitor nonlinear system can also be a good model for real applications.

In the article “An Integer-Order Memristive System with Two- to Four-Scroll Chaotic Attractors and Its Fractional-Order Version with a Coexisting Chaotic Attractor” by P. Zhou and M. Ke, based on a linear passive capacitor C , a linear passive inductor L , an active-charge-controlled memristor, and a fourth-degree polynomial function determined by charge, an integer-order memristive system is suggested. The proposed integer-order memristive system can generate two-scroll, three-scroll, and four-scroll chaotic attractors. The complex dynamics behaviors are investigated numerically. The Lyapunov exponent spectrum with respect to linear passive inductor L and the two-scroll, three-scroll, and four-scroll chaotic attractors are yielded by numerical calculation. Second, based on the integer-order memristive chaotic system with a four-scroll attractor, a fractional-order version memristive system is suggested. The complex dynamics behaviors of its fractional-order version are studied numerically. The largest Lyapunov exponent spectrum with respect to fractional-order p is yielded. The coexisting two kinds of three-scroll chaotic attractors and the coexisting three-scroll and four-scroll chaotic attractors can be found in its fractional-order version.

In the article “Dynamic Behaviors in Coupled Neuron System with the Excitatory and Inhibitory Autapse under Electromagnetic Induction” by Y. Xu et al., numerical simulation method is adopted with the aim of investigating the synchronous behavior in the neuronal system that is coupled by chemical and electrical synapses under electromagnetic induction. Within the improved model, the effects of electromagnetic induction on neurons are described with additive memristive current on the membrane variable, and the memristive current is dependent on the variation of magnetic flow. The simulation results show that the two coupling modes play an important role in the synchronization of the system. By increasing the chemical synaptic feedback gain, authors observe a transition from mixed oscillatory to periodic state at a critical value. In addition, two Hopf bifurcation points are found with the change of the external stimuli, and the state of neuron discharge is influenced by initial values. Furthermore, there is a domain of coupling strength and feedback gain values, in which the two-coupled neuron system is synchronized and longer time lag is not conducive to the system synchronization.

In the article “Evidence of Exponential Speed-Up in the Solution of Hard Optimization Problems” by F. L. Traversa et al., a noncombinatorial approach is applied to hard optimization problems that achieves an exponential speed-up and finds better approximations than the current state of the art. First, authors map the optimization problem into a Boolean circuit made of specially designed, self-organizing logic gates, which can be built with (nonquantum) electronic elements with memory. The equilibrium points of the circuit represent the approximation to the problem at hand. Then, authors solve its associated nonlinear ordinary differential equations numerically, towards the equilibrium

points. Authors demonstrate this exponential gain by comparing a sequential MATLAB implementation of authors' solver with the winners of the 2016 Max-SAT competition on a variety of hard optimization instances. Authors show empirical evidence that authors' solver scales linearly with the size of the problem, both in time and in memory, and argue that this property derives from the collective behavior of the simulated physical circuit. Authors' approach can be applied to other types of optimization problems, and the results presented here have far-reaching consequences in many fields.

In the article “Analysis and Implementation of a New Switching Memristor Scroll Hyperchaotic System and Application in Secure Communication” by P. Liu et al., a novel switching scroll hyperchaotic system based on a memristor device is proposed and applied to secure communication. The new system could be switched between the double-scroll chaotic system and the multiscroll one by switch $S1$ and switch $S2$. Authors gave the construction process of the novel system, its numerical simulations, and dynamical properties, firstly. Moreover, the memristive circuit implementation of the new switching system was presented and the results were also in agreement with those of numerical simulation. Finally, the new switching memristive system was applied to secure communication by means of the drive-response synchronization with chaotic masking. When the voice signal is a rising waveform, it is encrypted by the double-scroll memristive system. When the voice signal is a falling waveform, the multiscroll memristive system works. The voice signal is completely submerged in the chaotic signal and could not be distinguished at all. Security analyses show that it is a successful application to secure communication.

In the article “Investigation of Cortical Signal Propagation and the Resulting Spatiotemporal Patterns in Memristor-Based Neuronal Network” by K. Ding et al., it is shown that memristive neuronal network can represent plasticity phenomena observed in biological cortical synapses. A network of neuronal units as a two-dimensional excitable tissue is designed with 3-neuron Hopfield neuronal model for the local dynamics of each unit. The results show that the lattice supports spatiotemporal pattern formation without supervision. It is found that memristor-type coupling is more noticeable against resistor-type coupling, while determining the excitable tissue switch over different complex behaviors. The stability of the resulting spatiotemporal patterns against noise is studied as well. Finally, the bifurcation analysis is carried out for variation of memristor effect. Authors' study reveals that the spatiotemporal electrical activity of the tissue concurs with the bifurcation analysis. It is shown that the memristor coupling intensities, by which the system undergoes periodic behavior, prevent the tissue from holding wave propagation. Besides, the chaotic behavior in bifurcation diagram corresponds to turbulent spatiotemporal behavior of the tissue. Moreover, authors found that the excitable media are very sensitive to noise impact when the neurons are set close to their bifurcation point, so that the respective spatiotemporal pattern is not stable.

In the article “Fractional-Order Memristor Emulator Circuits” by C. Sánchez-López et al., the synthesis of

fractional-order memristor (FOM) emulator circuits is studied. To do so, a novel fractional-order integrator (FOI) topology based on current-feedback operational amplifier and integer-order capacitors is proposed. Then, the FOI is substituting the integer-order integrator inside flux- or charge-controlled memristor emulator circuits previously reported in the literature and in both versions: floating and grounded. This demonstrates that FOM emulator circuits can also be configured at incremental or decremental mode and the main fingerprints of an integer-order memristor are also holding up for FOMs. Theoretical results are validated through HSPICE simulations and the synthesized FOM emulator circuits can easily be reproducible. Moreover, the FOM emulator circuits can be used for improving future applications such as cellular neural networks, modulators, sensors, chaotic systems, relaxation oscillators, nonvolatile memory devices, and programmable analog circuits.

In the article “Memristor-Based Canonical Chua’s Circuit: Extreme Multistability in Voltage-Current Domain and Its Controllability in Flux-Charge Domain” by H. Bao et al., authors investigate extreme multistability and its controllability for an ideal voltage-controlled memristor emulator-based canonical Chua’s circuit. With the voltage-current model, the initial condition-dependent extreme multistability is explored through analyzing the stability distribution of line equilibrium point and then the coexisting infinitely many attractors are numerically uncovered in such a memristive circuit by the attraction basin and phase portraits. Furthermore, based on the accurate constitutive relation of the memristor emulator, a set of incremental flux-charge describing equations for the memristor-based canonical Chua’s circuit is formulated and a dimensionality reduction model is thus established. As a result, the initial condition-dependent dynamics in the voltage-current domain is converted into the system parameter-associated dynamics in the flux-charge domain, which is confirmed by numerical simulations and circuit simulations. Therefore, a controllable strategy for extreme multistability can be expediently implemented, which is greatly significant for seeking chaos-based engineering applications of multistable memristive circuits.

In the article “Three-Dimensional Memristive Hindmarsh–Rose Neuron Model with Hidden Coexisting Asymmetric Behaviors” by B. Bao et al., a novel three-dimensional memristive Hindmarsh–Rose (HR) neuron model is presented to describe complex dynamics of neuronal activities with electromagnetic induction. The proposed memristive HR neuron model has no equilibrium point but can show hidden dynamical behaviors of coexisting asymmetric attractors, which has not been reported in the previous references for the HR neuron model. Mathematical model based numerical simulations for hidden coexisting asymmetric attractors are performed by bifurcation analyses, phase portraits, attraction basins, and dynamical maps, which just demonstrate the occurrence of complex dynamical behaviors of electrical activities in neuron with electromagnetic induction. Additionally, circuit breadboard based experimental results well confirm the numerical simulations.

Conflicts of Interest

The authors declare that there is no conflict of interest regarding the publication of this article.


Acknowledgments

The editorial team would like to express appreciation to all authors for their valuable contributions and to all reviewers for their valuable comments. In addition, the editors would like to thank the Complexity journal’s Editorial Board for their valuable help and support regarding this special issue.

*Viet-Thanh Pham
Sundarapandian Vaidyanathan
Esterban Tlelo-Cuautle
Tomasz Kapitaniak*

Research Article

Fully Integrated Memristor and Its Application on the Scroll-Controllable Hyperchaotic System

Jie Jin ^{1,2} and Li Cui¹

¹*School of Information and Electrical Engineering, Hunan University of Science and Technology, Xiangtan 411201, China*

²*College of Information Science and Engineering, Jishou University, Jishou 416000, China*

Correspondence should be addressed to Jie Jin; jj67123@sina.com

Received 5 June 2018; Revised 13 September 2018; Accepted 30 September 2018; Published 10 January 2019

Guest Editor: Viet-Thanh Pham

Copyright © 2019 Jie Jin and Li Cui. This is an open access article distributed under the Creative Commons Attribution License, which permits unrestricted use, distribution, and reproduction in any medium, provided the original work is properly cited.

In this paper, a fully integrated memristor emulator using operational amplifiers (OAs) and analog multipliers is simulated. Based on the fully integrated memristor, a scroll-controllable hyperchaotic system is presented. By controlling the nonlinear function with programmable switches, the memristor-based hyperchaotic system achieves controllable scroll numbers. Moreover, the memristor-based hyperchaotic system is fully integrated in one single chip, and it achieves lower supply voltage, lower power dissipation, and smaller chip area. The fully integrated memristor and memristor-based hyperchaotic system are verified with the GlobalFoundries' 0.18 μm CMOS process using Cadence IC Design Tools. The postlayout simulation results demonstrate that the memristor-based fully integrated hyperchaotic system consumes 90.5 mW from ± 2.5 V supply voltage and it takes a compact chip area of 1.8 mm².

1. Introduction

Memristor and multiscroll chaos systems are two research hotspots in recent years. Although, memristor is not commercially available, many memristive emulators have been reported [1–5]. Based on these memristive emulators, various kinds of memristor-based chaotic circuits have been presented [6–12] and they effectively promote the development of the memristive circuit theories.

Most of the existing memristive emulators and memristor-based chaotic circuits are realized using commercially available off-the-shelf discrete components with breadboard or field programmable gate array (FPGA). The breadboard or FPGA-based chaotic circuits are difficult to achieve low-voltage and low-power conditions. As we all know, the fully integrated circuits have the advantages of lower supply voltage, less power consumption, more stable and convenient than their breadboard-based counterparts. Cruz and Chua [13, 14] realized fully integrated Chua's circuit and nonlinear resistor in 1992 and 1993. Elwakil et al. [15] realized another integrated chaotic system in 2002, which further verified the advantages of the integrated chaotic circuits. However,

the existing integrated chaotic circuits are very simple; they could not realize more complicated chaos.

In order to realize more practical and complicated integrated memristor-based chaotic circuits, a fully integrated memristor emulator and a scroll-controllable hyperchaotic system are presented and verified in this paper. The Cadence IC Design Tools post-layout simulation results verify that the presented fully integrated memristor and memristor-based scroll-controllable hyperchaotic system are all feasible and achievable and the fully integrated method will further promote the practical applications of chaotic circuits and systems.

2. Fully Integrated Scroll-Controllable Hyperchaotic System and Its Dynamics Analysis

2.1. Implementation of the Operational Amplifier. In a fully integrated chaotic system, complex and high-performance OA is not necessary, and the designed low-voltage and low-power two-stage OA with simple structure for the fully

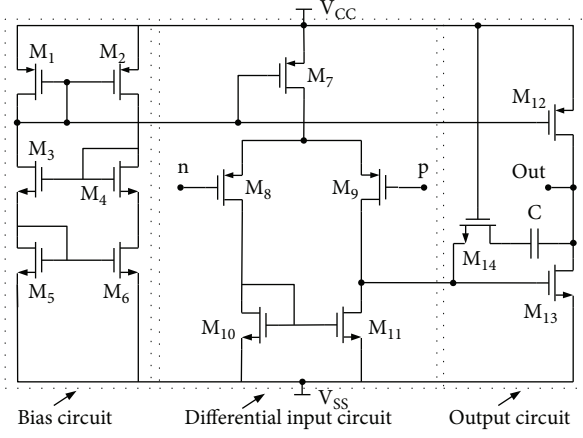


FIGURE 1: The designed OA.

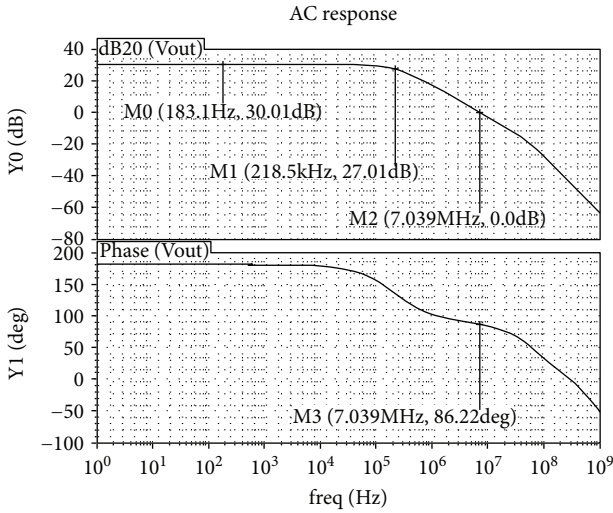


FIGURE 2: The amplitude and phase frequency of the OA.

integrated chaotic system is presented in Figure 1 [16]. The supply voltage of the designed operation amplifier is $V_{CC} = -V_{SS} = 2.5$ V. The P-channel transistors M_7 – M_9 [17] and N-channel transistors M_{10} – M_{11} consist of a double-ended input single-ended output differential input stage; M_{12} and M_{13} consist of the second common source amplifier stage; M_{14} and capacitor C consist of the frequency compensation network between the two stages; the transistors M_1 – M_6 consist of the bias circuit of the OA.

The simulated amplitude and phase-frequency characteristics of the operation amplifier are presented in Figure 2. From the marks M_0 – M_3 , it is clear that the voltage gain of the operation amplifier is about 30 dB, its 3 dB bandwidth is 218.5 kHz, and the phase margin is about 86.22°. Its static power consumption is about 5.85 mW with ± 2.5 V supply voltage.

2.2. Implementation of the Analog Multiplier. The analog multiplier used in the memristor is presented in Figure 3. The classic Gilbert structure [18–20] is adopted. M_4 and M_5 consist of the transconductance stage; M_6 – M_9 consist of

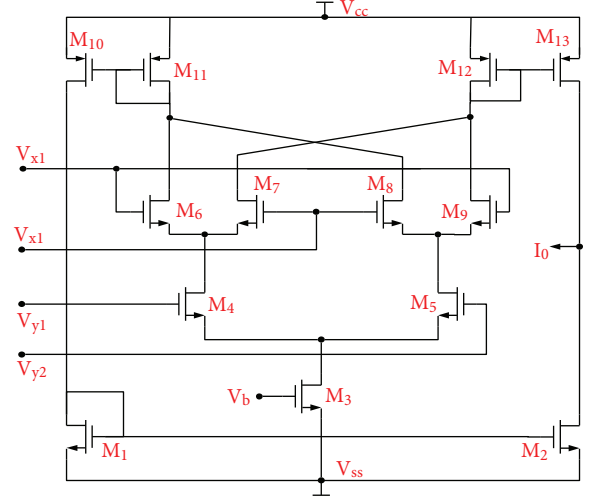


FIGURE 3: The designed analog multiplier.

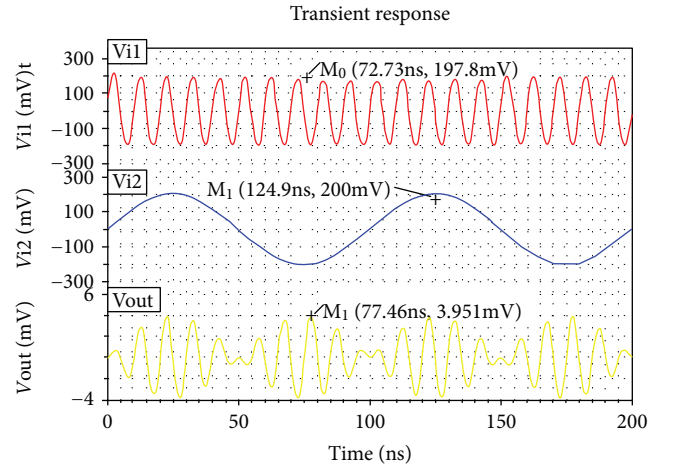


FIGURE 4: The transient response of the analog multiplier.

the Gilbert switch stage, and M_{10} – M_{13} consist of the load stage of the analog multiplier. The supply voltage of the designed analog multiplier is $V_{CC} = -V_{SS} = 2.5$ V.

The transient responses of the designed analog multiplier are presented in Figure 4. V_{i1} and V_{i2} are the two input voltages; their input powers are all -10 dBm, and their frequencies are 100 MHz and 10 MHz, respectively. V_{out} is the output voltage of the analog multiplier. From the above simulation results, it is clear that V_{i1} is the high-frequency carrier, V_{i2} is the low-frequency input signal, and the multiplication is realized in the output voltage V_{out} .

2.3. The Fully Integrated Memristor. Memristors could be classified as flux-dependent and charge-dependent memristors. A fully integrated flux-controlled memristor is adopted in this work, and its circuit realization using operation amplifier and multipliers is presented in Figure 5.

The voltage and current relation of the flux-controlled memristor could be expressed as

$$i = W(\varphi)v, \quad \dot{\varphi} = v, \quad (1)$$

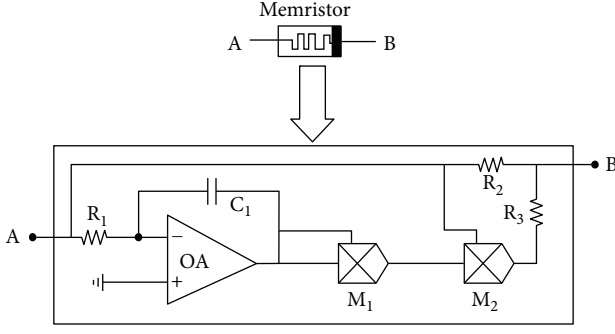


FIGURE 5: The fully integrated memristor.

where $W(\varphi)$ is an incremental memductance function [21]. In order to research the characteristics and application of memristor, various mathematical models and emulator circuits of memristor have been reported in recent years [1–3, 22]. According to [6, 23], a quadric nonlinearity is used to indicate memductance function:

$$W(\varphi) = a + 3b\varphi^2, \quad (2)$$

where a and b are two positive constants.

Figure 6 shows the Cadence simulation results of the frequency-dependent pinched hysteresis loop of the memristor in Figure 5 operating at various frequencies. The circuit elements used in the memristor are $R_1 = 250 \text{ k}\Omega$, $R_2 = 500 \text{ k}\Omega$, $R_3 = 40 \text{ k}\Omega$, $C_1 = 220 \text{ pF}$, and the supply voltages of the OA and multiplier are all $\pm 2.5 \text{ V}$.

Figure 6(a) is the simulation result while the frequency of the input voltage equals to 100 kHz, and a clear pinched hysteresis loop is obtained. Figure 6(b) is the simulation result while the frequency of the input voltage equals to 1 MHz; the edges of the pinched hysteresis loop become a bit blurry, and the center of the pinched hysteresis loop becomes narrow. Figure 6(c) is the simulation result while the frequency of the input voltage equals to 5 MHz; the edges of the pinched hysteresis loop become more blurred, and the center of the pinched hysteresis loop becomes more narrow. From the simulation results in Figure 6, it is clear that the fully integrated memristor could operate properly from 1 kHz to 1 MHz. Compared with the memristor using off-the-shelf discrete components with breadboard [24–28], the fully integrated memristor could be used in higher frequency applications.

2.4. The Programmable Staircase Function Circuit. The proposed fully integrated programmable staircase function circuit is presented in Figure 7, and it is realized using the designed OA in Figure 2. The circuit elements used in the memristor are $R_1 = R_4 = R_7 = 1 \text{ k}\Omega$, $R_2 = R_5 = R_8 = 350 \text{ k}\Omega$, $R_3 = R_6 = R_9 = 19.8 \text{ k}\Omega$, $R_{10} = 2.20 \text{ k}\Omega$, and $R_{11} = R_{12} = 10 \text{ k}\Omega$. The programmable MOS switches used in the proposed programmable staircase function circuit is presented in Figure 8. The programmable MOS switch consists of a NMOS and a PMOS transistor, and it can be turned on and off by controlling the bias voltages V_{s+} and V_{s-} [29, 30].

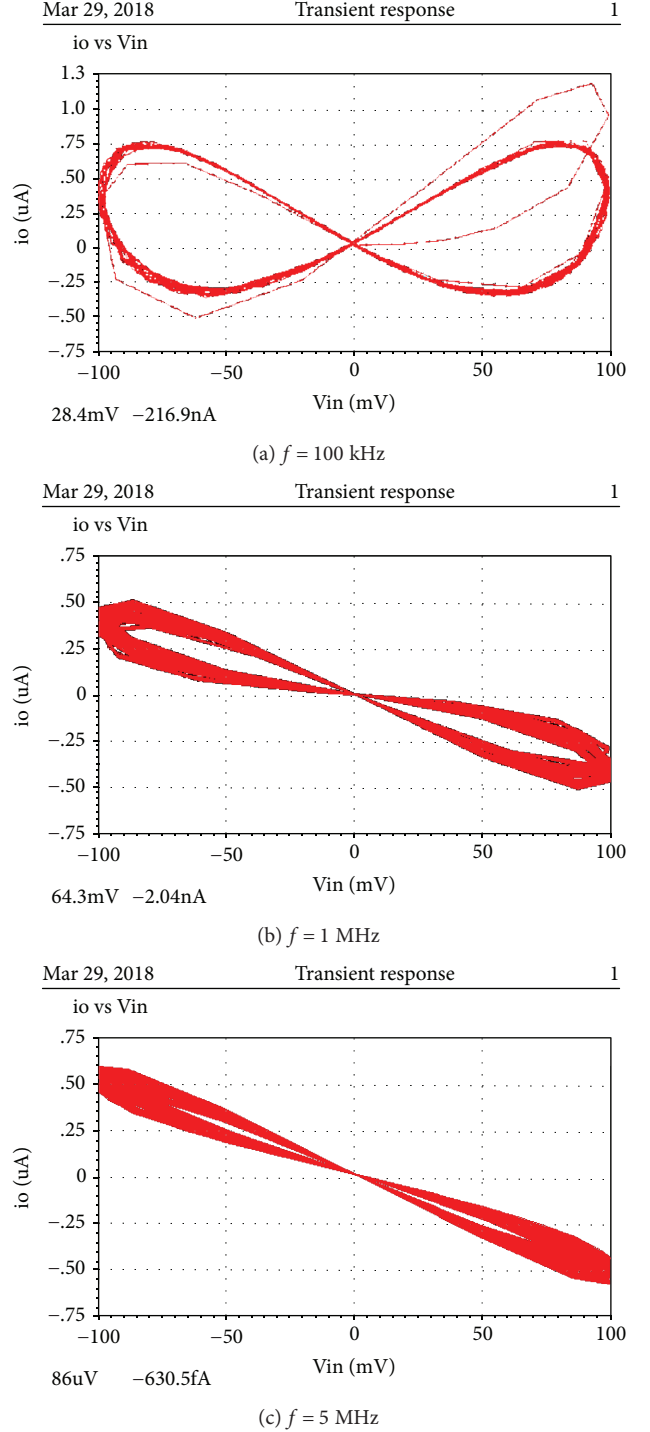


FIGURE 6: Cadence simulation results of the frequency-dependent pinched hysteresis loop operating at (a) 100 kHz, (b) 1 MHz, and (c) 5 MHz.

By controlling the switches S_1 , S_2 , and S_3 in Figure 7, the numbers of stairs could be changed. When the switches S_1 and S_3 are turned off, a stair is obtained (Figure 9(a) $N = 1$). When the switch S_2 is turned off, S_1 and S_3 are turned on and two stairs are obtained (Figure 9(b) $N = 2$). When the switches S_1 , S_2 , and S_3 are all turned on, three stairs are

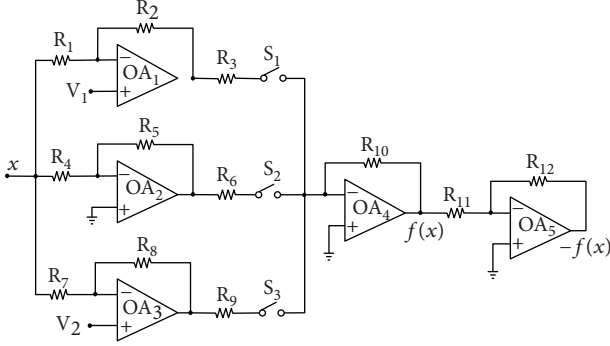


FIGURE 7: The programmable staircase function circuit.

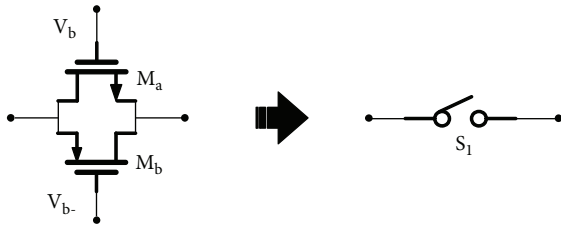


FIGURE 8: The digitally programmable MOS switch.

obtained (Figure 9(c) $N = 3$). As an example, when the switch S_2 is turned off, S_1 and S_3 are turned on; the simulated staircase function circuit with $N = 2$ is presented in Figure 9(d).

2.5. The Proposed Fully Integrated Scroll-Controllable Hyperchaotic System and Its Dynamics Analysis. The proposed fully integrated scroll-controllable hyperchaotic system is presented in Figure 10. It consists of a classic Jerk system [31–35] and a flux-controlled memristor in Figure 5. There are three integrators (OA_1 , OA_2 , and OA_4) and two reverse proportional operators (OA_3 and OA_5) in the fully integrated scroll-controllable hyperchaotic circuit. The circuit elements used in the chaotic circuit are $R_1 = R_2 = R = 4.9 \text{ k}\Omega$, $R_5 = R_6 = R_7 = R_8 = R_k = 9.45 \text{ k}\Omega$, $R_3 = R_4 = R_9 = R_{10} = 10 \text{ k}\Omega$, and $C_1 = C_2 = C_3 = C = 35 \text{ pF}$.

From Figure 10, the following expression could be obtained:

$$\begin{cases} \dot{x} = \frac{y}{RC}, \\ \dot{y} = \frac{z}{RC} - \frac{W(\varphi)z}{C}, \\ \dot{z} = -\frac{x}{R_k C} - \frac{y}{R_k C} - \frac{z}{R_k C} + \frac{f(x)}{R_k C}, \\ \dot{\varphi} = z, \end{cases} \quad (3)$$

where $W(\varphi)$ is the memductance of the memristor and $f(x)$ is the output of the staircase function circuit in Figure 5. The stairs of $f(x)$ can be changed by the programmable switches, and the scrolls of the chaotic system are controllable.

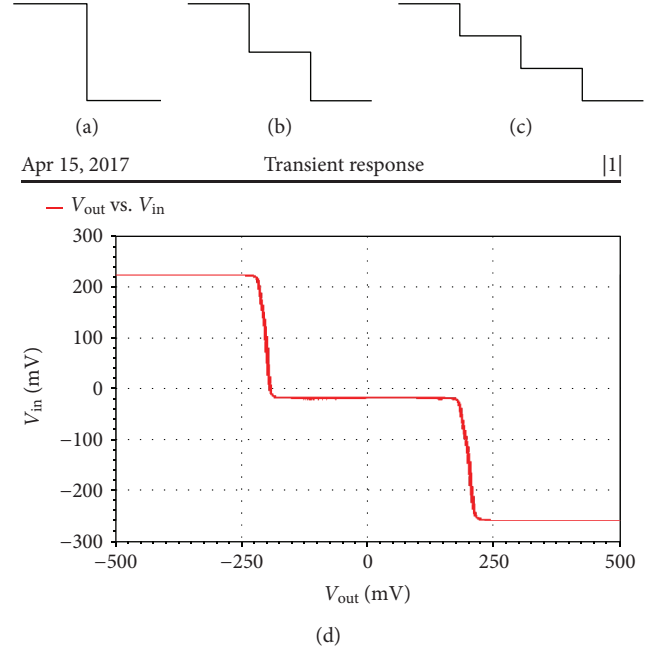
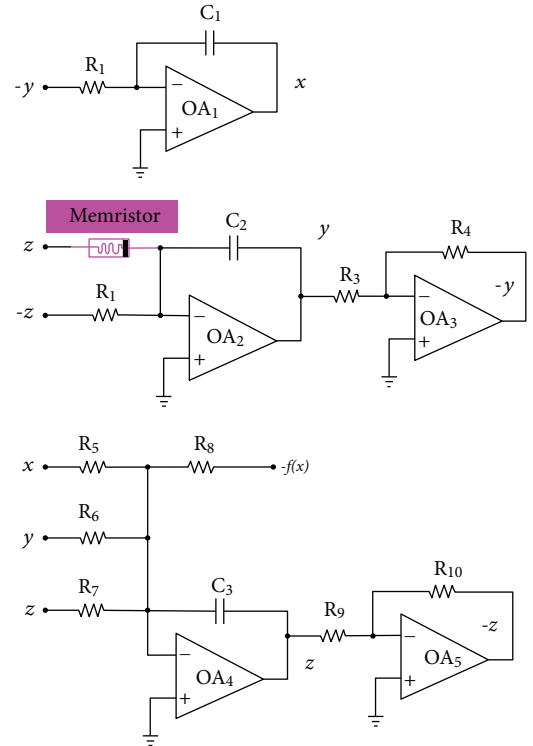
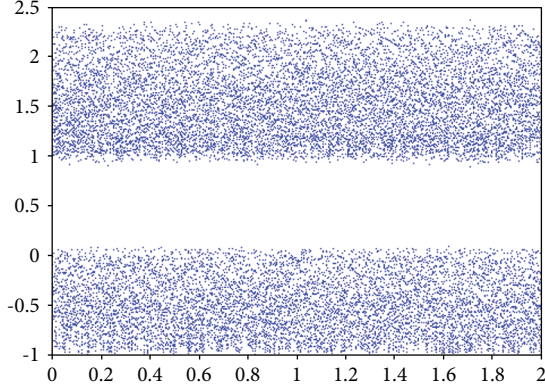
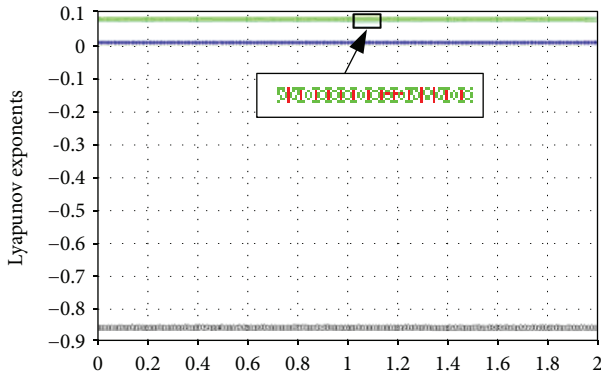
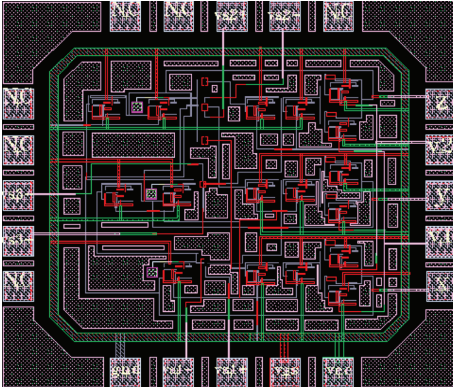
FIGURE 9: The staircase function: (a) $N = 1$, (b) $N = 2$, and (c) $N = 3$. (d) Simulated staircase function circuit with $N = 2$.

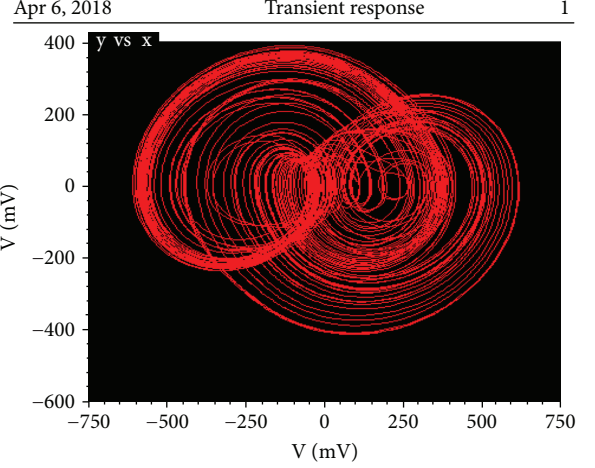
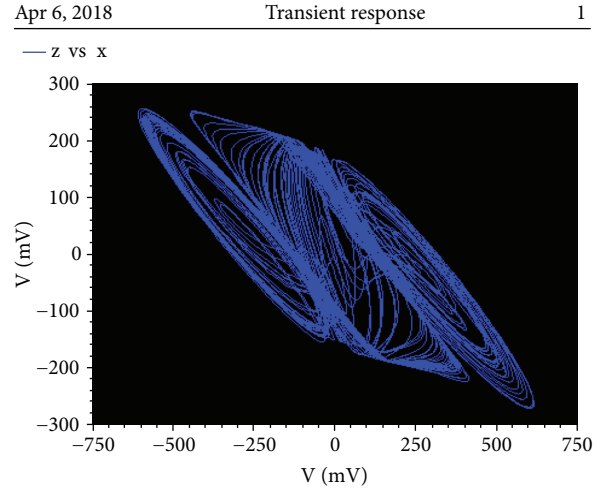
FIGURE 10: Proposed scroll-controllable hyperchaotic circuit.

In order to explore the nonlinear dynamics of the fully integrated hyperchaotic system, the Lyapunov exponents and bifurcation diagrams are investigated using the MATLAB simulation results.

FIGURE 11: Bifurcation diagram by adjusting α from 0 to 2.FIGURE 12: Lyapunov exponents by adjusting α from 0 to 2.FIGURE 13: Chip layout diagram of the chaotic circuit (1.8 mm²).

The dimensionless equations of the chaotic system could be expressed as

$$\begin{cases} \dot{x} = y, \\ \dot{y} = z - \alpha W(\varphi)z, \\ \dot{z} = -\beta(x + y + z) + f(x), \\ \dot{\varphi} = z, \end{cases} \quad (4)$$

FIGURE 14: The phase portrait in the x - y plane (S_2 is turned on, S_1 and S_3 are turned off).FIGURE 15: The phase portrait in the x - z plane (S_2 is turned on, S_1 and S_3 are turned off).

where $W(\varphi) = a + 3b\varphi^2$ and α and β are two positive parameters.

Let $\beta = 0.72$, the bifurcation diagram is presented in Figure 11. From Figure 11, it is clear that the system is chaotic, when α is changing from 0 to 2. The Lyapunov exponents of the system by adjusting α from 0 to 2 are presented in Figure 12. From Figure 12, it is clear that there are two Lyapunov exponents more than zero in the system and the proposed system is a hyperchaotic system. Considering Figures 11 and 12, both of the Lyapunov exponents and the bifurcation diagram indicate that the proposed system is chaotic and it could generate complex dynamic behaviors.

3. Postlayout Simulation Results of the Fully Integrated Scroll-Controllable Hyperchaotic Circuit

The proposed fully integrated scroll-controllable hyperchaotic system is verified using the Cadence IC Design Tools

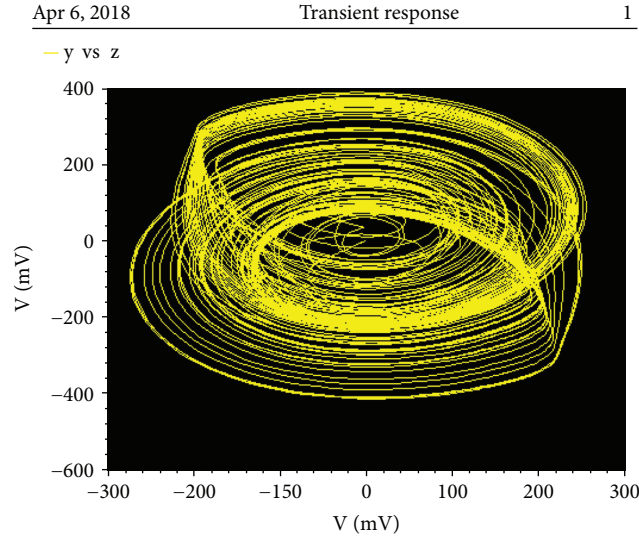


FIGURE 16: The phase portrait in the y - z plane (S_2 is turned on, S_1 and S_3 are turned off).

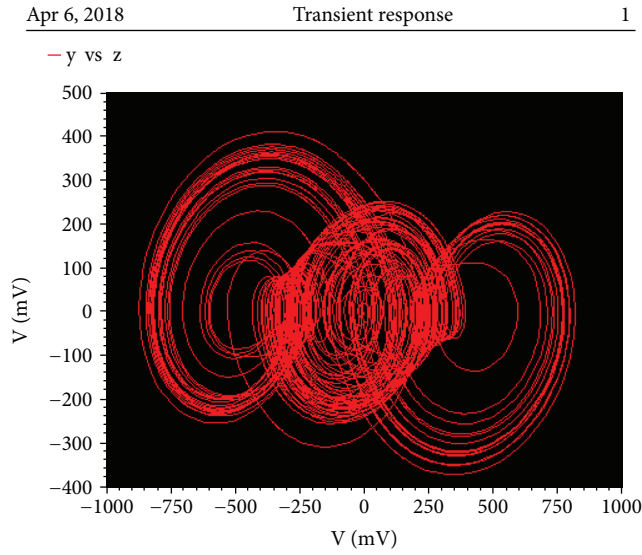


FIGURE 17: The phase portrait in the x - y plane (S_1 and S_3 are turned on, S_2 is turned off).

5.1.41 Spectre simulator with GlobalFoundries' $0.18\mu\text{m}$ CMOS technology. The supply voltage of the OAs and multipliers is all $\pm 2.5\text{ V}$, and the power consumption of the whole chaotic system is about 90.5 mW . According to the standard GlobalFoundries' $0.18\mu\text{m}$ CMOS process, there are two problems that should be considered in the full integration of chaotic circuits. First, the capacitors and inductors should not exceed 1 nF and 1 mH , because large capacitors and inductors cannot be realized in the standard integration process. Second, it is difficult to realize complex chaotic systems, because the supply voltages are very low in integrated circuits (less than 5 V).

The chip layout diagram of the chaotic oscillator is presented in Figure 13, and it takes a compact chip area of

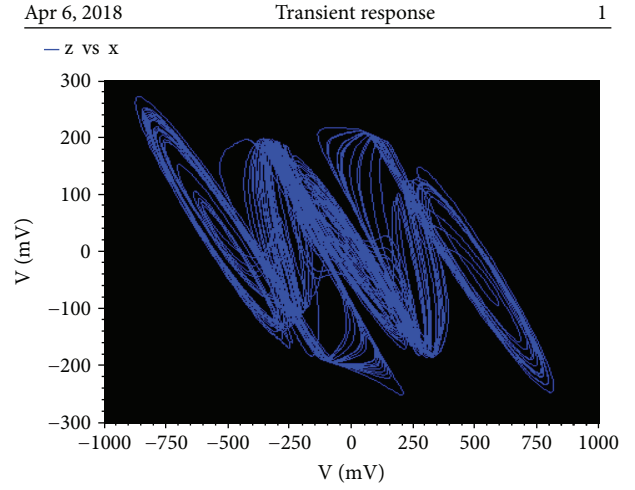


FIGURE 18: The phase portrait in the x - z plane (S_1 and S_3 are turned on, S_2 is turned off).

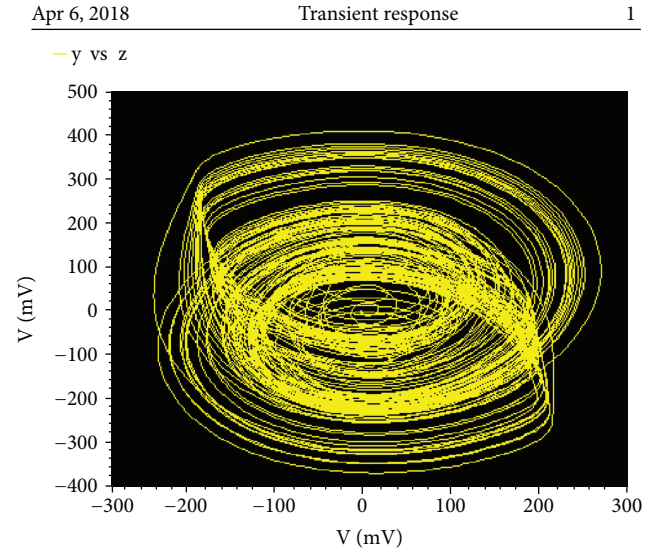


FIGURE 19: The phase portrait in the y - z plane (S_1 and S_3 are turned on, S_2 is turned off).

1.8 mm^2 including the testing pads. The Mentor Calibre software is used for the design rule check (DRC), layout versus schematic (LVS), and parasitic extraction (PEX) of the chaotic system. Based on the chip layout in Figure 13 and considering the parasitics extracted from the chip layout, the postlayout simulation results are presented in Figures 14–22.

When the switch S_2 is turned on, S_1 and S_3 are turned off, a single-stair nonlinear staircase function is added in the chaotic system, and the simulation results are presented in Figures 14–16.

Figures 14–16 are the phase portraits in the x - y , x - z , and y - z planes. Because the nonlinear staircase function is added in the x axis, there are two scrolls in the x - y and x - z planes and one scroll in the y - z plane.

When the switches S_1 and S_3 are turned on, S_2 is turned off and a two-stair nonlinear staircase function is added in

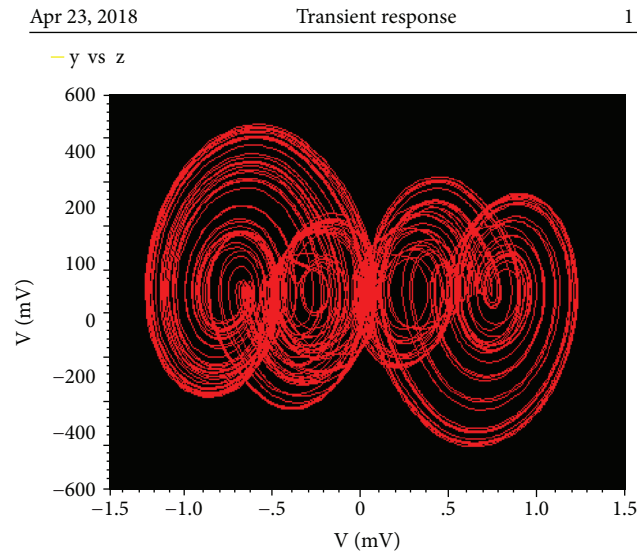


FIGURE 20: The phase portrait in the x - y plane (S_1 , S_2 , and S_3 are all turned on).

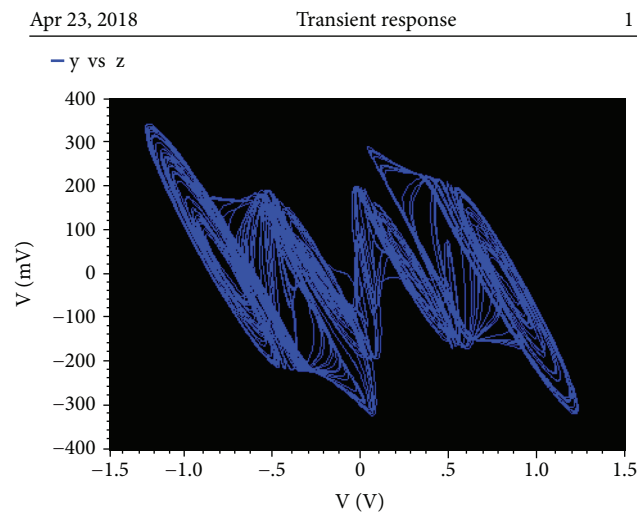


FIGURE 21: The phase portrait in the x - z plane (S_1 , S_2 , and S_3 are all turned on).

the chaotic system, and the simulation results are presented in Figures 17–19.

Figures 17–19 are the phase portraits in the x - y , x - z , and y - z planes. Similarly, the nonlinear staircase function is also added in the x axis, there are three scrolls in the x - y and x - z planes, and one scroll in the y - z plane.

When the switches S_1 , S_2 , and S_3 are all turned on, a three-stair nonlinear staircase function is added in the chaotic system, and the simulation results are presented in Figures 20–22.

Figures 20–22 are the phase portraits in the x - y , x - z , and y - z planes. Similarly, the nonlinear staircase function is also added in the x axis, there are four scrolls in the x - y and x - z planes, and one scroll in the y - z plane.

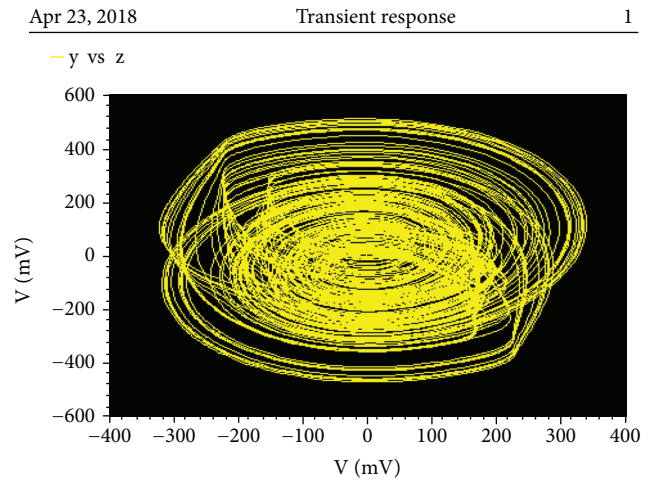


FIGURE 22: The phase portrait in the y - z plane (S_1 , S_2 , and S_3 are all turned on).

Obviously, by using programmable switches in the staircase circuit, it is easy to generate controllable scrolls in the proposed fully integrated scroll-controllable hyperchaotic system.

4. Conclusion

This work proposed a novel fully integrated memristor-based scroll-controllable hyperchaotic system. The chaotic system is verified via bifurcation diagram and Lyapunov exponents. In addition, the new chaotic system is realized using the designed OA and multiplier and simulated using Cadence IC Design Tools with the GlobalFoundries' 0.18 μm CMOS process. It is hoped that the investigation of this work will lead to more effective and systematic studies of fully integrated low-voltage and low-power chaotic circuits and enhance the practical applications of chaotic circuits.

Data Availability

The data used to support the findings of this study are available from the corresponding author upon request.

Conflicts of Interest

The authors declare that there is no conflict of interests regarding the publication of this paper.

Acknowledgments

This work is supported by the National Natural Science Foundation of China (no. 61561022), the Natural Science Foundations of Hunan Province (2017JJ3254), the Education Department of Hunan Province project (nos. 16B212 and 15C0550), and the Doctoral Scientific Research Foundation of Jishou University under Grant jsdxxcfxbskyxm07.

References

- [1] M. Di Ventra, Y. V. Pershin, and L. O. Chua, "Circuit elements with memory: memristors, memcapacitors, and meminductors," *Proceedings of the IEEE*, vol. 97, no. 10, pp. 1717–1724, 2009.
- [2] A. Ascoli, F. Corinto, and R. Tetzlaff, "Generalized boundary condition memristor model," *International Journal of Circuit Theory and Applications*, vol. 44, no. 1, pp. 60–84, 2016.
- [3] F. Corinto and A. Ascoli, "Memristive diode bridge with LCR filter," *Electronics Letters*, vol. 48, no. 14, pp. 824–825, 2012.
- [4] J. Secco, M. Biey, F. Corinto, A. Ascoli, and R. Tetzlaff, "Complex behavior in memristor circuits based on static nonlinear two-ports and dynamic bipole," in *2015 European Conference on Circuit Theory and Design (ECCTD)*, pp. 1–4, Trondheim, Norway, 2015.
- [5] L. Wang, E. Drakakis, S. Duan, P. He, and X. Liao, "Memristor model and its application for chaos generation," *International Journal of Bifurcation and Chaos*, vol. 22, no. 8, article 1250205, 2012.
- [6] V. T. Pham, C. Volos, S. Jafari, and T. Kapitaniak, "A novel cubic-equilibrium chaotic system with coexisting hidden attractors: analysis, and circuit implementation," *Journal of Circuits, Systems and Computers*, vol. 27, no. 4, article 1850066, 2018.
- [7] C. K. Volos, A. Akgul, V. T. Pham, and M. S. Baptista, "Antimonotonicity, crisis and multiple attractors in a simple memristive circuit," *Journal of Circuits, Systems and Computers*, vol. 27, no. 2, article 1850026, 2018.
- [8] V. T. Pham, A. Buscarino, L. Fortuna, and M. Frasca, "Simple memristive time-delay chaotic systems," *International Journal of Bifurcation and Chaos*, vol. 23, no. 4, article 1350073, 2013.
- [9] H. H. C. Iu, D. S. Yu, A. L. Fitch, V. Sreeram, and H. Chen, "Controlling chaos in a memristor based circuit using a twin-T notch filter," *IEEE Transactions on Circuits and Systems I: Regular Papers*, vol. 58, no. 6, pp. 1337–1344, 2011.
- [10] B. C. Bao, W. Hu, J. P. Xu, Z. Liu, and L. Zou, "Analysis and implementation of memristor chaotic circuit," *Acta Physica Sinica*, vol. 60, no. 12, pp. 1775–1785, 2011.
- [11] B. Bao, Z. Ma, J. Xu, Z. Liu, and Q. Xu, "A simple memristor chaotic circuit with complex dynamics," *International Journal of Bifurcation and Chaos*, vol. 21, no. 9, pp. 2629–2645, 2011.
- [12] C. Wang, H. Xia, and L. Zhou, "Implementation of a new memristor-based multiscroll hyperchaotic system," *Pramana*, vol. 88, no. 2, 2017.
- [13] J. M. Cruz and L. O. Chua, "A CMOS IC nonlinear resistor for Chua's circuit," *IEEE Transactions on Circuits and Systems I: Regular Papers*, vol. 39, no. 12, pp. 985–995, 1992.
- [14] J. M. Cruz and L. O. Chua, "An IC chip of Chua's circuit," *IEEE Transactions on Circuits and Systems I: Regular Papers*, vol. 40, no. 10, pp. 614–625, 1993.
- [15] A. S. Elwakil, K. N. Salama, and M. P. Kennedy, "An equation for generating chaos and its monolithic implementation," *International Journal of Bifurcation and Chaos*, vol. 12, no. 12, pp. 2885–2895, 2002.
- [16] J. Jin, "Programmable multi-direction fully integrated chaotic oscillator," *Microelectronics Journal*, vol. 75, pp. 27–34, 2018.
- [17] K. Xu, "Electro-optical modulation processes in Si-PMOSFET LEDs operating in the avalanche light emission mode," *IEEE Transactions on Electron Devices*, vol. 61, no. 6, pp. 2085–2092, 2014.
- [18] J. Jin, C. Wang, J. Sun, and S. Du, "Design and simulation of novel amplifier-based mixer for ISM band wireless applications," *International Journal of Circuit Theory and Applications*, vol. 43, no. 11, pp. 1794–1800, 2015.
- [19] J. Jin, K. Q. Zhou, and L. Zhao, "Designing RF ring oscillator using current-mode technology," *IEEE Access*, vol. 5, no. 99, pp. 5306–5312, 2017.
- [20] J. Jin, "Resonant amplifier-based sub-harmonic mixer for zero-IF transceiver applications," *Integration, the VLSI Journal*, vol. 57, pp. 69–73, 2017.
- [21] L. Chua, "Memristor-the missing circuit element," *IEEE Transactions on Circuit Theory*, vol. 18, no. 5, pp. 507–519, 1971.
- [22] L. Zhou, C. Wang, and L. Zhou, "A novel no-equilibrium hyperchaotic multi-wing system via introducing memristor," *International Journal of Circuit Theory and Applications*, vol. 46, no. 1, pp. 84–98, 2018.
- [23] B. Muthuswamy, "Implementing memristor based chaotic circuits," *International Journal of Bifurcation and Chaos*, vol. 20, no. 5, pp. 1335–1350, 2010.
- [24] C. Sánchez-López and L. E. Aguila-Cuapio, "A 860 kHz grounded memristor emulator circuit," *AEU - International Journal of Electronics and Communications*, vol. 73, no. 3, pp. 23–33, 2017.
- [25] C. Sánchez-López, M. A. Carrasco-Aguilar, and C. Muñiz-Montero, "A 16 Hz–160 kHz memristor emulator circuit," *AEU - International Journal of Electronics and Communications*, vol. 69, no. 9, pp. 1208–1219, 2015.
- [26] B. C. Bao, F. Feng, W. Dong, and S. H. Pan, "The voltage—current relationship and equivalent circuit implementation of parallel flux-controlled memristive circuits," *Chinese Physics B*, vol. 22, no. 6, article 068401, 2013.
- [27] A. Sodhi and G. Gandhi, "Circuit mimicking TiO₂ memristor: a plug and play kit to understand the fourth passive element," *International Journal of Bifurcation and Chaos*, vol. 20, no. 8, pp. 2537–2545, 2010.
- [28] B. C. Bao, J. P. Xu, G. H. Zhou, Z. H. Ma, and L. Zou, "Chaotic memristive circuit: equivalent circuit realization and dynamical analysis," *Chinese Physics B*, vol. 20, no. 12, article 120502, 2011.
- [29] P. E. Allen and D. R. Holberg, *CMOS Analog Circuit Design*, Oxford University Press, 2002.
- [30] J. Jin, C. Wang, J. Sun, Y. Tu, L. Zhao, and Z. Xia, "Novel digitally programmable multiphase voltage controlled oscillator and its stability discussion," *Microelectronics Reliability*, vol. 54, no. 3, pp. 595–600, 2014.
- [31] J. C. Sprott, "Some simple chaotic flows," *Physical Review E*, vol. 50, no. 2, pp. R647–R650, 1994.
- [32] J. C. Sprott, "Simple chaotic systems and circuits," *American Journal of Physics*, vol. 68, no. 8, pp. 758–763, 2000.
- [33] J. C. Sprott, "A new class of chaotic circuit," *Physics Letters A*, vol. 266, no. 1, pp. 19–23, 2000.
- [34] J. Ma, X. Wu, R. Chu, and L. Zhang, "Selection of multi-scroll attractors in Jerk circuits and their verification using Pspice," *Nonlinear Dynamics*, vol. 76, no. 4, pp. 1951–1962, 2014.
- [35] S. M. Yu and M. H. Liu, "Multi-scroll high-order general Jerk circuits," *Acta Physica Sinica*, vol. 55, no. 11, pp. 5707–5713, 2006.

Research Article

A Novel Memductor-Based Chaotic System and Its Applications in Circuit Design and Experimental Validation

Li Xiong^{1,2,3}, Yanjun Lu¹, Yongfang Zhang⁴, and Xinguo Zhang⁵

¹School of Mechanical and Precision Instrument Engineering, Xi'an University of Technology, Xi'an 710048, China

²School of Physics and Electromechanical Engineering, Hexi University, Zhangye 734000, China

³State Key Laboratory of ASIC & System, Fudan University, Shanghai 200433, China

⁴School of Printing, Packaging Engineering and Digital Media Technology, Xi'an University of Technology, Xi'an 710048, China

⁵School of Information Science and Engineering, Lanzhou University, Lanzhou 730000, China

Correspondence should be addressed to Yanjun Lu; yanjunlu@xaut.edu.cn

Received 16 April 2018; Revised 16 July 2018; Accepted 5 August 2018; Published 3 January 2019

Academic Editor: Viet-Thanh Pham

Copyright © 2019 Li Xiong et al. This is an open access article distributed under the Creative Commons Attribution License, which permits unrestricted use, distribution, and reproduction in any medium, provided the original work is properly cited.

This paper is expected to introduce a novel memductor-based chaotic system. The local dynamical entities, such as the basic dynamical behavior, the divergence, the stability of equilibrium set, and the Lyapunov exponent, are all investigated analytically and numerically to reveal the dynamic characteristics of the new memductor-based chaotic system as the system parameters and the initial state of memristor change. Subsequently, an active control method is derived to study the synchronous stability of the novel memductor-based chaotic system through making the synchronization error system asymptotically stable at the origin. Further to these, a memductor-based chaotic circuit is designed, realized, and applied to construct a new memductor-based secure communication circuit by employing the basic electronic components and memristor. Furthermore, the design principle of the memductor-based chaotic circuit is thoroughly analyzed and the concept of “the memductor-based chaotic circuit defect quantification index” is proposed for the first time to verify whether the chaotic output is consistent with the mathematical model. A good qualitative agreement is shown between the simulations and the experimental validation results.

1. Introduction

With the deep study of the chaotic systems and chaotic circuits, the concept of memristor was first put forwarded by Chua in 1971 [1]. Memristor is the fourth circuit component after capacitor, resistor, and inductor were coined, which is actually a nonlinear resistor with natural memory function. Nevertheless, we did not see significant progress on relevant research at that time on account of insufficient attention was paid to the memristor. The immature nanomanufacturing technology and difficult manufacturing of memristor with real materials all contributed to the slow progress on memristor [2]. It was not until 2008 that the HP Laboratories confirmed the existence of memristor and simultaneously a memristor-based real device was coined with its results published in *Nature* [3, 4]. Since then, memristor has become a hot research spot of chaos and it drew much more eyes from researchers engaged in various areas of

science and engineering [5–10]. It is well known that memristor has two models, namely, charge control and chain control. Among them, charge control exports memristor, while chain control exports memductor. If the memristor is a constant, it becomes the same concept as resistor. Correspondingly, the physical meaning of memductor is equivalent to conductance. Because the design of memductor is more convenient than the design of memristor in the design of chaotic circuits, the model of memductor is studied in this paper.

As a tunable nonlinear device with small size and low power consumption, memristor is quite suitable for the applications of high-frequency chaotic circuit, image encryption, and chaotic secure communication. It is no wonder that, in recent years, utilizing memristor to construct chaotic circuits has attracted close attention of quite a number of researchers [11–15]. Among them, Itoh and Chua adopted the memristor with a characteristic curve for the monotone

rise and piecewise linear to replace the diode in Chua's circuit and followed by the chaotic oscillation circuit based on memristor was derived [6]. Similarly, Muthuswamy and Kokate replaced the memristor with piecewise linear model instead of Chua's diode and analyzed the dynamic characteristics of the system after replacement. The results indicated that the chaotic characteristics of the system were more complex than that of the classical Chua's [7]. In 2010, Muthuswamy and Chua proposed the most simple third-order memristor chaotic circuit so far and in [8, 9] showed the experimental results of the corresponding hardware circuit, whose greatest feature was the simple structure. It was connected in series simply by a linear inductor, a linear capacitor, and a nonlinear memristor. In addition, Bao et al. carried on the research on the memristor chaotic circuit and realized a series of new Chua's memristor chaotic circuits by using the smooth model magnetic controlled memristor [10–12]. At present, the proposed memristor chaotic oscillation circuits of different structure and types [13–23] include the chaotic circuits with two memristors [16], integer-order memristor chaotic circuit [18], fractional-order memristor chaotic circuit [19], and memristor-based circuit for neural networks [23], whereas most of the researchers focus on theoretical analysis and numerical simulation for the memristive chaotic system and the experimental validation of the hardware circuit is rarely seen because those memristive chaotic circuits are theoretically established and their feasibility to be implemented by using hardware circuit is still not known. In particular, it is more difficult to design and implement a practical circuit for certain more complicated memductor chaotic systems. Therefore, we construct a novel memductor-based chaotic circuit and implement the experimental validation of the hardware circuit for above reason.

Moreover, in order to meet the security requirements of chaotic secure communication, researchers proposed a method to improve the predictability and complexity of the system by constructing hyperchaotic systems [24–26] and memristor-based chaotic systems, since memristor is a nonlinear component, whose memory ability [27–31] of the current by convection is not available in conventional chaotic circuit elements. In this way, it is especially suitable for the chaotic secure communication field [32–36]. Although the application research of memristor is just the beginning in the field of chaotic secure communication, it has great potentials and advantages in improving the confidentiality and security of chaotic secure communication system. So far, there is no literature to implement the memductor-based chaotic secure communication in chaotic modulation way. In this paper, chaotic modulation is adopted to implement the memductor-based secure communication based on the novel memductor-based chaotic circuit.

The contribution of this paper is that a new method for constructing ordinary chaotic system into memductor-based chaotic system is proposed by using memristor as nonlinear term. Then, we perform a detailed analysis, active control, synchronous stability analysis [37–40], and secure communication of the novel memductor-based chaotic system. The active control is implemented, and the synchronization stability results are determined by using Lyapunov

stability theory. The corresponding physical circuit implementation is also proposed to show the accuracy and efficiency of the memductor-based chaotic circuit. The analog circuit implementation results match with the Multisim and MATLAB simulation results. In addition, the concept of “the memductor-based chaotic circuit defect quantification index” is first proposed to verify whether the chaotic output is consistent with the mathematical model through deep analysis on the design principle of memductor-based chaotic circuit. Our research provides important theoretical and technical basis for the realization of the large-scale integrated circuit with memductor. This paper is expected to serve as a further step to apply memductor into real-world secure communication.

This paper falls into 6 parts. In Section 2, a novel 4D memductor-based chaotic system is constructed. In following Section 3, several qualitative issues about the novel memductor-based chaotic system, such as the basic dynamical behavior, divergence, stability of the equilibrium set, bifurcation, Poincaré map, and synchronous stability, are investigated analytically and numerically. In Section 4, the proposed memductor-based chaotic circuit is implemented in an analog electronic circuit. After that, a new memductor-based chaotic secure communication circuit is proposed based on the novel memductor-based chaotic circuit in Section 5. Finally, some conclusions and discussions are drawn in Section 6.

2. The Construction of a Novel Memductor-Based Chaotic System

2.1. A Specific Memductor Model. Apart from the three basic circuit components, including capacitor, resistor, and inductor, the fourth circuit component is memristor, which derives from the magnetic flux and charge in the circuit. And the resistance value of the memristor varies with the current flowing through the circuit. When the circuit is powered down, the resistance value of the memristor still remains valid before the power is broken. Therefore, memristor is actually a nonlinear resistor with natural memory function.

The memristor is defined as the relation between the magnetic flux and the charge quantity, that is,

$$d\phi = mdq. \quad (1)$$

Memristor can be divided into accumulation charge memristor and magnetic flux-controlled memristor. For a charge-controlled memristor, ϕ is easily obtained by

$$\phi = f(q). \quad (2)$$

For (2), differentiation can be easily obtained as follows:

$$\frac{d\phi}{dt} = \frac{df(q)}{dq} \frac{dq}{dt}. \quad (3)$$

Thus, $v(t)$ can be obtained as follows:

$$v(t) = \frac{df(q)}{dq} i(t). \quad (4)$$

According to Ohm's law, $v(t)$ is obtained as follows:

$$v(t) = m(q)i(t). \quad (5)$$

Thus, a memristance value is obtained as follows:

$$m(q) = \frac{df(q)}{dq}, \quad (6)$$

where $m(q)$ is the memristance, and its unit is Ohm (Ω). If the memristance value is a constant, then it becomes the same concept as resistance. It can also be obtained by a linear relationship between the current and the voltage.

For the magnetic flux-controlled memristor, q is easily obtained by

$$q = f(\phi). \quad (7)$$

From $i = dq/dt$, we can get

$$i(t) = w(\phi)v(t), \quad (8)$$

where $w(\phi)$ is the memductance. In the chaotic circuits, the use of memductor is more extensive. This is because the design of memductor in chaotic circuits is more convenient than memristor design.

Here, a magnetically controlled memristor is defined with a smooth cubic monotonic rise nonlinear characteristic curve. The model is a nonlinear memductor, and the nonlinearity is modeled by using a cubic curve model. The formula is described as follows:

$$q(\phi) = a\phi + b\phi^3. \quad (9)$$

Act on the equation ends of the sign with d/dt , that is,

$$\begin{aligned} \frac{dq(\phi)}{dt} &= \frac{d}{dt}(a\phi + b\phi^3) = \frac{d}{d\phi}(a\phi + b\phi^3) \frac{d\phi}{dt} \\ &= (a + 3b\phi^2) \frac{d\phi}{dt}. \end{aligned} \quad (10)$$

In consideration of $dq = idt$, $d\phi = udt$, and $\phi = \int udt$, we can obtain

$$i = (a + 3b\phi^2)u \quad (11)$$

and

$$i = au + 3bu \left(\int udt \right)^2. \quad (12)$$

Equation (11) is the VAR (volt ampere relation) expression of the memductor. It makes the physical concept of

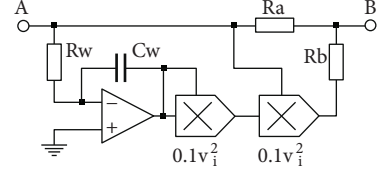


FIGURE 1: The alternative circuit of memristor.

memductor more distinct; thus, we can clearly see that the dimension of $(a + 3b\phi^2)$ is conductance. Equation (12) seems useless, but it is very important for engineering design. The specific circuit of memristor can be directly designed by (12). Even when the model represented by (10) changes, we can also design corresponding memductor-based or memristor-based circuits according to this method.

2.2. Realization Circuit of the Specific Memductor Element.

According to (12), the specific circuit of memristor can be designed directly. An equivalent memductor-based circuit consisting of operational amplifier, analog multiplier, resistor, and capacitor is shown in Figure 1.

Here, we assume that the B terminal is connected to the inverting input of the next-stage operational amplifier, so the B point has dummy ground and zero level. The A point is the voltage input, and it is set as u_A . The multiplier coefficient of analog multiplier is 0.1, and the relation between input and output voltage is described as $u_o = 0.1 u_i^2$. It is assumed that the normalized resistance is $10 \text{ k}\Omega$. Then, the output voltage of the operational amplifier is $-(300/R_w C_w) \int u_A dt$. And the output voltage of the operational amplifier after normalization is $-300 \int u_A dt$. After the first analog multiplication, the voltage is $30(\int u_A dt)^2$. After the second analog multiplication, the voltage is $3u_A (\int u_A dt)^2$. Therefore, the current flowing through R_b is easily obtained as follows:

$$i_{R_b} = \frac{3u_A (\int u_A dt)^2}{R_b}. \quad (13)$$

Thus, the current flowing through B point is obtained as follows:

$$i_B = \frac{u_A}{R_a} + \frac{3u_A (\int u_A dt)^2}{R_b}. \quad (14)$$

In the following, the circuit parameter design is carried out.

$$\begin{aligned} R_w &= 33.3 \Omega, \\ R_a &= \frac{10 \text{ k}\Omega}{a}, \\ R_b &= \frac{10 \text{ k}\Omega}{b}. \end{aligned} \quad (15)$$

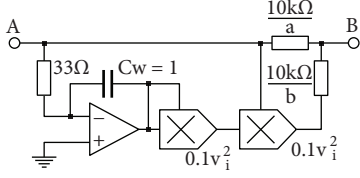


FIGURE 2: The alternative circuit of memductor based with specific parameters.

Then, the total current flowing through B is obtained as follows:

$$i_B = au_A + 3bu_A \left(\int u_A dt \right)^2. \quad (16)$$

In this way, the circuit structure and circuit parameter design of the memductance are realized. The equivalent memductor-based circuit with specific parameters is shown in Figure 2.

2.3. A Novel 4D Memductor-Based Chaotic System. The 3D chaotic system is described as follows:

$$\begin{cases} \dot{x} = \alpha(y - h(x)), \\ \dot{y} = x - y + z, \\ \dot{z} = -\beta y, \end{cases} \quad (17)$$

where

$$h(x) = m_1 x + m_2 f(x) = m_1 x + m_2 \left(\frac{1}{2} (|x+1| - |x-1|) \right), \quad (18)$$

and where x, y, z are the state variables and α, β, m_1, m_2 are the constant parameters of the 3D system. Here, replace $h(x)$ with the memductance $w(x)$; thus, a mathematical model of a chaotic circuit consisting of a memductor element is obtained as follows:

$$\begin{cases} \dot{x} = \alpha(y - w(x)), \\ \dot{y} = x - y + z, \\ \dot{z} = -\beta y, \end{cases} \quad (19)$$

where

$$w(x) = ax + 3bx \left(\int x dt \right)^2. \quad (20)$$

Therefore, according to the characteristics of the aforementioned specific memductor element and the specific realization circuit with memductor, a novel 4D memductor-based chaotic system is proposed based on the ordinary 3D

chaotic system (17). And the novel 4D memductor-based chaotic system is presented as follows:

$$\begin{cases} \dot{x} = \alpha(y + \xi x - cu - dxu^2), \\ \dot{y} = x - y + z, \\ \dot{z} = -\beta y - \gamma z, \\ \dot{u} = x, \end{cases} \quad (21)$$

where x, y, z, u are the state variables and $\alpha, \beta, \xi, \gamma, c, d$ are constant, positive parameters of the novel memductor-based chaotic system.

When choosing $\alpha = 16$, $\beta = 15$, $\xi = 0.25$, $c = 0.00625$, $d = 0.125$, and $\gamma = 0.5$, there exist typical chaotic attractors in system (21). That is, after adding 1D memristor to the ordinary 3D chaotic system, we need to find the appropriate parameters to satisfy the memductor-based system to produce new chaotic phenomena. For the constructed novel memductor-based chaotic system, four parameters ξ, γ, c, d are added. When the specific parameters are brought in, the equation becomes

$$\begin{cases} \dot{x} = 16(y + 0.25x - 0.00625u - 0.125xu^2), \\ \dot{y} = x - y + z, \\ \dot{z} = -15y - 0.5z, \\ \dot{u} = x. \end{cases} \quad (22)$$

However, the numerical solutions of the proposed 4D memductor-based chaotic system (22) are not able to be implemented by using general circuit components. Therefore, in practical applications, it often needs to be varied to make proper adjustments of these variables. Here, the method of scale transformation is to replace x, y, z , and u by $4x, 0.5y, 3z$, and u , respectively. After scale transformation, (22) becomes

$$\begin{cases} \dot{x} = 4x + 2y + 0.025u - 2xu^2, \\ \dot{y} = 8x - y + 6z, \\ \dot{z} = -2.5y - 0.5z, \\ \dot{u} = -4x. \end{cases} \quad (23)$$

Thus, the novel 4D memductor-based chaotic system after scale transformation is easily described as follows:

$$\begin{cases} \dot{x} = \xi x + \alpha y + cu - dxu^2, \\ \dot{y} = \eta x - y + \mu z, \\ \dot{z} = -\beta y - \gamma z, \\ \dot{u} = -\rho x, \end{cases} \quad (24)$$

where x, y, z, u are the state variables and $\alpha, \beta, \xi, \gamma, c, d, \eta, \mu, \rho$ are constant, positive parameters of the novel 4D memductor-based chaotic system. When choosing $\xi = 4$,

$\alpha = 2$, $c = 0.025$, $d = 2$, $\eta = 8$, $\mu = 6$, $\beta = 2.5$, $\gamma = 0.5$, and $\rho = 4$, there exist typical chaotic attractors in system (24).

3. Dynamical Analysis of the Novel Memductor-Based Chaotic System

3.1. Chaotic Attractors. The chaotic attractors with MATLAB simulation of the novel 4D memductor-based chaotic system (24) are shown in Figure 3. It can be seen from the numerical simulation results that the numerical range of each variable parameter is within -10 V to $+10\text{ V}$, and it fully conforms to the requirements of circuit design in practical applications. That is because the working voltage of electronic components generally ranges from -15 V to $+15\text{ V}$ in practical electronic circuits. As a result, it must be the equation of scaling if the memductor-based chaotic circuit is to be implemented.

3.2. Divergence and Stability of Equilibrium Set. The divergence of the novel 4D memductor-based chaotic system (24) is easily calculated as follows:

$$\nabla = \frac{\partial \dot{x}}{\partial x} + \frac{\partial \dot{y}}{\partial y} + \frac{\partial \dot{z}}{\partial z} + \frac{\partial \dot{u}}{\partial u} = \xi - du^2 - 1 - \gamma = 2.5 - 2u^2. \quad (25)$$

In this way, the system will be dissipative on the condition that the parameter becomes $|u| > \sqrt{5}/2$, because a necessary and sufficient condition for system (24) to be dissipative is that the divergence of the vector field is negative when the time tends to infinite. Furthermore, the corresponding dynamic characteristics will be presented.

Considering $\dot{x} = \dot{y} = \dot{z} = \dot{u} = 0$, then the equilibrium equation of system (24) is easily obtained as follows:

$$\begin{cases} \dot{x} = \xi x + \alpha y + cu - dxu^2 = 0, \\ \dot{y} = \eta x - y + \mu z = 0, \\ \dot{z} = -\beta y - \gamma z = 0, \\ \dot{u} = -\rho x = 0. \end{cases} \quad (26)$$

Clearly, the set of equilibrium points of the system (24) is obtained as follows:

$$E = \{(x, y, z, u) \mid x = y = z = 0, u = \sigma\}, \quad (27)$$

where σ is any real constant. That is, the set of points on the u coordinate is the equilibrium point and the system has an infinite set of equilibrium points. Through linearizing the system (24) near the equilibrium point, then the Jacobian matrix for system (24) at equilibrium point (27) is obtained as follows:

$$J_E = \begin{bmatrix} \xi - d\sigma^2 & \alpha & 0 & 0 \\ \eta & -1 & \mu & 0 \\ 0 & -\beta & -\gamma & 0 \\ -\rho & 0 & 0 & 0 \end{bmatrix}, \quad (28)$$

where $\xi = 4$, $\alpha = 2$, $d = 2$, $\eta = 8$, $\mu = 6$, $\beta = 2.5$, $\gamma = 0.5$, and $\rho = 4$. Then, the specific Jacobian matrix for system (24) at equilibrium point is easily obtained as follows:

$$J_E = \begin{bmatrix} 4 - 2\sigma^2 & 2 & 0 & 0 \\ 8 & -1 & 6 & 0 \\ 0 & -2.5 & -0.5 & 0 \\ -4 & 0 & 0 & 0 \end{bmatrix}. \quad (29)$$

The characteristic polynomial of the Jacobian matrix (29) is described as follows:

$$\text{Det}(J_E - \lambda I) = 0. \quad (30)$$

Therefore, the eigenvalues at the equilibrium point of the novel memductor-based chaotic system can be obtained as follows:

$$\begin{aligned} \lambda_1 &= 5.7332, \\ \lambda_{2,3} &= -1.6276 \pm 3.0918i, \\ \lambda_4 &= 0.0221, \\ |\sigma| &> 1.118. \end{aligned} \quad (31)$$

It can be concluded from (31) that the equilibrium point set of the system, which accords with the condition of chaos generation, is unstable.

3.3. Bifurcation, Lyapunov Exponents, and Poincaré Graph. The calculation of Lyapunov exponent is a method employed to quantitatively judge the chaos of system. When choosing $\xi = 4$, $\alpha = 2$, $c = 0.025$, $d = 2$, $\eta = 8$, $\mu = 6$, $\beta = 2.5$, $\gamma = 0.5$, and $\rho = 4$, the initial conditions are chosen as $x(0) = -0.17528$, $y(0) = -1.0872$, $z(0) = 1.6368$, and $u(0) = -3.2852$. The Lyapunov exponents of the novel memductor-based chaotic system are, respectively, calculated as follows: $L_1 = 0.0600$, $L_2 = 0.0065$, $L_3 = -0.0069$, and $L_4 = -10.4012$. Figure 4 shows the projection of a chaotic attractor generated by the novel memductor-based chaotic system on the $x - u$ plane. It represents the extreme sensitivity of the memristor-based chaotic system to the initial values [30]. When the initial value varies by 0.00001, there will be such a prominent difference in the result. It is obvious that the proposed memductor-based chaotic system is extremely sensitive to initial values. In Figure 5, the Lyapunov exponent spectrum of the novel memductor-based chaotic system is shown. Consequently, it is found that the novel memductor-based chaotic system is chaotic oscillation from the chaotic attractors and Lyapunov exponents.

In order to further verify the chaotic dynamical behavior of the novel memductor-based chaotic system (24), the bifurcation diagram and the Poincaré graph are strictly calculated. Through numerical analysis, the bifurcation diagram with parameter variation is shown in Figure 6, where α is a variable parameter. It is obvious that the system will undergo a huge change in topology when α is about 1.1. The Poincaré

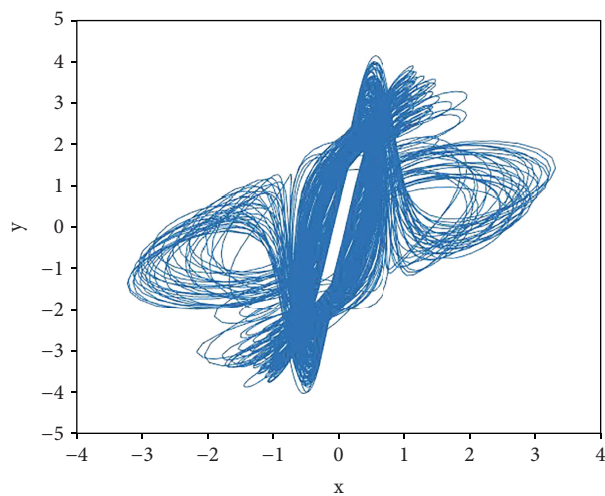
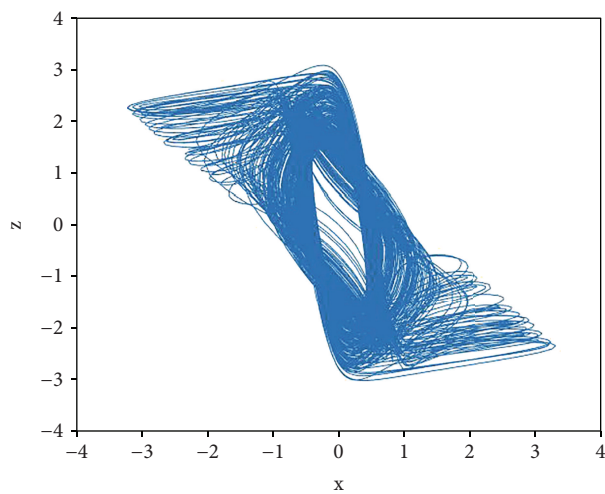
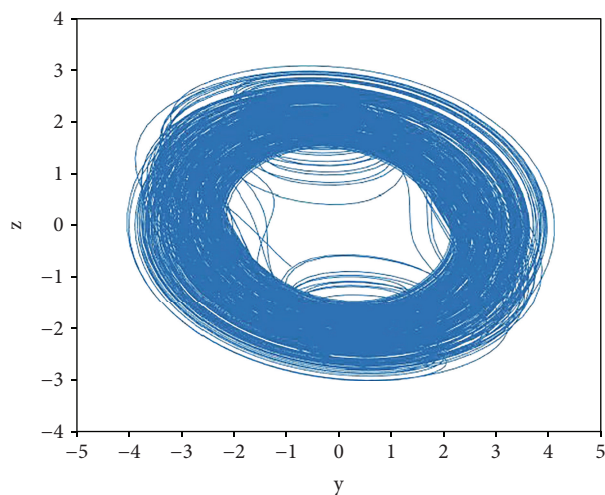
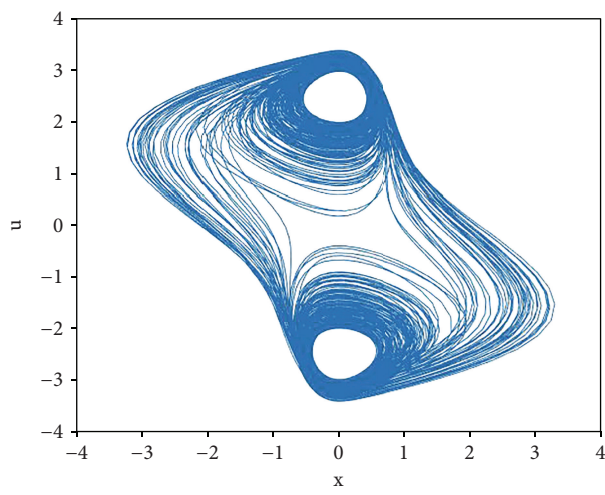
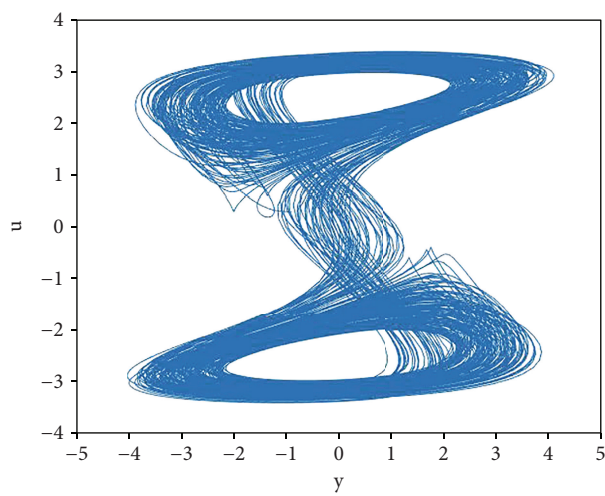
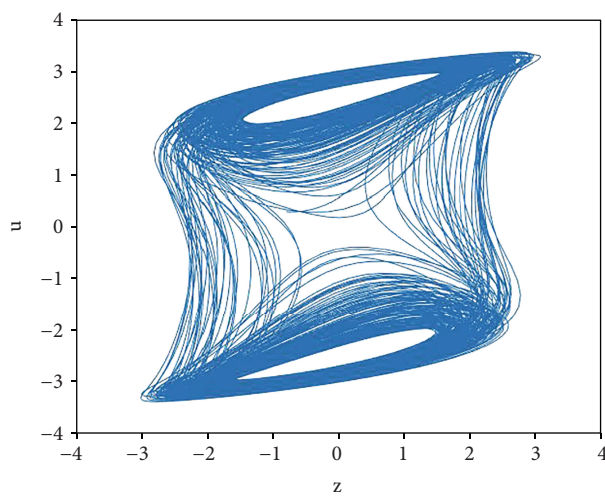
(a) xy plane(b) xz plane(c) yz plane(d) xu plane(e) yu plane(f) zu plane

FIGURE 3: The chaotic attractors of system (24) with MATLAB.

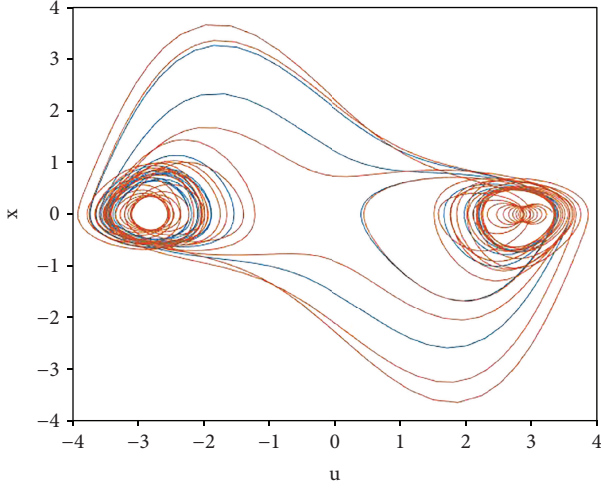
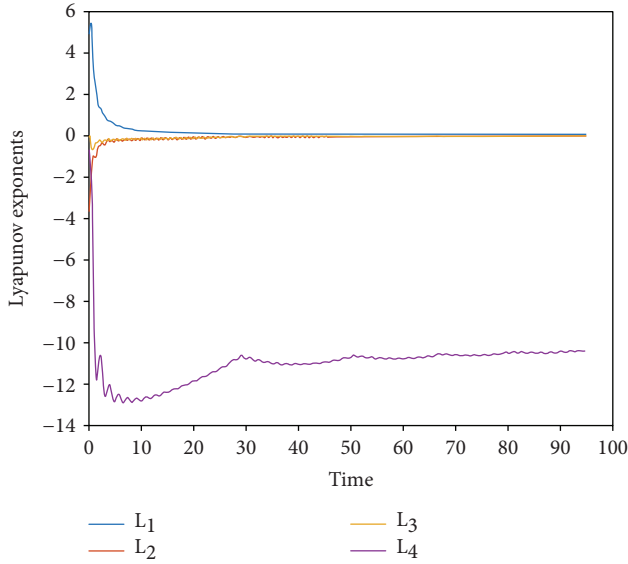
FIGURE 4: The chaotic attractor of ux plane.

FIGURE 5: The Lyapunov exponent spectrum.

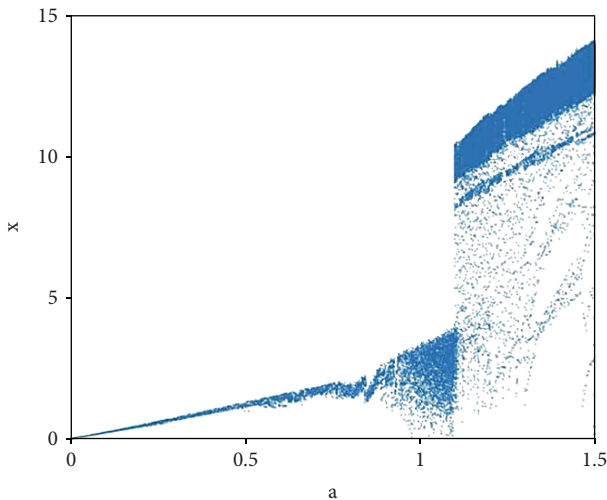


FIGURE 6: The bifurcation diagram.

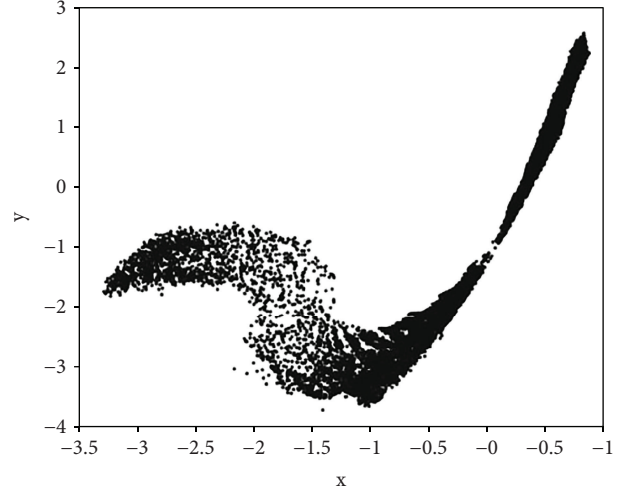


FIGURE 7: The Poincaré graph.

graph in $x - y$ plane is shown in Figure 7. The law of phase trajectory can be obtained by Poincaré map. It confirms the chaotic behavior of the proposed memductor-based chaotic system for the aforementioned set of parameters.

3.4. Synchronous Stability Analysis Based on Active Control. Chaotic synchronization means that the trajectory of a chaotic system converges to another chaotic system and maintains a consistent dynamic phenomenon from a physical standpoint [38]. Here, the chaotic drive system or the transmitter in the secure communication system is defined as follows:

$$\dot{X} = M(X, t). \quad (32)$$

Then, the chaotic response system or the receiver in the secure communication system is defined as follows:

$$\dot{Y} = M'(Y, t) + N, \quad (33)$$

where N is the controller, t is the time, and vectors are $X, Y \in \mathbb{R}^n$. And they have the n -dimensional elements (x_1, x_2, \dots, x_n) and (y_1, y_2, \dots, y_n) , respectively. In addition, the two chaotic systems can be the same or different, but their initial conditions are different. If the two chaotic systems are interrelated to some extent through the controller N , $X(t; t_0, X_0)$ and $Y(t; t_0, Y_0)$ are considered to be the solutions of system (32) and system (33), respectively, where they satisfy the smooth condition of the function, when \mathbb{R}^n has a subset of $W(t_0)$, and the initial value is satisfied to $X_0, Y_0 \in D(t_0)$, and then when $t \rightarrow \infty$ exists:

$$\zeta \equiv \lim_{t \rightarrow \infty} \|X(t; t_0, X_0) - Y(t; t_0, Y_0)\| \rightarrow 0. \quad (34)$$

Thus, it can be obtained that the chaotic response system (32) is synchronized with the chaotic drive system (33).

In this way, the active synchronization error system between the chaotic drive system and the chaotic response system is defined by $\dot{e} = \dot{y} - \dot{x}$, which means the asymptotic

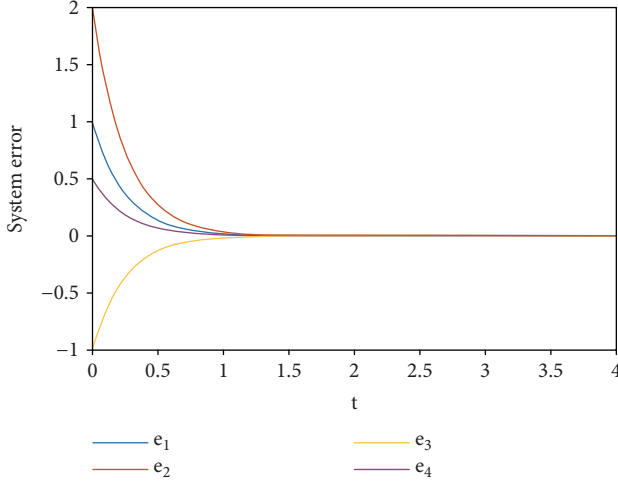


FIGURE 8: The history of synchronization errors.

stability at the origin of the synchronization error system on the basis of the Lyapunov stability theory. It is obvious that the controller N plays a key role in stabilizing the synchronization error system at the origin. Consequently, various synchronization methods will be realized by designing different controllers.

Then, the novel 4D memductor-based system (24) is rewritten. And we consider the novel memductor-based drive system which is described as follows:

$$\begin{cases} \dot{x}_1 = \xi x_1 + \alpha x_2 + cx_4 - dx_1 x_4^2, \\ \dot{x}_2 = \eta x_1 - x_2 + \mu x_3, \\ \dot{x}_3 = -\beta x_2 - \gamma x_3, \\ \dot{x}_4 = -\rho x_1. \end{cases} \quad (35)$$

When choosing $\xi = 4$, $\alpha = 2$, $c = 0.025$, $d = 2$, $\eta = 8$, $\mu = 6$, $\beta = 2.5$, $\gamma = 0.5$, and $\rho = 4$, the novel memductor-based system (35) is chaotic. Thereafter, the novel memductor-based response system is considered as follows:

$$\begin{cases} \dot{y}_1 = \xi y_1 + \alpha y_2 + cy_4 - dy_1 y_4^2 + u_1, \\ \dot{y}_2 = \eta y_1 - y_2 + \mu y_3 + u_2, \\ \dot{y}_3 = -\beta y_2 - \gamma y_3 + u_3, \\ \dot{y}_4 = -\rho y_1 + u_4, \end{cases} \quad (36)$$

where y_1, y_2, y_3, y_4 are the states and u_1, u_2, u_3, u_4 are the designed controllers, whereas the synchronization error based on the active control method is defined as follows:

$$\dot{e}_i = \dot{y}_i - \dot{x}_i, \quad (i = 1, 2, 3, 4). \quad (37)$$

According to (37), the synchronization error system between the memductor-based drive system (35) and the memductor-based response system (36) is easily obtained as follows:

$$\begin{cases} \dot{e}_1 = \xi e_1 + \alpha e_2 + ce_4 - d(y_1 y_4^2 - x_1 x_4^2) + u_1, \\ \dot{e}_2 = \eta e_1 - e_2 + \mu e_3 + u_2, \\ \dot{e}_3 = -\beta e_2 - \gamma e_3 + u_3, \\ \dot{e}_4 = -\rho e_1 + u_4. \end{cases} \quad (38)$$

Then, the active controller system is designed as follows:

$$\begin{cases} u_1 = -\xi e_1 - \alpha e_2 - ce_4 + d(y_1 y_4^2 - x_1 x_4^2) - k_1 e_1, \\ u_2 = -\eta e_1 + e_2 - \mu e_3 - k_2 e_2, \\ u_3 = \beta e_2 + \gamma e_3 - k_3 e_3, \\ u_4 = \rho e_1 - k_4 e_4, \end{cases} \quad (39)$$

where k_1, k_2, k_3, k_4 are the control gains, and they are positive values, respectively. Substituting (39) into (38), the active synchronization error system is obtained as follows:

$$\begin{cases} \dot{e}_1 = -k_1 e_1, \\ \dot{e}_2 = -k_2 e_2, \\ \dot{e}_3 = -k_3 e_3, \\ \dot{e}_4 = -k_4 e_4. \end{cases} \quad (40)$$

Next, the Lyapunov function V is defined as follows:

$$V = \frac{e_1^2 + e_2^2 + e_3^2 + e_4^2}{2}. \quad (41)$$

Thus, it is obvious that V is positively definite. Differentiating V ,

$$\begin{aligned} \dot{V} &= e_1 \dot{e}_1 + e_2 \dot{e}_2 + e_3 \dot{e}_3 + e_4 \dot{e}_4 \\ &= e_1(-k_1 e_1) + e_2(-k_2 e_2) + e_3(-k_3 e_3) + e_4(-k_4 e_4) \\ &= -k_1 e_1^2 - k_2 e_2^2 - k_3 e_3^2 - k_4 e_4^2. \end{aligned} \quad (42)$$

According to (42), $\dot{V} = -k_1 e_1^2 - k_2 e_2^2 - k_3 e_3^2 - k_4 e_4^2 \leq 0$ is easily obtained. That is to say, \dot{V} is negatively semidefinite. Based on the Lyapunov stability theory, if V is positively definite and \dot{V} is negatively semidefinite, then the system is consistent and stable at the origin of the equilibrium state [38]. Accordingly, the active synchronization error system (38) is asymptotically stable at the origin. Thus, $\lim_{t \rightarrow \infty} |e(t)| \rightarrow 0$. It is proved that the synchronization between the novel memductor-based drive system and the novel memductor-based response system is achieved. In the following numerical simulations, the initial values of the novel memductor-based system are chosen as $x_1(0) = -0.17528$, $x_2(0) = -1.0872$, $x_3(0) = 1.6368$, and $x_4(0) = -3.2852$. The control gains are chosen as $k_1 = k_2 = k_3 = k_4 = 10$.

The history of the synchronization errors between the novel memductor-based drive system and the novel memductor-based response system is shown in Figure 8. It is clear from Figure 8 that the active synchronization errors e_1, e_2, e_3, e_4 can be asymptotically stabilized at the origin in

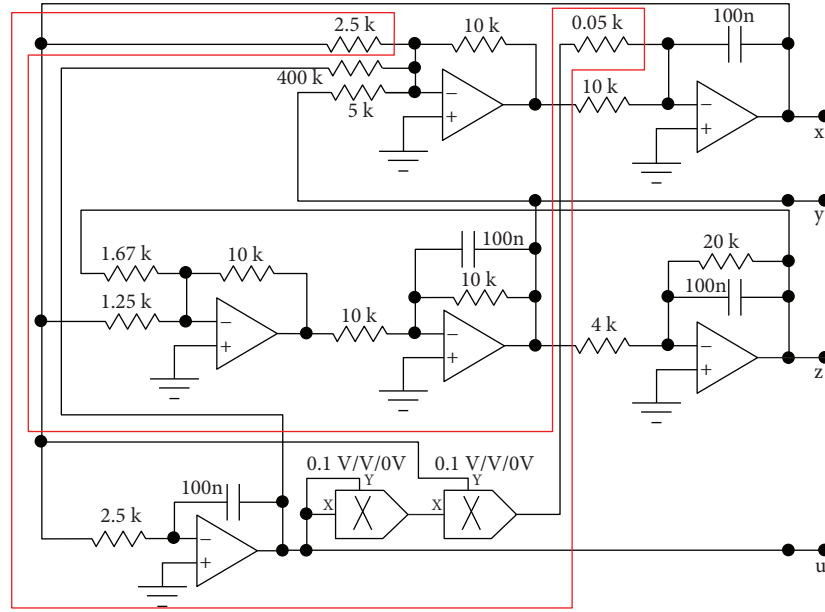


FIGURE 9: The novel memductor-based chaotic circuit schematic.

a very short period of time. The active control method is simple, practical, and easier to be implemented in an electronic circuit. It can be applied to other complex memductor-based chaotic systems to implement synchronization and chaotic secure communication.

4. Circuit Design and Hardware Implementation

4.1. Circuit Design. Based on the novel 4D memductor-based chaotic system (23), the normalized resistor is set as $R_{\text{normalization}} = 100 \text{ k}\Omega$ in order to design the memductor-based chaotic circuit. In view of the need for higher accuracy, the low-power AD633 analog multipliers are chosen in the

chaotic circuits, which enjoy the precision of laser trimming and remain stable between -10 V and $+10 \text{ V}$. Taking into considering the convenience of power supply and the feasibility of the circuit, as well as saving components, the selected operational amplifiers are LF347N and LF353N with the power supply voltage ranging from -15 V to $+15 \text{ V}$. In order to prevent the voltage in the circuit from exceeding the range of operational amplifier, the ranges of the variables in system (22) have been adjusted appropriately, and a new memductor-based chaotic system (23) was obtained after scale transformation. Because the precision provided by AD633 is $1/10 \text{ V}$, the input factor for analog multiplier is 0.1 V . Conclusively, the state equation of the memductor-based chaotic circuit is obtained by rewriting (23):

$$\begin{cases} \dot{x} = \frac{100 \text{ k}}{2.5 \text{ k}} \times 0.1x + \frac{100 \text{ k}}{5 \text{ k}} \times 0.1y + \frac{100 \text{ k}}{400 \text{ k}} \times 0.1u - \frac{100 \text{ k}}{0.05 \text{ k}} \times 0.001xu^2, \\ \dot{y} = \frac{100 \text{ k}}{1.25 \text{ k}} \times 0.1x - \frac{100 \text{ k}}{10 \text{ k}} \times 0.1y + \frac{100 \text{ k}}{1.67 \text{ k}} \times 0.1z, \\ \dot{z} = -\frac{100 \text{ k}}{4 \text{ k}} \times 0.1y - \frac{100 \text{ k}}{20 \text{ k}} \times 0.1z, \\ \dot{u} = -\frac{100 \text{ k}}{2.5 \text{ k}} \times 0.1x. \end{cases} \quad (43)$$

Thus, the novel memductor-based chaotic circuit schematic is designed as shown in Figure 9 according to (43). The circuit is divided into two parts: the nonmemristor part and the independent memristor part. The memristor part is

the red circuit marked in Figure 9. The rest of the circuit is the nonmemristor part, a linear part. What is seen from Figure 9 is that the novel memductor-based chaotic circuit is composed of six operational amplifiers and two analog

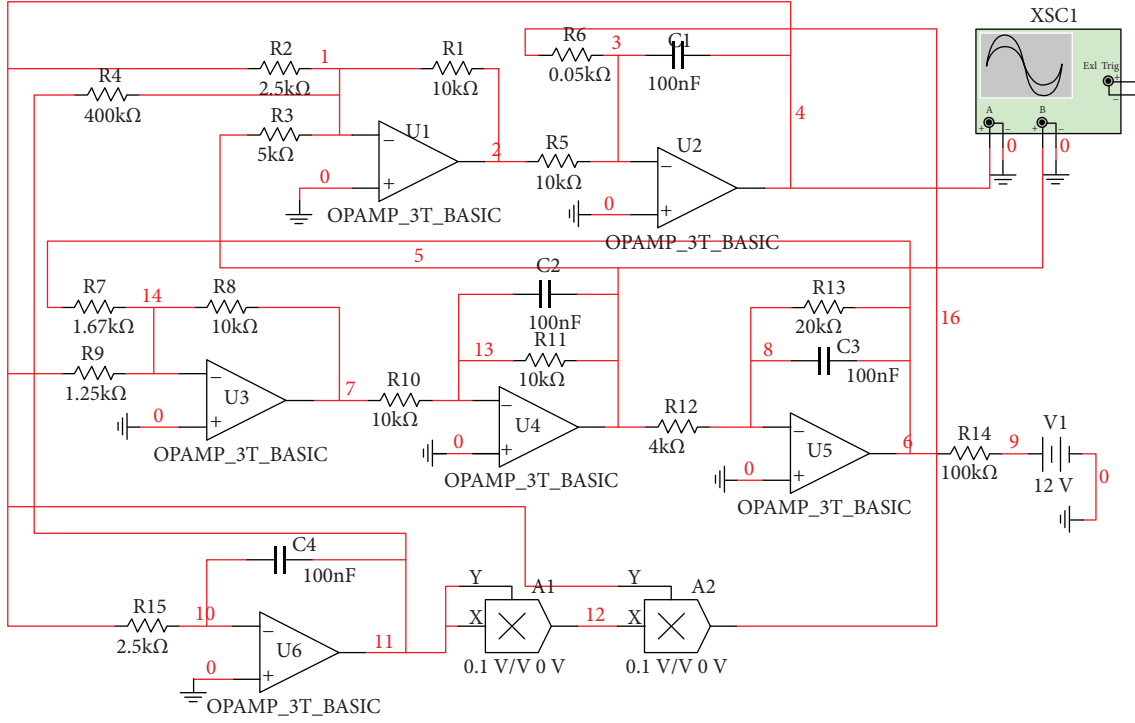


FIGURE 10: The novel memductor-based chaotic circuit with Multisim.

multipliers. It outputs four signal waveforms, six phase portraits, and stable fourth-order double vortex chaotic signals. Accordingly, Figure 10 shows the novel memductor-based chaotic circuit with Multisim.

All of the electronic components are easily available. The memductor-based chaotic phase portraits of the novel memductor-based chaotic circuit by Multisim are shown in Figure 11. It can be shown from the simulation results that it outputs six chaotic phase portraits of xy , xz , zy , xu , yu , and zu . Moreover, the Multisim simulation results are consistent with the MATLAB simulation results as shown in Figure 3. That is, it fully conforms to the requirements of circuit design in practical applications.

4.2. Hardware Implementation. Most researchers highlight the study of memristor chaos theory in numerical simulation; in that case, there is a certain deviation in the physical memristor circuit system. Based on the correct simulation results shown in Figure 11, with the purposes to verify that the novel memductor-based chaotic circuit enjoys high accuracy and good robustness and further study the chaotic dynamical characteristics of the novel memductor-based chaotic system (23), a practical electronic circuit is constructed by using some general electronic components such as operational amplifiers, analog multipliers, resistors, and capacitors according to the circuit model of Figure 9.

It should be noted that the problems easily occurring in the process of constructing the memductor-based chaotic circuit should be tackled. For example, the chaotic circuit is more sensitive to the initial value because of adding the memristor, and any minor change will lead to unpredictable results. Therefore, we chose the values of the resistors closer

to the simulation resistor to construct the circuit and test whether each module of the circuit works properly in the process of constructing. Afterwards, input voltage to the system and access the oscilloscope, the output phase portrait photos of the novel memductor-based chaotic circuit are shown in Figure 12. Figure 13 shows the experimental circuit board photo.

What should be seen from the experimental results shown in Figure 12 is that the phase portraits of the novel memductor-based chaotic attractors displayed by oscilloscope coincide with the simulation results of MATLAB and Multisim. That is, it proves true that the memductor-based chaotic attractors exist in real. The proposed memductor-based chaotic circuit design method provides a reliable and straightforward way for realizing memristive chaotic circuits, and the method plays a significant role in easily handling and avoiding the output voltage beyond the limitation of the amplifier linear region efficiency.

4.3. Experimental Results Analysis. Through careful experiments on the proposed memductor-based chaotic circuit shown in Figure 9, the following important conclusions can be obtained:

- (i) The impact of switching power seems to exist. Once the chaotic state is entered, the chaotic attractors begin to become stable. The memductor-based chaotic circuit characteristics of this phenomenon are presented as follows: when the power is turned on, two attractors contribute to establish a stable state of the circuit. One is a chaotic attractor, which tells the fact that the voltage amplitude is less than the

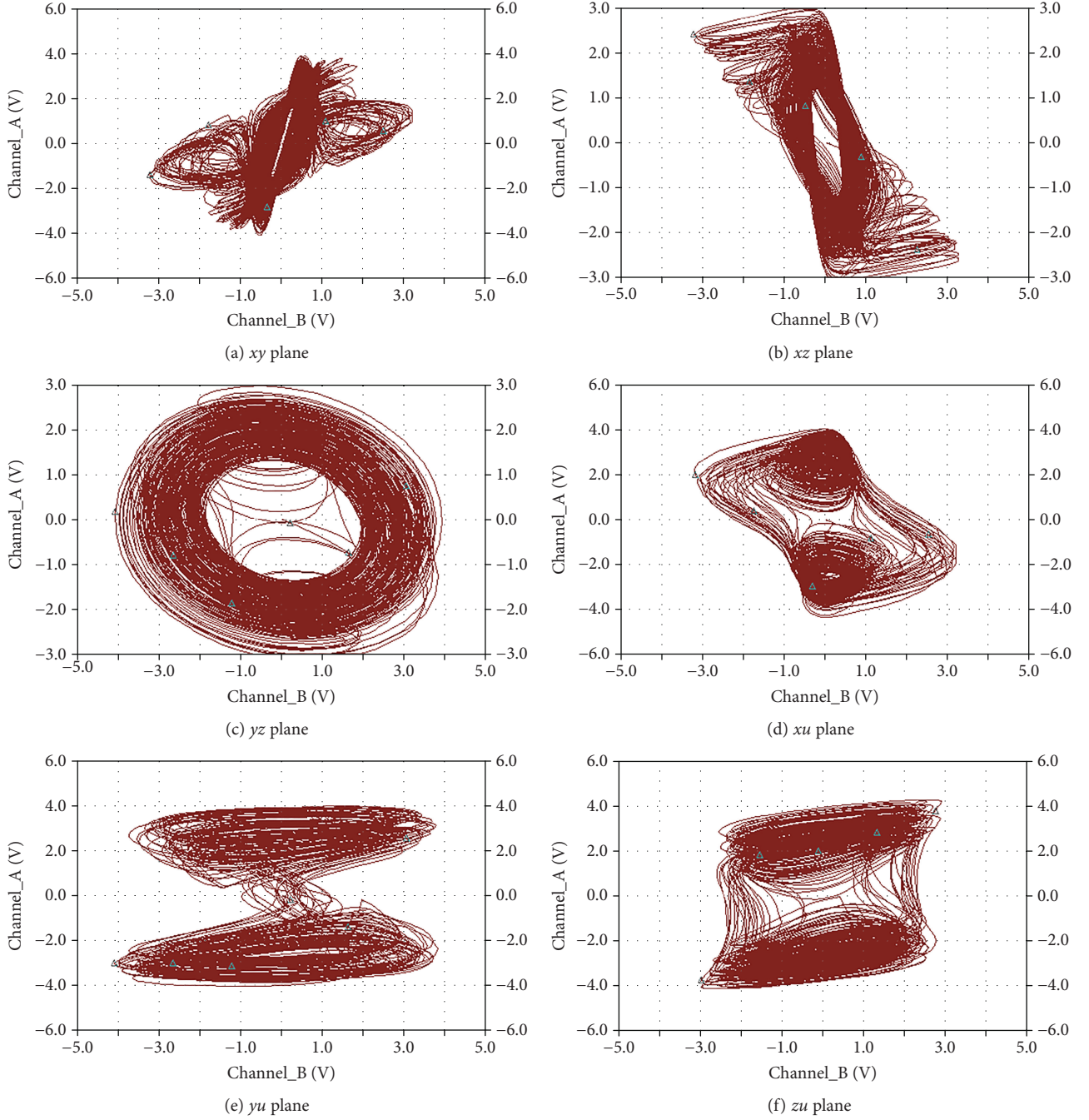


FIGURE 11: The chaotic attractors of the novel memductor-based chaotic circuit with Multisim.

supply voltage, and no amplitude limiting condition occurs. The other is the possibility of entering a state of limiting amplitude and not breaking out of the limiting amplitude state, but entering the traditional periodic oscillation, and this oscillation is a stable oscillation

- (ii) The ranges of the physical variables measured in this experiment are presented as follows: x ranges from -2.2 V to $+2.2\text{ V}$, y ranges from -4.4 V to $+4.4\text{ V}$, z ranges from -4.4 V to 4.4 V , and u ranges from -4.8 V to $+4.8\text{ V}$. This set of data is easy to be

controlled. So as long as the resistance of the 4 K resistor is adjusted, the amplitude of the chaos varies accordingly and the shape remains unchanged, which is extremely convenient

- (iii) A good memductor-based chaotic circuit must be designed without defects. One of the defects is the voltage limit of the regulated power supply. The defects may appear in designing of the operational amplifier and inverting integrator. As for the design defect of operational amplifier, the feedback resistor of the operational amplifier R_f is greater

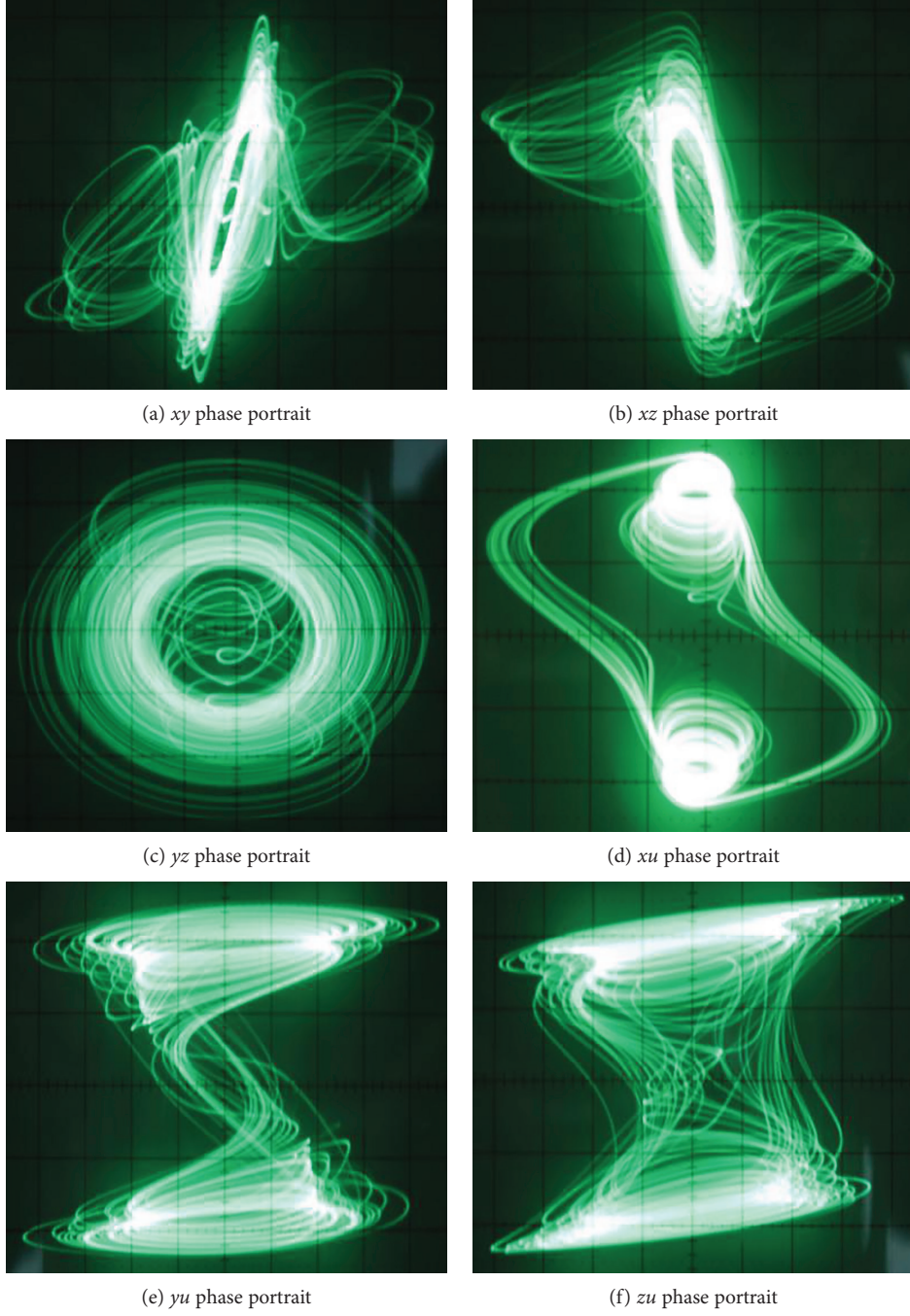


FIGURE 12: The output phase portrait photos.

than that of the input circuit R_{in} . That is, the design defect is presented as

$$R_f > R_{in}. \quad (44)$$

Moreover, if the operational amplifier is equipped with two input resistors, the design defect is presented as follows:

$$R_f > \frac{1}{(1/R_{in1}) + (1/R_{in2})}. \quad (45)$$

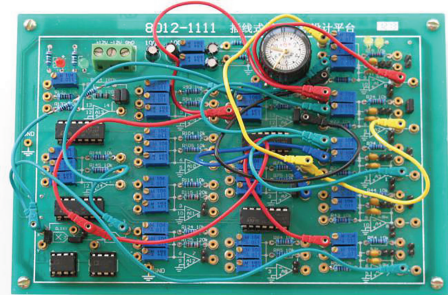


FIGURE 13: Experimental circuit board photo.

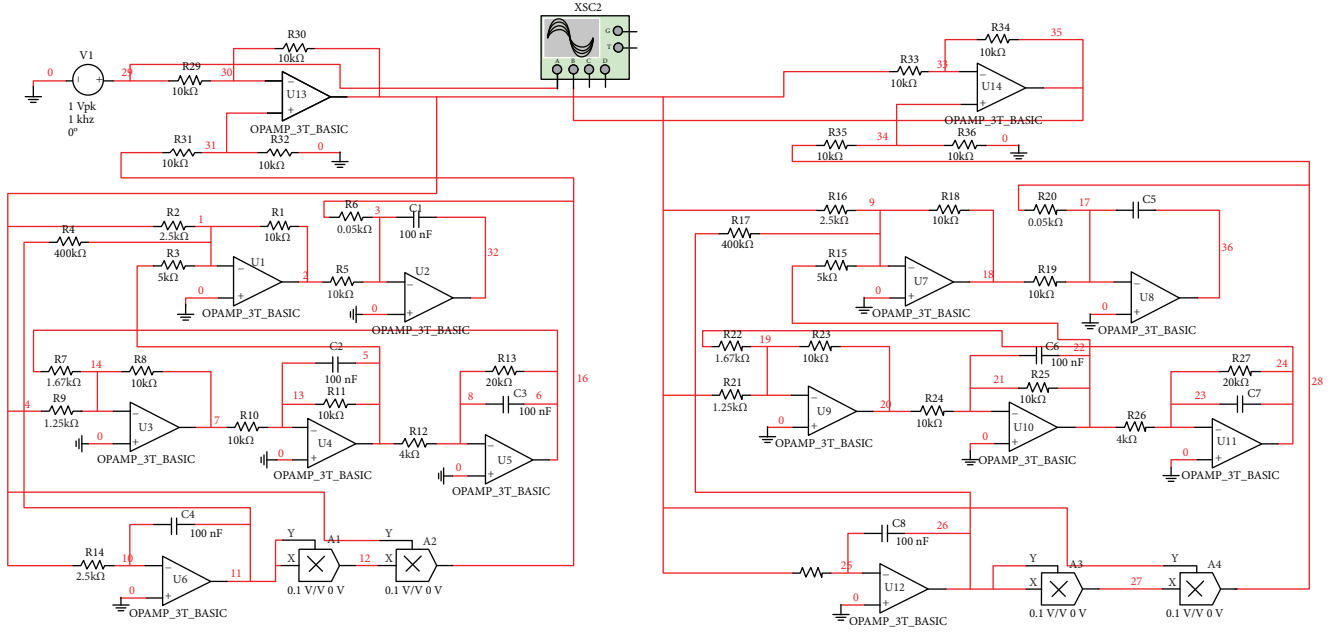


FIGURE 14: A novel memductor-based secure communication circuit by Multisim.

Therefore, both of these conditions may cause amplitude limiting distortion, which makes the design of memductor-based circuits deviates from the original intention of chaotic mathematical model.

And as for the design defect of the inverting integrator, the normalized resistance of the inverting integrator is set as $R_{\text{normalization}}$; thus, the possible defect of the memductor-based circuit design is presented as follows:

$$R_{\text{in}} < R_{\text{normalization}}, \quad (46)$$

which is hard to achieve, since in some cases, the mathematical model itself is involved, and it is not just the circuit design but also the circuit model involved. Therefore, the reason why the steady phase portraits have not been debugged is that the design of the operational amplifier violates (44) or (45).

- (iv) Here, a new concept, called “the memductor-based chaotic circuit defect quantification index”, is first proposed. The new concept of quantification consists of two parts logically. First of all, the single-stage defect coefficient is considered. For a stage operational amplifier, if the operational amplifier does not violate (44) and (45), the defect coefficient of the memductor-based chaotic circuit is equal to zero. If (44) and (45) are violated, the defect coefficient of the operational amplifier is defined as

$$\varepsilon_{\text{defect}} = \frac{R_f}{R_{\text{in}}} - 1 = \frac{R_f - R_{\text{in}}}{R_{\text{in}}}. \quad (47)$$

Secondly, the defect coefficient of the whole memductor-based circuit system is the sum of the defect coefficient at

all levels of the unit circuit. Physical experiments in this paper show that the chaotic output of the memductor-based circuit with the parameters shown in Figure 9 is the most stable, and they are consistent with the MATLAB and Multisim simulation results.

5. Application of the Proposed Memductor-Based Chaotic Circuit

Since the memductor-based chaotic signal is more sensitive to the initial value than the ordinary chaotic signal, it is especially suitable for the secure communication field. In order to improve the security of secure communication system, it is considered that the novel memductor-based chaotic system should be selected as the chaotic system. In the proposed memductor-based chaotic secure communication scheme, the memristive secure communication circuit is implemented by using some electronic components containing analog multipliers, operational amplifiers, resistors, and capacitors with a novel 4D memductor-based chaotic system as chaos generator. Based on the proposed memductor-based chaotic circuit shown in Figure 9, the memductor-based secure communication circuit schematic by Multisim is shown in Figure 14. Its circuit principle is carefully presented as follows:

It consists 14 operational amplifiers together with 4 analog multipliers. Its basic circuit is composed of two proposed identical memductor-based chaotic circuit units with a little change. The left side of the circuit is the transmitter and the right side of the circuit is the receiver. The inverting input end of transmitter-modulator is connected with the transmitted signal to be transmitted. The same phase input end is connected with the x output terminal of the novel memductor-based chaotic circuit. In this way, the receiving system and the transmitting system are easier to maintain synchronization, and the robustness of the memductor-

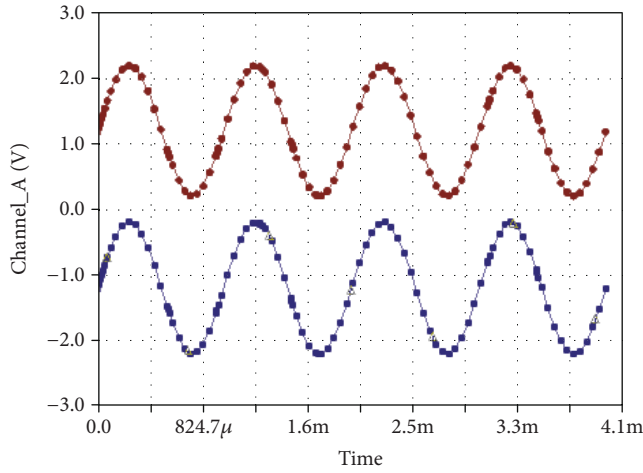


FIGURE 15: Transmitting and receiving waveforms.

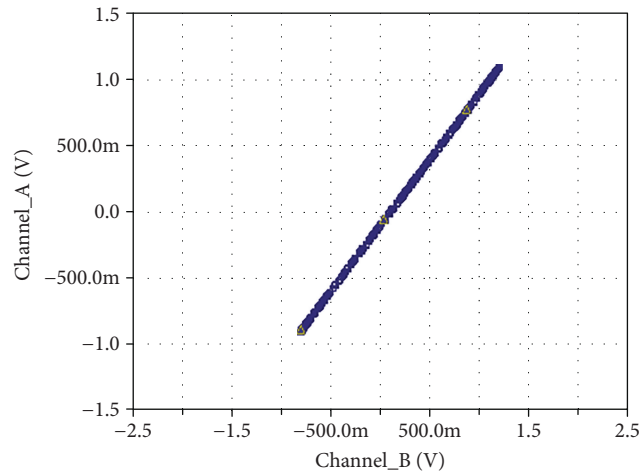


FIGURE 16: Synchronous phase portrait.

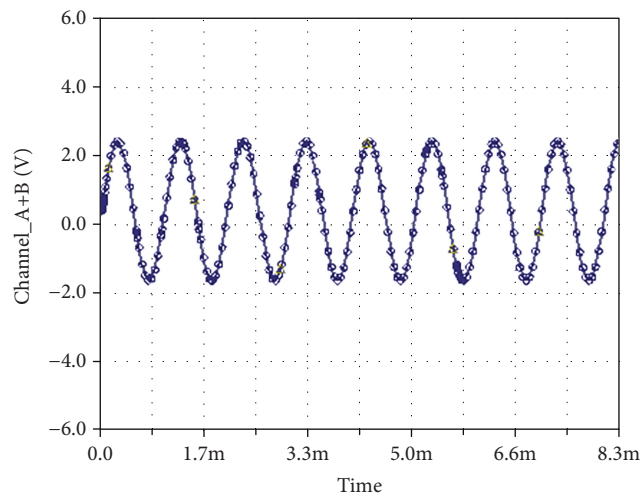


FIGURE 17: Superimposed signal waveform.

based chaotic circuit is also maintained. This method prevents effective information from being intercepted in the secure communication process.

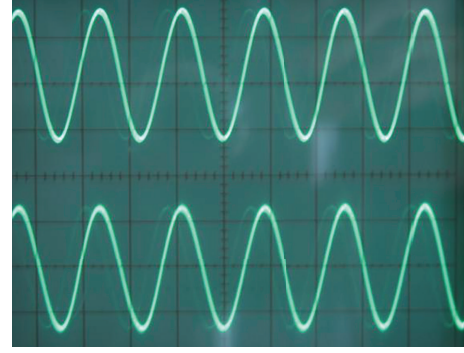


FIGURE 18: Transmitting and receiving signal photo.

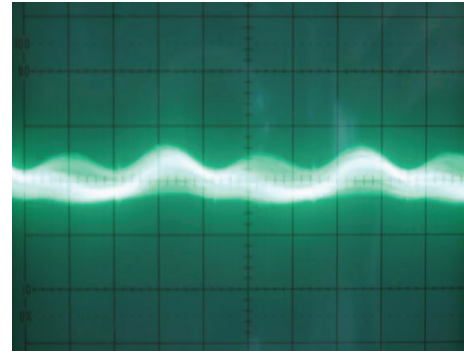


FIGURE 19: Modulation and demodulation waveform subtraction.

In what follows, the simulation experiments are presented to verify whether two identical parameters of the memductor-based chaotic circuits can effectively achieve the signal transmission and reception without distortion. Suppose an input sine wave with amplitude of 1 V and frequency of 1 kHz is given in the circuit simulation, the transmitting and receiving signal waveform by Multisim is shown in Figure 15. The synchronous phase portrait is shown in Figure 16. And Figure 17 shows the superimposed signal waveform of the modulation and demodulation signal. It is obvious from the simulation results that, no matter what kinds of signals are input, the two identical memductor-based chaotic circuits entirely maintain synchronization with each other if the component parameters of the transmitting circuit are exactly the same with the receiving circuit. Almost no distortion can be seen.

Subsequently, the hardware circuit experiments of the proposed chaotic secure communication circuit based on the memductor-based chaotic circuit are implemented successfully. To verify the above Multisim simulation results, accordingly, an input sine wave with amplitude of 1 V and frequency of 1 kHz is taken in the practical electronic circuit experiment. It should be noted that the transmitting and receiving signal waveform photo is shown in Figure 18. Figure 19 shows the modulation and demodulation waveform subtraction. It is evident that the difference between the two waves (i.e., noise) is only 10 microvolts when the most sensitive gear of the oscilloscope is 10 μV . The synchronous phase portrait photo is shown in Figure 20. Figure 21 shows the superimposed signal photo of the modulation

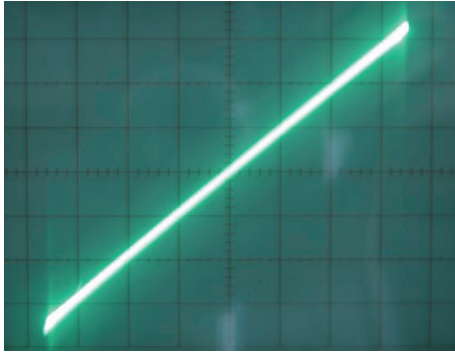


FIGURE 20: Synchronous phase portrait photo.

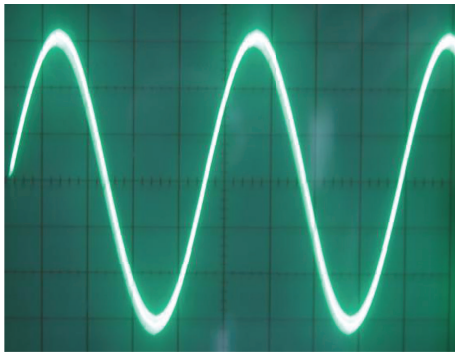


FIGURE 21: Superimposed signal photo.

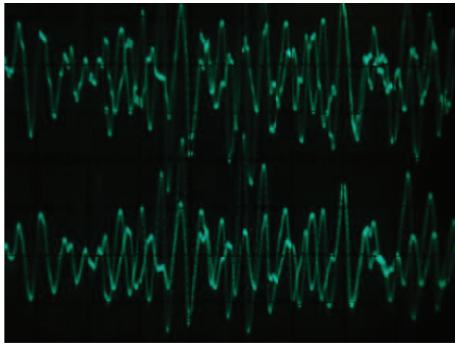


FIGURE 22: The transmitting modulation signal and the receiving demodulation signal photo.

and demodulation waveform. Figure 22 shows the transmitting modulation signal and the receiving demodulation signal waveform photo on the oscilloscope. According to the experimental measurement results of the memductor-based chaotic secure communication circuit, it is obvious that the transmitting and receiving signal waveform photo and the synchronous phase portrait photo displayed by oscilloscope coincide with the Multisim simulation results.

Nevertheless, the memductor-based chaotic circuits composed of conventional operational amplifiers and analog multipliers still have some limitations, mainly because of the frequency limitations of the operational amplifiers. As already shown in [38], the operational amplifiers allow us to implement any type of circuit that is useful in analog

processing applications. However, its performance in realizing chaotic circuits is limited. In work [38], the signals can be transmitted from 1 Hz to 500 kHz without distortion for the hyperchaotic secure communication circuit. When the signal frequency exceeds 500 kHz, the signal distortion will be very obvious. Thus, in order to transmit high-speed data, the chaotic attractors should work at high frequency. In addition, high frequency should be enhanced from the aspect of improving the security and confidentiality of chaotic secure communication circuits.

6. Conclusion

In this paper, a novel memductor-based chaotic system is proposed by adding a one-dimensional memristor equation to a particular three-dimensional chaotic system according to the physical nonlinear characteristics of memductor through looking for suitable parameters. And this paper is an attempt to investigate the dynamical behaviors and synchronous stability of the novel memductor-based chaotic system and realize these dynamics in a new physical circuit. What can be seen from the simulation results and experimental results is that they do not only output six phase portraits but also output stable fourth-order double vortex chaotic signals, respectively. In order to enhance the security performance of transmission signal and improve the vulnerability of the novel memristive system, the novel memductor-based chaotic circuit is applied to construct a new memductor-based chaotic secure communication circuit. Comparisons among Multisim simulation, MATLAB simulation results, and physical experimental results show that they are consistent with each other, and the attractors of the novel memductor-based chaotic system exist. What is more, the concept of “the memductor-based chaotic circuit defect quantification index” is proposed for the first time to verify whether the chaotic output is consistent with the mathematical model, which provides a powerful theoretical basis for the successful design and implementation of memductor-based chaotic circuits. These proposed circuit design methods can also be applied in other complex memristor-based chaotic systems.

Nevertheless, the conventional operational amplifiers have somewhat performance limitations in implementing memductor-based chaotic circuits. It is quite hard to improve the frequency response for analog implementation of chaotic oscillator when it is designed with integrated circuits. Perhaps the implementation based on FPGA can be used as a solution to observe memductor-based attractors at higher frequencies. Thus, our future research will devote to the circuit realization of memductor-based systems by using FPGA.

Data Availability

The data used to support the findings of this study are available from the corresponding author upon request.

Conflicts of Interest

The authors have declared that no competing interests exist.

Acknowledgments

The authors are greatly thankful for the help and support from the National Natural Science Foundation of China (Grant no. 51505375), Open Project of State Key Laboratory of Digital Manufacturing Equipment and Technology (Grant no. DMETKF2017014), Shaanxi Provincial Natural Science Foundation of China (Grant no. 2014JM2-5082), and Open Project of State Key Laboratory of ASIC & System (Grant no. 2018KF001).

References

- [1] L. Chua, "Memristor-the missing circuit element," *IEEE Transactions on Circuit Theory*, vol. 18, no. 5, pp. 507–519, 1971.
- [2] L. O. Chua and Sung Mo Kang, "Memristive devices and systems," *Proceedings of the IEEE*, vol. 64, no. 2, pp. 209–223, 1976.
- [3] J. M. Tour and T. He, "The fourth element," *Nature*, vol. 453, no. 7191, pp. 42–43, 2008.
- [4] D. B. Strukov, G. S. Snider, D. R. Stewart, and R. S. Williams, "The missing memristor found," *Nature*, vol. 453, no. 7191, pp. 80–83, 2008.
- [5] S. Kvatinsky, M. Ramadan, E. G. Friedman, and A. Kolodny, "VTEAM: a general model for voltage controlled memristors," *IEEE Transactions on Circuits and Systems II: Express Briefs*, vol. 62, no. 8, pp. 786–790, 2015.
- [6] M. Itoh and L. O. Chua, "Memristor oscillators," *International Journal of Bifurcation and Chaos*, vol. 18, no. 11, pp. 3183–3206, 2008.
- [7] B. Muthuswamy and P. P. Kokate, "Memristor-based chaotic circuits," *IETE Technical Review*, vol. 26, no. 6, pp. 417–426, 2009.
- [8] B. Muthuswamy, "Implementing memristor based chaotic circuits," *International Journal of Bifurcation and Chaos*, vol. 20, no. 5, pp. 1335–1350, 2010.
- [9] B. Muthuswamy and L. O. Chua, "Simplest chaotic circuit," *International Journal of Bifurcation and Chaos*, vol. 20, no. 5, pp. 1567–1580, 2010.
- [10] B. Bo-Cheng, X. Jian-Ping, and L. Zhong, "Initial state dependent dynamical behaviors in a memristor based chaotic circuit," *Chinese Physics Letters*, vol. 27, no. 7, article 070504, 2010.
- [11] B. C. Bao, Z. Liu, and J. P. Xu, "Steady periodic memristor oscillator with transient chaotic behaviours," *Electronics Letters*, vol. 46, no. 3, p. 228, 2010.
- [12] B. Bao, Z. Ma, J. Xu, Z. Liu, and Q. Xu, "A simple memristor chaotic circuit with complex dynamics," *International Journal of Bifurcation and Chaos*, vol. 21, no. 9, pp. 2629–2645, 2011.
- [13] S. P. Adhikari, M. P. Sah, H. Kim, and L. O. Chua, "Three fingerprints of memristor," *IEEE Transactions on Circuits and Systems I: Regular Papers*, vol. 60, no. 11, pp. 3008–3021, 2013.
- [14] A. Ascoli, F. Corinto, V. Senger, and R. Tetzlaff, "Memristor model comparison," *IEEE Circuits and Systems Magazine*, vol. 13, no. 2, pp. 89–105, 2013.
- [15] Q. H. Hong, Z. J. Li, J. F. Zeng, and Y. C. Zeng, "Design and simulation of a memristor chaotic circuit based on current feedback op amp," *Acta Physica Sinica*, vol. 63, no. 18, article 180502, 2014.
- [16] A. Buscarino, L. Fortuna, M. Frasca, and L. Valentina Gambuzza, "A chaotic circuit based on Hewlett-Packard memristor," *Chaos*, vol. 22, no. 2, article 023136, 2012.
- [17] A. Buscarino, L. Fortuna, M. Frasca, and L. V. Gambuzza, "A gallery of chaotic oscillators based on HP memristor," *International Journal of Bifurcation and Chaos*, vol. 23, no. 5, article 1330015, 2013.
- [18] I. Petras, "Fractional-order memristor-based Chua's circuit," *IEEE Transactions on Circuits and Systems II: Express Briefs*, vol. 57, no. 12, pp. 975–979, 2010.
- [19] L. Teng, H. H. C. Iu, X. Wang, and X. Wang, "Chaotic behavior in fractional-order memristor-based simplest chaotic circuit using fourth degree polynomial," *Nonlinear Dynamics*, vol. 77, no. 1–2, pp. 231–241, 2014.
- [20] S. Kvatinsky, E. G. Friedman, A. Kolodny, and U. C. Weiser, "TEAM: threshold adaptive memristor model," *IEEE Transactions on Circuits and Systems I: Regular Papers*, vol. 60, no. 1, pp. 211–221, 2013.
- [21] Q. Li, H. Zeng, and J. Li, "Hyperchaos in a 4D memristive circuit with infinitely many stable equilibria," *Nonlinear Dynamics*, vol. 79, no. 4, pp. 2295–2308, 2015.
- [22] A. Adamatzky and L. Chua, *Memristor Networks*, Springer International Publishing, Switzerland, 2014.
- [23] Y. Zhang, X. Wang, and E. G. Friedman, "Memristor-based circuit design for multilayer neural networks," *IEEE Transactions on Circuits and Systems I: Regular Papers*, vol. 65, no. 2, pp. 677–686, 2018.
- [24] E. E. Mahmoud, "Complex complete synchronization of two nonidentical hyperchaotic complex nonlinear systems," *Mathematical Methods in the Applied Sciences*, vol. 37, no. 3, pp. 321–328, 2013.
- [25] G. M. Mahmoud and E. E. Mahmoud, "Complete synchronization of chaotic complex nonlinear systems with uncertain parameters," *Nonlinear Dynamics*, vol. 62, no. 4, pp. 875–882, 2010.
- [26] E. E. Mahmoud, "Dynamics and synchronization of new hyperchaotic complex Lorenz system," *Mathematical and Computer Modelling*, vol. 55, no. 7–8, pp. 1951–1962, 2012.
- [27] A. Wu and Z. Zeng, "Global Mittag-Leffler stabilization of fractional-order memristive neural networks," *IEEE Transactions on Neural Networks and Learning Systems*, vol. 28, no. 1, pp. 206–217, 2017.
- [28] P. Jiang, Z. Zeng, and J. Chen, "On the periodic dynamics of memristor-based neural networks with leakage and time-varying delays," *Neurocomputing*, vol. 219, pp. 163–173, 2017.
- [29] R. Rakkiyappan, R. Sivasamy, and X. Li, "Synchronization of identical and nonidentical memristor-based chaotic systems via active backstepping control technique," *Circuits, Systems, and Signal Processing*, vol. 34, no. 3, pp. 763–778, 2015.
- [30] J. Ma, F. Wu, G. Ren, and J. Tang, "A class of initial-dependent dynamical systems," *Applied Mathematics and Computation*, vol. 298, pp. 65–76, 2017.
- [31] C. Yakopcic, T. M. Taha, G. Subramanyam, and R. E. Pino, "Generalized memristive device SPICE model and its application in circuit design," *IEEE Transactions on Computer-Aided Design of Integrated Circuits and Systems*, vol. 32, no. 8, pp. 1201–1214, 2013.
- [32] M. Halimi, K. Kemih, and M. Ghanes, "Circuit simulation of an analog secure communication based on synchronized chaotic Chua's system," *Applied Mathematics & Information Sciences*, vol. 8, no. 4, pp. 1509–1516, 2014.

- [33] E. Tlelo-Cuautle, V. H. Carbajal-Gomez, P. J. Obeso-Rodelo, J. J. Rangel-Magdaleno, and J. C. Núñez-Pérez, "FPGA realization of a chaotic communication system applied to image processing," *Nonlinear Dynamics*, vol. 82, no. 4, pp. 1879–1892, 2015.
- [34] A. D. Pano-Azucena, J. de Jesus Rangel-Magdaleno, E. Tlelo-Cuautle, and A. de Jesus Quintas-Valles, "Arduino-based chaotic secure communication system using multi-directional multi-scroll chaotic oscillators," *Nonlinear Dynamics*, vol. 87, no. 4, pp. 2203–2217, 2017.
- [35] L. Xiong, Y. J. Lu, Y. F. Zhang, X. G. Zhang, and P. Gupta, "Design and hardware implementation of a new chaotic secure communication technique," *PLoS One*, vol. 11, no. 8, article e0158348, 2016.
- [36] X. G. Zhang, H. T. Sun, J. L. Zhao, J. Z. Liu, Y. D. Ma, and T. W. Han, "Equivalent circuit in function and topology to Chua's circuit and the design methods of these circuits," *Acta Physica Sinica*, vol. 63, no. 20, pp. 200503–200508, 2014.
- [37] M. F. Hassan, "Synchronization of uncertain constrained hyperchaotic systems and chaos-based secure communications via a novel de-composed non-linear stochastic estimator," *Nonlinear Dynamics*, vol. 83, no. 4, pp. 2183–2211, 2016.
- [38] L. Xiong, Z. Liu, and X. Zhang, "Dynamical analysis, synchronization, circuit design, and secure communication of a novel hyperchaotic system," *Complexity*, vol. 2017, Article ID 4962739, 23 pages, 2017.
- [39] R. L. Filali, M. Benrejeb, and P. Borne, "On observer-based secure communication design using discrete-time hyperchaotic systems," *Communications in Nonlinear Science and Numerical Simulation*, vol. 19, no. 5, pp. 1424–1432, 2014.
- [40] C. Wang, Y. He, J. Ma, and L. Huang, "Parameters estimation, mixed synchronization, and antisynchronization in chaotic systems," *Complexity*, vol. 20, no. 1, p. 73, 2014.

Research Article

A New Memristor-Based 5D Chaotic System and Circuit Implementation

Rui Wang ^{1,2}, Mingjin Li ³, Zhaoling Gao ² and Hui Sun ^{2,4}

¹Tianjin Key Laboratory for Civil Aircraft Airworthiness and Maintenance, Civil Aviation University of China, Tianjin 300300, China

²College of Information Engineering and Automation, Civil Aviation University of China, Tianjin 300300, China

³Engineering Technology Department, Sichuan Airlines, Chengdu 610202, China

⁴Department of Engineering Design and Mathematics, University of the West of England, Frenchay Campus, Coldharbour Lane, Bristol, BS 161QY, UK

Correspondence should be addressed to Rui Wang; ruiwang@cauc.edu.cn and Hui Sun; h-sun@cauc.edu.cn

Received 30 June 2018; Revised 5 October 2018; Accepted 29 October 2018; Published 2 December 2018

Guest Editor: Viet-Thanh Pham

Copyright © 2018 Rui Wang et al. This is an open access article distributed under the Creative Commons Attribution License, which permits unrestricted use, distribution, and reproduction in any medium, provided the original work is properly cited.

This paper proposes a new 5D chaotic system with the flux-controlled memristor. The dynamics analysis of the new system can also demonstrate the hyperchaotic characteristics. The design and analysis of adaptive synchronization for the new memristor-based chaotic system and its slave system are carried out. Furthermore, the modularized circuit designs method is used in the new chaotic system circuit implementation. The Multisim simulation and the physical experiments are conducted, compared, and matched with each other which can demonstrate the existence of the attractor for the new system.

1. Introduction

Memristors are the fourth kind of circuit elements except for resistors, capacitors, and conductors and are conceived by Chua in 1971 through the basic symmetric principle [1]. Furthermore, the corresponding theory was applied to memristive devices in 1976 [2]. It took a long time to develop the hardware memristor model. Until 2008 HP labs first realized the memristor of nanoscale in the form of crossbar array [3]. Since memristors have the potential applications in the wide range of fields, memristor study becomes hotter, and a huge amount of researchers have paid immense attention on memristor studies from industry and academics, respectively [4, 5]. The typical examples include nonvolatile memories of nanoscale [6], memristor-based synapse in neuromorphic systems [7, 8], logic operations through material implication [9–12], and nonlinear dynamics in chaotic system [13–17].

With rapid development of memristor models, some studies combine the memristor and chaotic systems including dynamics analysis, image encryption applications and circuit implementations which have grown up quickly in recent years [18–22]. One of the typical early memristor-based

chaotic systems was developed by Itoh and Chua in 2008 [19]. This paper developed some nonlinear oscillators by using memristors based on Chua's oscillators. Petráš derived and investigated a fractional-order memristor-based Chua's circuit in [20]. Chua and Muthuswamy also discussed circuit topology and developed the simplest memristor-based circuits [21]. These papers demonstrate that the memristor oscillators own the special nonlinear dynamics due to memristors' extinguished characteristics. One of these significant characteristics is that the behaviors are dependent on initial states and circuit parameters. Li et al. proposed a scroll chaotic system circuit implementation by using HP memristor [22]. Ma et al. developed a four-wing hyperchaotic system by using a memristor adding over a three-dimensional chaotic system [16]. Dimitrios et al. found a new 4-D memristive chaotic system and investigated the behavior with hidden attractors of the system through numerical simulations [23]. Wang et al. proposed a flux-controlled memristor model and established a 4-D chaotic system with this model. The numerical analysis and circuit implementation simulation verification were conducted [24]. Mou et al. discussed the characteristics of dynamical behaviors of a fractional-order

4D hyperchaotic memristive system and circuit simulation verification [25]. Other memristor-based hyperchaotic systems were also investigated such as numerical analysis about a four-dimensional hyperchaotic system with memristor and conducted circuit simulation verifications [26–29]. There are also some other chaotic systems developed by memristive models and its applications [30–32].

The above memristor-based chaotic system literatures focus on four or lower-dimensional chaotic systems and investigate the detailed numerical analysis and the corresponding numerical and circuit implementation simulation verifications. However, the higher-dimensional (5-D or above) memristor-based hyperchaotic systems and the corresponding physical hardware experiments are not found. Therefore, the paper analyzes a new memristor-based hyperchaotic system and develops a circuit physical implementation method by using the modularized design method. This method is used to design the circuit without dimensions for chaotic circuit designs and is easy to be implemented in the circuit by using less circuit parts [33–38].

The novelty of this paper is to develop a new memristor-based 5D hyperchaotic system, design and analyze the adaptive synchronization of this new system, implement the physical experiment circuit hardware, and verify the existence of system attractors. The improved modularized design method is used to implement the circuit of the system to verify the existence of attractors.

The rest of the paper is organized as follows. Section 2 analyzes the fundamental characteristics of the new memristor-based chaotic system. Section 3 investigates the adaptive synchronization of the new memristor-based hyperchaotic system. Section 4 discusses the circuit implementation of the new system and verifies the existence of attractors. Conclusions are presented in Section 5.

2. Analysis of a New Memristor-Based Hyperchaotic System

In this section, numerical analyses are conducted for a flux-controlled memristor-based new 5D hyperchaotic system derived from Wang's 4D hyperchaotic system.

As illustrated in [16], memristor model is based on the fundamental characteristics of a flux-controlled memristor described below.

$$i = W(\varphi) v \quad (1)$$

where i and v are the current and the voltage of the device terminal, respectively. $W(\varphi)$ is the incremental memductance defined as

$$W(\varphi) = \frac{dq(\varphi)}{d\varphi} \quad (2)$$

This demonstrates that the characteristics of a memristor are a nonlinear function reflecting the relationship among the charge and flux across and through the device.

Furthermore, this paper consistently uses the smooth cubic monotone-increasing continuous nonlinearity described as follows [20–22, 33].

$$dq(\varphi) = m\varphi + n\varphi^3 \quad (3)$$

where $m, n > 0$.

Then the memductance is shown below

$$W(\varphi) = \frac{dq(\varphi)}{d\varphi} = m + 3n\varphi^2 \quad (4)$$

This paper develops a 5D memristor-based chaotic system which is derived from four-wing autonomous chaotic dynamics systems reported by Wang et al. [34, 37]

$$\begin{aligned} \dot{x} &= a(y - x) + 4yz \\ \dot{y} &= -x + 16y - xz + w \\ \dot{z} &= -bz + xy \\ \dot{w} &= -10y + 0.15xz \\ \dot{u} &= -x \end{aligned} \quad (5)$$

This system has four state variables x, y, z , and w , and $a, b \in \mathbb{R}^+$.

Substitute (4) into (5), a 5D memristor-based system is obtained.

$$\begin{aligned} \dot{x} &= a(y - x) + 4yz - kxW(u) \\ \dot{y} &= -x + 16y - xz + w \\ \dot{z} &= -bz + xy - xu - yw \\ \dot{w} &= -10y + 0.15xz - gzu \\ \dot{u} &= -x \end{aligned} \quad (6)$$

where

$$W(u) = m + 3nu^2, \quad (7)$$

and k, m, n, g are positive parameters.

2.1. Equilibria and Stability. The equilibrium points of System (6) can be calculated by solving the equations as shown below

$$\begin{aligned} a(y - x) + 4yz - kxW(u) &= 0 \\ -x + 16y - xz + w &= 0 \\ -bz + xy - xu - yw &= 0 \\ -10y + 0.15xz - gzu &= 0 \\ -x &= 0 \end{aligned} \quad (8)$$

where $m = 0.1, n = 0.01$, and $g = 0.3$.

System (6) has only one real equilibrium point with $(0, 0, 0, 0, 0)$ and has typical characteristics with a line equilibrium in $(0, 0, 0, 0, \delta)$, given δ a real constant.

First, analyze the zero equilibrium point $(0, 0, 0, 0, 0)$. The Jacobian matrix of System (6) on the zero equilibrium point is

$$J_0 = \begin{pmatrix} -a-0.1k & a & 0 & 0 & 0 \\ -1 & 16 & 0 & 1 & 0 \\ 0 & 0 & b & 0 & 0 \\ 0 & -10 & 0 & 0 & 0 \\ -1 & 0 & 0 & 0 & 0 \end{pmatrix}_{(0,0,0,0,0)} \quad (9)$$

and the corresponding polynomial is

$$f(\lambda) = \lambda(\lambda - b)f_1(\lambda) \quad (10)$$

and

$$f_1(\lambda) = \lambda^3 + (a - 16 + 0.1k)\lambda^2 + (10 - 15a - 1.6k)\lambda + 10a + k \quad (11)$$

It is obvious that 0 and $-b$ are eigenvalues of System(6) for the $(0, 0, 0, 0, 0)$ equilibrium point. According to Routh-Hurwitz condition, if and only if $a - 16 + 0.1k > 0$, $10 - 15a - 1.6k > 0$, $(10a + k) > 0$, and $(a - 16 + 0.1k)(10 - 15a - 1.6k) - (10a + k) > 0$ coexist, $f_1(\lambda)$ has the negative real number. However, the above four inequalities are not able to be realized simultaneously. Then not all real parts of the eigenvalues are negative. Therefore, it is not a stable equilibrium point.

Second, analyze the eigenvalues of Jacobian matrix of System (6) on the line equilibrium in $(0, 0, 0, 0, \delta)$.

$$J_1 = \begin{pmatrix} -a - k(0.1 + 0.03\delta^2) & a & 0 & 0 & 0 \\ -1 & 16 & 0 & 1 & 0 \\ -\delta & 0 & -b & 0 & 0 \\ 0 & -10 & -0.3\delta & 0 & 0 \\ -1 & 0 & 0 & 0 & 0 \end{pmatrix} \quad (12)$$

Typically, when $a = 14$ and $b = 78$, J_1^* is calculated as shown below

$$J_1^* = \begin{pmatrix} -14 - k(0.1 + 0.03\delta^2) & 14 & 0 & 0 & 0 \\ -1 & 16 & 0 & 1 & 0 \\ -\delta & 0 & -78 & 0 & 0 \\ 0 & -10 & -0.3\delta & 0 & 0 \\ -1 & 0 & 0 & 0 & 0 \end{pmatrix} \quad (13)$$

Two of the five eigenvalues of J_1^* are complex conjugates; therefore, it is difficult to determine the stability of the line equilibria.

2.2. Symmetry. System (6) is symmetric with respect to z axis since it is invariant when applying the coordinate transformations.

$$(x, y, z, w, u) \longleftrightarrow (-x, -y, z, -w, -u) \quad (14)$$

2.3. Dissipativity. Furthermore, dissipative characteristics analysis of System (6) is shown below. The system divergence is given by

$$\begin{aligned} \nabla V &= \frac{\partial \dot{x}}{\partial x} + \frac{\partial \dot{y}}{\partial y} + \frac{\partial \dot{z}}{\partial z} + \frac{\partial \dot{w}}{\partial w} + \frac{\partial \dot{u}}{\partial u} \\ &= -a - kW(u) + 16 - b \\ &= -k(m + 3nu^2) + 16 - a - b \end{aligned} \quad (15)$$

when $k > 0$, $m > 0$, $n > 0$, $16 - a - b < 0$, $-k(m + 3nu^2) + 16 - a - b < 0$, System (6) is dissipative. The paper selects $m = 0.1$, $n = 0.01$ for equation (7), and $k = 0.02$ for System (6).

2.4. Lyapunov Spectrum and Bifurcation Diagram. Fix parameters $a = 14$, $b = 78$ and vary the parameter k , and the graphs about the Lyapunov exponents versus k , bifurcation diagram, and phase portraits are shown in Figure 1.

Figure 1 shows that the Lyapunov exponents vary with the parameter k changes. In the five Lyapunov exponents, three of them are obviously negative when $k \in [0, 5.9]$. The top two lines in Figure 1(b) demonstrate that these two kinds of Lyapunov exponents are bigger than zero, and systems are hyperchaotic systems when k lies in this range. In this paper, k will be selected in this range.

When $a = 14$, $b = 78$, $k = 0.02$, $m = 0.1$, $n = 0.01$, and $g = 0.3$, the Lyapunov exponents are calculated as $L_1 = 1.0241$, $L_2 = 0.0137$, $L_3 = -0.1735$, $L_4 = -2.3787$, and $L_5 = -70.3244$. This system is a hyperchaotic system with two positive Lyapunov exponents. Therefore, the Kaplan-Yorke dimension of System (6) can be found below

$$D_{KY} = 4 + \frac{L_1 + L_2 + L_3 + L_4}{|L_5|} = 3.978466 \quad (16)$$

3. Adaptive Synchronization of a New Memristor-Based Hyperchaotic System

In this section, the adaptive controller was designed for the new memristor-based hyperchaotic system which was derived by Lyapunov stability theory inspired by [39].

First, consider the master System (6) with $a = 14$, $b = 78$, $k = 0.02$, $m = 0.1$, $n = 0.01$, and $g = 0.3$ shown as below

$$\begin{aligned} \dot{x} &= 14(y - x) + 4yz - kx(0.1 + 0.01u^2) \\ \dot{y} &= -x + 16y - xz + w \\ \dot{z} &= -78z + xy - xu - yw \\ \dot{w} &= -10y + 0.15xz - 0.3zu \\ \dot{u} &= -x \end{aligned} \quad (17)$$

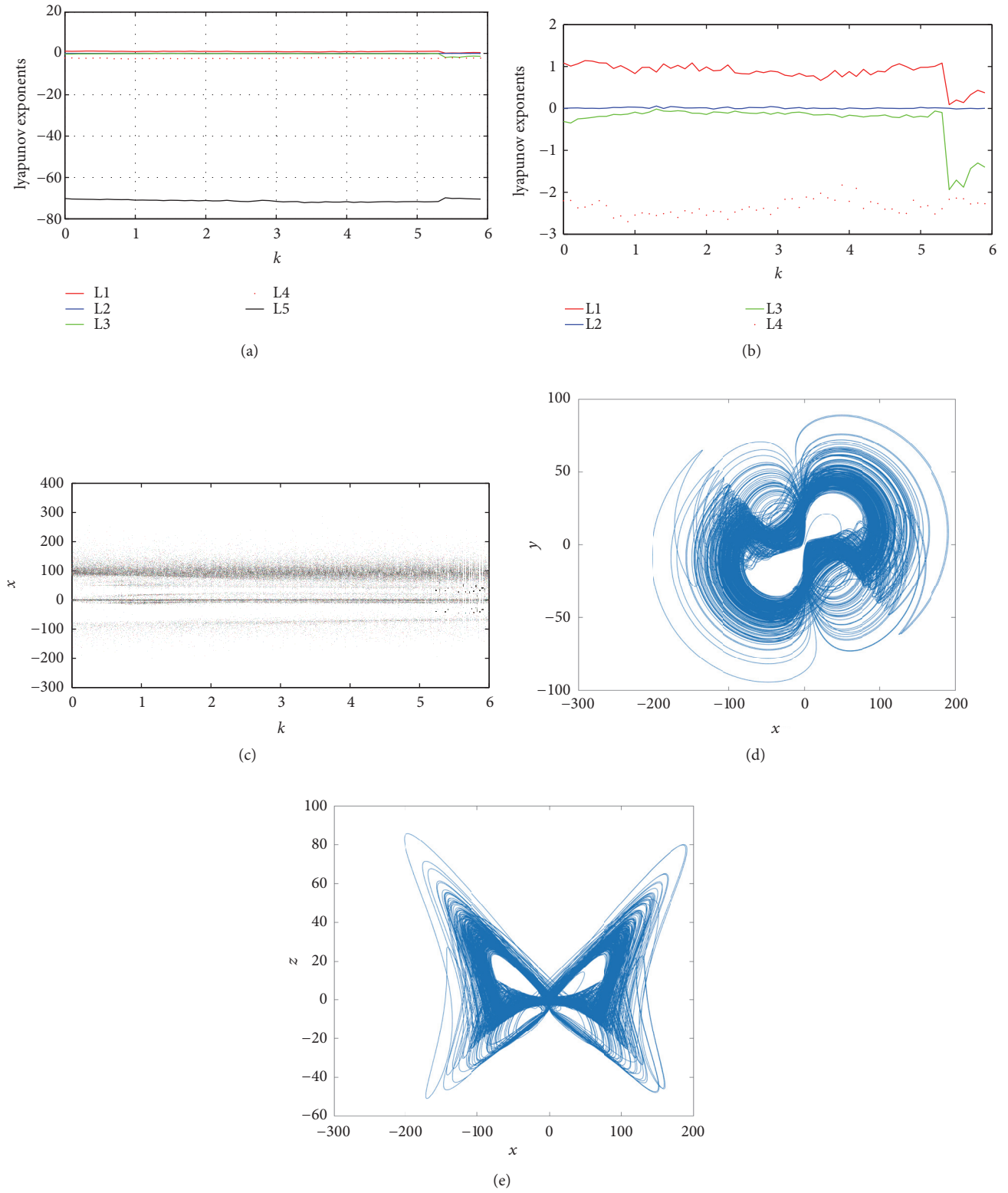


FIGURE 1: Lyapunov exponents versus the parameter k : (a) the full five exponents, (b) Lyapunov exponents L_1 - L_4 of System (6), (c) the bifurcation diagram of x vs. k for System (6) when $m = 0.1$, $n = 0.01$, and $g = 0.3$. (d)-(e) The phase portraits x - y and x - z for System (6) when $k = 0.02$, $m = 0.1$, $n = 0.01$, and $g = 0.3$.

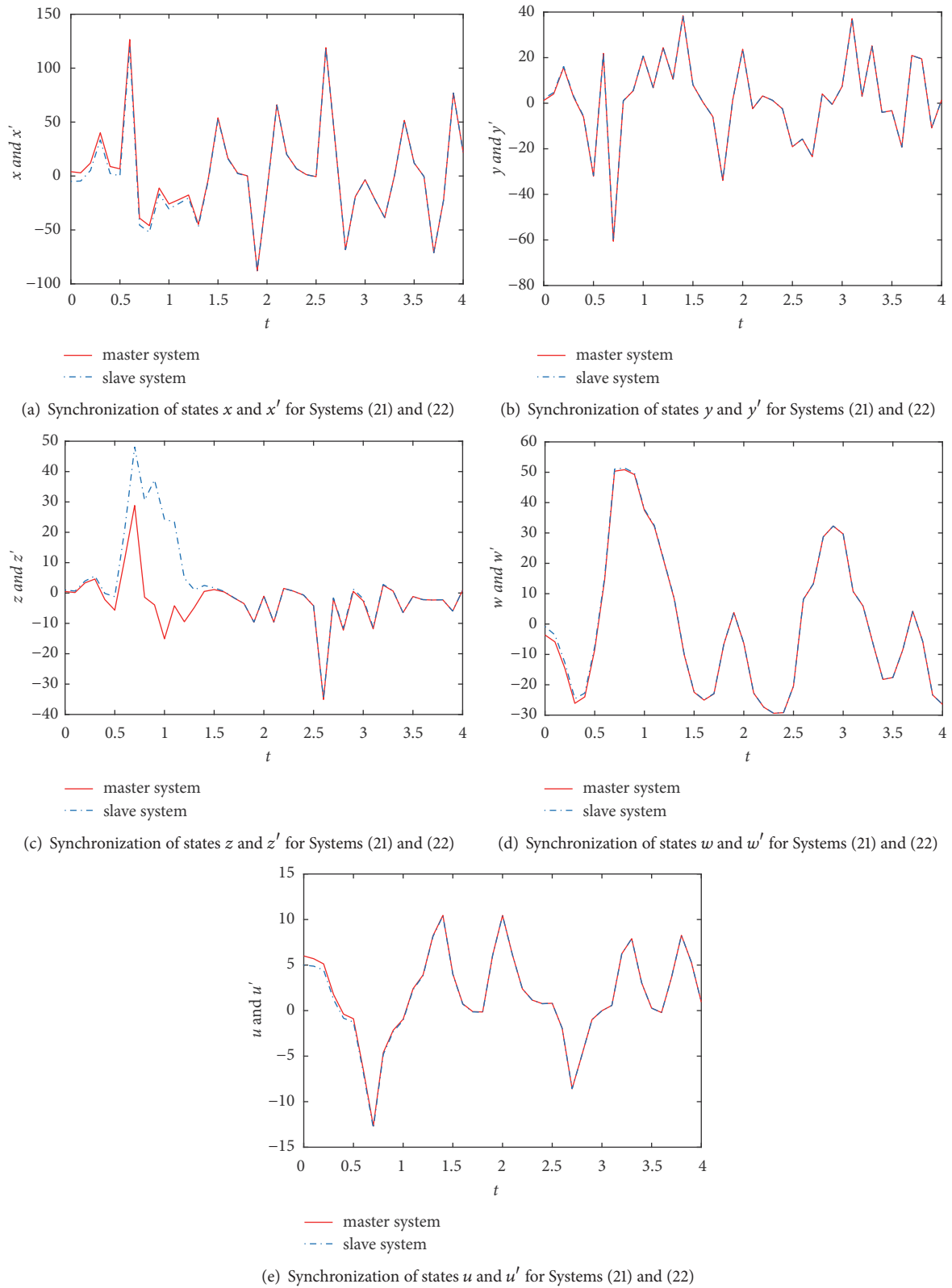
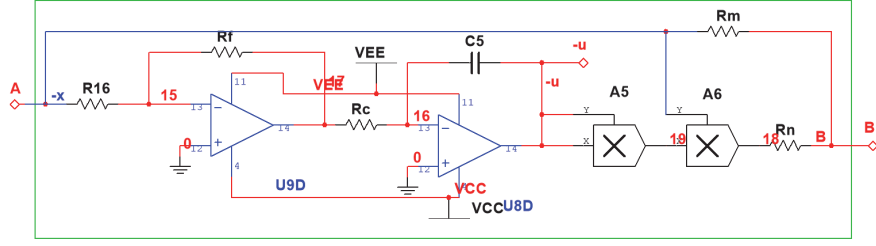
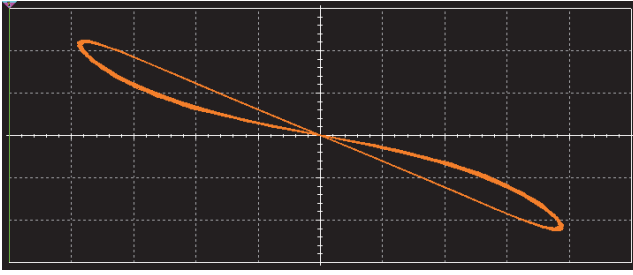


FIGURE 2: Synchronization of states for Systems (21) and (22).

FIGURE 3: $W(u)$ function-memristor channel.FIGURE 4: The relationship between x and $W(x)$ for the circuit as shown in Figure 3.

Second, consider the slave system shown as below

$$\begin{aligned}
 \dot{x}' &= 14(y' - x') + 4y'z' - kx'(0.1 + 0.01u'^2) + u_1 \\
 \dot{y}' &= -x' + 16y' - x'z' + w' + u_2 \\
 \dot{z}' &= -78z' + x'y' - x'u - y'w' + u_3 \\
 \dot{w}' &= -10y' + 0.15x'z' - 0.3z'u' + u_4 \\
 \dot{u}' &= -x' + u_5
 \end{aligned} \tag{18}$$

where u_i ($i = 1 \dots 5$) are adaptive controller, and x' , y' , z' , w' , u' are the new state variables.

Therefore, the synchronization errors among the Systems (17) and (18) are defined as follows.

$$\begin{aligned}
 e_1 &= x' - x \\
 e_2 &= y' - y \\
 e_3 &= z' - z \\
 e_4 &= w' - w \\
 e_5 &= u' - u
 \end{aligned} \tag{19}$$

Then the dynamics of the error can be calculated by substituting the master and slave systems as shown below

$$\begin{aligned}
 \dot{e}_1 &= a(e_2 - e_1) - 0.1ke_1 + 4(y'z' - yz) \\
 &\quad - 0.03k(x'u'^2 - xu^2) + u_1 \\
 \dot{e}_2 &= -e_1 + 16e_2 + e_4 - x'z' + xz + u_2 \\
 \dot{e}_3 &= -be_3 + x'y' - x'u' - y'w' - xy + xu + yw + u_3 \\
 \dot{e}_4 &= -10e_2 + 0.15x'z' - 0.15xz - 0.3z'u' + 0.3zu \\
 &\quad + u_4 \\
 \dot{e}_5 &= -e_1 + u_5
 \end{aligned} \tag{20}$$

where the adaptive controller u_i are defined by

$$\begin{aligned}
 u_1 &= -\hat{a}(t)(e_2 - e_1) + 0.1ke_1 - 4(y'z' - yz) \\
 &\quad + 0.03k(x'u'^2 - xu^2) - k_1e_1 \\
 u_2 &= e_1 - 16e_2 - e_4 + x'z' - xz - k_2e_2 \\
 u_3 &= \hat{b}(t)e_3 - x'y' + x'u' + y'w' + xy - xu - yw \\
 &\quad - k_3e_3 \\
 u_4 &= 10e_2 - 0.15x'z' + 0.15xz + 0.3z'u' - 0.3zu \\
 &\quad - k_4e_4 \\
 u_5 &= e_1 - k_5e_5
 \end{aligned} \tag{21}$$

where k_i ($i = 1, \dots, 5$) are the positive gains and $\hat{a}(t)$, $\hat{b}(t)$ are the estimations of the corresponding parameters a and b , respectively.

Correspondingly, the dynamics of the error is changed into

$$\begin{aligned}
 \dot{e}_1 &= (a - \hat{a}(t))(e_2 - e_1) - k_1e_1 \\
 \dot{e}_2 &= -k_2e_2 \\
 \dot{e}_3 &= (b - \hat{b}(t))e_3 - k_3e_3 \\
 \dot{e}_4 &= -k_4e_4 \\
 \dot{e}_5 &= -k_5e_5
 \end{aligned} \tag{22}$$

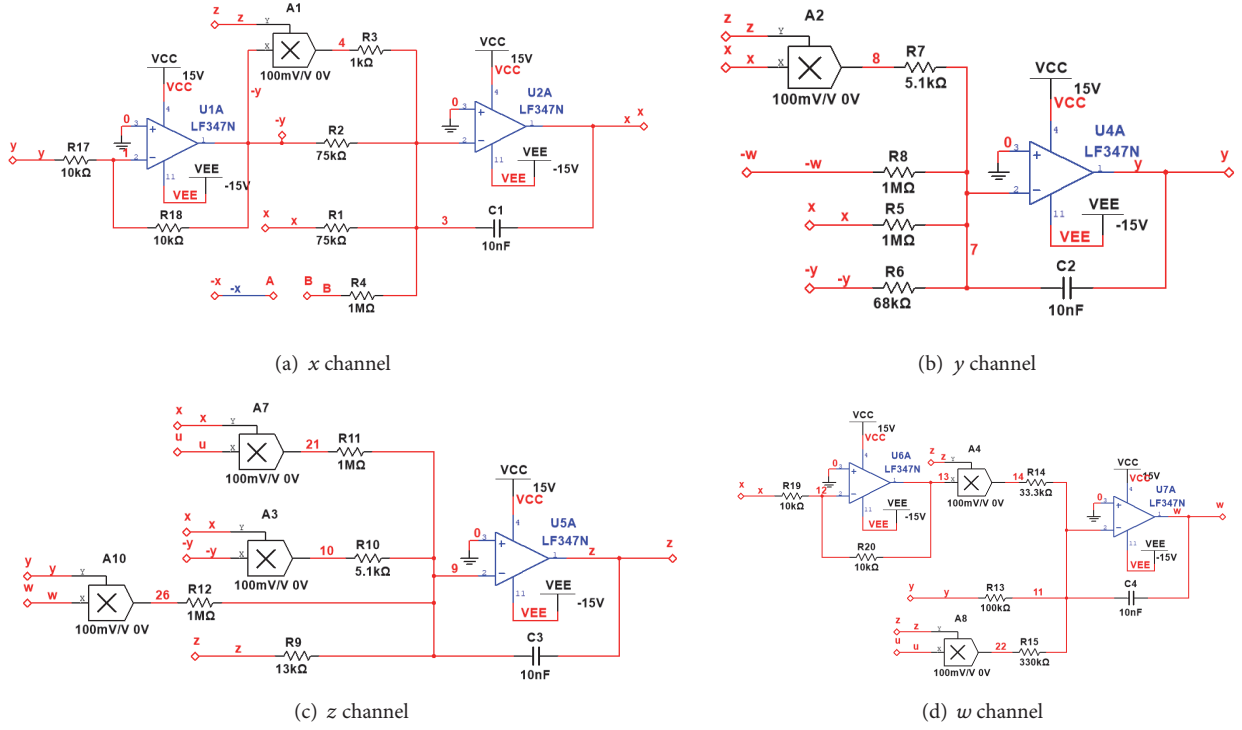


FIGURE 5: Modularized circuit channels for circuit implementation of the new memristor-based 5D hyperchaotic system.

Define the parameters for estimating errors as

$$\begin{aligned} e_a(t) &= a - \hat{a}(t) \\ e_b(t) &= b - \hat{b}(t) \end{aligned} \quad (23)$$

Substitute (23) into the dynamics (22), the simplified error dynamics is described as

$$\begin{aligned} \dot{e}_1 &= e_a(t)(e_2 - e_1) - k_1 e_1 \\ \dot{e}_2 &= -k_2 e_2 \\ \dot{e}_3 &= -e_b(t)e_3 - k_3 e_3 \\ \dot{e}_4 &= -k_4 e_4 \\ \dot{e}_5 &= -k_5 e_5 \end{aligned} \quad (24)$$

Correspondingly,

$$\begin{aligned} \dot{e}_a(t) &= -\hat{a}(t) \\ \dot{e}_b(t) &= -\hat{b}(t) \end{aligned} \quad (25)$$

Depending on the master and slave systems definitions and error dynamics transformations mentioned above, consider a Lyapunov function defined by

$$V = \frac{1}{2} (e_1^2 + e_2^2 + e_3^2 + e_4^2 + e_5^2 + e_a^2 + e_b^2) \quad (26)$$

Differentiate V along the trajectories for equations (24)-(25), \dot{V} can be obtained as

$$\begin{aligned} \dot{V} &= e_1 \dot{e}_1 + e_2 \dot{e}_2 + e_3 \dot{e}_3 + e_4 \dot{e}_4 + e_5 \dot{e}_5 + e_a \dot{e}_a + e_b \dot{e}_b \\ &= -k_1 e_1^2 - k_2 e_2^2 - k_3 e_3^2 - k_4 e_4^2 - k_5 e_5^2 \\ &\quad + e_a [-e_1^2 - e_1 e_2 - \hat{a}(t)] - e_b(t) [e_3^2 + \hat{b}(t)] \end{aligned} \quad (27)$$

Then, the parameter update law is

$$\begin{aligned} \dot{\hat{a}}(t) &= -e_1^2 - e_1 e_2 \\ \dot{\hat{b}}(t) &= -e_3^2 \end{aligned} \quad (28)$$

Theorem 1. The master and slave Systems (17)-(18) for a new memristor-based hyperchaotic system along with unknown parameters and positive gains k_i ($i = 1 \dots 5$) synchronize exponentially by using the adaptive controller (21) and the parameter update law (28).

Proof. Substitute the parameter update law (28) into the adaptive controller (21), then

$$\begin{aligned} \dot{V} &= -k_1 e_1^2 - k_2 e_2^2 - k_3 e_3^2 - k_4 e_4^2 - k_5 e_5^2 \leq -k' \|e\|^2 \\ &\leq 0 \end{aligned} \quad (29)$$

where $k' = \min\{k_1, k_2, k_3, k_4, k_5 \mid k_i \in \mathbb{R}^+, i = 1 \dots 5\}$. \square

It is obvious that $e(t) \rightarrow 0$ exponentially as time goes to infinite for all initial conditions of $e(0)$. According to Lyapunov stability theory, two systems are synchronized.

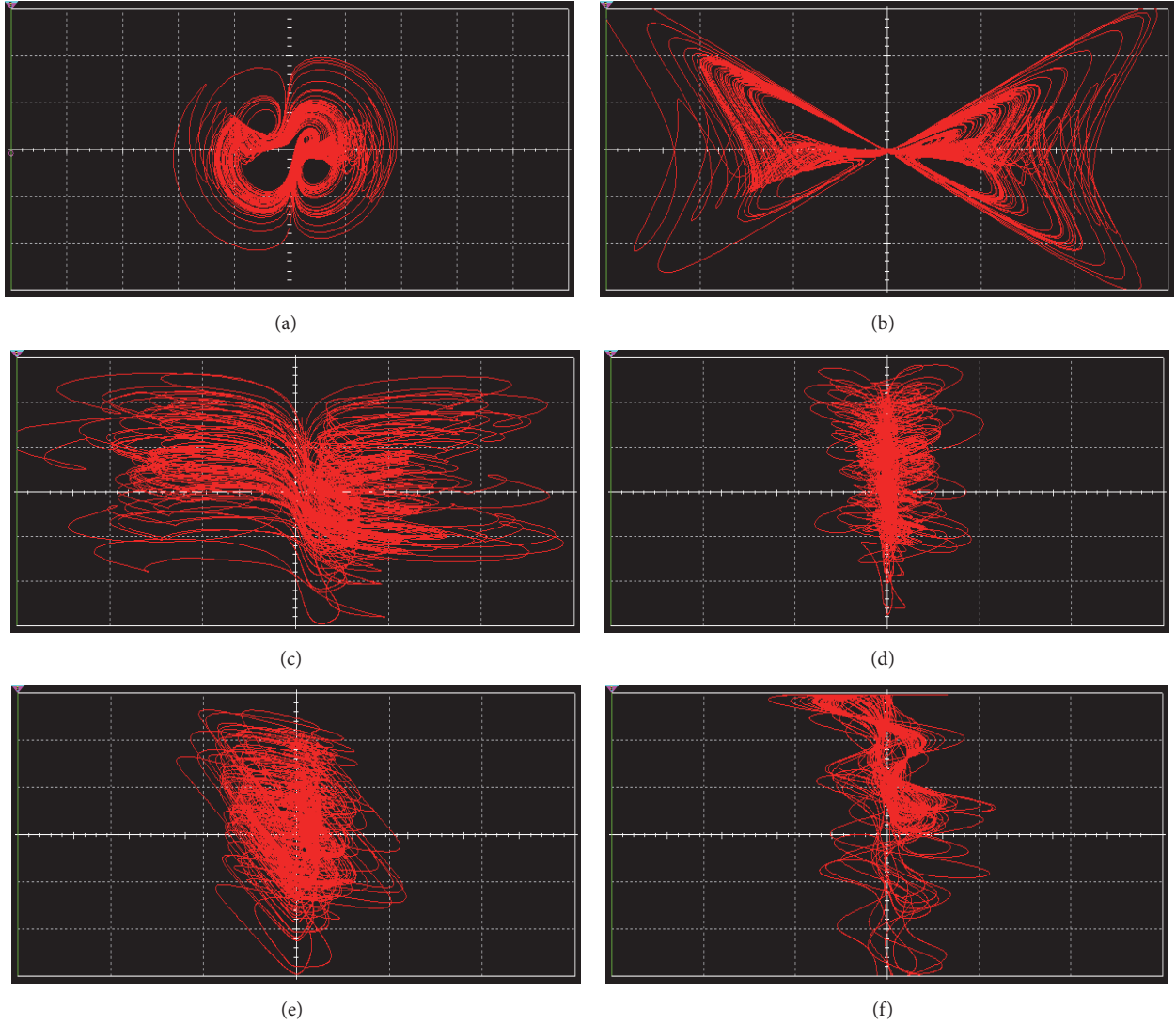


FIGURE 6: Multisim implementation of the chaotic System (17): (a) x - y plane with scales 5 V/div and 2 V/div, (b) x - z plane with scales 2 V/div and 1 V/div, (c) x - w plane with scales 2 V/div and 1 V/div, (d) z - w plane with scales 2 V/div and 1 V/div, (e) y - w plane with scales 2 V/div and 1 V/div, and (f) y - u plane with scales 2 V/div and 2 V/div.

Figure 2 is the simulation verification of synchronization for the master and the slave memristor-based hyperchaotic Systems (21) and (22) when selecting $k' = k_i = 4$ ($i = 1 \cdots 5$), and the systems choose the initial conditions for both systems, respectively, such that $x(0) = 4$, $y(0) = 1.2$, $z(0) = 0.5$, $w(0) = -3.6$, $u(0) = 6$ and $x'(0) = -5$, $y'(0) = 2$, $z'(0) = 1$, $w'(0) = -0.8$, $u'(0) = 5$. These figures demonstrate the synchronization of the master and slave Systems (21) and (22).

4. A New Memristor-Based Hyperchaotic System Circuit Implementation

In this section, modularized design methods will be implemented in the new memristor-based hyperchaotic systems

mentioned above. Multisim software is used to generate the circuit simulation results, and the corresponding physical circuit experiments are conducted to verify the hyperchaotic attractor existences of this hyperchaotic system.

(A1) *Memristors Circuit Implementation.* Figure 3 shows the circuit configuration of memristor inspired by [16].

In this memristor circuit, a factor $0.1/V$ multiplier AD633JN is used. Therefore, $m = R_f/R_m = 0.1$, $n = (100R_f/R_n)(0.01/V) = 0.01$, and

$$W = \frac{R_f}{R_m} + 3 \cdot \frac{100R_f}{R_n} \left(\frac{0.01}{V} \right) \cdot u^2 \quad (30)$$

where R_f is the feedback resistor of the amplifier.

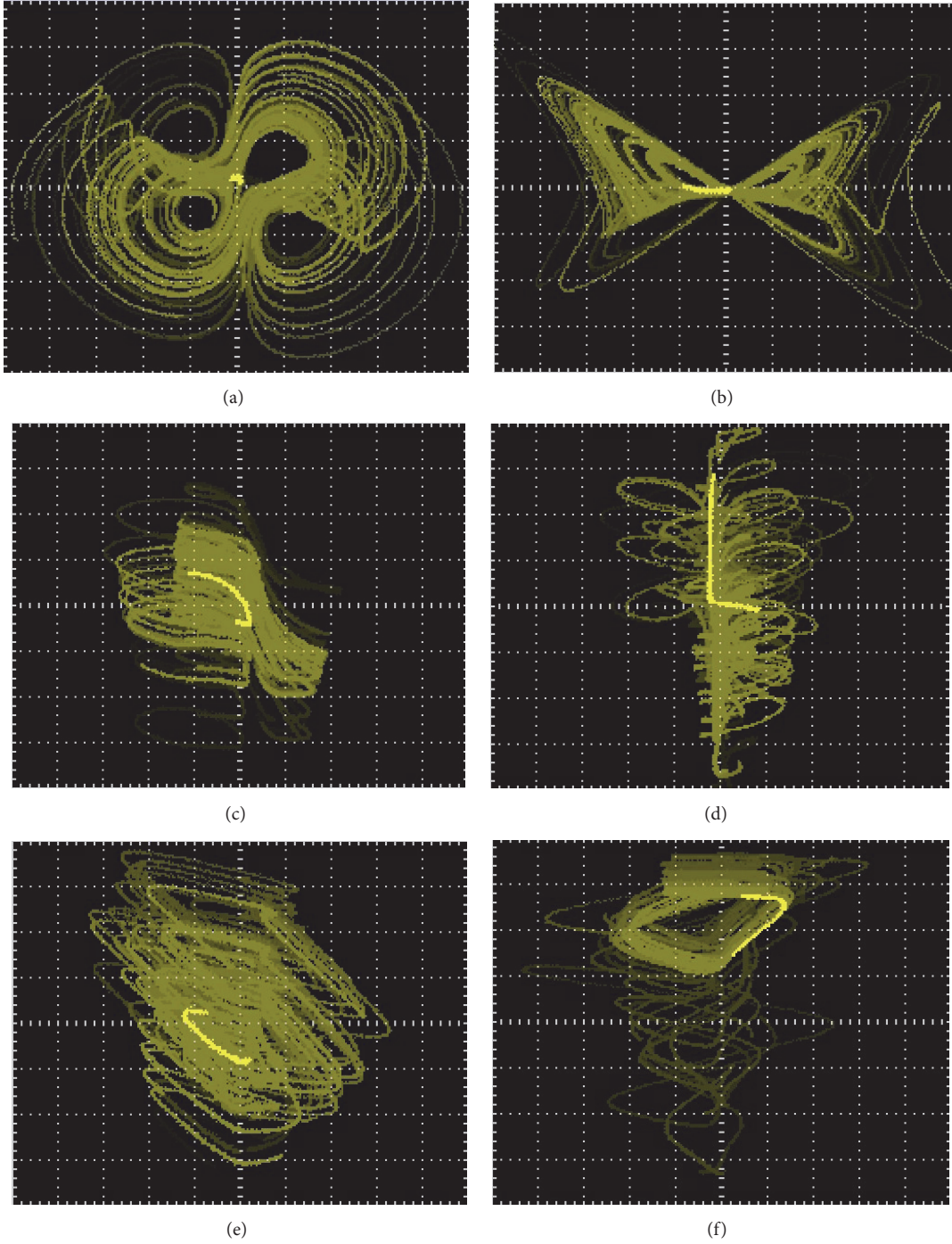


FIGURE 7: Physical circuit implementation hardware and digital oscilloscope diagrams of the chaotic System (17): (a) x - y plane with scales 2 V/div and 1 V/div, (b) x - z plane with scales 2 V/div and 1 V/div, (c) x - w plane with scales 2 V/div and 1 V/div, (d) z - w plane with scales 1 V/div and 1 V/div, (e) y - w plane with scales 1 V/div and 1 V/div, and (f) y - u plane with scales 1 V/div and 2 V/div.

Parameter k represents the strength of a memristor.

$$k = \frac{R_f}{mR_m} = \frac{R_f}{300nR_n} \quad (31)$$

In Figure 4, select the following resistors and the capacitor, $R_f = 2k\Omega$, $R_m = 1M\Omega$, $R_n = 66k\Omega$, $R_{15} = 200k\Omega$, $R_c = 1k\Omega$, $C_4 = 10nF$.

Figure 4 is the Multisim simulation for the flux-controlled memristor with x input with sinusoid signal. This demonstrates the typical closed loop characteristics of the memristor developed by equation (7) and part of equation (6).

(A2) *Memristor-Based Chaotic System Circuit Analysis.* The implementation of memristor-based chaotic system uses the

modularized design method applied on System (17). After the time-scale transformation method is applied on System (17), System (17) becomes System (32).

$$\begin{aligned}
\frac{dx}{dt} &= -\frac{1}{\tau_0 R_1 C_1} x - \frac{1}{\tau_0 R_2 C_1} (-y) \\
&\quad - \frac{1}{10\tau_0 R_3 C_1} (-y) z - \frac{1}{10\tau_0 R_4 C_1} kxW(u) \\
\frac{dy}{dt} &= -\frac{1}{\tau_0 R_5 C_2} x - \frac{1}{\tau_0 R_6 C_2} (-y) - \frac{1}{10\tau_0 R_7 C_2} xz \\
&\quad - \frac{1}{\tau_0 R_8 C_2} (-w) \\
\frac{dz}{dt} &= -\frac{1}{\tau_0 R_9 C_3} z - \frac{1}{10\tau_0 R_{10} C_3} x(-y) \\
&\quad - \frac{1}{10\tau_0 R_{11} C_3} xu - \frac{1}{10\tau_0 R_{12} C_3} yw \\
\frac{dw}{dt} &= -\frac{1}{\tau_0 R_{13} C_4} y - \frac{1}{10\tau_0 R_{14} C_4} x(-z) \\
&\quad - \frac{1}{10\tau_0 R_{15} C_4} zu \\
\frac{du}{dt} &= -\frac{1}{\tau_0 R_{16} C_5} x
\end{aligned} \tag{32}$$

where $\tau_0 = 100$.

Therefore,

$$\begin{aligned}
\frac{dx}{dt} &= -1400x - 1400(-y) - 400(-y)z \\
&\quad - 100kxW(u) \\
\frac{dy}{dt} &= -100x - 1600(-y) - 100xz - 100(-w) \\
\frac{dz}{dt} &= -7800z - 100x(-y) - 100xu - 100yw \\
\frac{dw}{dt} &= -1000y - 15x(-z) - 30zu \\
\frac{du}{dt} &= -100x
\end{aligned} \tag{33}$$

Furthermore, the paper employs the unified compression coefficient, $s = 1/20$, for each variable in order not to exceed the range of the oscilloscope used to the circuit. Then

$$\begin{aligned}
sx &\longrightarrow x \\
sy &\longrightarrow y \\
sz &\longrightarrow z \\
sw &\longrightarrow w
\end{aligned} \tag{34}$$

Substituting (34) into (33), we can obtain

$$\begin{aligned}
\frac{dx}{dt} &= -1400x - 1400(-y) - 8000(-y)z \\
&\quad - 100kxW(u) \\
\frac{dy}{dt} &= -100x - 1600(-y) - 2000xz - 100(-w) \\
\frac{dz}{dt} &= -7800z - 100x(-y) - 2000xu - 2000yw \\
\frac{dw}{dt} &= -1000y - 300x(-z) - 600zu \\
\frac{du}{dt} &= -100x
\end{aligned} \tag{35}$$

Comparing equations (35) to (32), parameters R and C in the circuit can be calculated when using the factor of 0.1 multiplier. $R_1=R_2=75k\Omega$, $R_3=1k\Omega$, $R_4=1M\Omega$, $R_5=1M\Omega$, $R_6=68k\Omega$, $R_7=5.1k\Omega$, $R_8=1M\Omega$, $R_9=13k\Omega$, $R_{10}=5.1k\Omega$, $R_{11}=R_{12}=1M\Omega$, $R_{13}=100k\Omega$, $R_{14}=33.3k\Omega$, $R_{15}=330k\Omega$, $R_{16}=220k\Omega$.

In the modularized circuit design for System (17), there are five channels for each variable. The circuit implementation uses analog amplifiers LF347N and AD633JN multipliers to implement the addition and the integral operations. Some additional R and C components are also selected in the circuit implementation. $R_{17}=R_{18}=R_{19}=R_{20}=10k\Omega$, $R_{21}=R_{22}=R_{23}=R_{24}=20k\Omega$, $C_1=C_2=C_3=C_4=C_5=10nF$, $R_f=2.2k\Omega$, $R_c=1k\Omega$, $R_m=1M\Omega$, $R_n=68k\Omega$.

The circuit channels for first four variables are shown in Figure 5, and the fifth one is shown in Figure 3.

(A3) Circuit Implementation for the New 5D Chaotic Systems. According to the circuit design, the Multisim simulation implementation for the memristor-based hyperchaotic System (17) is demonstrated in Figure 6. That shows the attractor phases graphs of different planes for System (17).

Attractor phases of System (17) as shown in Figure 6 own similar hyperchaotic characteristics with those of System (5) which are elaborated in [37]. It is known that practical analog devices are not ideal. Therefore, in reality, the voltages added on the amplifiers are not exceeding $\pm 13.5V$ in order to guarantee the system variable outputs do not exceed the amplifier linear region. This paper employs $\pm 12.5V$ across the amplifier in the physical circuits hardware, and the corresponding attractor phases graphs are shown in Figure 7.

Comparing Figure 6 to Figure 7, it is shown that the physical experiment attractor phase results match those conducted by Multisim and demonstrate the existence of the memristor-based hyperchaotic attractor for System (17). Furthermore, the memristor-based Wang hyperchaotic system has similar characteristics with those of the original Wang hyperchaotic system which is verified by the Multisim simulation and physical experimental results. The improved modularized method with compression coefficients is flexible, reliable, and straightforward to realize the physical implementation. The memristor-based hyperchaotic system has potential and

bright application physically. For example, it can realize the physical communication encryptions more reliably and easily. Future works will focus on the physical applications for communication encryptions by using the memristor-based hyperchaotic system.

5. Conclusions

The paper developed a new 5D memristor-based chaotic system with a flux-controlled memristor. The dynamics analysis of the system showed that the new system is a hyperchaotic system. The adaptive controller and update laws for the synchronization of the new system were designed and conducted. Furthermore, the modularized design method for the physical circuit experiment implementation is applied to realize the circuit by Multisim and physical experiments hardware. After the implementation of these circuits, then the comparisons between Multisim simulation and results from the physical experiments showed that these two kinds of results matched with each other and verified the existence of the attractors from the phase plane graphs. Furthermore, this new higher-dimensional chaotic system with memristor owns more complex dynamics and can be applied in a wide range of applications such as encryptions. This is also the future work for this work.

Data Availability

The data used to support the findings of this study are available from the corresponding author upon request.

Conflicts of Interest

The authors declare that there are no conflicts of interest regarding the publication of this paper.

Acknowledgments

This work was supported by grants from the project supported by the Scientific Research Starting Foundation for the Returned Overseas Chinese Scholars, Ministry of Education of China, Tianjin Key Laboratory of Civil Aircraft Airworthiness and Maintenance in CAUC (104003020106) and the National Basic Research Program of China (3122017009).

References

- [1] L. O. Chua, "Memristor—the missing circuit element," *IEEE Transactions on Circuit Theory*, vol. 18, no. 5, pp. 507–519, 1971.
- [2] K. J. Kuhn, "Considerations for ultimate CMOS scaling," *IEEE Transactions on Electron Devices*, vol. 59, no. 7, pp. 1813–1828, 2012.
- [3] D. B. Strukov, G. S. Snider, D. R. Stewart, and R. S. Williams, "The missing memristor found," *Nature*, vol. 453, pp. 80–83, 2008.
- [4] G. Wang, M. Cui, B. Cai, X. Wang, and T. Hu, "A Chaotic Oscillator Based on HP Memristor Model," *Mathematical Problems in Engineering*, vol. 2015, Article ID 561901, 12 pages, 2015.
- [5] L. Chua, "Memristor, hodgekin-huxley, and edge of chaos," *Nanotechnology*, vol. 24, no. 38, Article ID 383001, 2013.
- [6] P. Junsangsri and F. Lombardi, "Design of a hybrid memory cell using memristance and ambipolarity," *IEEE Transactions on Nanotechnology*, vol. 12, no. 1, pp. 71–80, 2013.
- [7] M. R. Azghadi, B. Linares-Barranco, D. Abbott, and P. H. W. Leong, "A Hybrid CMOS-Memristor Neuromorphic Synapse," *IEEE Transactions on Biomedical Circuits and Systems*, vol. 11, no. 2, pp. 434–445, 2017.
- [8] S. H. Jo, T. Chang, I. Ebong, B. B. Bhadviya, P. Mazumder, and W. Lu, "Nanoscale memristor device as synapse in neuromorphic systems," *Nano Letters*, vol. 10, no. 4, pp. 1297–1301, 2010.
- [9] J. Borghetti, G. S. Snider, P. J. Kuekes, J. J. Yang, D. R. Stewart, and R. S. Williams, "Memristive switches enable 'stateful' logic operations via material implication," *Nature*, vol. 464, no. 7290, pp. 873–876, 2010.
- [10] Y. Zhang, Y. Shen, X. Wang, and Y. Guo, "A novel design for memristor-based OR gate," *IEEE Transactions Circuits Systems II: Express Briefs*, vol. 62, p. 1, 2015.
- [11] X. Zhu, X. J. Yang, C. Q. Wu, N. Xiao, J. J. Wu, and X. Yi, "Performing stateful logic on memristor memory," *IEEE Transactions on Circuits and Systems II: Express Briefs*, vol. 60, no. 10, pp. 682–686, 2013.
- [12] Q. Chen, X. Wang, H. Wan, R. Yang, and J. Zheng, "A circuit design for multi-inputs stateful OR gate," *Physics Letters A*, vol. 380, no. 38, pp. 3081–3085, 2016.
- [13] L. Wang and S. Duan, "A chaotic attractor in delayed memristive system," *Abstract and Applied Analysis*, Art. ID 726927, 7 pages, 2012.
- [14] F. Setoudeh, A. Khaki Sedigh, and M. Dousti, "Analysis of a chaotic memristor based oscillator," *Abstract and Applied Analysis*, vol. 2014, 2014.
- [15] B. Muthuswamy, "Implementing memristor based chaotic circuits," *International Journal of Bifurcation and Chaos*, vol. 20, no. 5, pp. 1335–1350, 2010.
- [16] J. Ma, Z. Chen, Z. Wang, and Q. Zhang, "A four-wing hyperchaotic attractor generated from a 4D memristive system with a line equilibrium," *Nonlinear Dynamics*, vol. 81, no. 3, pp. 1275–1288, 2015.
- [17] J. Zhang, "Combination-combination hyperchaos synchronization of complex memristor oscillator system," *Mathematical Problems in Engineering*, vol. 2014, Article ID 591089, 13 pages, 2014.
- [18] Z.-H. Lin and H.-X. Wang, "Image encryption based on chaos with PWL memristor in Chua's circuit," in *Proceedings of the 2009 International Conference on Communications, Circuits and Systems, ICCAS 2009*, pp. 964–968, USA, July 2009.
- [19] M. Itoh and L. O. Chua, "Memristor oscillators," *International Journal of Bifurcation & Chaos*, vol. 18, pp. 3183–3206, 2008.
- [20] I. Petráš, "Fractional-order memristor-based Chua's circuit," *IEEE Transactions on Circuits and Systems II: Express Briefs*, vol. 57, no. 12, pp. 975–979, 2010.
- [21] B. Muthuswamy and L. O. Chua, "Simplest chaotic circuit," *International Journal of Bifurcation and Chaos*, vol. 20, no. 5, pp. 1567–1580, 2010.
- [22] H. Li, L. Wang, and S. Duan, "A memristor-based scroll chaotic system-design, analysis and circuit implementation," *International Journal of Bifurcation & Chaos*, vol. 24, no. 7, pp. 1–10, 2014.

- [23] D. A. Prousalis, C. K. Volos, I. N. Stouboulos, and I. M. Kyprianidis, "4-D memristive chaotic system with different families of hidden attractors, 2018.
- [24] C. Wang, H. Xia, and L. Zhou, "Implementation of a new memristor-based multiscroll hyperchaotic system," *Pramana—Journal of Physics*, vol. 88, no. 2, 2017.
- [25] J. Mou, K. Sun, H. Wang, and J. Ruan, "Characteristic Analysis of Fractional-Order 4D Hyperchaotic Memristive Circuit," *Mathematical Problems in Engineering*, vol. 2017, Article ID 2313768, 13 pages, 2017.
- [26] Y. Li, W. Chi, and X. Huang, "A New Memristor Based Hyperchaotic System," in *Proceedings of the 2012 5th International Workshop on Chaos-Fractals Theories and Applications (IWCFTA)*, pp. 131–135, Dalian, Liaoning, China, October 2012.
- [27] W. Shen, Z. Zeng, and G. Wang, "Feedback stabilization of memristor-based hyperchaotic systems," in *Proceedings of the 2013 IEEE 3rd International Conference on Information Science and Technology, ICIST 2013*, pp. 211–214, China, March 2013.
- [28] P. Liu, R. Xi, P. Ren, J. Hou, and X. Li, "Analysis and Implementation of a New Switching Memristor Scroll Hyperchaotic System and Application in Secure Communication," *Complexity*, vol. 2018, Article ID 3497640, 15 pages, 2018.
- [29] V.-T. Pham, C. Volos, and L. V. Gambuzza, "A memristive hyperchaotic system without equilibrium," *The Scientific World Journal*, vol. 2014, Article ID 368986, 2014.
- [30] V. T. Pham, S. Vaidyanathan, C. K. Volos, S. Jafari, and X. Wang, "A chaotic hyperjerk system based on memristive device," in *Advances and Applications in Chaotic Systems*, Springer International Publishing, 2016.
- [31] D. A. Prousalis, C. K. Volos, I. N. Stouboulos, and I. M. Kyprianidis, "Hyperchaotic memristive system with hidden attractors and its adaptive control scheme," *Nonlinear Dynamics*, vol. 90, no. 3, pp. 1681–1694, 2017.
- [32] A. G. Radwan, A. T. Azar, S. Vaidyanathan, J. M. Munoz-Pacheco, and A. Ouannas, "Fractional-Order and Memristive Nonlinear Systems: Advances and Applications," *Complexity*, vol. 2017, Article ID 3760121, 2 pages, 2017.
- [33] J. Ma, L. Wang, S. Duan, and Y. Xu, "A multi-wing butterfly chaotic system and its implementation," *International Journal of Circuit Theory and Applications*, vol. 45, no. 11, pp. 1873–1884, 2017.
- [34] J. Wang, H. Li, R. Wang, L. Wang, and Y. Wang, "A new four-dimensional smooth four-wing hyperchaotic system and its circuit implementation," *Journal of Shandong University (Natural Science)*, vol. 50, no. 11, pp. 104–112, 2015.
- [35] S. M. Yu, *Chaotic Systems and Chaotic Circuits- Principle, Design and its application in communications*, XiDian University Press, Xian, 1st edition, 2011.
- [36] S. M. Yu, W. K. S. Tang, and G. Chen, "Design and implementation of multi-wing butterfly chaotic attractors via Lorenz-type systems," *International Journal of Bifurcation & Chaos*, vol. 20, pp. 29–41, 2010.
- [37] R. Wang, H. Sun, J. Wang, L. Wang, and Y. Wang, "Applications of modularized circuit design in a new hyper-chaotic system circuit implementation," *Chinese Physics B*, vol. 24, Article ID 020501, 2015.
- [38] R. Wang, Q. Xie, Y. Huang, H. Sun, and Y. Sun, "Design of a switched hyperchaotic system and its application," *International Journal of Computer Applications in Technology*, vol. 57, no. 3, p. 207, 2018.
- [39] S. Vaidyanathan, V.-T. Pham, C. Volos, and X. Wang, "A Chaotic System with an Infinite Number of Equilibrium Points: Dynamics, Horseshoe, and Synchronization," *Advances in Mathematical Physics*, vol. 2016, Article ID 4024836, 8 pages, 2016.

Research Article

New Results on Fuzzy Synchronization for a Kind of Disturbed Memristive Chaotic System

Bo Wang^{1,2} and L. L. Chen¹

¹*School of Electrical and Information Engineering, Xihua University, Chengdu 610039, China*

²*School of Applied Mathematics, University Electronic Science and Technology of China, Chengdu 610054, China*

Correspondence should be addressed to Bo Wang; coolbie@163.com

Received 13 May 2018; Accepted 2 September 2018; Published 1 November 2018

Guest Editor: Viet-Thanh Pham

Copyright © 2018 Bo Wang and L. L. Chen. This is an open access article distributed under the Creative Commons Attribution License, which permits unrestricted use, distribution, and reproduction in any medium, provided the original work is properly cited.

This paper concerns the problem on the fuzzy synchronization for a kind of disturbed memristive chaotic system. First, based on fuzzy theory, the fuzzy model for a memristive chaotic system is presented; next, based on H-infinity technique, a multidimensional fuzzy controller and a single-dimensional fuzzy controller are designed to realize the synchronization of master-slave chaotic systems with disturbances. Finally, some typical examples are included to illuminate the correctness of the given control method.

1. Introduction

Since May 2008, by using nanotechnology physical techniques, HP laboratory research team successfully obtain the resistance with memory characteristic [1], which confirmed the concept of memristor proposed by Chua [2, 3]. As the fourth basic passive device, memristor establishes the relationship between the magnetic flux and the charge. It has been reported that memristor can be applied in the field of computer science [4], biological engineering [5], and electronic engineering [6]. Especially, memristor can be used to construct the chaotic circuits.

For chaotic circuits, the nonlinear device is the key component. In 2008, Itoh and Chua built the first memristor-based chaotic system by replacing the diode with a piecewise linear magnetron Chua's memristor [7]. Compared with the conventional nonlinear-device-based chaotic circuits, the memristor-based circuit has two main characteristics: first, the memristor-based circuit can produce the complicated dynamical behavior, which is different from the general chaotic dynamical behavior; secondly, the memristor-based circuit is more suitable to generate the high-frequency chaotic signal and have potential applications in chaotic secure communication, signal generator, and image process [8–12]. Hence, up to now, a number of memristor-based

chaotic circuit with different structures are proposed. For example, the chaotic circuit with one memristor is studied in [13, 14], the chaotic circuit with two memristor is concerned in [15, 16], the integer-order chaotic memristor circuit is investigated in [17, 18], and the fractional chaotic memristor circuit are researched in [19, 20].

Chaos synchronization is a common phenomenon and can be found in biological systems, chemical reactions, power converters, secure communication system, and so on. Fuzzy technique is a powerful tool [21–27] and especially suitable for the chaos synchronization in the case that disturbances exist. For general fuzzy control, the control input is multidimensional and requires all system state information. However, in practical engineering, it is not easy to get all system state information. The multidimensional control can not only increase the control cost but also result in disturbance input problem. Hence, it is meaningful to design a single-dimensional fuzzy controller which is just based on one system state variable. In addition, disturbance inputs exist in actual system widely, which should be considered in synchronization control. All these motivate our research.

The paper is schemed as follows: the fuzzy model for a memristor-based chaotic circuit is constructed and the preliminary knowledge will be given in Section 2; a multidimensional fuzzy controller and a single-dimensional

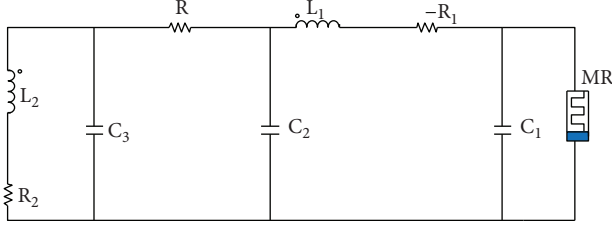


FIGURE 1: The memristor-based chaotic circuit.

fuzzy controller will be designed to achieve the chaos synchronization of the master-slave systems in Section 3; the typical simulation example will be included to validate the correctness of the scheme in Section 4; and finally, the paper will be concluded in Section 5.

Notations used in this paper are fairly standard. $\text{diag}\{\dots\}$ represents a block diagonal matrix, R^n is the n -dimensional Euclidean space, $R^{n \times m}$ denotes the set of $n \times m$ real matrix, the superscript T stands for matrix transposition, $\|\cdot\|_2$ refers to the Euclidean vector norm or the induced matrix 2-norm, and $\lambda_{\min}\{\cdot\}$ represents the maximum eigenvalue.

2. System Description and Preliminaries

First, consider a memristor-based circuit as Figure 1.

One can get the equivalent dynamic system as

$$\begin{aligned} C_1 \frac{dV_{C_1}(t)}{dt} &= i_{L_1}(t) - W(\varphi(t))V_{C_1}(t), \\ L_1 \frac{di_{L_1}(t)}{dt} &= V_{C_2}(t) - V_{C_1}(t) + R_1 i_{L_1}(t), \\ C_2 \frac{dV_{C_2}(t)}{dt} &= \frac{1}{R} (V_{C_3}(t) - V_{C_2}(t)) - i_{L_1}(t), \\ C_3 \frac{dV_{C_3}(t)}{dt} &= \frac{1}{R} (V_{C_2}(t) - V_{C_3}(t)) - i_{L_2}(t), \\ L_2 \frac{di_{L_2}(t)}{dt} &= V_{C_3}(t) - R_2 i_{L_2}, \\ \frac{d\varphi(t)}{dt} &= V_{C_1}(t). \end{aligned} \quad (1)$$

Define the state variable as

$$\begin{aligned} x_1(t) &= V_{C_1}(t), \\ x_2(t) &= R i_{L_1}(t), \\ x_3(t) &= V_{C_2}(t), \\ x_4(t) &= V_{C_3}(t), \\ x_5(t) &= R i_{L_2}(t), \\ x_6(t) &= \varphi(t). \end{aligned} \quad (2)$$

One can obtain the equivalent dynamical equation as

$$\begin{aligned} \dot{x}_1(t) &= r_1 [x_2(t) - \bar{W}(x_6(t))x_1(t)], \\ \dot{x}_2(t) &= r_2 [x_3(t) - x_1(t) + r_7 x_2(t)], \\ \dot{x}_3(t) &= r_3 [x_4(t) - x_3(t) - x_2(t)], \\ \dot{x}_4(t) &= r_4 [x_3(t) - x_4(t) - x_5(t)], \\ \dot{x}_5(t) &= r_5 [x_4(t) - r_6 x_5(t)], \\ \dot{x}_6(t) &= x_1(t), \end{aligned} \quad (3)$$

with

$$\bar{W}(x_6(t)) = RW(\varphi(t)) = \begin{cases} a, & |x_6(t)| \leq 1, \\ b, & |x_6(t)| > 1 \end{cases}, \quad (4)$$

where $x_i, i = 1, 2, \dots, 7$ is the state variable of the system and $r_i > 0, i = 1, 2, \dots, 7$ is the system parameter. The memristive system will possess the chaotic dynamical behavior when the system parameters are $r_1 = 5, r_2 = 2, r_3 = 2, r_4 = 4, r_5 = 3, r_6 = 0.1, r_7 = 0.8, a = 0.1$, and $b = 6$.

Next, consider the fuzzy modeling of the memristive chaotic system.

For $\dot{x}_1(t) = r_1(x_2(t) - \bar{W}(x_6(t))x_1(t))$.

Rule 1. If $x_1(t)$ is H_{11} , then

$$\dot{x}_1(t) = r_1(x_2(t) - ax_1(t)), \quad (5)$$

where H_{11} means $|x_6(t)| \leq 1$, and define

$$M_{11} = \begin{cases} 1, & |x_6(t)| \leq 1, \\ 0, & |x_6(t)| > 1. \end{cases} \quad (6)$$

Rule 2. If $x_1(t)$ is H_{12} , then

$$\dot{x}_1(t) = r_1(x_2(t) - bx_1(t)), \quad (7)$$

where H_{12} means $|x_6(t)| > 1$, and define

$$M_{12} = \begin{cases} 0, & |x_6(t)| \leq 1, \\ 1, & |x_6(t)| > 1. \end{cases} \quad (8)$$

Hence, the fuzzy model of the memristive chaotic system is defined as

$$\begin{bmatrix} \dot{x}_1(t) \\ \dot{x}_2(t) \\ \dot{x}_3(t) \\ \dot{x}_4(t) \\ \dot{x}_5(t) \\ \dot{x}_6(t) \end{bmatrix} = \begin{bmatrix} M_{11} & 0 & 0 & 0 & 0 & 0 \\ 0 & M_{11} & 0 & 0 & 0 & 0 \\ 0 & 0 & M_{11} & 0 & 0 & 0 \\ 0 & 0 & 0 & M_{11} & 0 & 0 \\ 0 & 0 & 0 & 0 & M_{11} & 0 \\ 0 & 0 & 0 & 0 & 0 & M_{11} \end{bmatrix}$$

$$\begin{aligned}
& \begin{bmatrix} r_1[x_2(t) - ax_1(t)] \\ r_2[x_3(t) - x_1(t) + r_7x_2(t)] \\ r_3[x_4(t) - x_3(t) - x_2(t)] \\ r_4[x_3(t) - x_4(t) - x_5(t)] \\ r_5[x_4(t) - r_6x_5(t)] \\ x_1(t) \end{bmatrix} \\
& + \begin{bmatrix} M_{12} & 0 & 0 & 0 & 0 & 0 \\ 0 & M_{12} & 0 & 0 & 0 & 0 \\ 0 & 0 & M_{12} & 0 & 0 & 0 \\ 0 & 0 & 0 & M_{12} & 0 & 0 \\ 0 & 0 & 0 & 0 & M_{12} & 0 \\ 0 & 0 & 0 & 0 & 0 & M_{12} \end{bmatrix} \\
& \cdot \begin{bmatrix} r_1[x_2(t) - bx_1(t)] \\ r_2[x_3(t) - x_1(t) + r_7x_2(t)] \\ r_3[x_4(t) - x_3(t) - x_2(t)] \\ r_4[x_3(t) - x_4(t) - x_5(t)] \\ r_5[x_4(t) - r_6x_5(t)] \\ x_1(t) \end{bmatrix}.
\end{aligned}$$

Above model can be rewritten as

$$\dot{x}(t) = \sum_{i=1}^2 \Theta_i A_i x(t), \quad (10)$$

where

$$\begin{aligned}
\Theta_i &= \text{diag} \{M_{1i}, M_{1i}, M_{1i}, M_{1i}, M_{1i}, M_{1i}\}, \\
A_1 &= \begin{bmatrix} -ar_1 & r_1 & 0 & 0 & 0 & 0 \\ -r_2 & r_2r_7 & r_2 & 0 & 0 & 0 \\ 0 & -r_3 & -r_3 & r_3 & 0 & 0 \\ 0 & 0 & r_4 & -r_4 & -r_4 & 0 \\ 0 & 0 & 0 & r_5 & -r_5r_6 & 0 \\ 1 & 0 & 0 & 0 & 0 & 0 \end{bmatrix}, \\
A_2 &= \begin{bmatrix} -br_1 & r_1 & 0 & 0 & 0 & 0 \\ -r_2 & r_2r_7 & r_2 & 0 & 0 & 0 \\ 0 & -r_3 & -r_3 & r_3 & 0 & 0 \\ 0 & 0 & r_4 & -r_4 & -r_4 & 0 \\ 0 & 0 & 0 & r_5 & -r_5r_6 & 0 \\ 1 & 0 & 0 & 0 & 0 & 0 \end{bmatrix}.
\end{aligned} \quad (11)$$

System (3) is supposed as the master system, and the slave system is constructed as

$$\begin{aligned}
\dot{y}_1(t) &= r_1(y_2(t) - \bar{W}(y_6(t))y_1(t)) + u_1(t) + w_1(t), \\
\dot{y}_2(t) &= r_2[y_3(t) - y_1(t) + r_7y_2(t)] + u_2(t) + w_2(t), \\
\dot{y}_3(t) &= r_3[y_3(t) - y_4(t) - y_2(t)] + u_3(t) + w_3(t), \\
\dot{y}_3(t) &= r_4[y_4(t) - y_3(t) - y_5(t)] + u_4(t) + w_4(t), \\
\dot{y}_5(t) &= r_5[y_4(t) - r_6y_5(t)] + u_5(t) + w_5(t), \\
\dot{y}_6(t) &= y_1(t) + u_6(t) + w_6(t),
\end{aligned} \quad (12)$$

where $y(t) = (y_1(t), y_2(t), y_3(t), y_4(t), y_5(t), y_6(t))^T$ is the state variable vector of the slave system and $w(t) = (w_1(t), w_2(t), w_3(t), w_4(t), w_5(t), w_6(t))^T$ is the disturbance input of the slave system.

Hence, the fuzzy model of the slave system can be represented as

$$\dot{y}(t) = \sum_{i=1}^2 \Theta_i A_i y(t) + w(t) + u(t), \quad (13)$$

where $u(t) = (u_1(t), u_2(t), u_3(t), u_4(t), u_5(t), u_6(t))^T$ is the synchronization fuzzy controller.

Define the synchronization error vector of the master-slave systems as

$$E(t) = y(t) - x(t), \quad (14)$$

where $E(t) = (e_1(t), e_2(t), e_3(t), e_4(t), e_5(t), e_6(t))^T$.

One can get the error dynamic system as

$$\begin{aligned}
\dot{E}(t) &= \dot{y}(t) - \dot{x}(t) = \sum_{i=1}^2 \Theta_i A_i y(t) - \sum_{i=1}^2 \Theta_i A_i x(t) \\
&+ w(t) + u(t) = \sum_{i=1}^2 \Theta_i A_i E(t) + w(t) + u(t).
\end{aligned} \quad (15)$$

In this paper, the following lemmas are concerned:

Lemma 1 (see [28]). If $f(t) \in L_\infty \cap L_2$ and $\dot{f}(t) \in L_\infty$, one can get

$$\lim_{t \rightarrow +\infty} f(t) = 0. \quad (16)$$

Definition 1. For nonzero $w(t) \in L_2[t_0, \infty]$ and under the assumption of zero initial condition, if there exists a positive scalar γ such that

$$\|E(t)\|_2 \leq \gamma \|w(t)\|_2. \quad (17)$$

Then, the slave system will synchronize to the master system with H_∞ norm bound γ .

3. Main Results

Based on fuzzy theory and Lyapunov theory, a controller is presented as follows.

Theorem 1. *If there exist scalar $K_j^i > 0, i = 1, 2, j = 1, \dots, 6$, design the multidimensional fuzzy controller with following control regulation*

$$u(t) = - \sum_{i=1}^2 \Theta_i k_i E(t), \quad (18)$$

with

$$\left\{ \begin{array}{l} k_1^1 = K_1^1 - r_1 a + 2, \\ k_2^1 = K_2^1 + \frac{(r_1 - r_2)^2}{4} + r_2 r_7 + 1, \\ k_3^1 = K_3^1 + \frac{(r_2 - r_3)^2}{4} - r_3 + 1, \\ k_4^1 = K_4^1 + \frac{(-r_3 - r_4)^2}{4} - r_4 + 1, \\ k_5^1 = K_5^1 + \frac{(r_5 - r_4)^2}{4} - r_5 r_6, \\ k_6^1 = K_6^1 + \frac{1}{4}, \\ k_1^2 = K_1^2 - r_1 b + 2, \\ k_2^2 = K_2^2 + \frac{(r_1 - r_2)^2}{4} + r_2 r_7 + 1, \\ k_3^2 = K_3^2 + \frac{(r_2 - r_3)^2}{4} - r_3 + 1, \\ k_4^2 = K_4^2 + \frac{(-r_3 - r_4)^2}{4} - r_4 + 1, \\ k_5^2 = K_5^2 + \frac{(r_5 - r_4)^2}{4} - r_5 r_6, \\ k_6^2 = K_6^2 + \frac{1}{4}, \end{array} \right. \quad (19)$$

$$\left[\begin{array}{cc} I - \sum_{i=1}^2 \Theta_i K_i & \frac{I}{2} \\ * & -\gamma^2 I \end{array} \right] < 0, \quad (20)$$

$$k_i = \text{diag} \{k_1^i, k_2^i, k_3^i, k_4^i, k_5^i, k_6^i\}, \quad (21)$$

$$K_i = \text{diag} \{K_1^i, K_2^i, K_3^i, K_4^i, K_5^i, K_6^i\}. \quad (22)$$

Then, the slave system (12) can synchronize to the master system (3) with H_∞ norm bound γ .

Proof 1. With (18), the error dynamic system can be transformed as

$$\begin{bmatrix} \dot{e}_1(t) \\ \dot{e}_2(t) \\ \dot{e}_3(t) \\ \dot{e}_4(t) \\ \dot{e}_5(t) \\ \dot{e}_6(t) \end{bmatrix} = \begin{bmatrix} M_{11} & 0 & 0 & 0 & 0 & 0 \\ 0 & M_{11} & 0 & 0 & 0 & 0 \\ 0 & 0 & M_{11} & 0 & 0 & 0 \\ 0 & 0 & 0 & M_{11} & 0 & 0 \\ 0 & 0 & 0 & 0 & M_{11} & 0 \\ 0 & 0 & 0 & 0 & 0 & M_{11} \end{bmatrix} \cdot \begin{bmatrix} r_1[e_2(t) - ae_1(t)] - k_1^1 e_1(t) + w_1(t) \\ r_2[e_3(t) - e_1(t) + r_7 e_2(t)] - k_2^1 e_2(t) + w_2(t) \\ r_3[e_4(t) - e_3(t) - e_2(t)] - k_3^1 e_3(t) + w_3(t) \\ r_4[e_3(t) - e_4(t) - e_5(t)] - k_4^1 e_4(t) + w_4(t) \\ r_5[e_4(t) - r_6 e_5(t)] - k_5^1 e_5(t) + w_5(t) \\ e_1(t) - k_6^1 e_6(t) + w_6(t) \end{bmatrix} + \begin{bmatrix} M_{12} & 0 & 0 & 0 & 0 & 0 \\ 0 & M_{12} & 0 & 0 & 0 & 0 \\ 0 & 0 & M_{12} & 0 & 0 & 0 \\ 0 & 0 & 0 & M_{12} & 0 & 0 \\ 0 & 0 & 0 & 0 & M_{12} & 0 \\ 0 & 0 & 0 & 0 & 0 & M_{12} \end{bmatrix} \cdot \begin{bmatrix} r_1[e_2(t) - be_1(t)] - k_1^2 e_1(t) + w_1(t) \\ r_2[e_3(t) - e_1(t) + r_7 e_2(t)] - k_2^2 e_2(t) + w_2(t) \\ r_3[e_4(t) - e_3(t) - e_2(t)] - k_3^2 e_3(t) + w_3(t) \\ r_4[e_3(t) - e_4(t) - e_5(t)] - k_4^2 e_4(t) + w_4(t) \\ r_5[e_4(t) - r_6 e_5(t)] - k_5^2 e_5(t) + w_5(t) \\ e_1(t) - k_6^2 e_6(t) + w_6(t) \end{bmatrix} \quad (23)$$

Choose the Lyapunov function candidate as

$$V(t) = \frac{1}{2} (e_1^2(t) + e_2^2(t) + e_3^2(t) + e_4^2(t) + e_5^2(t) + e_6^2(t)) \quad (24)$$

One can get the time derivative of $V(t)$ as

$$\dot{V}(t) = e_1(t) \{ M_{11} [r_1[e_2(t) - ae_1(t)] - k_1^1 e_1(t) + w_1(t)] + M_{12} [r_1[e_2(t) - be_1(t)] - k_1^2 e_1(t) + w_1(t)] \}$$

$$\begin{aligned}
& + e_2(t) \{ M_{11} r_2 [e_3(t) - e_1(t) + r_7 e_2(t)] - k_2^1 e_2(t) \\
& + w_2(t) \} + M_{12} [r_2 [e_3(t) - e_1(t) + r_7 e_2(t)] \\
& - k_2^2 e_2(t) + w_2(t)] \} + e_3(t) \{ M_{11} [r_3 [e_4(t) \\
& - e_3(t) - e_2(t)] - k_3^1 e_3(t) + w_3(t)] \\
& + M_{12} [r_3 [e_4(t) - e_3(t) - e_2(t)] - k_3^2 e_3(t) \\
& + w_3(t)] \} + e_4(t) \{ M_{11} [r_4 [e_5(t) - e_4(t) \\
& - e_5(t)] - k_4^1 e_4(t) + w_4(t)] + M_{12} [r_4 [e_5(t) \\
& - e_4(t) - e_5(t)] - k_4^2 e_4(t) + w_4(t)] \} \\
& + e_5(t) \{ M_{11} [r_5 [e_6(t) - r_6 e_5(t)] - k_5^1 e_5(t) + w_5(t)] \\
& + M_{12} [r_5 [e_6(t) - r_6 e_5(t)] - k_5^2 e_5(t) + w_5(t)] \} \\
& + e_6(t) \{ M_{11} [e_1(t) - k_6^1 e_6(t) + w_6(t)] \\
& + M_{12} [e_1(t) - k_6^2 e_6(t) + w_6(t)] \} \\
& = -r_1 (M_{11} a + M_{12} b) e_1^2(t) + (r_1 - r_2) e_1(t) e_2(t) \\
& + r_2 r_7 e_2^2(t) + (r_2 - r_3) e_2(t) e_3(t) - r_3 e_3^2(t) \\
& + (r_3 + r_4) e_3(t) e_4(t) - r_4 e_4^2(t) \\
& + (r_5 - r_4) e_4(t) e_5(t) - r_5 r_6 e_5^2(t) + e_1(t) e_6(t) \\
& - \sum_{j=1}^6 (M_{11} k_j^1 e_j^2(t) + M_{12} k_j^2 e_j^2(t)) + w^T(t) E(t) \\
& \leq -[r_1 (M_{11} a + M_{12} b) - 2 + M_{11} k_1^1 + M_{12} k_1^2] e_1^2(t) \\
& - \left[e_1(t) - (r_1 - r_2) e_2 \frac{t}{2} \right]^2 - \left[-\frac{(r_1 - r_2)^2}{4} \right. \\
& \left. - 1 - r_2 r_7 + M_{11} k_2^1 + M_{12} k_2^2 \right] e_2^2(t) \\
& - \left[e_2(t) - (r_2 - r_3) e_3 \frac{t}{2} \right]^2 - \left[-\frac{(r_2 - r_3)^2}{4} - 1 + r_3 \right. \\
& \left. + M_{11} k_3^1 + M_{12} k_3^2 \right] e_3^2(t) - \left[e_3(t) - (r_3 + r_4) e_4 \frac{t}{2} \right]^2 \\
& - \left[-\frac{(r_3 + r_4)^2}{4} - 1 + r_4 + M_{11} k_4^1 + M_{12} k_4^2 \right] e_4^2(t) \\
& - \left[e_4(t) - (r_5 - r_4) e_5 \frac{t}{2} \right]^2 - \left[-\frac{(r_5 - r_4)^2}{4} + r_5 r_6 \right. \\
& \left. + M_{11} k_5^1 + M_{12} k_5^2 \right] e_5^2(t) - \left[e_1(t) - e_6 \frac{t}{2} \right]^2 \\
& - \left[-\frac{1}{4} + M_{11} k_6^1 + M_{12} k_6^2 \right] e_6^2(t) + w^T(t) E(t). \tag{25}
\end{aligned}$$

With (19), one can conclude that

$$\dot{V}(t) \leq -E^T(t) \sum_{i=1}^2 \Theta_i K_i E(t) + w^T(t) E(t). \tag{26}$$

Consider the H_∞ performance index as

$$\begin{aligned}
J &= \int_{t_0}^{t_T} [E^T(t) E(t) - \gamma^2 w^T(t) w(t)] dt \\
&= \int_{t_0}^{t_T} [E^T(t) E(t) - \gamma^2 w^T(t) w(t) + \dot{V}(t)] dt \\
&\quad + V(t_0) - V(t_T). \tag{27}
\end{aligned}$$

For $V(t_0) = 0$ and $V(t_T) \geq 0$,

$$\begin{aligned}
J &\leq \int_{t_0}^{t_T} [E^T(t) E(t) - \gamma^2 w^T(t) w(t) + \dot{V}(t)] dt \\
&= \int_{t_0}^{t_T} \eta^T(t) \Omega \eta(t) dt, \tag{28}
\end{aligned}$$

where

$$\begin{aligned}
\eta(t) &= [E^T(t), w^T(t)]^T, \\
\Omega &= \begin{bmatrix} I - \sum_{i=1}^2 \Theta_i K_i & \frac{I}{2} \\ * & -\gamma^2 I \end{bmatrix}. \tag{29}
\end{aligned}$$

Consider (20), it can be concluded that $J \leq 0$. Based on Definition 1, slave system (12) can synchronize to master system (3) with H_∞ norm bound γ .

Next, consider the design for the single-dimensional fuzzy synchronization controller.

Construct the slave system as

$$\begin{aligned}
\dot{y}_1(t) &= r_1 (y_2(t) - \bar{W}(y_6(t)) y_1(t)), \\
\dot{y}_2(t) &= r_2 [y_3(t) - y_1(t) + r_7 y_2(t)] + w(t) + u(t), \\
\dot{y}_3(t) &= r_3 [y_4(t) - y_3(t) - y_2(t)], \\
\dot{y}_4(t) &= r_4 [y_3(t) - y_4(t) - y_5(t)], \\
\dot{y}_5(t) &= r_5 [y_4(t) - r_6 y_5(t)], \\
\dot{y}_6(t) &= y_1(t), \tag{30}
\end{aligned}$$

where $u(t)$ is the single-dimensional synchronization fuzzy controller.

Theorem 2. *If there exist scalar $k^i > 0, i = 1, 2$, design the single-dimensional fuzzy controller with following control regulation*

$$u(t) = - \sum_{i=1}^2 M_{1i} k_i e_2(t), \tag{31}$$

where

$$k_i = (k^i + r_7)r_2$$

$$\begin{bmatrix} -(M_{11}a + M_{12}b) & 0 & 0 & 0 \\ 0 & 1 - (M_{11}k^1 + M_{12}k^2) & 0 & \frac{1}{2r_2} \\ 0 & 0 & -r_6 & 0 \\ 0 & \frac{1}{2r_2} & 0 & -\gamma^2 \end{bmatrix} \leq 0. \quad (32)$$

Then, slave system (30) with any initial conditions can synchronize to master system (3) with H_∞ norm bound γ .

Proof 2. With (31), the error dynamic system can be transformed as

$$\begin{bmatrix} \dot{e}_1(t) \\ \dot{e}_2(t) \\ \dot{e}_3(t) \\ \dot{e}_4(t) \\ \dot{e}_5(t) \\ \dot{e}_6(t) \end{bmatrix} = \begin{bmatrix} M_{11} & 0 & 0 & 0 & 0 & 0 \\ 0 & M_{11} & 0 & 0 & 0 & 0 \\ 0 & 0 & M_{11} & 0 & 0 & 0 \\ 0 & 0 & 0 & M_{11} & 0 & 0 \\ 0 & 0 & 0 & 0 & M_{11} & 0 \\ 0 & 0 & 0 & 0 & 0 & M_{11} \end{bmatrix} \cdot \begin{bmatrix} r_1[e_2(t) - ae_1(t)] \\ r_2[e_3(t) - e_1(t) + r_7e_2(t)] + w(t) - k^1e_2(t) \\ r_3[e_4(t) - e_3(t) - e_2(t)] \\ r_4[e_3(t) - e_4(t) - e_5(t)] \\ r_5[e_4(t) - r_6e_5(t)] \\ e_1(t) \end{bmatrix} + \begin{bmatrix} M_{12} & 0 & 0 & 0 & 0 & 0 \\ 0 & M_{12} & 0 & 0 & 0 & 0 \\ 0 & 0 & M_{12} & 0 & 0 & 0 \\ 0 & 0 & 0 & M_{12} & 0 & 0 \\ 0 & 0 & 0 & 0 & M_{12} & 0 \\ 0 & 0 & 0 & 0 & 0 & M_{12} \end{bmatrix} \cdot \begin{bmatrix} r_1[e_2(t) - be_1(t)] \\ r_2[e_3(t) - e_1(t) + r_7e_2(t)] + w(t) - k^2e_2(t) \\ r_3[e_4(t) - e_3(t) - e_2(t)] \\ r_4[e_3(t) - e_4(t) - e_5(t)] \\ r_5[e_4(t) - r_6e_5(t)] \\ e_1(t) \end{bmatrix}. \quad (33)$$

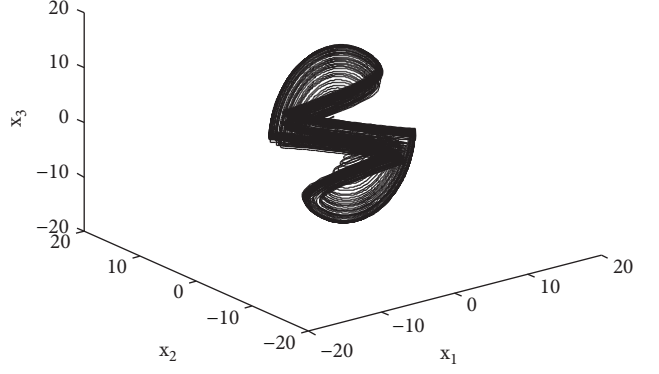


FIGURE 2: Attractor of the memristive chaotic system.

Choose the Lyapunov function candidate as

$$V_0(t) = \frac{1}{2r_1}e_1^2(t) + \frac{1}{2r_2}e_2^2(t) + \frac{1}{2r_3}e_3^2(t) + \frac{1}{2r_4}e_4^2(t) + \frac{1}{2r_5}e_5^2(t). \quad (34)$$

One can get the time derivative of $V_0(t)$ as

$$\begin{aligned} \dot{V}_0(t) &= \frac{1}{r_1}e_1(t)\dot{e}_1(t) + \frac{1}{r_2}e_2(t)\dot{e}_2(t) + \frac{1}{r_3}e_3(t)\dot{e}_3(t) \\ &\quad + \frac{1}{r_4}e_4(t)\dot{e}_4(t) + \frac{1}{r_5}e_5(t)\dot{e}_5(t) \\ &= e_1(t)\{M_{11}[e_2(t) - ae_1(t)] + M_{12}[e_2(t) - be_1(t)]\} \\ &\quad + e_2(t)\{M_{11}[e_3(t) - e_1(t) + r_7e_2(t)] \\ &\quad + M_{12}[e_3(t) - e_1(t) + r_7e_2(t)] + w(t)/r_2 + u(t)/r_2\} \\ &\quad + e_3(t)\{M_{11}[e_4(t) - e_3(t) - e_2(t)] \\ &\quad + M_{12}[e_4(t) - e_3(t) - e_2(t)]\} \\ &\quad + e_4(t)\{M_{11}[e_3(t) - e_4(t) - e_5(t)] \\ &\quad + M_{12}[e_3(t) - e_4(t) - e_5(t)]\} \\ &\quad + e_5(t)\{M_{11}[e_4(t) - r_6e_5(t)] + M_{12}[e_4(t) - r_6e_5(t)]\} \\ &= e_1(t)\{M_{11}[e_2(t) - ae_1(t)] + M_{12}[e_2(t) - be_1(t)]\} \\ &\quad + e_2(t)\{M_{11}[e_3(t) - e_1(t) - k^1e_2(t)] \\ &\quad + M_{12}[e_3(t) - e_1(t) - k^2e_2(t)]\} \\ &\quad + e_3(t)\{M_{11}[e_4(t) - e_3(t) - e_2(t)] \\ &\quad + M_{12}[e_4(t) - e_3(t) - e_2(t)]\} \\ &\quad + e_4(t)\{M_{11}[e_3(t) - e_4(t) - e_5(t)] \\ &\quad + M_{12}[e_3(t) - e_4(t) - e_5(t)]\} \\ &\quad + e_5(t)\{M_{11}[e_4(t) - r_6e_5(t)] \\ &\quad + M_{12}[e_4(t) - r_6e_5(t)]\} + e(t)_2w(t)/r_2 \\ &= -(M_{11}a + M_{12}b)e_1^2(t) - (M_{11}k^1 + M_{12}k^2)e_2^2(t) \\ &\quad - (e_3(t) - e_4(t))^2 - r_6e_5^2(t) + e_2(t)w(t)/r_2. \end{aligned} \quad (35)$$

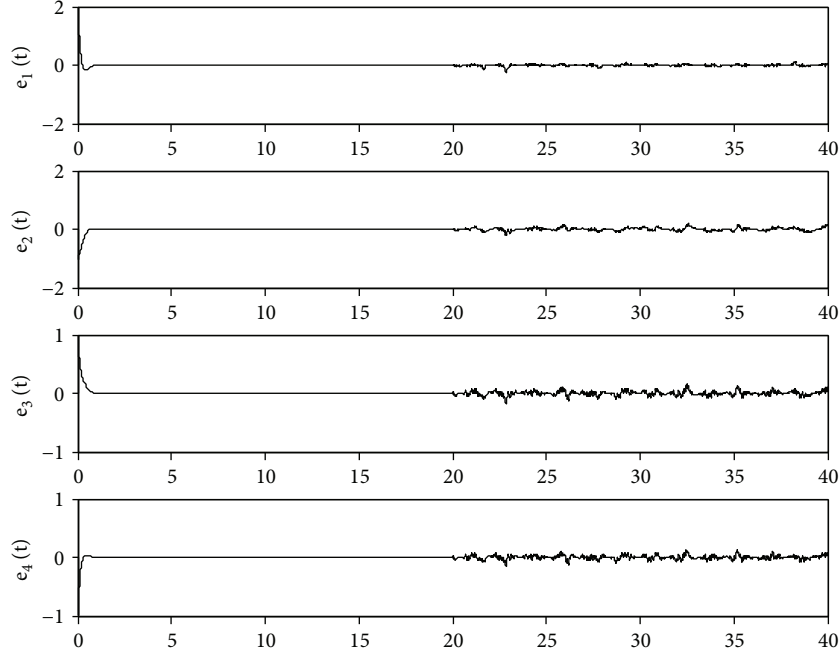


FIGURE 3: Time response of synchronization error variables with multidimensional fuzzy controller.

With (31), one can conclude that

$$\dot{V}_0(t) \leq -\bar{E}^T(t) \sum_{i=1}^2 \bar{\Theta}_i \bar{K}_i \bar{E}(t) + \frac{1}{r_2} w(t) e_2(t), \quad (36)$$

where

$$\begin{aligned} \bar{K}_1 &= \text{diag} \{a, k^1, r_6\} \geq 0, \\ \bar{K}_2 &= \text{diag} \{b, k^2, r_6\} \geq 0, \\ \bar{E} &= [e_1(t), e_2(t), e_5(t)]^T, \\ \bar{\Theta}_i &= \text{diag} \{M_{1i}, M_{1i}, M_{1i}\}. \end{aligned} \quad (37)$$

Consider the H_∞ performance index as

$$\begin{aligned} J &= \int_{t_0}^{t_T} [e_2^2(t) - \gamma^2 w^T(t) w(t)] dt \\ &= \int_{t_0}^{t_T} [e_2^2(t) - \gamma^2 w^T(t) w(t) + \dot{V}_0(t)] dt \\ &\quad + V(t_0) - V(t_T). \end{aligned} \quad (38)$$

For $V(t_0) = 0$ and $V(t_T) \geq 0$,

$$J \leq \int_{t_0}^{t_T} [e_2^2(t) - \gamma^2 w^T(t) w(t) + \dot{V}_0(t)] dt = \int_{t_0}^{t_T} \eta^T(t) \Omega \eta(t) dt, \quad (39)$$

where

$$\eta(t) = [\bar{E}^T(t), w^T(t)]^T, \quad \Omega = \begin{bmatrix} -(M_{11}a + M_{12}b) & 0 & 0 & 0 \\ 0 & 1 - (M_{11}k^1 + M_{12}k^2) & 0 & \frac{1}{2r_2} \\ 0 & 0 & -r_6 & 0 \\ 0 & \frac{1}{2r_2} & 0 & -\gamma^2 \end{bmatrix}. \quad (40)$$

Consider (32), it can be concluded that $J \leq 0$. Based on Definition 1, slave system (30) can synchronize to master system (3) with H_∞ norm bound γ .

4. Example and Simulation

First, consider the dynamics of the memristive chaotic system, and the simulation result is shown in Figure 2.

Next, we study the synchronization control of the master-slave systems. In the simulation, the system initial values are $y(0) = [1, -1, 0.5, -1, 2, -1]^T$ and $x(0) = 0.001 \times [1, 1, 1, 1, 1, 1]^T$. The disturbance input is $w(t) = w_i(t) = 2 \sin(2t) \sin(e^t/(t+1))$, $t \geq 20$ s. Let $\gamma = 0.4$, and based on Theorem 1, the control parameters for the multidimensional fuzzy controller are $k_1 = \text{diag} \{4.06, 7.41, 1.56, 8.56, 2.21, 2.81\}$ and $k_2 = \text{diag} \{-35.43, 7.41, 1.56, 8.56, 2.21, 2.81\}$; the simulation result is shown in Figure 3. Then, based on Theorem 2, the control parameters for the single-dimensional fuzzy controller are $k_1 = 9.73$ and $k_2 = 7.38$; the simulation result is shown in Figure 4.

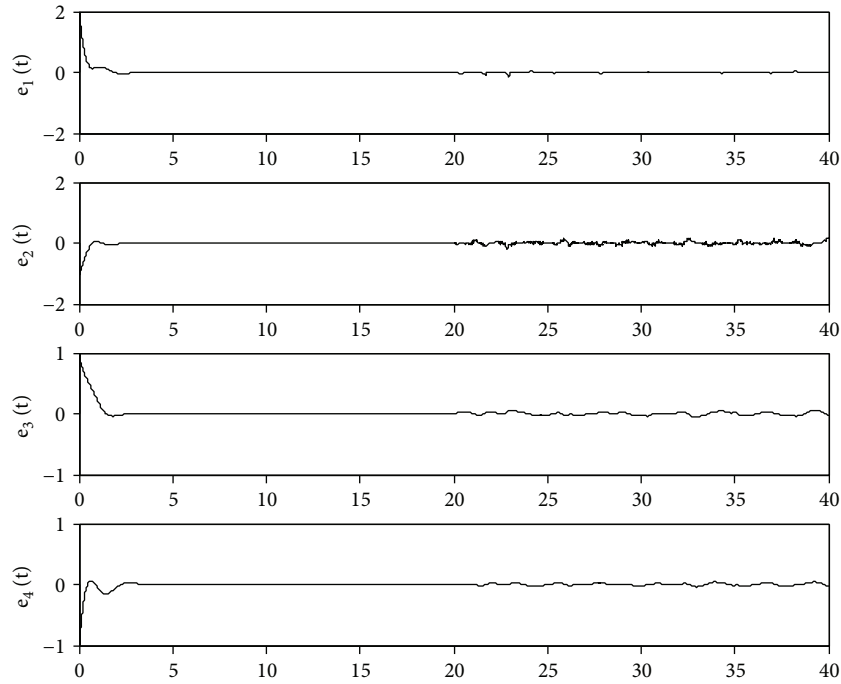


FIGURE 4: Time response of synchronization error variables with single-dimensional fuzzy controller.

Remark 2. Figure 3 depicts the time response of the synchronization error variables of the memristive master-slave systems with the multidimensional fuzzy controller. Figure 4 depicts the time response of the synchronization error variables of the master-slave systems with the single-dimensional fuzzy controller. It can be seen that although there exists just one disturbance $w(t)$ for single-dimensional fuzzy control, the disturbance has impact on all error synchronization variables. In addition, it can be seen that both controllers can be able to realize the synchronization of the master-slave systems; the multidimensional fuzzy controller has the better control performance and realizes the chaos synchronization during 2.0 seconds. However, the possession of the good control performance is at the cost of the acquirement of all system state information. In addition, multidimensional control may introduce more disturbance input. The single-dimensional synchronization controller has the general control performance but requires just one system state information, which can decrease the control cost and the disturbance input. Hence, two kinds of controllers are useful and recommended for the different applied cases.

Remark 3. For the nonlinear disturbed chaotic system, the fuzzy modeling technique is adopted to realize the exact linearization control, which can eliminate the constraint on the system nonlinear term, compared with the general nonlinear control method; in addition, H-infinity approach is introduced to deal with the case that disturbances exist.

5. Conclusion

This paper focuses on the fuzzy synchronization for a new memristive chaotic system with disturbances. Based on fuzzy

theory and Lyapunov stability theory, we have built the fuzzy model for the memristive chaotic system. Then, by using H-infinity technique, we have presented two kinds of fuzzy controllers for the possible application in chaos synchronization of slave-master systems. Finally, we have included some example to demonstrate the effectiveness of the given fuzzy controllers. In addition, the proposed results can be extended to the memristive chaotic control system with delay or event trigger, which is our future work.

Data Availability

The data used to support the findings of this study are included within the article.

Conflicts of Interest

The authors declare that there is no conflict of interests regarding the publication of this paper.

Acknowledgments

This work is partially supported by the National Key Basic Research Program, China (2012CB215202), the Graduate Innovation Fund of Xihua University (ycjj2018015), the Open Research Fund of Key Laboratory of Fluid and Power Machinery of Ministry of Education, and the National Natural Science Foundation of China (51475453, 11472297).

References

- [1] D. B. Strukov, G. S. Snider, D. R. Stewart, and R. S. Williams, "The missing memristor found," *Nature*, vol. 453, no. 7191, pp. 80–83, 2008.

- [2] L. O. Chua, "Memristors - the missing circuit element," *IEEE Transactions on Circuit Theory*, vol. 18, no. 5, pp. 507–519, 1971.
- [3] L. O. Chua and S. M. Kang, "Memristive devices and systems," *Proceedings of the IEEE*, vol. 64, no. 2, pp. 209–223, 1976.
- [4] Y. C. Yang, F. Pan, Q. Liu, M. Liu, and F. Zeng, "Fully room-temperature-fabricated nonvolatile resistive memory for ultra-fast and high-density memory application," *Nano Letters*, vol. 9, no. 4, pp. 1636–1643, 2009.
- [5] Y. V. Pershin and M. Di Ventra, "Experimental demonstration of associative memory with memristive neural networks," *Neural Networks*, vol. 23, no. 7, pp. 881–886, 2010.
- [6] S. Shin, K. Kim, and S.-M. Kang, "Memristor applications for programmable analog ICs," *IEEE Transactions on Nanotechnology*, vol. 10, no. 2, pp. 266–274, 2011.
- [7] M. Itoh and L. O. Chua, "Memristor oscillators," *International Journal of Bifurcation and Chaos*, vol. 18, no. 11, pp. 3183–3206, 2008.
- [8] B. Wang, S. M. Zhong, and X. C. Dong, "On the novel chaotic secure communication scheme design," *Communications in Nonlinear Science and Numerical Simulation*, vol. 39, pp. 108–117, 2016.
- [9] B. Wang, F. C. Zou, and Y. Zhang, "New memristive chaotic system and the application in digital watermark," *Optik*, vol. 172, pp. 873–878, 2018.
- [10] B. Wang, F. C. Zou, and J. Cheng, "A memristor-based chaotic system and its application in image encryption," *Optik*, vol. 154, pp. 538–544, 2018.
- [11] V. K. Rai, S. Tripathy, and J. Mathew, "Memristor based random number generator: architectures and evaluation," *Procedia Computer Science*, vol. 125, pp. 576–583, 2018.
- [12] B. Wang, L. L. Chen, and J. Cheng, "New result on maximum entropy threshold image segmentation based on P system," *Optik*, vol. 163, pp. 81–85, 2018.
- [13] H. H. C. Iu, D. S. Yu, A. L. Fitch, V. Sreeram, and H. Chen, "Controlling chaos in a memristor based circuit using a Twin-T notch filter," *IEEE Transactions on Circuits and Systems I: Regular Papers*, vol. 58, no. 6, pp. 1337–1344, 2011.
- [14] B. Muthuswamy, "Implementing memristor based chaotic circuits," *International Journal of Bifurcation and Chaos*, vol. 20, no. 05, pp. 1335–1350, 2010.
- [15] R. K. Budhathoki, M. P. D. Sah, C. Yang, H. Kim, and L. Chua, "Transient behaviors of multiple memristor circuits based on flux charge relationship," *International Journal of Bifurcation and Chaos*, vol. 24, no. 2, article 1430006, 2014.
- [16] A. Buscarino, L. Fortuna, M. Frasca, and L. V. Gambuzza, "A chaotic circuit based on Hewlett-Packard memristor," *Chaos*, vol. 22, no. 2, article 023136, 2012.
- [17] R. Riaz, "First order mem-circuits: modeling, nonlinear oscillations and bifurcations," *IEEE Transactions on Circuits and Systems I: Regular Papers*, vol. 60, no. 6, pp. 1570–1583, 2013.
- [18] A. Buscarino, L. Fortuna, M. Frasca, and L. V. Gambuzza, "A gallery of chaotic oscillators based on HP memristor," *International Journal of Bifurcation and Chaos*, vol. 23, no. 5, article 1330015, 2013.
- [19] I. Petráš, "Fractional-order memristor-based Chua's circuit," *IEEE Transactions on Circuits and Systems II: Express Briefs*, vol. 57, no. 12, pp. 975–979, 2010.
- [20] L. Teng, H. H. C. Iu, X. Wang, and X. Wang, "Chaotic behavior in fractional-order memristor-based simplest chaotic circuit using fourth degree polynomial," *Nonlinear Dynamics*, vol. 77, no. 1-2, pp. 231–241, 2014.
- [21] B. Wang, X. Zhang, and X. Dong, "Novel secure communication based on chaos synchronization," *IEICE Transactions on Fundamentals of Electronics, Communications and Computer Sciences*, vol. E101.A, no. 7, pp. 1132–1135, 2018.
- [22] L. Zhang, Z. Ning, and P. Shi, "Input-output approach to control for fuzzy Markov jump systems with time-varying delays and uncertain packet dropout rate," *IEEE Transactions on Cybernetics*, vol. 45, no. 11, pp. 2449–2460, 2015.
- [23] B. Wang, J. Cheng, and F. C. Zou, "Stochastic finite-time H_∞ filtering for nonlinear Markovian jump systems with partly known transition probabilities," *Proceedings of the Institution of Mechanical Engineers Part I-Journal of Systems and Control Engineering*, 2018.
- [24] R. Sakthivel, T. Saravanakumar, Y. K. Ma, and S. Marshal Anthoni, "Finite-time resilient reliable sampled-data control for fuzzy systems with randomly occurring uncertainties," *Fuzzy Sets and Systems*, vol. 329, pp. 1–18, 2017.
- [25] B. Wang, D. Zhang, J. Cheng, and J. H. Park, "Fuzzy model-based nonfragile control of switched discrete-time systems," *Nonlinear Dynamics*, vol. 93, no. 4, pp. 2461–2471, 2018.
- [26] M. J. Park and O. M. Kwon, "Stability and stabilization of discrete-time T-S fuzzy systems with time-varying delay via Cauchy-Schwartz-based summation inequality," *IEEE Transactions on Fuzzy Systems*, vol. 25, no. 1, pp. 128–140, 2017.
- [27] K. Zhang, B. Jiang, and V. Cocquempot, "Fuzzy unknown input observer-based robust fault estimation design for discrete-time fuzzy systems," *Signal Processing*, vol. 128, pp. 40–47, 2016.
- [28] K. Narendra and A. Annaswamy, *Stable Adaptive Systems*, Prentice-Hall, Englewood Cliffs, 1989.

Research Article

Exact Analysis and Physical Realization of the 6-Lobe Chua Corsage Memristor

Zubaer I. Mannan, Changju Yang, Shyam P. Adhikari, and Hyongsuk Kim 

Division of Electronics and Information Engineering and Intelligent Robots Research Center (IRRC), Chonbuk National University, Jeonju, Jeonbuk 567-54896, Republic of Korea

Correspondence should be addressed to Hyongsuk Kim; hskim@jbnu.ac.kr

Received 20 April 2018; Accepted 11 July 2018; Published 1 November 2018

Academic Editor: Viet-Thanh Pham

Copyright © 2018 Zubaer I. Mannan et al. This is an open access article distributed under the Creative Commons Attribution License, which permits unrestricted use, distribution, and reproduction in any medium, provided the original work is properly cited.

A novel generic memristor, dubbed the *6-lobe Chua corsage memristor*, is proposed with its nonlinear dynamical analysis and physical realization. The proposed corsage memristor contains *four* asymptotically stable equilibrium points on its complex and diversified dynamic routes which reveals a *4-state nonlinear memory device*. The higher degree of versatility of its dynamic routes reveal that the proposed memristor has a variety of dynamic paths in response to different initial conditions and exhibits a highly nonlinear *contiguous* DC *V-I* curve. The DC *V-I* curve of the proposed memristor is endowed with an explicit *analytical parametric representation*. Moreover, the derived *three formulas*, exponential trajectories of state $x_n(t)$, time period t_{fn} , and minimum pulse amplitude V_A , are required to analyze the movement of the state trajectories on the piecewise linear (PWL) dynamic route map (DRM) of the corsage memristor. These *formulas* are universal, that is, applicable to any PWL DRM curves for any DC or pulse input and with any number of segments. Nonlinear dynamics and circuit and system theoretic approach are employed to explain the *asymptotic quad-stable behavior* of the proposed corsage memristor and to design a novel real memristor emulator using *off-the-shelf* circuit components.

1. Introduction

Memristor, the acronym of memory resistor, is one of the most propitious elements in the emerging memory sector due to its exclusive attributes under DC or AC excitations, as well as its miniature nanoscale physical dimension. Extensive research is ongoing on memristors and the memristive system after the seminal paper published by *hp* in 2008 [1]. Memristor, the fourth basic circuit element, was postulated by Chua [2] and later generalized to a broader class of dynamical devices which exhibit interesting and valuable circuit-theoretic properties [3].

Recently, several researchers investigated the multistate phenomena in generic and extended memristors [4–7]. This important research direction could lead to another stage of technical innovation in the memristor area. The principle

of the multistate memristor can be explained using the nonlinear dynamics theory as well as circuit and system theoretic concepts [4–6]. For example, the locally active generic Chua corsage memristor exhibits an asymptotical stability via the supercritical Hopf bifurcation [8–9]. Once an initial state is set, the state alters following its nonlinear dynamic route. The state changing is repeated until the state reaches a particular state which is termed as an “attractor.” In this type of memristors, the state space contains various attractors and each attractor has its own basin of attraction [10]. When inputs or noises are applied at a stable equilibrium state of the generic corsage memristor, the equilibrium state is moved by the amount of time integral of the inputs. However, unless the state moves beyond the boundary of current basin of attraction, the state returns back to its original equilibrium state (attractor) [8, 9]. Therefore, it can

become a robust memory device. Since a part of the previous programming history of the corsage memristor is lost in this procedure, the phenomenon is known as “local fading memory” in bistable and multistate memory devices [4].

Another feature of this type of multistate corsage memristor is the alteration of the stable equilibrium states. In this case, a sufficiently large amplitude with short pulse width or a minimum pulse amplitude with lengthy pulse width is applied across the memristor to switch the state from one stable equilibrium state to another stable state by converging into the basin of a new stable attractor. In this way, the equilibrium state of a multistate corsage memristor is changed to a new stable state where the resistances or conductances of each stable equilibrium state are distinguishably different from each other [7]. The alteration of the stable equilibrium states of corsage memristors is determined by the function of its input and initial condition, and henceforth, the corsage memristors exhibit multistability and eventually can be used as multistate memory devices.

In this paper, we demonstrate a novel quad-stable generic memristor, dubbed the *6-lobe Chua corsage memristor*. The dynamic routes of the 6-lobe corsage memristor have *four* asymptotically stable equilibrium points and *three* unstable equilibrium points at the DC input voltage $V=0$ V. The *four* asymptotically stable equilibrium points of the proposed memristor define the corresponding four distinct resistance levels and can be used to develop a multibit-per-cell memory device similar to the unidirectional spin Hall magnetoresistance [11]. The multistable memory states are distinguishable by resistance levels in accordance to stable equilibrium points where the memory states can be defined with a pair of bits. To ease the demonstration of the switching kinetics of multistable memory states of the proposed memristor, we derived *three universal formulas* regarding the exponential state $x_n(t)$, the time period t_{fn} , and the minimum pulse amplitude V_A .

In addition to the theoretical insights, we have designed and built a real emulator circuit of the proposed corsage memristor. For the physical realization of the piecewise linear 6-lobe Chua corsage memristor, we use the Graetz bridge [12] circuit in parallel with an *active and locally active* resistor [5]. Concepts from circuit and system theory, and techniques from nonlinear dynamics theory, are employed in this paper to elucidate the key mechanisms underlying the emergence of switching strategies of quad-stable memory.

The rest of the paper is organized as follows: the 6-lobe corsage memristor is designed and introduced in Section 2. The parametric representation and DC V - I curve are analyzed in Section 3. The switching kinetics and the physical implementation of the proposed corsage memristor are described in Sections 4 and 5, respectively, followed by the concluding remarks in Section 6.

2. 6-Lobe Chua Corsage Memristor Model

The *6-lobe Chua corsage memristor* is an extension of the 1st-order locally active Chua corsage memristor [8]. It is a

piecewise linear (PWL) memristor whose state-dependent Ohm's law and state equation are as follows:

$$i = G(x)v, \quad (1)$$

where

$$G(x) = G_0 x^2, \quad (2)$$

and

$$\frac{dx}{dt} = f(x) + v, \quad (3)$$

where

$$f(x) = 33 - x + |x - 6| - |x - 12| + |x - 20| - |x - 30| + |x - 42| - |x - 56|, \quad (4)$$

and x , i , and v denote the memristor state, current, and voltage, respectively. In practice, G_0 is a scaling constant chosen to fit the intrinsic memductance scale of the memristor. In this paper, we choose $G_0 = 10^{-6}$ so that the current of the 6-lobe Chua corsage memristor can be measured in *milliamperes (mA)* [7].

2.1. Frequency-Dependent Pinched Hysteresis Loops. The frequency-dependent pinched hysteresis loops of a device, when driven by any periodic input current or voltage source with a zero DC component, are a signature of a memristor or memristive system [13]. The 6-lobe Chua corsage memristor defined in (1), (2), (3), and (4) exhibits frequency-dependent pinched hysteresis loops when it is driven by a sinusoidal input signal $v(t) = A \sin(\omega t)$ where $A = 5$ V, as shown in Figure 1. The input voltage $v(t)$ and the corresponding memristor current $i(t)$ are shown in the upper-right side of Figure 1(a), and the memristor state $x(t)$ and memductance $G(t)$ are shown in the lower-right side of Figure 1(a), whereas the left side of Figure 1(a) shows the memristive circuit diagram with AC excitation. The frequency-dependent pinched hysteresis loops are shown in Figure 1(b) for frequencies $\omega = 1$ rad/s, 10 rad/s, 20 rad/s, and 100 rad/s. The lobe area of the pinched hysteresis loops shrinks as the frequency increases and tends to a straight line for $\omega \geq 100$ rad/s as shown in Figure 1(b) [14]. It follows that the proposed corsage memristor is a generic memristor [15].

2.2. Dynamic Routes with Their Phase Portrait. The dynamic route of a nonlinear system prescribes the dynamics of nonlinear differential equations [14]. The dynamic route of the *short-circuited* ($v=0$ V), namely, the *power-off-plot (POP)*, 6-lobe Chua corsage memristor is shown in Figure 2 where (5) is used to plot the loci of $dx/dt|_{v=0}$ versus x .

$$\frac{dx}{dt}\bigg|_{v=0} = \hat{f}(x) = 33 - x + |x - 6| - |x - 12| + |x - 20| - |x - 30| + |x - 42| - |x - 56|. \quad (5)$$

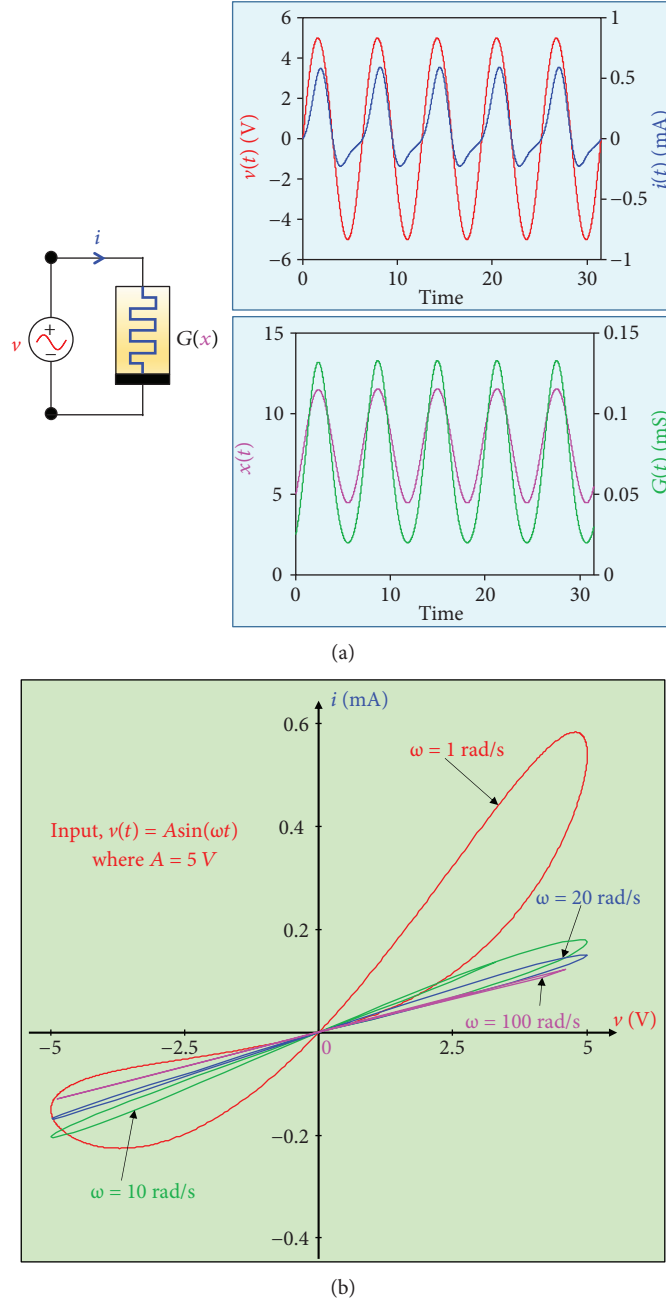


FIGURE 1: Frequency-dependent pinched hysteresis loop fingerprint of the 6-lobe Chua corsage memristor, calculated with initial state $x(0) = 5$: (a) the input voltage $v(t)$ (in red), corresponding memristor current $i(t)$ (in blue), memristor state $x(t)$ (in magenta), and memconductance $G(t)$ (in green) of the 6-lobe Chua corsage memristor; (b) frequency-dependent pinched hysteresis loops for zero-mean periodic input $v(t) = A \sin(\omega t)$ where $A = 5$ V and frequency $\omega = 1$ rad/s, 10 rad/s, 20 rad/s, and 100 rad/s.

The arrowheads in Figure 2 indicate the *direction of motion* of the state variable x from any initial state $x(0)$.

Figure 2 shows that for any initial state $x(0)$ on the *upper half* of the POP, where $dx/dt > 0$, the state variable $x(t)$ must move to the *right* as $x(t)$ increases with time, depicted by the purple arrowheads pointing to the right in Figure 2. On the contrary, for any initial state $x(0)$ on the *lower half* of the POP, where $dx/dt < 0$, the state variable $x(t)$ decreases with time and must move to the left, depicted by the black arrowheads pointing to the left in Figure 2. In the

theory of *nonlinear dynamics* [16], the stationary points where $dx/dt = 0$ or $\hat{f}(x)$ intersects the x -axis; are known as *equilibrium points*. Figure 2 shows that $\hat{f}(x)$ intersects the x -axis at seven points, namely, $x = X_{Q1} = 3$ (Q_1), $x = X_{Q2} = 9$ (Q_2), $x = X_{Q3} = 15$ (Q_3), $x = X_{Q4} = 25$ (Q_4), $x = X_{Q5} = 35$ (Q_5), $x = X_{Q6} = 49$ (Q_6), and $x = X_{Q7} = 63$ (Q_7). The equilibrium points Q_1 , Q_3 , Q_5 , and Q_7 are stable whereas Q_2 , Q_4 , and Q_6 are unstable equilibrium points because the state variable $x(t)$ diverges away from Q_2 , Q_4 , and

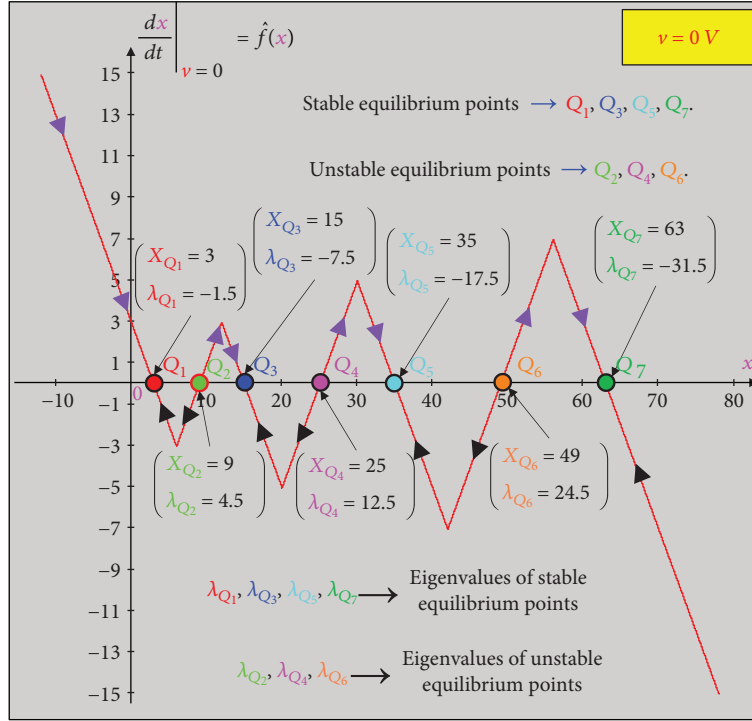


FIGURE 2: Dynamic route map of the 6-lobe Chua corsage memristor at $V=0$ V is called the *power-off-plot* (POP).

Q_6 . Moreover, the equilibrium points Q_1 , Q_3 , Q_5 , and Q_7 in Figure 2 are stable as the corresponding eigenvalues of those equilibrium points are negative real numbers whereas Q_2 , Q_4 , and Q_6 are unstable as the eigenvalues are positive [17].

Figure 2 shows that for any initial state $x(0) > X_Q + \delta x$, where $X_Q \in \{X_{Q_2}, X_{Q_4}, X_{Q_6}\}$, the unstable equilibrium points Q_2 , Q_4 , and Q_6 converge to stable equilibrium points Q_3 , Q_5 , and Q_7 , respectively, to their right as shown with purple arrowheads. In contrast, for any initial state $x(0) < X_Q - \delta x$, Q_2 , Q_4 , and Q_6 converge to stable equilibrium points Q_1 , Q_3 , and Q_5 , respectively, to their left as shown with black arrowheads.

The phase portrait of stable equilibrium states Q_1 , Q_3 , Q_5 , and Q_7 is shown in Figure 3 where the dotted straight lines represent the separatrices between two stable equilibrium states and pass through the unstable equilibrium points Q_2 , Q_4 , and Q_6 , respectively. Similar to Figure 2, Figure 3 also shows that for any $x(0) > (X_{Q_2} \text{ or } X_{Q_4} \text{ or } X_{Q_6})$, the trajectories of $x(t)$ converge to Q_3 , Q_5 , and Q_7 , respectively, as shown with purple arrowheads. Conversely, for $x(0) < (X_{Q_2} \text{ or } X_{Q_4} \text{ or } X_{Q_6})$, $x(t)$ converges to Q_1 , Q_3 , and Q_5 , respectively, as shown with black arrowheads.

The dynamic routes in Figure 2 and the phase portrait in Figure 3 illustrate that the proposed memristor can be used as a 4-state or multibit-per-cell (2-bit) memory device at $v=0$ V.

The more stable equilibrium states of the 6-lobe corsage memristor increases the memory efficiency per device 50% and 25% compared to 2-lobe and 4-lobe corsage memristors, respectively, and eventually enhance the

capability to represent a desired function more closely than 2-lobe or 4-lobe corsage memristors.

3. Parametric Representation and the DC V-I Curve

In mathematics, parametric representation of an object is a collection of parametric equations which are used to express the coordinates of the points that make up a geometric object [18] where those parametric equations are defined by a group of quantities based on a function of one or more independent variables [19].

3.1. Parametric Representation. The parametric representation of the 6-lobe Chua corsage memristor can be derived by equating state (3) to zero ($dx/dt=0$) and solving for the following equilibrium points (6) for each DC input voltage $v=V$, at the DC equilibrium state $x=X(V)$:

$$\begin{aligned} \frac{dx}{dt} = & (33 - x + |x - 6| - |x - 12| + |x - 20| - |x - 30| \\ & + |x - 42| - |x - 56|) + v = 0. \end{aligned} \quad (6)$$

The DC voltage of the proposed corsage memristor is given explicitly by

$$\begin{aligned} V = & -(33 - x + |x - 6| - |x - 12| + |x - 20| - |x - 30| \\ & + |x - 42| - |x - 56|) \triangleq \hat{v}(X). \end{aligned} \quad (7)$$

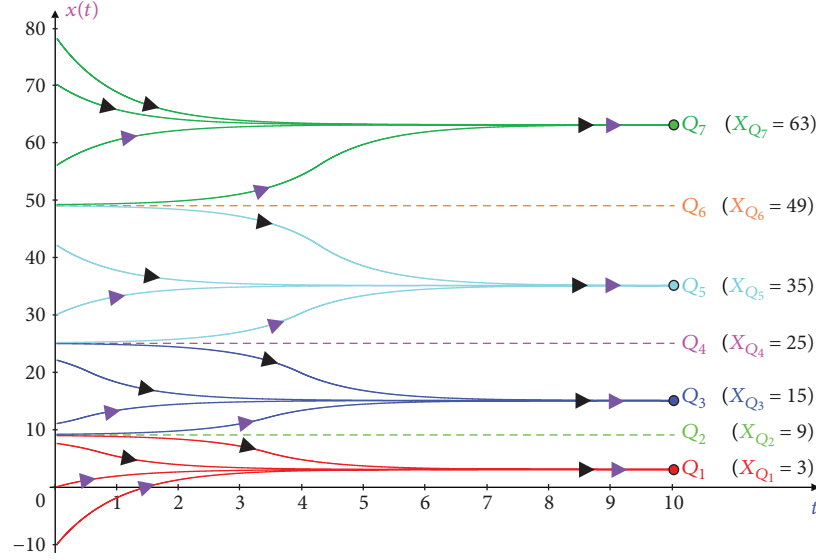


FIGURE 3: Phase portrait of the stable equilibrium states Q_1 , Q_3 , Q_5 , and Q_7 . The horizontal dotted lines are the separatrices and pass through the unstable equilibrium states Q_2 , Q_4 , and Q_6 , respectively.

The parametric representation of the DC current of the 6-lobe cossage memristor can be derived by substituting V given by (7) for v in (1) with $G_0 = 10^{-6}$, namely,

$$I = -G_0 X^2 (33 - x + |x - 6| - |x - 12| + |x - 20| - |x - 30| + |x - 42| - |x - 56|) \triangleq \hat{i}(X). \quad (8)$$

The parametric representations of the proposed cossage memristor are shown in Figure 4 where Figures 4(a) and 4(b) show the loci of the parametric representation of $V = \hat{v}(x)$ versus X and $I = \hat{i}(x)$ versus X , respectively. The loci of the parametrically represented $V = \hat{v}(x)$ versus $I = \hat{i}(x)$ are shown in Figure 4(c).

For convenience of readers, several points of the parametric representation of $V = \hat{v}(x)$ and $I = \hat{i}(x)$ of the 6-lobe Chua cossage memristor over the range $\chi = \{X: -12 \leq X \leq 78\}$ are listed in Table 1.

3.2. DC V - I Plot. A circuit-theoretic approach is used to derive the DC V - I loci of the voltage-controlled 6-lobe Chua cossage memristor. Each DC value of voltage V and current I is computed using the following steps:

- (1) For each value of V listed in Table 1, we calculate all equilibria $x = X_k$, $1 \leq k \leq 7$, of the proposed memristor using state (3) where $dx/dt = 0$

$$V = -(33 - x + |x - 6| - |x - 12| + |x - 20| - |x - 30| + |x - 42| - |x - 56|) \triangleq \hat{v}(X). \quad (9)$$

- (2) Then we determine the DC current $i = I$ of the memristor corresponding to each equilibrium point $X = X_1, X_2, \dots, X_N$, $1 \leq N \leq 7$:

$$I = -G_0 X^2 (33 - x + |x - 6| - |x - 12| + |x - 20| - |x - 30| + |x - 42| - |x - 56|) \triangleq \hat{i}(X). \quad (10)$$

- (3) Finally, we draw the DC V - I curve by plotting the coordinates (V, I) on the V - I plane for each value of X .

The DC V - I loci of the 6-lobe cossage memristor is shown in Figure 5 over the input voltage range $-10 \text{ V} \leq V \leq 10 \text{ V}$ where the solid curves correspond to stable equilibrium states and the dash curves correspond to unstable equilibrium states. Since the DC V - I curve contains six contiguous lobes, henceforth call it the “six lobe cossage V - I curve.” The seven different colored DC V - I branches in Figure 5 represent the equilibrium points of the corresponding colors in Figure 3. At $v = 0 \text{ V}$, the state variables are $x = 3$ (red DC V - I curve Q_1), $x = 9$ (fluorescent green DC V - I curve Q_2), $x = 15$ (blue DC V - I curve Q_3), $x = 25$ (magenta DC V - I curve Q_4), $x = 35$ (cyan DC V - I curve Q_5), $x = 49$ (brown DC V - I curve Q_6), and $x = 63$ (green DC V - I curve Q_7). As the values of the state variable of each DC V - I branch at the origin are different, their slopes (i.e., conductances $G(x)$) at the origin are also different according to (2), as tabulated in the upper-left inset of Figure 5. The tabulated upper-left inset shows that the red DC V - I curve represents the lower conductance state (higher resistance state) whereas the green DC V - I curve represents the higher conductance state (lower resistance state). Moreover, the lower-right inset of Figure 5 shows a zoomed portion of the red DC V - I curve over

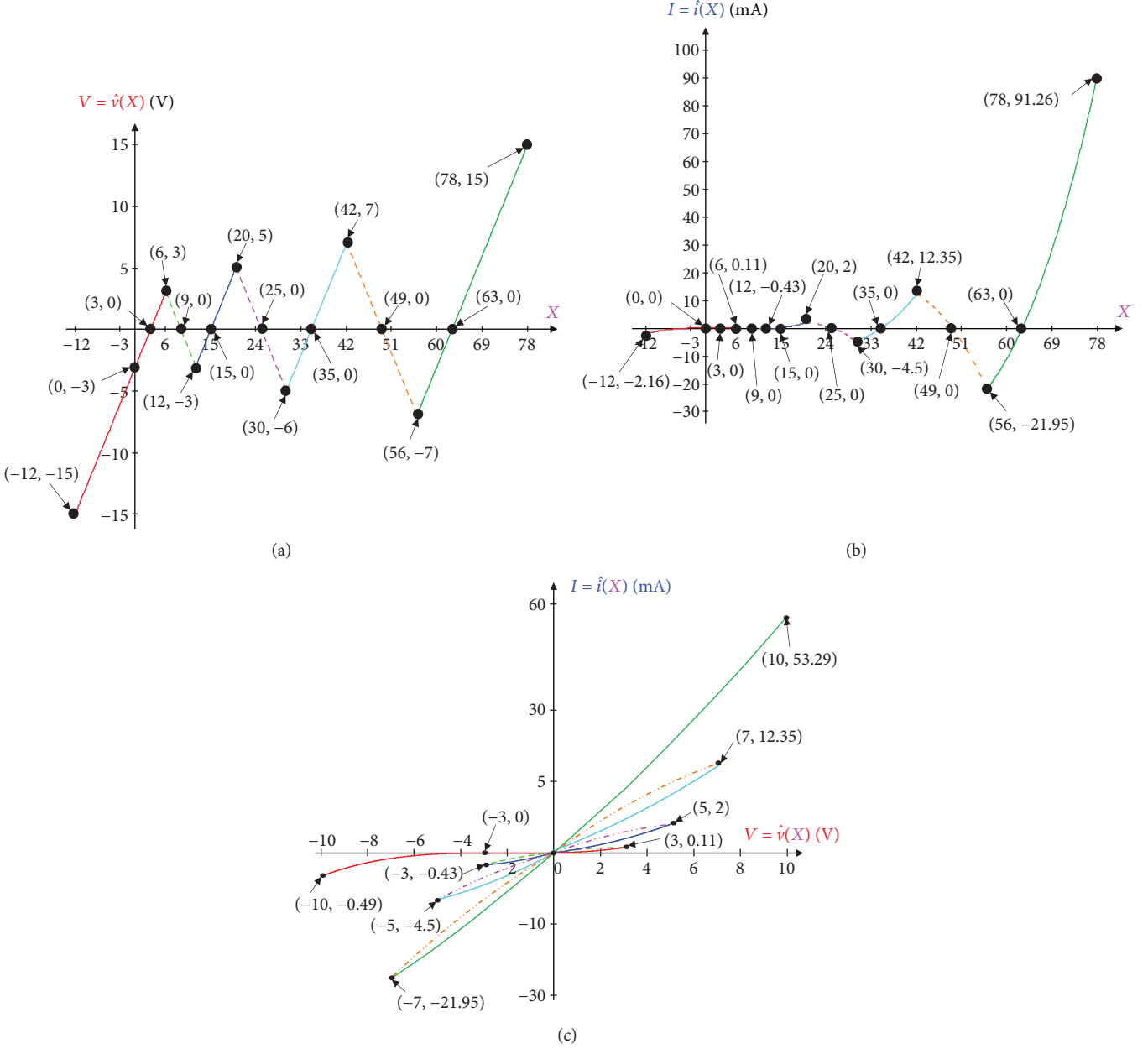


FIGURE 4: Parametric representations of the 6-lobe Chua corsage memristor (a) voltage $V = \hat{v}(X)$ versus state variable X and (b) current $I = \hat{i}(X)$ versus state variable X , for each value of $\chi = \{X: -12 \leq X \leq 78\}$. (c) DC V - I plot, where the coordinates (V, I) of each point are extracted from (a) and (b), for each value of $\chi = \{X: -7 \leq X \leq 73\}$ for better illustration.

the range $-5 \text{ V} \leq V \leq 2 \text{ V}$. The zoomed red DC V - I curve contains a *negative-slope region* over the voltage range $-3 \text{ V} < V < -1 \text{ V}$ which affirms that the proposed corsage memristor is locally active over the $-3 \text{ V} < V < -1 \text{ V}$ range as $\text{Re}Z(i\omega) < 0$ for DC input voltage ($\omega = 0$) [8]. The locally active negative slope region of the 6-lobe Chua corsage memristor is significant in circuit theory as it might give rise to complexity through which *complex phenomenon and information processing* might emerge [20, 21].

One of the most important features of the 6-lobe corsage memristor is the contiguousness of its DC V - I curve which is

different from many other published nonlinear DC V - I curves which exhibit several *disconnected* branches [14].

Another impressive feature is that the parametric representation and the DC V - I curve of the proposed corsage memristor has an explicit analytical equation, which rarely happens.

4. Switching Strategies of Memory States

The *power-off-plot* in Figure 2 shows that the 6-lobe Chua corsage memristor can be used as a *4-state* or *2-bit*

TABLE 1: Numerical values of the 6-lobe corsage memristor obtained from parametric representation over $-12 \leq X \leq 78$.

X	$V = \hat{v}(X)$ (V)	$I = \hat{i}(X)$ (mA)
-12	-15	-2.16
0	-3	0
3	0	0
6	3	0.11
9	0	0
10	-1	-0.1
12	-3	-0.43
15	0	0
20	5	2
25	0	0
30	-5	-4.5
35	0	0
40	5	8
42	7	12.35
49	0	0
50	-1	-2.5
56	-7	-21.95
60	-3	-10.8
63	0	0
70	7	34.3
78	15	91.26

memory device at $v = 0$ V. Conceptually, the simplest way to switch the memory states of the 6-lobe corsage memristor is to apply a square pulse with an appropriate pulse amplitude V_A and pulse width Δw . For a successful switching between the memory states of the proposed corsage memristor, the square pulse should have a minimum pulse width for an appropriate pulse amplitude, V_A . Any square pulse with less than the minimum pulse width results in switching failure.

The switching kinetics of the 6-lobe Chua corsage memristor can be represented through its *dynamic route map* (DRM). The solution of each straight-line segment of the dynamic route map of our corsage memristor is an exponential function where the complete solution $\mathbf{x}(t)$ is made of a sequence of the exponential waveforms, joined at the various breakpoints in the dynamic routes. In this paper, we derived the following universal exponential state variable $x_n(t)$ formula related to a straight-line segment around an equilibrium point Q_n of the piecewise linear DRM (detailed derivation of $x_n(t)$, t_{fn} , and V_A are provided in the supplementary document (available here).):

$$x_n(t) = Q_n - mv(t) \left(1 - e^{m(t-t_{0n})} \right) - (Q_n - x(t_{0n})) e^{m(t-t_{0n})}, \quad (11)$$

where m represents the sign value of the straight-line slope,

$$m = \text{sgn} \left(\frac{(dx/dt)|_{\text{start}} - (dx/dt)|_{\text{end}}}{x_{\text{start}} - x_{\text{end}}} \right), \quad (12)$$

and t_{0n} is the initial time of the segment whereas $x(t_{0n})$ represents the initial state at t_{0n} . The universal formula of the time, t_{fn} , required for the trajectory of $x_n(t)$ to move from any initial point $x(t_{0n})$ to the end of the straight-line segment is also derived as follows:

$$t_{fn} = t_{0n} + \underbrace{\frac{1}{m} \ln \left[\frac{(Q_n - mv(t) - x(t_{fn}))}{(Q_n - mv(t) - x(t_{0n}))} \right]}_{\Delta t_{fn}}. \quad (13)$$

The appropriate pulse amplitude V_A is computed by replacing $t = t_{fn}$ in (11) and substituting the value of t_{fn} from (13) to (11) where the resultant equation is shown as follows:

$$V_A > Q_{n-1} - x(t_{0(n-1)}), \quad (14)$$

where Q_{n-1} and $x(t_{0(n-1)})$ represent, respectively, the immediate before equilibrium point and the initial state of the resultant memory state Q_n .

The derived universal formulas in (11), (12), (13), and (14) are applicable for any piecewise linear DRM curve of any number of segments and any DC or pulse input $v(t)$. Such exponential analytical solutions can be derived from no nonlinear functions other than the PWL functions.

The dynamic route map (DRM) in Figure 6(a) shows an application of successful switching for an appropriate pulse amplitude V_A and pulse width Δw where the 6-lobe corsage memristor switches from high-resistance (low conductance) state Q_1 to low-resistance (high conductance) state Q_5 . To switch from Q_1 to Q_5 , we choose the pulse amplitude $V_A = 5.5$ V which satisfies the condition $V_A > [(Q_4 - x(t_{04})) = 5]$. To compute the appropriate pulse width Δw , we choose the final state (with input V_A) $x_{\Delta w}(t) = 26.5$ for a square pulse $v(t)$ by satisfying the condition $x_{\Delta w}(t) > Q_4$, as shown in Figure 6(a). For $x_{\Delta w}(t) \leq Q_4$, the proposed corsage memristor fails to switch from memory state Q_1 to Q_5 and converges to memory state Q_3 . However, pulse width Δw is equal to the time required for the trajectories to move from $x_1(t_{01})$ to $x_{\Delta w}(t)$ and can be computed by summing the time needed for each individual straight-line segment to reach the terminal points and express as

$$\Delta w = \Delta t_{f1} + \Delta t_{f2} + \Delta t_{f3} + \Delta t_{f4}. \quad (15)$$

The total time period t_f required to move from memory state Q_1 to Q_5 is expressed as

$$t_f = \Delta w + \Delta t_{f4wv} + \Delta t_{f5}, \quad (16)$$

as shown in Figure 6. The sequence of exponential $x(t)$ obtained from (11) is shown as follows:

$$x(t) = \begin{cases} x_1(t) = Q_1 + v(t) \left(1 - e^{-(t-t_{01})}\right) - (Q_1 - x_1(t_{01}))e^{-(t-t_{01})}, & t_{01} \leq t < t_{f1}, \\ x_2(t) = Q_2 - v(t) \left(1 - e^{-(t-t_{02})}\right) - (Q_2 - x_2(t_{02}))e^{-(t-t_{02})}, & t_{02} \leq t < t_{f2}, \\ x_3(t) = Q_3 + v(t) \left(1 - e^{-(t-t_{03})}\right) - (Q_3 - x_3(t_{03}))e^{-(t-t_{03})}, & t_{03} \leq t < t_{f3}, \\ x_4(t) = Q_4 - v(t) \left(1 - e^{-(t-t_{04})}\right) - (Q_4 - x_4(t_{04}))e^{-(t-t_{04})}, & t_{04} \leq t < t_{f4}, \\ x_{4wv}(t) = Q_4 - v(t) \left(1 - e^{-(t-t_{04wv})}\right) - (Q_4 - x_{4wv}(t_{04wv}))e^{-(t-t_{04wv})}, & t_{04wv} \leq t < t_{f4wv}, \\ x_5(t) = Q_5 + v(t) \left(1 - e^{-(t-t_{05})}\right) - (Q_5 - x_5(t_{05}))e^{-(t-t_{05})}, & t_{05} \leq t, \end{cases} \quad (17)$$

and by inserting the initial states, equilibrium points, and time period for the trajectories to move from

initial states to final states, the $x(t)$ can be expressed as follows:

$$x(t) = \begin{cases} x_1(t) = 3 + v(t) \left(1 - e^{-(t-t_{01})}\right), & (t_{01} = 0) \leq t < (t_{f1} = 0.778), \\ x_2(t) = 9 - v(t) \left(1 - e^{-(t-t_{02})}\right) - 3e^{-(t-t_{02})}, & (t_{02} = t_{f1} = 0.778) \leq t < (t_{f2} = 2.008), \\ x_3(t) = 15 + v(t) \left(1 - e^{-(t-t_{03})}\right) - 3e^{-(t-t_{03})}, & (t_{03} = t_{f2} = 2.008) \leq t < (t_{f3} = 4.841), \\ x_4(t) = 25 - v(t) \left(1 - e^{-(t-t_{04})}\right) - 5e^{-(t-t_{04})}, & (t_{04} = t_{f3} = 4.841) \leq t < (t_{f4} = 7.48), \\ x_{4wv}(t) = 25 - v(t) \left(1 - e^{-(t-t_{04wv})}\right) + 1.5e^{-(t-t_{04wv})}, & (t_{04wv} = t_{f4} = 7.48) \leq t < (t_{f4wv} = 8.684), \\ x_5(t) = 35 + v(t) \left(1 - e^{-(t-t_{05})}\right) - 5e^{-(t-t_{05})}, & (t_{05} = t_{f4wv} = 8.684) \leq t. \end{cases} \quad (18)$$

The memory state switching from Q_1 to Q_5 in Figure 6(a) shows that the applied square pulse with $V_A = 5.5$ V is equivalent to translating the red curve $f(x)$ upwards by 5.5 units, as shown by the blue curve. The dynamic route starting from Q_1 ($x = 3$), at $t = 0^-$, would jump abruptly from Q_1 on the red curve to a point directly above Q_1 on the blue curve (yellow circle) at $t = 0^+$ (shown with the upward green arrow) as the pulse input increases from 0 V to 5.5 V. Since the blue curve is located above the x -axis (where $dx/dt > 0$) over the range of interest, its motion can only move to the right, until time $t = \Delta w$. When the square pulse returns to zero at $t = \Delta w$, the point (shown with the green circle) on the blue curve reverts back abruptly to the point $x_{\Delta w}(t = \Delta w) = 26.5$ on the red curve (shown with the light cyan circle followed by the downward green arrowhead), whereupon the dynamics must continue to move along the dynamic route indicated by the black arrowheads, until it converges to the low-resistance memory state Q_5 ($x = 35$).

The exponential trajectories of the $x(t)$ related with the individual piecewise linear segments are shown in Figure 6(b). Observe from Figure 6(b) that the total time period (t_f) needed for the $x(t)$ trajectories to reach Q_5 from Q_1 is the summation of all the time periods needed for an individual trajectory to propagate through the piecewise linear segments which is $t_f = \Delta w + \Delta t_{f4wv} + \Delta t_{f5} = 17.2$ s.

To switch back from the low-resistance (high conductance) state Q_5 to the high-resistance (low conductance) state Q_1 of our corsage memristor, we simply applied a negative voltage pulse with amplitude $V_A = -5.5$ V and pulse width $\Delta w_b = 7.684$ s where Δw_b is computed using (15). The dynamic route and the state trajectories $x(t)$ of switching back kinetics from memory states Q_5 to Q_1 is shown in Figures 7(a) and 7(b), respectively. In Figure 7(a), at $t_b = \Delta w_b$, the state variable $x_{\Delta w_b}(t_b = \Delta w_b) = 8.9$ and the slope $dx/dt < 0$ at that linear segment for which the state variable $x(t)$ must move to the right and eventually converge

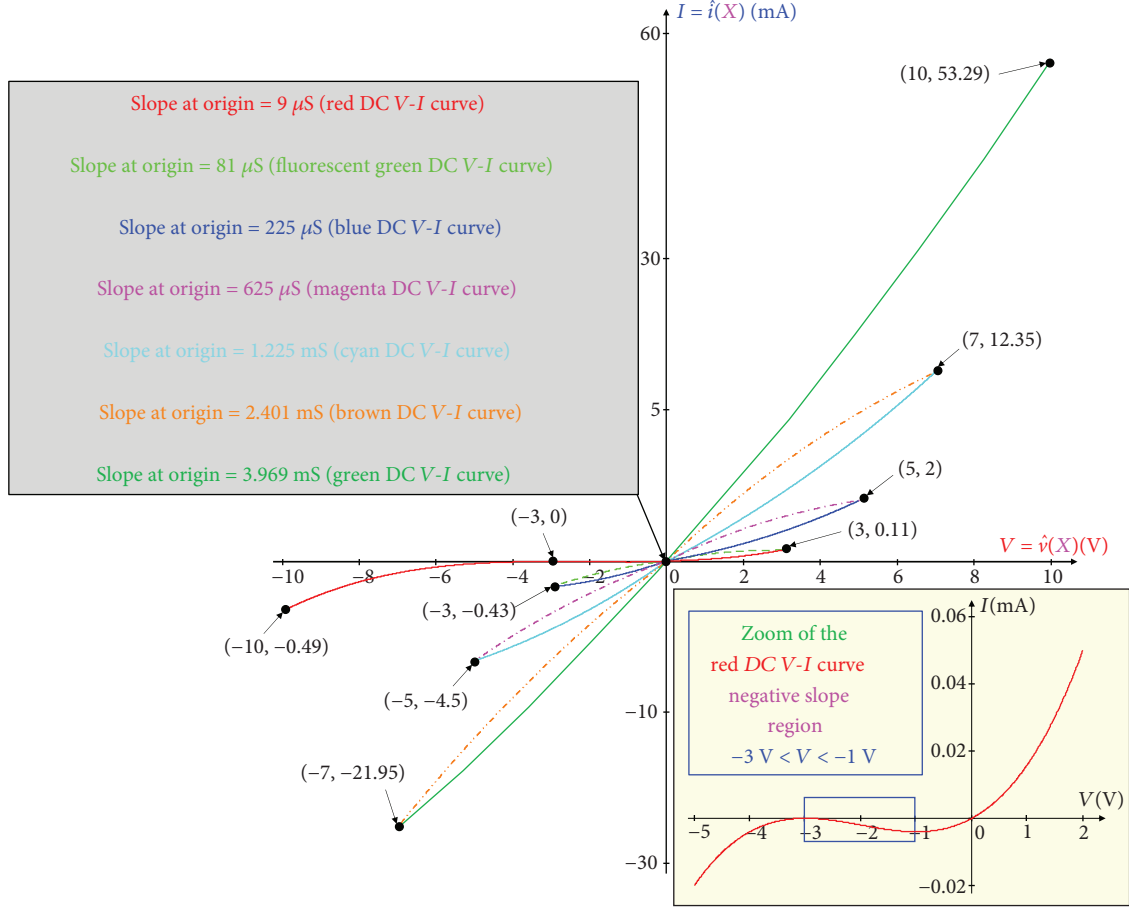


FIGURE 5: DC V - I plot of the 6-lobe corsage memristor over input voltage $-10 \text{ V} \leq V \leq 10 \text{ V}$. The left inset shows the conductance values at $V=0 \text{ V}$. The right inset shows the zoomed portion of the red DC V - I curve over the voltage range $-5 \text{ V} \leq V \leq 2 \text{ V}$.

to the equilibrium memory state Q_1 ($x=3$). The similar phenomenon with exponential trajectories of $x(t)$ is shown in Figure 7(b) where the $x(t)$ decreases as the time increases and converges to $x(t_{f1b})=3$ where $x(t_{f1b})=3$ is regarded as the Q_1 memory state. To switch back from Q_5 to Q_1 , the total time $t_{fb}=20.701 \text{ s}$ is needed as shown in Figure 7(b).

The pulse amplitude V_A and the pulse width Δw play a crucial role in the switching kinetics of the memory states of the 6-lobe Chua corsage memristor. An inappropriate pulse amplitude or pulse width may result in switching failures. To choose the appropriate pulse amplitude V_A , we already provided (14) whereas we illustrate the inappropriate pulse width scenario in Figure 8. In Figure 8, we provide the same pulse amplitude $V_A=5.5 \text{ V}$ to switch from memory state Q_1 to Q_5 with a different pulse width $\Delta w=7 \text{ s}$. Observe from Figure 8(b) that the exponential trajectories are converging to memory state Q_3 ($x=15$) rather than converging to memory state Q_5 ($x=35$). The reason behind such switching failure is the pulse width as at $t=\Delta w$ and the state variable $x_{\Delta w}(t=\Delta w)=23.812$ which lies in the left-hand side of Q_4 ($x=25$), as shown in Figure 8(a). According to Section 2.2, any point that lies in the left side of Q_4 ($x=25$) follows the dynamic route $dx/dt < 0$ (as shown with the black

arrowhead in Figure 2) and converges to equilibrium state Q_3 , and in this case, the state variable $x(t)$ follows the same route $dx/dt < 0$ and converges to Q_3 ($x=15$) as $x_{\Delta w}(t=\Delta w) < Q_4$.

For convenience of the readers, we plotted the hyperbolic relationship between the pulse amplitude V_A versus the pulse width Δw of the switching memory states between Q_1 and Q_5 of our 6-lobe corsage memristor as shown in Figure 9.

5. Physical Realization of the 6-Lobe Chua Corsage Memristor

For physical realization of the 6-lobe Chua corsage memristor, we modified the circuit in Figure 1(a) with the switching kinetics closer to the behavioral attributes of our 7-segment PWL hypothetical memristor which is shown in Figure 10. The novel circuit consists of the cascade between a passive nonlinear-resistive two-port and a dynamic first-order one-port [5]. The passive nonlinear-resistive two-port is composed of parallel connected Graetz bridges [12] with opposite diode directions whereas the dynamic first-order one-port is made up of a C - R parallel circuit.

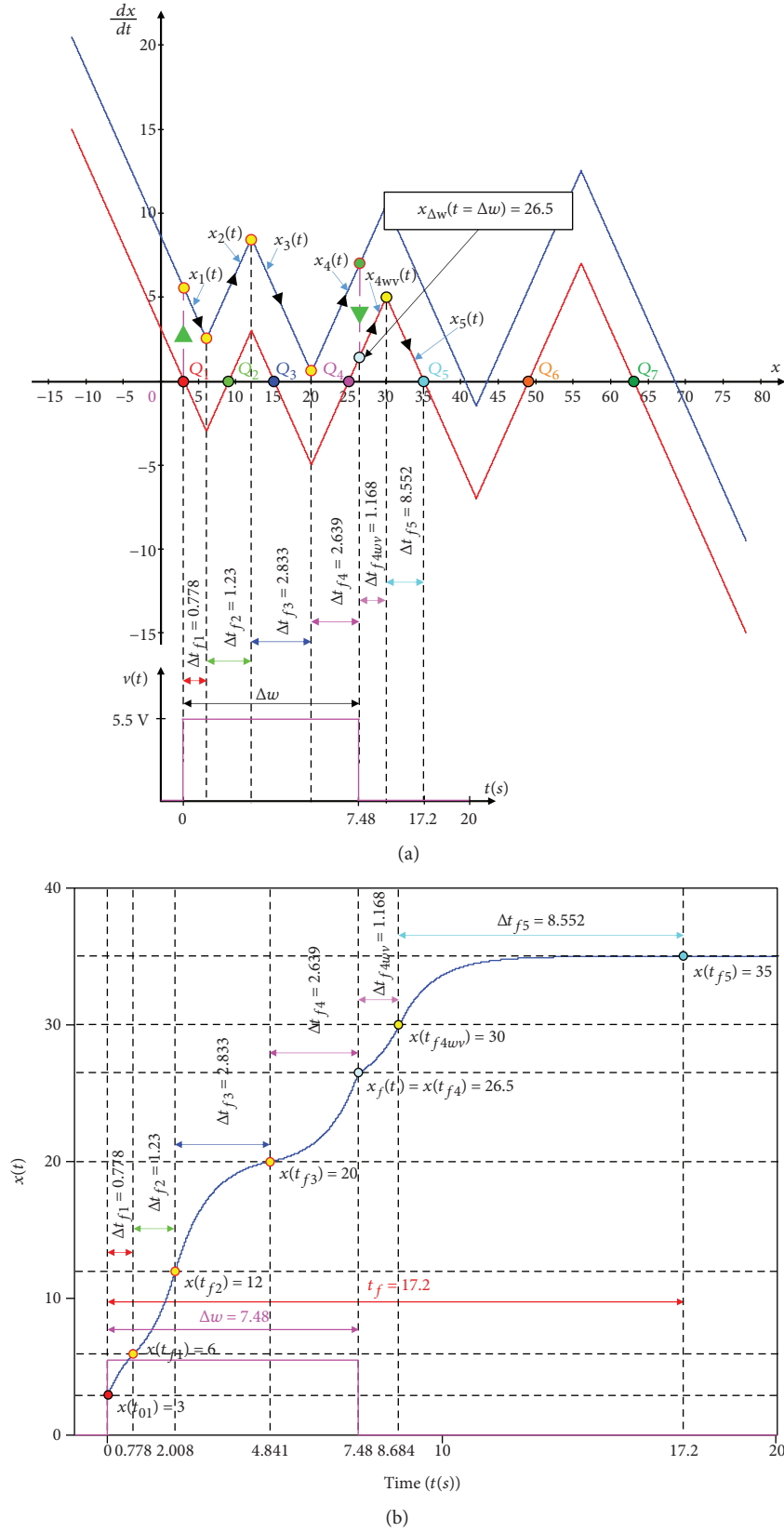


FIGURE 6: Memory state switching kinetics of the 6-lobe Chua corsage memristor from memory state Q_1 to Q_5 for an input square pulse $V_A = 5.5$ V and $\Delta w = 7.48$ s. (a) Dynamic routes of the switching kinetics of the 6-lobe Chua corsage memristor. The two magenta-color vertical line segments indicate an instantaneous jump between the red and the blue piecewise-linear plots in the dynamic route map. (b) Movement of the exponential trajectories of $x(t)$ with respect to time t .

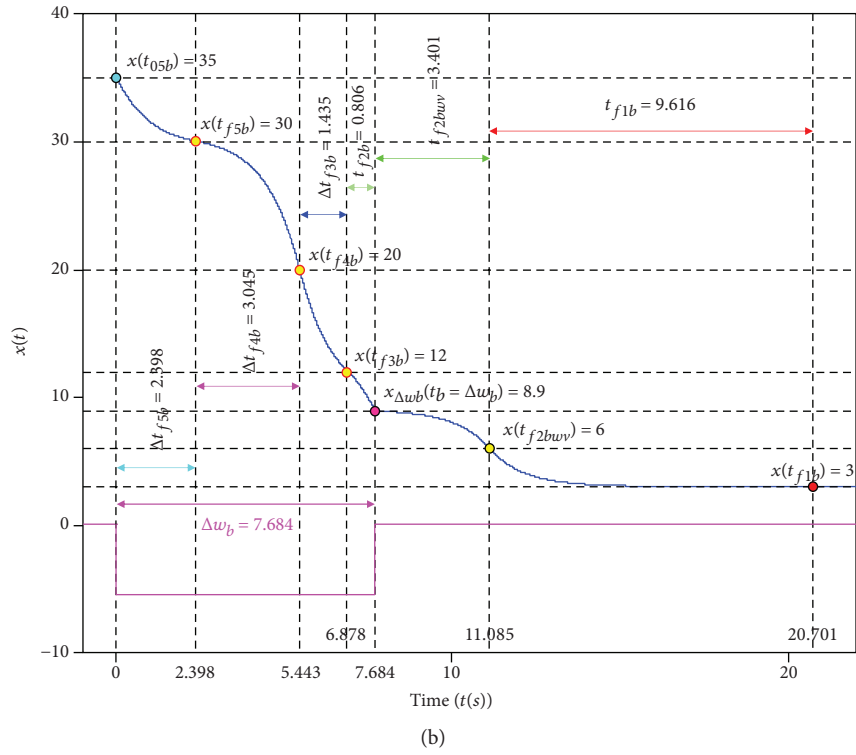
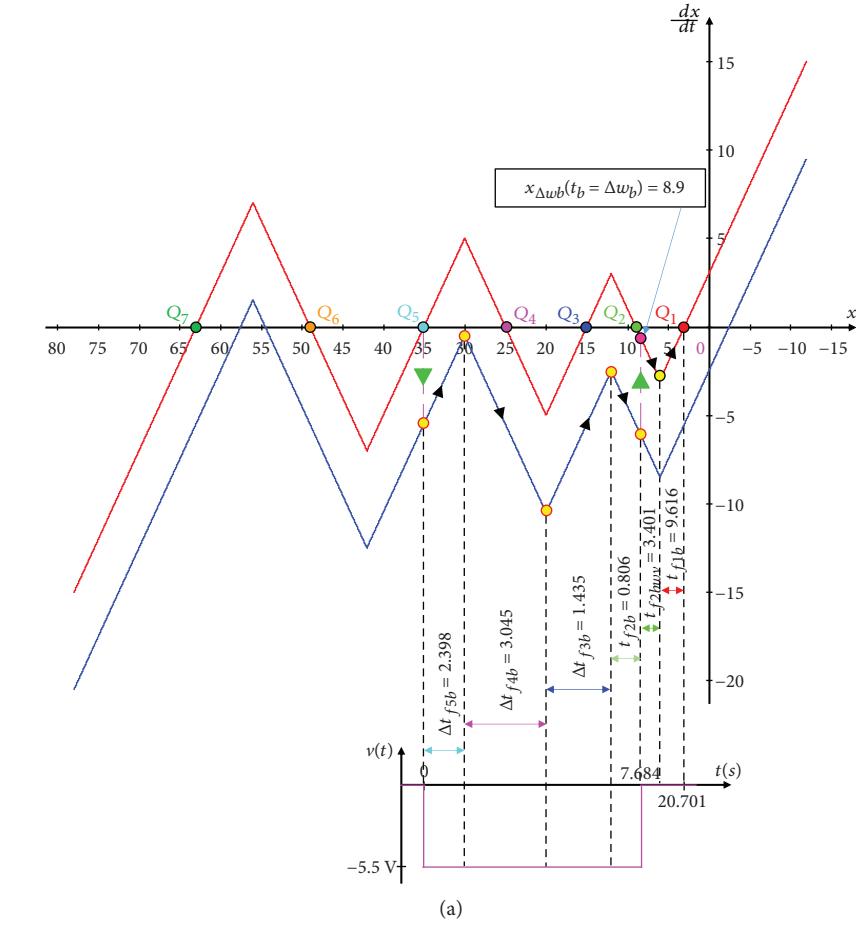


FIGURE 7: Switching kinetics from low-resistance state Q_5 to high-resistance state Q_1 for an input square pulse $V_A = -5.5$ V and $\Delta w_b = 7.684$ s. (a) Dynamic routes of the switching-back kinetics of the proposed cossage memristor. (b) Movement of the exponential trajectories of $x(t)$ with respect to time t .

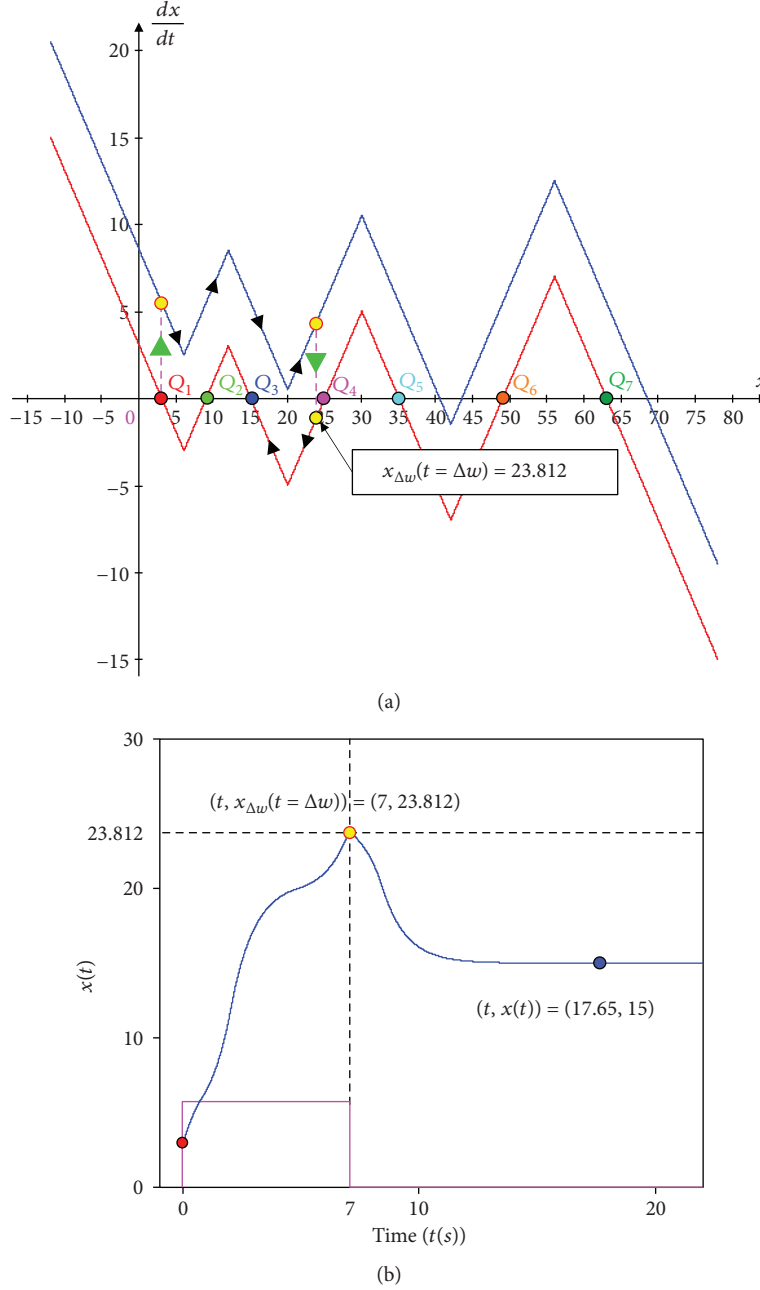


FIGURE 8: Switching failures of the 6-lobe corsage memristor from Q_1 to Q_5 for a pulse amplitude $V_A = 5.5$ V and pulse width $\Delta w = 7$ s. (a) Dynamic routes of the switching kinetics and (b) movement of the exponential trajectories of $x(t)$ with respect to time t . The switching failure happens due to insufficient pulse width.

The *active and locally active* resistor R_0 in Figure 10 should exhibit the contiguous six breakpoints on its DC V - I curve similar to the 6-lobe Chua corsage memristor. To design the nonlinear resistor R_0 , we applied the circuit-theoretic analysis on an op-amp circuit [22] to obtain the desired DC V - I breakpoints at specific voltages. According to [22], the driving-point characteristic of a single positive and negative feedback op-amp circuit provides *two* breakpoints on its piecewise linear DC V - I curve. To obtain a *six*-breakpoint piecewise linear DC V - I curve, we combine three op-amp circuits in parallel as shown in Figure 11.

The current i coming out from the parallel op-amp circuit in Figure 11 provides a piecewise linear DC V - I curve with *six* breakpoints when plotted in the V - I plane.

The active and locally active two-port (marked with the black box) in Figure 11 consists of three op-amp circuits (marked with red, blue, and magenta boxes) in parallel. The circuit parameters and the components of the three op-amp circuit in Figure 11 are similar for each box except the negative feedback resistances (R_{41} , R_{42} , and R_{43}) which determine the effective saturation voltage E_{sat} of an individual op-amp circuit. The saturation voltage E_{sat} along with

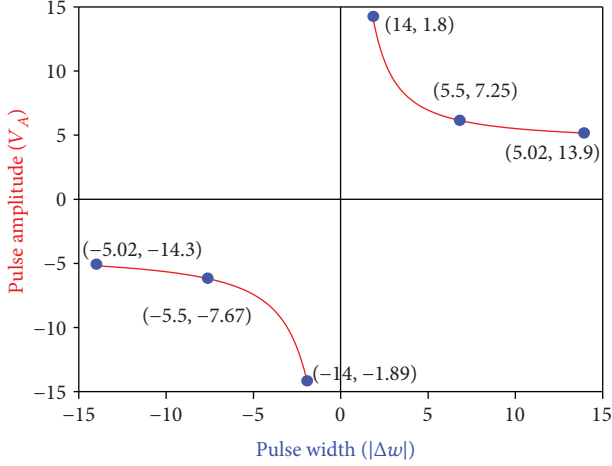


FIGURE 9: Relationship between the pulse amplitude V_A and pulse width Δw for the switching kinetics of the 6-lobe cossage memristor.

the negative feedback resistance play a key role to achieve the V - I breakpoints at specified voltages such as $V = 3$ V, $V = 5$ V, and $V = 7$ V. The op-amp circuits in Figure 11 also contain a positive feedback path where the difficulty arises with the driving-point and transfer function. To resolve this problem, we replace the op-amp circuit in the red box (in Figure 11) by its three ideal models, such as the “Linear region,” “+Saturation region,” and “-Saturation region” as shown in Figures 12(a)–12(c), respectively.

The Linear region of the op-amp circuit in Figure 12(a) shows that the potential difference between the noninverting terminal (v_+) and the inverting terminal (v_-) is zero, so the differential voltage $v_d = (v_+ - v_-) = 0$ and eventually inverting terminal voltage,

$$v_- = v_+ = v_x = v. \quad (19)$$

The following relation between output voltage v_{03} and inverting terminal voltage v_- can be computed by the voltage divider rule

$$v_- = v_x = \left(\frac{R_{33}}{R_{33} + R_{43}} \right) v_{03} = \beta v_{03}, \quad (20)$$

where $\beta = R_{33}/(R_{33} + R_{43})$ and henceforth

$$v = \beta v_{03}. \quad (21)$$

Pedagogically, in the linear region, the relation between the saturation voltage ($\pm E_{\text{sat}}$) and output voltage v_{03} is as follows:

$$-E_{\text{sat}} < v_{03} < E_{\text{sat}}, \quad (22)$$

for which, in the Linear region, the relation between the input voltage v and saturation voltage ($\pm E_{\text{sat}}$) is

$$-\beta E_{\text{sat}} < v < \beta E_{\text{sat}}. \quad (23)$$

The loop

$$\textcircled{4} - \textcircled{3} - \textcircled{1} - \textcircled{4} \quad (24)$$

provides linear region current i_{lin} as

$$i_{\text{lin}} = \frac{1}{R_{73}} \left[v \left(1 + \frac{R_{73}}{R_{63}} \right) - v_{03} \right]. \quad (25)$$

For the +Saturation region shown in Figure 12(b), the relation between the output voltage v_{03} and the saturation voltage E_{sat} is as follows:

$$v_{03} = E_{\text{sat}}, \quad (26)$$

and the differential voltage $v_d > 0$, so that $(v_+ - v_-) > 0$, and eventually the relationship between input voltage and saturation voltage is

$$v \geq \beta E_{\text{sat}}. \quad (27)$$

The current for the +Saturation region $i_{+\text{sat}}$ is computed as follows:

$$i_{+\text{sat}} = \frac{1}{R_{73}} \left[v \left(1 + \frac{R_{73}}{R_{63}} \right) - E_{\text{sat}} \right]. \quad (28)$$

For the -Saturation region shown in Figure 12(c), the relation between the output voltage v_{03} and the saturation voltage E_{sat} is

$$v_{03} = -E_{\text{sat}}, \quad (29)$$

and $v_d < 0$, so that $(v_+ - v_-) < 0$, and henceforth, the relationship between the input voltage and saturation voltage is

$$v \leq -\beta E_{\text{sat}}, \quad (30)$$

and the -Saturation region current is computed as

$$i_{-\text{sat}} = \frac{1}{R_{73}} \left[v \left(1 + \frac{R_{73}}{R_{63}} \right) + E_{\text{sat}} \right]. \quad (31)$$

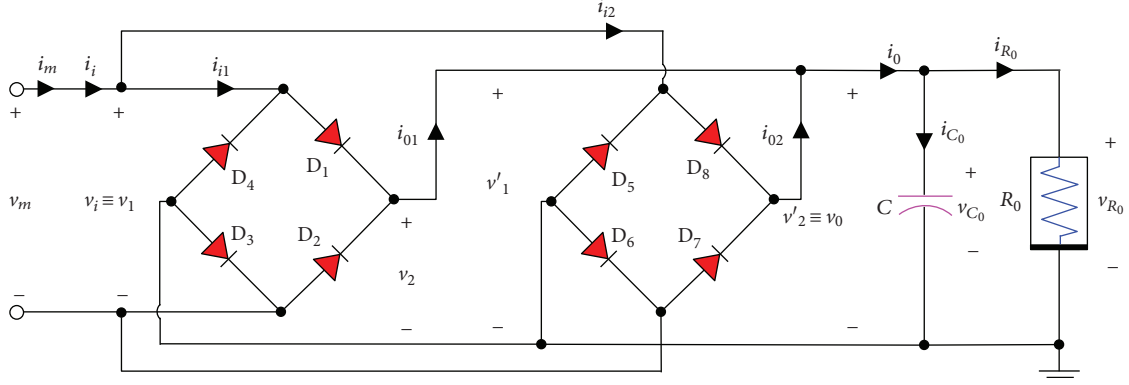


FIGURE 10: Circuit diagram of the real 6-lobe Chua corsage memristor emulator with quad-stable input dynamics.

The current i_3 flowing out of the op-amp circuit in Figure 11 is computed by adding all currents (i_{lin} , i_{+sat} , and i_{-sat}):

$$i_3 = \left\{ \underbrace{\left[\frac{1}{R_{73}} \left[v \left(1 + \frac{R_{73}}{R_{63}} \right) - v_{03} \right] \right]}_{\text{Linear region}} + \underbrace{\left[\frac{1}{R_{73}} \left[v \left(1 + \frac{R_{73}}{R_{63}} \right) - E_{sat} \right] \right]}_{\text{+Saturation region}} + \underbrace{\left[\frac{1}{R_{73}} \left[v \left(1 + \frac{R_{73}}{R_{63}} \right) + E_{sat} \right] \right]}_{\text{-Saturation region}} \right\} \quad (32)$$

Plotting the output voltage v_{03} and input current i_3 with respect to the input voltage v of the op-amp circuit with positive and negative feedback paths over the specified ranges of all the three regions provides a *piecewise linear* curve as shown in Figure 13(a). The op-amp circuit enclosed in the red box in Figure 11 exhibits *two* breakpoints at $V = \pm 7$ V with circuit parameters $R_{33} = 1$ K, $R_{43} = 1$ K, $R_{63} = 100$ K, $R_{73} = 1$ K, and $E_{sat} = 14$ V over the input voltage range $-14 \text{ V} \leq V \leq 14 \text{ V}$. The mathematical simulation results shown in Figure 13 shows that the linear region of the op-amp circuit lies in the range $-7 \text{ V} \leq V \leq 7 \text{ V}$ (as $\beta E_{sat} = 7 \text{ V}$) whereas the positive and negative saturation regions lie at $V > 7 \text{ V}$ and $V < -7 \text{ V}$, respectively. Moreover, the output voltage v_{03} at the positive and negative saturation regions are $v_{03} = +E_{sat} = +14 \text{ V}$ and $v_{03} = -E_{sat} = -14 \text{ V}$, respectively, and in the linear region, v_{03} increases proportionately to the input voltage v . However, the current i_3 of the op-amp circuit increases linearly in the saturation region and decreases in an inversely proportional manner to the input voltage v in the linear region.

Similarly, following the circuit-theoretic concepts mentioned above, the input currents i_2 and i_1 of the op-amp circuits in Figure 11 are computed as

$$i_2 = \left\{ \underbrace{\left[\frac{1}{R_{72}} \left[v \left(1 + \frac{R_{72}}{R_{62}} \right) - v_{02} \right] \right]}_{\text{Linear region}} + \underbrace{\left[\frac{1}{R_{72}} \left[v \left(1 + \frac{R_{72}}{R_{62}} \right) - E_{sat} \right] \right]}_{\text{+Saturation region}} + \underbrace{\left[\frac{1}{R_{72}} \left[v \left(1 + \frac{R_{72}}{R_{62}} \right) + E_{sat} \right] \right]}_{\text{-Saturation region}} \right\} \quad (33)$$

and

$$i_1 = \left\{ \underbrace{\left[\frac{1}{R_{71}} \left[v \left(1 + \frac{R_{71}}{R_{61}} \right) - v_{01} \right] \right]}_{\text{Linear region}} + \underbrace{\left[\frac{1}{R_{71}} \left[v \left(1 + \frac{R_{71}}{R_{61}} \right) - E_{sat} \right] \right]}_{\text{+Saturation region}} + \underbrace{\left[\frac{1}{R_{71}} \left[v \left(1 + \frac{R_{71}}{R_{61}} \right) + E_{sat} \right] \right]}_{\text{-Saturation region}} \right\} \quad (34)$$

The loci of v_{02} versus v and i_2 versus v and v_{01} versus v and i_1 versus v are shown in Figures 13(b) and 13(c), respectively.

The total current i flowing out of the 3 parallel connected op-amp circuits in Figure 11 is equal to the summation of the

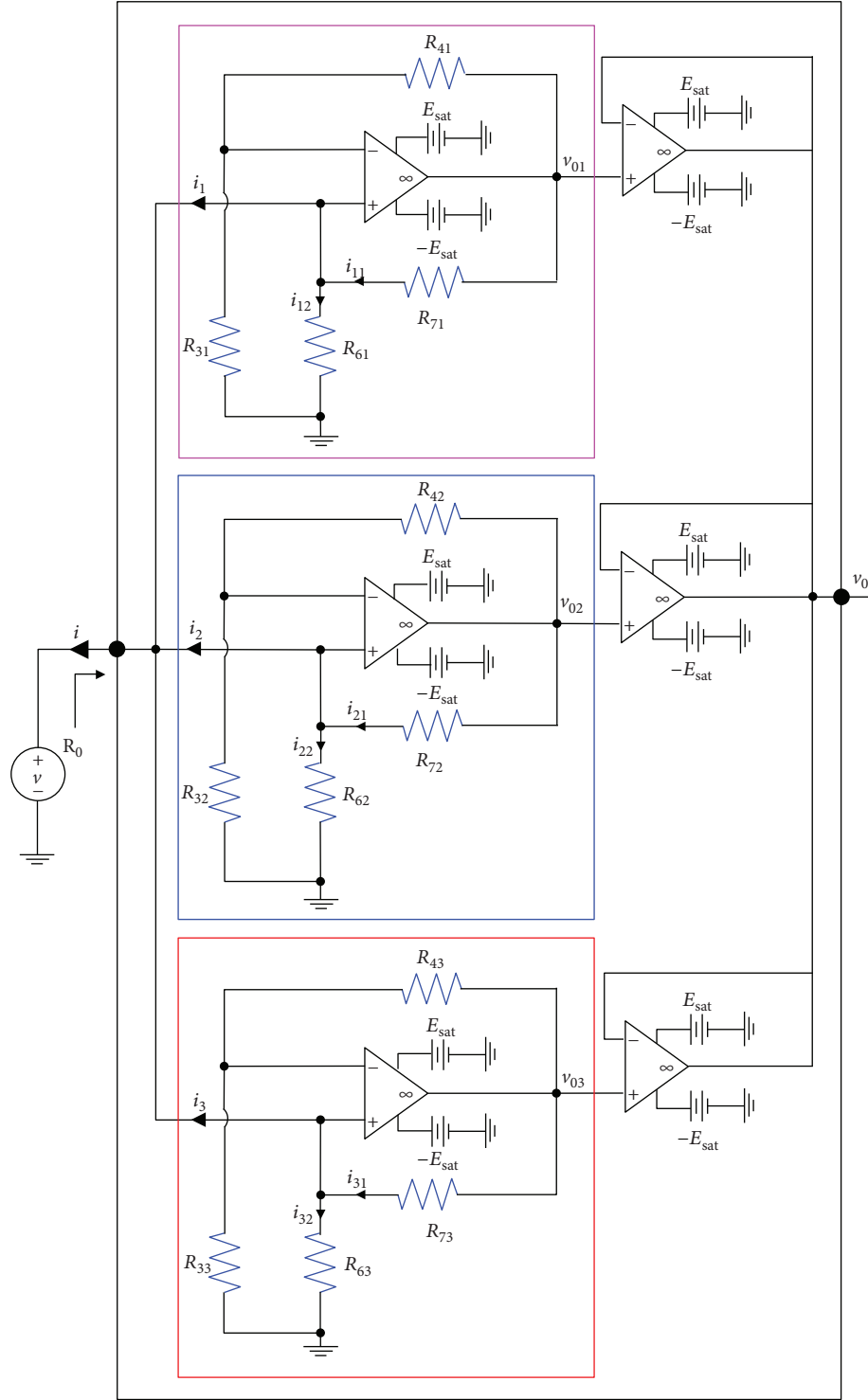


FIGURE 11: Circuit diagram of nonlinear resistor R_0 of the real 6-lobe corsage memristor using off-the-shelf components.

three currents (i_1 , i_2 , and i_3) of the individual op-amp circuits and computed as

$$i = i_1 + i_2 + i_3. \quad (35)$$

The six-breakpoint V - I curve of nonlinear resistor R_0 is shown in Figure 14. Mathematical simulation results of

current i and the equivalent nonlinear resistance R_0 are shown in Figure 14(a) with the parameters (the measured resistor values of circuit implementation are used in mathematical and SPICE simulations) $R_{31} = R_{32} = R_{33} = 0.985\text{K}$, $R_{61} = R_{62} = R_{63} = 100.5\text{K}$, $R_{71} = R_{72} = R_{73} = 1.001\text{K}$, $R_{41} = 3.888\text{K}$, $R_{42} = 1.797\text{K}$, $R_{43} = 0.987\text{K}$, and $E_{\text{sat}} = 14\text{V}$. The plots of the current i and the active and locally active

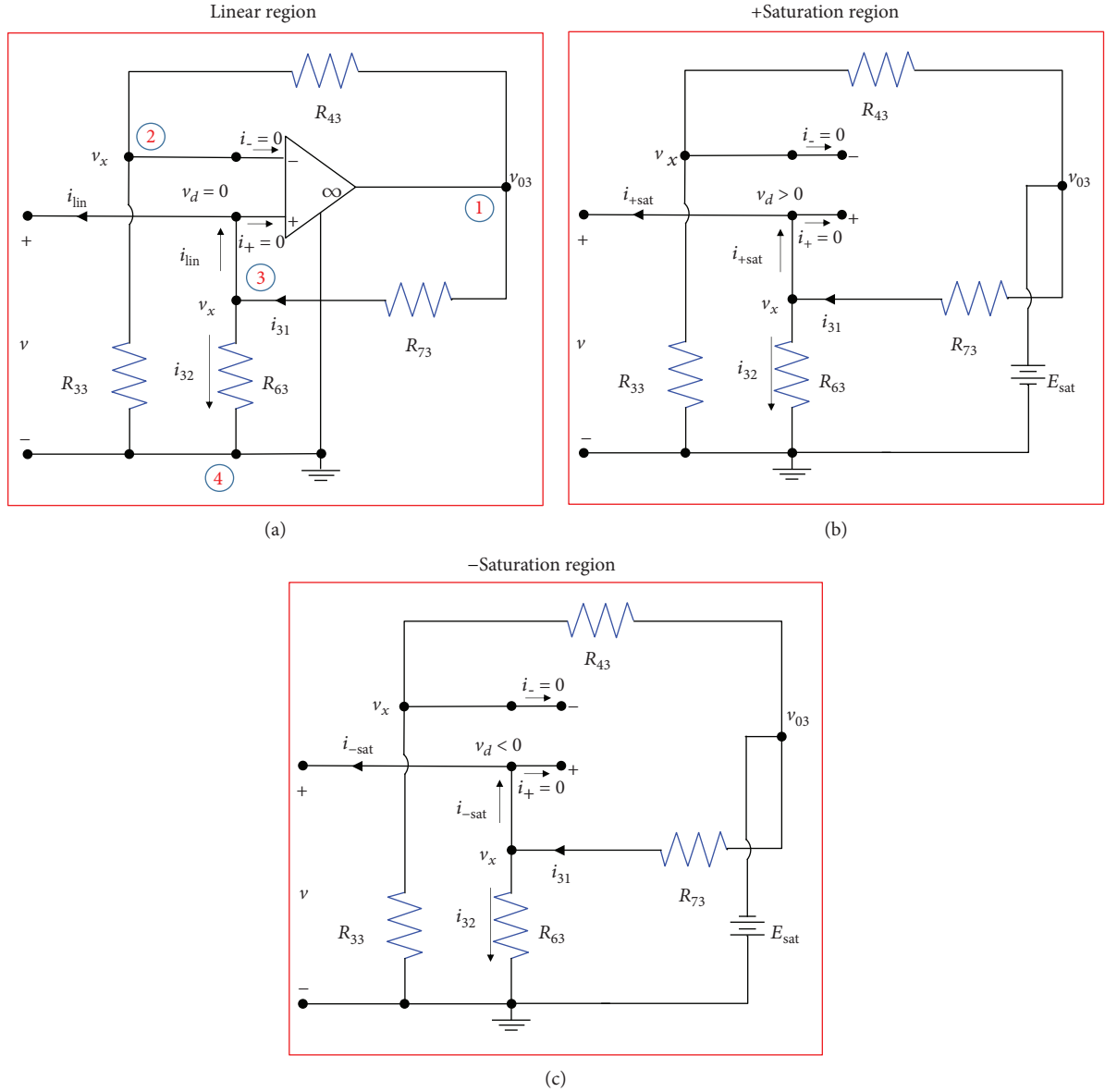


FIGURE 12: Region-based ideal models of the op-amp circuit: (a) Linear region, (b) +Saturation region, and (c) -Saturation region.

resistance R_0 obtained by SPICE simulation and the actual circuit implementation are shown in Figures 14(b) and 14(c), respectively.

The mathematical simulation presented in Figure 14(a) shows that the V - I curve and the resistance value of the non-linear resistor R_0 has *six* breakpoints at $V = \pm 6.99$ V, ± 4.95 V, and ± 2.82 V. The slope of R_0 is different between these breakpoints and hence defines different memory states. Similar to the mathematical model, the plots of the V - I curve and the nonlinear resistance R_0 obtained by SPICE simulation and the circuit implementation also have *six* breakpoints at $V = \pm 6.9$ V, ± 4.89 V, and ± 2.77 V and $V = \pm 5.74$ V, ± 4.05 V, and ± 2.15 V, respectively. The insets in Figures 14(a)–14(c) show the zoomed figure of R_0 near the origin and show that $R_0 = 0$ at input voltage $V = 0$ V.

The nonlinear resistance waveform obtained from the SPICE modelling in Figure 14(b) shows that the R_0 is

constant at resistance 147.47Ω for an input voltage range -2.77 V $< V < 2.77$ V, except for a tiny interval at the origin ($V = 0$ V). However, for 2.77 V $< V < 4.89$ V and 4.89 V $< V < 6.9$ V, the R_0 increases linearly from 147.47Ω to 216.07Ω and from 216.07Ω to 336.10Ω , respectively, whereas for $V > 6.9$ V, R_0 increases almost linearly. Due to the linear increment of R_0 with a constant slope over the above-mentioned voltage range, it can be acclaimed that the real 6-lobe cossage memristor emulator contains *four* different memory states, namely, R_{01} , R_{02} , R_{03} , and R_{04} where $R_{01} = (R_0 = 147.47 \Omega)$, $R_{02} = (147.47 \Omega < R_0 \leq 216.07 \Omega)$, $R_{03} = (216.07 \Omega < R_0 \leq 336.10 \Omega)$, and $R_{04} = (R_0 > 336.10 \Omega)$.

Similar to the SPICE model, the mathematical and the circuit implementation plots of R_0 also contains the *four* different memory states as shown in Figures 14(a) and 14(b), respectively. The fluctuation of R_0 at the -2.16 V $< V < 2.16$ V voltage range in Figure 14(c) is negligibly small and can be

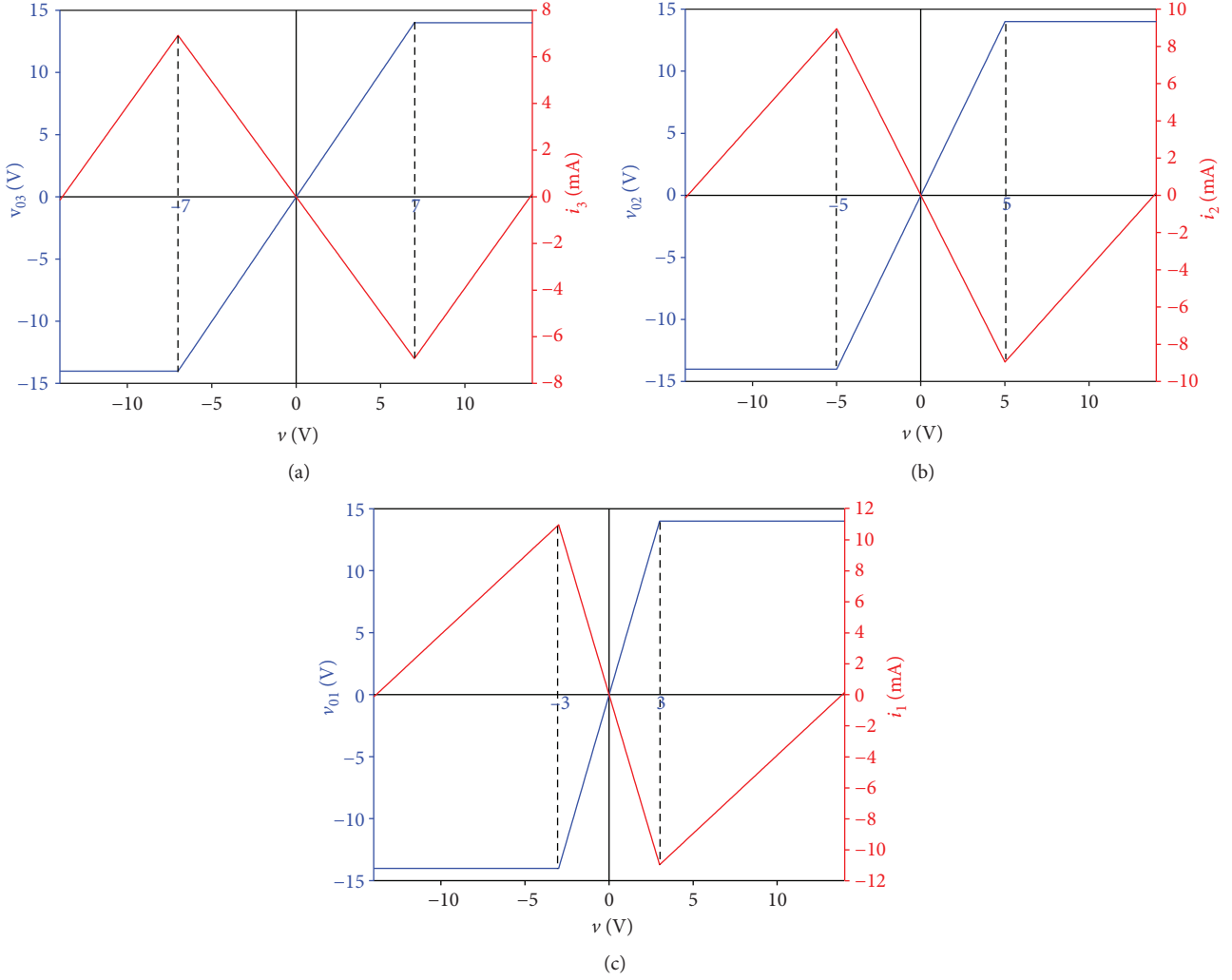


FIGURE 13: Mathematical simulation of input currents (i_3 , i_2 , and i_1) and output voltages (v_{03} , v_{02} , v_{01}) with respect to input voltage v . Loci of (a) v_{03} versus v and i_3 versus v , (b) v_{02} versus v and i_2 versus v , and (c) v_{01} versus v and i_1 versus v of the individual op-amp circuits.

regarded as $R_0 = 137 \Omega$. The fluctuation was induced due to computational difficulties at $V = 0$ V in the oscilloscope. Although the resistance R_0 of the mathematical model of the 6-lobe cossage memristor and the real emulator are quantitatively different, they are also qualitatively identical.

The breakpoints of the V - I curve of the nonlinear resistor R_0 in mathematical simulation, shown in Figure 14(a) and the *SPICE* simulation shown in Figure 14(b), are slightly different. This deviation happens due to the nonideal circuit components of the *SPICE* module. Moreover, the V - I curve breakpoints of R_0 measured from the circuit implementation is further deviated from the mathematical and *SPICE* simulation. The reason behind such deviation is the nonideal characteristic of the op-amp circuit as well as the noise induced from the DC power supply and the oscilloscope probe. Another reason for such deviation is the used op-amp's rated saturation voltage ($E_{\text{sat}} = 13.7$ V) which is slightly less than the mathematical and *SPICE* saturation voltage $E_{\text{sat}} = 14$ V.

Although the breakpoints of the DC V - I curve in Figure 5 and the breakpoints of Figure 14 are quantitatively different, they are qualitatively similar. In this artifact, one of our

primary motives is to show that the basic method explained in [4, 5] and [14] can be used to convert the DC V - I curve of any real nonlinear resistor into a memristor. We prove this analogy by analyzing the parallel connected op-amp circuit in Figure 11 which has the capabilities to emulate the attributes of the 6-lobe Chua cossage memristor as it exhibits a 7-segment *PWL* DC V - I curve as shown in Figure 14.

The *SPICE* simulation of switching of memory states of the real 6-lobe Chua cossage memristor emulator (in Figure 10) is shown in Figure 15. Figure 15(a) shows the example of successful switching between the memory states R_{01} and R_{03} . To switch from R_{01} to R_{03} , a pulse input $V_A = 5.5$ V with a pulse width $\Delta w = 7.5$ s is applied across our real emulator circuit in Figure 10. Observe from Figure 15(a) that the resistance $R_0 = 147.47 \Omega$ at $t = 0^+$, and it gradually increases during the pulse period Δw and saturated at $R_0 = 216.5 \Omega$ and remained there although the input voltage become zero for $t \geq \Delta w$. The saturated resistance $R_0 = 216.5 \Omega$ lies over the memory state $R_{03} = (216.07 \Omega < R_0 \leq 336.10 \Omega)$ which confirms the successful switching from memory state R_{01} to R_{03} for an input pulse $V_A = 5.5$ V

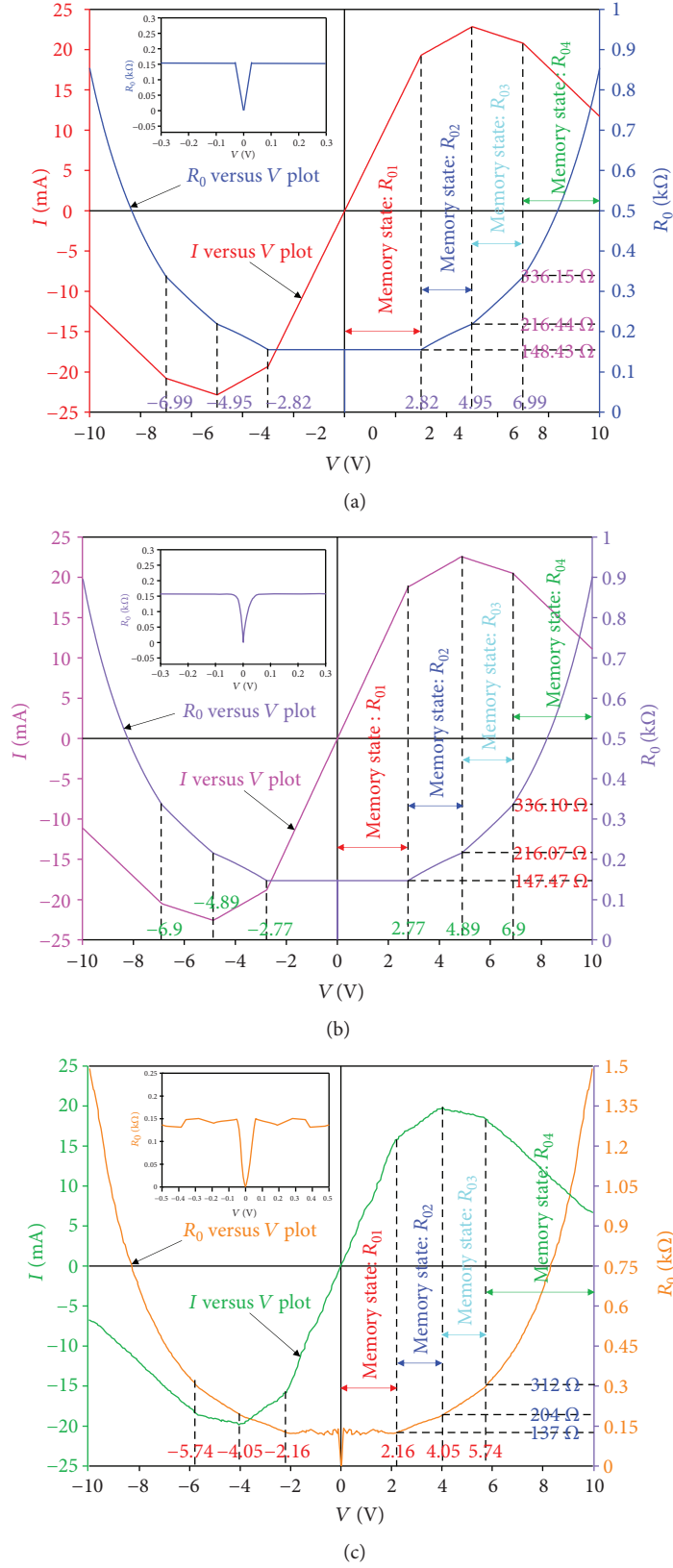


FIGURE 14: DC current I versus DC voltage V and DC resistance $R_0 = (V/I)$ derived and measured from the 6-lobe corsage memristor emulator. (a) I versus V and R_0 versus V plot of mathematical model, (b) I versus V and R_0 versus V plot of spice circuit simulation, and (c) I versus V and R_0 versus V plot of the actual circuit implementation.

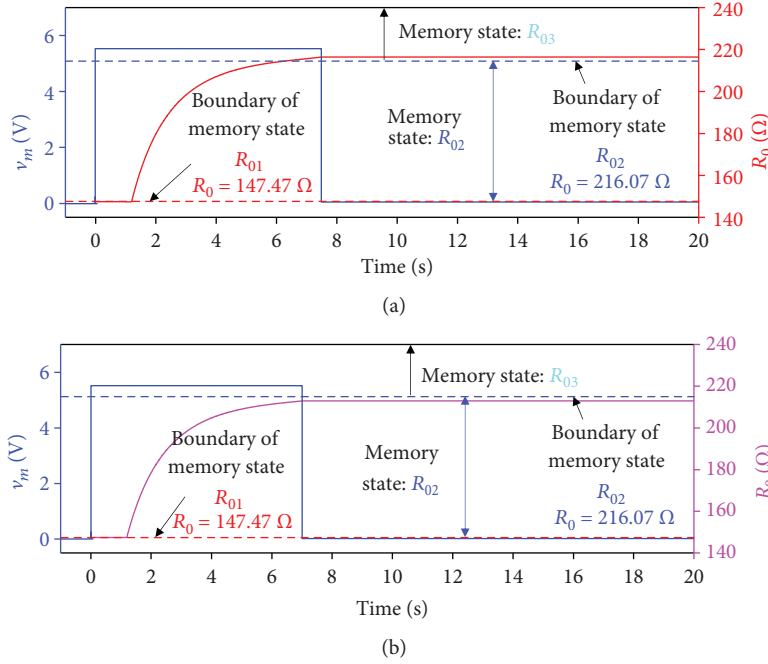


FIGURE 15: Switching kinetics of the memory states of real 6-lobe Chua corsage memristor emulator. (a) Successful switching: the corsage memristor emulator switches from memory state R_{01} to R_{03} with a resultant resistance $R_0 = 216.5 \Omega$ for an input pulse $V_A = 5.5 \text{ V}$ and pulse width $\Delta w = 7.5 \text{ s}$. (b) Switching failure: the proposed corsage memristor emulator fails to switch from R_{01} to R_{03} for an input pulse $V_A = 5.5 \text{ V}$ and pulse width $\Delta w = 7 \text{ s}$ as the resultant resistance $R_0 = 215.6 \Omega$ lies in the memory state range R_{02} .

and $\Delta w = 7.5 \text{ s}$. However, to fit the resistance scale, we truncated the $t \leq 0$ part of the R_0 in Figure 15(a) as that part is insignificant because at $t = 0^+$, R_0 immediately rises from $R_0 = 0 \Omega$ to $R_0 = 147.47 \Omega$.

In this paper, we also demonstrate the switching failure scenario of the real 6-lobe Chua corsage memristor as shown in Figure 15(b). In Figure 15(b), a pulse input $V_A = 5.5 \text{ V}$ with a pulse width $\Delta w = 7 \text{ s}$ is applied across our real emulator. The nonlinear resistance R_0 is saturated at $R_0 = 215.6 \Omega$ and remained there as the time increases although the voltage becomes $v(t) = 0$ for $t \geq \Delta w$. The resultant resistance $R_0 = 215.6 \Omega$ lies over the memory state $R_{02} = (147.47 \Omega < R_0 \leq 216.07 \Omega)$ which confirms the failure of switching as our intention is to switch from memory state R_{01} to R_{03} for an input pulse $V_A = 5.5 \text{ V}$ and $\Delta w = 7 \text{ s}$, but we converge on memory state R_{02} .

The switching failure scenario gives us the insights that the emulator circuit of our proposed corsage memristor is also dependent on the appropriate pulse amplitude and the pulse width like its mathematical model. To illustrate the relationship of pulse amplitude and the pulse width in our real emulator circuit, we plot the *pulse amplitude V_A versus pulse width $|\Delta w|$* curve as shown in Figure 16. The hyperbolic relationship in Figure 16 shows that the maximum pulse amplitude V_A requires less pulse width Δw to switch from one memory state to another state whereas the minimum pulse amplitude requires maximum pulse width.

6. Conclusion

The recent interest in inherently nonlinear memristor devices is bringing to a new life to the theory of nonlinear

circuits and systems. In this paper, we design and build a highly nonlinear novel device, namely, the 6-lobe Chua corsage memristor, and its real emulator circuit using the nonlinear circuit theory. The proposed generic memristor can be used as a multistate, specifically 4-state, memory device with an increased efficiency of 50% compared to the 2-lobe and bistable extended memristor whereas the efficiency of the proposed memristor increased by 25% compared to the 4-lobe corsage memristor. Moreover, due to the presence of more equilibrium points compared to the 2-lobe or 4-lobe corsage memristors, the proposed corsage memristor exhibits a higher variety of dynamic routes in response to different initial conditions $x(0)$ which enhance the capability to represent a desired function more closely than 2-lobe or 4-lobe corsage memristors. Due to the diversified dynamic routes and the enhancement in stable memory states, the proposed corsage memristor is more versatile and effective than its predecessor 2-lobe and 4-lobe corsage memristors. Moreover, the diversified dynamic routes reveal a contiguous highly nonlinear DC V - I curve with *six* distinct *contiguous* hysteresis lobes, unlike the most published highly nonlinear disconnected DC V - I curves. Furthermore, the *universal formulas*, derived in Section 4, ease the demonstration of the switching kinetics of the 6-lobe corsage memristor and assist to switch the memory states precisely with an appropriate pulse amplitude and pulse width in accordance to an initial condition $x(0)$. The universal formulas are applicable to any device which exhibits a PWL dynamic route map with any *number of segments* for any *DC or pulse input*. Following the introduction of a purely mathematical memristor model with quad stability (2-bit memory system) at DC and pulse input, this paper elucidates the mechanisms behind the

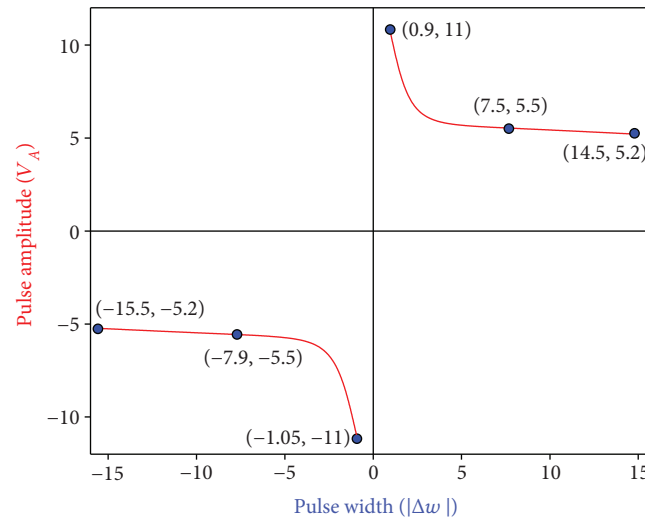


FIGURE 16: Relation between amplitude V_A versus pulse width Δw of the real 6-lobe Chua corsage memristor emulator.

emergence of the first real emulated 6-lobe Chua corsage memristor using *off-the-shelf* elements. Nonlinear system theoretic concepts were applied to the model of the two-port memristive element to gain a deep insight into the quad-stable characteristic of its dynamics where the quantitative attributes of the real emulator might not be similar to the mathematical model but they are qualitatively same.

Data Availability

The data used to support the findings of this study are available from the first author or corresponding author upon request.

Conflicts of Interest

The authors declare that they have no conflicts of interest.

Acknowledgments

The authors would like to thank Professor Leon Chua for his wonderful assistance for revising the manuscript and technical advice. This work was supported in part by the National Research Foundation of Korea (NRF) grant funded by the Korean Government (2016R1A2B4015514), the “Cooperative Research Program for Agriculture Science and Technology Development (Project no. PJ0120642016),” the Rural Development Administration, Republic of Korea, and the US Air Force Office of Scientific Research under Grant no. FA9550-18-1-0016.

Supplementary Materials

Finding of universal formulas. Figure 1: dynamic routes of the switching kinetics of the 6-lobe Chua corsage memristor. The two magenta-color vertical line segments indicate an instantaneous jump between the red and the blue piecewise-linear plots in the dynamic route map. Figure 2: movement of the exponential trajectories of $x(t)$ with respect to time t . (*Supplementary Materials*)

References

- [1] D. B. Strukov, G. S. Snider, D. R. Stewart, and R. S. Williams, “The missing memristor found,” *Nature*, vol. 453, no. 7191, pp. 80–83, 2008.
- [2] L. Chua, “Memristor—the missing circuit element,” *IEEE Transactions on Circuit Theory*, vol. 18, no. 5, pp. 507–519, 1971.
- [3] L. O. Chua and S. M. Kang, “Memristive devices and systems,” *Proceedings of the IEEE*, vol. 64, no. 2, pp. 209–223, 1976.
- [4] A. Ascoli, R. Tetzlaff, and L. O. Chua, “The first ever real bistable memristors—part I: theoretical insights on local fading memory,” *IEEE Transactions on Circuits and Systems II: Express Briefs*, vol. 63, no. 12, pp. 1091–1095, 2016.
- [5] A. Ascoli, R. Tetzlaff, and L. O. Chua, “The first ever real bistable memristors—part II: design and analysis of a local fading memory system,” *IEEE Transactions on Circuits and Systems II: Express Briefs*, vol. 63, no. 12, pp. 1096–1100, 2016.
- [6] S. Stathopoulos, A. Khat, M. Trapatseli et al., “Multibit memory operation of metal-oxide bi-layer memristors,” *Scientific Reports*, vol. 7, no. 1, article 17532, 2017.
- [7] Z. I. Mannan, C. Yang, and H. Kim, “Oscillation with 4-lobe Chua corsage memristor,” *IEEE Circuits and Systems Magazine*, vol. 18, no. 2, pp. 14–27, 2018.
- [8] Z. I. Mannan, H. Choi, and H. Kim, “Chua corsage memristor oscillator via Hopf bifurcation,” *International Journal of Bifurcation and Chaos*, vol. 26, no. 4, 2016.
- [9] Z. I. Mannan, H. Choi, V. Rajamani, H. Kim, and L. Chua, “Chua corsage memristor: phase portraits, basin of attraction, and coexisting pinched hysteresis loops,” *International Journal of Bifurcation and Chaos*, vol. 27, no. 3, 2017.
- [10] S. H. Strogatz, “Phase plane,” in *Nonlinear Dynamics and Chaos*, pp. 145–150, Addison-Wesley Publishing Co., MA, USA, 2nd edition, 1994, ch. 6, sec 6.1–6.3.
- [11] C. O. Avci, M. Mann, A. J. Tan, P. Gambardella, and G. S. D. Beach, “A multi-state memory device based on the unidirectional spin Hall magnetoresistance,” *Applied Physics Letters*, vol. 110, no. 20, 2017.
- [12] R. Strzelecki and G. S. Zinoviev, “Overview of power electronics converters and controls,” in *Power Electronics in Smart*

- Electrical Energy Networks, Power Systems*, pp. 55–105, Springer-Verlag Limited, London, 2008.
- [13] S. P. Adhikari, M. P. Sah, H. Kim, and L. O. Chua, “Three fingerprints of memristor,” *IEEE Transactions on Circuits and Systems I: Regular Papers*, vol. 60, no. 11, pp. 3008–3021, 2013.
 - [14] L. Chua, “If it’s pinched it’s a memristor,” *Semiconductor Science and Technology*, vol. 29, no. 10, 2014.
 - [15] L. Chua, “Everything you wish to know about memristors but are afraid to ask,” *Radioengineering*, vol. 24, no. 2, pp. 319–368, 2015.
 - [16] L. O. Chua, *Introduction to Nonlinear Network Theory*, McGraw-Hill, New York, USA, 1969.
 - [17] J. J. E. Slotine and W. Li, “Advance stability theory,” in *Applied Nonlinear Control*, Prentice-Hall, Inc., New Jersey, 1991.
 - [18] G. B. Thomas and R. L. Finney, *Calculus and Analytic Geometry*, Addison-Wesley Publishing Co., MA, USA, 5th edition, 1979.
 - [19] Stover and E. W. Weisstein, “Parametric equations,” *Math-World—A Wolfram Web Resource*, 2017, <http://mathworld.wolfram.com/ParametricEquations.html>.
 - [20] K. Mainzer and L. Chua, *Local Activity Principle: the Cause of Complexity and Symmetry Breaking*, Imperial College Press, UK, 2013.
 - [21] M. P. Sah, Z. I. Mannan, H. Kim, and L. Chua, “Oscillator made of only one memristor and one battery,” *International Journal of Bifurcation and Chaos*, vol. 25, no. 3, 2015.
 - [22] L. O. Chua, C. A. Desoer, and E. A. Kuh, “Operational-amplifier circuits,” in *Linear and Nonlinear Circuits McGraw Hill*, pp. 187–212, New York, USA, 1985, ch. 4, sec. 3.

Research Article

On Designing Feedback Controllers for Master-Slave Synchronization of Memristor-Based Chua's Circuits

Ke Ding ^{1,2}

¹*School of Information Technology, Jiangxi University of Finance and Economics, Nanchang 330013, China*

²*Jiangxi E-commerce High Level Engineering Technology Research Centre, Jiangxi University of Finance and Economics, Nanchang 330013, China*

Correspondence should be addressed to Ke Ding; keding@jxufe.edu.cn

Received 26 April 2018; Accepted 22 July 2018; Published 16 October 2018

Academic Editor: Viet-Thanh Pham

Copyright © 2018 Ke Ding. This is an open access article distributed under the Creative Commons Attribution License, which permits unrestricted use, distribution, and reproduction in any medium, provided the original work is properly cited.

This paper is concerned with designing feedback controllers for master-slave synchronization of two chaotic memristor-based Chua's circuits. The memductance function of memristor-based Chua's circuits is a bounded function with a bounded derivative which is more generalized than those piecewise constant-valued functions or quadratic functions in some existing papers. The main contributions are that one master-slave synchronization criterion is established for two chaotic memristor-based Chua's circuits, and the feedback controller gain is easily obtained by solving a set of linear matrix inequalities. One numerical example is given to illustrate the effectiveness of the design method.

1. Introduction

Since the memristor, a missing circuit element, was first introduced by Chua in 1971 [1] and was realized in 2008 [2], memristor-based Chua's circuits have received some attention, see, for example, [3–5].

When some equipment of circuits in oscillators were replaced by memristors, complex and dynamical properties were revealed in the circuits. Chaotic attractors have been studied in memristor-based Chua's circuits in which the memductance functions of memristors were characterized by a piecewise constant-valued function [3, 6, 7] or a quadratic function [4, 5, 8, 9]. It should be pointed out that the memductance function of memristor can be represented by a bounded function with a bounded derivative [2], which is more generalized than those piecewise constant-valued functions or quadratic functions in some existing papers [3, 4]. However, to the best of author's knowledge, there is no result available in the existing published literature to study memristor-based Chua's circuits with abovementioned memductance function, which is the first motivation of this paper.

Chaotic synchronization and chaos control have received much attention due to its theoretical importance and practical applications [10–33]. Due to the existence of memristors, the product of the memductance function and voltage can give rise to chaotic behaviors in circuits. Most research efforts [3–5, 7–9, 17–19] were made to chaotic behaviors of memristor-based circuits, rather than master-slave synchronization and chaos control for two memristor-based circuits. Zhang et al. [6] conducted stability analysis for a single circuit with a piecewise constant-valued memductance function, but they did not consider the synchronization problem of two circuits. In [15, 16], synchronization of memristor-based Chua's circuits has been investigated, in which the memductance elements were piecewise linear functions. In addition, the memristor with a passive nonlinearity and a piecewise constant-valued memductance function is essential to generate the high signal-to-noise ratio which is not suitable for achieving the secure communication [5]. Therefore, the memristor with nonlinear memductance function which is suitable for secure communication should be worth studying. The memristor in which the memductance function is a bounded function with a bounded

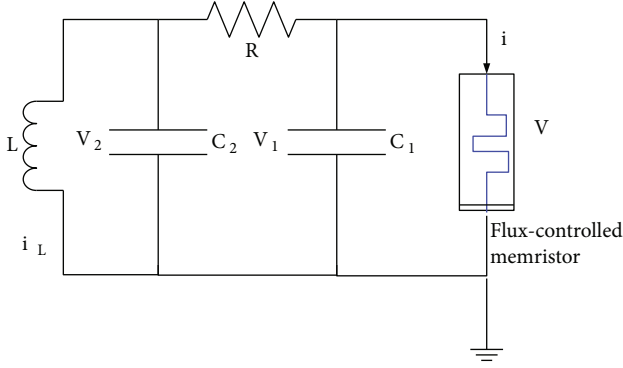


FIGURE 1: The memristor-based chaotic Chua's circuit.

derivative can satisfy this criterion, but the mathematical model of corresponding circuit is a set of nonlinear differential equations as well as the corresponding error systems derived by the master-slave scheme. Thus, how to derive master-slave synchronization criteria for two memristor-based Chua's circuits in which the memductance function is a bounded function with a bounded derivative and how to design a feedback controller matrix gain to achieve synchronization is the second motivation of this paper.

In this paper, we will deal with the problem of the controller design for master-slave synchronization of chaotic memristor-based Chua's circuits. The master-slave scheme will be constructed by using an error state feedback control. We will derive one synchronization criterion. Based on the obtained synchronization criterion, we will give the sufficient conditions on the existence of an error state feedback controller. Moreover, we will obtain the controller gain. We will also use one numerical example to illustrate the effectiveness of the synchronization criterion and the design method.

Notation 1. \mathbb{R}^n denotes the n -dimensional Euclidean space. $\mathbb{R}^{m \times n}$ is the set of all $m \times n$ real matrices. For symmetric matrices P and Q , the notation $P > Q$ (respectively, $P \geq Q$) means that matrix $P - Q$ is positive definite (respectively, positive semidefinite). $\lambda_{\max}(P)$ and $\lambda_{\min}(P)$ are the maximum and minimum eigenvalues of the matrix P , respectively.

2. Memristor-Based Chua's Circuits

The memristor in Chua's circuits is a two-terminal element. The magnetic flux of memristor between the terminals is a function of the electric charge which passes through the device [1]. A flux-controlled memristor can be characterized by the incremental memductance function $\omega(\phi)$ describing the flux-dependent rate of change of charge [2], i.e., $\omega(\phi) = dq(\phi)/d\phi$. Therefore, the voltage $v(t)$ across and the current $i(t)$ through the memristor can be described as $i(t) = \omega(\phi)v(t)$ [3].

Figure 1 shows a smooth flux-controlled memristor-based Chua's circuit, where v_1 and v_2 are the voltages across capacitors C_1 and C_2 , respectively; i_L is the current through the inductances L ; R is a linear resistor; the Chua's diode is replaced by a memristor. The mathematical model of the

Chua's circuit with the memristor can be described as

$$\begin{cases} \frac{dv_1(t)}{dt} = \frac{1}{C_1} \left(\frac{v_2(t) - v_1(t)}{R} - \omega(\phi(t))v_1(t) \right), \\ \frac{dv_2(t)}{dt} = \frac{1}{C_2} \left(\frac{v_1(t) - v_2(t)}{R} - i_L(t) \right), \\ \frac{di_L(t)}{dt} = \frac{1}{L} v_2(t), \\ \frac{d\phi(t)}{dt} = v_1(t), \end{cases} \quad (1)$$

with the initial condition $v_1(0) = v_{1_0}$, $v_2(0) = v_{2_0}$, $i_L(0) = i_{L_0}$, $\phi(0) = \phi_0$.

Let $f(\cdot)$ and $g(\cdot): \mathbb{R} \rightarrow \mathbb{R}$ be two differentiable functions. In this paper, we mainly focus on the following nonlinearity, i.e., $q(\phi(t)) = a\phi(t) + bg(\phi(t))$, $\omega(\phi(t)) = a + bf(\phi(t))$, $dq(\phi)/d\phi = f(\phi)$, and $i(t) = (a + bf(\phi(t)))v(t)$, where a and b are the parameters of electronic equipment. Besides $f(\phi)$ is differentiable, we assume that $f(\phi)$ is a bounded function and $df(\phi)/d\phi$ is a bounded function where, i.e., there exist two scales $\mu_f > 0$ and $\mu_{f'} > 0$ such that

$$|f(\phi)| \leq \mu_f, \quad \left| \frac{df(\phi)}{d\phi} \right| \leq \mu_{f'}, \quad \forall \phi \in \mathbb{R}. \quad (2)$$

Rescaling the parameters of the circuit as $x_1(t) = v_1(t)$, $x_2(t) = v_2(t)$, $x_3(t) = i_L(t)$, $x_4(t) = \phi(t)$, $\tau = t/RC_2$, $\alpha = C_2/C_1$, $\beta = C_2R/L$, $\gamma = C_2R$, $v_1 = aR$, and $v_2 = bR$, we obtain the following dimensionless form for system (1):

$$\begin{cases} \frac{dx_1(\tau)}{d\tau} = \alpha(x_2(\tau) - (1 + v_1)x_1(\tau) - v_2x_1(\tau)f(x_4(\tau))), \\ \frac{dx_2(\tau)}{d\tau} = x_1(\tau) - x_2(\tau) - Rx_3(\tau), \\ \frac{dx_3(\tau)}{d\tau} = \beta x_2(\tau), \\ \frac{dx_4(\tau)}{d\tau} = \gamma x_1(\tau), \end{cases} \quad (3)$$

where the initial condition is $x_1(0) = v_{1_0}$, $x_2(0) = v_{2_0}$, $x_3(0) = i_{L_0}$, and $x_4(0) = \phi_0$. Let $x(\tau) = (x_1(\tau), x_2(\tau), x_3(\tau), x_4(\tau))^T \in \mathbb{R}^4$, and

$$A = \begin{pmatrix} -\alpha(1 + v_1) & \alpha & 0 & 0 \\ 1 & -1 & -R & 0 \\ 0 & \beta & 0 & 0 \\ \gamma & 0 & 0 & 0 \end{pmatrix}. \quad (4)$$

Then, system (3) can be rewritten as

$$\frac{dx(\tau)}{d\tau} = Ax(\tau) + \varphi(x(\tau)), \quad (5)$$

where $\varphi(x(\tau)) = v_3 x_1(\tau) f(x_4(\tau))$ and $v_3 = -\alpha v_2$.

Remark 1. In [3–5, 7–9, 17–19], dynamical behaviors of the single memristor-based Chua's circuit have been studied. In this paper, the synchronization of two memristor-based Chua's circuits is investigated.

Remark 2. In [6, 15, 16], the memductance elements of memristor-based Chua's circuits were either piecewise linear functions or piecewise constant-valued memductance functions. It is well known that the memristor with a passive nonlinearity or a piecewise constant-valued memductance function is easy to generate the high signal-to-noise ratio which is not suitable for achieving the secure communication [5]. Thus, the memristor with nonlinear memductance function should be investigated. The memristor with bounded memductance functions and bounded derivatives which is suitable for secure communication can satisfy this criterion. Moreover, the mathematical model of corresponding circuit is easily to set up. Thus, it is worth studying master-slave synchronization for two memristor-based Chua's circuits in which the memductance function is a bounded function with a bounded derivative. It is also worth designing a feedback controller matrix gain to achieve synchronization.

3. Master-Slave Synchronization

Let $z(\tau) = (z_1(\tau) z_2(\tau) z_3(\tau) z_4(\tau))^T \in \mathbb{R}^4$. We construct a master-slave synchronization scheme for system (5).

$$\mathcal{M} : \frac{dx(\tau)}{d\tau} = Ax(\tau) + \varphi(x(\tau)), \quad (6)$$

$$\mathcal{S} : \frac{dy(\tau)}{d\tau} = Ay(\tau) + \varphi(y(\tau)) + u(\tau), \quad (7)$$

$$\mathcal{C} : u(\tau) = K(x(\tau) - y(\tau)), \quad (8)$$

with master system \mathcal{M} , slave system \mathcal{S} , and controller \mathcal{C} .

Defining a signal $e(t) = x(t) - y(t) = (e_1(\tau) e_2(\tau) e_3(\tau) e_4(\tau))^T \in \mathbb{R}^4$ with $e_i(t) = x_i(t) - y_i(t)$, $i = 1, 2, 3, 4$, we have the error system

$$\frac{de(\tau)}{d\tau} = (A - K)e(\tau) + \tilde{\varphi}(e(\tau)), \quad (9)$$

where

$$\tilde{\varphi}(e(\tau)) = \varphi(x(\tau)) - \varphi(y(\tau)). \quad (10)$$

The initial values of (6) and (7) are $x(0) = (x_1(0), x_2(0), x_3(0), x_4(0))^T$ and $y(0) = (y_1(0), y_2(0), y_3(0), y_4(0))^T$, respectively. Thus,

$$e(0) = (e_1(0), e_2(0), e_3(0), e_4(0))^T, \quad (11)$$

with $e_i(0) = x_i(0) - y_i(0)$, $i = 1, 2, 3, 4$.

It follows from (10) and the differential mean value theorem that

$$\begin{aligned} \tilde{\varphi}(e(\tau)) &= \varphi(x(\tau)) - \varphi(y(\tau)) \\ &= v_3(x_1(\tau)f(x_4(\tau)) - y_1(\tau)f(y_4(\tau))) \end{aligned} \quad (12)$$

where $\xi \in (\min \{x_4(\tau), y_4(\tau)\}, \max \{x_4(\tau), y_4(\tau)\})$. Notice that the error system (9) can be rewritten as

$$\frac{de(\tau)}{d\tau} = (A + B(\tau) - K)e(\tau), \quad (13)$$

where

$$B(\tau) = \begin{pmatrix} b_{11}(\tau) & 0 & 0 & b_{14}(\tau) \\ 0 & 0 & 0 & 0 \\ 0 & 0 & 0 & 0 \\ 0 & 0 & 0 & 0 \end{pmatrix}, \quad (14)$$

with

$$\begin{aligned} b_{11}(\tau) &= v_3 f(y_4(\tau)), b_{14}(\tau) \\ &= v_3 x_1(\tau) \frac{df(\varsigma)}{d\varsigma} \Big|_{\varsigma=\xi}, \\ &\in (\min \{x_4(\tau), y_4(\tau)\}, \max \{x_4(\tau), y_4(\tau)\}). \end{aligned} \quad (15)$$

Choosing the proper parameters of system (3), there exist some chaotic attractors which indicate that for any initial condition x_0 within the domain of system (3), there are bounds $\mu_i(x_0) > 0$, $i = 1, 2, 3, 4$, such that

$$|x_i(t, x_0)| \leq \mu_i(x_0), \quad \forall t > 0, i = 1, 2, 3, 4. \quad (16)$$

From inequalities (2) and (16), we know that

$$|b_{11}(\tau)| \leq |v_3| \mu_f, |b_{14}(\tau)| \leq |v_3| \mu_1(x_0) \mu_{f'}. \quad (17)$$

Therefore, the error system (13) can be modeled as a polytopic system.

Let

$$\begin{aligned}
 B_1 &= \begin{pmatrix} |v_3|\mu_f & 0 & 0 & |v_3|\mu_1(x_0)\mu_{f'} \\ 0 & 0 & 0 & 0 \\ 0 & 0 & 0 & 0 \\ 0 & 0 & 0 & 0 \end{pmatrix}, \\
 B_2 &= \begin{pmatrix} -|v_3|\mu_f & 0 & 0 & |v_3|\mu_1(x_0)\mu_{f'} \\ 0 & 0 & 0 & 0 \\ 0 & 0 & 0 & 0 \\ 0 & 0 & 0 & 0 \end{pmatrix}, \\
 B_3 &= \begin{pmatrix} |v_3|\mu_f & 0 & 0 & -|v_3|\mu_1(x_0)\mu_{f'} \\ 0 & 0 & 0 & 0 \\ 0 & 0 & 0 & 0 \\ 0 & 0 & 0 & 0 \end{pmatrix}, \\
 B_4 &= \begin{pmatrix} -|v_3|\mu_f & 0 & 0 & -|v_3|\mu_1(x_0)\mu_{f'} \\ 0 & 0 & 0 & 0 \\ 0 & 0 & 0 & 0 \\ 0 & 0 & 0 & 0 \end{pmatrix}.
 \end{aligned} \tag{18}$$

It is clear that $B_i (i = 1, 2, 3, 4)$ are the vertices of $B(\tau)$.

This paper intends to derive synchronization criteria for two memristor-based Chua's circuits and to design the controller (8), i.e., to find the controller gain K , such that the system described by (13) is asymptotically stable, which means that the system described by (6), (7), and (8) synchronizes.

4. Controller Design

4.1. A Synchronization Criterion. This subsection aims to derive a synchronization criterion for two memristor-based Chua's circuits. Choose the quadratic Lyapunov function.

$$V(\tau, e(\tau)) = e^T(\tau)Pe(\tau), \tag{19}$$

where $P \in \mathbb{R}^4 \times 4$, $P = P^T > 0$.

Applying Lyapunov's direct method, we obtain the following result.

Proposition 1. *The error system described by (11) and (13) is asymptotically stable if there exists a matrix $P = P^T > 0$ such that*

$$P(A + B_i - K) + (A + B_i - K)^T P < 0, \quad i = 1, 2, 3, 4. \tag{20}$$

Proof 1. Taking the derivative of $V(\tau, e(\tau))$ with respect to τ along the trajectory of (13) yields

$$\begin{aligned}
 \frac{dV(\tau, e(\tau))}{d\tau} &= e^T(\tau)P(A + B(\tau) - K)e(\tau) \\
 &\quad + e^T(\tau)(A + B(\tau) - K)^T Pe(\tau).
 \end{aligned} \tag{21}$$

A sufficient condition for the asymptotic stability of system (13) is that there exists a matrix $P = P^T > 0$ such that

$$P(A + B(\tau) - K) + (A + B(\tau) - K)^T P < 0. \tag{22}$$

It is easy to see that LMI (22) can be ensured by LMIs (20). This ends the proof.

If the menductance function is a linear piecewise constant-valued function, i.e.,

$$\begin{cases} w(\phi(t)) = \kappa_1, & \text{for } \phi(t) \geq 1, \\ w(\phi(t)) = \kappa_2, & \text{for } \phi(t) < 1, \end{cases} \tag{23}$$

we obtain the following dimensionless form for system (1):

$$\frac{dx(\tau)}{d\tau} = \hat{A}_i x(\tau), \quad i = 1, 2, \tag{24}$$

by rescaling the parameters of the circuit as (3), where

$$\begin{aligned}
 \hat{A}_1 &= \begin{pmatrix} \theta_1 & \alpha & 0 & 0 \\ 1 & -1 & R & 0 \\ 0 & \beta & 0 & 0 \\ \gamma & 0 & 0 & 0 \end{pmatrix}, \\
 \hat{A}_2 &= \begin{pmatrix} \theta_2 & \alpha & 0 & 0 \\ 1 & -1 & R & 0 \\ 0 & \beta & 0 & 0 \\ \gamma & 0 & 0 & 0 \end{pmatrix},
 \end{aligned} \tag{25}$$

$\theta_1 = -\alpha(1 + \kappa_1 R)$, $\theta_2 = -\alpha(1 + \kappa_2 R)$, and the initial condition is $x_1(0) = v_{1_0}$, $x_2(0) = v_{2_0}$, $x_3(0) = i_{L_0}$, and $x_4(0) = \phi_0$. The switched rule is if $x_4 \geq 1$, then $(dx(\tau))/d\tau = \hat{A}_1 x(\tau)$; if $x_4 < 1$, then $(dx(\tau))/d\tau = \hat{A}_2 x(\tau)$. The chaotic behaviors of model (24) have been studied in [3, 6, 7].

We construct a master-slave synchronization scheme for system (24).

$$\begin{aligned}
 \mathcal{M} : \frac{dx(\tau)}{d\tau} &= \hat{A}_i x(\tau), \quad i = 1, 2, \\
 \mathcal{S} : \frac{dy(\tau)}{d\tau} &= \hat{A}_i y(\tau) + u_i(\tau), \quad i = 1, 2, \\
 \mathcal{C} : u_i(\tau) &= K_i(x(\tau) - y(\tau)), \quad i = 1, 2,
 \end{aligned} \tag{26}$$

with master system \mathcal{M} , slave system \mathcal{S} , and controller \mathcal{C} . Defining an error signal $e(\tau) = x(\tau) - y(\tau)$, we obtain the error system.

$$\frac{de(\tau)}{d\tau} = B_i e(\tau), \quad i = 1, 2, 3, 4, \tag{27}$$

where $B_1 = B_2 = 0$, $B_3 = \hat{A}_1 - \hat{A}_2$, $B_4 = -B_3$, $C_1 = C_4 = -\hat{A}_1 + K_1$, and $C_2 = C_3 = -\hat{A}_2 + K_2$. The initial value is the same as

that defined in (11). The switched rule is if $x_4 \geq 1, y_4 \geq 1$, then $(de(\tau))/d\tau = B_1x(\tau) - C_1e(\tau)$; if $x_4 < 1, y_4 < 1$, then $(de(\tau))/d\tau = B_2x(\tau) - C_2e(\tau)$; if $x_4 \geq 1, y_4 < 1$, then $(de(\tau))/d\tau = B_3x(\tau) - C_3e(\tau)$; if $x_4 < 1, y_4 \geq 1$, then $(de(\tau))/d\tau = B_4x(\tau) - C_4e(\tau)$.

We choose the quadratic Lyapunov function.

$$V(\tau, e(\tau)) = e^T(\tau)e(\tau). \quad (28)$$

Taking the derivative of (28) with respect to τ along the trajectory of (27), we can derive the following state estate which can be stated as the error system described by (27) and (11) converges exponentially to the following ball M with a convergence rate $r/2$, where $M = \{e \in \mathbb{R}^4 \mid \|e\|^2 \leq |q/r|\}$ with $q = \max \{q_1, q_2, q_3, q_4\}$, $q_i = \lambda_{\max}(\rho^T B_i^T B_i \rho)$, $\rho^T = (\mu_1(x_0), \mu_2(x_0), \mu_3(x_0), \mu_4(x_0))$, $r = \min \{r_1, r_2, r_3, r_4\}$, and $r_i = \lambda_{\min}(C_i^T + C_i - I_4)$, $i = 1, 2, 3, 4$.

4.2. The Controller Design. In this subsection, we will design the controller (8) based on the synchronization criterion derived in Section 4.1.

Applying Proposition 1, we establish the following result.

Proposition 2. *The error system described by (11) and (13) is asymptotically stable if there exists a matrix $\tilde{P} = \tilde{P}^T > 0$ and a matrix Y of appropriate dimensions such that*

$$(A + B_i)\tilde{P} + \tilde{P}(A + B_i)^T - Y - Y^T < 0, \quad i = 1, 2, 3, 4. \quad (29)$$

Moreover, the feedback controller gain matrix is given by $K = Y\tilde{P}^{-1}$.

Proof 2. Pre- and postmultiplying both sides of (20) with P^{-1} gives

$$(A + B_i)P^{-1} + P^{-1}(A + B_i)^T - KP^{-1} - P^{-1}K < 0, \quad i = 1, 2, 3, 4. \quad (30)$$

Setting $\tilde{P} = P^{-1}$ and $Y = KP^{-1}$ yields (29).

5. Simulation Results

In this section, in order to illustrate the effectiveness of the derived results, we consider a memristor-based Chua's circuit (1) in which the parameters are chosen as $R = 2 \times 10^3 \Omega$, $C_1 = 6.8 \times 10^{-9} \text{ nF}$, $C_2 = 6.8 \times 10^{-8} \text{ nF}$, and $L = 1.8 \times 10^{-2} \text{ mH}$. Thus, we have $\alpha = 10$, $\beta = 7.5 \times 10^{-3}$, $\gamma = 1.36 \times 10^{-4}$.

For the initial value $(0.11, 0.11, 0, 0)$ of (6), we give Figures 2 and 3 for system (3) with $f(x_4(\tau)) = \arctan x_4(\tau)$ and $f(x_4(\tau)) = \sin^2 x_4(\tau)$ to illustrate the chaotic attractors in the $x_4 - x_1$ plane. We can also obtain the values for $\mu_1(x_0)$, μ_f , $\mu_{f'}$, b_{11} , and b_{14} , respectively. If $f(x_4(\tau)) = \arctan x_4(\tau)$, then $a = -1.3550 \times 10^{-4}$, $b = 6.0930 \times 10^{-4}$, $\mu_f = 1$, $\mu_{f'} = (\pi/2)\mu_1(x_0) = 400$, $b_{11} = nu_3 \arctan y_4(t)$, and $b_{14} = (v_3 x_1(\tau))/1 + \xi^2$. If $f(x_4(\tau)) = \sin^2 x_4(\tau)$, then $a = -5.9900 \times$

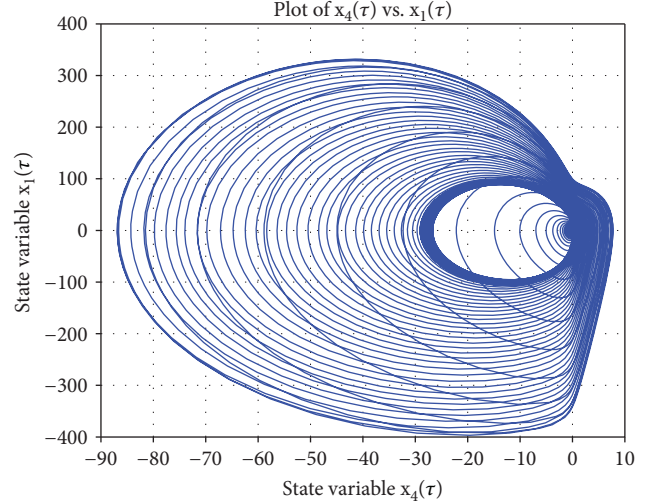


FIGURE 2: The chaotic attractors of system (3) with $f(x_4(\tau)) = \arctan x_4(\tau)$.

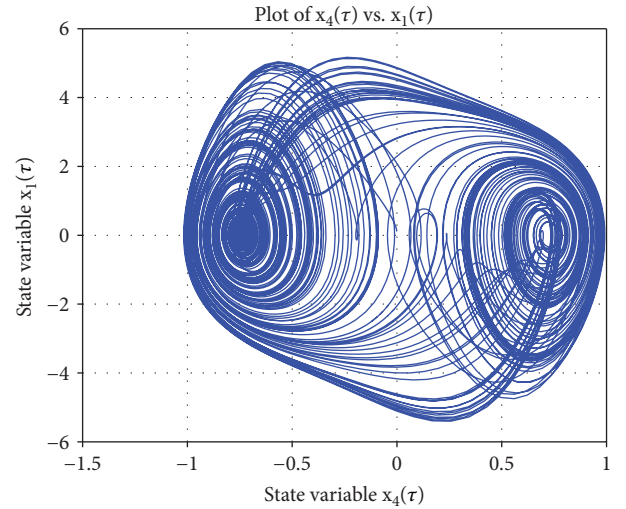


FIGURE 3: The chaotic attractors of system (3) with $f(x_4(\tau)) = \sin^2 x_4(\tau)$.

TABLE 1: The feedback gain matrix derived by Proposition 2.

$f(x_4(\tau))$	K
$\arctan x_4(\tau)$	$\begin{pmatrix} -10 & 10 & 0 & 691750 \\ 10 & 0 & -1000 & 0 \\ 0 & -1000 & 0 & 0 \\ -40 & 0 & 0 & 9360 \end{pmatrix}$
$\sin^2 x_4(\tau)$	$\begin{pmatrix} 0 & 0 & 0 & 6959000 \\ 0 & 0 & -1000 & 0 \\ 0 & -1000 & 0 & 0 \\ -1620 & 0 & 0 & 200 \end{pmatrix}$

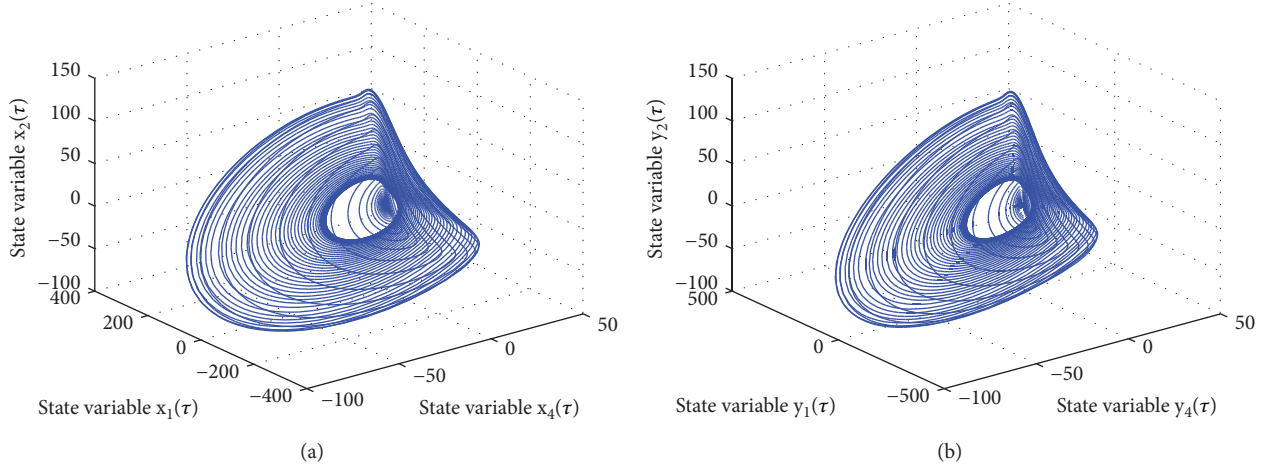


FIGURE 4: (a) Simulation result for master system with $f(x_4(\tau)) = \arctan x_4(\tau)$ and K derived by Proposition 2. (b) Simulation result for slave system with $f(x_4(\tau)) = \arctan x_4(\tau)$ and K derived by Proposition 2.

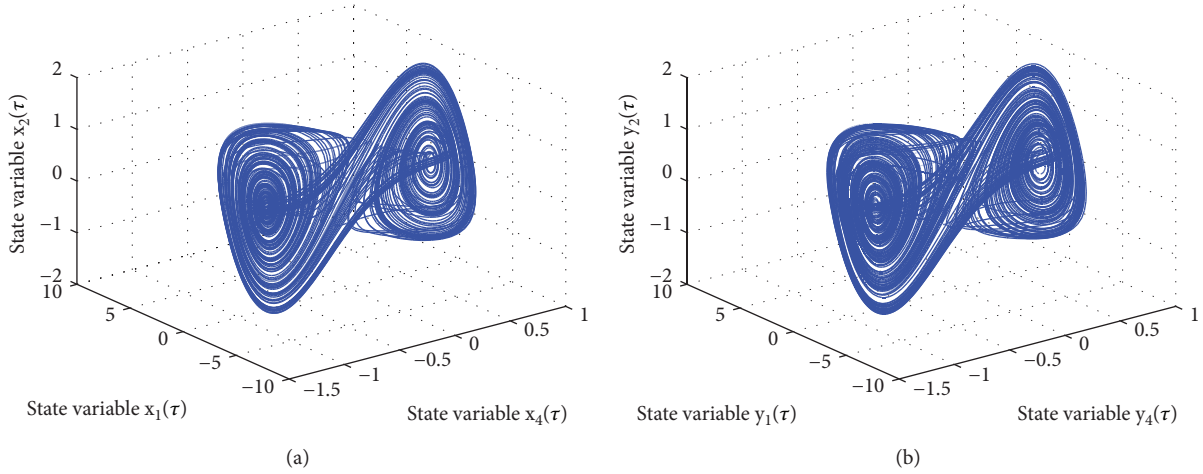


FIGURE 5: (a) Simulation result for master system with $f(x_4(\tau)) = \sin^2 x_4(\tau)$ and K derived by Proposition 2. (b) Simulation result for slave system with $f(x_4(\tau)) = \sin^2 x_4(\tau)$ and K derived by Proposition 2.

10^{-4} , $b = 6.0930 \times 10^{-4}$, $\mu_f = 1$, $\mu_{f'} = 1\mu_1(x_0) = 6$, $b_{11} = v_3 \sin^2 y_4(\tau)$, and $b_{14} = v_3 x_1(\tau) \sin(2\xi)$.

We choose the initial condition of master system (6) as $(x_{1_0}, x_{2_0}, x_{3_0}, x_{4_0}) = (0.11, 0.11, 0, 0)$ and the initial condition of slave system (7) as $(y_{1_0}, y_{2_0}, y_{3_0}, y_{4_0}) = (0.12, 0.12, 0.01, 0.01)$. From Proposition 2, we obtain the feedback gain matrix K for $f(x_4(\tau)) = \arctan x_4(\tau)$ and $f(x_4(\tau)) = \sin^2 x_4(\tau)$, respectively, which are listed in Table 1.

The simulation results for master, slave, and error systems for $f(x_4(\tau)) = \arctan x_4(\tau)$ and $f(x_4(\tau)) = \sin^2 x_4(\tau)$ and the feedback controller gain derived by Proposition 2 are illustrated in Figures 4 and 5, from which one can clearly see that the master and slave systems are synchronized, which means that the design method is effective.

6. Conclusions and Future Works

We have addressed the problem of the controller design for master-slave synchronization of memristor-based Chua's circuits and constructed a master-slave scheme by using

an error state feedback control. We have derived a master-slave synchronization criterion and provided the sufficient conditions on the existence of an error feedback controller. Moreover, we have obtained the error state feedback controller gain by solving a set of LMIs. The effectiveness of the synchronization criterion and the design method has been illustrated through one numerical example. It should be pointed out that we only consider the state feedback control for synchronization of memristor-based Chua's circuits in this paper. To design the time-delayed controller is our future research focus.

Data Availability

The data used to support the findings of this study are included within the article.

Conflicts of Interest

The author declares that there is no conflict of interest regarding the publication of this paper.

Acknowledgments

This work is partially supported by the National Natural Science Foundation of China under Grant 61561023, the key project of Youth Science Fund of Jiangxi China under Grant 20133ACB21009, the project of Science and Technology Fund of Jiangxi Education Department of China under Grant GJJ160429, and the project of Jiangxi E-Commerce High Level Engineering Technology Research Centre.

References

- [1] L. Chua, "Memristor. The missing circuit element," *IEEE Transactions on Circuit Theory*, vol. 18, no. 5, pp. 507–519, 1971.
- [2] D. B. Strukov, G. S. Snider, D. R. Stewart, and R. S. Williams, "The missing memristor found," *Nature*, vol. 453, no. 7191, pp. 80–83, 2008.
- [3] M. Itoh and L. O. Chua, "Memristor oscillators," *International Journal of Bifurcation and Chaos*, vol. 18, no. 11, pp. 3183–3206, 2008.
- [4] B. Muthuswamy, "Implementing memristor based chaotic circuits," *International Journal of Bifurcation and Chaos*, vol. 20, no. 5, pp. 1335–1350, 2010.
- [5] B. Muthuswamy and P. Kokate, "Memristor-based chaotic circuits," *IETE Technical Review*, vol. 26, no. 6, pp. 417–429, 2009.
- [6] J. Zhang, H. Zhang, and G. Zhang, "Controlling chaos in a memristor-based Chua's circuit," in *2009 International Conference on Communications, Circuits and Systems*, Milpitas, CA, USA, September 2009.
- [7] I. Petras, "Fractional-order memristor-based Chua's circuit," *IEEE Transactions on Circuits and Systems II: Express Briefs*, vol. 57, no. 12, pp. 975–979, 2010.
- [8] B. C. Bao, Z. Liu, and J. P. Xu, "Steady periodic memristor oscillator with transient chaotic behaviours," *Electronics Letters*, vol. 46, no. 3, p. 228, 2010.
- [9] I. M. Kyprianidis, C. K. Volos, and I. N. Stouboulos, "Chaotic dynamics from a nonlinear circuit based on memristor with cubic nonlinearity," *AIP Conference Proceedings*, vol. 1203, pp. 626–631, 2010.
- [10] V. T. Pham, S. Jafari, X. Wang, and J. Ma, "A chaotic system with different shapes of equilibria," *International Journal of Bifurcation and Chaos*, vol. 26, no. 4, article 1650069, 2016.
- [11] V. T. Pham, S. Jafari, and T. Kapitaniak, "Constructing a chaotic system with an infinite number of equilibrium points," *International Journal of Bifurcation and Chaos*, vol. 26, no. 13, article 1650225, 2016.
- [12] S. Vaidyanathan, A. T. Azar, and A. Boulkroune, "A novel 4-D hyperchaotic system with two quadratic nonlinearities and its adaptive synchronisation," *International Journal of Automation and Control*, vol. 12, no. 1, pp. 5–26, 2018.
- [13] J. L. Valtierra, E. Tlelo-Cuautle, and A. Rodriguez-Vazquez, "A switched-capacitor skew-tent map implementation for random number generation," *International Journal of Circuit Theory and Applications*, vol. 45, no. 2, pp. 305–315, 2017.
- [14] V.-T. Pham, C. Volos, S. Jafari, and T. Kapitaniak, "A novel cubic equilibrium chaotic system with coexisting hidden attractors: analysis, and circuit implementation," *Journal of Circuits, Systems, and Computers*, vol. 27, no. 4, article 1850066, 2018.
- [15] S. Wen, Z. Zeng, and T. Huang, "Adaptive synchronization of memristor-based Chua's circuits," *Physics Letters A*, vol. 376, no. 44, pp. 2775–2780, 2012.
- [16] S. Wen, Z. Zeng, T. Huang, and Y. Chen, "Fuzzy modeling and synchronization of different memristor-based chaotic circuits," *Physics Letters A*, vol. 377, no. 34–36, pp. 2016–2021, 2013.
- [17] Y. Zhao, Y. Jiang, J. Feng, and L. Wu, "Modeling of memristor-based chaotic systems using nonlinear Wiener adaptive filters based on back-slash operator," *Chaos, Solitons and Fractals*, vol. 87, pp. 12–16, 2016.
- [18] J. Wu, L. Wang, G. Chen, and S. Duan, "A memristive chaotic system with heart-shaped attractors and its implementation," *Chaos, Solitons and Fractals*, vol. 92, pp. 20–29, 2016.
- [19] Z. T. Njitacke, J. Kengne, H. B. Fotsin, A. N. Negou, and D. Tchiotso, "Coexistence of multiple attractors and crisis route to chaos in a novel memristive diode bridge-based Jerk circuit," *Chaos, Solitons and Fractals*, vol. 91, pp. 180–197, 2016.
- [20] Z. Tu, J. Cao, A. Alsaedi, and F. Alsaedi, "Global dissipativity of memristor-based neutral type inertial neural networks," *Neural Networks*, vol. 88, pp. 125–133, 2017.
- [21] G. Wen, Y. Wan, J. Cao, T. Huang, and W. Yu, "Master-slave synchronization of heterogeneous systems under scheduling communication," *IEEE Transactions on Systems, Man, and Cybernetics: Systems*, vol. 48, no. 3, pp. 473–484, 2018.
- [22] Y. Liu, Z. Wang, J. Liang, and X. Liu, "Synchronization and state estimation for discrete-time complex networks with distributed delays," *IEEE Transactions on Systems, Man, and Cybernetics, Part B (Cybernetics)*, vol. 38, no. 5, pp. 1314–1325, 2008.
- [23] Y. Liu, Z. Wang, J. Liang, and X. Liu, "Stability and synchronization of discrete-time Markovian jumping neural networks with mixed mode-dependent time delays," *IEEE Transactions on Neural Networks*, vol. 20, no. 7, pp. 1102–1116, 2009.
- [24] Y. Liu, Z. Wang, J. Liang, and X. Liu, "Synchronization of coupled neutral-type neural networks with jumping-mode-dependent discrete and unbounded distributed delays," *IEEE Transactions on Cybernetics*, vol. 43, no. 1, pp. 102–114, 2013.
- [25] F. Yang, Z. Wang, D. W. C. Ho, and M. Gani, "Robust H_∞ control with missing measurements and time delays," *IEEE Transactions on Automatic Control*, vol. 52, no. 9, pp. 1666–1672, 2007.
- [26] F. Yang and Y. Li, "Set-membership fuzzy filtering for nonlinear discrete-time systems," *IEEE Transactions on Systems, Man, and Cybernetics, Part B (Cybernetics)*, vol. 40, no. 1, pp. 116–124, 2010.
- [27] F. Yang, Q. L. Han, and Y. Liu, "Distributed H_∞ state estimation over a filtering network with time-varying and switching topology and partial information exchange," *IEEE Transactions on Cybernetics*, 2018.
- [28] Z. I. Mannan, H. Choi, and H. Kim, "Chua corsage memristor oscillator via Hopf bifurcation," *International Journal of Bifurcation and Chaos*, vol. 26, no. 4, p. 1630009, 2016.
- [29] Z. I. Mannan, C. Yang, and H. Kim, "Oscillation with 4-lobe Chua corsage memristor," *IEEE Circuits and Systems Magazine*, vol. 18, no. 2, pp. 14–27, 2018.

- [30] F. Corinto, A. Ascoli, and M. Gilli, "Nonlinear dynamics of memristor oscillators," *IEEE Transactions on Circuits and Systems I: Regular Papers*, vol. 58, no. 6, pp. 1323–1336, 2011.
- [31] B. Bao, T. Jiang, G. Wang, P. Jin, H. Bao, and M. Chen, "Two-memristor-based Chua's hyperchaotic circuit with plane equilibrium and its extreme multistability," *Nonlinear Dynamics*, vol. 89, no. 2, pp. 1157–1171, 2017.
- [32] Q. Lu, Q. L. Han, B. Zhang, D. Liu, and S. Liu, "Cooperative control of mobile sensor networks for environmental monitoring: an event-triggered finite-time control scheme," *IEEE Transactions on Cybernetics*, vol. 47, no. 12, pp. 4134–4147, 2017.
- [33] Q. Lu, Q. L. Han, and S. Liu, "A cooperative control framework for a collective decision on movement behaviors of particles," *IEEE Transactions on Evolutionary Computation*, vol. 20, no. 6, pp. 859–873, 2016.

Research Article

Family of Bistable Attractors Contained in an Unstable Dissipative Switching System Associated to a SNLF

J. L. Echenausía-Monroy , J. H. García-López, R. Jaimes-Reátegui, D. López-Mancilla, and G. Huerta-Cuellar 

Dynamical Systems Laboratory, CULagos, University of Guadalajara, 1144 Enrique Díaz de León St., Paseos de la Montaña, Lagos de Moreno, Jalisco 47460, Mexico

Correspondence should be addressed to J. L. Echenausía-Monroy; jose.luis.echenausia@gmail.com and G. Huerta-Cuellar; g.huerta@lagos.udg.mx

Received 27 April 2018; Revised 13 July 2018; Accepted 30 July 2018; Published 15 October 2018

Academic Editor: Viet-Thanh Pham

Copyright © 2018 J. L. Echenausía-Monroy et al. This is an open access article distributed under the Creative Commons Attribution License, which permits unrestricted use, distribution, and reproduction in any medium, provided the original work is properly cited.

This work presents a multiscroll generator system, which addresses the issue by the implementation of 9-level saturated nonlinear function, SNLF, being modified with a new control parameter that acts as a bifurcation parameter. By means of the modification of the newly introduced parameter, it is possible to control the number of scrolls to generate. The proposed system has richer dynamics than the original, not only presenting the generation of a global attractor; it is capable of generating monostable and bistable multiscrolls. The study of the basin of attraction for the natural attractor generation (9-scroll SNLF) shows the restrictions in the initial conditions space where the system is capable of presenting dynamical responses, limiting its possible electronic implementations.

1. Introduction

Over the last few years, the development and implementation of chaotic oscillators have been extensively studied, taking a special interest in the generation of systems with multiscrolls in their phase space, such as the Lorenz [1] and Chua [2] systems, which present a double-scroll attractor. There are several methods to obtain multiscroll behavior, for example, by adding breakpoints to Chua's function [3, 4], by using a system with hysteresis [5, 6], implementing step functions, using sine/cosine functions, or by generating piecewise linear functions [7–10]. The disadvantage of these methods is that the systems have more fixed points than scrolls generated, so increasing the number of scrolls in the phase space turns into a more complex task to address. As an alternative to this dilemma arises, the conception of a saturated nonlinear function, SNLF, which is based on the operational amplifiers performance [11, 12], which guarantees to find as many

scrolls as segmentation points the function possesses, being a simpler way to approach the topic in the scrolls generation.

An example of this kind of systems can be described within the theory of unstable dissipative systems, UDS [13, 14], which characterizes the systems of three differential equations based on the location of the eigenvalues that it possesses. UDS's are classified as type I or type II, where the order of the type represents the number of eigenvalues with negative real part. In general, any three-dimensional dynamic system is considered an UDS if and only if it has a combination of eigenvalues that coincide with the definition of a hyperbolic saddle-node, and the sum of these components is negative, i.e., the dissipation condition is fulfilled [15]. Examples of these systems are found in Rössler [16], Lorenz [1], and Chua [2], among some other systems [17–19]. This kind of combination in the eigenvalues favors the appearance of multiscroll behavior, by means of the implementation of the appropriated nonlinear function.

In recent years, the design and control of systems with multiple scrolls have been a subject of interest for the scientific community, having a great impact in their application, such as secure communication systems, neuronal modeling, and generation of pseudorandom systems [20–23]. In this work, the modification in a multiscroll dynamics by means of controlling the associated nonlinear function is presented, introducing a new control parameter. This new control parameter helps to generate a specific number of scrolls, generating regions of coexisting attractors, as well as the generation of attractors with double-wing and three equilibrium points.

This work is structured as follows: the first section contains an introduction that describes previous works and theoretical principles of the system. The second section shows the UDS definition and the description of the multiscroll generator system. In the third section, the methodology and results of the studied system are shown. The analysis of the bifurcation diagrams exhibits the coexistence of two attractors for fixed set parameters, bistability, which is illustrated by the construction of the corresponding basins of attractions. The main conclusions are shown in the last section.

2. Theoretical Background

2.1. Unstable Dissipative Systems Theory. In the same spirit as [13, 24, 25], it is considered as a system of autonomous differential equations of third order,

$$\dot{\mathbf{X}} = \mathbf{A}\mathbf{X} + \mathbf{B}\mathbf{f}(\mathbf{x}), \quad (1)$$

where $\mathbf{X} = [x, y, z]^T \in \mathbb{R}^3$ is the state vector, $\mathbf{A} = [a_{i,j}] \in \mathbb{R}^{3 \times 3}$ is a constant matrix, $\mathbf{B} = [b_1, b_2, b_3]^T \in \mathbb{R}^3$ is a constant position vector, and $\mathbf{f}(\mathbf{x})$ is a nonlinear function. The behavior of the system is governed by the eigenvalues of the matrix \mathbf{A} , which generates a great variety of characteristic values, presenting special attention to those saddle-node points that have a stable and an unstable variety. This kind of eigenvalues is responsible for both stretching and successive folding in the dynamic of the system, which favors the generation of multiscrolls [14, 26].

A system can be considered as an UDS type I if their equilibrium points correspond to a hyperbolic-saddle-node, i.e., one eigenvalue is negative real (dissipative component) and the other two are complex conjugated with positive real part (unstable and oscillatory component), where the sum of the components must be less than zero. By other side, an UDS type II, eq. (1), is described in the opposite way, i.e., one eigenvalue is positive real (unstable component) and the other two are complex conjugated with negative real part (dissipative and oscillatory component), and the sum of them must be less than zero [13].

2.2. Multiscroll Generator. The multiscroll generator system studied is described by a set of three coupled differential equations that makes use of the definition of a saturated nonlinear function, SNLF, as a method for the scroll generation [12, 27], eq. (2).

$$\begin{aligned} \dot{x} &= y, \\ \dot{y} &= z, \\ \dot{z} &= -\alpha_1 x - \alpha_2 y - \alpha_3 z + \alpha_4 f(x, q), \end{aligned} \quad (2)$$

where x, y, z are the state variables, $f(x, q)$ is the SNLF, q is the upper limit of scrolls to generate, and $\alpha_{1,2,3,4}$ are the system parameters that define the behavior of the dynamic. This work is focused on the region for which the system is defined as a UDS I. Within this proposition, the multiscroll appearance is possible, by generating a conservative component that causes the oscillation of the system over an equilibrium point, while the other two dissipative components favor the visit to other fixed points, resulting in the dynamics of a multiscroll system. The operation region of the system is defined by the combination of the system parameters, in this case, the following consideration is contemplated: $\alpha = \alpha_1 = \alpha_2 = \alpha_3 = \alpha_4$.

Considering the previous condition, it is possible to examine the behavior of the equilibrium points by sweeping the control parameter and finding the operation zone where their eigenvalues are consistent with an UDS I definition. The control parameter variation is developed by means of the characteristic polynomial of the system described in eq. (2), $\lambda^3 + \alpha(\lambda^2 + \lambda + 1) = 0$, and are plotted by considering the split of the real and imaginary component of each eigenvalue, $\lambda_j = \sigma_j + i\omega_j$, $j = 1, 2, 3$, being σ_j the real part, and ω_j the imaginary part. Figure 1 shows the analysis of the eigenvalues over a range value defined as $\alpha = [-2, 2]$, Figure 1(a) shows the operation zone delimited by $0 < \alpha < 1$. Figures 1(b) and 1(c) confirm the conditions for the UDS I definition. λ_1 the real negative eigenvalue, and $\lambda_{2,3}$ the complex conjugated eigenvalues with positive real part.

It is well known [11, 12, 27] that it is possible to define a series of saturated functions, based on the behavior of an operational amplifier (op-amp) configured as voltage comparator, in order to generate as many plateaus (commutation surfaces) as desired, and thus guarantee the generation of the same number of scrolls. In general, the mathematical construction of a SNLF is defined as

$$f(x_{k,h,p,q}) = \sum_{m=-p}^q f_m(x_{k,h}), \quad (3)$$

where $k > 0$ is the slope that connects the plateaus in the saturated function, $h > 2$ is the delay time of the saturated function, defined by the op-amp switching speed, p and q are positive integers defined as the smallest integer that result from dividing the number of scrolls by 2, $m = 1, 2, 3, \dots, n$, where n defines the number of scrolls to generate. The function $f(x)$ is defined as follows

$$f_m(x_{k,h}) = \begin{cases} 2k, & f x > mh + 1, \\ k(x - mh) + k, & \text{if } |x - mh| \leq 1, \\ 0, & f x < mh - 1, \end{cases} \quad (4)$$

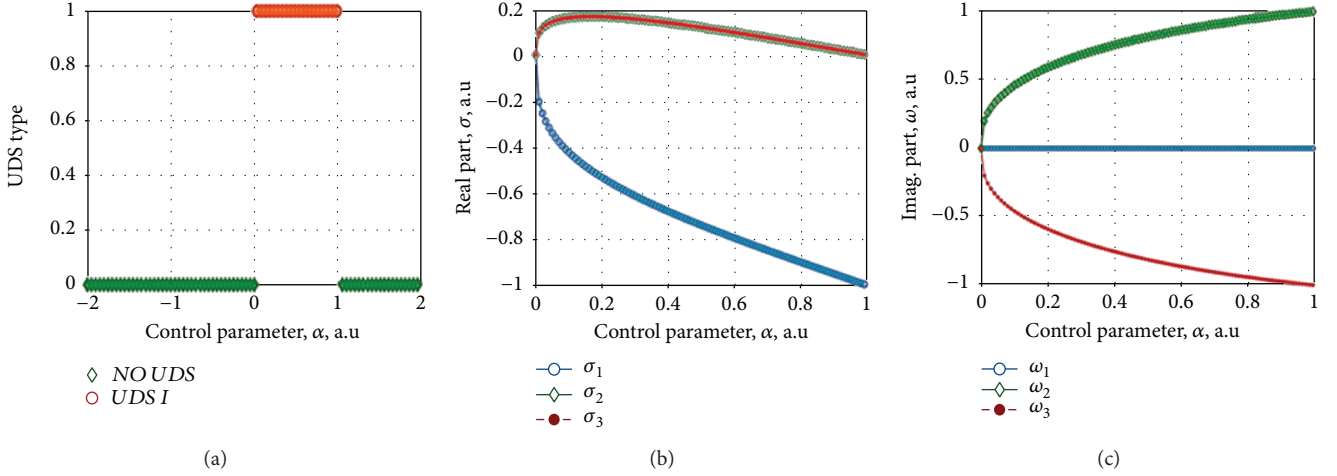


FIGURE 1: Eigenvalues analysis as a function of the control parameter α . (a) Control parameter analysis showing the UDS I region. (b) and (c) real and imaginary parts for the UDS I, respectively.

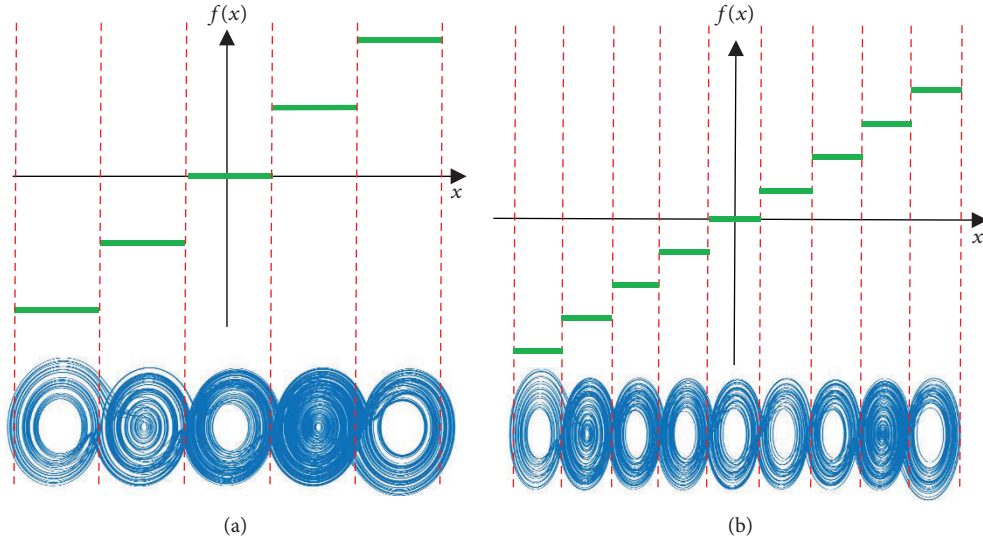


FIGURE 2: (a) Saturated nonlinear function with $n = 5$ and its corresponding attractor of five multiscrolls. (b) Saturated nonlinear function with $n = 9$ and its corresponding attractor of nine multiscrolls.

and

$$f_{m-1}(x_{k,h}) = \begin{cases} 0, & \text{if } x > mh \pm 1, \\ k(x \pm mh) - k, & \text{if } |x \pm mh| \leq 1, \\ -2k, & \text{if } x < -mh - 1. \end{cases} \quad (5)$$

Figure 2 shows the graphical representation of eq. (4) and (5) (green) and their corresponding attractor (blue). The breakpoints are plotted with a red dotted line, where the system switches between the different generated commutation surfaces. At the middle of each switching surface, the equilibrium point is located, where each scroll oscillates. Figure 2(a) SNLF generated with $n = 5$, whereas Figure 2(b) shows a SNLF with $n = 9$. Notice the relation between the number of switching surfaces and generated scrolls.

The SNLF contemplated for this study is constructed based on [11], eq. (4) and (5), for the generation up to nine scrolls as in Figure 2(b), but it is studied with a new bifurcation parameter ζ , modifying the original system, eq. (2) [28, 29]. This new parameter works as an individual control gain for the nonlinear function. This allows the possibility to study the bifurcation diagrams for a defined set of parameters in the model and generates more than one single attractor. The modified system is described by

$$\begin{aligned} \dot{x} &= y, \\ \dot{y} &= z, \\ \dot{z} &= -\alpha[x + y + z - \zeta f(x, q)], \end{aligned} \quad (6)$$

where α is a control parameter and ζ is the bifurcation parameter. This modification allows to analyze the

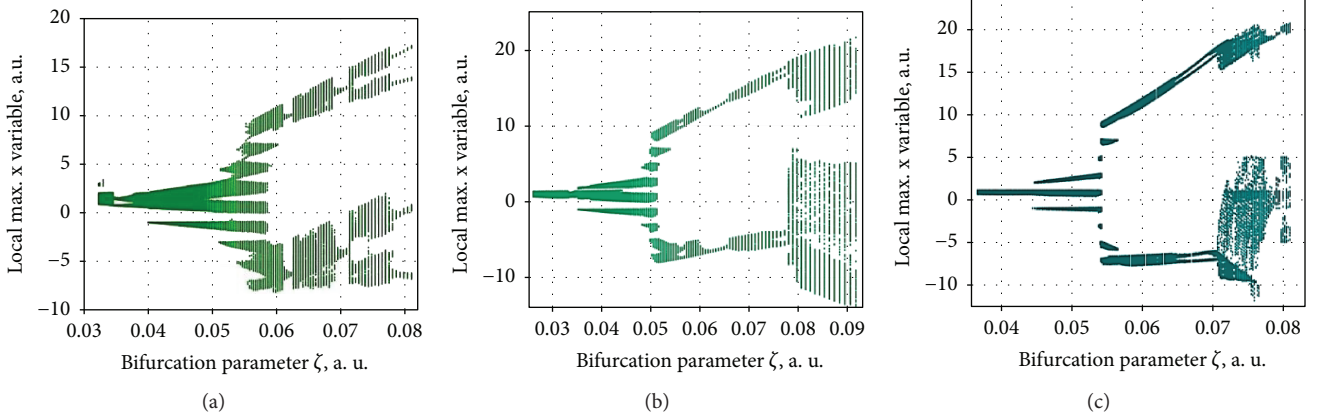


FIGURE 3: Bifurcation diagram for the dynamical control parameter (a) $\alpha = 0.45$, (b) $\alpha = 0.70$, (c) $\alpha = 0.90$.

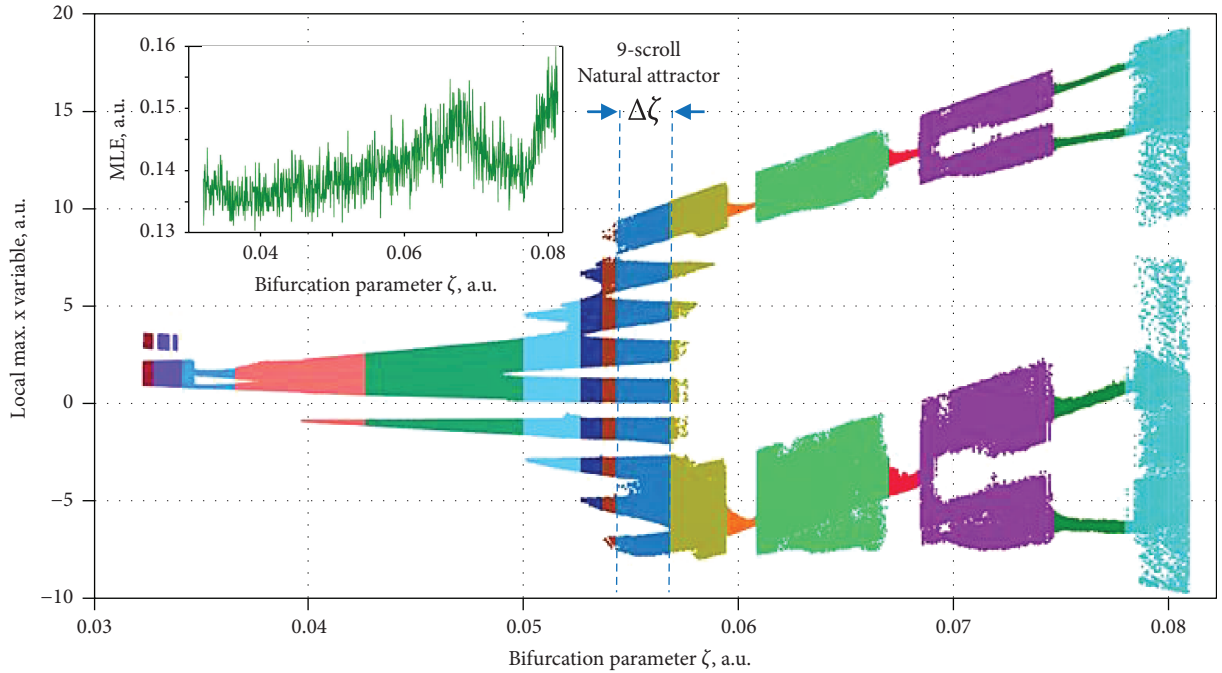


FIGURE 4: Bifurcation diagram for the dynamical control parameter $\alpha = 0.45$.

behavior of the system through numerical simulation in a better way. In this case, the implementation of an Rk4 integrator is used.

3. Methodology and Results

Considering the restrictions of the system, eq. (6), given the region of operation under the conditions of an UDS I, the control parameter is analyzed in the interval $0.05 \leq \alpha \leq 0.95$ with a step size $\Delta\alpha = 0.05$.

The dynamical system, eq. (6), is analyzed by a gradual change of the bifurcation parameter ζ for the different α values. For this purpose, the construction of bifurcation diagrams of local maximums of the state variable $x(t)$, are calculated by means of randomly changing the initial condition of the three state variables.

Analyzing the dynamical system, Figure 3, it is observed that the behavior of the different bifurcation diagrams has a dependence on the control parameter α , but obtaining in each one of them a control in the generation of multiscrolls. However, it is more interesting to describe the dynamical evolution that the system exhibits for a value $\alpha = 0.45$ in Figure 3(a). This is because the scrolls generation is produced gradually, obtaining a greater number of generated dynamics, unlike the behavior displayed in other values of the control parameter.

The 9-scroll natural attractor region $\Delta\zeta$ is shown in Figure 4. At the left top of this figure, the last largest Lyapunov exponent (MLE) is shown, corresponding to the same bifurcation diagram. Notice that it is always a positive value, in concordance with UDS I definition. This bifurcation diagram is plotted by a color combination, where each color

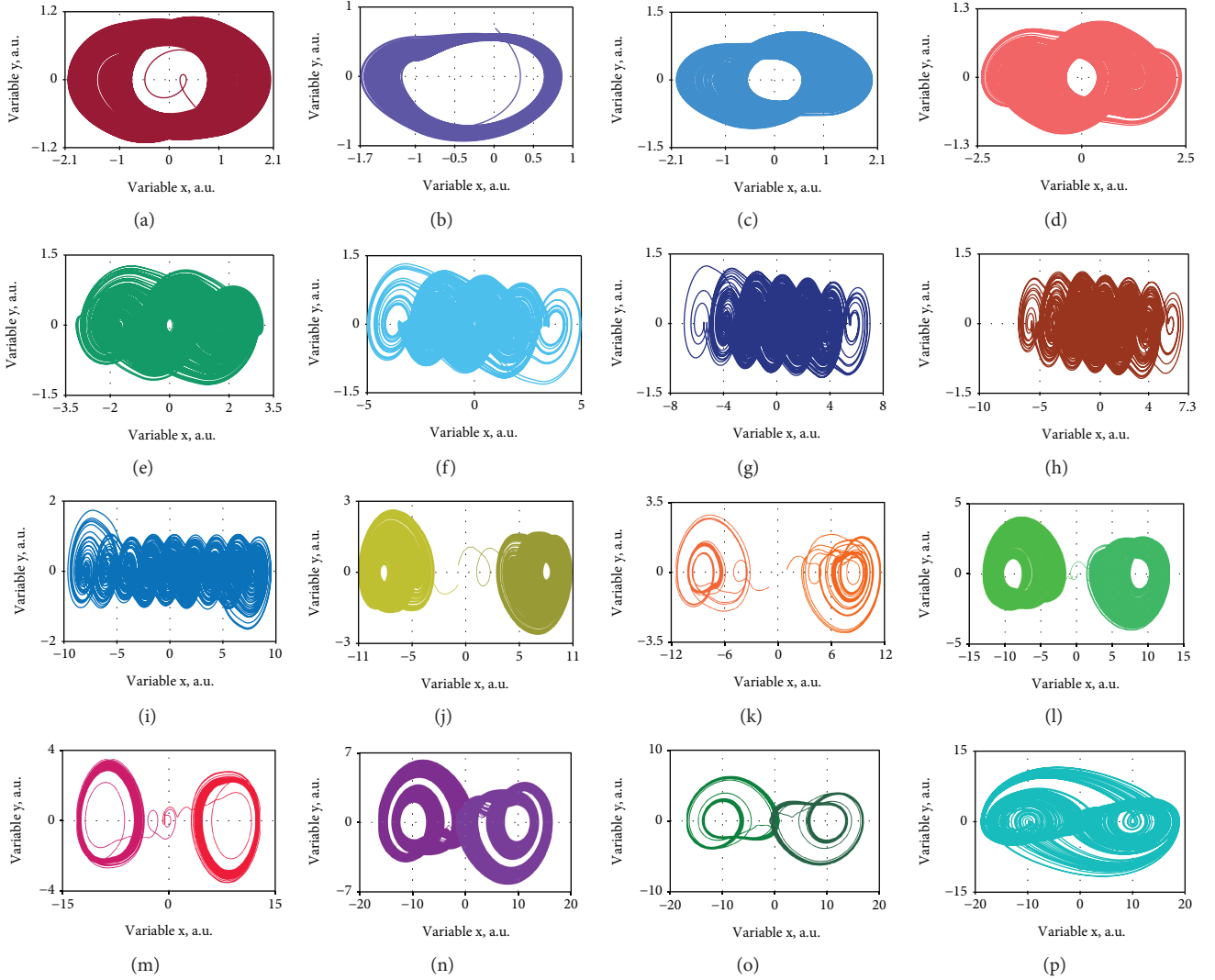


FIGURE 5: Space phase for each attractor identified into the bifurcation diagram, Figure 4, for the control parameter $\alpha = 0.45$.

represents a different behavior in the system, related to the corresponding attractors displayed in Figure 5.

Table 1 describes the different behavior of the bifurcation diagram of Figure 4 as well as the corresponding attractors of Figure 5. The bistability referred in Table 1 indicates the coexistence of two identical attractors located at symmetrical equilibrium points. Notice that from Figures 5(j)–5(o) the bistable attractors are shown in the same phase space and plotted with different colors for easier visualization, i.e., in Figure 5(m) the pink scroll represents the lower part of the bifurcation diagram, while the red scroll is the upper part in the same diagram for $0.0670 < \zeta < 0.0690$.

4. Discussion

With the premise that every UDS I system has large basins of attraction [30], the analysis of the dynamical system, eq. (6), is determined for each value of the dynamical parameter α ,

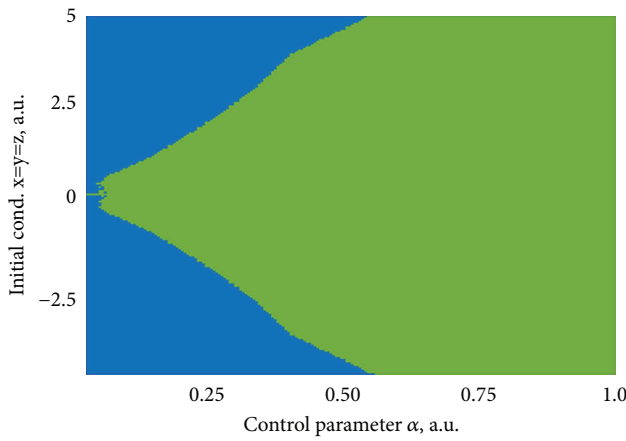
by means of the exploration of the bifurcation parameter ζ , being $\alpha = 0.05$ the first explored value.

An analysis of the dynamical response of the natural system attractor (nine multiscrolls) in a bidimensional space $\alpha v s x_{ci} = y_{ci} = z_{ci}$, where ci represents the initial condition, is shown in Figure 6. It can clearly be seen that meanwhile the α value is increased, the area of initial conditions grows (green points), while the nonexistence of the dynamical response is shown by every blue point. As a result, $\alpha = 0.3$ is the minimum value in which it is possible to perform the characterization of the system, eq. (6), as defined in the previous section. This fact limits the possible electronic implementation of the model.

As in [28, 29], in this work, the bifurcation parameter ζ is dependent on the dynamical parameter α , as shown in Figure 3. This effect can be visualized in Figure 7(a) that shows the ration $\Delta\zeta/\zeta(\alpha)$. As a result, the ration has a maximum point for $\alpha = 0.3$. The operation region relative size, $\zeta(\alpha)$, is normalized to its $\zeta(\alpha)_{\max}$ to improve the

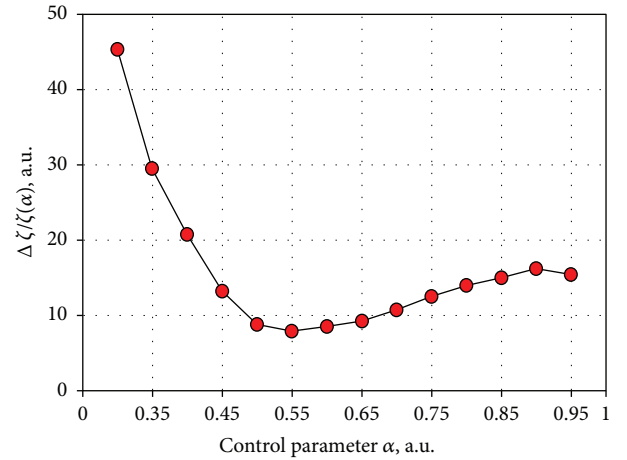
TABLE 1: Behavior analysis of Figures 4 and 5.

ζ interval	Attractor type	Bistability	Fig.
0.0310–0.0320	Single-wing deformed	No	Figure 5(a)
0.0320–0.0335	Single-wing	No	Figure 5(b)
0.0335–0.0350	Single-wing deformed	No	Figure 5(c)
0.0350–0.0420	Single-wing with 3 equilibrium points	No	Figure 5(d)
0.0420–0.0500	3-scroll	No	Figure 5(e)
0.0500–0.0510	5-scroll	No	Figure 5(f)
0.0510–0.0520	7-scroll	No	Figure 5(g)
0.0520–0.0530	8-scroll	No	Figure 5(h)
0.0530–0.0570	9-scroll (natural attractor)	No	Figure 5(i)
0.0570–0.0590	Single-wing	Yes	Figure 5(j)
0.0590–0.0610	Coherent single-wing	Yes	Figure 5(k)
0.0610–0.0670	Single-wing	Yes	Figure 5(l)
0.0670–0.0690	Single-wing	Yes	Figure 5(m)
0.0690–0.0740	Coherent single-wing	Yes	Figure 5(n)
0.0740–0.0780	Coherent single-wing	Yes	Figure 5(o)
0.0780–0.0820	Double-scroll with 3 equilibrium points	No	Figure 5(p)

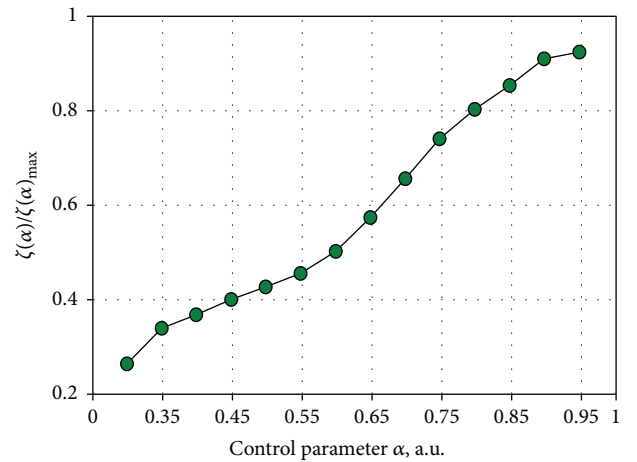
FIGURE 6: Bidimensional space $\alpha vs x_{ci} = y_{ci} = z_{ci}$ for the natural system attractor by means of the dynamical parameter modification.

visualization, $\zeta(\alpha)/\zeta(\alpha)_{\max}$, Figure 7(b). The values $\alpha < 0.3$ are omitted due to the results shown in Figure 6.

As a result of the bifurcation diagrams shown in Figures 3 and 4 and to the bistable attractors shown in Figure 5, an analysis is developed in search of bistable behavior in all the control parameters of the system for which its response is defined as an UDS I. The study in search of bistable dynamics is developed in the following way: given a control parameter α , the bifurcation parameter ζ is fixed, and the basins of attraction of the system, eq. (6), are calculated under the modification of two of the three state variables for the space of initial conditions defined as $x, y = [-4, 4], z = 0$. The results shown by the basins of attraction confirm the bistable behavior for any α value and are validated by analyzing the attractors generated for different explored initial conditions, Figure 8, where each column corresponds to a α value.



(a)



(b)

FIGURE 7: (a) Ration curve of the 9-scroll operation zone and (b) normalized operation zone for every dynamical value.

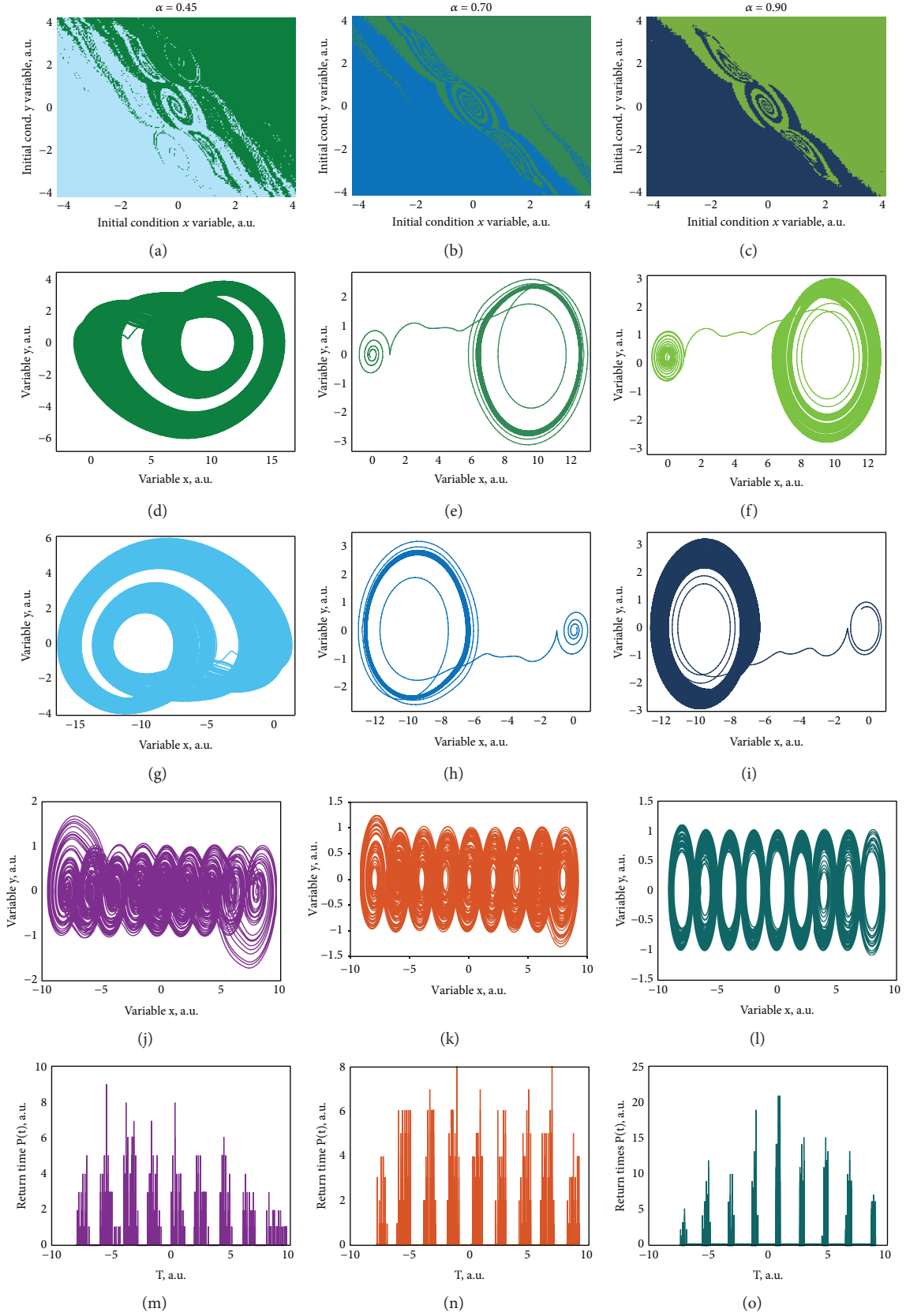


FIGURE 8: (a–c) Basins of attraction for the coexisting coherent single-wing attractor. (d–i) Coexisting attractors for each basin of attraction. (j–l) Natural system attractor. (m–o) Return time distribution calculated by the Poincare section for the natural system attractor. Columns from left to right correspond to $\alpha = 0.45, 0.70, 0.90$.

Figures 8(a)–8(c) shows three different basins of attraction calculated for different α values under the conditions for the generation of a coexisting coherent single-wing attractor. The corresponding coexisting attractors are plotted in Figures 8(d)–8(i), where the color of the attractor is related to the color in their corresponding basin of attraction.

Analyzing the resulting basins of coexisting attractors, Figures 8(a)–8(c), it is evident that while the dynamical parameter of the system is increased, the basin tends to look more defined, where the state borders are better distinguished. This means that for small values in α , the system requires a very small variation in the initial condition, or a very low noise level, to leave the actual state and converge to another coexisting equilibrium point. Meanwhile, for larger values in the dynamical parameter, the system obtains robustness by requiring significantly larger changes to leave one state and converge to another one. This phenomenon can be visualized if the return times of the attractor are calculated via the Poincaré section, from the natural attractors of each analyzed α value, Figures 8(j)–8(o). The distribution of these return times tends to gain some order similar to a normal distribution, Figure 8(o), becoming in softer transitions between each of the equilibrium points.

5. Conclusions

In this work, a multiscroll system of three-dimensional autonomous equations with a parameter ζ has been presented and studied. The parameter ζ controls the number of generated scrolls, being up to nine the maximum number of scrolls using a saturated nonlinear function. The studied system exhibits the generation of emergent behaviors from a single-wing up to a 9-scroll attractor. On the other hand, bistable states such as a single scroll, coherent single-wing, and a monostable double-scroll attractor with three equilibrium points are also obtained. The understanding of the UDS I systems has also been extended, proving that these systems have considerably large basins of attraction, but not at every value where the system fully satisfies the requirements established by the UDS theory.

The described model, in addition to involving a relatively easy implementation [27, 31], is able to control the number of scrolls to be generated, with the additional advantage of having bistable dynamics. This factor increases the potential technological applications, as in secure communication systems, neuronal systems, and control of electric motors with variable torque. The corresponding analogical implementation, in order to compare the presented results, is proposed as future work.

Data Availability

The data used to support the findings of this study are available from the corresponding author upon request.

Conflicts of Interest

The authors declare that there is no conflict of interest regarding the publication of this paper.

Acknowledgments

J. L. E. M. acknowledges CONACYT for the financial support (National Fellowship CVU-706850, No. 582124) and the University of Guadalajara, CULagos (Mexico). This work was supported by the University of Guadalajara under the project “research laboratory equipment for academic groups in optoelectronics from CULAGOS”, R-0138/2016, Agreement RG /019/2016-UdeG, Mexico. The authors acknowledge J.O. Esqueda-de la Torre for his help in improving the grammar.

References

- [1] E. N. Lorenz, “Deterministic nonperiodic flow,” *Journal of the Atmospheric Sciences*, vol. 20, no. 2, pp. 130–141, 1963.
- [2] L. Chua, *The Genesis of Chua’s Circuit*, Electronics Research Laboratory, College of Engineering, University of California, Berkeley, CA, USA, 1992.
- [3] M. E. Yalcin, J. A. K. Suykens, and J. Vandewalle, “Experimental confirmation of 3- and 5-scroll attractors from a generalized Chua’s circuit,” *IEEE Transactions on Circuits and Systems I: Fundamental Theory and Applications*, vol. 47, no. 3, pp. 425–429, 2000.
- [4] J. A. K. Suykens, A. Huang, and L. O. Chua, “A family of n -scroll attractors from generalized Chua’s circuit,” *Archiv für Elektronik und Übertragungstechnik*, vol. 53, no. 3, pp. 131–137, 1997.
- [5] R. W. Newcomb and N. El-Leithy, “Chaos generation using binary hysteresis,” *Circuits, Systems, and Signal Processing*, vol. 5, no. 3, pp. 321–341, 1986.
- [6] J. Lü, F. Han, X. Yu, and G. Chen, “Generating 3-D multiscroll chaotic attractors: a hysteresis series switching method,” *Automatica*, vol. 40, no. 10, pp. 1677–1687, 2004.
- [7] M. E. Yalçın, S. Özoğuz, J. A. K. Suykens, and J. Vandewalle, “ n -scroll chaos generators: a simple circuit model,” *Electronics Letters*, vol. 37, no. 3, pp. 147–148, 2001.
- [8] W. K. S. Tang, G. Q. Zhong, G. Chen, and K. F. Man, “Generation of n -scroll attractors via sine function,” *IEEE Transactions on Circuits and Systems I: Fundamental Theory and Applications*, vol. 48, no. 11, pp. 1369–1372, 2001.
- [9] L. Chua, M. Komuro, and T. Matsumoto, “The double scroll family,” *IEEE Transactions on Circuits and Systems*, vol. 33, no. 11, pp. 1072–1118, 1986.
- [10] J. A. K. Suykens and J. Vandewalle, “Generation of n -double scrolls ($n=1, 2, 3, 4, \dots$),” *IEEE Transactions on Circuits and Systems I: Fundamental Theory and Applications*, vol. 40, no. 11, pp. 861–867, 1993.
- [11] J. Lü, G. Chen, X. Yu, and H. Leung, “Design and analysis of multiscroll chaotic attractors from saturated function series,” *IEEE Transactions on Circuits and Systems I: Regular Papers*, vol. 51, no. 12, pp. 2476–2490, 2004.
- [12] J. Lu, S. Yu, H. Leung, and G. Chen, “Experimental verification of multidirectional multiscroll chaotic attractors,” *IEEE Transactions on Circuits and Systems I: Regular Papers*, vol. 53, no. 1, pp. 149–165, 2006.

- [13] E. Campos-Cantón, J. G. Barajas-Ramírez, G. Solís-Perales, and R. Femat, "Multiscroll attractors by switching systems," *Chaos: An Interdisciplinary Journal of Nonlinear Science*, vol. 20, no. 1, article 013116, 2010.
- [14] E. Campos-Cantón, R. Femat, and G. Chen, "Attractors generated from switching unstable dissipative systems," *Chaos: An Interdisciplinary Journal of Nonlinear Science*, vol. 22, no. 3, article 033121, 2012.
- [15] E. Ott, "Strange attractors and chaotic motions of dynamical systems," in *The Theory of Chaotic Attractors*, pp. 103–119, Springer, 1981.
- [16] O. E. Rössler, "An equation for continuous chaos," *Physics Letters A*, vol. 57, no. 5, pp. 397–398, 1976.
- [17] M. E. Yalçın, J. A. K. Suykens, J. Vandewalle, and S. Özoğuz, "Families of scroll grid attractors," *International Journal of Bifurcation and Chaos*, vol. 12, no. 1, pp. 23–41, 2002.
- [18] G. Q. Zhong, K. F. Man, and G. Chen, "A systematic approach to generating n-scroll attractors," *International Journal of Bifurcation and Chaos*, vol. 12, no. 12, pp. 2907–2915, 2002.
- [19] J. Lü, T. Zhou, G. Chen, and X. Yang, "Generating chaos with a switching piecewise-linear controller," *Chaos: An Interdisciplinary Journal of Nonlinear Science*, vol. 12, no. 2, pp. 344–349, 2002.
- [20] J. H. Park, D. H. Ji, S. C. Won, and S. M. Lee, " \mathcal{H}_∞ synchronization of time-delay chaotic systems," *Applied Mathematics and Computation*, vol. 204, no. 1, pp. 170–177, 2008.
- [21] O. M. Kwon, J. H. Park, and S. M. Lee, "Secure communication based on chaotic synchronization via interval time-varying delay feedback control," *Nonlinear Dynamics*, vol. 63, no. 1-2, pp. 239–252, 2011.
- [22] W. Yu, J. Cao, K. W. Wong, and J. Lü, "New communication schemes based on adaptive synchronization," *Chaos: An Interdisciplinary Journal of Nonlinear Science*, vol. 17, no. 3, article 033114, 2007.
- [23] M. E. Yalcin, J. A. K. Suykens, and J. Vandewalle, "True random bit generation from a double-scroll attractor," *IEEE Transactions on Circuits and Systems I: Regular Papers*, vol. 51, no. 7, pp. 1395–1404, 2004.
- [24] L. J. Ontañón-García, E. Jiménez-López, E. Campos-Cantón, and M. Basin, "A family of hyperchaotic multi-scroll attractors in \mathbf{R}^n ," *Applied Mathematics and Computation*, vol. 233, pp. 522–533, 2014.
- [25] A. D. Pano-Azucena, J. de Jesus Rangel-Magdaleno, E. Tlelo-Cuautle, and A. de Jesus Quintas-Valles, "Arduino-based chaotic secure communication system using multi-directional multi-scroll chaotic oscillators," *Nonlinear Dynamics*, vol. 87, no. 4, pp. 2203–2217, 2017.
- [26] L. J. Ontañón-García, E. Jiménez-López, and E. Campos-Cantón, "Generation of multiscroll attractors by controlling the equilibria," *IFAC Proceedings Volumes*, vol. 45, no. 12, pp. 111–114, 2012.
- [27] E. T. Cuautle, D. G. H. Rodríguez, J. H. Santillán, V. H. Arreola, and L. A. C. Cantera, "Simulation and experimental realization of multi-scroll chaotic oscillators," *Journal of Engineering Science and Technology Review*, vol. 6, no. 4, pp. 1–8, 2013.
- [28] M.-S. Abdelouahab and N.-E. Hamri, "A new chaotic attractor from hybrid optical bistable system," *Nonlinear Dynamics*, vol. 67, no. 1, pp. 457–463, 2012.
- [29] E. Campos-Cantón, I. Campos-Cantón, J. S. González-Salas, and F. Cruz-Ordaz, "A parameterized family of single-double-triple-scroll chaotic oscillations," *Revista Mexicana de Física*, vol. 54, no. 6, pp. 411–415, 2008.
- [30] L. J. Ontañón-García, E. Campos-Cantón, and R. Femat, "Analog electronic implementation of a class of hybrid dissipative dynamical system," *International Journal of Bifurcation and Chaos*, vol. 26, no. 1, article 1650018, 2016.
- [31] J. L. Echenausía-Monroy, J. R. Sevilla-Escoboza, and G. Huerta-Cuéllar, "Control para la generación de multi-enroscados mediante la generación de interfaces virtuales," in *2do. Congreso Iberoamericano de Instrumentación y Ciencias Aplicadas, SOMI XXXI*, Guatemala, Guatemala, 2016.

Research Article

Dynamical Behavior of a 3D Jerk System with a Generalized Memristive Device

Wei Feng ^{1,2}, Yi-Gang He ¹, Chun-Lai Li ³, Xun-Min Su,³ and Xiao-Qing Chen³

¹School of Electrical Engineering and Automation, Hefei University of Technology, Hefei 230009, China

²School of Mathematics and Computer Science, Panzhihua University, Panzhihua 617000, China

³College of Physics and Electronics, Hunan Institute of Science and Technology, Yueyang 414006, China

Correspondence should be addressed to Yi-Gang He; yghe@hfut.edu.cn and Chun-Lai Li; hnistlichl@163.com

Received 18 May 2018; Accepted 28 June 2018; Published 19 August 2018

Academic Editor: Viet-Thanh Pham

Copyright © 2018 Wei Feng et al. This is an open access article distributed under the Creative Commons Attribution License, which permits unrestricted use, distribution, and reproduction in any medium, provided the original work is properly cited.

As a new type of electronic components, a memristive device is receiving worldwide attention and can enrich the dynamical behaviors of the oscillating system. In this paper, we propose a 3D jerk system by introducing a generalized memristive device. It is found that the dynamical behaviors of the system are sensitive to the initial conditions even the system parameters are fixed, which results in the coexistence of multiple attractors. And there exists different transition behaviors depending on the selection of the parameters and initial values. Thereby, it is one important type of the candidate system for secure communication since the reconstruction of accurate state space becomes more difficult. Moreover, we build a hardware circuit and the experimental results effectively confirm the theoretical analyses.

1. Introduction

As the fourth basic circuit element besides resistance, inductance, and capacitance, the memristor was postulated by Chua in 1971, to link the charge with the flux [1]. And the concept of the memristive system was further extended by Chua and Kang [2]. However, research on the memristor had not been received much interest until 2008, when the solid-state realization of the memristor was reported by the scholars in Hewlett-Packard Laboratory [3]. The memristor belongs to a nonvolatile two-terminal passive device with variable quantity called memristance, which connects the electric flux applied to the device with the electric charge passing through in a particular direction. When the electrical field in the memristor is removed, the memristance may remain unchanged, thus holding memory characteristic [4, 5]. It was proved that the memory characteristic of the memristor could not be reproduced by any combination of the other three fundamental elements. Therefore, the memristor could be in fact considered as a new electronic element in electrical circuit theory, which is generally called as the fourth element [1].

In 2009, Chua put forward the other two hypothetical circuit elements called memcapacitor and meminductor from the nanoworld [6–8], which have closely the same characteristics as the memristor depending on the past states through which the system has evolved, so they are all called to be memory circuit elements.

As the new circuit element, the memristor has potential applications in the construction of the new generation of computers and memories and has been found to have significant applications in memristor oscillators, memristor-based neural networks, and memristor-based charge pump locked loops [9, 10]. Additionally, a memristive circuit is propitious to generate chaotic signal for the intrinsic nonlinearity and plasticity properties [11–13]. Different from the conventional nonlinear systems, the most significant feature of the memristor-based nonlinear system is that the long-term dynamical behaviors extremely rely on the initial state of the memristor, which leads to the emergence of multistability or coexisting many attractors [14, 15]. The phenomenon of multistability has attracted a lot of research enthusiasm recently. In many cases, the multistability exists in dynamical systems with stable equilibrium, no-equilibrium,

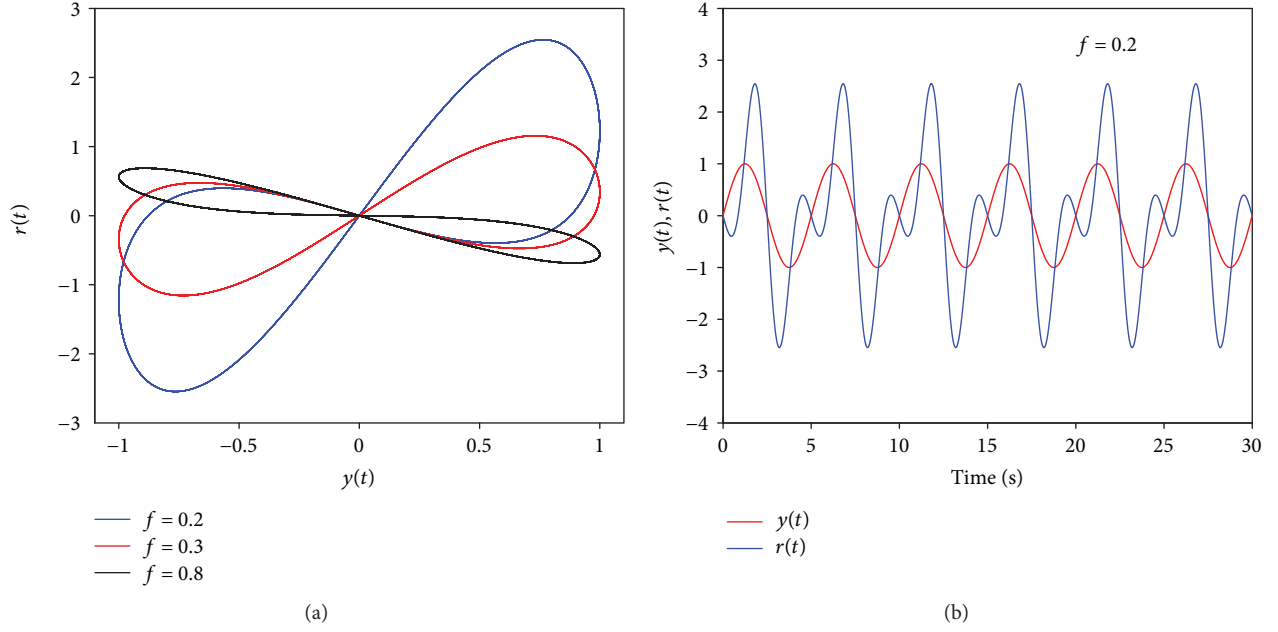


FIGURE 1: (a) Relationship curves of input and output under different frequencies and (b) the time-domain waveforms when $f = 0.2$ Hz.

or a line of equilibrium, in which one cannot use the Shilnikov method to explain the chaos [14–18].

In this paper, we introduce a generalized memristive device by extending the definition of the memristor and propose a 3D jerk system based on the memristive element. Basic dynamical properties of the jerk system are displayed and studied. Specially, the coexistence of multiple attractors is investigated by analyzing the bifurcation map, spectrum of Lyapunov exponent, and distribution of the stable region in the initial value space. And there exist different transition behaviors depending on the selection of the parameters and initial values. Thereby, this system exhibits a rich and complex dynamics relying on the system parameters, initial values, and time evolution, which are of significance for secure communication since the reconstruction of accurate state space becomes more difficult. Moreover, we build a hardware circuit and the experimental results effectively confirm the theoretical analysis.

2. Generalized Memristive Device

By extending the definition of the memristive system [2, 19–21], we introduce a generalized memristive device, depicted by the following relation:

$$\begin{aligned} \frac{dx}{dt} &= y, \\ r &= (x^2 - 2)y. \end{aligned} \quad (1)$$

In relation (1), $x(t)$ denotes the internal state variable of the memristive element; $y(t)$ and $r(t)$ are complementary constitutive variables representing the input and output, respectively.

To study the fingerprint, we consider a sinusoidal stimulus $y = h \sin(\omega t) = h \sin(2\pi f t)$ with the amplitude h and

the frequency ω or f , connected across the terminals of the memristive element [22–24]. Thus, we have

$$\begin{aligned} x(t) &= \int_{-\infty}^t y(\tau) d\tau = \int_{-\infty}^0 y(\tau) d\tau + \int_0^t y(\tau) d\tau \\ &= x(0) + \frac{h}{2\pi f} [1 - \cos(2\pi f t)]. \end{aligned} \quad (2)$$

And we further obtain the output of the memristive element, as

$$r = (x^2 - 2)y = \left[\left(x(0) + \frac{h}{2\pi f} (1 - \cos(2\pi f t)) \right)^2 - 2 \right] h \sin(2\pi f t). \quad (3)$$

As we know that the resulting output not only depends on the initial state of the memristive element but also depends on the frequency and amplitude of the sinusoidal input. Figure 1(a) depicts the relations of input and output of the memory element for sinusoidal stimulus at different frequencies, when $h = 1$ and $x(0) = 1$. Figure 1(b) shows the corresponding time domain waveform of $f = 0.2$. Figure 2(a) depicts the relations of input and output of the memory element with $h = 1$ and $f = 0.2$ under different initial states. Figure 2(b) depicts the relations of input and output of the memory element with $x(0) = 1$ and $f = 0.2$ under different amplitudes of the sinusoidal signal.

From the simulation results in Figures 1 and 2, it can be seen that the memory device is not passive and behaves as a linear negative commutator in the limit of infinite frequency. Besides, there exist at most two values of the output $r(t)$ for any designated input $y(t)$ [20].

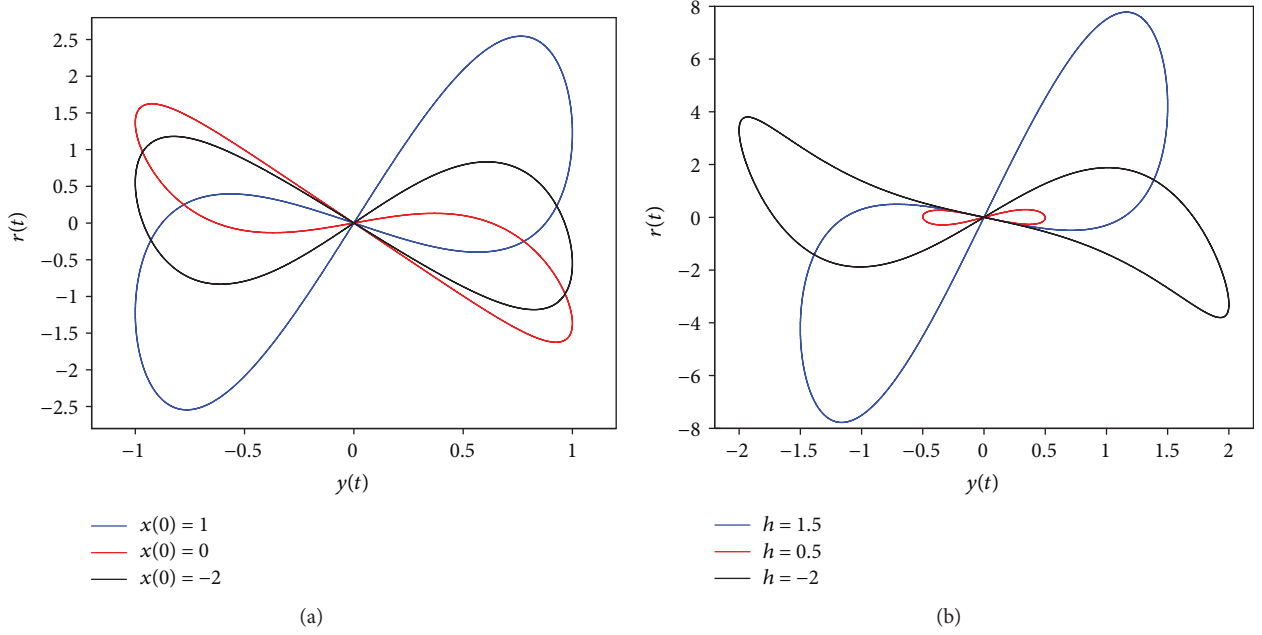


FIGURE 2: Relationship curves of input and output under (a) different initial states and (b) different amplitudes of the sinusoidal signal.

3. Model of a Memristor-Based Jerk System

Jerk system is of interest within the nonlinear dynamics domain for the simple mathematical form yet rich dynamics. A jerk system is depicted by the third-order ordinary differential equation as $d^3x/dt^3 = J(d^2x/dt^2, dx/dt, x)$, in which the function $J(\cdot)$ is nonlinear. From the point of view of mechanics, the function $J(\cdot)$ corresponds to the first-time derivative of acceleration; thus, it is called to be a jerk or jolt [25–27].

In this work, we introduce a 3D jerk system which possesses the generalized memristive element of (1):

$$\begin{aligned} \frac{dx}{dt} &= y, \\ \frac{dy}{dt} &= dz, \\ \frac{dz}{dt} &= -az + bx - cx^3 + kr, \end{aligned} \quad (4)$$

where $r = (x^2 - 2)y$, x, y, z are the state variables, and a, b, c, k are the positive system parameters.

The volume contraction of system (4) can be described by the Lie derivative:

$$\nabla V = \left(\frac{\partial \dot{x}}{\partial x} \right) + \left(\frac{\partial \dot{y}}{\partial y} \right) + \left(\frac{\partial \dot{z}}{\partial z} \right) = -a. \quad (5)$$

This signifies that the dissipativity of system (4) is negative. Thereby, the limit sets of system (4) will infinitely converge to zero volume, and the asymptotic motion at time through the flow will settle onto an attractor.

We obtain the three equilibrium points of system (4) as $E_0(0, 0, 0)$, $E_1(\sqrt{b/c}, 0, 0)$, and $E_2(-\sqrt{b/c}, 0, 0)$, by simple mathematical derivation. When letting the parameter set

$P = (a, b, c, d, k) = (0.5, 0.8, 0.6, 3.0, 1)$, we get the typical equilibrium points and the corresponding characteristic roots, as below

$$\begin{aligned} E_0(0, 0, 0): \lambda_1 &= -1.12415 - 1.88224i, \\ \lambda_2 &= -1.12415 + 1.88224i, \lambda_3 = 1.2483, \\ E_{1,2}(\pm 1.1547, 0, 0): \lambda_1 &= -2.54216, \lambda_2 = 0.771078 - 2.03122i, \\ \lambda_3 &= 0.771078 + 2.03122i. \end{aligned} \quad (6)$$

Therefore, the equilibrium point E_0 is a saddle node of index 1, and the equilibrium points E_1 and E_2 are both saddle-focus points of index 2. Accordingly, the three equilibrium points are all instable.

With the parameter set P , we get the Lyapunov exponents as 0.165274, 0, and -0.662735 and the Kaplan-Yorke dimension as 2.2494, implying a fractional feature with chaotic behavior, as depicted in Figure 3.

4. Dynamics of a Memristor-Based Jerk System

4.1. Impact of System Parameters. We first select the parameter set P except let b vary in the region $(0.6, 0.82)$, the bifurcation diagram and the Lyapunov exponent spectrum are displayed in Figure 4. It is known from Figure 4 that the system trajectory evolves from a fixed point to multiple period-doubling bifurcations, finally falls into a chaotic state. And there exists an obvious periodic window near $b = 0.75$. The Feigenbaum's constant can be acquired by $F_n = (\rho_n - \rho_{n-1})/(\rho_{n+1} - \rho_n)$, where ρ_n is the critical parameter value at which a period-doubling bifurcation emerges. It is agreed that the ratio F_n will converge to the ideal value 4.669 as n increases. Thus, the ratio on the parameter b is reckoned as $(0.7241 - 0.6782)/(0.7341 - 0.7241) = 4.59$, which

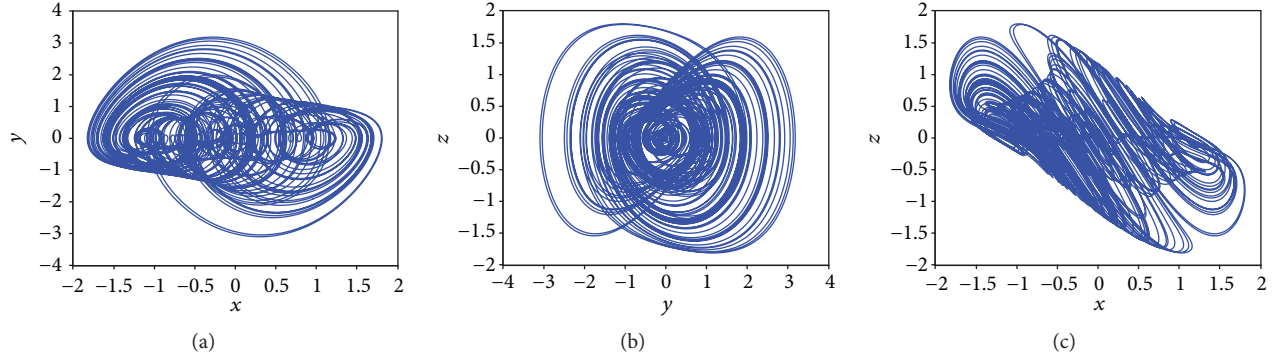


FIGURE 3: (a) x - y phase portrait, (b) y - x phase portrait, (c) x - z phase portrait.

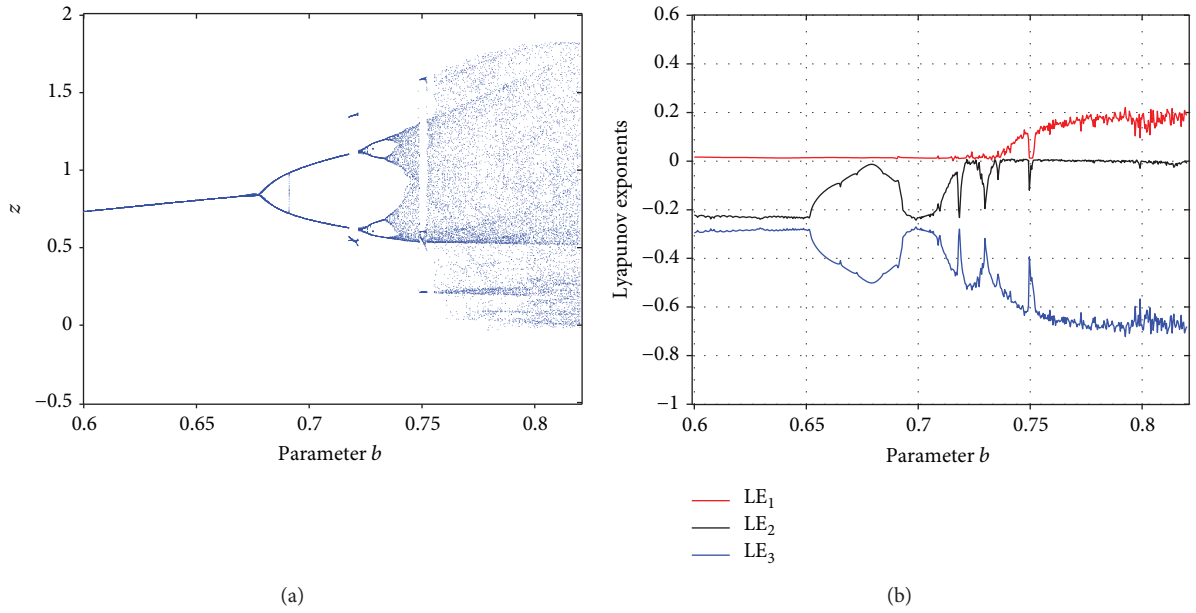


FIGURE 4: (a) Bifurcation diagram and (b) Lyapunov exponent spectrum versus parameter b .

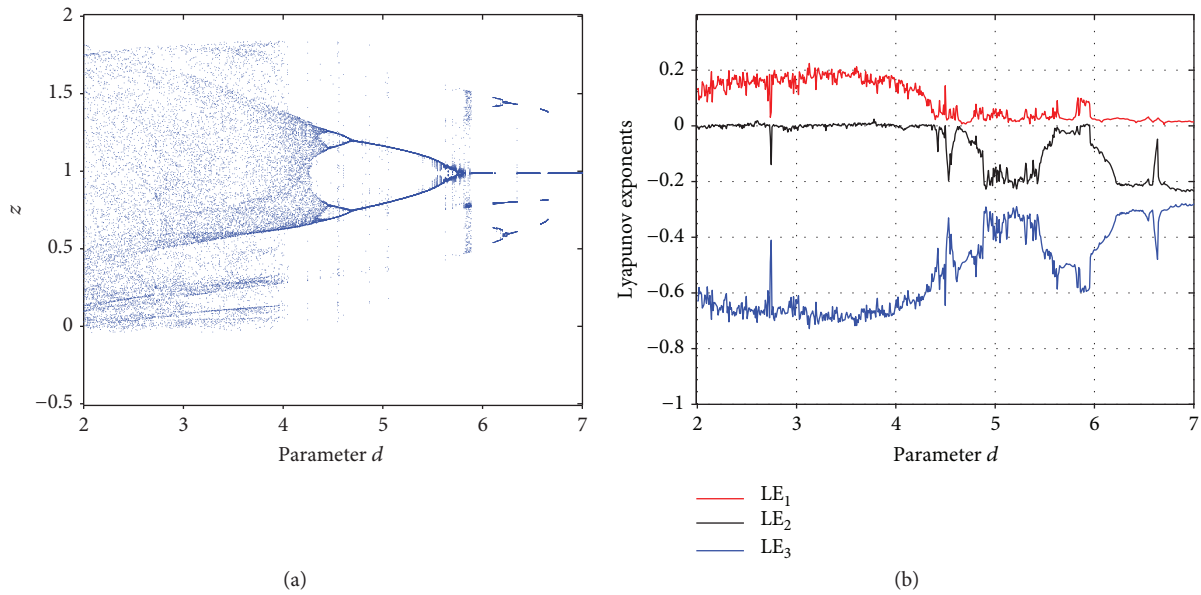
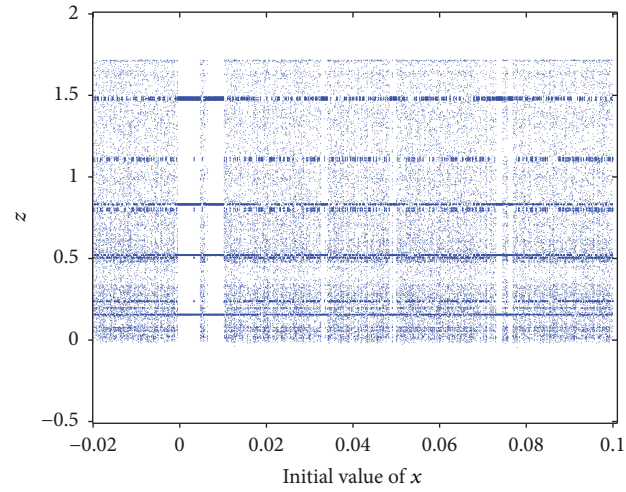
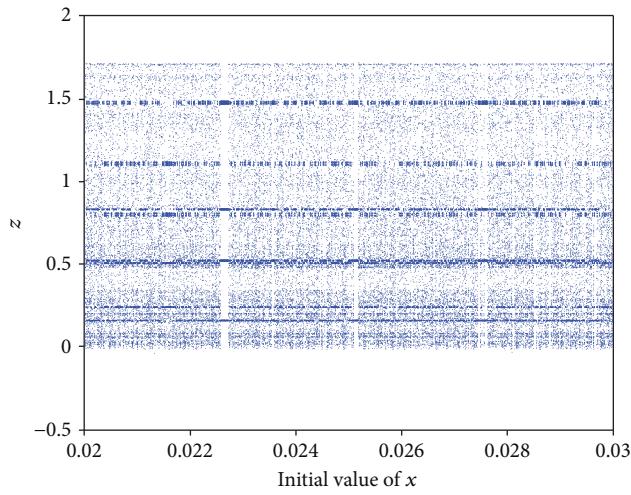


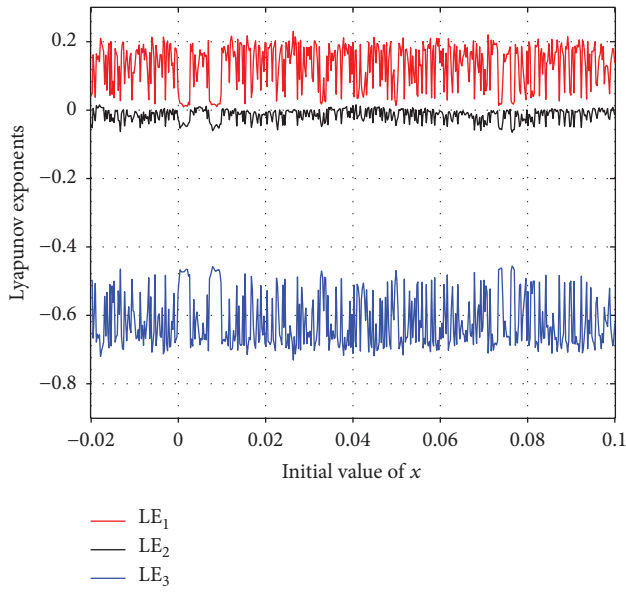
FIGURE 5: (a) Bifurcation diagram and (b) Lyapunov exponent spectrum versus parameter d .



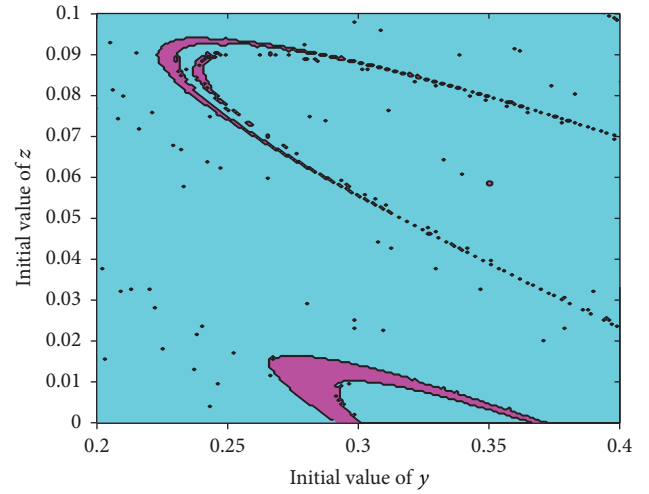
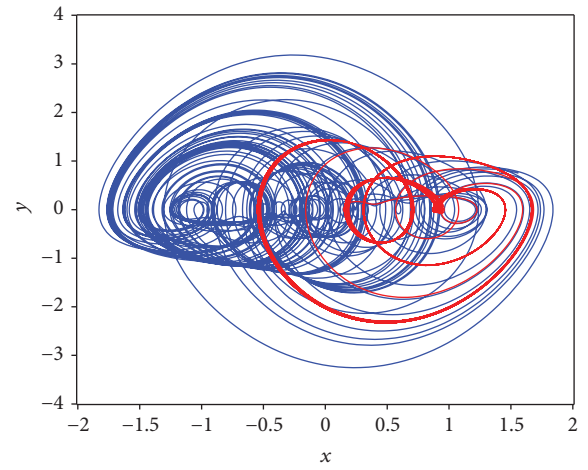
(a)



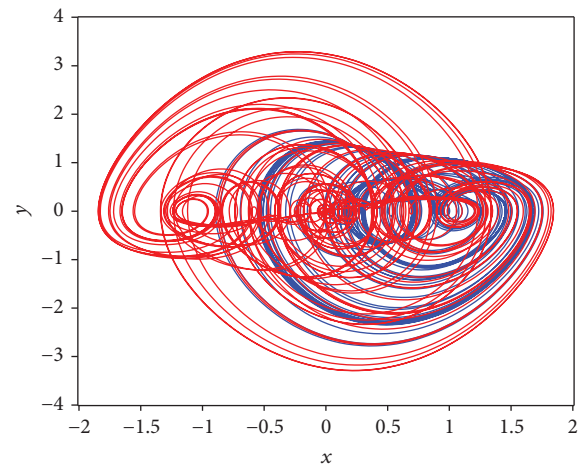
(b)



(c)

FIGURE 6: (a, b) Bifurcation diagram and (c) Lyapunov exponent spectrum versus $x(0)$.FIGURE 7: Dynamical map with $y(0)$ and $z(0)$.

(a)

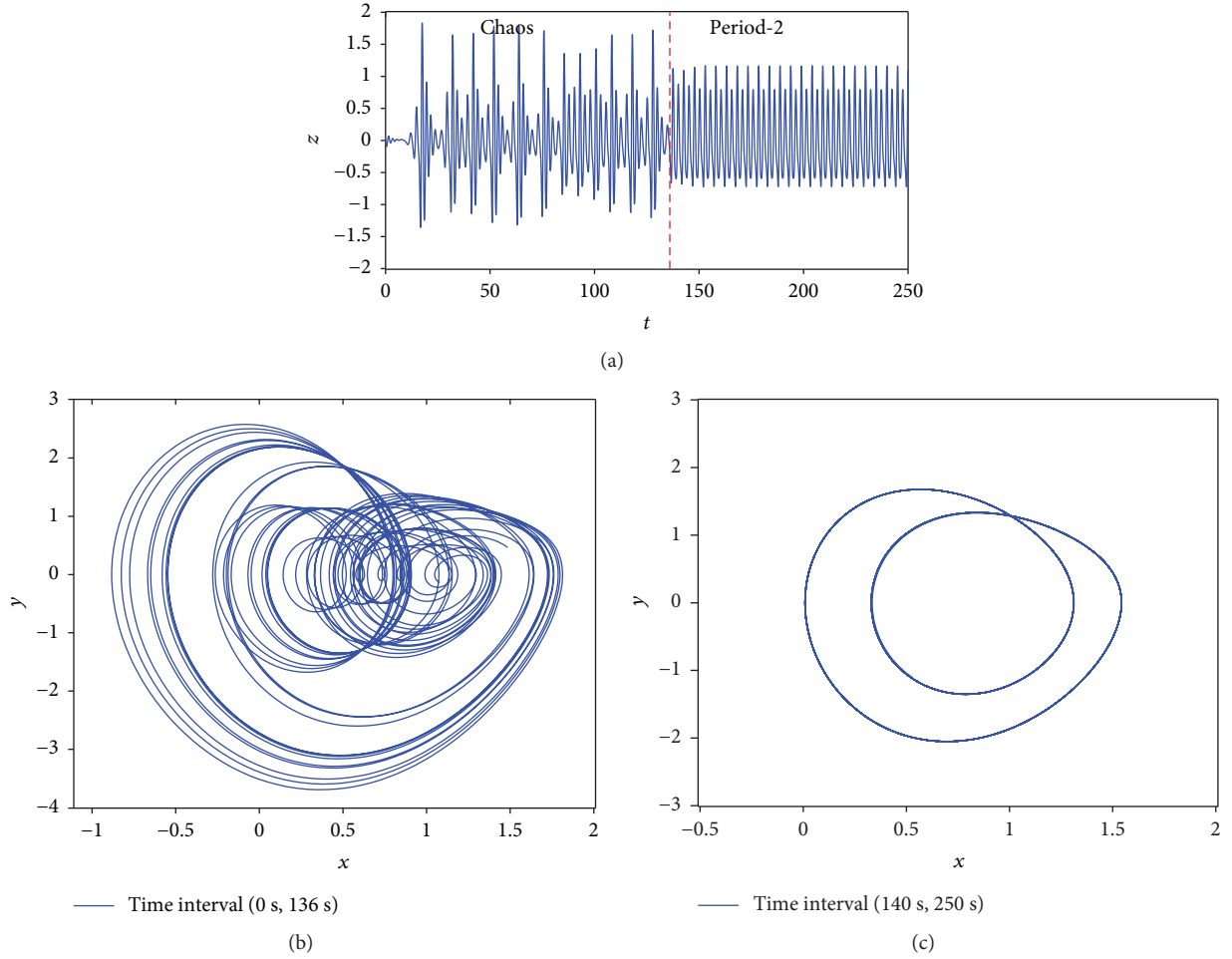


(b)

FIGURE 8: Attractors on x - y plane with different initial conditions.

TABLE 1: Multistable behavior of system (4) with $a = 0.5$, $b = 0.8$, $c = 0.6$, $d = 3$, and $k = 0.95$.

Initial condition	Lyapunov exponent	Dynamical behavior
(0.01, 0.2, 0.09)	0.173334, 0.009299, -0.682633	2-Scroll chaotic attractor
(0.01, 0.23, 0.09)	0.0017705, -0.062944, -0.484761	Period-3 mode
(0.01, 0.4, 0)	0.050191, -0.0047652, -0.502539	1-Scroll chaotic attractor
(0.01, 0.4, 0.022)	0.148570, -0.001767, -0.646803	2-Scroll chaotic attractor

FIGURE 9: (a) Time-domain waveform of variable z in the region of (0 s, 250 s); (b) the phase portrait in time interval of (0 s, 136 s); (c) the phase portrait in time interval of (140 s, 250 s).

approximately equals to 4.669 with a relative deviation (decline) of 1.69%.

Figure 5 depicts the bifurcation diagram and the Lyapunov exponent spectrum when selecting parameter set P except d varying in the region $[2, 7]$. It is obvious that the dynamics of system (4) switch among the chaotic state and periodic orbit by inverse period-doubling Feigenbaum tree, with the increase of parameter d . And the Feigenbaum's constant is reckoned as $(5.732 - 4.666)/(4.666 - 4.445) = 4.8235$, which is approximately equal to 4.669 with a relative deviation (rise) of 3.31%.

4.2. Coexisting Attractors. We assign the parameters of system (4) as $a = 0.5$, $b = 0.8$, $c = 0.6$, $d = 3$, and $k = 0.95$ and take the initial conditions $y(0) = 0.3$ and $z(0) = 0.015$. When let

$x(0)$ as the bifurcation parameter varying in the region $(-0.02, 0.1)$, the bifurcation diagram and its Lyapunov exponent spectra are plotted in Figure 6. It is found that when initial value of x increases from -0.02 , system (4) starts from a chaotic state and abruptly breaks into a periodic state via tangent bifurcation at -0.005 , and system turns into the normal chaotic state at 0.0035 then degrades into a periodic state at 0.0065 via chaos crisis; the periodic state continues until the tangent bifurcation at $x(0) = 0.012$. As depicted by the enlarged view in Figure 6(b), similar switching process will happen in other ranges or smaller local ranges, showing a multifractal process.

When assigning the same parameters and $x(0) = 0.01$, the dynamic dependence on both initial conditions $y(0)$ and $z(0)$ is also studied by the dynamical map, through

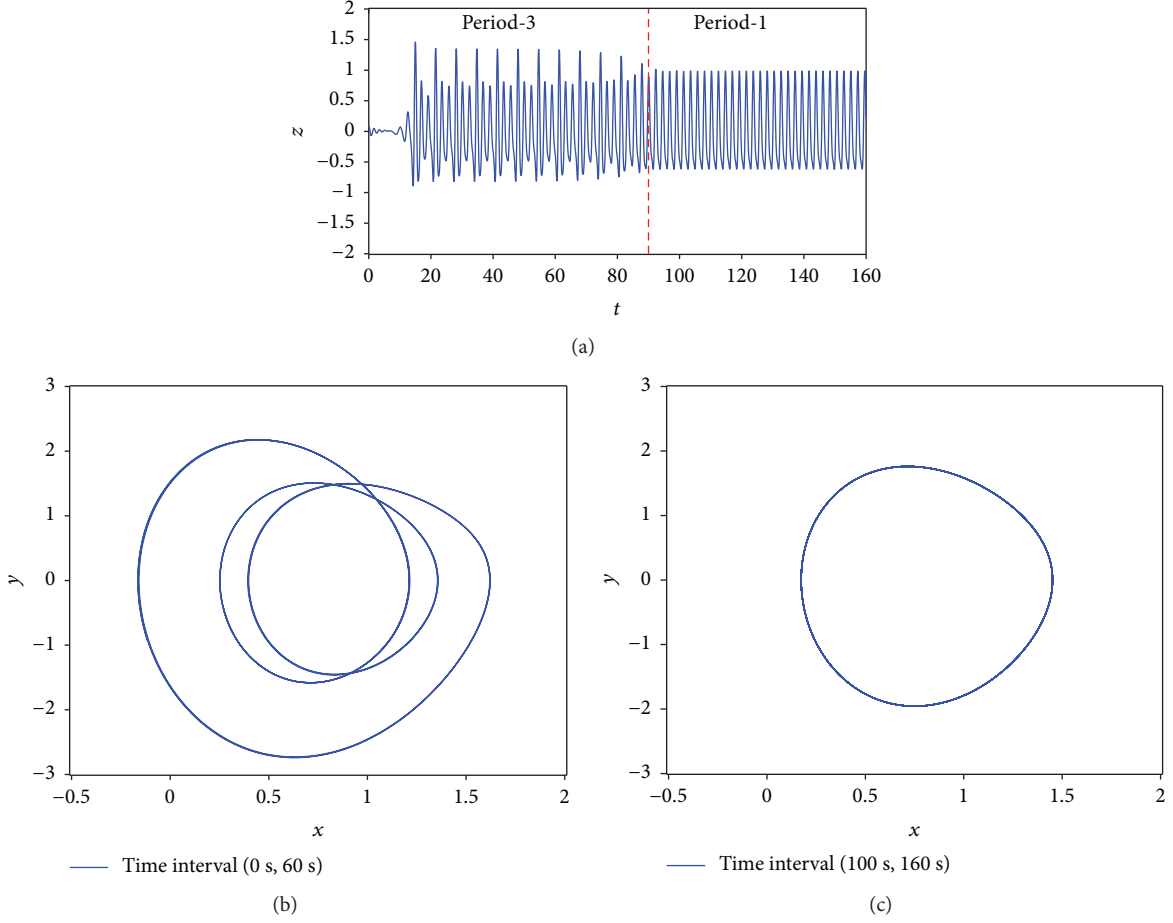


FIGURE 10: (a) Time-domain waveform of variable z in the region of (0 s, 160 s); (b) the phase portrait in time interval of (0 s, 60 s); (c) the phase portrait in time interval of (100 s, 160 s).

numerical simulation, as shown in Figure 7. In the dynamical map, the system is chaotic in the cyan region, stable in the pink region, and periodic in the blue region.

All these results of initial sensitivity indicate that there exists palpable feature of coexisting attractors in system (4). As the representative examples, Figure 8 displays the attractors on x - y plane with $a = 0.5$, $b = 0.8$, $c = 0.6$, $d = 3$, and $k = 0.95$ and different initial conditions. Figure 8(a) displays that the initial condition (0.01, 0.2, 0.09) leads to a 2-scroll chaotic mode and the initial condition (0.01, 0.23, 0.09) leads to a period-3 mode. Figure 8(b) displays that the initial condition (0.01, 0.4, 0) leads to a 1-scroll chaotic attractor and the initial condition (0.01, 0.4, 0.022) leads to a 2-scroll chaotic attractor. The typical multistable behaviors are summarized in Table 1.

4.3. Transient Dynamics. As discussed above, the dynamic mode of the reported system strongly depends not only on the parameters but also on the initial conditions. Another important phenomenon is that the dynamic mode also strongly depends on state evolution time, called to be the transition behavior.

Taking $a = 0.5$, $b = 0.8$, $c = 0.6$, $d = 5$, $k = 1$ and the initial condition (0.01, 0.2, 0.01), we depict the time trajectory in the

region of (0 s, 250 s) and the phase portraits in time intervals of (0 s, 136 s) and (140 s, 250 s), as shown in Figure 9. As we find that the dynamics convert from transient chaos to period-2 behavior.

Taking $a = 0.5$, $b = 0.8$, $c = 0.6$, $d = 6.6$, $k = 1$ and the initial condition (0.01, 0, 0.1), we depict the time trajectory in the region of (0 s, 160 s) and the phase portraits in time intervals of (0 s, 60 s) and (100 s, 160 s), as shown in Figure 10, from which we find the dynamics transition from transient period-3 to period-1 behaviors.

Figure 11 depicts the case of $a = 0.5$, $b = 0.8$, $c = 0.6$, $d = 3$, $k = 0.95$ and the initial condition (0.01, 0.26, 0.01). As we find that the system (4) is chaotic in the region of (0 s, 1050 s) and is in the mode of period-4 in the region of (1050 s, 2000 s).

5. Circuit Realization of a Memristor-Based Jerk System

The circuit realization is important for the chaotic system, especially by adopting commercially common electronic components [28–30]. In this section, we build an electronic circuit to physically realize the reported system for different cases, based on the improved module-based technique

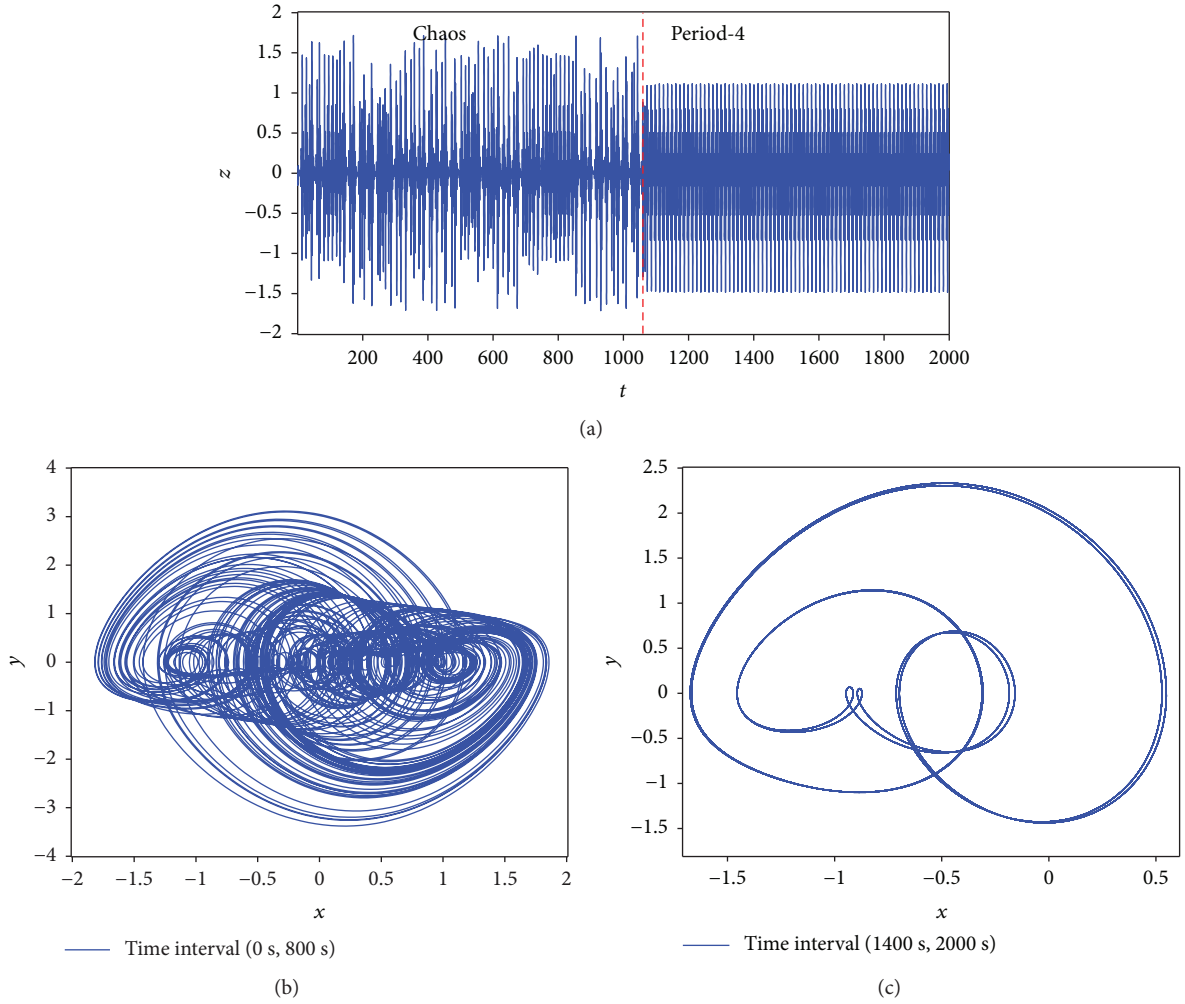


FIGURE 11: (a) Time-domain waveform of variable z in the region of (0 s, 2000 s); (b) the phase portrait in time interval of (0 s, 800 s); (c) the phase portrait in time interval of (1400 s, 2000 s).

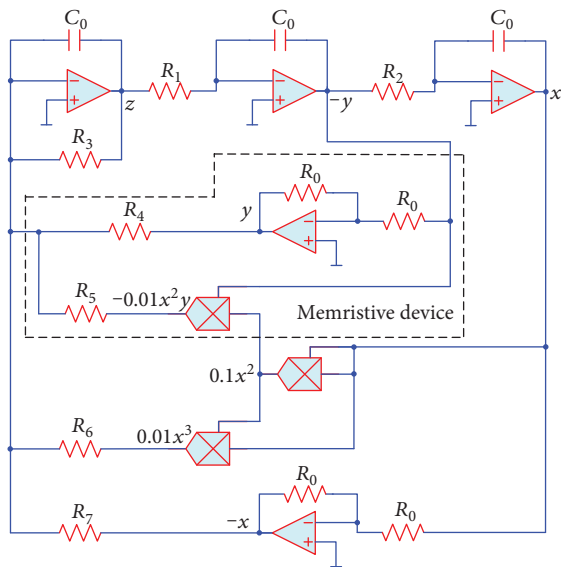


FIGURE 12: Electronic circuit realization of the emulating system (4).

[31–34]. The electronic circuit is designed as the jerk form by using the dimensionless state equations, as depicted in Figure 12, which is simple with less circuit elements. In this design, the operations of integral, addition, and inverse are realized by the operational amplifier TL082 chip and the multiply operation is realized by the AD633JN chip. Moreover, time-scale transformation is considered in our experiment to guarantee capturing of the wave effectively, which is determined by the time constant R_0C_0 in the integrator. Accordingly, we obtain the circuit state equation from Figure 12, as follows

$$\begin{aligned}
 \frac{dx}{dt} &= \frac{1}{R_2C_0}y, \\
 \frac{dy}{dt} &= \frac{1}{R_1C_0}z, \\
 \frac{dz}{dt} &= -\frac{1}{R_3C_0}z + \frac{1}{R_7C_0}x - \frac{1}{100R_6C_0}x^3 \\
 &\quad + \frac{1}{100R_5C_0}x^2y - \frac{1}{R_4C_0}y.
 \end{aligned} \tag{7}$$

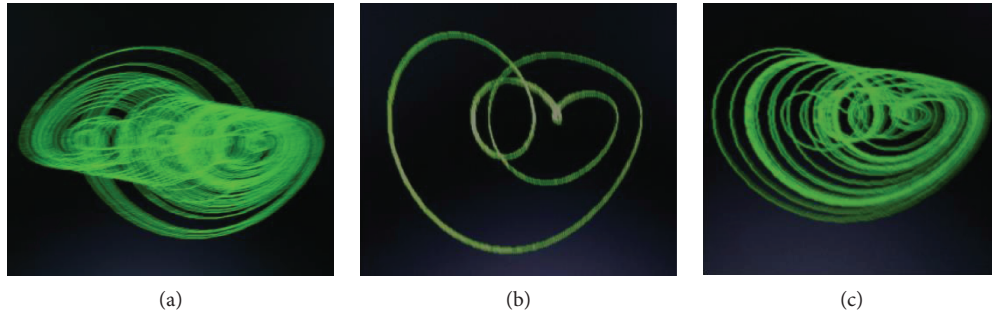


FIGURE 13: Experimental observation of (a) 2-scroll chaotic behavior; coexistence of (b) period-3 behavior and (c) 1-scroll chaotic behavior on the x - y plane.

We first select the system parameter as $a = 0.5$, $b = 0.8$, $c = 0.6$, $d = 3$, $k = 1$. When setting $R_0 = 10\text{ k}\Omega$ and $C_0 = 500\text{ nF}$, the other resistances are derived as $R_1 = 33.3k$, $R_2 = 100k$, $R_3 = 200k$, $R_4 = 50k$, $R_5 = 1k$, $R_6 = 1.667k$, and $R_7 = 125k$. The experimental result of the 2-scroll chaotic attractor on x - y plane captured from the analog oscilloscope is depicted in Figure 13(a), which agrees well with the numerical simulation in Figure 3.

To experimentally confirm the coexisting attractors, we consider the system parameters as $a = 0.5$, $b = 0.8$, $c = 0.6$, $d = 3$, and $k = 0.95$. In this case, the parameter values of circuit element in Figure 12 are invariable except for $R_4 = 52.63k$ and $R_5 = 1.053k$. We switch on and off the power supply for randomly selecting the initial states, the experimental results in Figures 13(b) and 13(c) show the period-3 mode and 1-scroll chaotic attractor, which, respectively, agrees well with the numerical simulations in Figure 8 of initial conditions (0.01, 0.23, 0.09) and (0.01, 0.4, 0).

6. Conclusions

As the fourth basic circuit element, the memristor builds the missing bridges between flux and charge. The memory characteristic of memristor will lead to complicated dynamical behaviors of oscillating systems. The jerk system is of interest within the field of nonlinear dynamics for the simple mathematical form. Therefore, it is worth to study the dynamics of the memristor-based jerk system. In this paper, we propose a 3D jerk system by introducing a generalized memristive device. The dynamical behavior of the system is sensitive to the initial conditions, which results in the coexistence of multiple attractors. And there exist different transition behaviors depending on the selection of the parameters and initial values. Thereby, it is difficult for the third party to reconstruct the accurate state space of the reported system since the dynamics extremely rely on the system parameters, initial values, and time evolution, which are significant for secure communication.

Data Availability

The figure data and table data used to support the findings of this study are included within the article.

Conflicts of Interest

The authors declare that there is no conflict of interest regarding the publication of this paper.

Acknowledgments

This work was supported by the National Natural Science Foundation of China (no. 51577046), the State Key Program of National Natural Science Foundation of China (no. 51637004), the National Key Research and Development Plan “important scientific instruments and equipment development” (no. 2016YFF0102200), Science and Technology Program of Hunan Province (no. 2016TP1021), the Research Foundation of Education Bureau of Hunan Province of China (no. 16B113), and Natural Science Foundation of Hunan Province (No. 2016JJ4036).

References

- [1] L. Chua, “Memristor-the missing circuit element,” *IEEE Transactions on Circuit Theory*, vol. 18, no. 5, pp. 507–519, 1971.
- [2] L. O. Chua and S. M. Kang, “Memristive devices and systems,” *Proceedings of the IEEE*, vol. 64, no. 2, pp. 209–223, 1976.
- [3] D. B. Strukov, G. S. Snider, D. R. Stewart, and R. S. Williams, “The missing memristor found,” *Nature*, vol. 453, no. 7191, pp. 80–83, 2008.
- [4] Y. Zhao, Y. Jiang, J. Feng, and L. Wu, “Modeling of memristor-based chaotic systems using nonlinear Wiener adaptive filters based on backslash operator,” *Chaos, Solitons & Fractals*, vol. 87, pp. 12–16, 2016.
- [5] Y. Zhao, X. Zhang, J. Xu, and Y. Guo, “Identification of chaotic memristor systems based on piecewise adaptive Legendre filters,” *Chaos, Solitons & Fractals*, vol. 81, pp. 315–319, 2015.
- [6] M. Di Ventra, Y. V. Pershin, and L. O. Chua, “Circuit elements with memory: memristors, memcapacitors, and meminductors,” *Proceedings of the IEEE*, vol. 97, no. 10, pp. 1717–1724, 2009.
- [7] K. Rajagopal, A. Akgul, S. Jafari, and B. Aricioglu, “A chaotic memcapacitor oscillator with two unstable equilibria and its fractional form with engineering applications,” *Nonlinear Dynamics*, vol. 91, no. 2, pp. 957–974, 2018.
- [8] V. T. Pham, S. Jafari, S. Vaidyanathan, C. Volos, and X. Wang, “A novel memristive neural network with hidden attractors

- and its circuitry implementation," *Science China Technological Sciences*, vol. 59, no. 3, pp. 358–363, 2016.
- [9] Y. B. Zhao, C. K. Tse, J. C. Feng, and Y. C. Guo, "Application of memristor-based controller for loop filter design in charge-pump phase-locked loops," *Circuits, Systems, and Signal Processing*, vol. 32, no. 3, pp. 1013–1023, 2013.
 - [10] C. Yakopcic, T. M. Taha, G. Subramanyam, R. E. Pino, and S. Rogers, "A memristor device model," *IEEE Electron Device Letters*, vol. 32, no. 10, pp. 1436–1438, 2011.
 - [11] A. Buscarino, L. Fortuna, M. Frasca, L. V. Gambuzza, and G. Sciuto, "Memristive chaotic circuits based on cellular nonlinear networks," *International Journal of Bifurcation and Chaos*, vol. 22, no. 3, article 1250070, 2012.
 - [12] H. Bao, N. Wang, B. Bao, M. Chen, P. Jin, and G. Wang, "Initial condition-dependent dynamics and transient period in memristor-based hypogenetic jerk system with four line equilibria," *Communications in Nonlinear Science and Numerical Simulation*, vol. 57, pp. 264–275, 2018.
 - [13] B. Bao, T. Jiang, G. Wang, P. Jin, H. Bao, and M. Chen, "Two-memristor-based Chua's hyperchaotic circuit with plane equilibrium and its extreme multistability," *Nonlinear Dynamics*, vol. 89, no. 2, pp. 1157–1171, 2017.
 - [14] D. Kim, M. Jin, and P. H. Chang, "Control and synchronization of the generalized Lorenz system with mismatched uncertainties using backstepping technique and time-delay estimation," *International Journal of Circuit Theory and Applications*, vol. 45, no. 11, pp. 1833–1848, 2017.
 - [15] Z. Wang, W. Sun, Z. Wei, and S. Zhang, "Dynamics and delayed feedback control for a 3D jerk system with hidden attractor," *Nonlinear Dynamics*, vol. 82, no. 1–2, pp. 577–588, 2015.
 - [16] H. Saberi Nik, S. Effati, and J. Saberi-Nadjafi, "New ultimate bound sets and exponential finite-time synchronization for the complex Lorenz system," *Journal of Complexity*, vol. 31, no. 5, pp. 715–730, 2015.
 - [17] S. Jafari, A. Ahmadi, A. J. M. Khalaf, H. R. Abdolmohammadi, V. T. Pham, and F. E. Alsaadi, "A new hidden chaotic attractor with extreme multi-stability," *AEU - International Journal of Electronics and Communications*, vol. 89, pp. 131–135, 2018.
 - [18] Y.-X. Tang, A. Jalil M Khalaf, K. Rajagopal, V.-T. Pham, S. Jafari, and Y. Tian, "A new nonlinear oscillator with infinite number of coexisting hidden and self-excited attractors," *Chinese Physics B*, vol. 27, no. 4, article 040502, 2018.
 - [19] V. T. Pham, S. Vaidyanathan, C. K. Volos, S. Jafari, and X. Wang, "A chaotic hyperjerk system based on memristive device," in *Advances and Applications in Chaotic Systems*, Springer, Cham, 2016.
 - [20] B. Bao, X. Zou, Z. Liu, and F. Hu, "Generalized memory element and chaotic memory system," *International Journal of Bifurcation and Chaos*, vol. 23, no. 8, article 1350135, 2013.
 - [21] Z. Galias, "Automatized search for complex symbolic dynamics with applications in the analysis of a simple memristor circuit," *International Journal of Bifurcation and Chaos*, vol. 24, no. 7, article 1450104, 2014.
 - [22] Y. V. Pershin and M. Di Ventra, "Memory effects in complex materials and nanoscale systems," *Advances in Physics*, vol. 60, no. 2, pp. 145–227, 2011.
 - [23] D. Batas and H. Fiedler, "A memristor SPICE implementation and a new approach for magnetic flux-controlled memristor modeling," *IEEE Transactions on Nanotechnology*, vol. 10, no. 2, pp. 250–255, 2011.
 - [24] V. T. Pham, S. Vaidyanathan, C. K. Volos, S. Jafari, N. V. Kuznetsov, and T. M. Hoang, "A novel memristive time-delay chaotic system without equilibrium points," *The European Physical Journal Special Topics*, vol. 225, no. 1, pp. 127–136, 2016.
 - [25] J. C. Sprott, "Some simple chaotic jerk functions," *American Journal of Physics*, vol. 65, no. 6, pp. 537–543, 1997.
 - [26] J. Kengne, Z. T. Njitacke, and H. B. Fotsin, "Dynamical analysis of a simple autonomous jerk system with multiple attractors," *Nonlinear Dynamics*, vol. 83, no. 1–2, pp. 751–765, 2016.
 - [27] J. Kengne, A. N. Negou, and D. Tchitsop, "Antimonotonicity, chaos and multiple attractors in a novel autonomous memristor-based jerk circuit," *Nonlinear Dynamics*, vol. 88, no. 4, pp. 2589–2608, 2017.
 - [28] V. T. Pham, S. Jafari, X. Wang, and J. Ma, "A chaotic system with different shapes of equilibria," *International Journal of Bifurcation and Chaos*, vol. 26, no. 4, article 1650069, 2016.
 - [29] V. T. Pham, C. Volos, S. Jafari, and T. Kapitaniak, "A novel cubic-equilibrium chaotic system with coexisting hidden attractors: analysis, and circuit implementation," *Journal of Circuits, Systems and Computers*, vol. 27, no. 4, article 1850066, 2018.
 - [30] J. He, S. Yu, and J. Lü, "Constructing higher-dimensional non-degenerate hyperchaotic systems with multiple controllers," *International Journal of Bifurcation and Chaos*, vol. 27, no. 9, article 1750146, 2017.
 - [31] C. L. Li, H. M. Li, W. Li et al., "Dynamics, implementation and stability of a chaotic system with coexistence of hyperbolic and non-hyperbolic equilibria," *AEU - International Journal of Electronics and Communications*, vol. 84, pp. 199–205, 2018.
 - [32] C. H. Wang, H. Xu, and F. Yu, "A novel approach for constructing high-order Chua's circuit with multi-directional multi-scroll chaotic attractors," *International Journal of Bifurcation and Chaos*, vol. 23, no. 2, article 1350022, 2013.
 - [33] Q. Wang, S. Yu, C. Guyeux, J. M. Bahi, and X. Fang, "Theoretical design and circuit implementation of integer domain chaotic systems," *International Journal of Bifurcation and Chaos*, vol. 24, no. 10, article 1450128, 2014.
 - [34] A. T. Azar, C. Volos, N. A. Gerodimos et al., "A novel chaotic system without equilibrium: dynamics, synchronization, and circuit realization," *Complexity*, vol. 2017, Article ID 7871467, 11 pages, 2017.

Research Article

Chaos and Symbol Complexity in a Conformable Fractional-Order Memcapacitor System

Shaobo He,^{1,2} Santo Banerjee^{3,4} , and Bo Yan²

¹*School of Physics and Electronics, Central South University, Changsha 410083, China*

²*School of Computer Science and Technology, Hunan University of Arts and Science, Changde 415000, China*

³*Institute for Mathematical Research, Universiti Putra Malaysia, Serdang, Selangor, Malaysia*

⁴*Malaysia-Italy Centre of Excellence for Mathematical Science, Universiti Putra Malaysia, Serdang, Selangor, Malaysia*

Correspondence should be addressed to Santo Banerjee; santoban@gmail.com

Received 27 April 2018; Accepted 5 July 2018; Published 5 August 2018

Academic Editor: Viet-Thanh Pham

Copyright © 2018 Shaobo He et al. This is an open access article distributed under the Creative Commons Attribution License, which permits unrestricted use, distribution, and reproduction in any medium, provided the original work is properly cited.

Application of conformable fractional calculus in nonlinear dynamics is a new topic, and it has received increasing interests in recent years. In this paper, numerical solution of a conformable fractional nonlinear system is obtained based on the conformable differential transform method. Dynamics of a conformable fractional memcapacitor (CFM) system is analyzed by means of bifurcation diagram and Lyapunov characteristic exponents (LCEs). Rich dynamics is found, and coexisting attractors and transient state are observed. Symbol complexity of the CFM system is estimated by employing the symbolic entropy (SybEn) algorithm, symbolic spectral entropy (SybSEn) algorithm, and symbolic C_0 (Syb C_0) algorithm. It shows that pseudorandom sequences generated by the system have high complexity and pass the rigorous NIST test. Results demonstrate that the conformable memcapacitor nonlinear system can also be a good model for real applications.

1. Introduction

In 1971, Chua postulated the concept of memristor that describes a relationship between flux and charge [1]. In 2008, researchers in Hewlett-Packard announced that a solid-state implementation of memristor has been successfully fabricated [2]. Since then, designing memory circuits has received significant attention of researchers, and many different kinds of memristor-based circuits have been designed [3–5]. In 2009, Ventra et al. [6] reported memcapacitors and meminductors. Compared with memristors, memcapacitors and meminductors have received much less attention. Currently, memcapacitor and meminductor can be designed based on the memristor. For example, Biolek and Biolkova [7] designed a memcapacitor model based on memristor by means of off-the-shelf circuits. As a matter of fact, memory electronic elements are usually designed nonlinearly. Thus, chaos can be easily found in those memory

electronic element-based circuits [8–16]. Bao et al. [8–11] presented many valuable works on chaotic memristor circuits. For instance, their most recent work reported quasiperiodic behavior and chaotic bursting in a third-order autonomous memristive oscillator [11]. Moreover, Mou et al. [12] designed a memory circuit with two memcapacitors that exhibited complex phenomena of state transition and transient chaos accompanied with time evolution and coexisting states. Fractional calculus has been studied for about 300 years, and there are a large number of literatures reporting chaos in the fractional-order nonlinear systems [17–20]. Moreover, fractional-order memory electronic element-based systems increasingly attracted attention of scholars [21, 22]. Since not much research exists about the fractional-order memcapacitor system, a fractional-order system with two memcapacitors is considered in this paper.

All of the abovementioned systems are integer-order systems or fractional-order chaotic systems under Caputo

definition or Riemann-Liouville (R-L) definition [23]. In 2014, Khalil et al. [24] proposed a new fractional derivative, and it is called the conformable fractional (CF) derivative. Since the CF definition is prominently compatible with the integer-order derivative, it has been widely studied in different research fields [25–28]. For example, İskender Eroğlu et al. [26] proposed an optimal boundary temperature control for a time-conformable fractional heat conduction equation. However, to our best knowledge, there are only two literatures reporting numerical analysis of CF chaotic systems. He et al. [29] firstly solved the nonlinear CF equations by the conformable Adomian decomposition method (CADM) and found chaos in the CF simplified Lorenz system. Later, Ruan et al. [30] investigated dynamics of a CF memristor system based on CADM, and rich dynamical behaviors were found. It shows that the CF nonlinear systems also generate chaos, and it is an interesting topic to explore complexity in these systems. Recently, Ünal and Gökdoğan [31] modified the differential transform method (DTM) and applied this method to solve CF nonlinear equations. But it has not been used to solve CF chaotic systems. Thus, in this paper, we will use conformable DTM to solve the CF memcapacitor system and analyze this system numerically.

Meanwhile, measuring complexity is also an important method to analyze dynamics of chaotic systems. It reflects the security of the system to some extent. When a system has higher complexity, it means that the time series generated by the system is more random. Currently, there are several methods to measure complexity of time series, such as the permutation entropy (PE) [32], sample entropy (SampEn) [33], spectral entropy (SE) [34], and C_0 algorithms [35]. It should be noted out that complexity of chaotic systems is mainly estimated based on the original time series, and complexity analysis of nonlinear symbol sequence has aroused interests of researchers [36, 37]. Meanwhile, there are many kinds of pseudorandom sequence generation algorithms. How complexity and dynamics of a chaotic system are determined by the pseudorandom quantization algorithms should be investigated. And whether the CFM system can be actually used in real applications should be verified.

The rest of the article is organized as follows. In Section 2, definitions of conformable fractional derivative and a numerical solution algorithm are proposed. Solution of the CFM system is obtained. In Section 3, dynamics of the CFM system is analyzed by means of Lyapunov characteristic exponents (LCEs), bifurcation diagram, and phase portraits. In Section 4, three different symbol complexity measuring algorithms are designed and the complexity of the CFM system is analyzed. Meanwhile, the NIST test is carried out. Finally, we summarize the results in Section 5.

2. Definitions and Numerical Solution Algorithm

In this section, the system model and definitions about conformable fractional derivative are presented. A numerical solution algorithm for conformable fractional nonlinear systems is designed based on the differential transform method.

TABLE 1: Parameters for the three kinds of chaotic attractors.

Type	(a_1, b_1)	(a_2, b_2)
I	$(-0.17, 10)$	$(0.25, 0.6)$
II	$(0.15, 10)$	$(-0.2, 0.6)$
III	$(-0.17, 10)$	$(-0.2, 0.6)$

2.1. The Conformable Fractional Memcapacitor System. Mou et al. [12] proposed a circuit with memcapacitor, and it is denoted by

$$\begin{aligned}\dot{x} &= cf_1(z), \\ \dot{y} &= (d - e)f_2(y) + ef_1(z), \\ \dot{z} &= e(f_2(y) - f_1(z)) - x,\end{aligned}\tag{1}$$

where c, d , and e are the system parameters, x, y , and z are the state variables, and $f_1(z) = a_1z + b_1z^3$ and $f_2(y) = a_2y + b_2y^3$ represent the two memcapacitors in the circuit in which a_1, b_1, a_2 , and b_2 are the intrinsic parameters of the two memcapacitors. In [12], $c = 8.96$, $d = 4$, and e is the bifurcation parameter. Moreover, there are three different sets of intrinsic parameters for different types of attractors. The three sets of intrinsic parameters are shown in Table 1.

By introducing the conformable fractional derivative to the system, the conformable fractional memcapacitor (CFM) system is defined as

$$\begin{aligned}T_{t_0}^{q_1}x &= cf_1(z), \\ T_{t_0}^{q_2}y &= (d - e)f_2(y) + ef_1(z), \\ T_{t_0}^{q_3}z &= e(f_2(y) - f_1(z)) - x,\end{aligned}\tag{2}$$

where $T_{t_0}^q$ is the conformable fractional derivative and $0 < q_1, q_2, q_3 \leq 1$. Definitions and characteristics of the conformable fractional derivative are given as follows.

Definition 1 [24]. For a given function $f : [0, \infty) \rightarrow \mathbb{R}$, its conformable fractional derivative of order α is defined by

$$T_{t_0}^q f(t) = \lim_{\varepsilon \rightarrow 0} \frac{f(t + \varepsilon t^{1-q}) - f(t)}{\varepsilon},\tag{3}$$

where $t > t_0 \geq 0$ and $q \in (0, 1]$.

Let $q \in (0, 1]$ and f, g be q -differentiable at a point $t > t_0 \geq 0$. Then,

- (1) $T_{t_0}^q(af + bg) = a(T_{t_0}^q f) + b(T_{t_0}^q g)$, for all $a, b \in \mathbb{R}$;
- (2) $T_{t_0}^q(t^p) = pt^{p-q}$, for all $p \in \mathbb{R}$;
- (3) $T_{t_0}^q(\lambda) = 0$, for all constant functions $f(t) = \lambda$;
- (4) $T_{t_0}^q(fg) = f(T_{t_0}^q g) + g(T_{t_0}^q f)$;
- (5) $T_{t_0}^q(f/g) = (g(T_{t_0}^q f) - f(T_{t_0}^q g))/g^2$;
- (6) $T_{t_0}^q f(t) = t^{1-q}(df/dt)(t)$.

Definition 2 [24]. The conformable fractional integral of function $f : [q, \infty) \rightarrow \mathbb{R}$ is defined by

$$(I_{t_0}^q f)(t) = \int_{t_0}^t \frac{f(x)}{(x - t_0)^{1-q}} dx, \quad (4)$$

where $t > t_0 \geq 0$, $q \in (0, 1]$, and f is q -differentiable at $[t_0, t]$.

2.2. Conformable Fractional Differential Transform Method. The differential transform method is one of the most effective methods for semianalytic analysis of differential equations. Here, the conformable fractional differential transform method (CFDTM) is introduced to solve the conformable fractional chaotic system.

Assume that f is an infinitely q -differentiable function, for $0 < q \leq 1$ at a neighborhood of a point t_0 . Then, f has the fractional power series expansion [31].

$$f(t) = \sum_{k=0}^{\infty} \frac{(T_{t_0}^q f)(t_0)(t - t_0)^{qk}}{q^k k!}, \quad (5)$$

where $t_0 < t < t_0 + R^{1/q}$, $R > 0$, and $(T_{t_0}^q f)^{(k)}(t_0)$ denotes the conformable fractional derivative for k times. Define the conformable fractional differential transform of $f(t)$ as

$$F_q(k) = \frac{1}{q^k k!} \left[(T_{t_0}^q f)^{(k)}(t) \right]_{t=t_0}, \quad (6)$$

where $(T_{t_0}^q f)^{(k)}(t)$ denotes the application of the fractional derivative for k times. Thus, the inverse conformable fractional differential transform of $F(k)$ is defined as

$$f(t) = \sum_{k=0}^{\infty} F_q(k)(t - t_0)^{qk}. \quad (7)$$

Lemma 1 [31]. If $f(t) = u(t) \pm v(t)$, then $F_q(k) = U_q(k) \pm V_q(k)$.

Lemma 2 [31]. If $f(t) = \alpha u(t)$, then $F_q(k) = \alpha U_q(k)$.

Lemma 3 [31]. If $f(t) = u(t)^3 = u(t)u(t)u(t)$, then $F_q(k) = \sum_{i=0}^k \sum_{j=0}^i \sum_{l=0}^j U_q(l)U_q(j-l)U_q(k-j)$.

The multistep CFDTM method is proposed to solve the CFM system. Divide the time interval $[0, T]$ into small subintervals $[t_n, t_{n+1}]$, where $n = 0, 1, 2, \dots, N$, $t_N = T$, and $t_{n+1} - t_n = h$. According to (7), the solution of the system over interval $[t_n, t_{n+1}]$ is given by

$$\begin{aligned} x(t_{n+1}) &\approx \sum_{k=0}^D X(k)h^{kq_1}, \\ y(t_{n+1}) &\approx \sum_{k=0}^D Y(k)h^{kq_2}, \\ z(t_{n+1}) &\approx \sum_{k=0}^D Z(k)h^{kq_3}, \end{aligned} \quad (8)$$

where

$$\begin{aligned} X(k+1) &= \frac{1}{q_1(k+1)} cF_1^k, \\ Y(k+1) &= \frac{1}{q_2(k+1)} \left[(d-e)F_2^k + eF_1^k \right], \\ Z(k+1) &= \frac{1}{q_3(k+1)} \left[e(F_2^k - F_1^k) - X(k) \right], \end{aligned} \quad (9)$$

and

$$\begin{aligned} F_1^k &= a_1 Z(k) + b_1 \sum_{i=0}^k \sum_{j=0}^i \sum_{l=0}^j Z(l)Z(j-l)Z(k-j), \\ F_2^k &= a_2 Y(k) + b_2 \sum_{i=0}^k \sum_{j=0}^i \sum_{l=0}^j Y(l)Y(j-l)Y(k-j). \end{aligned} \quad (10)$$

It should be pointed out that

$$\begin{aligned} X(0) &= x(t_n), \\ Y(0) &= y(t_n), \\ Z(0) &= z(t_n). \end{aligned} \quad (11)$$

It means that $x(t_{n+1})$, $y(t_{n+1})$, and $z(t_{n+1})$ can be obtained based on $x(t_n)$, $y(t_n)$, and $z(t_n)$, and the solution can be given as $\mathbf{x}(t_{n+1}) = F(\mathbf{x}(t_n))$. As for the contribution of this section, there are two aspects that could be specified. Firstly, it is the first time that the solution of the conformable fractional-order chaotic (memcapacitor) system is obtained by employing DTM. Secondly, we modified the method as the multistep CFDTM method by dividing the solution into subintervals $[t_n, t_{n+1}]$, and the obtained solution can be represented as $\mathbf{x}(t_{n+1}) = F(\mathbf{x}(t_n))$. Thus, the numerical solution of the conformable fractional-order chaotic system can be obtained in MATLAB.

In addition, we choose $D = 3$ for the approximation of the system. Let $e = 6.9$; phase diagrams with different derivative orders are shown in Figure 1. As shown in Figure 1, type I and type III attractors do not change much with the decrease of derivative orders while type II attractor is changed from chaos to periodical circle. Obviously, these three types of attractors are different. According to [12], there is no steady state in the type I system and type III system, but the type II system is steady when $0 < e < 4$.

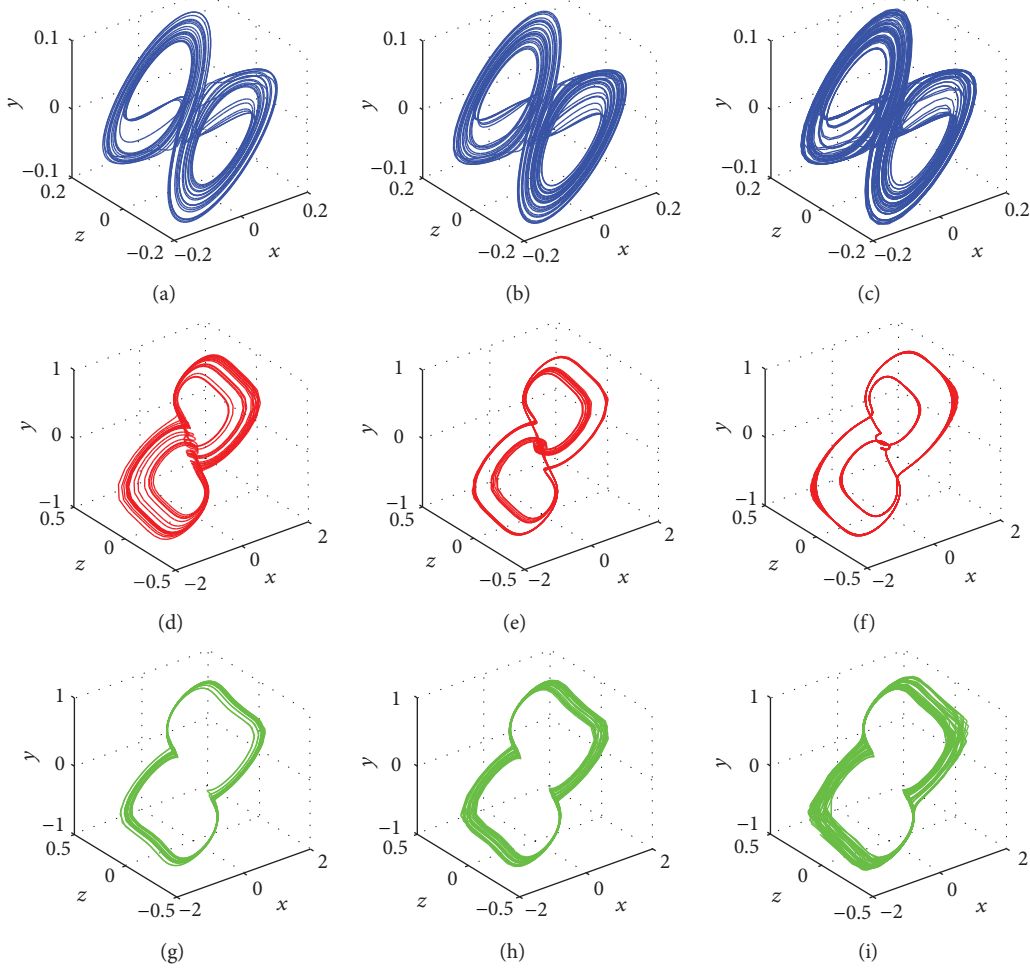


FIGURE 1: Different types of chaotic attractors in the CFM system with different fractional derivative orders: (a) type I attractor with $q_1 = q_2 = q_3 = 0.95$; (b) type I attractor with $q_1 = q_2 = q_3 = 0.9$; (c) type I attractor with $q_1 = q_2 = q_3 = 0.8$; (d) type II attractor with $q_1 = q_2 = q_3 = 0.95$; (e) type II attractor with $q_1 = q_2 = q_3 = 0.9$; (f) type II attractor with $q_1 = q_2 = q_3 = 0.8$; (g) type III attractor with $q_1 = q_2 = q_3 = 0.95$; (h) type III attractor with $q_1 = q_2 = q_3 = 0.9$; (i) type III attractor with $q_1 = q_2 = q_3 = 0.8$.

3. Dynamical Analysis of the CFM System

3.1. LCE Calculation Algorithm. As mentioned above, the solution of the CFM system can be written as $\mathbf{x}(t_{n+1}) = F(\mathbf{x}(t_n))$; thus, it is actually shown as a given map $\mathbf{x}(n+1) = F(\mathbf{x}(n))$. Here, the QR decomposition method is employed to calculate the LCEs of the system. The computational process is denoted as

$$qr[\mathbf{J}_n \mathbf{J}_{n-1} \cdots \mathbf{J}_1] = qr[\mathbf{J}_n \mathbf{J}_{n-1} \cdots \mathbf{J}_2 (\mathbf{J}_1 \mathbf{Q}_0)] = \mathbf{Q}_n \mathbf{R}_n \cdots \mathbf{R}_2 \mathbf{R}_1, \quad (12)$$

where $qr[\cdot]$ represents the QR decomposition function, \mathbf{J} is the Jacobian matrix of the given map, \mathbf{Q} is an orthogonal matrix, and \mathbf{R} is an upper triangular matrix. All LCEs are calculated according to the upper triangular matrix, and they are given by [38]

$$\lambda_\eta = \frac{1}{Mh} \sum_{i=1}^M \ln |R_i(\eta, \eta)|, \quad (13)$$

TABLE 2: LCEs of the CFM system with different derivative orders.

Type	$q_1 = q_2 = q_3 = 0.95$	$q_1 = q_2 = q_3 = 0.90$	$q_1 = q_2 = q_3 = 0.80$
I	0.0987, 0, -3.4849	0.1290, 0, -4.7279	0.2287, 0, -8.4289
II	0.1099, 0, -6.422	0.0855, 0, -7.1556	0, 0, -16.1767
III	0.0531, 0, -9.0147	0.0789, 0, -12.4373	0.2831, 0, -28.5537

where $\eta = 1, 2, 3$ (dimension of the system) and M is the maximum iteration number. Here, the Jacobian matrix is obtained by the MATLAB symbolic operation function $J = \text{Jacobian}(\cdot)$. LCEs of attractors in Figure 1 are calculated, and the results are shown in Table 2.

3.2. Bifurcation and Chaos. As with [12], we also treat parameter e as a bifurcation parameter. Meanwhile, dynamics with the variation of fractional derivative orders q_1 , q_2 , and q_3 is also analyzed. Since type II attractor changes more with the decrease of derivative orders, it is chosen as the representation of the three kinds of chaotic attractors for further

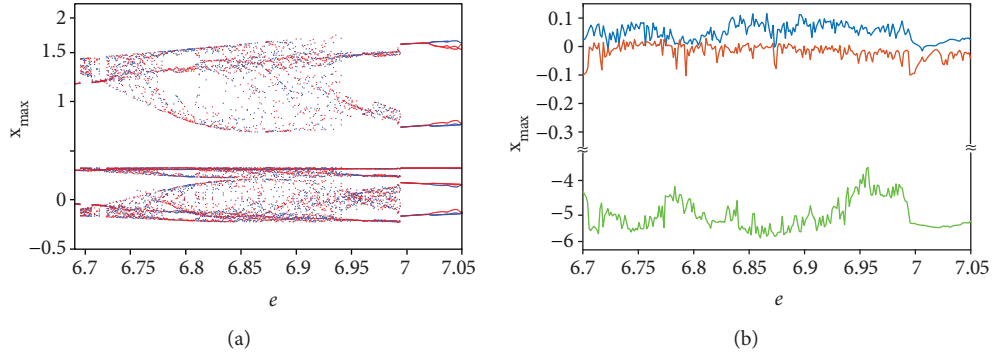


FIGURE 2: Dynamics of the CFM system with parameter e varying: (a) bifurcation diagram; (b) LCEs.

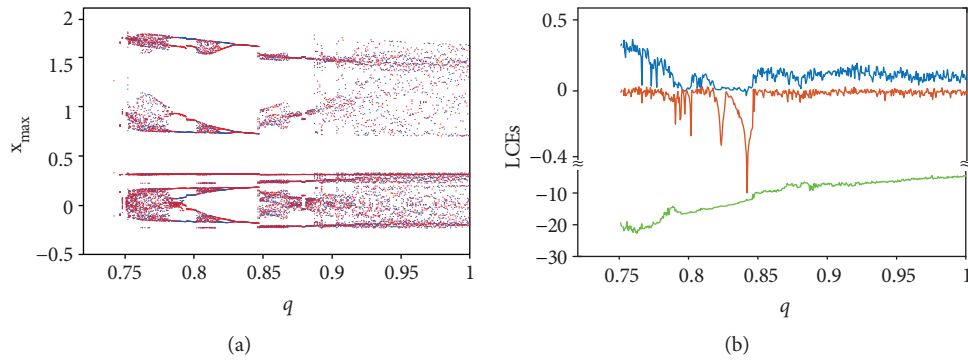


FIGURE 3: Dynamics of the CFM system with derivative order $q_1 = q_2 = q_3 = q$ varying: (a) bifurcation diagram; (b) LCEs.

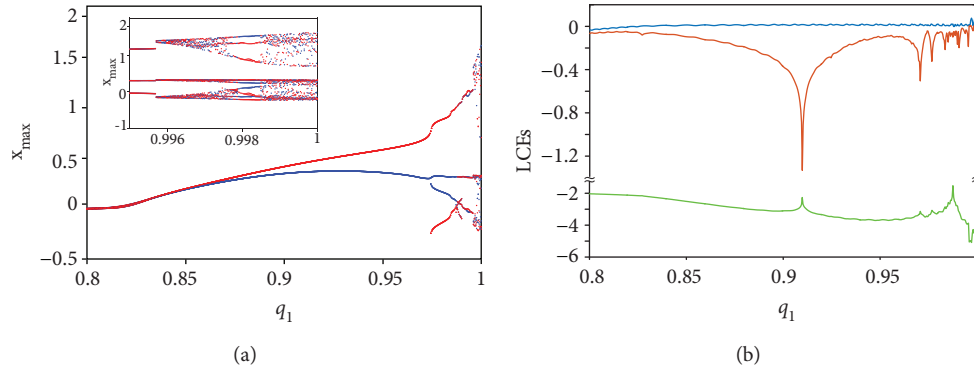


FIGURE 4: Dynamics of the CFM system with derivative order $q_2 = q_3 = 1$ and q_1 varying: (a) bifurcation diagram; (b) LCEs.

analysis. When plotting bifurcation diagrams, the initial condition for the blue dots is $[x(t_0), y(t_0), z(t_0)] = [0.1, 0, 0]$, while the initial condition for the red dots is $[x(t_0), y(t_0), z(t_0)] = [-0.1, 0, 0]$.

Case 1. Fix $q_1 = q_2 = q_3 = 0.95$ and vary parameter e from 6.7 to 7.05 with a step size of 0.0007. The bifurcation diagram and LCEs with parameter e varying are shown in Figure 2. It shows that dynamical behaviors of the CFM system change with the variation of parameter e . The system is chaotic when $q \in [6.7, 0.7561] \cup [0.7617, 6.9974]$, while the system is periodical when $q \in (0.7561, 0.7617) \cup (6.9974, 7.05)$.

Case 2. Let $e = 6.9$ and $q_1 = q_2 = q_3 = q$. Vary q from 0.72 to 1 where the variation step size is 0.002. As shown in Figure 3(a), the system is divergent when $q < 0.75$. When $q \in [0.7568, 0.802] \cup (0.817, 0.8496)$, the system is periodical while the chaotic interval is $q \in [0.75, 0.7568] \cup (0.802, 0.817) \cup [0.8496, 1]$. LCE curves agree well with the analysis results. It shows that rich dynamics is found with the decrease of q .

Case 3. Let $e = 6.9$ and $q_2 = q_3 = 1$, and vary q_1 from 0.995 to 1 with a step size of 0.00056. The bifurcation diagram and its corresponding LCEs are shown in Figure 4. The system is

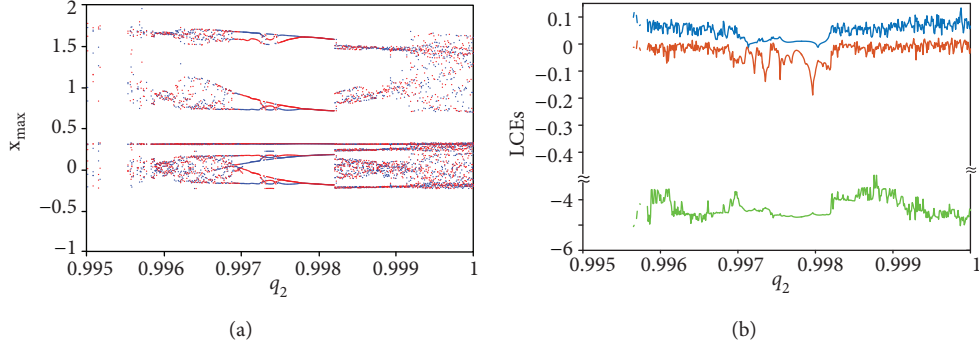


FIGURE 5: Dynamics of the CFM system with derivative order $q_1 = q_3 = 1$ and q_2 varying: (a) bifurcation diagram; (b) LCEs.

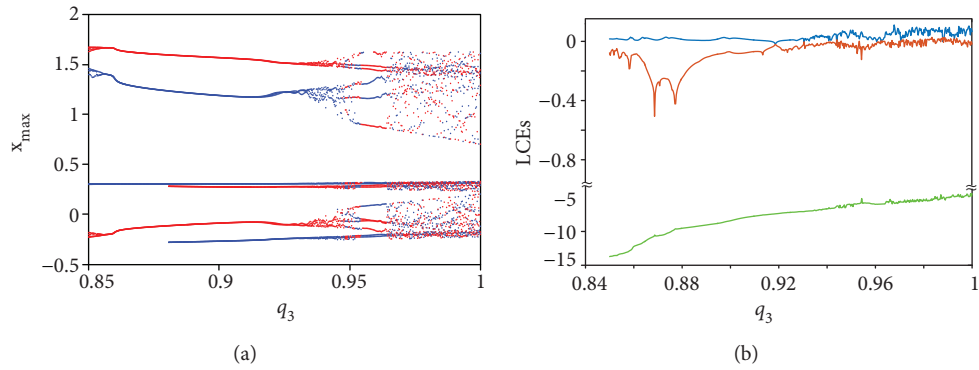


FIGURE 6: Dynamics of the CFM system with derivative order $q_2 = q_3 = 1$ and q_1 varying: (a) bifurcation diagram; (b) LCEs.

chaotic when $q \in [0.9958, 0.9975] \cup [0.9984, 1]$, while the system is nonchaotic for the rest values of q_1 .

Case 4. Let $e = 6.9$ and $q_1 = q_3 = 1$, and vary q_2 from 0.995 to 1 with a step size of 0.00001. The bifurcation diagram and its corresponding LCEs are shown in Figure 5. When $q_2 < 0.9959$, the transient state is found. The system is chaotic at the beginning and then becomes divergent finally. The system is periodical when $q \in [0.9967, 0.9982]$, while for the rest range, the system is chaotic.

Case 5. Let $e = 6.9$ and $q_1 = q_2 = 1$, and vary q_3 from 0.995 to 1 with a step size of 0.00001. The bifurcation diagram and its corresponding LCEs with derivative order q_3 are shown in Figure 6. The system is chaotic when $q \in [0.942, 0.95] \cup [0.961, 1]$, and the system is periodical when $q \in [0.85, 0.942] \cup [0.95, 0.961]$.

As shown above, after introducing the conformable fractional derivative, the system still has rich dynamical behaviors like parameter e and derivative orders q_1 , q_2 , and q_3 . Moreover, when varying one derivative order and the other two to be equal to 1, the chaotic region shrinks much, compared with that when all derivative orders are varied simultaneously. The minimum order for chaos in the CFM system is 2.25, when the system is solved by CFDTM. Meanwhile, according to Figures 3–6, the system is chaotic when $q_1 =$

$q_2 = q_3 = 1$. However, when the derivative orders become smaller, the periodical state can be observed. It means that derivative orders can change the dynamics of the system distinctly. Thus, the conformable derivative orders q_1 , q_2 , and q_3 are also the bifurcation parameters. Chaotic pseudorandom sequence (CPRS) has been widely used in real applications. In the next section, complexity of the CPRS generated by the CFM system is measured and the potential application values of the system are discussed.

3.3. Coexisting Attractors and Transient State. As shown in the above bifurcation diagrams, when the initial conditions are different, the red and blue dots show two different routes to chaos. Moreover, the coexistence of multiple attractors is produced mainly due to the reason that symmetry and invariance exist in the system. For the CFM system, it is symmetric and invariant under the transformation $(x, y, z) \rightarrow (-x, -y, -z)$ for all values of parameter e . Thus, the coexistence of multiple attractors should be observed. As mentioned above, two different sets of initial conditions are chosen which are $[x(t_0), y(t_0), z(t_0)] = [0.1, 0, 0]$ and $[x(t_0), y(t_0), z(t_0)] = [-0.1, 0, 0]$. Coexisting attractors under different orders are shown in Figure 7. Obviously, the phase portraits of the CFM system with two symmetric initial values are symmetric, and the system can generate coexisting periodical cycles, chaotic attractors.

In some cases, there is no steady state in the system, and dynamical behaviors of the system are different under certain

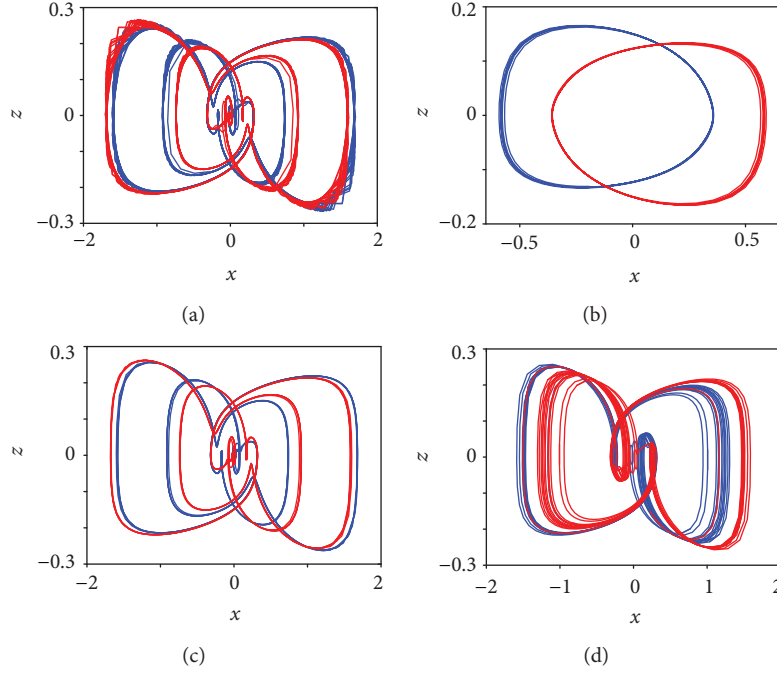


FIGURE 7: Coexisting attractors of the CFM system where $e = 6.9$. The blue line is obtained with the initial condition $[x(t_0), y(t_0), z(t_0)] = [0.1, 0, 0]$, and the red line is obtained with the initial condition $[x(t_0), y(t_0), z(t_0)] = [-0.1, 0, 0]$: (a) $q_1 = q_2 = q_3 = 0.79$; (b) $q_2 = q_3 = 1$, $q_1 = 0.95$; (c) $q_1 = q_3 = 1$, $q_2 = 0.997$; (d) $q_1 = q_2 = 1$, $q_3 = 0.948$.

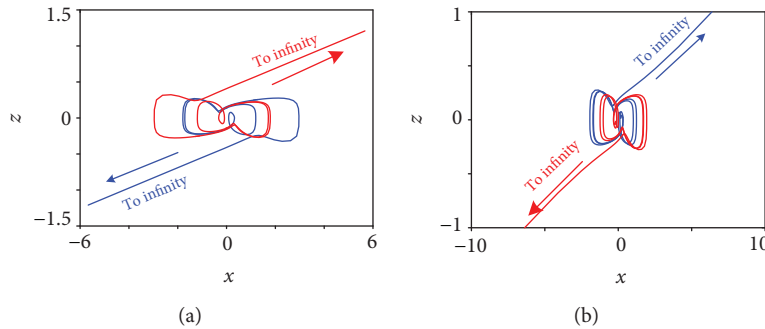


FIGURE 8: Transient state in the CFM system where the blue line is obtained with the initial condition $[x(t_0), y(t_0), z(t_0)] = [0.1, 0, 0]$ and the red line is obtained with the initial condition $[x(t_0), y(t_0), z(t_0)] = [-0.1, 0, 0]$: (a) $q_2 = 0.9955$; (b) $q_2 = 0.9958$.

parameters when starting from a different initial state. As mentioned above, when $e = 6.9$, $q_1 = q_3 = 1$, and $q_2 < 0.9959$, the system has a transient state. Here, phase diagrams with $q_2 = 0.9955$ and 0.9958 are shown in Figure 8, where initial conditions are the same as those mentioned above. The coexisting state and transient state are observed as shown in Figure 8. The system becomes divergent through different directions with different initial conditions, and it is chaotic at the beginning and becomes divergent finally.

4. Complexity Analysis of the CFM System

In this section, complexity of the CFM system is analyzed by means of symbolic complexity measures. Generally, if the system has higher complexity, it means that the system is securer in practical applications. Besides, it is more

convenient to calculate complexity since it just needs a segment of time series. Thus, complexity analysis result provides a basis for parameter choice of chaotic systems.

4.1. Symbolic Complexity Measures. In real application, a chaotic time series should be discretized as a pseudorandom sequence or symbolic sequence, which usually varies between 0 and 1 (0-1 time series) or varies from 0 to 255 (8-bit numbers). Here, complexity of chaotic symbolic time series is analyzed using different algorithms including the symbolic entropy (SybEn) algorithm, symbolic spectral entropy (SybSEn) algorithm, and symbolic C_0 (Syb C_0) algorithm. These three complexity algorithms are defined as follows.

Step 1 (pseudorandom process). Here, suppose that there is a chaotic series defined as $\{x(n), n = 0, 1, 2, \dots, N-1\}$; it is

discretized as $\{s(n), n = 0, 1, 2, \dots, N-1\}$ by employing the following method:

$$s(n) = \begin{cases} 0, & \text{if } \min(x) \leq x(n) < \Delta x, \\ 1, & \text{if } \Delta x \leq x(n) < 2\Delta x, \\ \vdots & \\ 255, & \text{if } 255\Delta x \leq x(n) \leq \max(x), \end{cases} \quad (14)$$

where $\Delta x = (\max(x) - \min(x))/256$. Thus, $\{s(n), n = 0, 1, 2, \dots, N-1\}$ is an 8-bit number time series.

Step 2 (calculating SybEn). Count the number of each symbol (from 0 to 255), and obtain the probability of each symbol as

$$P_i = \frac{\#\{i : s(n) = i, \quad n = 0, 1, \dots, N-1\}}{N}, \quad (15)$$

where $\#$ stands for number and $i = 0, 1, \dots, 255$. Thus, SybEn is defined by

$$\text{SybEn} = - \sum_{i=0}^{255} P_i \log(P_i). \quad (16)$$

Step 3 (discrete Fourier transformation (DFT)). Before the DFT, the following normalization is employed to the symbol time series, and it is denoted as

$$S(n) = \frac{s(n) - \text{mean}(s)}{\text{std}(s)}, \quad (17)$$

where $\text{mean}(s)$ and $\text{std}(s)$ are the mean value and the standard deviation of the time series s , respectively, and $n = 0, 1, \dots, N-1$. Thus, the mean value of the new time is zero and there is no direct current signal. DFT is carried out on time series S , and it is given by

$$X(k) = \sum_{n=0}^{N-1} S(n) e^{-j2\pi nk/N}, \quad (18)$$

where $k = 0, 1, \dots, N-1$ and j is the imaginary unit.

Step 4 (calculating SybSEn). If the power of a discrete power spectrum with the k th frequency is $|X(k)|^2$, then the “probability” of this frequency is defined as

$$\rho_k = \frac{|X(k)|^2}{\sum_{k=0}^{N/2-1} |X(k)|^2}. \quad (19)$$

When the DFT is employed, the summation runs from $k = 0$ to $k = N/2 - 1$. The normalization of SybSEn is denoted by [34]

$$\text{SybSEn} = - \frac{1}{\ln(N/2)} \sum_{k=0}^{N/(2-1)} \rho_k \ln \rho_k. \quad (20)$$

$\ln(N/2)$ is the entropy of the completely random signal.

Step 5 (inverse DFT). Define the mean square value of $X(k)$ as

$$G_N = \frac{1}{N} \sum_{k=0}^{N-1} |X(k)|^2. \quad (21)$$

Let

$$\tilde{X}(k) = \begin{cases} X(k), & \text{if } |X(k)|^2 > rG_N, \\ 0, & \text{if } |X(k)|^2 \leq rG_N, \end{cases} \quad (22)$$

where $r(r > 0)$ is the control parameter. The inverse DFT of $\tilde{X}(k)$ is

$$\tilde{S}(n) = \frac{1}{N} \sum_{k=0}^{N-1} \tilde{X}(k) e^{j2\pi nk/N}, \quad (23)$$

where $n = 0, 1, \dots, N-1$. $\tilde{S}(n)$ reflects the regular part of the time series with detailed information removed.

Step 6 (calculating SybC₀). SybC₀ complexity is defined as [35]

$$\text{SybC}_0 = \sum_{n=0}^{N-1} \frac{|S(n) - \tilde{S}(n)|^2}{\Omega}. \quad (24)$$

where $\Omega = \sum_{n=0}^{N-1} |S(n)|^2$.

The three complexity measuring algorithms estimate complexity of an 8-bit symbol time series from different aspects. Firstly, SybEn analyzes complexity in the time domain while SybSEn and SybC₀ are defined in the frequency domain. Secondly, SybEn and SybSEn are defined based on the definition of the Shannon entropy while SybC₀ reflects the ratio of an irregular part in the time series. Let $e = 6.9$ and $q_1 = q_2 = q_3 = 0.95$; we obtain a type II chaotic time series x . The time series is shown in Figure 9(a), and the symbol time series is illustrated in Figure 9(b). By employing (15) and (19), plots of the two different “probabilities” are shown in Figures 9(c) and 9(d), respectively. According to (22) and (24), we illustrate the irregular part of the time series with $r = 10$, where the red line represents $|S(n)|^2$ and the green line represents $|S(n) - \tilde{S}(n)|^2$ which shows the “difference” or “irregular part.”

As shown in Figure 9, the principles of different algorithms are different. For SybEn and SybSEn, if the probability density is more uniform, values of entropy are larger, while if the proportion of the green part is larger, values of SybC₀ are larger. As a result, larger values of SybEn, SybSEn, and SybC₀ mean that the system has higher complexity. In this paper, to analyze the complexity of the CMF system, the time series x with a length of 55000 is sampled with $\tau = 10$; thus, $x = x(1 : 10 : 55000)$. Finally, the sampled time series is changed into a symbol time series. For SybC₀ complexity, we choose $r = 10$.

4.2. Complexity Analysis. Complexity of the CFM system is analyzed by means of SybEn, SybSEn, and SybC₀. Firstly,

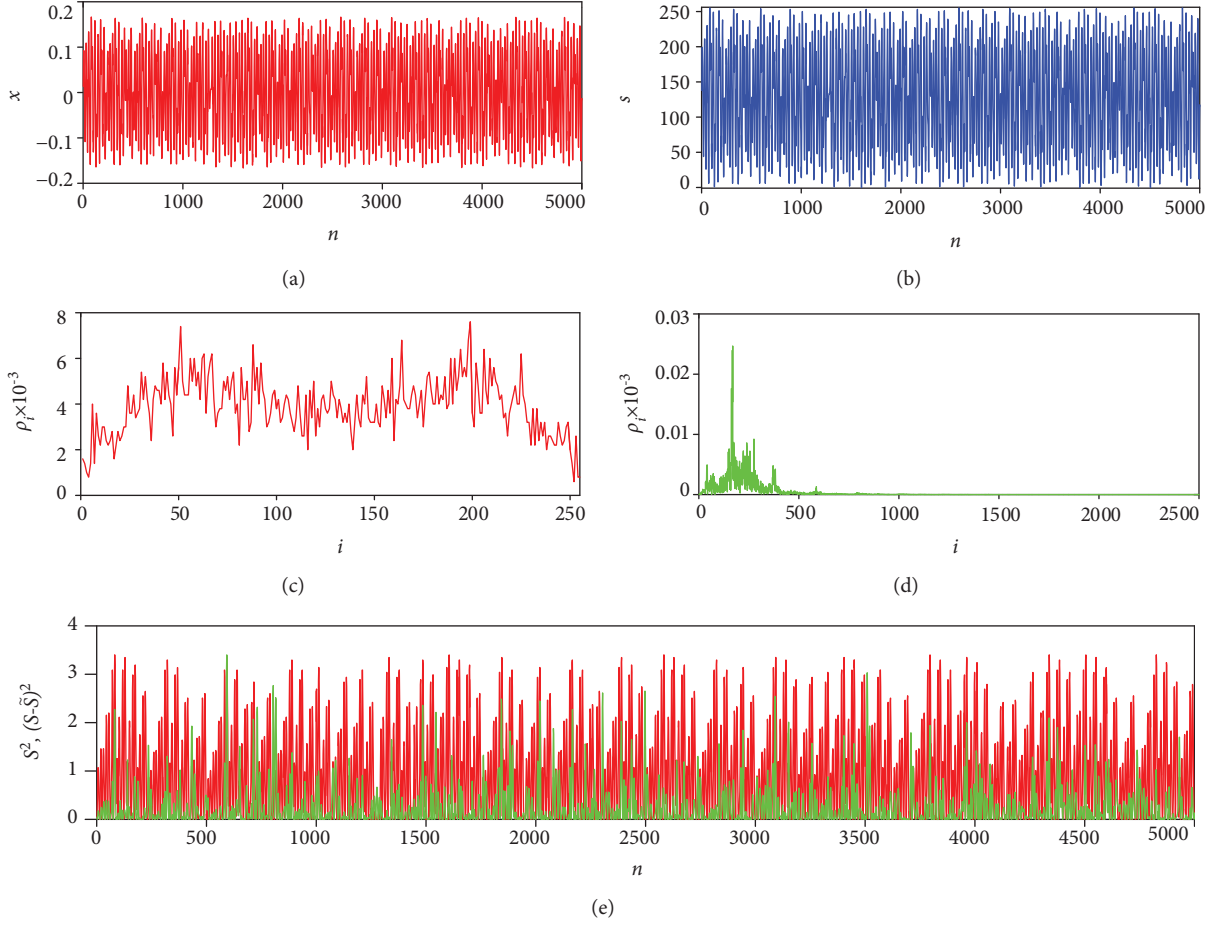


FIGURE 9: Analysis of complexity algorithms: (a) original time series x ; (b) pseudorandom sequence s ; (c) probability of each symbol P_i ; (d) probability of the frequency ρ_i ; (e) irregular part in the SybC₀ algorithm.

TABLE 3: SybEn complexity of the CFM system with different derivative orders.

Type	$q_1 = q_2 = q_3 = 0.95$	$q_1 = q_2 = q_3 = 0.90$	$q_1 = q_2 = q_3 = 0.80$
I	5.4834	5.4646	5.4868
II	4.7810	4.7422	4.6255
III	4.8680	4.8711	4.9467

TABLE 4: SybSEn complexity of the CFM system with different derivative orders.

Type	$q_1 = q_2 = q_3 = 0.95$	$q_1 = q_2 = q_3 = 0.90$	$q_1 = q_2 = q_3 = 0.80$
I	0.4497	0.5131	0.5589
II	0.5635	0.6135	0.3190
III	0.3580	0.3776	0.5386

SybEn, SybSEn, and SybC₀ of different types of CFM systems with different derivative orders are analyzed, and the results are shown in Tables 3–5, respectively. As with Figure 1 and Table 2, values of derivative orders are set as $q_1 = q_2 = q_3 = 0.95, 0.90$, and 0.80 and $e = 6.9$. It shows that complexity

TABLE 5: SybC₀ complexity of the CFM system with different derivative orders.

Type	$q_1 = q_2 = q_3 = 0.95$	$q_1 = q_2 = q_3 = 0.90$	$q_1 = q_2 = q_3 = 0.80$
I	0.1263	0.1756	0.2885
II	0.1913	0.2424	0.0776
III	0.1795	0.1963	0.3128

analysis results agree well with the LCE analysis results. When the system is chaotic, higher complexity can be found. Moreover, the system has relative higher complexity when the derivative orders are smaller. It should be pointed out that SybEn cannot distinguish the chaotic state and periodical state well similar to SybSEn and SybC₀. Actually, it is also one of the reasons why we furtherly design complexity analysis methods in the frequency domain.

Complexity of the CFM system with parameter e varying is analyzed, and results are shown in Figure 10. Here, $q_1 = q_2 = q_3 = q$ equals to 0.95 , and parameter e varies from 6.7 to 7.05 with a step size of 0.0007 . As shown in Figure 10, SybSEn and SybC₀ agree with the maximum LCEs better than SybEn, and they identify more periodical windows which show relative lower complexity.

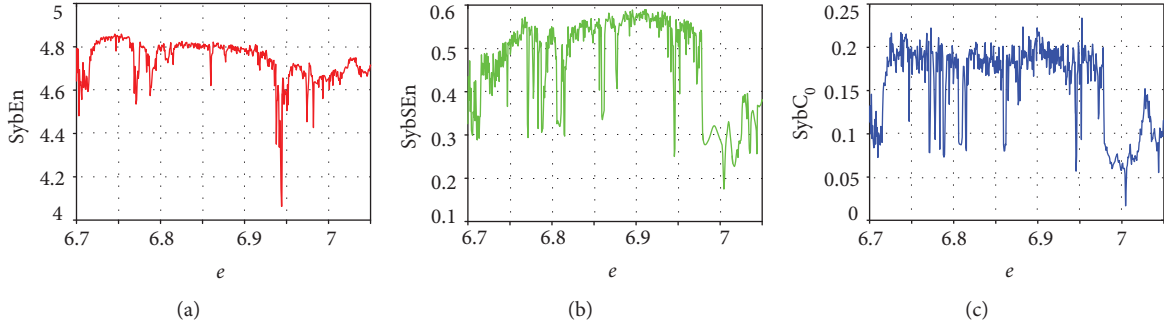


FIGURE 10: Complexity analysis results of the CFM system with parameter e varying: (a) SybEn; (b) SybSEn; (c) SybC₀.

Complexity of the type II CFM system with parameter $e = 6.9$ and derivative orders q_1 , q_2 , and q_3 varying is analyzed, and the analysis results are shown in Figure 11. Let $q_1 = q_2 = q_3 = q$ and let it vary from 0.75 to 1. Complexity analysis results are shown in Figures 11(a)–11(c). As shown in Figures 11(b) and 11(c), complexity of the system increases with the decrease of order q , which means that the system has higher complexity with smaller values of q . Thus, the system has a good application value in the engineering field. Fix $q_2 = q_3 = 1$ and vary q_1 from 0.995 to 1, and the complexity results are shown in Figures 11(d)–11(f). Fix $q_1 = q_2 = 1$ and vary q_3 from 0.996 to 1, and the complexity results are displayed in Figures 11(g)–11(i). Moreover, let $q_1 = q_2 = 1$ and vary q_3 from 0.85 to 1, and the complexity results are illustrated in Figures 11(j)–11(l). As shown in those figures, complexity of the CFM system does not increase with the decrease of derivative order q_1 , q_2 , or q_3 . When $q_1 = q_2 = q_3 = 1$, the integer-order system is chaotic with high complexity, but the low-complexity region can be found when the fractional derivative orders decrease. In real application, one should choose those orders with which the system generates high-complexity time series.

According to Figures 11 and 12, SybEn, SybSEn, and SybC₀ complexity analysis results are consistent with the corresponding maximum LCEs to a certain degree. Overall, SybSEn and SybC₀ analysis results agree better with the corresponding maximum LCE results than with those of SybEn. Compared with calculating LCEs, calculating SybEn, SybSEn, and SybC₀ needs much less time and it is more convenient in real application since results can be obtained with a time series. On the one hand, it shows that the system has a potential application value in practice. On the other hand, it provides a basis for parameter choice of the CFM system in real applications.

SybSEn and SybC₀ complexity in the q - e parameter plane is calculated, and the results are shown in Figure 12. Here, the parameter varies from 6.7 to 7.05 similar to that mentioned above, while derivative order q varies from 6.5 to 1, simultaneously. As shown in Figure 12, the minimum order for chaos is about 0.65 when $e = 6.7$. Meanwhile, it shows that the system has higher complexity.

The pseudorandom time series $s(n)$ by (14) fluctuates with the original system variables. As we all know that a chaotic system is a good source for entropy. There are many different kinds of chaotic systems that can be used

for designing a pseudorandom sequence generator (PRSG), such as the Lorenz system [39], logistic map, sine map, and 2D-SIMM [40]. And these PRSGs are widely used in real application fields such as image encryption [41], speech encryption [42], and chaotic watermark [43]. The quantization algorithms used in this applications are more complex than the method given in (14). One of the most commonly used methods is designed by expressing the original number or its converted number as a 64-bit binary number as $DB_{63} \cdots DB_0$; then, one can obtain a new 8-bit number by choosing $DB_7 \cdots DB_0$. The details of this method are given as follows.

The original number is converted as

$$\varphi(n) = \text{round}(x(n) \times 10^w), \quad (25)$$

where $n = 0, 1, 2, \dots, N-1$ and w is a control number. Here, in this paper, $w = 10$. Thus, $\varphi(n)$ is an integer number and it can be expressed as

$$\varphi(n) = DB_{63}DB_{62} \cdots DB_1DB_0. \quad (26)$$

By choosing the first 8-bit number, a new symbol time series $s(n)$ is given as

$$s(n) = DB_7 \cdots DB_1DB_0. \quad (27)$$

Obviously, $s(n)$ can be expressed as a decimal integer number varying from 0 to 255, as mentioned above. By using this quantization algorithm, complexity of pseudorandom sequences generated by different chaotic systems is calculated and the results are shown in Table 6. The length of each segment symbol time series is 5000, and complexity of such 100 time series is calculated. The results are given as mean \pm std of complexity values in these windows. As shown in Table 6, entropy or complexity of different chaotic pseudorandom sequences is at about the same high level. It shows that as with other different chaotic systems, the CFM system is also a good system for high entropy.

According to Table 6, complexity of the CFM system is high as other systems. Thus, it is necessary to check whether the pseudorandom sequence generated by this system passes the test suite of NIST. The package used for the NIST test is sts-2.1.2 which can be downloaded from the website. Two indicators, which are p values and the proportion of passing sequences, are used to show whether the sequence passes the test or not. The minimum value for p value is 0.0001. It

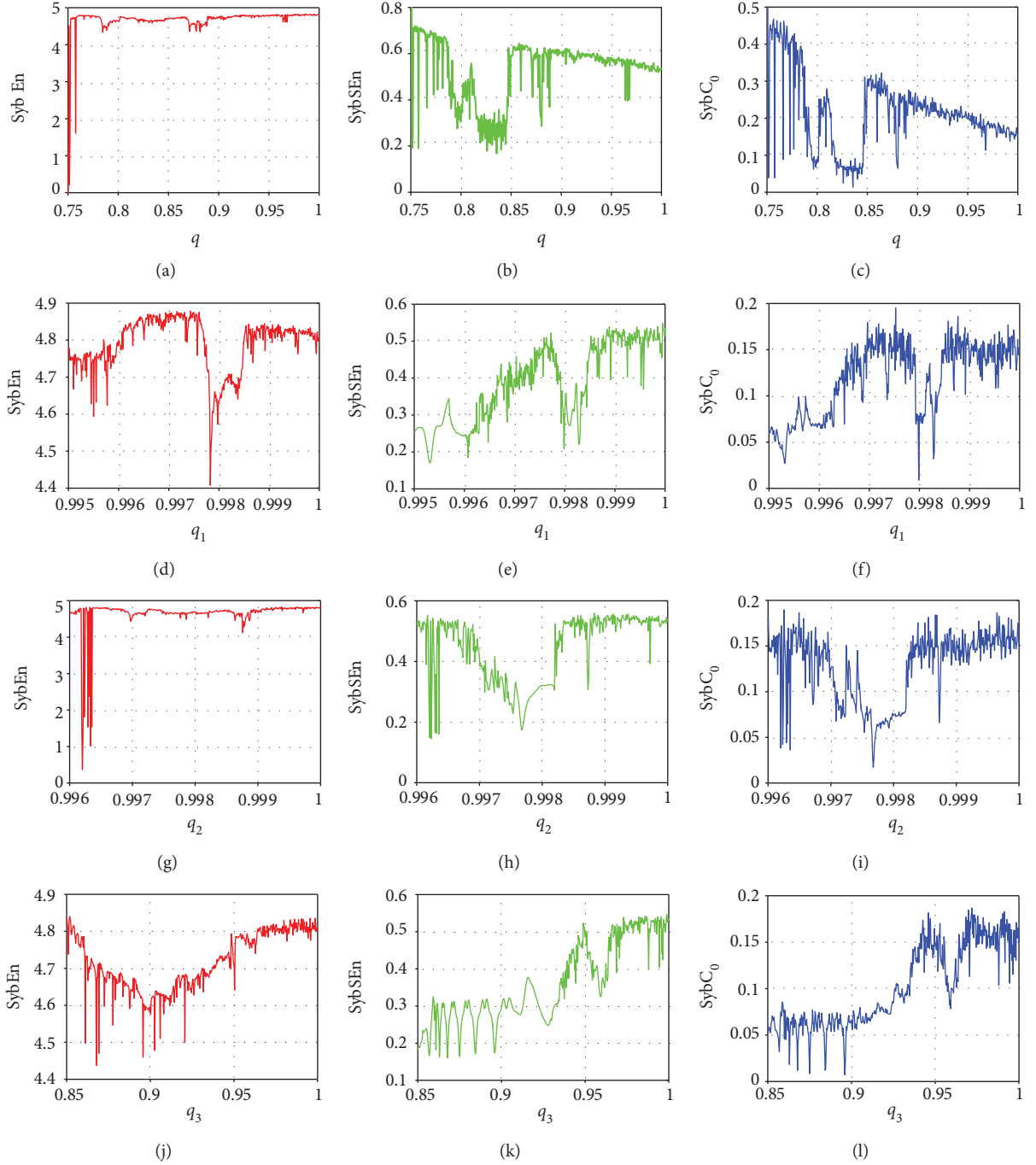


FIGURE 11: Complexity analysis results of the CFM system with derivative orders varying: (a) SybEn with $q_1 = q_2 = q_3 = q$ varying; (b) SybSEn with $q_1 = q_2 = q_3 = q$ varying; (c) SybC₀ with $q_1 = q_2 = q_3 = q$ varying; (d) SybEn with $q_2 = q_3 = 1$ and q_1 varying; (e) SybSEn with $q_2 = q_3 = 1$ and q_1 varying; (f) SybC₀ with $q_2 = q_3 = 1$ and q_1 varying; (g) SybEn with $q_1 = q_3 = 1$ and q_2 varying; (h) SybSEn with $q_1 = q_3 = 1$ and q_2 varying; (i) SybC₀ with $q_1 = q_3 = 1$ and q_2 varying; (j) SybEn with $q_1 = q_2 = 1$ and q_3 varying; (k) SybSEn with $q_1 = q_2 = 1$ and q_3 varying; (l) SybC₀ with $q_1 = q_2 = 1$ and q_3 varying.

means that when the p value is larger than 0.0001 and the confidence interval satisfies

$$\left[(1 - \eta) - 3\sqrt{\frac{(1 - \eta)\eta}{M}}, (1 - \eta) + 3\sqrt{\frac{(1 - \eta)\eta}{M}} \right], \quad (28)$$

where M is the sample size and η is the given significance level, then the pseudorandom bit generator passes the test successfully. In our test, the length of the pseudorandom sequence is 10^6 , and $\eta = 0.01$ with a confidence interval given by [96.015%, 1]. The test result is illustrated in Table 7. For those items including C. Sums (2 times), N.O. Temp (148

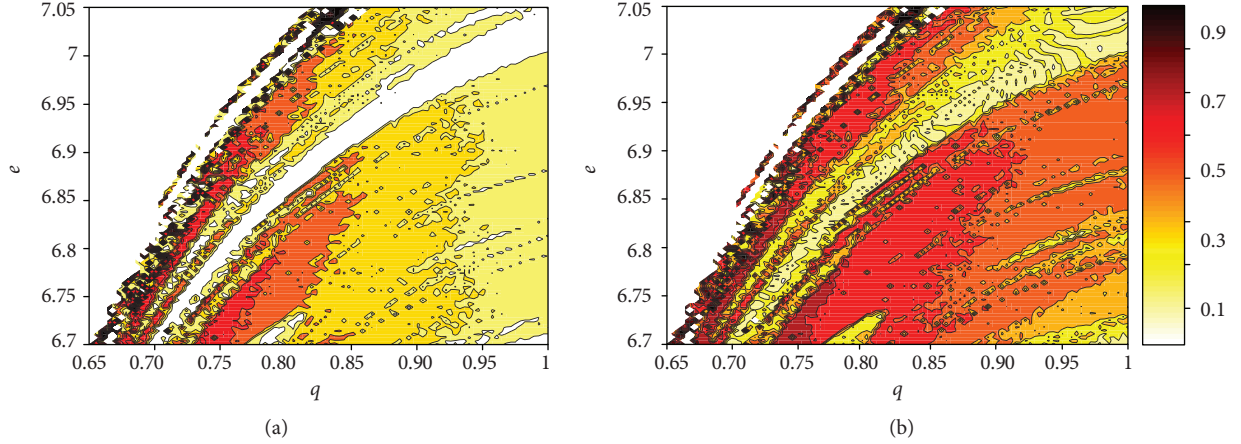
FIGURE 12: Complexity analysis results of the CFM system in the e - q parameter plane: (a) SybSEn; (b) SybC₀.

TABLE 6: Complexity measuring results of different chaotic pseudorandom sequences with the second quantization method.

Systems	Equations	SybEn	SybSEn	SybC ₀
CFM system	$T_{t_0}^{q_1} x = cf_1(z)$			
	$T_{t_0}^{q_2} y = (d - e)f_2(y) + ef_1(z)$			
	$T_{t_0}^{q_3} z = e(f_2(y) - f_1(z)) - x$	5.4825 ± 0.0036	0.9466 ± 0.0014	0.9995 ± 0.0014
Lorenz system	$\dot{x} = 10(y - x)$			
	$\dot{y} = 28x - xz - y$			
	$\dot{z} = (xy - 8z)/3$	5.5206 ± 0.0012	0.9583 ± 0.0003	$0.9995 \pm 4.4 \times 10^{-4}$
Logistic map	$x(n+1) = 4x(n)(1 - x(n))$	5.4962 ± 0.0053	0.9461 ± 0.0012	0.9994 ± 0.0015
Sine map	$x(n+1) = 4 \sin(\pi x(n))$	5.4966 ± 0.0043	0.9459 ± 0.0013	0.9992 ± 0.0019
2D-SIMM	$x(n+1) = 10 \sin(\pi y(n)) \sin(10/x(n))$			
	$y(n+1) = 10 \sin(\pi x(n+1)) \sin(10/y(n))$	5.4966 ± 0.0046	0.9461 ± 0.0014	0.9996 ± 0.0013

times), R. Excur. (8 times), R. Excur. V. (18 times), and Serial (2 times), we only illustrate the lowest values of p value and proportion. It is shown in Table 7 that all p values are larger than 0.0001 and the computed proportion for each test lies inside the confidence interval. Hence, the tested binary sequences generated by the proposed pseudorandom bit generator are random.

In this section, two different pseudorandom quantization algorithms are designed. As shown in Figures 9(a) and 9(b), fluctuation of pseudorandom sequence obtained by the first method given (14) agrees well with the original time series. Thus, it is the reason why complexity analysis results match well with the corresponding maximum LCEs. It provides a good symbol sequence for complexity analysis of chaotic systems when analyzed by complexity measuring methods. However, according to Table 6, pseudorandom sequences generated by different systems by employing the second method have the same level of high complexity. Meanwhile, the pseudorandom sequence passes all the NIST tests. It means that the obtained sequence is random. As with other chaotic systems, the CFM system is also a good secret key generator for real applications including information encryption, secure communication, and chaotic digital watermark.

TABLE 7: NIST test result of binary sequences generated by the CFM system.

Tests	p value	Proportion	Success
Frequency (1)	0.3345	97/100	✓
B. Frequency (1)	0.6163	100/100	✓
C. Sums (2)	0.9558	99/100	✓
Runs (1)	0.1816	99/100	✓
Longest Run (1)	0.2133	99/100	✓
Rank (1)	0.3191	99/100	✓
FFT (1)	0.1968	99/100	✓
N.O. Temp (148)	0.0288	97/100	✓
O. Temp (1)	0.7197	97/100	✓
Universal (1)	0.5341	99/100	✓
App. Entropy (1)	0.8165	57/58	✓
R. Excur. (8)	0.010	57/58	✓
R. Excur. V. (18)	0.0179	58/58	✓
Serial (2)	0.5544	99/100	✓
L. Complexity (1)	0.1025	99/100	✓

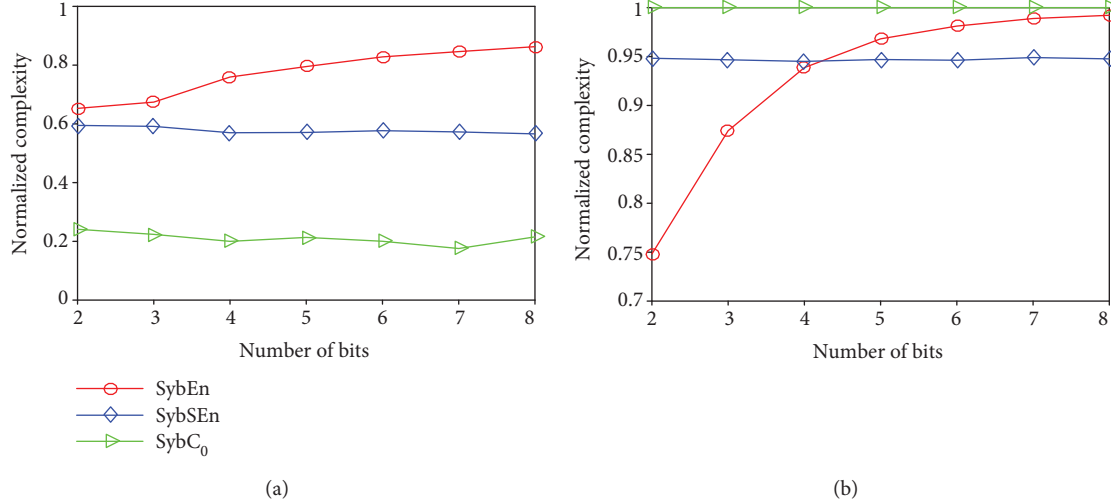


FIGURE 13: Relation between the number of quantization levels and its complexity: (a) quantization method one; (b) quantization method two.

Finally, it is necessary to explain why we choose 8-bit or 256-quantization-level symbols to form the numbers and how complexity analysis result is determined by the quantization levels. Let $e = 6.9$ and $q_1 = q_2 = q_3 = 0.95$. A segment of type II chaotic time series is used to calculate the complexity. The relation between the number of quantization levels and its complexity measuring results is shown in Figure 13, where SybEn is normalized via dividing $\ln(m)$. Here, m is the number of bits or 2^m is the quantization levels. It shows that the values of the two frequency domain methods, namely, SybC₀ and SybSEn, do not change with the quantization levels. However, values of SybEn (the time-domain method) increase but tend to become stable with the quantization levels. Meanwhile, the 8-bit number is widely used in real applications. Thus, 8-bit or 256-quantization-level symbol sequences are employed for complexity analysis.

5. Conclusions

In this work, we introduced the conformable fractional calculus in a nonlinear system with two memcapacitors (CFM system). The conformable fractional differential transform method is employed to solve the nonlinear conformable differential system for the first time. The ALCE calculation algorithm is designed based on the obtained solution, and bifurcation and chaos in the CFM system are explored. It shows that the CFM system has rich dynamics with the variation of system parameter and derivative orders. Meanwhile, coexisting attractors and transient state were observed under some specific parameters. Three symbol complexity measuring algorithms are designed, namely, symbolic entropy (SybEn) algorithm, symbolic spectral entropy (SybSEn) algorithm, and symbolic C₀ (SybC₀) algorithm. Complexity analysis results match well with the corresponding maximum LCE analysis results. Finally, by using a proper quantization algorithm, the obtained pseudorandom sequence has high complexity as other common chaotic systems and is randomly verified by the NIST test. It shows

that the memory electronic element-based systems have a potential engineering application value.

Data Availability

The data used to support the findings of this study are included within the article.

Conflicts of Interest

The authors declare that there is no conflict of interest regarding the publication of this paper.

Acknowledgments

Shaobo He acknowledges the support from the Post-Doctoral Innovation Talent Support Program (no. BX20180386), the National Natural Science Foundation of China (no. 11747150), the Natural Science Foundation of Hunan Province (no. 2018JJ4015), and the Foundation of Hunan University of Arts and Science (nos. E07016048 and 17BSQD07).

References

- [1] L. O. Chua, "Memristor-the missing circuit element," *IEEE Transactions on Circuit Theory*, vol. 18, no. 5, pp. 507–519, 1971.
- [2] D. B. Strukov, G. S. Snider, D. R. Stewart, and R. S. Williams, "The missing memristor found," *Nature*, vol. 453, no. 7191, pp. 80–83, 2008.
- [3] H. Kim, M. P. Sah, C. Yang, T. Roska, and L. O. Chua, "Neural synaptic weighting with a pulse-based memristor circuit," *IEEE Transactions on Circuits and Systems I: Regular Papers*, vol. 59, no. 1, pp. 148–158, 2012.
- [4] Y. Babacan, F. Kaçar, and K. Gürkan, "A spiking and bursting neuron circuit based on memristor," *Neurocomputing*, vol. 203, pp. 86–91, 2016.

- [5] C. Sánchez-López, J. Mendoza-López, M. A. Carrasco-Aguilar, and C. Muñoz-Montero, "A floating analog memristor emulator circuit," *IEEE Transactions on Circuits and Systems II: Express Briefs*, vol. 61, no. 5, pp. 309–313, 2017.
- [6] M. D. Ventra, Y. V. Pershin, and L. O. Chua, "Circuit elements with memory: memristors, memcapacitors, and meminductors," *Proceedings of the IEEE*, vol. 97, no. 10, pp. 1717–1724, 2009.
- [7] D. Bielek and V. Biolkova, "Mutator for transforming memristor into memcapacitor," *Electronics Letters*, vol. 46, no. 21, pp. 1428–1429, 2010.
- [8] B. C. Bao, Q. Xu, H. Bao, and Q. Xu, "Extreme multistability in a memristive circuit," *Electronics Letters*, vol. 52, no. 12, pp. 1008–1010, 2016.
- [9] B. C. Bao, P. Y. Wu, H. Bao, M. Chen, and Q. Xu, "Chaotic bursting in memristive diode bridge-coupled Sallen-Key lowpass filter," *Electronics Letters*, vol. 53, no. 16, pp. 1104–1105, 2017.
- [10] B. C. Bao, L. Xu, Z. M. Wu, M. Chen, and H. Wu, "Coexistence of multiple bifurcation modes in memristive diode-bridge-based canonical Chua's circuit," *International Journal of Electronics*, vol. 105, no. 7, pp. 1159–1169, 2018.
- [11] B. C. Bao, P. Y. Wu, H. Bao, Q. Xu, and M. Chen, "Numerical and experimental confirmations of quasi-periodic behavior and chaotic bursting in third-order autonomous memristive oscillator," *Chaos, Solitons & Fractals*, vol. 106, pp. 161–170, 2018.
- [12] J. Mou, K. Sun, J. Ruan, and S. He, "A nonlinear circuit with two memcapacitors," *Nonlinear Dynamics*, vol. 86, no. 3, pp. 1735–1744, 2016.
- [13] L. Zou, Y. Peng, Y. Feng, and Z. Tu, "Stabilization and synchronization of memristive chaotic circuits by impulsive control," *Complexity*, vol. 2017, Article ID 5186714, 10 pages, 2017.
- [14] J. Kengne, A. N. Negou, and D. Tchiotso, "Antimonotonicity, chaos and multiple attractors in a novel autonomous memristor-based jerk circuit," *Nonlinear Dynamics*, vol. 88, no. 4, pp. 2589–2608, 2017.
- [15] S. Kumar, J. P. Strachan, and R. S. Williams, "Chaotic dynamics in nanoscale NbO₂ Mott memristors for analogue computing," *Nature*, vol. 548, no. 7667, pp. 318–321, 2017.
- [16] B. Wang, F. C. Zou, and J. Cheng, "A memristor-based chaotic system and its application in image encryption," *Optik - International Journal for Light and Electron Optics*, vol. 154, pp. 538–544, 2018.
- [17] S. B. He, K. H. Sun, and H. H. Wang, "Complexity analysis and DSP implementation of the fractional-order Lorenz hyperchaotic system," *Entropy*, vol. 17, no. 12, pp. 8299–8311, 2015.
- [18] S. B. He, K. H. Sun, and H. H. Wang, "Solution and dynamics analysis of a fractional-order hyperchaotic system," *Mathematical Methods in the Applied Sciences*, vol. 39, no. 11, pp. 2965–2973, 2016.
- [19] K. Rajagopal, A. Karthikeyan, and A. K. Srinivasan, "FPGA implementation of novel fractional-order chaotic systems with two equilibriums and no equilibrium and its adaptive sliding mode synchronization," *Nonlinear Dynamics*, vol. 87, no. 4, pp. 2281–2304, 2017.
- [20] R. Zhang and S. Yang, "Robust synchronization of two different fractional-order chaotic systems with unknown parameters using adaptive sliding mode approach," *Nonlinear Dynamics*, vol. 71, no. 1–2, pp. 269–278, 2013.
- [21] K. Rajagopal, L. Guessas, A. Karthikeyan, A. Srinivasan, and G. Adam, "Fractional order memristor no equilibrium chaotic system with its adaptive sliding mode synchronization and genetically optimized fractional order PID synchronization," *Complexity*, vol. 2017, no. 4, 19 pages, 2017.
- [22] D. Cafagna and G. Grassi, "On the simplest fractional-order memristor-based chaotic system," *Nonlinear Dynamics*, vol. 70, no. 2, pp. 1185–1197, 2012.
- [23] R. Gorenflo and F. Mainardi, "Fractional calculus: integral and differential equations of fractional order," *Mathematics*, vol. 49, no. 2, pp. 277–290, 2012.
- [24] R. Khalil, M. A. Horani, A. Yousef, and M. Sababheh, "A new definition of fractional derivative," *Journal of Computational and Applied Mathematics*, vol. 264, no. 5, pp. 65–70, 2014.
- [25] T. Abdeljawad, "On conformable fractional calculus," *Journal of Computational and Applied Mathematics*, vol. 279, pp. 57–66, 2014.
- [26] B. B. İskender Eroğlu, D. Avcı, and N. Özdemir, "Optimal control problem for a conformable fractional heat conduction equation," *Acta Physica Polonica A*, vol. 132, no. 3, pp. 658–662, 2017.
- [27] M. S. Hashemi, "Invariant subspaces admitted by fractional differential equations with conformable derivatives," *Chaos, Solitons & Fractals*, vol. 107, pp. 161–169, 2018.
- [28] N. A. Khan, O. A. Razzaq, and M. Ayaz, "Some properties and applications of conformable fractional Laplace transform (CFLT)," *Journal of Fractional Calculus and Applications*, vol. 9, no. 1, pp. 72–81, 2018.
- [29] S. B. He, K. H. Sun, X. Y. Mei, B. Yan, and S. Xu, "Numerical analysis of a fractional-order chaotic system based on conformable fractional-order derivative," *The European Physical Journal Plus*, vol. 132, no. 1, pp. 1–11, 2017.
- [30] J. Ruan, K. Sun, J. Mou, S. He, and L. Zhang, "Fractional-order simplest memristor-based chaotic circuit with new derivative," *The European Physical Journal Plus*, vol. 133, no. 1, pp. 1–10, 2018.
- [31] E. Ünal and A. Gökdoğan, "Solution of conformable fractional ordinary differential equations via differential transform method," *Optik - International Journal for Light and Electron Optics*, vol. 128, pp. 264–273, 2017.
- [32] S. A. Makarkin, A. V. Starodubov, and Y. A. Kalinin, "Application of permutation entropy method in the analysis of chaotic, noisy, and chaotic noisy series," *Technical Physics*, vol. 62, no. 11, pp. 1714–1719, 2017.
- [33] S. N. Yu and M. Y. Lee, "Wavelet-based multiscale sample entropy and chaotic features for congestive heart failure recognition using heart rate variability," *Journal of Medical and Biological Engineering*, vol. 35, no. 3, pp. 338–347, 2015.
- [34] C. C. Hwang, "On the normalized spectral entropy of the chaotic states," *Journal of Non-Equilibrium Thermodynamics*, vol. 21, no. 3, pp. 270–277, 1996.
- [35] Z. J. Cai and J. Sun, "Convergence of C₀ complexity," *International Journal of Bifurcation and Chaos*, vol. 19, no. 3, pp. 977–992, 2009.
- [36] W. Yao and J. Wang, "Double symbolic joint entropy in nonlinear dynamic complexity analysis," *AIP Advances*, vol. 7, no. 7, pp. 1031–1051, 2017.
- [37] Y. Li, Y. Yang, G. Li, M. Xu, and W. Huang, "A fault diagnosis scheme for planetary gearboxes using modified multi-scale symbolic dynamic entropy and mRMR feature selection," *Mechanical Systems and Signal Processing*, vol. 91, pp. 295–312, 2017.

- [38] H. F. V. Bremen, F. E. Udadia, and W. Proskurowski, "An efficient QR based method for the computation of Lyapunov exponents," *Physica D: Nonlinear Phenomena*, vol. 101, no. 1-2, pp. 1-16, 1997.
- [39] C. Sparrow, "The Lorenz equations: bifurcations, chaos, and strange attractors," in *Applied Mathematical Sciences* Springer, New York.
- [40] W. H. Liu, K. H. Sun, and C. X. Zhu, "A fast image encryption algorithm based on chaotic map," *Optics and Lasers in Engineering*, vol. 84, pp. 26-36, 2016.
- [41] R. Parvaz and M. Zarebnia, "A combination chaotic system and application in color image encryption," *Optics & Laser Technology*, vol. 101, pp. 30-41, 2018.
- [42] J. S. Long, "A speech encryption using fractional chaotic systems," *Nonlinear Dynamics*, vol. 65, no. 1-2, pp. 103-108, 2010.
- [43] P. Raj and M. Gurjar, "Discrete wavelet transform and chaotic map based watermark hiding in medical images," *International Journal of Computer Applications*, vol. 177, no. 1, pp. 21-26, 2017.

Research Article

An Integer-Order Memristive System with Two- to Four-Scroll Chaotic Attractors and Its Fractional-Order Version with a Coexisting Chaotic Attractor

Ping Zhou ^{1,2} and Meihua Ke¹

¹Center of System Theory and Its Applications, Chongqing University of Posts and Telecommunications, Chongqing 400065, China

²Key Laboratory of Network Control and Intelligent Instrument of Ministry of Education, Chongqing University of Posts and Telecommunications, Chongqing 400065, China

Correspondence should be addressed to Ping Zhou; zhouping@cqupt.edu.cn

Received 19 April 2018; Accepted 28 June 2018; Published 30 July 2018

Academic Editor: Viet-Thanh Pham

Copyright © 2018 Ping Zhou and Meihua Ke. This is an open access article distributed under the Creative Commons Attribution License, which permits unrestricted use, distribution, and reproduction in any medium, provided the original work is properly cited.

First, based on a linear passive capacitor C , a linear passive inductor L , an active-charge-controlled memristor, and a fourth-degree polynomial function determined by charge, an integer-order memristive system is suggested. The proposed integer-order memristive system can generate two-scroll, three-scroll, and four-scroll chaotic attractors. The complex dynamics behaviors are investigated numerically. The Lyapunov exponent spectrum with respect to linear passive inductor L and the two-scroll, three-scroll, and four-scroll chaotic attractors are yielded by numerical calculation. Second, based on the integer-order memristive chaotic system with a four-scroll attractor, a fractional-order version memristive system is suggested. The complex dynamics behaviors of its fractional-order version are studied numerically. The largest Lyapunov exponent spectrum with respect to fractional-order p is yielded. The coexisting two kinds of three-scroll chaotic attractors and the coexisting three-scroll and four-scroll chaotic attractors can be found in its fractional-order version.

1. Introduction

Chaos is an interesting phenomenon in nonlinear systems. High irregularity, unpredictability, and complexity are the typical characteristics of chaotic systems [1, 2]. These typical characteristics have great applications in the following fields: data encryption [3], secure communication [4–7], power grid protection [8, 9], and so on [10–16]. Therefore, more and more attentions have been attracted on the study of chaotic systems in the last few decades [17–20]. In 1971, Chua reported the fourth circuit element named memristor [21], and a solid-state implementation of a memristor has been successfully realized in Hewlett-Packard in 2008 [22]. After then, the applications of a memristor have caught many attentions in nonlinear science [23–28]. Meanwhile, chaotic and hyperchaotic attractors have been found in many memristor-based circuits [21, 23–26]. For example, Muthuswamy and Chua provided a memristor-based circuit with a

single-scroll chaotic attractor [24], Bao et al. reported a memristor-based circuit with a double-scroll chaotic attractor [25], Teng et al. found a memristor-based circuit with double-scroll and four-scroll chaotic attractors [26], and so on [27, 28]. On the other hand, many real physical systems such as electromagnetic wave propagation, dielectric polarization, and heat conduction can be described by fractional-order differential equations [29, 30]. Meanwhile, chaotic phenomenon has been discussed in many fractional-order nonlinear systems such as the fractional-order electronic circuits [31], the fractional-order gyroscopes [32], the fractional-order chaotic brushless DC motor [12], the fractional-order microelectromechanical system [33], and the fractional-order neural networks [34, 35]. So, more attentions have been paid to research the chaotic behaviors of fractional-order nonlinear systems.

Motivated by the above considerations, first, based on a memristor-based chaotic circuit reported by Muthuswamy

and Chua [24], Bao et al. [25], and Teng et al. [26], an integer-order memristive chaotic system with two-scroll, three-scroll, and four-scroll chaotic attractors is provided in this paper. It is noticed that there is only a single-scroll chaotic attractor in [24], only a double-scroll chaotic attractor in [25], and only double-scroll and four-scroll chaotic attractors in [26]. However, there are two-scroll, three-scroll, and four-scroll chaotic attractors in our memristive system. Meanwhile, the Lyapunov exponent spectrum, and phase diagram for our memristive chaotic system are obtained. Second, based on the proposed integer-order memristive chaotic system with a four-scroll chaotic attractor, a fractional-order version chaotic system is suggested. We find that the coexisting three-scroll and four-scroll chaotic attractors and coexisting two kinds of three-scroll chaotic attractors are emerged in the fractional-order version. To the best of our knowledge, this result is rarely reported.

The outline of this paper is organized as follows. In Section 2, the concept of a memristor and some memristor-based system are briefly reviewed. Based on the review, we present an integer-order memristive chaotic system with two-scroll, three-scroll, and four-scroll chaotic attractors and some basic dynamics behaviors are obtained. In Section 3, based on the integer-order memristive chaotic system with a four-scroll chaotic attractor, we present its fractional-order version and we find that there are coexisting chaotic attractors in its fractional-order system. In Section 4, the conclusion is given.

2. An Integer-Order Memristive Chaotic System

The charge-controlled memristor [24, 26] is described by a nonlinear I - V characteristic as $V_M = M(q)I_M$ and $\dot{q} = F(q, I_M)$. Here, V_M , I_M , and q are the voltage, current, and charge associated to the device, respectively. $M(q)$ is the memristance, and $F(q, I_M)$ is the internal state function. In [24, 26], two schematics of the simplest memristor-based chaotic circuit with a linear passive inductor, linear passive capacitor, and a nonlinear active memristor have been reported. The state equations represent the current-voltage relation for the linear passive capacitor, and the inductor is described as

$$\begin{aligned} \frac{CdV_C}{dt} &= I_L, \\ \frac{LdI_L}{dt} &= -(V_C + M(q)I_L), \end{aligned} \quad (1)$$

where V_C denotes the voltage of the linear passive capacitor C and I_L denotes the current of the linear passive inductor L .

In [24], the memristance $M(q)$ is defined as $M(q) = \beta(q^2 - 1)$, and the internal state function $F(q, I_M)$ is defined as $F(q, I_M) = I_M - (\alpha + I_M)q$, where $I_M = -I_L$. The memristor-based circuit in [24] has a single-scroll chaotic attractor (for more details, see [24]), and its dynamics are described by

$$\begin{aligned} \frac{CdV_C}{dt} &= I_L, \\ \frac{LdI_L}{dt} &= -(V_C + \beta(q^2 - 1)I_L), \\ \frac{dq}{dt} &= -I_L - (\alpha - I_L)q. \end{aligned} \quad (2)$$

In [26], the memristance is chosen as $M(q) = \delta q^4 + \gamma q^2 - \beta$ and the internal state function is chosen as $F(q, I_M) = I_M - (\alpha - I_M^2)q$, where $I_M = -I_L$. The memristor-based circuit in [26] has double-scroll and four-scroll chaotic attractors (for more details, see [26]), and its dynamics are shown as

$$\begin{aligned} \frac{CdV_C}{dt} &= I_L, \\ \frac{LdI_L}{dt} &= -(V_C + (\delta q^4 + \gamma q^2 - \beta)I_L), \\ \frac{dq}{dt} &= -I_L - (\alpha - I_L^2)q. \end{aligned} \quad (3)$$

Now, based on [24, 26], an integer-order memristive system is suggested in our paper. The memristance is defined as $M(q) = \delta q^4 - \beta$, and the internal state function is defined as $F(q, I_M) = I_M - (\alpha - I_M^2)q$. So, the integer-order memristive chaotic system in this paper is suggested as

$$\begin{aligned} \frac{CdV_C}{dt} &= I_L, \\ \frac{LdI_L}{dt} &= -(V_C + (\delta q^4 - \beta)I_L), \\ \frac{dq}{dt} &= -I_L - (\alpha - I_L^2)q, \end{aligned} \quad (4)$$

where $C = 1F$, $\delta = 0.5$, $\beta = 2.4$, $\alpha = 0.75$, and $1H \leq L \leq 8H$.

The equilibrium points of system (4) can be calculated by

$$\begin{aligned} I_L &= 0, \\ -(V_C + (\delta q^4 - \beta)I_L) &= 0, \\ -I_L - (\alpha - I_L^2)q &= 0. \end{aligned} \quad (5)$$

Obviously, only $(I_L, V_C, q) = (0, 0, 0)$ is the equilibrium point in system (4). The Jacobian matrix J at this equilibrium point is

$$J = \begin{bmatrix} 0 & 1 & 0 \\ -\frac{1}{L} & \frac{2.4}{L} & 0 \\ 0 & -1 & -0.75 \end{bmatrix}, \quad (6)$$

and its eigenvalues are $\lambda_1 = 0.5(2.4/L) + \sqrt{(2.4/L)^2 - 4/L}$, $\lambda_2 = 0.5(2.4/L) - \sqrt{(2.4/L)^2 - 4/L}$, and $\lambda_3 = -0.75$. If $(2.4/L)^2 - 4/L \geq 0$, then $\lambda_{1,2} > 0$. If $(2.4/L)^2 - 4/L < 0$, then $\text{Re}(\lambda_{1,2}) > 0$. So, the equilibrium point $(I_L, V_C, q) = (0, 0, 0)$ in system (4) is unstable.

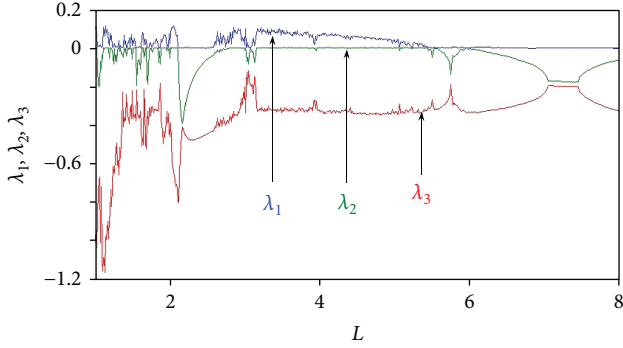


FIGURE 1: The Lyapunov exponent spectrum varies as linear passive inductor L .

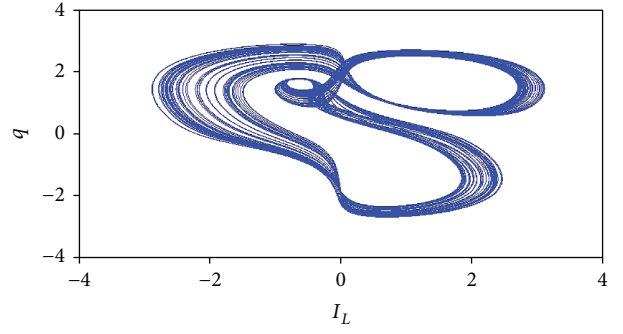


FIGURE 3: Three-scroll chaotic attractor in integer-order memristive system (4).

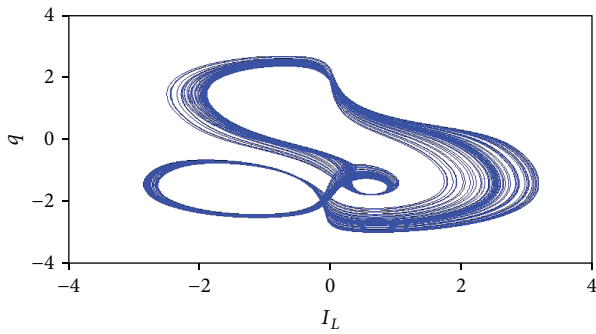


FIGURE 2: Three-scroll chaotic attractor in integer-order memristive system (4).

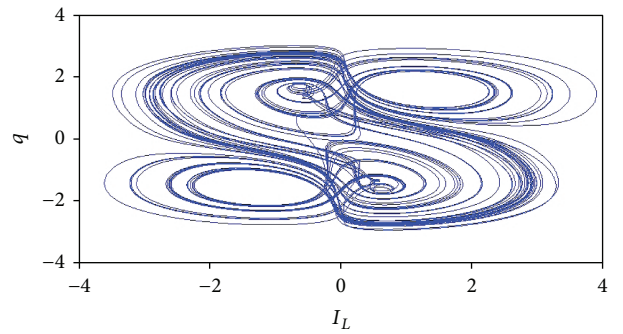


FIGURE 4: Four-scroll chaotic attractor in integer-order memristive system (4).

By numerical calculation, the Lyapunov exponent spectrum of integer-order memristive system (4) with respect to linear passive inductor L can be obtained and is displayed in Figure 1.

According to Figure 1, the maximum Lyapunov exponent λ_1 is positive for the suitable L . The positive Lyapunov exponent λ_1 indicates that the chaotic attractor is emerged in system (4). Next, some results are shown as follows:

2.1. Two Kinds of Three-Scroll Chaotic Attractors Are Emerged in System (4). Letting $L = 1.734$, the Lyapunov exponents are $\lambda_1 = 0.0168$, $\lambda_2 = 0$, and $\lambda_3 = -0.3275$. The Lyapunov dimension is $D_L = 2 + \lambda_1/|\lambda_3| = 2.051$; so, system (4) is fractal. The chaotic attractor is shown in Figure 2. The result in Figure 2 indicates that the three-scroll chaotic attractor is emerged in system (4).

Letting $L = 1.8$, the Lyapunov exponents are $\lambda_1 = 0.0246$, $\lambda_2 = 0$, and $\lambda_3 = -0.3152$. The Lyapunov dimension is $D_L = 2 + \lambda_1/|\lambda_3| = 2.078$; so, system (4) is fractal. The chaotic attractor is shown in Figure 3. The result in Figure 3 indicates that the three-scroll chaotic attractor is emerged in system (4).

According to Figures 2 and 3, we find that two kinds of three-scroll chaotic attractors are emerged in our integer-order memristive chaotic system.

2.2. The Four-Scroll Chaotic Attractor Is Emerged in System (4). Letting $L = 1.4$, the Lyapunov exponents are $\lambda_1 = 0.0663$,

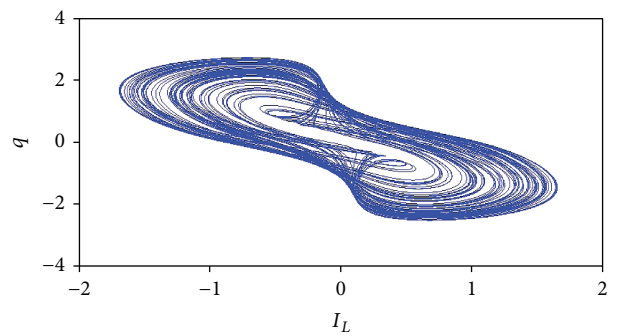


FIGURE 5: Two-scroll chaotic attractor in integer-order memristive system (4).

$\lambda_2 = 0$, and $\lambda_3 = -0.3593$. The Lyapunov dimension is $D_L = 2 + \lambda_1/|\lambda_3| = 2.1845$; so, system (4) is fractal. The chaotic attractor is displayed in Figure 4. The result in Figure 4 indicates that the four-scroll chaotic attractor is emerged in system (4).

2.3. The Two-Scroll Chaotic Attractor Is Emerged in System (4). Letting $L = 4$, the Lyapunov exponents are $\lambda_1 = 0.0397$, $\lambda_2 = 0$, and $\lambda_3 = -0.3364$. The Lyapunov dimension is $D_L = 2 + \lambda_1/|\lambda_3| = 2.1180$; so, system (4) is fractal. The chaotic attractor is displayed in Figure 5. The result in Figure 5 indicates that the two-scroll chaotic attractor is emerged in system (4).

According to the above results, the proposed integer-order memristive chaotic system (4) in this paper can generate two- to four-scroll chaotic attractors. This result is different with many previous results [21, 23–28].

3. A Fractional-Order Memristive Chaotic System with Coexisting Chaotic Attractors

In this section, based on integer-order memristive chaotic system (4), a fractional-order version with coexisting chaotic attractors is given.

According to Figure 4 in Section 2, the four-scroll chaotic attractor is emerged in integer-order memristive system (4) with $C = 1F$, $\delta = 0.5$, $\beta = 2.4$, $\alpha = 0.75$, and $L = 1.4$. Now, based on this case, a fractional-order version memristive system is suggested, which is shown as follows:

$$\begin{aligned}\frac{d^p V_C(t)}{dt^p} &= I_L(t), \\ \frac{d^p I_L(t)}{dt^p} &= -\frac{[V_C(t) + (0.5q^4(t) - 2.4)I_L(t)]}{1.4}, \\ \frac{d^p q(t)}{dt^p} &= -I_L(t) - (0.75 - I_L^2(t))q(t).\end{aligned}\quad (7)$$

Here, $0.92 \leq p \leq 1$ is the fractional-order version and $d^p V_C(t)/dt^p = \int_0^t (t-\tau)^{-p} dV_C(\tau)/\Gamma(1-p)$, $d^p I_L(t)/dt^p = \int_0^t$

$(t-\tau)^{-p} dI_L(\tau)/\Gamma(1-p)$, and $d^p q(t)/dt^p = \int_0^t (t-\tau)^{-p} dq(\tau)/\Gamma(1-p)$.

Now, by the improved version of Adams-Bashforth-Moulton numerical algorithm [36], nonlinear fractional-order system (7) with initial condition $(I_L(0), V_C(0), q(0))$ can be discretized as follows:

$$\begin{aligned}V_C(n+1) &= V_C(0) + \frac{\tau^p}{\Gamma(p+2)} \left[I_L^s(n+1) + \sum_{j=0}^n \alpha_{j,n+1} I_L(j) \right], \\ I_L(n+1) &= I_L(0) + \frac{\tau^p}{\Gamma(p+2)} \cdot \left[\frac{-(V_C^s(n+1) + (0.5(q^s(n+1))^4 - 2.4)I_L^s(n+1))}{1.4} \right. \\ &\quad \left. + \sum_{j=0}^n \frac{\alpha_{j,n+1} (-(V_C(j) + (0.5 - (q(j))^4 - 2.4)I_L(j)))}{1.4} \right], \\ q(n+1) &= q(0) + \frac{\tau^p}{\Gamma(p+2)} \cdot \left[I_L^s(n+1) - (0.75 - (I_L^s(n+1))^2)q^s(n+1) \right. \\ &\quad \left. + \sum_{j=0}^n \alpha_{j,n+1} (-I_L(j) - (0.75 - (I_L(j))^2)q(j)) \right],\end{aligned}\quad (8)$$

where

$$\begin{aligned}V_C^s(n+1) &= V_C(0) + \frac{1}{\Gamma(p)} \sum_{j=0}^n \beta_{j,n+1} I_L(j), \\ I_L^s(n+1) &= I_L(0) + \frac{1}{\Gamma(p)} \sum_{j=0}^n \beta_{j,n+1} \left(\frac{-(V_C(j) + (0.5(q(j))^4 - 2.4)I_L(j))}{1.4} \right), \\ q^s(n+1) &= q(0) + \frac{1}{\Gamma(p)} \sum_{j=0}^n \beta_{j,n+1} (-I_L(j) - (0.75 - (I_L(j))^2)q(j)), \\ \alpha_{j,n+1} &= \begin{cases} n^{p+1} - (n-p)(n+1)^p, & j=0, \\ (n-j+2)^{p+1} + (n-j)^{p+1} - 2(n-j+1)^{p+1}, & 1 \leq j \leq n, \\ 1, & j=n+1, \end{cases} \\ \beta_{j,n+1} &= \frac{\tau^p [(n-j+1)^p - (n-j)^p]}{p}, \quad 0 \leq j \leq n.\end{aligned}\quad (9)$$

The approximation error is as follows:

$$\begin{aligned}|V_C(t_n) - V_C(n)| &= o(\tau^{1+p}), \\ |I_L(t_n) - I_L(n)| &= o(\tau^{1+p}), \\ |q(t_n) - q(n)| &= o(\tau^{1+p}).\end{aligned}\quad (10)$$

In this numerical algorithm, T is the total time length of numerical calculation, N is the iterative calculation

time, and $\tau = T/N$ is the step length. So, $t_n = n\tau$ ($n = 0, 1, 2, \dots, N$).

Next, we study the dynamical behaviors for fractional-order system (7) by the improved version of Adams-Bashforth-Moulton numerical algorithm [36]. First, using numerical calculation, the largest Lyapunov exponents (Largest LE) of fractional-order system (7) with respect to fractional-order p can be obtained, which is shown in Figure 6.

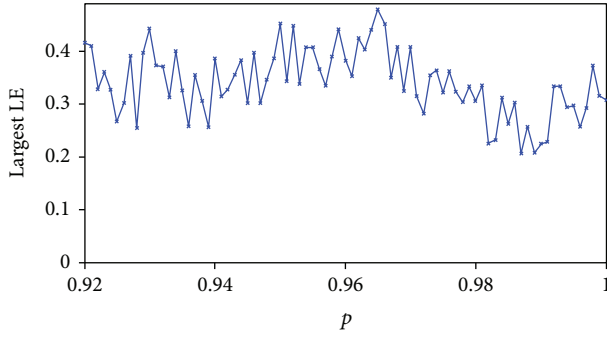


FIGURE 6: The Largest LE varies as fractional-order p .

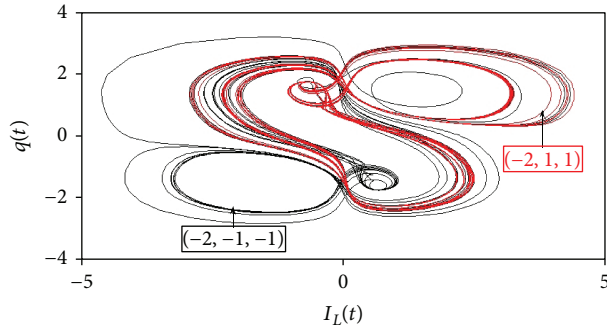


FIGURE 7: The coexisting three-scroll and four-scroll chaotic attractors in system (7).

According to Figure 6, the largest Lyapunov exponent is larger than zero for $0.92 \leq p \leq 1$. The positive largest Lyapunov exponent indicates that the chaotic attractor is emerged in fractional-order system (7). Next, some results are shown as follows:

3.1. Coexisting Three- and Four-Scroll Chaotic Attractors in System (7) for $p = 0.935$. Letting $p = 0.935$, the Largest LE is 0.3251. Therefore, fractional-order system (7) has chaotic behavior. The chaotic attractor can be obtained by numerical calculation. Here, we find that there are coexisting three-scroll and four-scroll chaotic attractors which depend on the initial conditions. For example, let the initial condition be $(-2, -1, -1)$ and $(-2, 1, 1)$. The four-scroll chaotic attractor (black line) and three-scroll chaotic attractor (red line) are shown in Figure 7.

3.2. Coexisting Two Kinds of Three-Scroll Chaotic Attractors in System (7) for $p = 0.94$. Letting $p = 0.94$, the Largest LE is 0.3864. Therefore, fractional-order system (7) has chaotic behavior. The chaotic attractor can be obtained by numerical calculation. Here, we find that there are coexisting two kinds of three-scroll chaotic attractors which depend on the initial conditions. For example, let the initial condition be $(-2, -1, -1)$ and $(-2, 1, 1)$. The two kinds of three-scroll chaotic attractors (black line, red line) are shown in Figure 8.

3.3. Four-Scroll Chaotic Attractor in System (7) for $p = 0.99$. Letting $p = 0.99$, the Largest LE is 0.2247. Therefore, fractional-order system (7) has chaotic behavior. By numerical

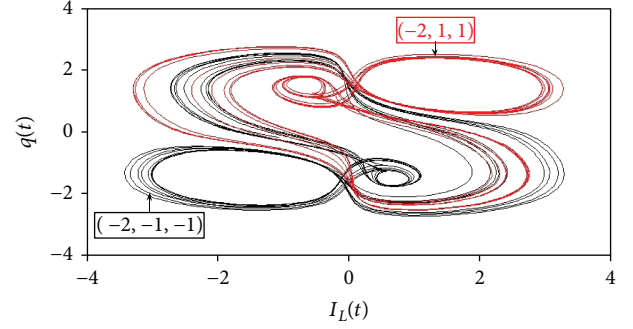


FIGURE 8: The coexisting two kinds of three-scroll chaotic attractors in system (7).

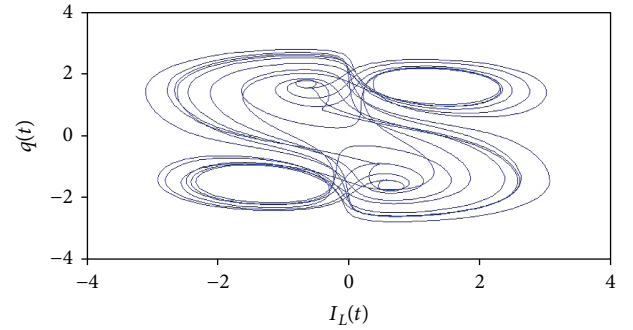


FIGURE 9: Four-scroll chaotic attractor in system (7).

calculation, we find that the four-scroll chaotic attractor is emerged in fractional-order system (7). The four-scroll chaotic attractor is shown in Figure 9.

According to Figure 9, four-scroll chaotic attractor is emerged in fractional-order system (7). This result is just as that of integer-order memristive chaotic system (4) with $L = 1.4$.

According to Figure 8, the coexisting two kinds of three-scroll chaotic attractors are obtained in fractional-order system (7) and the two kinds of three-scroll chaotic attractors do not exist in integer-order memristive chaotic system (4) with $L = 1.4$. So, two kinds of three-scroll chaotic attractor are newly produced.

According to Figure 7, the coexisting three-scroll and four-scroll chaotic attractors are emerged in fractional-order system (7). But, there is only a four-scroll chaotic attractor in integer-order memristive chaotic system (4) with $L = 1.4$. So, the three-scroll chaotic attractor is newly produced.

In summary, for integer-order memristive chaotic system (4) with $L = 1.4$, there is only a four-scroll chaotic attractor. However, for its fractional-order version, it can produce two kinds of new three-scroll chaotic attractors and has coexisting three-scroll and four-scroll chaotic attractors. These results in Section 3 are rarely reported in the previous literature.

4. Conclusions

By a linear passive capacitor C , a linear passive inductor L , and an active-charge-controlled memristor, an integer-order

memristive system is devised in this paper. The memristance $M(q)$ is defined as a fourth-degree polynomial function determined by charge, that is, $M(q) = \delta q^4 - \beta$. By numerical calculation, the Lyapunov exponent spectrum of the proposed memristor-based chaotic circuit with respect to linear passive inductor L is yielded. The proposed integer-order memristive system can generate two-scroll, three-scroll, and four-scroll chaotic attractors for suitable linear passive inductor L .

Furthermore, based on the proposed integer-order memristive system with a four-scroll chaotic attractor for $L = 1.4$, a fractional-order version memristive system is given. By numerical calculation, we obtain the largest Lyapunov exponent with respect to fractional-order p . This fractional-order version memristive system can newly produce two kinds of three-scroll chaotic attractors, and the coexisting three-scroll and four-scroll chaotic attractors are obtained.

Disclosure

The data used in our manuscript is obtained by MATLAB program.

Conflicts of Interest

The authors declare that there are no conflicts of interest regarding the publication of this paper.


References

- [1] G. Chen and X. Dong, *From Chaos to Order: Methodologies, Perspectives and Applications*, World Scientific, Singapore, 1998.
- [2] J. C. Sprott, *Chaos and Time-Series Analysis*, Oxford University Press, Oxford, UK, 2003.
- [3] P. Muthukumar, P. Balasubramaniam, and K. Ratnavelu, "Synchronization of a novel fractional order stretch-twist-fold (STF) flow chaotic system and its application to a new authenticated encryption scheme (AES)," *Nonlinear Dynamics*, vol. 77, no. 4, pp. 1547–1559, 2014.
- [4] T. Yang and L. O. Chua, "Impulsive stabilization for control and synchronization of chaotic systems: theory and application to secure communication," *IEEE Transactions on Circuits and Systems I: Fundamental Theory and Applications*, vol. 44, no. 10, pp. 976–988, 1997.
- [5] A. N. Miliou, I. P. Antoniadis, S. G. Stavrinos, and A. N. Anagnostopoulos, "Secure communication by chaotic synchronization: robustness under noisy conditions," *Nonlinear Analysis*, vol. 8, no. 3, pp. 1003–1012, 2007.
- [6] H. Li, G. Chen, T. Huang, Z. Dong, W. Zhu, and L. Gao, "Event-triggered distributed average consensus over directed digital networks with limited communication bandwidth," *IEEE Transactions on Cybernetics*, vol. 46, no. 12, pp. 3098–3110, 2016.
- [7] H. Li, G. Chen, T. Huang, and Z. Dong, "High-performance consensus control in networked systems with limited bandwidth communication and time-varying directed topologies," *IEEE Transactions on Neural Networks and Learning Systems*, vol. 28, no. 5, pp. 1043–1054, 2017.
- [8] Y. Y. Dai, G. Chen, Z. Y. Dong, Y. S. Xue, D. J. Hill, and Y. Zhao, "An improved framework for power grid vulnerability analysis considering critical system features," *Physica A: Statistical Mechanics and its Applications*, vol. 395, pp. 405–415, 2014.
- [9] J. Ni, C. Liu, K. Liu, and X. Pang, "Variable speed synergetic control for chaotic oscillation in power system," *Nonlinear Dynamics*, vol. 78, no. 1, pp. 681–690, 2014.
- [10] J. M. Ottino, F. J. Muzzio, M. Tjahjadi, J. G. Franjione, S. C. Jana, and H. A. Kusch, "Chaos, symmetry, and self-similarity: exploiting order and disorder in mixing processes," *Science*, vol. 257, no. 5071, pp. 754–760, 1992.
- [11] P. Zhou and W. Zhu, "Function projective synchronization for fractional-order chaotic systems," *Nonlinear Analysis: Real World Applications*, vol. 12, no. 2, pp. 811–816, 2011.
- [12] P. Zhou, R. J. Bai, and J. M. Zheng, "Stabilization of a fractional-order chaotic brushless DC motor via a single input," *Nonlinear Dynamics*, vol. 82, no. 1–2, pp. 519–525, 2015.
- [13] D. Q. Wei, L. Wan, X. S. Luo, S. Y. Zeng, and B. Zhang, "Global exponential stabilization for chaotic brushless DC motors with a single input," *Nonlinear Dynamics*, vol. 77, no. 1–2, pp. 209–212, 2014.
- [14] G. Chen, C. Li, and Z. Y. Dong, "Parallel and distributed computation for dynamical economic dispatch," *IEEE Transactions on Smart Grid*, vol. 8, pp. 1026–1027, 2017.
- [15] C. Wang, R. Chu, and J. Ma, "Controlling a chaotic resonator by means of dynamic track control," *Complexity*, vol. 21, no. 1, 378 pages, 2015.
- [16] Y. Feng, Z. Wei, U. E. Kocamaz, A. Akgül, and I. Moroz, "Synchronization and electronic circuit application of hidden hyperchaos in a four-dimensional self-exciting homopolar disc dynamo without equilibria," *Complexity*, vol. 2017, Article ID 7101927, 11 pages, 2017.
- [17] P. Zhou and M. Ke, "A new 3D autonomous continuous system with two isolated chaotic attractors and its topological horseshoes," *Complexity*, vol. 2017, Article ID 4037682, 7 pages, 2017.
- [18] V. T. Pham, C. Volos, S. Jafari, and T. Kapitaniak, "Coexistence of hidden chaotic attractors in a novel no-equilibrium system," *Nonlinear Dynamics*, vol. 87, no. 3, pp. 2001–2010, 2017.
- [19] J. Kengne, Z. T. Njitacke, and H. B. Fotsin, "Dynamical analysis of a simple autonomous jerk system with multiple attractors," *Nonlinear Dynamics*, vol. 83, no. 1–2, pp. 751–765, 2016.
- [20] Q. Lai and S. Chen, "Coexisting attractors generated from a new 4D smooth chaotic system," *International Journal of Control, Automation and Systems*, vol. 14, no. 4, pp. 1124–1131, 2016.
- [21] L. Chua, "Memristor-the missing circuit element," *IEEE Transactions on Circuit Theory*, vol. 18, no. 5, pp. 507–519, 1971.
- [22] D. B. Strukov, G. S. Snider, D. R. Stewart, and R. S. Williams, "The missing memristor found," *Nature*, vol. 453, no. 7191, pp. 80–83, 2008.
- [23] B. Muthuswamy, "Implementing memristor based chaotic circuits," *International Journal of Bifurcation and Chaos*, vol. 20, no. 5, pp. 1335–1350, 2010.
- [24] B. Muthuswamy and L. O. Chua, "Simplest chaotic circuit," *International Journal of Bifurcation and Chaos*, vol. 20, no. 5, pp. 1567–1580, 2010.
- [25] B. Bao, Z. Ma, J. Xu, Z. Liu, and Q. Xu, "A simple memristor chaotic circuit with complex dynamics," *International Journal of Bifurcation and Chaos*, vol. 21, no. 9, pp. 2629–2645, 2011.

- [26] L. Teng, H. H. C. Iu, X. Wang, and X. Wang, "Chaotic behavior in fractional-order memristor-based simplest chaotic circuit using fourth degree polynomial," *Nonlinear Dynamics*, vol. 77, no. 1-2, pp. 231–241, 2014.
- [27] J. Kengne, A. N. Negou, and D. Tchiotso, "Antimonotonicity, chaos and multiple attractors in a novel autonomous memristor-based jerk circuit," *Nonlinear Dynamics*, vol. 88, no. 4, pp. 2589–2608, 2017.
- [28] S. Sabarathinam, C. K. Volos, and K. Thamilmaran, "Implementation and study of the nonlinear dynamics of a memristor-based Duffing oscillator," *Nonlinear Dynamics*, vol. 87, no. 1, pp. 37–49, 2017.
- [29] I. Podlubny, *Fractional Differential Equations*, Academic Press, San Diego, CA, USA, 1999.
- [30] R. Hilfer, *Applications of Fractional Calculus in Physics*, World Scientific, Singapore, 2000.
- [31] T. T. Hartley, C. F. Lorenzo, and H. Killory Qammer, "Chaos in a fractional order Chua's system," *IEEE Transactions on Circuits and Systems I: Fundamental Theory and Applications*, vol. 42, no. 8, pp. 485–490, 1995.
- [32] M. P. Aghababa and H. P. Aghababa, "The rich dynamics of fractional-order gyros applying a fractional controller," *Proceedings of the Institution of Mechanical Engineers, Part I: Journal of Systems and Control Engineering*, vol. 227, no. 7, pp. 588–601, 2013.
- [33] M. P. Aghababa, "Chaos in a fractional-order micro-electro-mechanical resonator and its suppression," *Chinese Physics B*, vol. 21, no. 10, article 100505, 2012.
- [34] C. Song and J. Cao, "Dynamics in fractional-order neural networks," *Neurocomputing*, vol. 142, pp. 494–498, 2014.
- [35] E. Kaslik and S. Sivasundaram, "Nonlinear dynamics and chaos in fractional-order neural networks," *Neural Networks*, vol. 32, pp. 245–256, 2012.
- [36] C. Li and G. Peng, "Chaos in Chen's system with a fractional order," *Chaos, Solitons & Fractals*, vol. 22, no. 2, pp. 443–450, 2004.

Research Article

Dynamic Behaviors in Coupled Neuron System with the Excitatory and Inhibitory Autapse under Electromagnetic Induction

Ying Xu,¹ Ya Jia ,¹ John Billy Kirunda,¹ Jian Shen,^{1,2} Mengyan Ge,¹ Lulu Lu,¹ and Qiming Pei³

¹*Institute of Biophysics and Department of Physics, Central China Normal University, Wuhan 430079, China*

²*College of Electronics and Information Engineering, South-Central University for Nationalities, Wuhan 430074, China*

³*School of Physics and Optoelectronic Engineering, Yangtze University, Jingzhou 434023, China*

Correspondence should be addressed to Ya Jia; jiay@mail.ccnu.edu.cn

Received 4 April 2018; Revised 3 June 2018; Accepted 25 June 2018; Published 26 July 2018

Academic Editor: Viet-Thanh Pham

Copyright © 2018 Ying Xu et al. This is an open access article distributed under the Creative Commons Attribution License, which permits unrestricted use, distribution, and reproduction in any medium, provided the original work is properly cited.

The induced current produced by electromagnetic induction can adjust the membrane potential of neuron through the feedback of a magnetic flux-controlled memristor. We adopt the numerical simulation method with the aim of investigating the synchronous behavior in the neuronal system that is coupled by chemical and electrical synapses under electromagnetic induction. Within the improved model, the effects of electromagnetic induction on neurons are described with additive memristive current on the membrane variable, and the memristive current is dependent on the variation of magnetic flow. The simulation results show that the two coupling modes play an important role in the synchronization of the system. By increasing the chemical synaptic feedback gain, we observe a transition from mixed oscillatory to periodic state at a critical value. In addition, two Hopf bifurcation points are found with the change of the external stimuli, and the state of neuron discharge is influenced by initial values. Furthermore, there is a domain of coupling strength and feedback gain values, in which the two coupled neuron system is synchronized and longer time lag is not conducive to the system synchronization.

1. Introduction

A neural system, which is made up of a large number of neurons, is a complex information network. Different types of discharge patterns can be switched under the control of external stimulation or bifurcation parameter. In order to understand the regulating function of the nervous system, many models of neuronal electrical activity have been proposed. Commonly used models include the FitzHugh-Naguma model [1], Morris-Lecar neuron model [2], Hindmarsh-Rose model [3, 4], Nagumo-Sato neuron model [5], and Wilson-Cowan neuron model [6]. These models that describe neuron dynamics with a set of differential equations are almost derived from the Hodgkin-Huxley [7] model or the simplified version. Some results from biological experiments [8–10] can be explained by theoretical neuron models, such as the Morris-Lecar neuron model. In this model, the membrane potential exhibits quiescent, spiking, or bursting state by changing the

external forced current [11]. Neurons do not work in isolation, but they interact to affect the processing of information. There are two forms of synaptic coupling found in the real nervous system, namely, electrical synapse and chemical synapse. The synchronization phenomena are a typical manifestation of the rhythms of group movement; that is, all neurons in the system have a certain connection at the same time or rhythm [12–14]. Bazhenov et al. [15] designed a coupled linear chain of Hindmarsh-Rose model neurons with reciprocal inhibition between neighboring neurons that exhibited synchronous oscillations. Zhang et al. [16] proposed a class of synchronization problems of nonlinear time-delay dynamic networks with a nonuniform impulse effect. Burić et al. [17] studied the synchronization of Hindmarsh-Rose neurons with a time-delayed fast threshold modulation synapse. Xu et al. [18] analyzed the synchronization behavior and mode selection in neural networks under the coupling of chemical or electrical synapses. Yao et al. [19] investigated the influence of

coupling strength, time delay, and network topology on synchronization behavior in delay-coupled networks of chaotic pendulums. Gokul and Kapitaniak [20] studied the synchrony of coupling multistable systems which have hidden attractors with each other. In coupled oscillators or coupled neurons, synchronization may occur because of the appropriate coupling effect [21–24]. Interestingly, the stochastic and coherence resonance [25–27] of the nervous system is induced by appropriate noise intensity and external periodic stimulus. The synchronization of the coupling system is an interesting research field. It is challenging to analyze the dynamic mechanism caused by the variation of the coupling parameters and modes of the system. The synchronization phenomena in Hindmarsh-Rose (HR) neurons that are connected by electrical coupling and chemical coupling, moreover, complete synchronization, phase synchrony, and antisynchrony of neurons are realized [28, 29]. The neural electrical activity has also been widely studied and verified in the circuit [30–35]. For example, Vaidyanathan et al. [36–38] designed electronic circuits to study the feasibility of the 3D novel jerk chaotic system with hyperbolic sinusoidal nonlinearity. Conti and Turchetti [39] performed a circuit to realize approximate identity neural network for the analog synthesis nonlinear dynamical system. Pham et al. [40] proved the existence of chaotic behavior in a three-dimensional autonomous chaotic system with a circular equilibrium by using OrCAD PSpice software and experimental.

It is necessary to study the effects of electromagnetic induction on neuronal cells [41–44]. The changes of membrane potential can induce electromagnetic induction between neurons. As reviewed in [45, 46], the effects of electromagnetic radiation in *Homo sapiens* include electrical activity of neurons, energy metabolism, genomic responses, neurotransmitter balance, blood-brain barrier permeability, cognitive function, sleep, brain tumors, and other encephalopathy. Lu et al. [47–49] investigated the effects of high- and low-frequency signal stimulus on neural activity under electromagnetic radiation. According to Faraday's law of induction, the magnetic field is a result of fluctuations in the action potential. That is, the distribution of electromagnetic field both inside and outside neurons can be changed by the fluctuation of the membrane potential. Therefore, a new three-variable ML neuron model is established by introducing an additional variable as magnetic flux which adjusts the membrane potential via a memristor [50, 51].

The following study is based on the proposed Morris-Lecar neuron model with consideration of magnetic flux, in which the dynamic characteristics of the neurons are studied by using bifurcation diagrams and time series of the discharge. A preliminary synchronization analysis was conducted in the excitatory and inhibitory neural system. The study revealed that excitatory and inhibitory neurons can be synchronized under the appropriate coupling strength. The synchronization behavior of the system is also affected by the time lag when the coupling strength and the feedback gain are maintained.

2. Model and Scheme

The Morris-Lecar (ML) equations were originally developed as a mathematical model of muscle fiber. For the neuron,

the effect of electromagnetic induction should be considered during the discharge process of the membrane potential. The electric activity will change because of the fluctuation of electromagnetic induction and ion concentration in the process of ion exchange. We modify the basic ML model, including the impact of the electromagnetic radiation. The improved ML neuronal model [44] contains three variables, and the dynamic properties are described as follows:

$$\begin{aligned} c \frac{dV}{dt} &= g_{Ca} m_{\infty}(V)(V_{Ca} - V) + g_K \omega(V)(V_K - V) + g_L(V_L - V) \\ &\quad - k\rho(\varphi)V + I_{ext}, \\ \frac{d\omega}{dt} &= \lambda_{\omega}(V)(\omega_{\infty}(V) - \omega), \\ \frac{d\varphi}{dt} &= k_1 V - k_2 \varphi, \end{aligned} \quad (1)$$

with

$$\begin{aligned} m_{\infty}(V) &= 0.5 + 0.5 \tanh\left(\frac{V - V_1}{V_2}\right), \\ \omega_{\infty}(V) &= 0.5 + 0.5 \tanh\left(\frac{V - V_3}{V_4}\right), \\ \lambda_{\omega}(V) &= \phi \cosh\left(\frac{V - V_3}{2V_4}\right), \end{aligned} \quad (2)$$

where V and ω denote the variables for the membrane potential (mV) and gate channel, respectively. Parameter c is the capacitance of the membrane ($\mu\text{F}/\text{cm}^2$). The g_{Ca} , g_K , and g_L denote the maximum conductance (mS) of calcium ion, potassium ion, and leak ion, respectively. V_{Ca} , V_K , and V_L are the reversal potential (mV) corresponding to these channels. $m_{\infty}(V)$ and $\omega_{\infty}(V)$ define the value of the opening probability for the calcium ion channel and the potassium ion channel in the steady state, where V_1 , V_2 , V_3 , and V_4 are the parameters of the steady system, and $\lambda_{\omega}(V)$ defines the rate constant for the opening of potassium ion channel. The parameter ϕ is marked as the variation between the fast and the slow scales of neurons.

As described in [52, 53], the variations of the intercellular and extracellular ion concentration can induce electromagnetic induction, which can be expressed by magnetic flux according to Faraday's law of electromagnetic induction. The induced current produced by electromagnetic induction can adjust the membrane potential by the feedback of the memristor. The memristor in model (1) can be divided into two ways: the charge controlled and the magnetic controlled. For the potassium ion-channel memristor, the second term in the right of (1) can be rewritten as $i_K = G_K(\omega)v_K$ with $v_K \Leftrightarrow V - V_K$ and $G_K \Leftrightarrow g_K \omega$, and G_K is the potassium memductance function. The fourth term in the right of (1) can be rewritten as $i_{\varphi} = G_{\varphi}(\varphi)v_{\varphi}$ with $v_{\varphi} \Leftrightarrow V$ and $G_{\varphi} \Leftrightarrow k\rho(\varphi)$, which defines another first-order memristor, and the conductance value of the memristor depends on the input current. The expression of $\rho(\varphi) = \alpha + 3\beta\varphi^2$ denotes the memory conductance of a magnetic flux-controlled memristor [54], it is used to calculate the effect of feedback regulation on the

membrane potential when the magnetic flux is changed, and α and β are fixed parameters. Therefore, as in [54], the induced current and electromagnetic induction can be described by

$$i' = \frac{dq(\varphi)}{dt} = \frac{dq(\varphi)}{d\varphi} \frac{d\varphi}{dt} = \rho(\varphi) \frac{d\varphi}{dt} = \frac{d\varphi}{dt} (\alpha + 3\beta\varphi^2), \quad \frac{d\varphi}{dt} = kV. \quad (3)$$

The variable i' represents induction current. The term $-k\rho(\varphi)V$ represents the inhibitory modulation of membrane potential, and it describes the induced current induced by electromagnetic induction. The parameter k is the induction coefficient, and its value depends mainly on the medium itself. I_{ext} is the external forcing current. The terms k_1x and $k_2\varphi$ in the (1) mean the influence of membrane potential on magnetic flux and leakage of magnetic flux, respectively.

For the analysis of the possibility and stability of the synchronized dynamics between two neurons under bidirectional coupling, the dynamic equations are given by

$$\begin{aligned} c \frac{dV_{\alpha,\beta}}{dt} &= g_{\text{Ca}} m_{\infty}(V_{\alpha,\beta}) (V_{\text{Ca}} - V_{\alpha,\beta}) + g_{\text{K}} \omega_{\alpha,\beta} (V_{\text{K}} - V_{\alpha,\beta}) \\ &\quad + g_{\text{L}} (V_{\text{L}} - V_{\alpha,\beta}) - k\rho(\varphi_{\alpha,\beta}) V_{\alpha,\beta} + I_{\text{ext}} + I_{\text{syn}} \\ &\quad + C(V_{\alpha,\beta} - V_{\beta,\alpha}), \\ \frac{d\omega_{\alpha,\beta}}{dt} &= \lambda_{\omega}(V_{\alpha,\beta}) (\omega_{\infty}(V_{\alpha,\beta}) - \omega_{\alpha,\beta}), \\ \frac{d\varphi_{\alpha,\beta}}{dt} &= k_1 V_{\alpha,\beta} - k_2 \varphi_{\alpha,\beta}, \end{aligned} \quad (4)$$

where the subscripts α and β are a pair of coupled ML neurons under electromagnetic radiation. C denotes coupling intensity between adjacent neurons.

In order to simulate the chemical synapse feedback of neurons, we shall use the so-called fast threshold modulation scheme proposed by Somers and Kopell [55] and often used by others, for example, [56, 57]. This chemically feedback form, which clearly combines the time lag of the synapse, is provided by the following functions:

$$I_{\text{syn}} = -\frac{H_{\text{syn}}(V_{\alpha\beta} - V_{\text{syn}})}{1 + \exp[-\sigma(V_{\alpha\beta}(t - \tau) - \theta)]}. \quad (5)$$

The variable parameter H_{syn} is the feedback gain at time t with itself connected at time $t - \tau$. The symbol τ indicates the time lag (ms) of the signal propagation. C is coupling strength between two neurons. V_{syn} represents the synaptic reversal potential (mV), which depends on the presynaptic neurons and receiver. The chemical coupling is characterized by the difference between the synaptic reversal potential and the synaptic potential. A positive or negative sign of the difference corresponds to an excitatory or inhibitory effect of the synapse. If the synapsis is excitatory, $V_{\text{syn}} = 15$ mV, and if the synapsis is inhibitory, $V_{\text{syn}} = -10$ mV. The parameter θ is a synaptic threshold. Considering that the neuron membrane

potential value of the improved ML model is between -17 mV and 15 mV, $\theta = 4$ mV is selected to ensure that the spike of the V is over the threshold, and the quiescent state of the V is less than the threshold. That is, the membrane potential of the presynaptic neuron is more than θ , and it can play a role in the postsynaptic neuron [58, 59]. σ is the ratio constant to the start of excitement or inhibition. In this paper, we focus on the collective behavior of the two coupled neuron system driven by the excitatory and inhibitory autapse, and the schematic diagram is shown in Figure 1. Parameters of the improved ML neuronal model are given as $c = 20 \mu\text{F}$, $V_{\text{Ca}} = 120$ mV, $V_{\text{K}} = -84$ mV, $V_{\text{L}} = -60$ mV, $g_{\text{Ca}} = 4$ mS, $g_{\text{K}} = 8$ mS, $g_{\text{L}} = 2$ mS, $V_1 = -1.2$ mV, $V_2 = 18$ mV, $V_3 = 12$ mV, $V_4 = 17.4$ mV, $\phi = 0.067$, $k_1 = 0.1$, $k_2 = 0.01$, and $\sigma = -1$.

To characterize the synchronization in the system of coupled spiking neurons, a method of calculating the error function is introduced in the following [24]:

$$e = \sqrt{(V_{\alpha} - V_{\beta})^2 + (\omega_{\alpha} - \omega_{\beta})^2 + (\varphi_{\alpha} - \varphi_{\beta})^2}. \quad (6)$$

Equation (6) indicates that the lower the value of e corresponds with the better synchronization in the system.

3. Results and Discussion

In this section, first of all, the bifurcation is theoretically analyzed to reveal the dynamic mechanism of the discharge mode in the improved model (1). Then the fourth-order Runge-Kutta method is used to calculate the improved ML neuronal model, the step of time h is selected as 0.01, and the transient period for calculating is 5000 time units.

Let

$$\begin{aligned} \frac{dV}{dt} &= f(V, \omega, \varphi), \\ \frac{d\omega}{dt} &= g(V, \omega, \varphi), \\ \frac{d\varphi}{dt} &= h(V, \omega, \varphi), \end{aligned} \quad (7)$$

and $(V_s, \omega_s, \varphi_s)$ is the equilibrium point; that is,

$$f(V_s, \omega_s, \varphi_s) = g(V_s, \omega_s, \varphi_s) = h(V_s, \omega_s, \varphi_s) = 0. \quad (8)$$

If the parameter $k = 0.1$, the system (8) can be written in the form

$$\begin{aligned} 4m_{\infty}(V_s)(120 - V_s) + 8\omega_s(-84 - V_s) + 2(-60 - V_s) - 0.1(0.1 + 0.03\varphi_s^2)V_s + I_{\text{ext}} &= 0, \\ \omega_s &= \omega_{\infty} = 0.5 + 0.5 \tanh\left(\frac{V_s + 12}{17.4}\right), \\ \varphi_s &= 10V_s, \end{aligned} \quad (9)$$

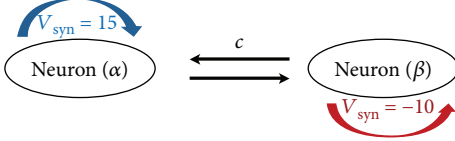


FIGURE 1: A schematic diagram of the coupled neuron system.

and thus,

$$2\left(1 + \tanh \frac{V_s + 1.2}{18}\right) - 4\left(1 + \tanh \frac{V_s - 12}{17.4}\right) - 2(60 + V_s) - 0.1V_s(0.1 + 3V_s^2) + I_{\text{ext}} = 0. \quad (10)$$

Obviously, the expression of the equilibrium point $(V_s, \omega_s, \varphi_s)$ can be obtained by (10). Then we analyze the stability of the equilibrium point with I_{ext} as the bifurcation parameter. It is noted that the stability of the equilibrium point is determined by the eigenvalue of its Jacob matrix; that is, when all the eigenvalues are a negative real part, then the equilibrium point is stable; otherwise, it may be marginally stable or unstable [60]. The appearance of a pair of pure imaginary eigenvalues signifies Hopf bifurcation [61].

At the equilibrium point $(V_s, \omega_s, \varphi_s)$, the linearization Jacobi matrix of the improved model is that

$$\mathbf{J}(V_s, \omega_s, \varphi_s) = \begin{bmatrix} \frac{1}{c} \left[-4m_\infty V_s + (480 - 4V_s) \frac{\partial m_\infty}{\partial V} - 8\omega_s - 2.01 - 0.003\varphi_s^2 \right] & \frac{8}{c}(84 + V_s) & -0.006 \frac{V_s \varphi_s}{c} \\ (\omega_\infty - \omega_s) \frac{\partial \lambda_\infty}{\partial V} + \lambda_\infty \frac{\partial m_\infty}{\partial V} & -\lambda_\infty & 0 \\ 0.1 & 0 & 0.01 \end{bmatrix}. \quad (11)$$

Therefore, the characteristic determinant of this system at the equilibrium point is

$$|\mathbf{J}(V_s, \omega_s, \varphi_s) - \lambda \mathbf{I}| = \begin{vmatrix} \frac{1}{c} \left[-4m_\infty V_s + (480 - 4V_s) \frac{\partial m_\infty}{\partial V} - 8\omega_s - 2.01 - 0.003\varphi_s^2 \right] - \lambda & -\frac{8}{c}(84 + V_s) & -0.006 \frac{V_s \varphi_s}{c} \\ (\omega_\infty - \omega_s) \frac{\partial \lambda_\infty}{\partial V} + \lambda_\infty \frac{\partial m_\infty}{\partial V} & -\lambda_\infty - \lambda & 0 \\ 0.1 & 0 & 0.01 - \lambda \end{vmatrix} = 0, \quad (12)$$

where

$$\begin{aligned} \frac{\partial m_\infty}{\partial V} &= \frac{19}{36} - \frac{1}{2} \tanh^2 \left(\frac{V_s + 1.2}{18} \right), \\ \frac{\partial \omega_\infty}{\partial V} &= \frac{46}{87} - \frac{1}{2} \tanh^2 \left(\frac{V_s - 12}{17.4} \right), \\ \frac{\partial \omega_\infty}{\partial V} &= \frac{46}{87} - \frac{1}{2} \tanh^2 \left(\frac{V_s - 12}{17.4} \right). \end{aligned} \quad (13)$$

If the Jacobi matrix has one eigenvalue of the negative real part and two zero real parts at a critical value of the bifurcation parameter, then we usually say that a Hopf bifurcation occurs [61]. According to the relationship between λ and I_{ext} , we calculate the branch of the equilibrium point which undergoes two Hopf bifurcations at parameter $I_{\text{ext}1} = -27.99$ and $I_{\text{ext}2} = 23.79$. Obviously, they correspond to the bifurcation points HB in Figure 2(b). Similarly, the

corresponding bifurcation points can be obtained by changing the parameter k .

The results of the bifurcation analysis for the system with the electromagnetic effect described by (1) are numerically simulated. In the bifurcation analysis, the influence of the external forcing current I_{ext} on the discharge behavior of the neuron under different electromagnetic effects known as induction coefficient k is investigated. The system will have the process of “resting-exciting-silent” by increasing the external forcing current. In Figure 2, several typical bifurcation diagrams for the different external forcing currents, without ($k = 0$) and with ($k \neq 0$) the electromagnetic effects, are plotted, respectively.

Figure 2 shows the bifurcation with I_{ext} as the bifurcation parameter for six different values of the induction coefficient. The equilibrium point of the system has undergone five changes without electromagnetic radiation, as shown in Figure 2(a). In the beginning, the system has only a stable equilibrium point, and the action potential of the neuron will

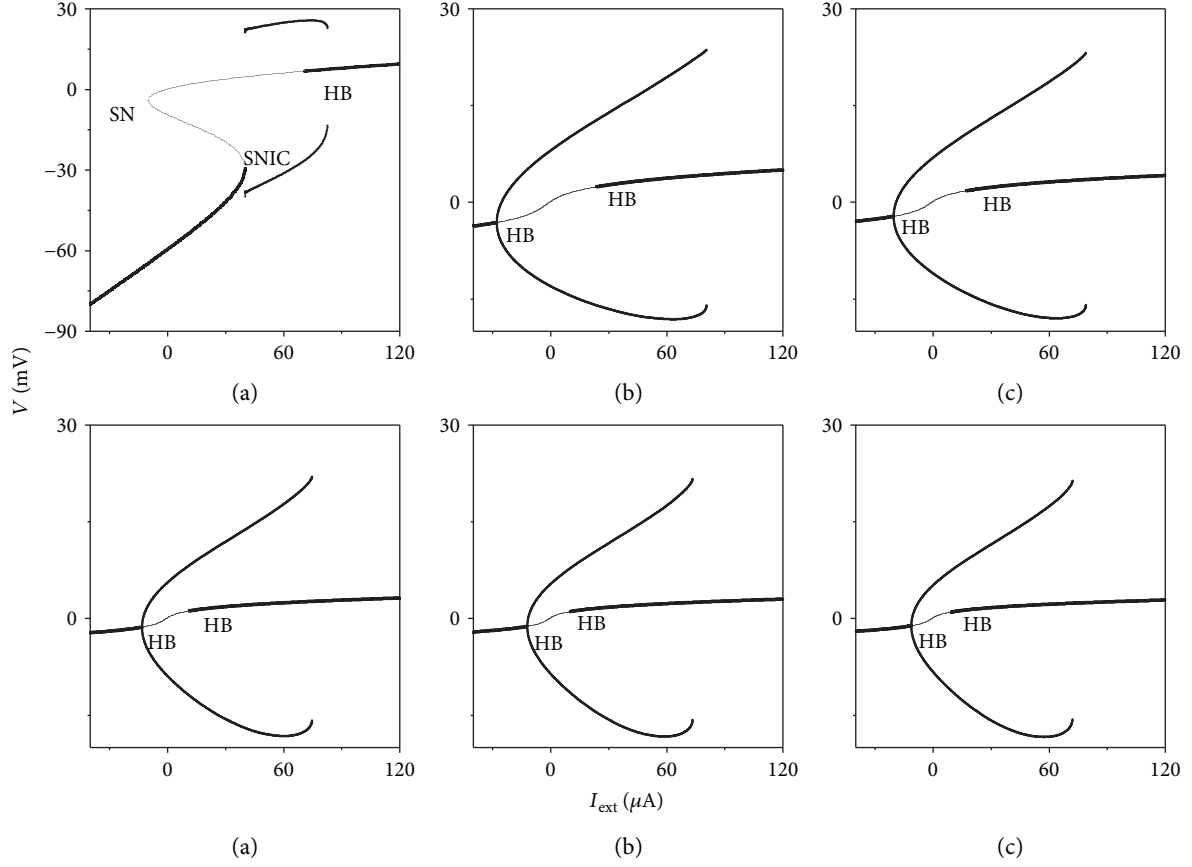


FIGURE 2: The bifurcation diagrams of V_{\max} and V_{\min} for the improved ML neuronal model driven by an external forcing current at $k_1 = 0.1$ and $k_2 = 0.01$; for (a) $k = 0$, (b) $k = 0.1$, (c) $k = 0.2$, (d) $k = 0.4$, (e) $k = 0.5$, and (f) $k = 0.6$.

eventually converge to a fixed value. When $I_{\text{ext}} > -9.93 \mu\text{A}$, there exist three equilibrium points, of which two are unstable, and the action potential of the neuron will still converge to a fixed value. As the external current increases, the excitability of neurons in the saddle node bifurcation threshold is obtained, the threshold is $I_{\text{ext}} = 40 \mu\text{A}$, and at this time, the membrane potential of the neuron is periodic discharge. On further increased I_{ext} , bistable state can be generated at $I_{\text{ext}} = 70.4 \mu\text{A}$, which corresponds to a subcritical Hopf bifurcation point. The limit cycle vanishes $I_{\text{ext}} = 82.5 \mu\text{A}$, and the system has only a stable state. The properties and positions of the bifurcation points have changed thoroughly, considering the neuron system after the electromagnetic effect, and the results are found in Figures 2(b)–2(f). There are two Hopf bifurcation points of the ML neuron system with the electromagnetic effect. The results in Figure 3(b) confirm the Hopf bifurcation points at $I_{\text{ext}} = -28.48 \mu\text{A}$ and $23.55 \mu\text{A}$. As the induction coefficient k increases, a similar phenomenon is observed and the corresponding bifurcations are summarized in Table 1.

It can be noted from Table 1 that parameters describe the interaction between membrane potential and magnetic flux which is further increased to $k = 0.6$, the threshold of excitability is increased to a higher value corresponding to $I_{\text{ext}} = -11.39 \mu\text{A}$ (see Figure 1 and Table 1). However, the position of the second bifurcation point was reduced from 23.55 mV

to 9.0 mV . That is to say, with the increase of the induction coefficient k , the region of the limit cycle in the system is gradually compressed. It should be pointed out that the system has a Hopf bifurcation point HOPF1 with a negative value of parameter I_{ext} (see Table 1), which will not be considered in the following text since it loses the biophysical meaning. At the same time, in the numerical simulation, we find that when $I_{\text{ext}} > \text{HOPF2}$, the selection of the initial value of the system is as important as the external current. Based on the analysis of the bifurcation diagram of V_{\max} and V_{\min} for the improved ML neuronal model, the external forcing currents $I_{\text{ext}} = 40 \mu\text{A}$, $I_{\text{ext}} = 50 \mu\text{A}$, $I_{\text{ext}} = 60 \mu\text{A}$, $I_{\text{ext}} = 70 \mu\text{A}$, and $I_{\text{ext}} = 80 \mu\text{A}$ are chosen to impose on the neuron. The type of membrane potential discharge at different initial values is calculated in Figure 3.

The results in Figure 3 show that the initial values of V_0 and ω_0 have a great influence on the discharge of neurons in the improved ML model. The oscillating areas of the membrane potential are reduced by the increase of the external stimulation current; that is, the red area in the picture becomes smaller. The oscillating region of the membrane potential is found to be banded, which indicates the changes in the initial value of φ_0 with little effects on the discharge of neurons as shown in Figure 3, a2–e2 and a3–e3.

The results in Figure 4 show that the initial value region that produces the oscillations of the membrane potential is

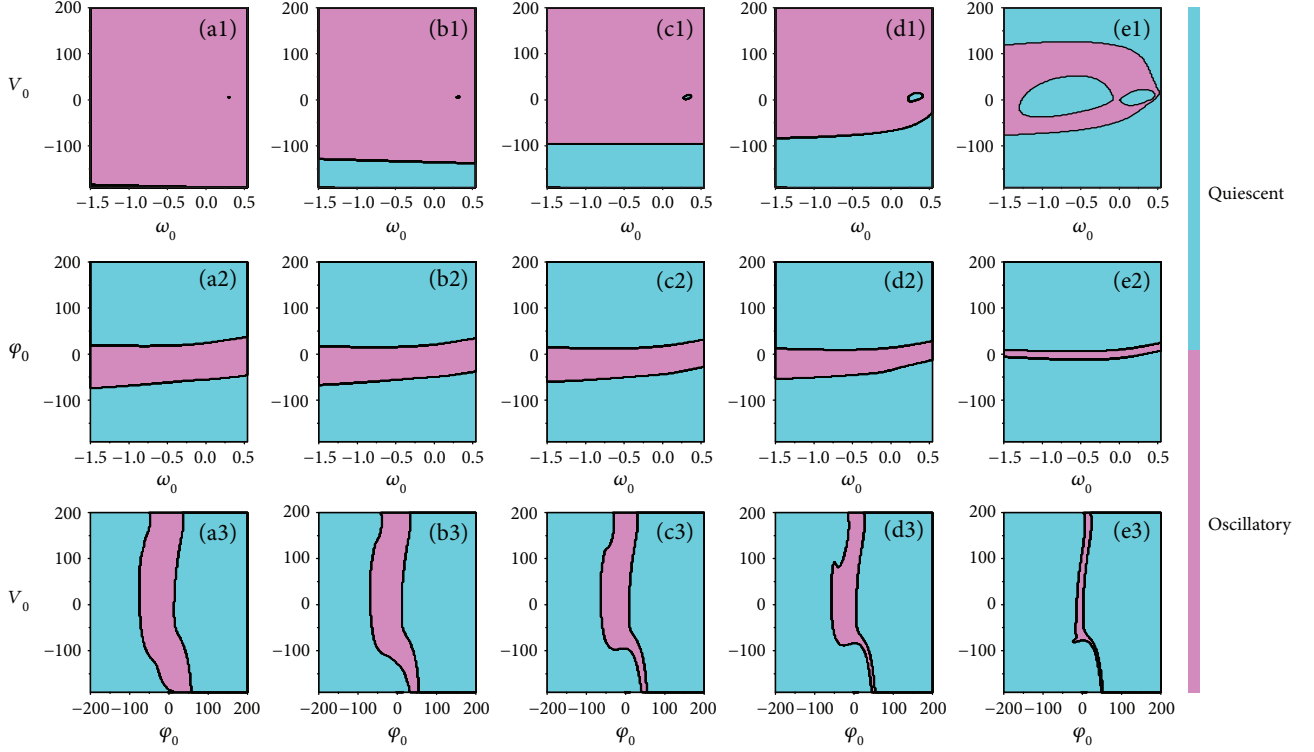


FIGURE 3: The regional distribution diagram of resting state and oscillating state under different initial values, for (a1–e1) $\varphi_0 = 0.1$ and $I_{\text{ext}} = 40, 50, 60, 70$, and 80 ; for (a2–e2) $V_0 = 80$ and $I_{\text{ext}} = 40, 50, 60, 70$, and 80 ; and for (a3–e3) $\omega_0 = -1.5$ and $I_{\text{ext}} = 40, 50, 60, 70$, and 80 .

TABLE 1: Summary of the type and position of bifurcation point.

k		0.1	0.2	0.4	0.5	0.6
$I_{\text{ext}} (\mu\text{A})$	HOPF1	-28.48	-20.75	-13.74	-12.27	-11.39
	HOPF2	23.55	17.40	10.97	10.17	9.0

reduced by the increase of the external stimulation current. Most interesting, the study found that the selection of the initial value will also be influenced by the induction coefficient k under the same external stimulus current. This discovery is in accordance with the bifurcation diagram of Figure 2. Therefore, it is very important to choose the appropriate initial value with the different induction coefficients k . According to the initial value area shown in Figures 3 and 4, sampled time series for membrane potential and phase portraits are plotted in Figure 5.

The improved ML neural model can exhibit several kinds of oscillations. When the initial value is determined, the electric activity depends on the external forcing current. The change of electrical activity between the quiescent state and the spiking state can be observed by selecting different external forcing currents. The phase portraits of the external forcing currents (μA) are chosen as 0, 10, 20, 30, 40, and 80 in Figure 5(a). And Figures 5(b) and 5(c) show the time series of the membrane potential for $I_{\text{ext}} = 0, 40$, and 80 .

The numerical results in Figure 5(a) show that the regions of limit cycles become larger with increasing the external forcing current. There exist some thresholds in the system, which determines the conversion of the discharge

mode of the neuron membrane potential. In the absence of external excitation, the neuron can still be discharged under the electromagnetic effect, as shown by the blue curve in Figure 5(b). With increasing the external forcing current, the amplitude of the neuron membrane potential will increase gradually; in other words, the amplitude of the periodic oscillation is related to the area size of the limit cycle. When the external forcing current is increased to a certain threshold, the system will change from the oscillating state to the resting state, as depicted in Figure 5(c).

Meanwhile, we studied the collective behavior of the two neurons driven by the excitatory autapse and inhibitory autapse in the case of electric coupling. The initial values are $V_0 = 100 \text{ mV}$, $\omega_0 = -1.5 \mu\text{A}$, and $\varphi_0 = 0.1$, and the external forcing current $I_{\text{ext}} = 40 \mu\text{A}$ is chosen for its simplicity; the induction coefficient is $k = 0.1$. At first, the inter-spike interval of the β -neuron membrane potential (as in ISI representation) at different feedback gain H_{syn} is calculated, and the results are plotted in Figures 6 and 7.

Presented results show clearly that feedback gain H_{syn} as well as coupling strengths plays an important role in the modes of electrical activities. When the value of H_{syn} is smaller, the rich discharge modes are observed in Figure 6. The value of the bifurcation point is also affected by the coupling intensity. It is found that the mode of β -neuron discharge does not exhibit periodicity, unless larger feedback gain could be applied. In essence, there may be two types of autapse in the system, and the increase of H_{syn} makes the difference in the discharge of the two neurons increasing; that is,

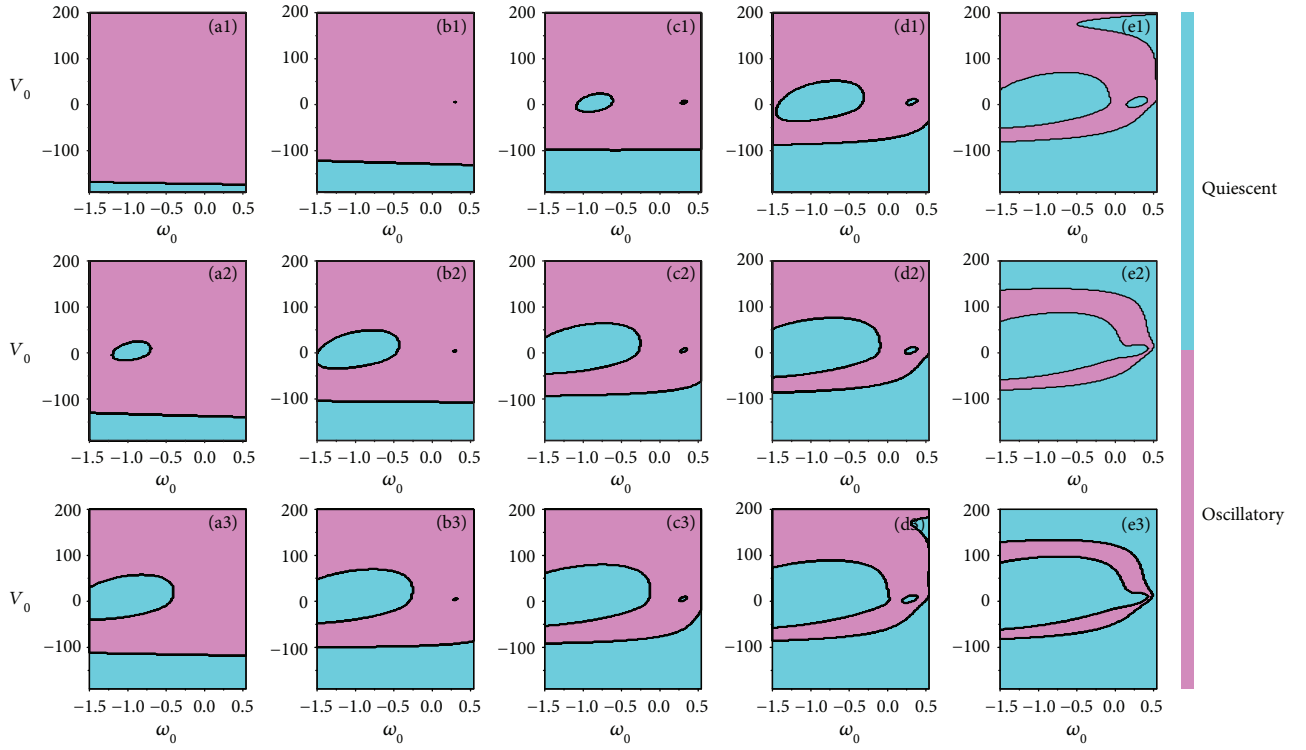


FIGURE 4: The regional distribution diagram of the resting state and oscillating state under different initial values at $\varphi_0 = 0.1$, for (a1–e1) $k = 0.2$ and $I_{\text{ext}} = 30, 40, 50, 60$, and 70 ; for (a2–e2) $k = 0.3$ and $I_{\text{ext}} = 30, 40, 50, 60$, and 70 ; and for (a3–e3) $k = 0.4$ and $I_{\text{ext}} = 30, 40, 50, 60$, and 70 .

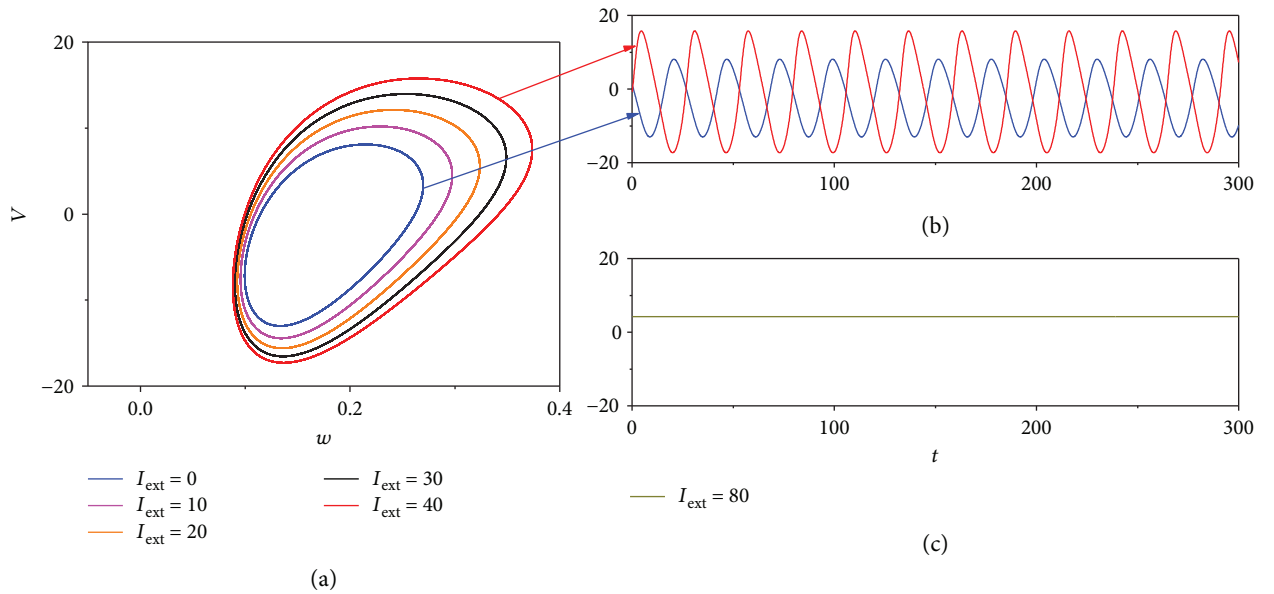


FIGURE 5: Sampled time series for membrane potential and phase portraits when different currents are calculated at the initial values $V_0 = 100$, $\omega_0 = -0.1$, and $\varphi_0 = 0.1$, and the induction coefficient is $k = 0.1$.

the inhibitory neurons tend to be quiescent and hence cannot affect the excitatory neurons. However, it can be observed that the modes of electrical activities depend significantly on the values of the synaptic feedback gain.

Within a certain coupling strength, if the error e tends to zero with the time increased, the coupled neurons are fully synchronized. According to the analysis of the results of Figure 6, the sampled time series for membrane potential

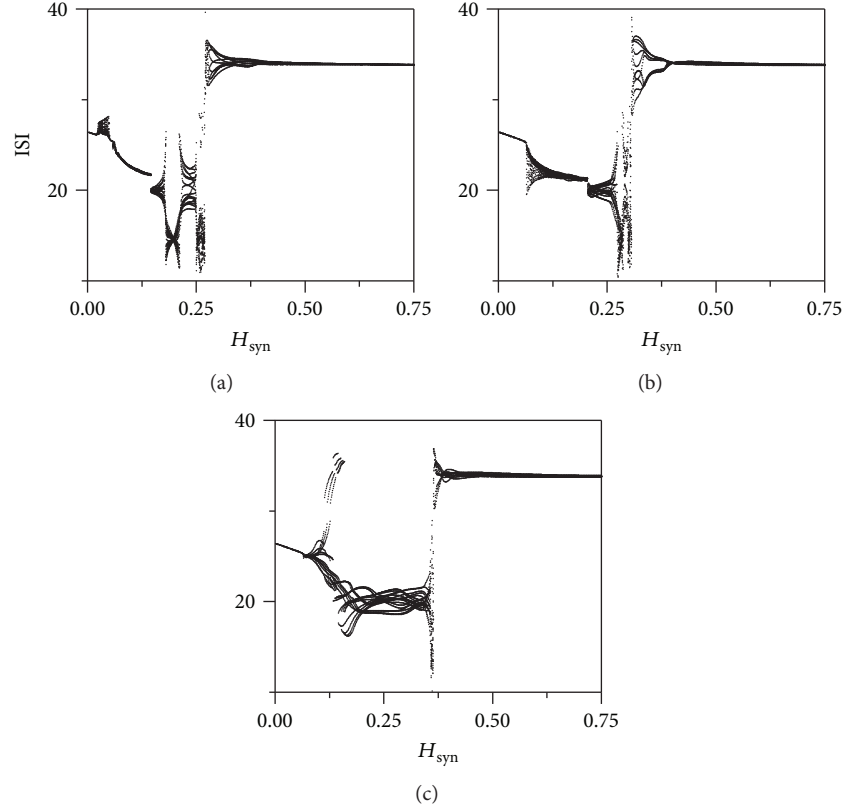


FIGURE 6: Bifurcation diagram associated with feedback gain H_{syn} for different coupling strengths. The time lag $\tau = 50$, (a) $C = 0.1$; (b) $C = 0.5$; and (c) $C = 1$.

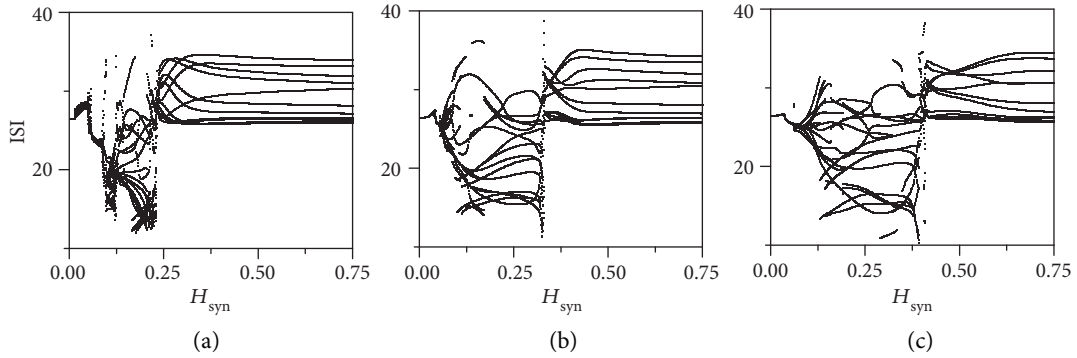


FIGURE 7: Bifurcation diagram associated with feedback gain H_{syn} for different coupling strengths. The time lag $\tau = 100$, (a) $C = 0.1$; (b) $C = 0.5$; and (c) $C = 1$.

and phase portraits of the coupling strength $C = 0.5$ are calculated with different feedback gains H_{syn} ; the results are plotted in Figure 8.

The phase portraits and time series of the membrane potential of two coupled neurons are illustrated in Figure 8. The limit cycle is shown in Figure 8(a1), indicating that the β -neuron is periodic discharge. The region of the two limit cycles is different in Figure 8, (a2), and the value of the V is within the range of -20 mV to 20 mV. The phase portrait of (V_β, V_α) is located near the corner line of the first quadrant, which means the occurrence of approximate synchronization. The error e (blue line) is found to exhibit periodic

oscillations in Figure 8, (a3). Interestingly, when the coupling strength C is further increased, the phase portrait of (V_β, V_α) tends to have a straight line, and the results are shown in Figure 9.

The results in Figure 9 confirmed that the phase portrait of (V_β, V_α) coincides with a straight line, which is located on the angle bisector of the first quadrant. With appropriate time lag and feedback gain, the two coupled neuron system will synchronize with the increase of the coupling strength between neurons. For the improved model in this paper, the numerical results show that phase synchrony can be achieved by selecting the appropriate coupling intensity of

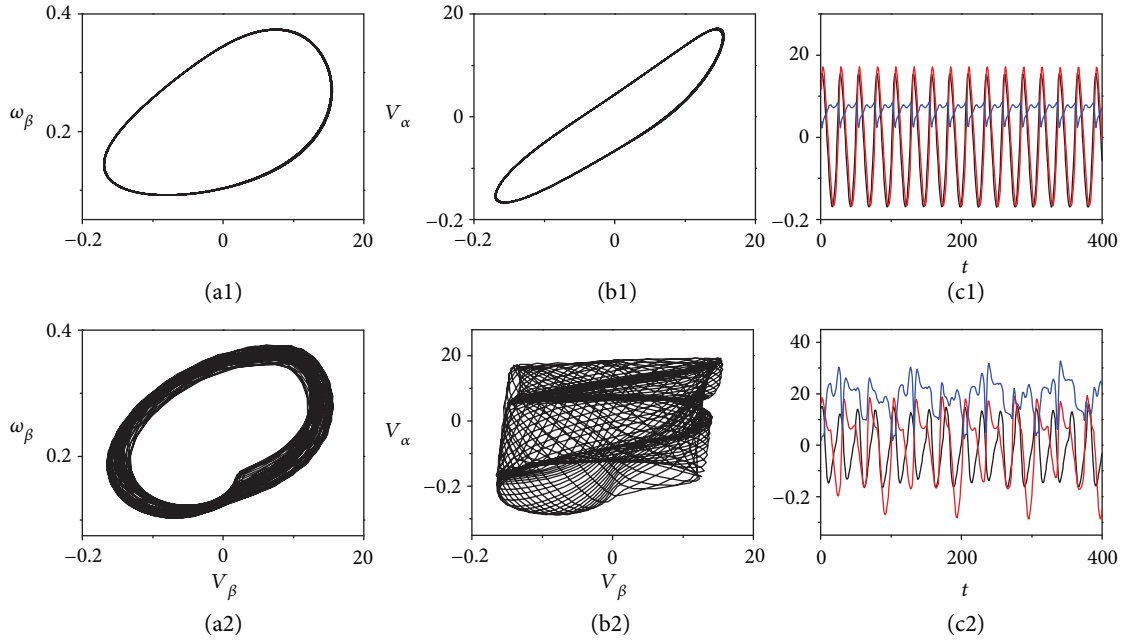


FIGURE 8: Numerical simulation of the two neuron system. The parameters are chosen as $C = 0.5$ and $\tau = 50$ ms. (a1) The phase portrait of (V_β, ω_β) , $H_{\text{syn}} = 0.03$. (a2) The phase portrait of (V_β, V_α) , $H_{\text{syn}} = 0.03$. (a3) The time series of V_β (black line), V_α (red line), and e (blue line), $H_{\text{syn}} = 0.03$. (b1) The phase portrait of (V_β, ω_β) , $H_{\text{syn}} = 0.32$. (b2) The phase portrait of (V_β, V_α) , $H_{\text{syn}} = 0.32$. (b3) The time series of V_β (black line), V_α (red line), and e (blue line), $H_{\text{syn}} = 0.32$.

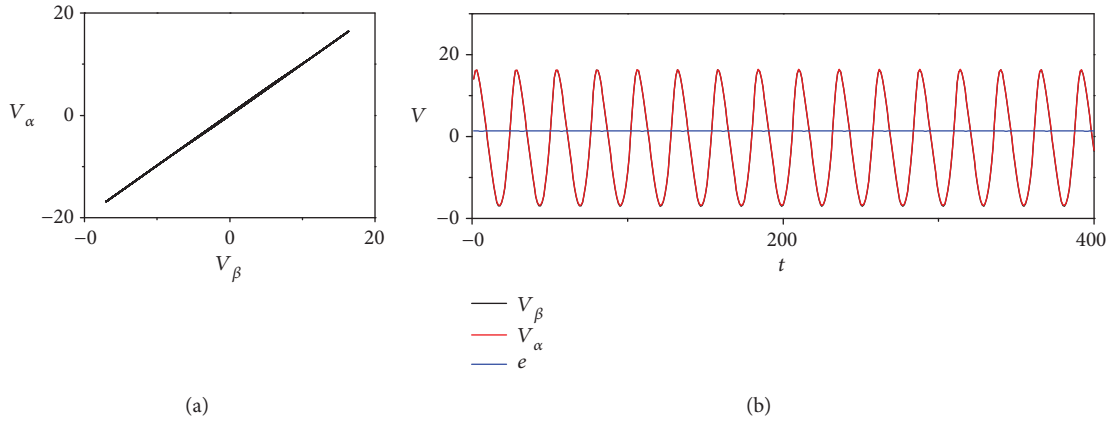


FIGURE 9: Phase portraits and sampled time series of membrane potential are calculated at coupling strength $C = 20$, feedback gain $H_{\text{syn}} = 0.03$, and time lag $\tau = 50$ ms.

the two neurons with electromagnetic radiation. The effect of time lag in autapse should also be considered; for example, the time lag is increased to 100 ms, and some results are found in Figures 7 and 10.

Results presented in Figure 7 reveal that the oscillatory pattern is largely influenced by the synaptic delay. For suitably long values of τ , a complex oscillatory pattern can be observed. Interestingly, however, if the H_{syn} is sufficiently high, we can observe the emergence of a periodic firing, which implies that there is a transition from chaos to periodic discharge in the system. Theoretically, under sufficiently long synaptic delay condition, neurons have enough time to fire more than once during a whole periodic cycle, before the

synaptic currents caused by the first synchronous spiking within the same periodic cycle start to affect their firing [62].

It is found in Figure 10 that spiking and bursting discharge behaviors of β -neuron reappear depending on the gain and delay of the autapse. The error e is observed to increase obviously through the time lag from 50 ms to 100 ms. But what is more interesting is that the increment of τ makes the amplitude of the membrane potential of α -neuron (excitatory) decrease in Figure 10, (a3). This trend may be that the role of the autapse is suppressed in the appropriate feedback gain and time lag. Therefore, the time lag plays a crucial role in the dynamics of the coupled system. Numerical studies on the synchronization of the two coupled

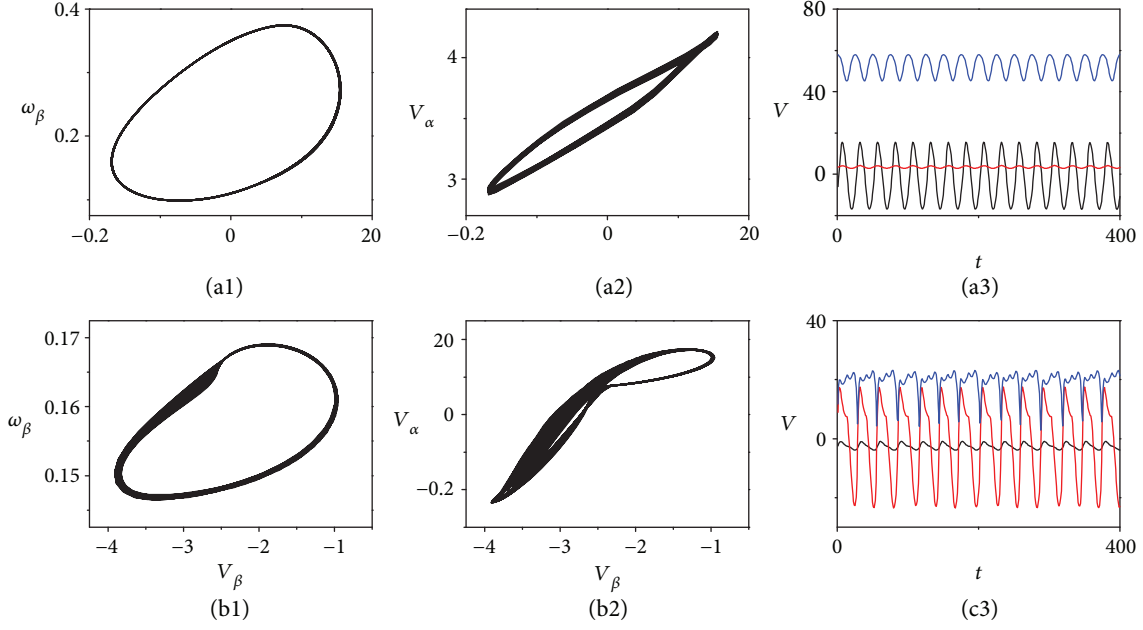


FIGURE 10: Numerical simulations of the two neuron system. the parameters are chosen as $C = 0.5$ and $\tau = 100$ ms. (a1) The phase portrait of (V_β, ω_β) , $H_{\text{syn}} = 0.1$. (a2) The phase portrait of (V_β, V_α) , $H_{\text{syn}} = 0.1$. (a3) The time series of V_β (black line), V_α (red line), and e (blue line), $H_{\text{syn}} = 0.1$. (b1) The phase portrait of (V_β, ω_β) , $H_{\text{syn}} = 0.4$. (b2) The phase portrait of (V_β, V_α) , $H_{\text{syn}} = 0.4$. (b3) The time series of V_β (black line), V_α (red line), and e (blue line), $H_{\text{syn}} = 0.4$.

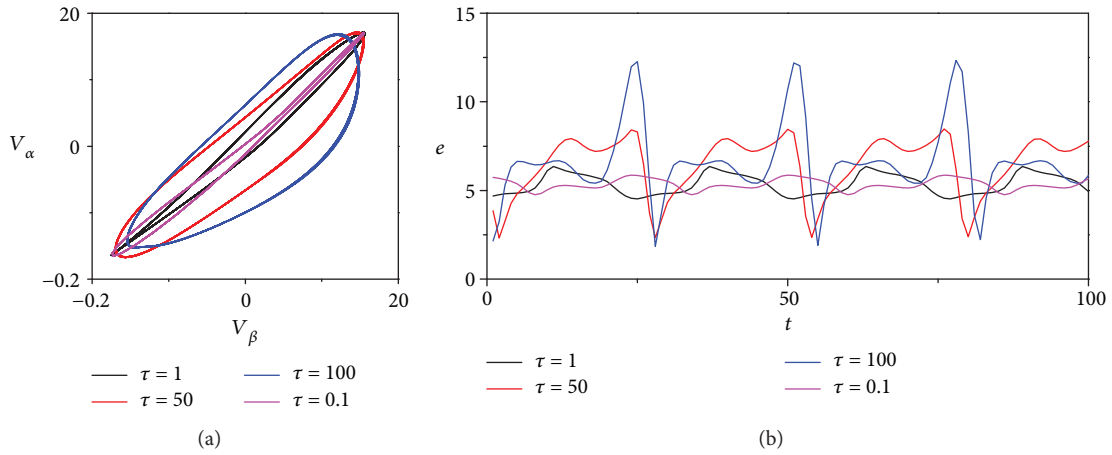


FIGURE 11: Phase portraits and error e when different time-lag are calculated at $H_{\text{syn}} = 0.03$, and the coupling strength $C = 0.5$.

neuron system are affected with time lag, and the results are shown in Figure 11.

The trajectories when $H_{\text{syn}} = 0.03$ indicate that the system of the two coupled neuron system is in the oscillation in Figure 11. When the time lag is 0.1, the membrane potential error e of the neurons is smaller. Although the electrical coupling plays a dominant role in the synchronization of the system, the feedback gain from the synapse and time lag are equally important. The increment of time lag is not conducive to the synchronization of the coupling neuron system. This conclusion is consistent with the result of Figure 10.

4. Conclusions

In this paper, the dynamics of the improved Morris-Lecar neuron model under electromagnetic induction were investigated using bifurcation diagrams and time series of discharge; phase portraits of the neuron under different conditions are investigated in a numerical manner as well. By analyzing the simple numerical simulation of the improved model, the basic dynamic behaviors are obtained by introducing an external forcing current. In the case of the electromagnetic induction, the mechanism of neuron firing has been changed. That is, two Hopf bifurcation points

are found with changing the external forcing current. Comparing these results with a previous work [33, 58], the bifurcation diagram has an obvious difference due to the consideration of electromagnetic induction based on the ML neural model. In fact, the fluctuation in membrane potential and signal propagation in the neuronal system can generate an induced electrical field and additive current in the media due to electromagnetic induction. As a result, the membrane potential of a neuron can be adjusted slightly by induction field and induced current associated with the variation of magnetic flux. By analyzing the interspike interval series of neural firing, we find that the improved model can generate electrical activity with multiple modes. These results are consistent with the observation observed in the experiment [8]. Meanwhile, the preliminary synchronization analysis of a system of excitatory and inhibitory neurons was conducted. In this aspect, it was unveiled that the neurons in the system can be synchronized by selecting an appropriate coupling strength. A longer time lag is not conducive to the system synchronization, and the higher the feedback gain H_{syn} and the longer the time lag τ are, the more obvious the electrical mode changes in the two coupled neuron system; this conclusion is in accordance with previous experiments [63]. Synchronization phenomena are associated with either brain functions [64] or pathological brain states in the neural system. For example, Stam and Bruin used synchronization likelihood to characterize statistical interdependencies between EEG and MEG (magneto encephalography) signals in early and mild Alzheimer's disease [65, 66]. Rubchinsky et al. [67] presented extensive experimental documentation of the relevance of synchronized oscillations to motor behavior in Parkinson's disease, and they confirmed that the real pathological state is not completely synchronous but showed a complex weak synchronization and highly intermittent dynamics. These results could provide potential theoretical supports for the treatment of neurological diseases.

Data Availability

The data used to support the findings of this study are available from the corresponding author upon request.

Conflicts of Interest

The authors declare that they have no conflicts of interest.

Acknowledgments

The authors gratefully thank Professor Jun Ma from the Lanzhou University of Technology for his constructive suggestions. This work was supported by the National Natural Science Foundation of China, under Grant nos. 11775091, 11474117, and 11605014.

References

- [1] R. FitzHugh, "Impulses and physiological states in theoretical models of nerve membrane," *Biophysical Journal*, vol. 1, no. 6, pp. 445–466, 1961.
- [2] C. Morris and H. Lecar, "Voltage oscillations in the barnacle giant muscle fiber," *Biophysical Journal*, vol. 35, no. 1, pp. 193–213, 1981.
- [3] J. L. Hindmarsh and R. M. Rose, "A model of the nerve impulse using two first-order differential equations," *Nature*, vol. 296, no. 5853, pp. 162–164, 1982.
- [4] M. Storace, D. Linaro, and E. de Lange, "The Hindmarsh–Rose neuron model: an bifurcation analysis and piecewise-linear approximations," *Chaos: An Interdisciplinary Journal of Nonlinear Science*, vol. 18, no. 3, article 033128, 2008.
- [5] J. Nagumo and S. Sato, "On a response characteristic of a mathematical neuron model," *Kybernetik*, vol. 10, no. 3, pp. 155–164, 1972.
- [6] H. R. Wilson and J. D. Cowan, "Excitatory and inhibitory interactions in localized populations of model neurons," *Biophysical Journal*, vol. 12, no. 1, pp. 1–24, 1972.
- [7] A. L. Hodgkin and A. F. Huxley, "The dual effect of membrane potential on sodium conductance in the giant axon of Loligo," *The Journal of Physiology*, vol. 116, no. 4, pp. 497–506, 1952.
- [8] H. Gu, W. Ren, Q. Lu, S. Wu, M. Yang, and W. Chen, "Integer multiple spiking in neuronal pacemakers without external periodic stimulation," *Physics Letters A*, vol. 285, no. 1–2, pp. 63–68, 2001.
- [9] M. T. M. Koper and B. D. Aguda, "Experimental demonstration of delay and memory effects in the bifurcations of nickel electrodisolution," *Physical Review E*, vol. 54, no. 1, pp. 960–963, 1996.
- [10] H. Gu, "Experimental observation of transition from chaotic bursting to chaotic spiking in a neural pacemaker," *Chaos: An Interdisciplinary Journal of Nonlinear Science*, vol. 23, no. 2, p. 023126, 2013.
- [11] K. Tsumoto, H. Kitajima, T. Yoshinaga, K. Aihara, and H. Kawakami, "Bifurcations in Morris–Lecar neuron model," *Neurocomputing*, vol. 69, no. 4–6, pp. 293–316, 2006.
- [12] D. Golomb and J. Rinzel, "Clustering in globally coupled inhibitory neurons," *Physica D: Nonlinear Phenomena*, vol. 72, no. 3, pp. 259–282, 1994.
- [13] L. M. Pecora and T. L. Carroll, "Paper 9 - Synchronization in chaotic systems," in *Controlling Chaos*, T. Kapitaniak, Ed., vol. 6, pp. 142–145, Academic Press, San Diego, CA, USA, 1996. <http://www.sciencedirect.com/science/article/pii/B9780123968401500400>.
- [14] F. Varela, J. P. Lachaux, E. Rodriguez, and J. Martinerie, "The brainweb: phase synchronization and large-scale integration," *Nature Reviews Neuroscience*, vol. 2, no. 4, pp. 229–239, 2001.
- [15] M. Bazhenov, R. Huerta, M. I. Rabinovich, and T. Sejnowski, "Cooperative behavior of a chain of synaptically coupled chaotic neurons," *Physica D: Nonlinear Phenomena*, vol. 116, no. 3–4, pp. 392–400, 1998.
- [16] W. Zhang, Y. Tang, X. Wu, and J. A. Fang, "Synchronization of nonlinear dynamical networks with heterogeneous impulses," *IEEE Transactions on Circuits and Systems I: Regular Papers*, vol. 61, no. 4, pp. 1220–1228, 2014.
- [17] N. Burić, K. Todorović, and N. Vasović, "Synchronization of bursting neurons with delayed chemical synapses," *Physical Review E*, vol. 78, no. 3, article 036211, 2008.
- [18] Y. Xu, Y. Jia, J. Ma, T. Hayat, and A. Alsaedi, "Collective responses in electrical activities of neurons under field coupling," *Scientific Reports*, vol. 8, no. 1, p. 1349, 2018.
- [19] C. Yao, M. Zhan, J. Shuai, J. Ma, and J. Kurths, "Insensitivity of synchronization to network structure in chaotic pendulum

- systems with time-delay coupling,” *Chaos*, vol. 27, no. 12, article 126702, 2017.
- [20] P. M. Gokul and T. Kapitaniak, “Synchronization in coupled multistable systems with hidden attractors,” *Mathematical Problems in Engineering*, vol. 2017, Article ID 5214235, 6 pages, 2017.
 - [21] M. Zhan, G. Hu, and J. Yang, “Synchronization of chaos in coupled systems,” *Physical Review E*, vol. 62, no. 2, pp. 2963–2966, 2000.
 - [22] W. Zou and M. Zhan, “Complete periodic synchronization in coupled systems,” *Chaos*, vol. 18, no. 4, article 043115, 2008.
 - [23] G. Zhang, F. Wu, C. Wang, and J. Ma, “Synchronization behaviors of coupled systems composed of hidden attractors,” *International Journal of Modern Physics B*, vol. 31, no. 26, article 1750180, 2017.
 - [24] Y. Xu, Y. Jia, J. Ma, A. Alsaedi, and B. Ahmad, “Synchronization between neurons coupled by memristor,” *Chaos, Solitons & Fractals*, vol. 104, pp. 435–442, 2017.
 - [25] M. Gosak, M. Marhl, and M. Perc, “Pacemaker-guided noise-induced spatial periodicity in excitable media,” *Physica D: Nonlinear Phenomena*, vol. 238, no. 5, pp. 506–515, 2009.
 - [26] A. A. M. Yousif, L. Lu, M. Ge, Y. Xu, and Y. Jia, “Effects of intrinsic and extrinsic noises on transposons kinetics,” *Chinese Physics B*, vol. 27, no. 3, article 030501, 2018.
 - [27] Y. Xu, Y. Jia, M. Ge, L. Lu, L. Yang, and X. Zhan, “Effects of ion channel blocks on electrical activity of stochastic Hodgkin–Huxley neural network under electromagnetic induction,” *Neurocomputing*, vol. 283, pp. 196–204, 2018.
 - [28] Q. Y. Wang, Q. S. Lu, G. R. Chen, and D. H. Guo, “Chaos synchronization of coupled neurons with gap junctions,” *Physics Letters A*, vol. 356, no. 1, pp. 17–25, 2006.
 - [29] Y. Wu, J. Xu, and W. Jin, “Synchronous behaviors of two coupled neurons,” in *Advances in Neural Networks – ISSN 2005. ISSN 2005*, vol. 3496 of Lecture Notes in Computer Science, pp. 302–307, Springer, Berlin, Heidelberg, 2005.
 - [30] V.-T. Pham, C. Volos, S. Jafari, and T. Kapitaniak, “A novel cubic–equilibrium chaotic system with coexisting hidden attractors: analysis, and circuit implementation,” *Journal of Circuits, Systems and Computers*, vol. 27, no. 4, article 1850066, 2018.
 - [31] G. Ren, J. Tang, J. Ma, and Y. Xu, “Detection of noise effect on coupled neuronal circuits,” *Communications in Nonlinear Science and Numerical Simulation*, vol. 29, no. 1–3, pp. 170–178, 2015.
 - [32] M. Ozer and N. H. Ekmekci, “Effect of channel noise on the time-course of recovery from inactivation of sodium channels,” *Physics Letters A*, vol. 338, no. 2, pp. 150–154, 2005.
 - [33] L. Xue, J. Wang, B. Deng, and F. Dong, “Inhibitory chemical coupling of electronic Morris-Lecar neuron model and its bifurcation analysis,” in *2008 30th Annual International Conference of the IEEE Engineering in Medicine and Biology Society*, pp. 2461–2464, Vancouver, BC, Canada, August 2008.
 - [34] M. Nouri, G. R. Karimi, A. Ahmadi, and D. Abbott, “Digital multiplierless implementation of the biological FitzHugh–Nagumo model,” *Neurocomputing*, vol. 165, pp. 468–476, 2015.
 - [35] E. Tlelo-Cuautle, L. G. de la Fraga, V.-T. Pham, C. Volos, S. Jafari, and A. d. J. Quintas-Valles, “Dynamics, FPGA realization and application of a chaotic system with an infinite number of equilibrium points,” *Nonlinear Dynamics*, vol. 89, no. 2, pp. 1129–1139, 2017.
 - [36] S. Vaidyanathan, C. Volos, V.-T. Pham, K. Madhavan, and B. A. Idowu, “Adaptive backstepping control, synchronization and circuit simulation of a 3-D novel jerk chaotic system with two hyperbolic sinusoidal nonlinearities,” *Archives of Control Sciences*, vol. 24, no. 3, pp. 375–403, 2014.
 - [37] S. Vaidyanathan and C. Volos, “Analysis and adaptive control of a novel 3-D conservative no-equilibrium chaotic system,” *Archives of Control Sciences*, vol. 25, no. 3, pp. 333–353, 2015.
 - [38] S. T. Kingni, V.-T. Pham, S. Jafari, G. R. Kol, and P. Wofo, “Three-dimensional chaotic autonomous system with a circular equilibrium: analysis, circuit implementation and its fractional-order form,” *Circuits, Systems, and Signal Processing*, vol. 35, no. 6, pp. 1933–1948, 2016.
 - [39] M. Conti and C. Turchetti, “Approximate identity neural networks for analog synthesis of nonlinear dynamical systems,” *IEEE Transactions on Circuits and Systems I: Fundamental Theory and Applications*, vol. 41, no. 12, pp. 841–858, 1994.
 - [40] V.-T. Pham, C. Volos, S. Jafari, Z. Wei, and X. Wang, “Constructing a novel no-equilibrium chaotic system,” *International Journal of Bifurcation and Chaos*, vol. 24, no. 5, p. 1450073, 2014.
 - [41] H. Akiyama, Y. Shimizu, H. Miyakawa, and M. Inoue, “Extra-cellular DC electric fields induce nonuniform membrane polarization in rat hippocampal CA1 pyramidal neurons,” *Brain Research*, vol. 1383, pp. 22–35, 2011.
 - [42] C. Wang and J. Ma, “A review and guidance for pattern selection in spatiotemporal system,” *International Journal of Modern Physics B*, vol. 32, no. 6, article 1830003, 2018.
 - [43] J. Ma and J. Tang, “A review for dynamics in neuron and neuronal network,” *Nonlinear Dynamics*, vol. 89, no. 3, pp. 1569–1578, 2017.
 - [44] M. Lv, C. Wang, G. Ren, J. Ma, and X. Song, “Model of electrical activity in a neuron under magnetic flow effect,” *Nonlinear Dynamics*, vol. 85, no. 3, pp. 1479–1490, 2016.
 - [45] K.-A. Hossmann and D. M. Hermann, “Effects of electromagnetic radiation of mobile phones on the central nervous system,” *Bioelectromagnetics*, vol. 24, no. 1, pp. 49–62, 2003.
 - [46] A. E. Kaprana, A. D. Karatzanis, E. P. Prokopakis et al., “Studying the effects of mobile phone use on the auditory system and the central nervous system: a review of the literature and future directions,” *European Archives of Oto-Rhino-Laryngology*, vol. 265, no. 9, pp. 1011–1019, 2008.
 - [47] L. Lu, Y. Jia, W. Liu, and L. Yang, “Mixed stimulus-induced mode selection in neural activity driven by high and low frequency current under electromagnetic radiation,” *Complexity*, vol. 2017, Article ID 7628537, 11 pages, 2017.
 - [48] M. Ge, Y. Jia, Y. Xu, and L. Yang, “Mode transition in electrical activities of neuron driven by high and low frequency stimulus in the presence of electromagnetic induction and radiation,” *Nonlinear Dynamics*, vol. 91, no. 1, pp. 515–523, 2018.
 - [49] L. Lulu, J. Ya, X. Ying, G. Mengyan, Y. Lijian, and Z. Xuan, “Energy dependence on modes of electric activities of neuron driven by different external mixed signals under electromagnetic induction,” *SCIENCE CHINA Technological Sciences*, vol. 61, 2018.
 - [50] C. K. Volos, I. M. Kyprianidis, I. N. Stouboulos, and S. Vaidyanathan, “A new concept in synchronization of coupled neuromorphic circuits,” *Journal of Engineering Science and Technology Review*, vol. 8, no. 2, pp. 157–173, 2015.
 - [51] L. O. Chua and S. M. Kang, “Memristive devices and systems,” *Proceedings of the IEEE*, vol. 64, no. 2, pp. 209–223, 1976.

- [52] L. Shi, X. Yang, Y. Li, and Z. Feng, "Finite-time synchronization of nonidentical chaotic systems with multiple time-varying delays and bounded perturbations," *Nonlinear Dynamics*, vol. 83, no. 1-2, pp. 75–87, 2016.
- [53] F. Wu, C. Wang, Y. Xu, and J. Ma, "Model of electrical activity in cardiac tissue under electromagnetic induction," *Scientific Reports*, vol. 6, no. 1, p. 28, 2016.
- [54] L. Chua, "Memristor-the missing circuit element," *IEEE Transactions on Circuit Theory*, vol. 18, no. 5, pp. 507–519, 1971.
- [55] D. Somers and N. Kopell, "Rapid synchronization through fast threshold modulation," *Biological Cybernetics*, vol. 68, no. 5, pp. 393–407, 1993.
- [56] I. Belykh, E. de Lange, and M. Hasler, "Synchronization of bursting neurons: what matters in the network topology," *Physical Review Letters*, vol. 94, no. 18, article 188101, 2005.
- [57] C. A. S. Batista, R. L. Viana, F. A. S. Ferrari, S. R. Lopes, A. M. Batista, and J. C. P. Coninck, "Control of bursting synchronization in networks of Hodgkin–Huxley-type neurons with chemical synapses," *Physical Review E*, vol. 87, no. 4, article 042713, 2013.
- [58] Y. Tao, H. Gu, and X. Ding, "Spatial coherence resonance and spatial pattern transition induced by the decrease of inhibitory effect in a neuronal network," *International Journal of Modern Physics B*, vol. 31, no. 26, article 1750179, 2017.
- [59] Q. Wang, H. Zhang, M. Perc, and G. Chen, "Multiple firing coherence resonances in excitatory and inhibitory coupled neurons," *Communications in Nonlinear Science and Numerical Simulation*, vol. 17, no. 10, pp. 3979–3988, 2012.
- [60] Y. X. Fu, Y. M. Kang, and Y. Xie, "Subcritical Hopf bifurcation and stochastic resonance of electrical activities in neuron under electromagnetic induction," *Frontiers in Computational Neuroscience*, vol. 12, p. 6, 2018.
- [61] Q. Zhang, *Bifurcation and Chaos Theory and Application*, Tianjin University Press, Tianjin, 2015.
- [62] D. Guo, Q. Wang, and M. Perc, "Complex synchronous behavior in interneuronal networks with delayed inhibitory and fast electrical synapses," *Physical Review E*, vol. 85, no. 6, pp. 878–896, 2012.
- [63] J. Ma, X. Song, W. Jin, and C. Wang, "Autapse-induced synchronization in a coupled neuronal network," *Chaos, Solitons & Fractals*, vol. 80, pp. 31–38, 2015.
- [64] A. Riehle, S. Grün, M. Diesmann, and A. Aertsen, "Spike synchronization and rate modulation differentially involved in motor cortical function," *Science*, vol. 278, no. 5345, pp. 1950–1953, 1997.
- [65] J. J. Palop, J. Chin, and L. Mucke, "A network dysfunction perspective on neurodegenerative diseases," *Nature*, vol. 443, no. 7113, pp. 768–773, 2006.
- [66] C. J. Stam and E. A. de Bruin, "Scale-free dynamics of global functional connectivity in the human brain," *Human Brain Mapping*, vol. 22, no. 2, pp. 97–109, 2004.
- [67] L. L. Rubchinsky, C. Park, and R. M. Worth, "Intermittent neural synchronization in Parkinson's disease," *Nonlinear Dynamics*, vol. 68, no. 3, pp. 329–346, 2012.

Research Article

Evidence of Exponential Speed-Up in the Solution of Hard Optimization Problems

Fabio L. Traversa,¹ Pietro Cicotti,² Forrest Sheldon,³ and Massimiliano Di Ventra³ 

¹MemComputing Inc., San Diego, CA 92130, USA

²San Diego Supercomputer Center, La Jolla, CA 92093, USA

³Department of Physics, University of California, La Jolla, San Diego, CA 92093, USA

Correspondence should be addressed to Massimiliano Di Ventra; diventra@physics.ucsd.edu

Received 17 April 2018; Accepted 29 May 2018; Published 3 July 2018

Academic Editor: Viet-Thanh Pham

Copyright © 2018 Fabio L. Traversa et al. This is an open access article distributed under the Creative Commons Attribution License, which permits unrestricted use, distribution, and reproduction in any medium, provided the original work is properly cited.

Optimization problems pervade essentially every scientific discipline and industry. A common form requires identifying a solution satisfying the maximum number among a set of many conflicting constraints. Often, these problems are particularly difficult to solve, requiring resources that grow exponentially with the size of the problem. Over the past decades, research has focused on developing heuristic approaches that attempt to find an approximation to the solution. However, despite numerous research efforts, in many cases even approximations to the optimal solution are hard to find, as the computational time for further refining a candidate solution also grows exponentially with input size. In this paper, we show a *noncombinatorial* approach to hard optimization problems that achieves an *exponential speed-up* and finds better approximations than the current state of the art. First, we map the optimization problem into a Boolean circuit made of specially designed, *self-organizing* logic gates, which can be built with (nonquantum) electronic elements with memory. The equilibrium points of the circuit represent the approximation to the problem at hand. Then, we solve its associated *nonlinear* ordinary differential equations numerically, towards the equilibrium points. We demonstrate this exponential gain by comparing a sequential MATLAB implementation of our solver with the winners of the 2016 Max-SAT competition on a variety of hard optimization instances. We show empirical evidence that our solver scales *linearly* with the size of the problem, both in time and memory, and argue that this property derives from the *collective* behavior of the simulated physical circuit. Our approach can be applied to other types of optimization problems, and the results presented here have far-reaching consequences in many fields.

1. Introduction

In real-life applications, it is common to encounter problems where one needs to find the best solution within a vast set of possible solutions. These *optimization problems* are routinely faced in many commercial segments, including transportation, goods delivery, software packages or hardware upgrades, network traffic and congestion management, and circuit design, to name just a few [1, 2]. Many of these problems can be easily mapped into *combinatorial optimization problems*, namely, they can be written as Boolean formulas with many constraints (clauses) among different variables (either negated or not, i.e., literals) with the constraints themselves related by some logical proposition [1].

It is typical to write the Boolean formulas as *conjunctions* (the logical ANDs, also represented by the symbol \wedge) of *disjunctions* (the logical ORs, represented by the symbol \vee), in the so called *conjunctive normal form* (CNF). The CNF representation is universal in that any Boolean formula can be written in this form [3].

A simple example of a CNF formula $\phi(x)$ is

$$\phi(x) = (\neg x_1 \vee x_2) \wedge (\neg x_2 \vee \neg x_3 \vee x_4) \wedge (x_1 \vee \neg x_2 \vee x_3 \vee \neg x_4) \wedge (\neg x_1 \vee x_4) \wedge (x_1 \vee x_2 \vee \neg x_4), \quad (1)$$

in which we have four variables, x_j , with $j = 1, 2, 3, 4$, five clauses, and fourteen literals (the symbol \neg indicates

negation). The problem is then to find an assignment satisfying the maximum number of clauses, that is, in which as many clauses as possible have at least one literal that is true. Such a clause is then said to be satisfied, otherwise it is unsatisfied [3], and the problem itself is known as Max-SAT (maximum satisfiability).

A Max-SAT problem whose CNF representation has exactly k literals ($k \geq 2$) per clause is called Max-EkSAT. Max-EkSAT is a ubiquitous optimization problem with widespread industrial applications. We will focus on its solution as a test bed in the main text and refer the reader to the appendix where we have applied our approach to a wide range of optimization problems, including weighted Max-SAT, [4] for its application to machine learning and [5] for the solution of the worst cases of a satisfiable problem known as the subset sum.

Max-EkSAT lies in the NP-hard class, meaning that any problem in NP can be reduced to it in polynomial time [1]. More informally, we expect that worst case instances will require resources which grow (at least) exponentially in the input size to solve, and additionally, problems in this class generally also require exponential resources in order to check a proposed solution. Due to this, complete algorithms that attempt to solve Max-EkSAT instances quickly become infeasible for large problems. Much research has instead focused on incomplete solvers that perform a stochastic local search, by generating an initial assignment and iteratively improving upon it. This approach has proven effective at approximating and sometimes solving large instances of SAT and other problems. For instance, in recent Max-SAT competitions [6], incomplete solvers outpace complete solvers by two orders of magnitude on random and crafted benchmarks. However, they too suffer from the same exponential time dependence as complete solvers for sufficiently large or hard instances [7–9].

It has further been shown, using probabilistically checkable proofs [10], that many classes of combinatorial optimization problems (including the Max-EkSAT) have an *inapproximability gap*. This means that no algorithm can overcome, in polynomial time, a fraction of the optimal solution, unless $NP = P$ [10, 11]. In other words, for heuristics to improve on their approximation beyond this limit would require exponentially increasing time. For example, for the Max-E3SAT, it has been proved that if $NP \neq P$, then there is no algorithm that can give an approximation better than $7/8$ of the optimal number of satisfied clauses [11].

Despite these difficulties, it is often necessary to solve or approximate optimization problems such as these as quickly as possible, and the quality of the approximation can have direct outcomes on the cost to businesses, the speed of our internet connections, or the efficiency of our shipping, to name a few important cases. In what follows, we outline a novel approach to generating approximations to Max-EkSAT and demonstrate its efficacy on a variety of instances both generated to provide the worst cases within the inapproximability gap and drawn from Max-SAT competitions [6].

2. The Memcomputing Approach

In this work, we consider a radically different *noncombinatorial* approach to hard optimization problems. Our approach is based on the *simulation* of *digital memcomputing machines* (DMMs) [5, 12, 13]. A brief introduction of these machines is provided in the appendix. The reader interested in a more in-depth discussion is urged to look at the extensive papers [5, 12]. The practical realization of DMMs can be accomplished using standard circuit elements and those with memory (time nonlocality, hence the name “memcomputing” [14]).

Time nonlocality allows us to build logic gates that *self-organize* into their logical proposition, *irrespective* of whether the signal comes from the traditional input or output [12]. We call them *self-organizing logic gates* (SOLGs), and circuits built out of them, *self-organizing logic circuits* (SOLCs). Our approach then follows these steps.

- (1) We first construct the Boolean circuit that represents the problem at hand (e.g., the Max-EkSAT of Figure 1).
- (2) We replace the traditional (unidirectional) Boolean gates of this Boolean circuit with SOLGs.
- (3) We feed the appropriate terminals with the required output of the problem (e.g., the logical 1 if we are interested in checking its satisfiability).
- (4) Finally, the electronic circuit built out of these SOLGs can be described by *nonlinear* ordinary differential equations, which can be solved to find the equilibrium (steady-state) points. These equilibria represent the approximation to the optimization problem [12].

The procedure of how we transform a combinatorial optimization problem into an electronic circuit as well as a sketch of its numerical solution is discussed further in the appendix (see also [12]). The important point to note is that SOLGs and SOLCs manifest *long-range order* due to the presence of instantons [15]. Instantons connect topologically inequivalent critical points in the phase space, hence generating *nonlocality* in the system. This translates into a *collective* dynamical behavior that allows gates at an *arbitrary* distance to correlate very efficiently so that, when a terminal of one gate needs to change its truth value to satisfy that gate’s logical proposition, a terminal at any other gate may provide the correct truth assignment while satisfying its own logical proposition [5]. As we will explain later, this is the key feature that allows these memcomputing machines to solve complex problems efficiently, without the need to explore a vast space of possibilities, as standard combinatorial approaches would do.

3. Results and Discussion

This radical change of perspective manifests its power already in comparing simulations of DMMs with those performed by the winners of the 2016 Max-SAT competition

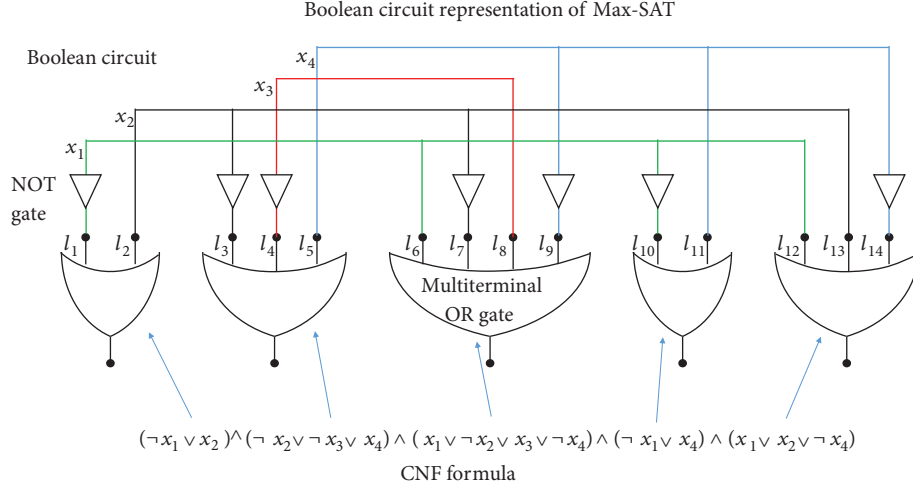


FIGURE 1: Example of the mapping between a Boolean satisfiability formula in conjunctive normal form and a Boolean circuit made of multiterminal OR and NOT gates. Each clause of the SAT formula is mapped into an OR with as many terminals as the literals in the clause (the satisfiability of this multiterminal OR requires that at least one terminal has a truth value of 1). The global optimum of the SAT formula, that is, the maximum number of satisfied clauses, corresponds to the maximum number of OR gates with output one. This Boolean circuit is then transformed into a self-organizing logic circuit by substituting each standard Boolean gate with a self-organizing logic gate [12], and each OR output is fed with a DC voltage generator representing the logic value of 1.

[6] on the competition benchmarks. When run on similar hardware, our solver, which we named Falcon [12, 16, 17], performs orders of magnitude faster than the winners in the incomplete track of the competition, and in some cases it finds the solution when the best solvers did not.

Since a direct comparison is difficult across hardware and implementations (our solver is written in MATLAB which is notoriously inefficient compared with the compiled languages of the competition solvers). Nevertheless, these tests already provide strong indication of the advantages of our approach using digital memcomputing machines over traditional combinatorial optimization.

However, in order to form a direct comparison and more clearly show the *exponential speed-up* of our approach, we have crafted three Max-SAT problems with increasing levels of difficulty. We then compared our memcomputing solver against two of the best solvers of the 2016 Max-SAT competition (CCLS [18] and DeciLS [19]—a new version of CnC-LS—kindly provided by their developers) which are specifically designed to solve these types of problems, but employing very different solution strategies.

Random 3-SAT instances may be generated by selecting 3 variables out of n , joining them in a 3-SAT clause where each is randomly negated and then repeating this for the desired number of clauses M . These instances are known to undergo a SAT/UNSAT transition when the ratio of clauses to variables, $M/n = \rho$ (hereafter the “density”), crosses the critical value $\rho_c \approx 4.3$ [20, 21]. Exponential time is required to demonstrate that an instance is UNSAT [22] and thus must also be required to solve the corresponding Max-SAT, offering a simple way to generate benchmarks.

However, the difficulty of computing approximations for these instances varies widely. This can be partially attributed

to the fluctuations in variable occurrences and their negations [23] leading to “fields” which point towards the optima. More balanced instances may be produced by starting with a Random-XORSAT instance (also called hyperSAT [24]), that is, a set of Boolean formulas defined by the XOR of Boolean variables (the XOR symbol is \oplus) and converting it to a Max-SAT instance.

Each XORSAT clause may be converted to a block of four SAT clauses, for example,

$$x \oplus y \oplus z = 1 \rightarrow (x \vee y \vee z) \wedge (x \vee \neg y \vee \neg z) \wedge (\neg x \vee \neg y \vee z) \wedge (\neg x \vee y \vee \neg z), \quad (2)$$

in which a variable and its negation appear symmetrically. The special structure of XORSAT gives rise to a global algorithm when the instance is satisfiable, allowing for a solution in polynomial time using Gaussian elimination [24]. However, when unsatisfiable, occurring for $\rho > 4 \cdot 0.918 \approx 3.7$, this same structure makes these problems very difficult for local search solvers [22, 25]. In addition, the choice of instances out of XORSAT clauses makes them particularly difficult also for algorithms based on message passing [26].

A basic understanding of this difficulty can be obtained by considering that changing a variable assignment affects positively (namely, contributes a true literal to) the same number of clauses as those affected negatively (where the literal is false), because of the balanced occurrences of the variables. Therefore, for any combinatorial approach, when a certain amount of satisfied clauses is reached, any further improvement requires many *simultaneous* variable flips, which is a *nonlocal* type of assignment. In other words, the distance between two assignments at successive approximations becomes of the same order of the input length $|x|$. This means that going from an assignment x to a better one y , if they have a distance $d(x, y) = \sum_j (x_j - y_j)^2 = O(|x|)$, would

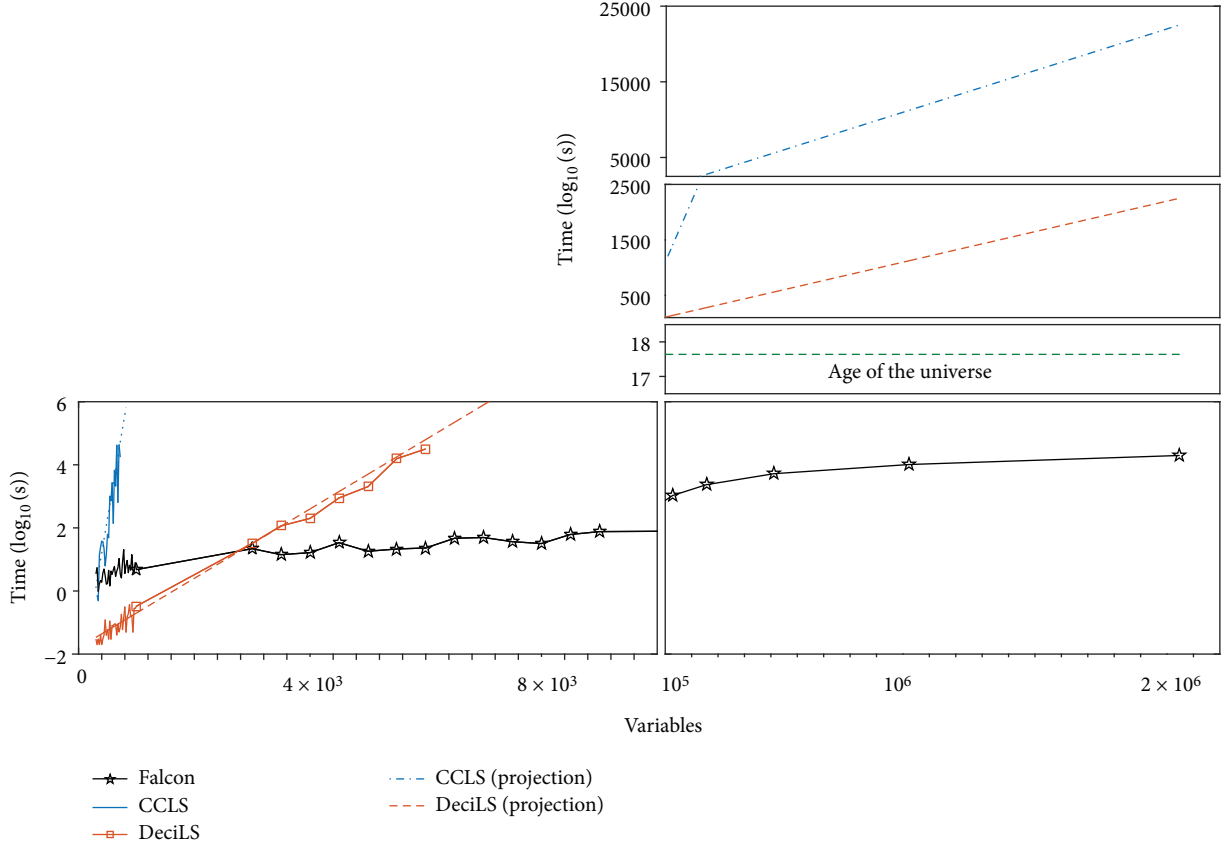


FIGURE 2: Simulation time comparison between incomplete solvers CCLS and DeciLS against our solver, Falcon, for the balanced and constrained delta-Max-E3SAT. A threshold of 1.5% of unsatisfiable clauses has been set. We have then tested how long CCLS, DeciLS, and our solver Falcon take to overcome this limit with increasing number of variables. All calculations have been performed on a single thread of an Intel Xeon E5-2680 v3 with 128 Gb DRAM shared on 24 threads. The local solvers require an exponentially increasing time to reach that limit already visible at a few hundred variables for the CCLS and a few thousands for the DeciLS. Our solver has been tested up to 2×10^6 variables and required order of 10^4 seconds for that maximum number of variables. We show also the estimate of time that would have been required these local solvers to run up to 2×10^6 variables. The estimated time (dashed and dashed-dotted lines) has been calculated using a linear regression of the $\log_{10}(\text{time})$ versus the number of variables.

require checking $O(2^{d(x,y)})$ variable flips, which is the number of configurations that is exponential with respect to the distance $d(x, y)$ (the actual calculation requires the enumeration of all possible flips of 1, 2, \dots , $d(x, y)$ literals because the distance $d(x, y)$ is not known a priori. Hence, the actual number of flips is $\sum_{k=0}^{d(x,y)} \binom{|x|}{k} \geq 2^{d(x,y)}$.

While more difficult, these instances also display some variation in resolution time. In order to obtain instances of more predictable difficulty, we impose a further constraint requiring all variables to appear the same number of times (or as near as possible while remaining consistent with the number of clauses $M = \rho N$), that is, the variable occurrences are distributed as a δ -function. This variant is harder than the previous one because of the additional balance induced by the variable distribution, and our results indicate that they display much lower variability in their difficulty.

In the following, we will call “random-Max-E3SAT” a Max-E3SAT completely generated at random. This will be used as an “easy” problem to test the performance of all solvers. We refer to “hyper-Max-E3SAT” as the Max-E3SAT generated from a random Max-E3XOR and finally

to “delta-Max-E3SAT” as a problem generated by the Max-E3XOR with δ -function distribution of variables.

As it is evident in Figure 2, while the balanced structure of Max-XORSAT poses a challenge to local search algorithms, our memcomputing solver easily overcomes these limits because, due to the collective (instantonic) behavior of the circuit, the dynamics evolve towards deep minima very close to the global optimum (see also the appendix). The reason is that, as already anticipated, the collective state of the machine allows simultaneous, *nonlocal* change of literals belonging to gates arbitrarily far from each other [15]. This change is consistent with the physics and the topology of the memcomputing circuit that naturally drive the system towards the maximum number of satisfied SOLGs, without recourse to any combinatorial selection scheme.

The optimum for all problems can be estimated using an ensemble of small instances for which it is easier to find a fairly good approximation. For example, instances of about 300 variables and density (clauses/variables) of $\rho = 5$ provide a good indication of the global optimum in terms of percentage of unsatisfied clauses. We found that for the random-

Max-E3SAT, the optimum is expected at about 0.4% of unsatisfied clauses, while for both the hyper- and delta-Max-E3SAT, this value is about 1.3%. The difference between these values is not surprising. As mentioned previously, it is well known that for the latter two problems the transition from satisfiable to unsatisfiable is around a density of $\rho \approx 3.7$, while for random-Max-E3SAT, it is around $\rho \approx 4.3$. We have then chosen the same density of $\rho = 5$ for the random-, hyper-, and delta-Max-E3SAT.

In order to prove the superior efficiency of our noncombinatorial approach for this class of hard problems, we have evaluated their scaling properties up to 2×10^6 variables (while keeping the density constant). We recall that the simulations of DMMs have been done using a MATLAB code, while CCLS and DeciLS are compiled codes. Therefore, the level of optimization is expected to be higher in the compiled codes, making a direct performance comparison harder, although for large problem sizes, our solver has much better performance compared to CCLS and DeciLS. Nevertheless, we are more interested in the scaling of the approximation time. Specifically, for hard cases where incomplete solvers diverge exponentially in time, our solver diverges *linearly*. This is the most important test and the central result of our paper. It is shown in Figure 2.

The hard inapproximability limit and its exponential nature for both the combinatorial heuristics CCLS and DeciLS is clearly visible in Figure 2, where we have set a threshold of 1.5% of unsatisfiable clauses for the delta-Max-E3SAT. We have then tested how long CCLS, DeciLS, and our solver Falcon take to overcome this limit with increasing number of clauses. All calculations have been done on a single core of an Intel Xeon E5-2680 v3.

The exponential blowup of CCLS and DeciLS is already evident for small instances of the problem, while our noncombinatorial approach performs *linearly*, in both time and memory, for *any* number of variables we have tested so far. In fact, we have tested our solver up to 2×10^6 variables, requiring $\sim 10^4$ seconds to reach the target 1.5% threshold. The heuristic solvers, if they could run up to the same number of variables, would require, in the best case, about $\sim 10^{2500}$ seconds, which is $\sim 10^{2480}$ times the estimated age of the universe.

To better highlight the *linear* scaling of our solver, we compare it in Figure 3 with CCLS (qualitatively, all other incomplete solvers should perform similarly). Each plot of Figure 3 displays the percentage of unsatisfied clauses versus time, normalized with respect to the number of variables n . Clearly, linear scaling for these hard problems is a very desirable feature and very difficult to achieve with combinatorial approaches. However, the reason for such linear scaling is subtle.

Regarding *memory*, since we simulate (integrate) differential equations in time, and the circuit scales linearly with the number of literals, the linear scaling in memory requirements of our simulations is easy to understand (see also the appendix). On the other hand, linear scaling in simulation *time* implies *constant* scaling, namely, *independent* of the problem size, when we look at the “machine time,” which is

the number of (differential equation discretized time) steps for the simulation to reach equilibrium. The reason for this unexpected machine time constant scaling can be found again in the long-range order of the dynamics of the system [15] (see also the appendix). As we have shown analytically in [15] using topological field theory, this long-range order leads to nondecreasing spatial (and temporal) correlations in memcomputing machines. In fact, Figure 3 clearly shows that self-organizing logic circuits relax close to the predicted global minimum, while the CCLS does so only for the (“easy”) random-Max-E3SAT. This is further illustrated in Figure 4 of the appendix for random-, hyper-, and delta-Max-E3SAT.

4. Conclusions

In conclusion, we have shown empirical evidence that a *non-combinatorial* approach—based on the simulation of digital memcomputing machines—to the solution of hard combinatorial optimization problems outperforms *exponentially* heuristics specifically designed to solve such problems. In particular, with our approach, we were able to find far better approximations to hard instances with millions of variables in a few hours on a single core, with *linear scaling* both in time and memory of the processor. For the same sizes, winners of the 2016 Max-SAT competition would require several orders of magnitude more than the age of the universe to find the same approximations. Of course, these numerical results are not intended to prove that there are polynomial solutions to NP-hard problems. Rather, they show that physics-inspired approaches can help tremendously in solving some of the most complex problems faced in academia and industry. We thus hope that this work will motivate further research along these lines.

Appendix

Methods

The noncombinatorial approach we discuss here is based on the concept of universal memcomputing machines (UMMs) [13] introduced by two of us (Fabio L. Traversa and Massimiliano Di Ventra). UMMs are a class of computing machines composed of interconnected memory units. The *topology* of such network is chosen to solve the specific problem at hand. UMMs use the *collective* state of the interconnected memory units to perform computation [12, 27], so they can take advantage of long-range correlations that can significantly boost the efficiency of the computation [12, 15]. If the input and output of UMMs can be mapped into strings of integers, belonging to a limited subset of \mathbb{N} , we obtain the digital (hence scalable) version of UMMs (DMMs) [12]. In particular, we consider DMMs whose input and output can be mapped into \mathbb{Z}_2 .

A possible, practical realization of DMMs is self-organizing logic circuits (SOLCs) composed of SOLGs [12]. SOLGs are logic gates that can accept inputs from *any* terminals and self-organize their internal state to satisfy their logic relations. For example, a self-organizing OR (SO-OR) is

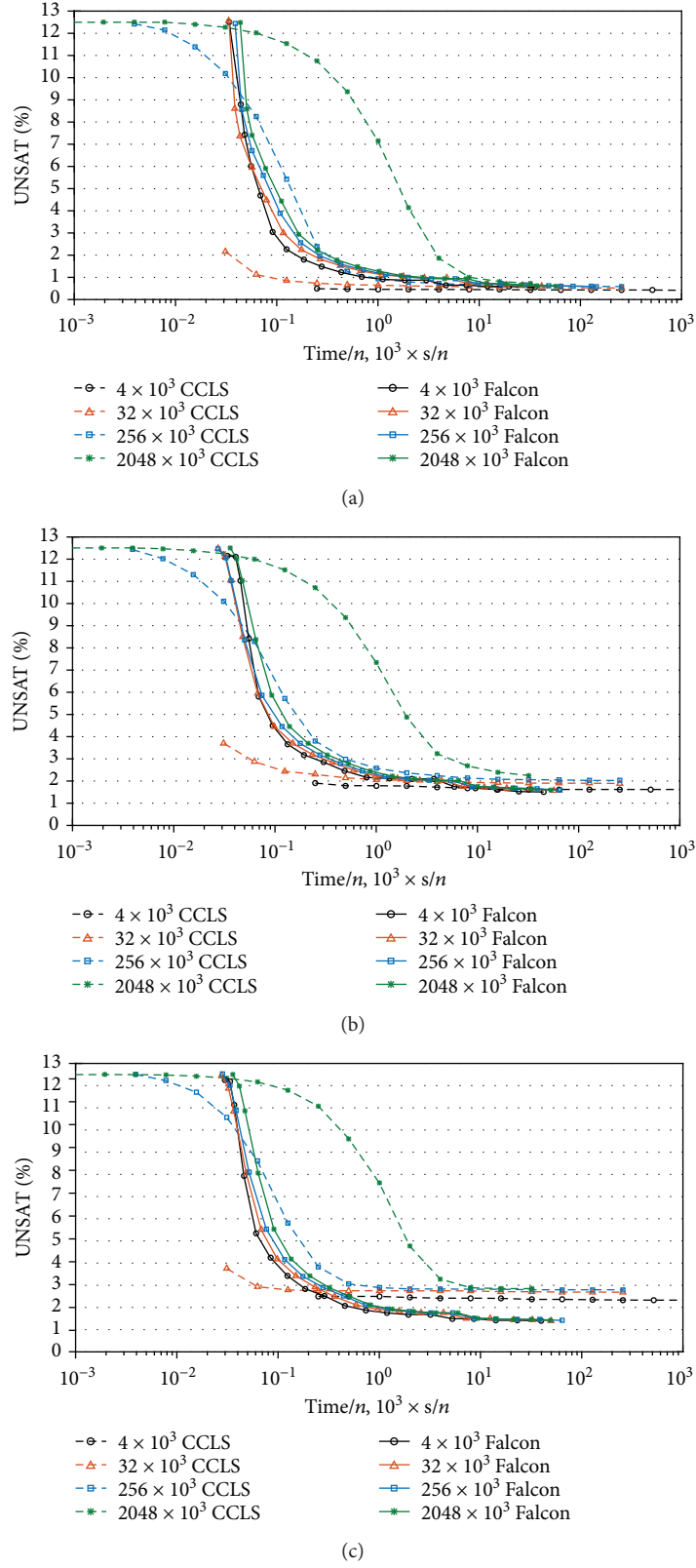
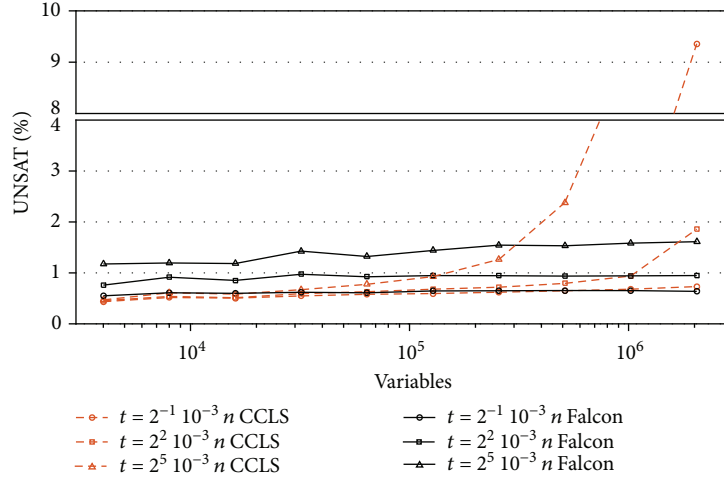
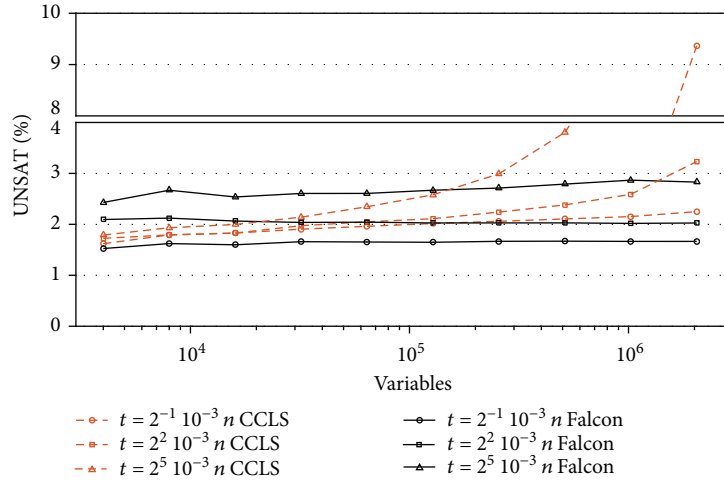


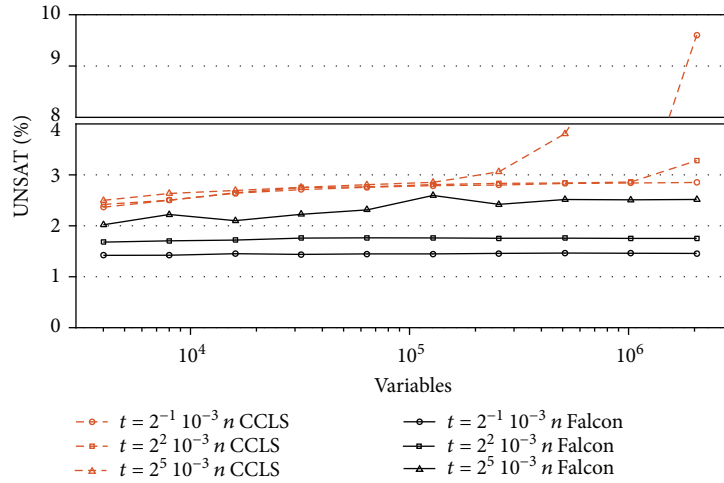
FIGURE 3: Comparison between the incomplete solver CCLS versus our noncombinatorial solver, Falcon, for (a) random-Max-E3SAT, (b) hyper-Max-E3SAT, and (c) delta-Max-E3SAT. In these plots, the percentage of unsatisfied clauses versus the time normalized with respect to the number of variables is shown to highlight the linear scaling of our solver. All calculations have been performed on a single thread of an Intel Xeon E5-2680 v3 with 128 Gb DRAM shared on 24 threads.



(a)



(b)



(c)

FIGURE 4: Comparison between the CCLS solver versus our solver, Falcon, for (a) random-Max-E3SAT, (b) hyper-Max-E3SAT, and (c) delta-Max-E3SAT. In these plots, the percentage of unsatisfied clauses versus the number of variables is shown. Different curves are for different simulation time-outs (in seconds) following the relation $t_{\text{out}} = kn$ with $n = |x|$ and k an integer given in the legend. All calculations have been performed on a single thread of an Intel Xeon E5-2680 v3 with 128 Gb DRAM shared on 24 threads.

a 3-terminal gate whose internal machinery drives the terminal states to satisfy the relation $x_0 = x_1 \vee x_2$, where x_0 is the state of the conventional output terminal, and x_1 and x_2 are the states of the conventional input terminals. Therefore, unlike conventional logic gates, the SO-OR can be fed also at the output terminal. If we set x_0 to some state, the SO-OR then will self-organize to give logically consistent states x_1 and x_2 .

We can use SOLCs to solve combinatorial problems by expressing them in Boolean format and then mapping the latter onto logic circuits. As a relevant example for this work, we can take the Max-SAT problem written in CNF. When we transform the SAT into a Boolean circuit, we have multiterminal OR gates connected together in order to represent a logic formula (see Figure 1 of the main text). Hence, we can substitute conventional logic gates by SOLGs and set all output of the SO-ORs to logical 1. We now let the SOLC to self-organize to satisfy the largest number of SO-ORs.

We have previously shown [12] that SOLCs can be realized via standard (nonquantum) electronic components (we employ the realization described in [12], just slightly modified to deal with CNF formulas).

One of the key components of SOLGs is the *dynamic correction module* we have designed to correct the inconsistent logic gate configurations. While the design and details of this component can be found in [12], we recall here its working principle. The error correction module dynamically reads the voltages at the terminals of the gate and injects a large current when the gate is in an inconsistent configuration, a small current otherwise.

The nonquantum electronic nature of SOLCs can be fully described by a system of *nonlinear* ordinary differential equations of the type

$$\dot{x}(t) = \mathbf{F}(x(t)), \quad (3)$$

where $x = \{v_j, x_i\} \in X$ (X is the phase space) is the collection of voltages, v_j , at the terminals and the internal state variables, x_i , of the electronic elements with memory; \mathbf{F} is a system of nonlinear ordinary differential equations, representing the flow vector field [12]. We can then efficiently simulate them by numerical integration. Therefore, SOLCs are nothing other than dynamical systems. In this case, a solution of the problem we want to solve (e.g., the Max-SAT) employing a DMM is mapped into an equilibrium point of the dynamical system. The system is engineered in such a way that, starting from *any* initial condition (generally chosen at random), it evolves to converge into an equilibrium.

We have discussed in [12] (see also [5]) the relevant properties that the dynamical systems representing DMMs should have to behave in this way. Among them, an important feature, fundamental to guarantee the convergence, is that they are *point dissipative* [28]. This implies that the dynamical system has bounded orbits (no divergences), and it is endowed with an asymptotically stable global attractor, that is, a compact set in the phase space that attracts any other point. This feature has also allowed us to prove that no chaotic behavior can emerge if equilibrium points are present [29], as well as absence of periodic orbits [30].

Finally, the point dissipative property guarantees convergence to equilibrium *irrespective* of the initial conditions.

We can finally summarize the power of these machines with the following hierarchical picture. DMMs use the *topology* of the internal connectivity of its elements to represent the problem to solve (this is called *information overhead* in [12]). Then, the collective state of the machine can manipulate all inputs, outputs, and connecting variables in a massively parallel fashion (*intrinsic parallelism* [12]).

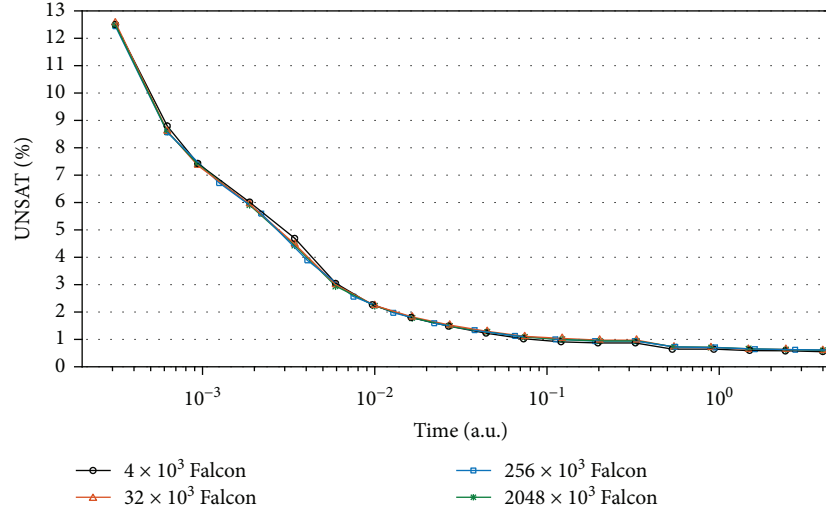
In addition, the nonlinearity of the dynamical system equations induces a transient instantonic phase with *long-range order*, both in space and time [15]. This long-range order allows the system to converge exponentially fast to the equilibrium points that are associated to the approximations of optimization problems, by exploring a subspace (that scales at most polynomially with input size) of the phase space. This subspace is considerably smaller than the entire phase space itself [15].

In fact, as briefly discussed in the main text, the particular realization of DMMs we have presented in this work (similar to the ones in [12]) supports infinite-range correlations in the infinite input size limit, as shown in [15]. This enables an ideal scale-free behavior (namely, one where the correlations *do not* decay) of the SOLC. This was derived analytically using topological field theory in [15] and can also be supported numerically from Figure 5 as follows.

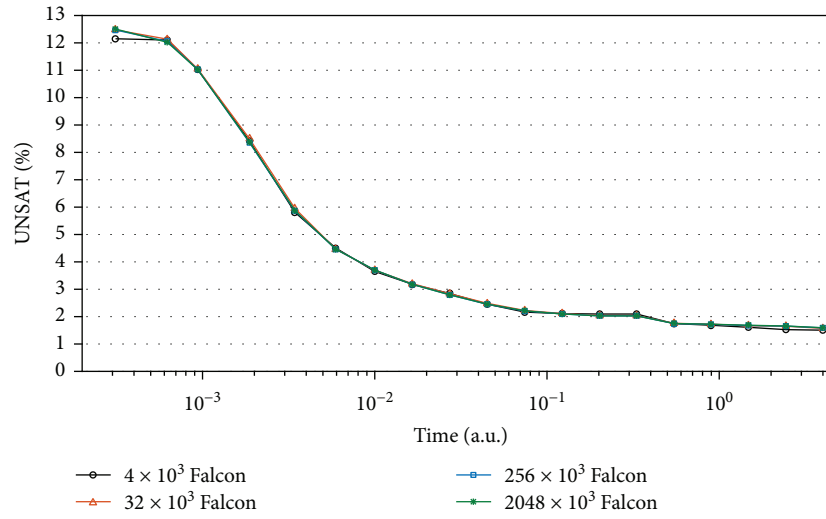
In order to simulate the system, we have employed a time step size-controlled forward-integration scheme for the differential equations that describe it [31]. Since the number of variables of the problem grows linearly with the input size because the number of gates grows only linearly, each time step to be simulated requires only a linear number of floating point operations and a memory linearly growing with input size. Then, the simulation time is just a linear function of the machine time. In Figure 5, it is reported the same as in Figure 3 of the main text but with the SOLC time (not normalized) on the x -axis. It is evident that the relaxation of the system is independent of the input size (ideal scale-free scaling). This is a very interesting and rare result for an extensive interconnected system. All these ingredients are necessary for the correct, efficient operation of a DMM.

The approximations to an optimization problem found by DMMs are very close to the global minimum of the problem, and this is guaranteed by the topology of the connectivity. This is clearly demonstrated in Figure 4 where the unsatisfied clauses are plotted versus variables for different simulation times, scaled linearly by the number of variables. While for the random-Max-E3SAT, both our solver and the CCLS approach the 0.4% minimum; in the case of the hyper-Max-E3SAT, CCLS reaches a hard *inapproximability limit* of about 2% for large instances. As expected, the delta-Max-E3SAT, instead, is a much worse case, and the inapproximability limit for CCLS is at about 3%.

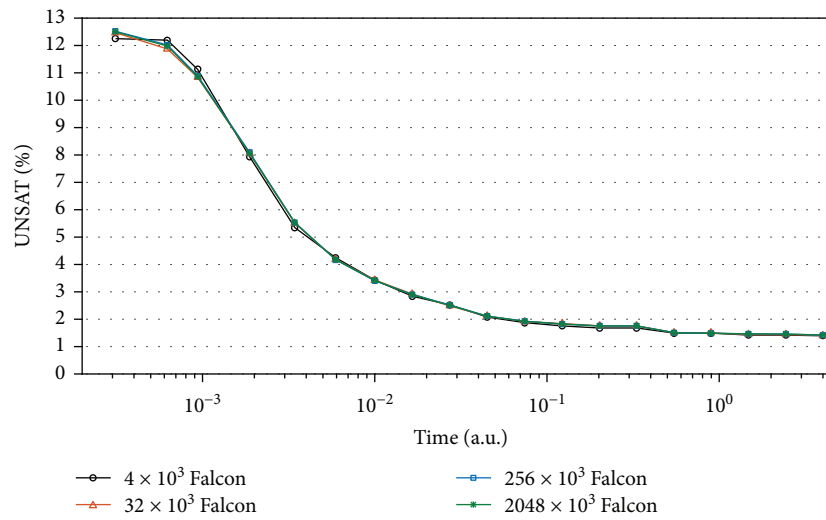
In contrast, our noncombinatorial approach directly reaches the global minimum in all cases. Interestingly, our solver shows slightly better performances for the delta-Max-E3SAT (the most difficult of the three cases) as can be seen by taking a closer look at Figure 4.



(a)



(b)



(c)

FIGURE 5: Percentage of unsatisfied clauses versus the machine time (i.e., simulated time steps) is shown to highlight the linear scaling of our solver, Falcon, for (a) random-Max-E3SAT, (b) hyper-Max-E3SAT, and (c) delta-Max-E3SAT. All calculations have been performed on a single thread of an Intel Xeon E5-2680 v3 with 128 Gb DRAM shared on 24 threads.

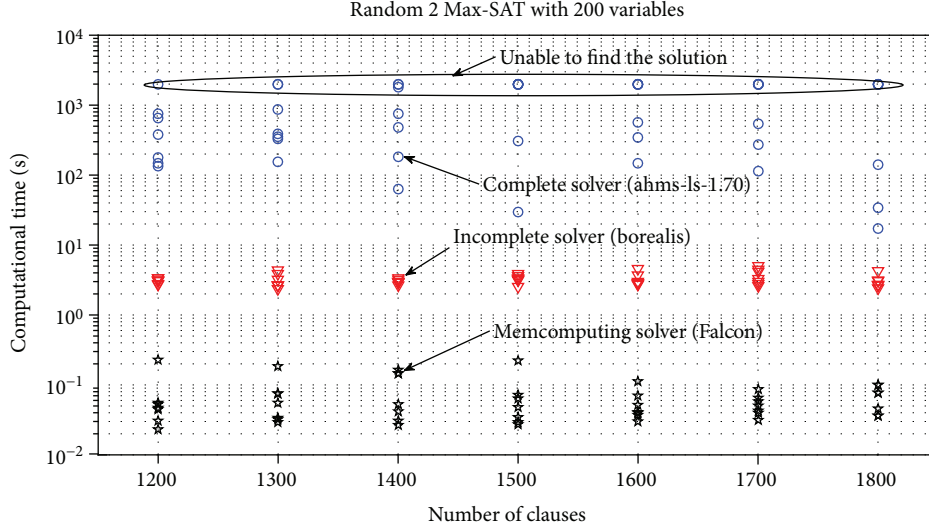


FIGURE 6: Results from the 2016 Max-SAT competition for the random Max-2SAT problem compared with our memcomputing solver, Falcon.

A Brief Survey on Max-SAT Solvers

As mentioned in the main text, there are two main (combinatorial) approaches to solve or approximate the Max-SAT problem. The first is based on the exhaustive exploration of the solution space and leads to the so-called “complete” solvers [7, 22]. The complete solvers use algorithms typically based on the branch-and-bound approach [1, 19] in which a greedy bound is first put on the optimum and then this is used to prune the resulting search tree. Despite this pruning, they still scale exponentially with input size $|x|$ because they exhaustively search a space $\mathbb{Z}_2^{O(|x|)} = \{0, 1\}^{O(|x|)}$. However, when the computation is finished, complete solvers are guaranteed to have found the global optimum of the Max-SAT.

Incomplete solvers [7, 8], in comparison, cannot guarantee the optimality of their solution as they do not explore the entire solution space. Instead, they proceed by generating an initial assignment and iteratively improving upon it. This trade-off allows them to find solutions, when they do, much more quickly than complete algorithms. In the most recent Max-SAT competition [6], incomplete track solvers found solutions of two orders of magnitude faster than complete track solvers in random and crafted benchmarks.

The quintessential incomplete solver is WalkSAT [8] which proceeds through a stochastic local search. After an initial assignment is generated, an unsatisfied clause is selected and one variable from the clause has its assignment flipped. This will leave this clause satisfied but may alter the state of other clauses in which the variable occurs. The procedure is continued for a specified number of steps or until a solution is found. Most current local search solvers work similarly with various heuristics to select the next variable flip and utilize restarts and/or noise and a host of other features.

We compared our solver, Falcon, with two of the best solvers from the 2016 Max-SAT competition, CCLS [18] and DeciLS [19]. CCLS won the crafted track for unweighted

Max-SAT and performed near the top of the random track. It performs a local search (LS) with configuration checking (CC), and the binary provided took no tuning parameters. Local search solvers will often retrace flips many times leading to an inefficient search. Configuration checking keeps track of when neighboring variables have been flipped and only allows a variable to be flipped again when at least one of its neighbors has changed its assignment. DeciLS is an updated version of CnC-LS which won the industrial track for unweighted Max-SAT and combines a unit propagation based decimation (Deci) and local search (LS) with restarts. An assignment is first generated through unit propagation-based decimation [22] in which conflicts are allowed, and the result is given to a local search for a specified number of steps. The process is then restarted, and the best result of the previous search is used to guide the subsequent decimation and resolve conflicts. This allows the solver to explore very different reasoning chains and areas of the solution space. We used the parameters values recommended in [19] for good performance across a range of instances, and subsequent tuning has indicated that the results are insensitive to changes in this range.

Weighted Partial Max-SAT

In order to more efficiently map a large number of maximization problems into Max-SAT, it is sometimes useful to consider a variant: *weighted* partial Max-SAT [1, 19]. Weighted partial Max-SAT is a version of Max-SAT for which a subset of clauses *must* be satisfied (“hard” clauses), while the remaining clauses (“soft” clauses) may be weighted, and the sum of the weights of satisfied clauses must be maximized. The Max-SAT is a particular case of the weighted partial Max-SAT in which all clauses are soft and have the same weight.

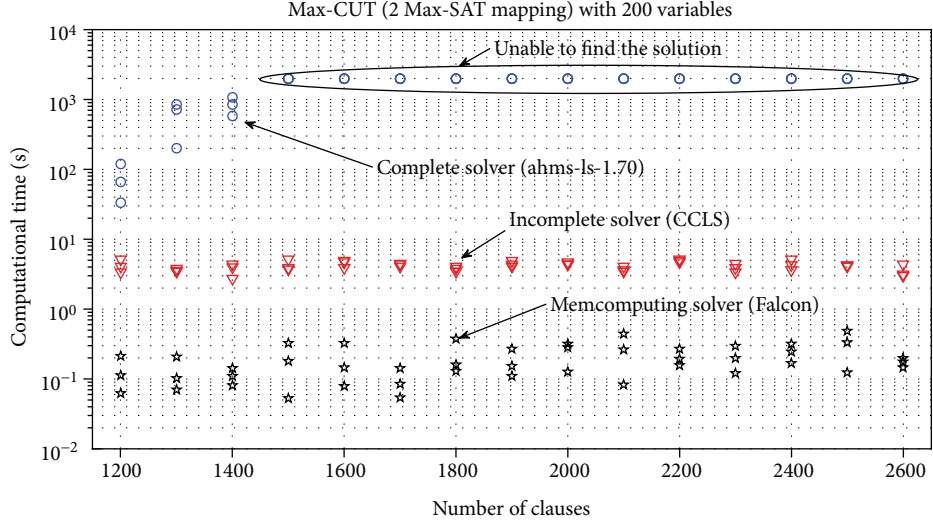


FIGURE 7: Results from the 2016 Max-SAT competition for the Max-CUT problem compared with our memcomputing solver, Falcon.

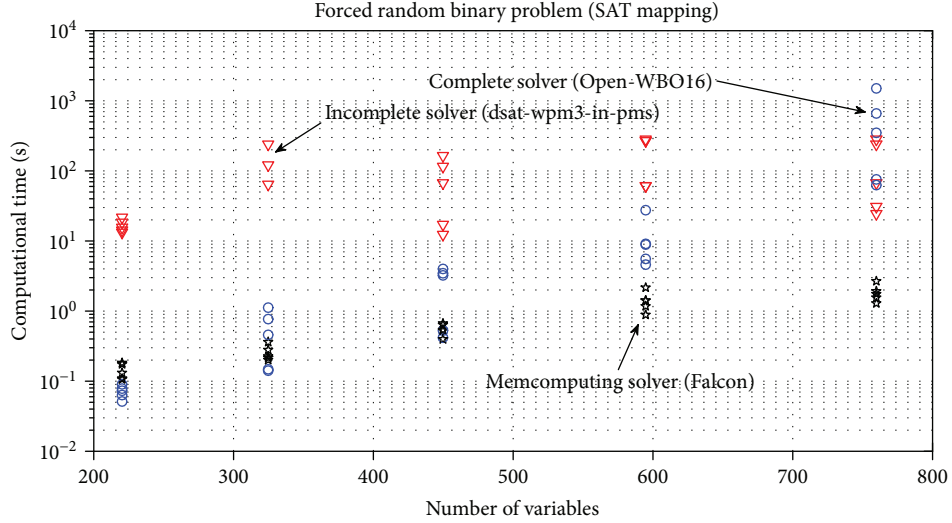


FIGURE 8: Results from the 2016 Max-SAT competition for the forced random binary problem compared with our memcomputing solver, Falcon.

Because of the presence of hard clauses, the weighted partial Max-SAT is, in general, harder than the Max-SAT for all kind of solvers. In fact, this is one of the main reasons heuristics are often unable to find even approximations to those problems (see, e.g., Figures 8 and 9).

Including weights and hard clauses in self-organizing logic circuits (SOLCs) is simple. Recalling that each OR gate representing a clause has attached at each terminal a dynamic correction module that injects a large current when the gate is in an inconsistent configuration, we can tune the maximum current allowed for each correction module in the following way. We set the maximum current injected by the dynamic correction modules connected to the SO-OR gates proportionally to the weights of the clauses. For the hard clauses, we can set the maximum current injected by the dynamic correction modules connected to the hard SO-OR gates, larger than the sum of all maximum currents injected by

the dynamic correction modules connected to all soft SO-OR gates connected to that hard SO-OR gate. This will guarantee that the hard clauses will have always the priority on the soft clauses.

Comparison from the 2016 Max-SAT Competition

We have tested SOLCs on problems taken from the 2016 Max-SAT competition and compared them against the results of the winners of each category of that competition. Even if the comparison is not completely fair because our code is written in MATLAB while the other codes are written in compiled languages, and the benchmark is not the same because we ran on different processors (we ran all our simulations on an Intel Xeon E5-2680 v3 but used the same

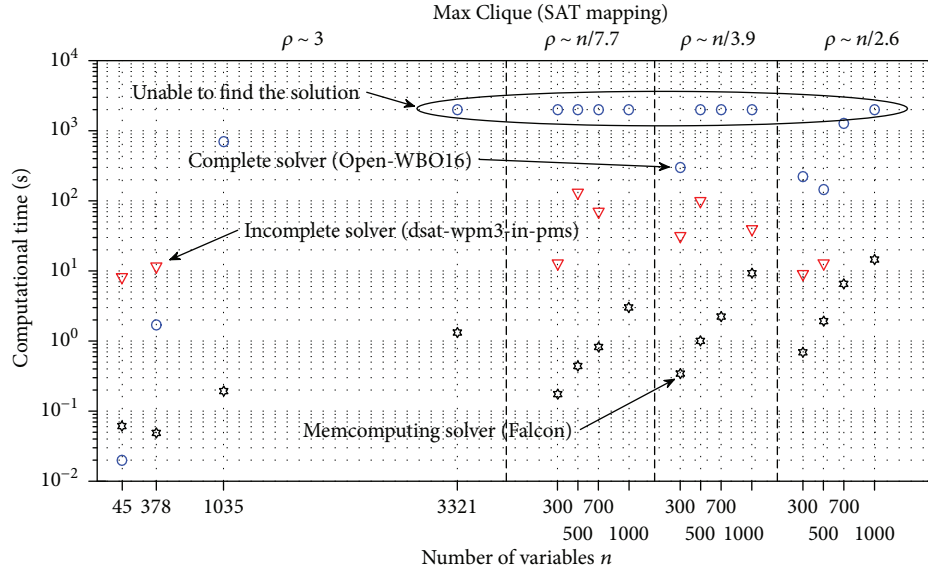


FIGURE 9: Results from the 2016 Max-SAT competition for the Max Clique problem compared with our memcomputing solver, Falcon.

number of threads allowed in the Max-SAT competition), the results are still interesting.

In Figures 6 and 7, we compare the random Max-2SAT and random Max-CUT instances, which are non-weighted problems [1]. In those cases, the scaling is similar to the heuristics, but the absolute time is orders of magnitude lower.

Of more interest are the results of Figures 8 and 9. These correspond to two problems (called forced random binary and Max Clique [1]) that, when mapped, become weighted partial Max-SAT instances. As discussed, these are especially hard. In fact, oftentimes, the best heuristics could not even find approximations because they were not able to satisfy all hard clauses, while our solver always does.

Data Availability

All calculations reported here have been performed by one of us (Pietro Cicotti) on a single processor of the Comet cluster of the San Diego Supercomputer Center, which is an NSF resource funded under award number 1341698. Apart from the instances freely available from the 2016 Max-SAT competition [6], the authors would be delighted to provide, upon request, all instances of the constrained delta-Max-E3SAT used to generate Figure 2 and those related to all the other figures in this work.

Conflicts of Interest

Fabio L. Traversa and Massimiliano Di Ventra are the cofounders of MemComputing Inc. This company is commercializing the software used in the simulations of this work.

Acknowledgments

The authors sincerely thank Dr. Shaowei Cai for providing the authors with the binary compiled codes CCLS and

DeciLS. The authors also thank Haik Manukian and Robert Sinkovits for helpful discussions. Massimiliano Di Ventra and Fabio L. Traversa acknowledge partial support from the Center for Memory Recording Research at UCSD. Massimiliano Di Ventra and Forrest Sheldon acknowledge partial support from the MemComputing Inc.



References

- [1] K. S. Christos and H. Papadimitriou, *Combinatorial Optimization*, Dover Publications Inc., 1998.
- [2] S. H. Z. Edwin and K. P. Chong, *An Introduction to Optimization*, John Wiley & Sons Inc., 2013.
- [3] M. R. Garey and D. S. Johnson, *Computers and Intractability: a Guide to the Theory of NP-Completeness*, W. H. Freeman & Co., New York, NY, USA, 1990.
- [4] H. Manukian, F. L. Traversa, and M. Di Ventra, *arXiv*, vol. 1801, article 00512, 2018.
- [5] M. Di Ventra and F. L. Traversa, *Journal of Applied Physics*, vol. 123, no. 18, article 180901, 2018.
- [6] <http://www.maxsat.udl.cat/16/index.html>.
- [7] C. P. Gomes, H. Kautz, A. Sabharwal, and B. Selman, *Handbook of Knowledge Representation*, F. Van Harmelen, V. Lifschitz, and B. Porter, Eds., vol. 1, Elsevier, 2008.
- [8] H. A. Kautz, A. Sabharwal, and B. Selman, *Handbook of Satisfiability*, A. Biere, M. Heule, and H. van Maaren, Eds., vol. 185, IOS press, 2009.
- [9] J. Hromkovic, *Algorithmics for Hard Problems: Introduction to Combinatorial Optimization, Randomization, Approximation, and Heuristics*, Springer, 2010.
- [10] U. Feige, "A threshold of $\ln n$ for approximating set cover," *Journal of the ACM*, vol. 45, no. 4, pp. 634–652, 1998.
- [11] J. Hastad, "Some optimal inapproximability results," *Journal of the ACM*, vol. 48, no. 4, pp. 798–859, 2001.
- [12] F. L. Traversa and M. Di Ventra, "Polynomial-time solution of prime factorization and NP-complete problems with digital

- memcomputing machines,” *Chaos: An Interdisciplinary Journal of Nonlinear Science*, vol. 27, no. 2, article 023107, 2017.
- [13] F. L. Traversa and M. Di Ventra, “Universal memcomputing machines,” *IEEE transactions on neural networks and learning systems*, vol. 26, no. 11, pp. 2702–2715, 2015.
- [14] M. Di Ventra and Y. V. Pershin, “The parallel approach,” *Nature Physics*, vol. 9, no. 4, pp. 200–202, 2013.
- [15] M. Di Ventra, F. L. Traversa, and I. V. Ovchinnikov, “Topological field theory and computing with instantons,” *Annalen der Physik*, vol. 529, no. 12, article 1700123, 2017.
- [16] F. L. Traversa, Y. V. Pershin, and M. Di Ventra, “Memory models of adaptive behavior,” *IEEE Transactions on Neural Networks and Learning Systems*, vol. 24, no. 9, pp. 1437–1448, 2013.
- [17] F. L. Traversa, F. Bonani, Y. V. Pershin, and M. Di Ventra, “Dynamic computing random access memory,” *Nanotechnology*, vol. 25, no. 28, article 285201, 2014.
- [18] C. Luo, S. Cai, W. Wu, Z. Jie, and K. Su, “CCLS: an efficient local search algorithm for weighted maximum satisfiability,” *IEEE Transactions on Computers*, vol. 64, no. 7, pp. 1830–1843, 2015.
- [19] S. Cai, C. Luo, and H. Zhang, “From decimation to local search and back: a new approach to MaxSAT,” in *Proceedings of the Twenty-Sixth International Joint Conference on Artificial Intelligence (IJCAI-17)*, pp. 571–577, Melbourne, Australia, August 2017.
- [20] B. Selman, H. Levesque, and D. Mitchell, “A new method for solving hard satisfiability problems,” in *Proceedings of the Tenth National Conference on Artificial Intelligence (AAAI-92)*, pp. 440–446, San Jose, CA, USA, July 1992.
- [21] S. Kirkpatrick and B. Selman, “Critical behavior in the satisfiability of random boolean expressions,” *Science*, vol. 264, no. 5163, pp. 1297–1301, 1994.
- [22] S. Cocco, R. Monasson, A. Montanari, and G. Semerjian, *Analyzing Search Algorithms with Physical Methods*, Computational Complexity and Statistical Physics, 2006.
- [23] W. Barthel, A. K. Hartmann, M. Leone, F. Ricci-Tersenghi, M. Weigt, and R. Zecchina, *Physical Review Letters*, vol. 88, no. 18, article 188701, 2002.
- [24] F. Ricci-Tersenghi, M. Weigt, and R. Zecchina, “Simplest random K-satisfiability problem,” *Physical Review E*, vol. 63, no. 2, 2001.
- [25] H. Jia, C. Moore, and B. Selman, *International Conference on Theory and Applications of Satisfiability Testing*, Springer, 2004.
- [26] M. Mezard and A. Montanari, *Information, Physics, and Computation*, Oxford University Press, 2009.
- [27] F. L. Traversa, C. Ramella, F. Bonani, and M. Di Ventra, “Memcomputing NP-complete problems in polynomial time using polynomial resources and collective states,” *Science Advances*, vol. 1, no. 6, article e1500031, 2015.
- [28] J. Hale, “Asymptotic behavior of dissipative systems,” in *Mathematical Surveys and Monographs*, vol. 25, American Mathematical Society, Providence, Rhode Island, 2nd edition, 2010.
- [29] M. Di Ventra and F. L. Traversa, *Physics Letters A*, vol. 381, no. 38, pp. 3255–3257, 2017.
- [30] M. Di Ventra and F. L. Traversa, “Absence of periodic orbits in digital memcomputing machines with solutions,” *Chaos: An Interdisciplinary Journal of Nonlinear Science*, vol. 27, no. 10, article 101101, 2017.
- [31] J. S. R. Bulirsch, *Introduction to Numerical Analysis*, Springer, 2010.

Research Article

Analysis and Implementation of a New Switching Memristor Scroll Hyperchaotic System and Application in Secure Communication

Ping Liu,¹ Rui Xi,¹ Pengbo Ren,¹ Jialin Hou¹ ,¹ and Xiang Li² 

¹College of Mechanical and Electrical Engineering, Shandong Agricultural University, Taian 271018, China

²State Key Laboratory of Crop Biology, College of Life Sciences, Shandong Agricultural University, Taian 271018, China

Correspondence should be addressed to Xiang Li; lixiang@sdau.edu.cn

Received 27 February 2018; Revised 22 April 2018; Accepted 27 May 2018; Published 2 July 2018

Academic Editor: Viet-Thanh Pham

Copyright © 2018 Ping Liu et al. This is an open access article distributed under the Creative Commons Attribution License, which permits unrestricted use, distribution, and reproduction in any medium, provided the original work is properly cited.

This paper proposed a novel switching scroll hyperchaotic system based on a memristor device and explored its application to secure communication. The new system could be switched between the double-scroll chaotic system and multiscroll one by switch S1 and switch S2. We gave the construction process of the novel system, its numerical simulations, and dynamical properties, firstly. Moreover, the memristive circuit implementation of the new switching system was presented and the results were also in agreement with those of numerical simulation. Finally, the new switching memristive system was applied to secure communication by means of the drive-response synchronization with chaotic masking. When the voice signal is a rising waveform, it is encrypted by the double-scroll memristive system. When the voice signal is a falling waveform, the multiscroll memristive system works. The voice signal is completely submerged in the chaotic signal and could not be distinguished at all. Security analyses show that it is a successful application to secure communication.

1. Introduction

Chaotic systems based on memristor have widely attracted attention recently. It has many applications such as in secure communication [1–4], neural network [5–9], and chemical route [10]. A lot of researches on memristive chaotic (hyperchaotic) system have been reported, for example, global synchronization [11], state estimation [12], time delay [13], and adaptive synchronization [14] of the memristive chaotic system. On the other hand, scroll chaotic systems have been explored in many papers extensively. For instance, Ma et al. introduced simulation and circuit implementation of 12-scroll chaotic system in [15]. Chen et al. investigated the generation of grid multiscroll chaotic attractors in [16]. In [17], Chen et al. studied the fractional-order multiscroll chaotic system. And in [18–19], García-Martínez et al. and Liu et al. discussed the multiscroll hyperchaotic system and its application to secure communication, but the memristor has not been introduced to chaotic system to produce multiscroll.

With respect to the chaotic system based on memristor, its application to secure communication has been studied in many works, such as in [1–4], since memristors are nonlinear elements with memory function, which are different from resistors, capacitors, and inductors. So the applications to secure communication based on chaotic system with memristor have become a hot topic. Meanwhile, researches on application of the scroll chaotic system have also existed. Whether the memristive chaotic (hyperchaotic) system or the scroll system, application to secure communication has been very common. Till now, secure communication based on the switching memristor scroll hyperchaotic system has not been explored. Thus, it has a great significance to investigate the switching memristive scroll hyperchaotic system and its application to secure communication.

The rest of the paper was organized as follows. Section 2 introduced the construction, numerical simulations, and dynamic analysis of the switching scroll hyperchaotic system based on a memristor. The circuit implementation was given in Section 3. In Section 4, application to voice encryption was

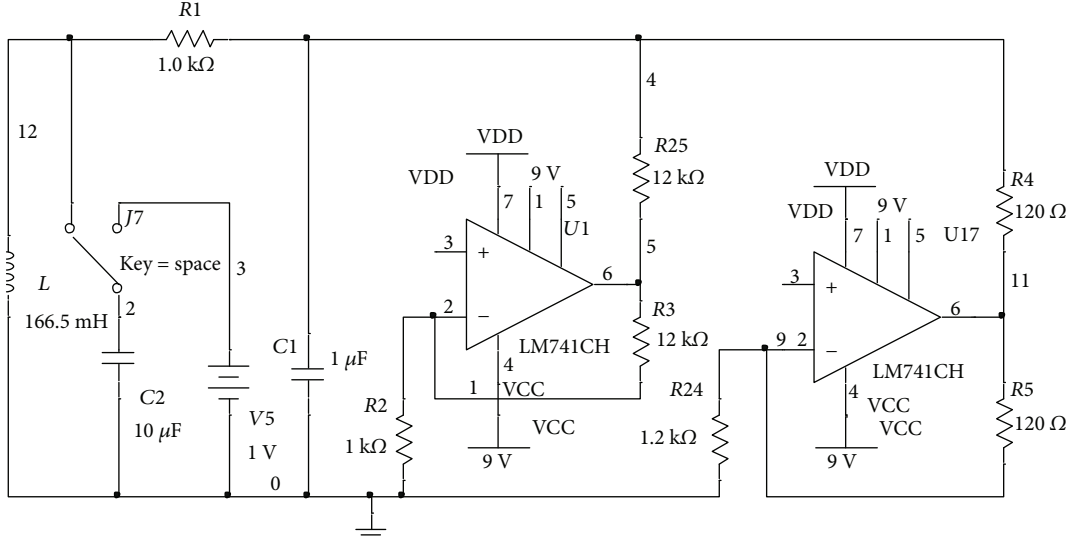


FIGURE 1: Chua's circuit diagram.

discussed using the drive-response synchronization with chaotic masking and some conclusions are given in the last.

2. System Construction and Dynamic Analysis

2.1. System Construction. The Chua's circuit is composed of a linear resistor, a linear inductor, two linear capacitors, and a nonlinear Chua's diode as shown in Figure 1.

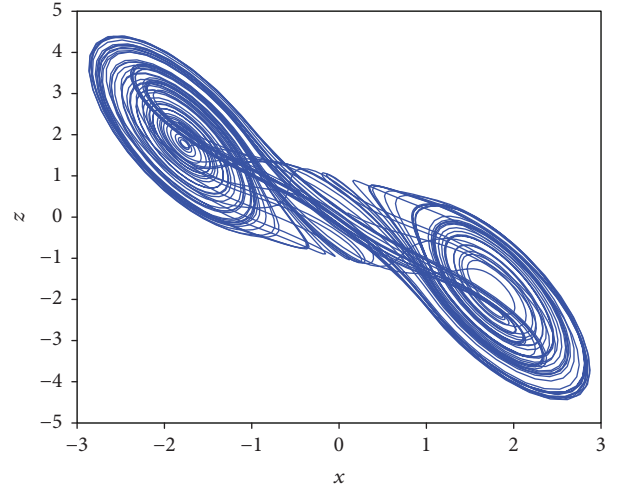
Based on Figure 1, the differential equation [20] could be obtained as

$$\begin{aligned} \frac{dx}{dt} &= a[(y - x) + f(x)], \\ \frac{dy}{dt} &= (x - y) + z, \\ \frac{dz}{dt} &= -by, \end{aligned} \quad (1)$$

where $f(x) = [-5x - 1.5(|x + 1| + |x - 1|)]/7$, when taking system parameters $a = 10$ and $b = 15$ with initial values $x(0) = y(0) = z(0) = 0.1$, we can get the projection on the $x - z$ phase plane of the double-scroll attractors shown in Figure 2.

In Figure 1, the resistor R and the Chua's diode are replaced by a magnetically controlled memristor M and a linear function, respectively. So, we can get a new hyperchaotic memristive circuit demonstrated by Figure 3. The memristor is the fourth kind of basic passive circuit element which is proposed by Professor Chua. There are two mathematical definitions of memristor, which are charge-controlled memristor and flux-controlled memristor, respectively [21]. The expression of a charge-controlled memristor is

$$\begin{aligned} v(t) &= M(q(t))i(t), \\ M(q(t)) &= \frac{d\varphi(q)}{dq}. \end{aligned} \quad (2)$$

FIGURE 2: A projection of the double-scroll attractor onto the (x, z) plane.

The flux-controlled memristor could be expressed as

$$\begin{aligned} i(t) &= W(\varphi(t))v(t), \\ W(\varphi) &= \frac{dq(\varphi)}{d\varphi}. \end{aligned} \quad (3)$$

And basic model of the memristor can be found in [22]. The definition of memristor was extended in [23],

$$\begin{aligned} y(t) &= g(z, u, t)u(t), \\ \frac{dz}{dt} &= f(u, z, t), \end{aligned} \quad (4)$$

where $u(t)$ and $y(t)$ are the input signal and output signal of the memristor, respectively. z is the system state variable. The input of the magnetically controlled memristor is voltage u ,

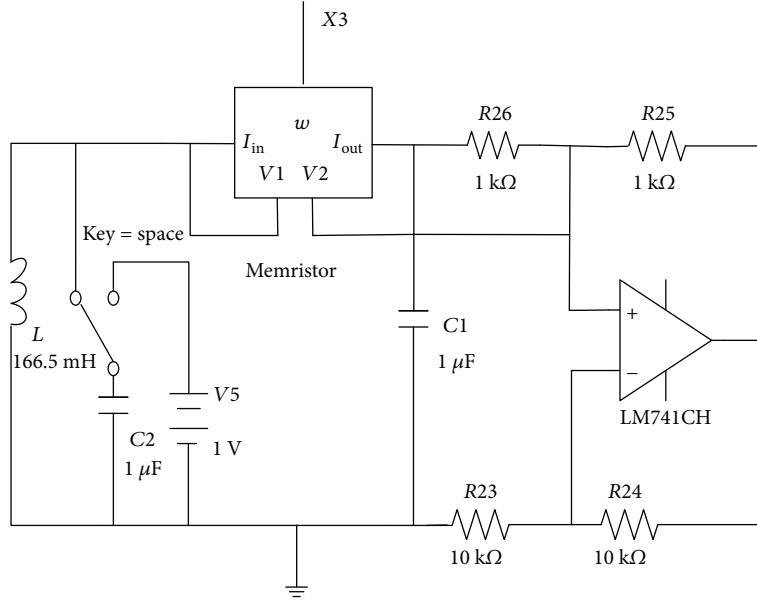
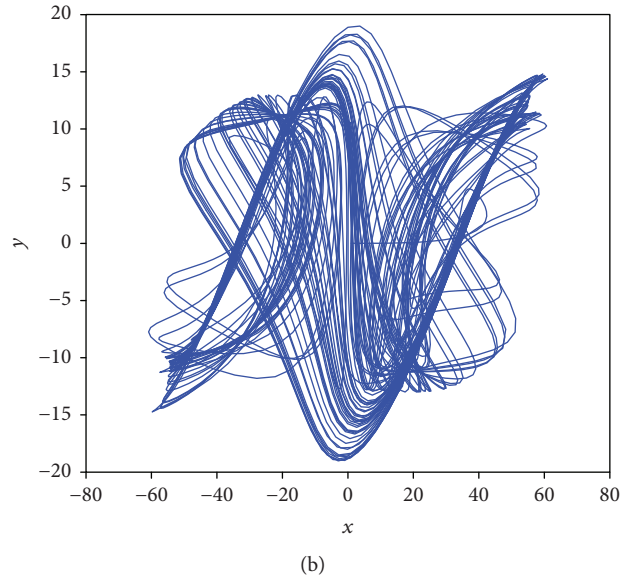
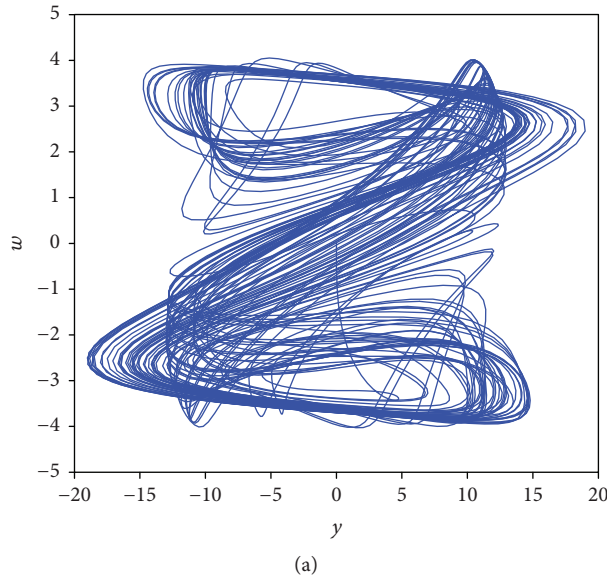


FIGURE 3: The new hyperchaotic memristive circuit.

FIGURE 4: Projections of the double-scroll hyperchaotic attractors onto the (y, w) and (x, y) plane. (a) (y, w) plane. (b) (x, y) plane.

the output is the current i following through the memristor, and flux ϕ is the state variable.

According to the definition of memristor, we obtain a novel expression as

$$\begin{aligned} i &= W(\phi)u, \\ \frac{d\phi}{dt} &= u_2 - u_1 - c\phi, \end{aligned} \quad (5)$$

where $W(\phi)$ is called memory conductance, let $W(\phi) = 0.1\phi^2$. According to the Kirchhoff's law and component parameter constraints, circuit dynamic equation could be obtained as

$$\begin{aligned} C1 \frac{dv_1}{dt} &= [W(\phi)(V_2 - V_1) + g(V_1)], \\ C2 \frac{dv_2}{dt} &= W(\phi)(V_1 - V_2) + I_i, \\ L \frac{dI_i}{dt} &= -V_2, \\ RC \frac{d\phi}{dt} &= V_2 - V_1 - c\phi, \end{aligned} \quad (6)$$

where $\tau_0 = RC$ is the time constant. Dimensionless time $\tau = t/\tau_0$ could be obtained by the scaling time and state space. The dimensional state variable $x = V_1$, $y = V_2$, $z = Ri$, $w = \phi$,

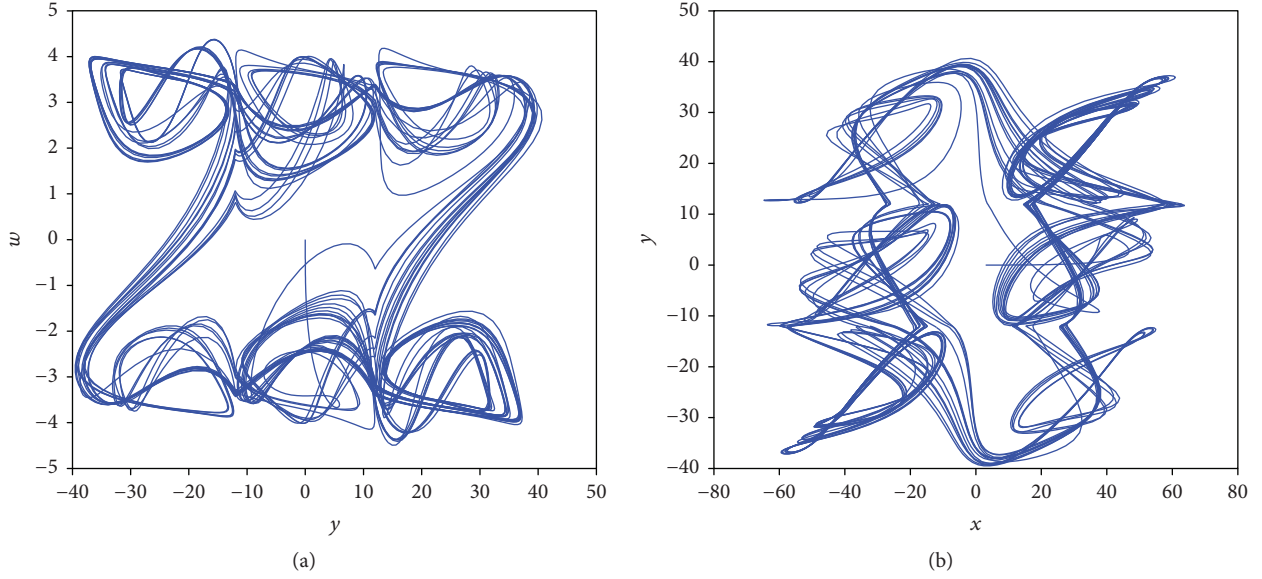


FIGURE 5: Projections of the 2×3 multiscroll hyperchaotic attractors onto the (y, w) and (x, y) plane. (a) (y, w) plane. (b) (x, y) plane.

$a = C/C_1$, $C = C_2$, $b = cR^2/L$, $f(w) = W(\phi)/R$, and $g(x) = g(V_1)/R$, so we can obtain

$$\begin{aligned} \frac{dx}{dt} &= a[f(w)(y-x) + g(x)], \\ \frac{dy}{dt} &= f(w)(x-y) + z, \\ \frac{dz}{dt} &= -by, \\ \frac{dw}{dt} &= y - x - cw, \end{aligned} \quad (7)$$

where $f(w) = dw^2$, $g(x) = 0.9x$, and a, b, c , and d are system parameters. The simulation results are given in Figure 4 by taking initial values $x(0) = 1$, $y(0) = z(0) = w(0) = 0$, and parameters $a = 10$, $b = 60$, $c = 10$, and $d = 0.1$. Then, based on (7), the N-scroll is realized in y direction by using the step function.

There are two forms of step function, when

$$h(y) = A \left\{ \sum_{i=1}^M \text{sgn}[y + (2i-1)A] + \sum_{i=1}^M \text{sgn}[y - (2i-1)A] \right\}, \quad M \geq 1, \quad (8)$$

$2M + 1$ scrolls could be generated in y direction.

When

$$h(y) = A \left\{ -\text{sgn}(y) + \sum_{i=0}^{N-1} \text{sgn}[y + (2i)A] + \sum_{i=0}^{N-1} \text{sgn}[y - (2i)A] \right\}, \quad N \geq 0, \quad (9)$$

$2N$ scrolls could be generated in y direction.

N-scroll could be obtained by a reasonable set of step function parameters. For example, when $M = 1$, $A = 12$,

$$h(y) = 12[\text{sgn}(y - 12) + \text{sgn}(y + 12)]. \quad (10)$$

The 2×3 multiscroll hyperchaotic system based on a memristor device is obtained as

$$\begin{aligned} \frac{dx}{dt} &= a[f(w)(y-x-h(y)) + g(x)], \\ \frac{dy}{dt} &= f(w)(x-y+h(y)) + z, \\ \frac{dz}{dt} &= -b(y-h(y)), \\ \frac{dw}{dt} &= y - x - h(y) - cw. \end{aligned} \quad (11)$$

When system parameters are $a = 10$, $b = 60$, $c = 10$, and $d = 0.1$ with initial values $x(0) = 3$ and $y(0) = z(0) = w(0) = 0$, simulation results are presented in Figure 5.

Similarly, 2×5 and 2×6 multiscroll hyperchaotic system could be also obtained by taking $M = 2$, $A = 12$, and $N = 3$, $A = 12$, and

$$\begin{aligned} h(y) &= 12[\text{sgn}(y + 12) + \text{sgn}(y - 12) \\ &\quad + \text{sgn}(y + 36) + \text{sgn}(y - 36)], \\ h(y) &= 12[\text{sgn}(y) + \text{sgn}(y - 24) + \text{sgn}(y + 24) \\ &\quad + \text{sgn}(y - 48) + \text{sgn}(y + 48)], \end{aligned} \quad (12)$$

respectively.

When selecting system parameters $a = 10$, $b = 60$, $c = 10$, and $d = 0.1$ with initial values $x(0) = 3$ and $y(0) = z(0) = w(0) = 0$, the numerical simulations of 2×5 and 2×6 multiscroll hyperchaotic system are shown in Figures 6 and 7.

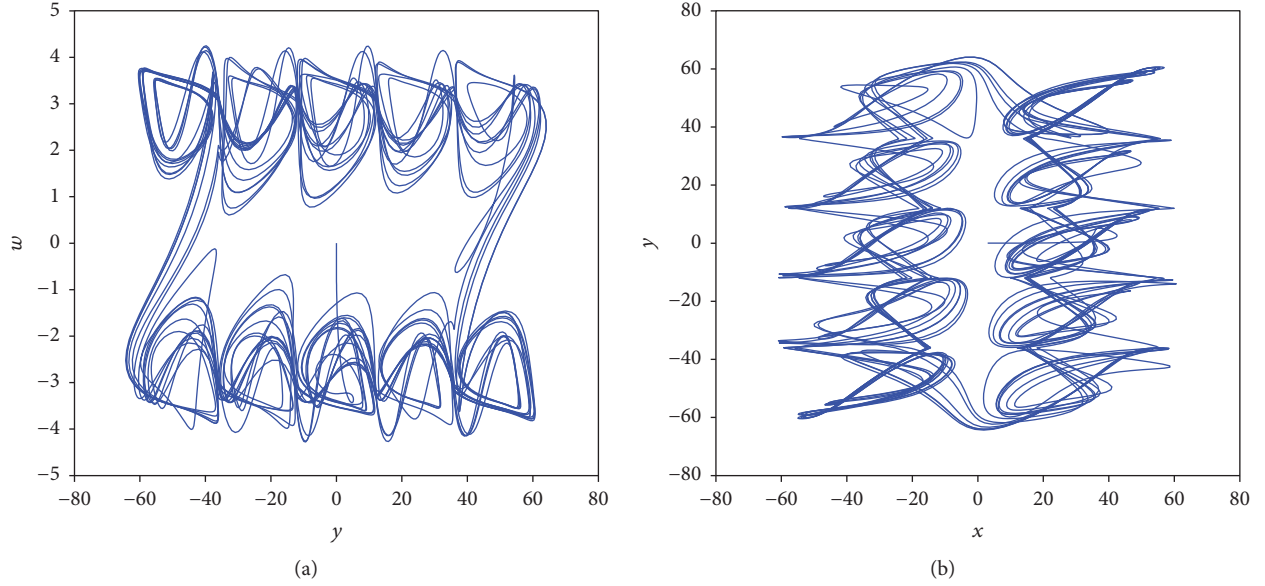


FIGURE 6: Projections of the 2×5 multiscroll hyperchaotic attractors onto the (y, w) and (x, y) plane. (a) (y, w) plane. (b) (x, y) plane.

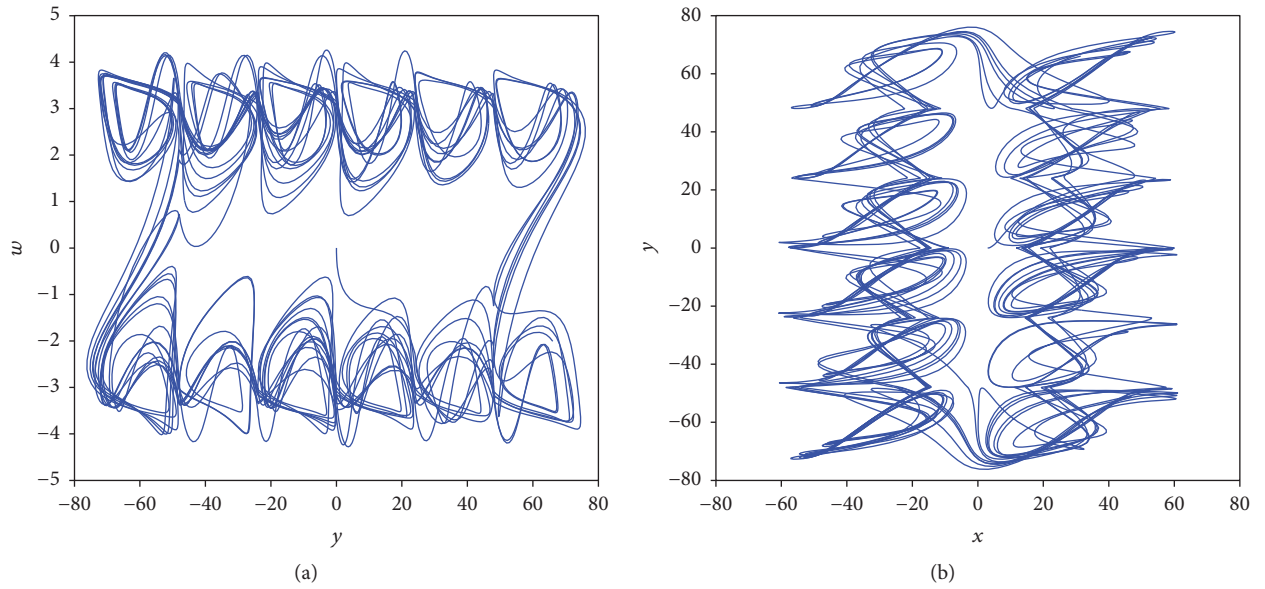


FIGURE 7: Projections of the 2×6 multiscroll hyperchaotic attractors onto the (y, w) and (x, y) plane. (a) (y, w) plane. (b) (x, y) plane.

2.2. Dynamic Analysis

2.2.1. The Double-Scroll Memristive System Is Taken as an Example to Analyse the Dynamic Properties

(1) *Lyapunov Exponents.* When selecting system parameters $a = 10$, $b = 60$, $c = 10$, and $d = 0.1$ with initial values $x(0) = 1$ and $y(0) = z(0) = w(0) = 0$, we can get the Lyapunov exponents diagram as shown in Figure 8.

From Figure 8, we can see that the chaotic system has two positive Lyapunov exponents. So, the system is a hyperchaotic system and has two scrolls.

(2) *Bifurcation Diagram.* Lyapunov exponents and bifurcation diagram of the system due to the variation of parameter

b is displayed in Figure 9. We could see that when $35 < b < 43$ and $54 < b < 70$, the system shows chaotic behavior.

(3) *Dissipation.* Generation of chaotic behavior is decided by whether the system has a dissipative structure or not [24]. The dissipative formula of the system is

$$\nabla V = \frac{\partial \dot{x}}{\partial x} + \frac{\partial \dot{y}}{\partial y} + \frac{\partial \dot{z}}{\partial z} + \frac{\partial \dot{w}}{\partial w} = 0.9a - c < 0, \quad (13)$$

so the system is dissipative, converging at an exponential rate $e^{0.9a-c}$ until it becomes 0. When $t \rightarrow \infty$, every volume element which contains trajectories of the system shrinks to zero with the rate of exponential convergent.

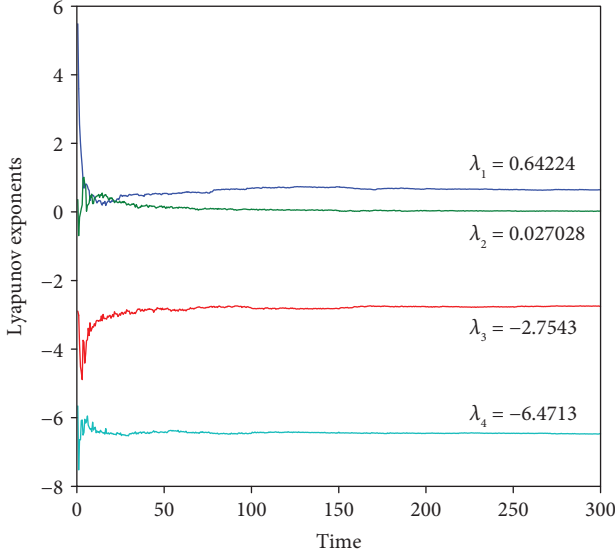


FIGURE 8: Lyapunov exponents diagram.

(4) *Equilibrium Points and Stability.* The Jacobian matrix of the system is

$$\begin{pmatrix} 9 - w^2 & w^2 & 0 & 2w(y - x) \\ 0.1w^2 & -0.1w^2 & 1 & 0.2w(x - y) \\ 0 & -60 & 0 & 0 \\ -1 & 1 & 0 & -10 \end{pmatrix}. \quad (14)$$

The equilibrium points of the system could be calculated by making (7) as 0. We could get three equilibrium points as

$$\begin{aligned} S_0 &= (0, 0, 0, 0), \\ S_1 &= (30, 0, -27, -3) \\ S_2 &= (-30, 0, 27, 3). \end{aligned} \quad (15)$$

The Jacobian matrix at point S_0 becomes

$$\begin{pmatrix} 9 & 0 & 0 & 0 \\ 0 & 0 & 1 & 0 \\ 0 & -60 & 0 & 0 \\ -1 & 1 & 0 & -10 \end{pmatrix}. \quad (16)$$

Eigenvalues at point S_0 are $\lambda_1 = -10$, $\lambda_2 = 9$, $\lambda_3 = 7.746i$, and $\lambda_4 = -7.746i$. The Jacobian matrix at point S_1 and S_2 becomes

$$\begin{pmatrix} 0 & 9 & 0 & 180 \\ 0.9 & -0.9 & 1 & -18 \\ 0 & -60 & 0 & 0 \\ -1 & 1 & 0 & -10 \end{pmatrix}. \quad (17)$$

The Equilibria S_1 and S_2 could have eigenvalues $\lambda_1 = -5.9483 + 13.6659i$, $\lambda_2 = -5.9483 - 13.6659i$, $\lambda_3 = 0.4983 + 6.9549i$, and $\lambda_4 = 0.4983 - 6.9549i$, which are called saddle points of index 2 since the two complex conjugate eigenvalues have positive real parts [25, 26]. It is clear that S_0 is the first type saddle point since the real eigenvalue is positive [25, 26]. It is noticed that the scrolls are generated only around the equilibria of saddle points of index 2 [25, 26]. Moreover, equilibria S_1 and S_2 correspond to the two saturated plateaus, which are responsible for generating the two scrolls in the double-scroll attractor. However, the equilibrium point S_0 corresponds to the saturated slope and is responsible for connecting these two symmetrical scrolls.

2.2.2. The Dynamic Analysis of 2×3 Multiscroll Hyperchaotic System. The dynamic analysis of 2×3 multiscroll hyperchaotic system is introduced briefly as follows. Let

$$\frac{dx}{dt} = \frac{dy}{dt} = \frac{dz}{dt} = \frac{dw}{dt} = 0. \quad (18)$$

Equation of equilibrium points could be obtained as

$$\begin{aligned} a[f(w)(y - x - h(y)) + g(x)] &= 0, \\ f(w)(x - y + h(y)) + z &= 0, \\ -b(y - h(y)) &= 0, \\ y - x - h(y) - cw &= 0. \end{aligned} \quad (19)$$

From (19), we could get the coordinate of system equilibrium points in the y -axis as $y = h(y)$, that is, $y = 0, \pm 12, \pm 24$, $x = \pm 30$. The figures of equilibrium points and chaotic attractors of the multiscroll hyperchaotic system are demonstrated in Figure 10. Therefore, the number of equilibrium points in the y -axis direction is 5×2 . The solid points represent the second type saddle point, which correspond to the six saturated plateaus and are responsible for generating the six scrolls in the 2×3 -scroll attractors. The hollow points represent the first type saddle point, which correspond to the saturated slope and are responsible for connecting these six symmetrical scrolls.

3. The Circuit Implementation of the Switching Scroll Hyperchaotic System

3.1. The Circuit Implementation of the Double-Scroll Hyperchaotic System. Circuit diagram of the double-scroll hyperchaotic system is displayed in Figure 3. With respect to the memristor shown in Figure 11(a), its internal circuit structure could be obtained in [27], shown in Figure 11(b). Circuit implementation results are shown in Figure 12, which are in agreement with numerical simulation results in Figure 4.

Symbolic function circuit is designed by the saturated output voltage of the operational amplifier to achieve step function. The saturated voltage of the operational amplifier in Figure 13 is E .

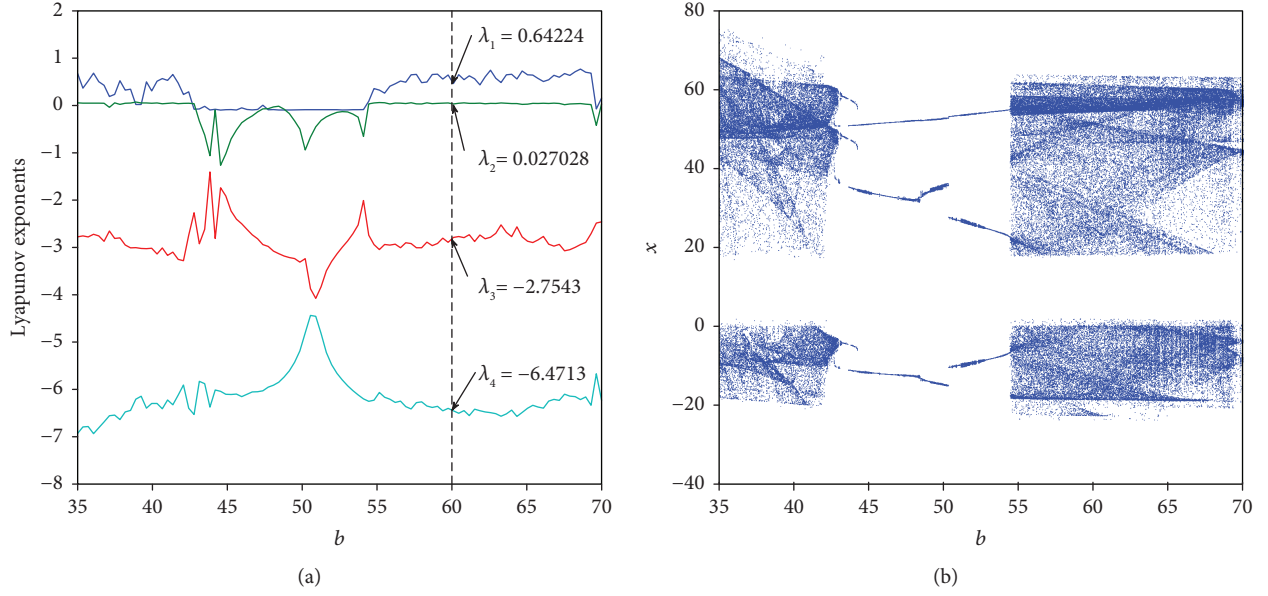


FIGURE 9: Lyapunov exponents and bifurcation diagram with respect to parameter b . (a) Lyapunov exponents diagram. (b) Bifurcation diagram.

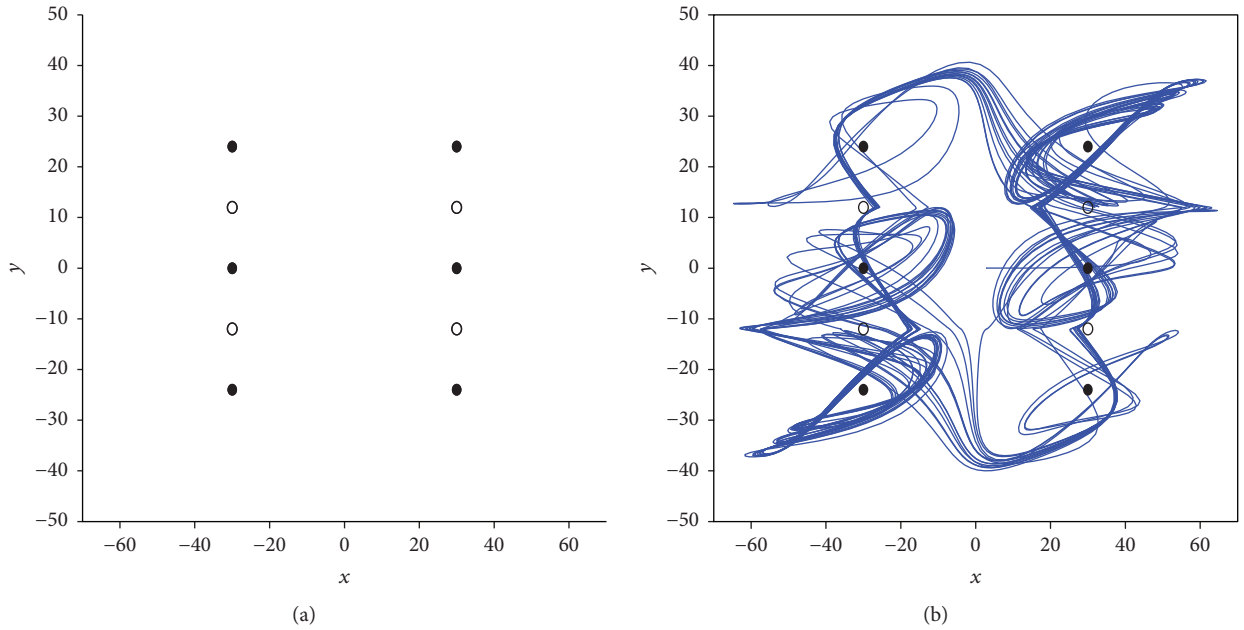


FIGURE 10: Equilibrium points and attractors of the 2×3 multiscroll hyperchaotic system. (a) Equilibrium points. (b) 2×3 multiscroll attractors.

$$V_{\text{out}} = -\frac{R3}{R2} \times \frac{R5}{R4} \times E \times [\text{sgn}(V_{\text{in}} + V_5) + \text{sgn}(V_{\text{in}} - V_8)]. \quad (20)$$

The step function circuit designed by the method is easy to expand and achieve, that is, more complex function could be realized by increasing the number of corresponding comparison circuit. In the following part, we choose the 2×3 scroll system as an example to discuss the multiscroll system. Based on Figure 13, step function is connected between the capacitor $C1$ and the ground to get the circuit

diagram of the multiscroll hyperchaotic system shown in Figure 14, and its circuit simulation results are displayed in Figure 15 which are in accordance with the numerical simulation results.

4. Applications to Secure Communication

4.1. Drive-Response Synchronization of the Switching Systems. The synchronization of the switching systems is briefly stated as follows. The drive system from (11) is

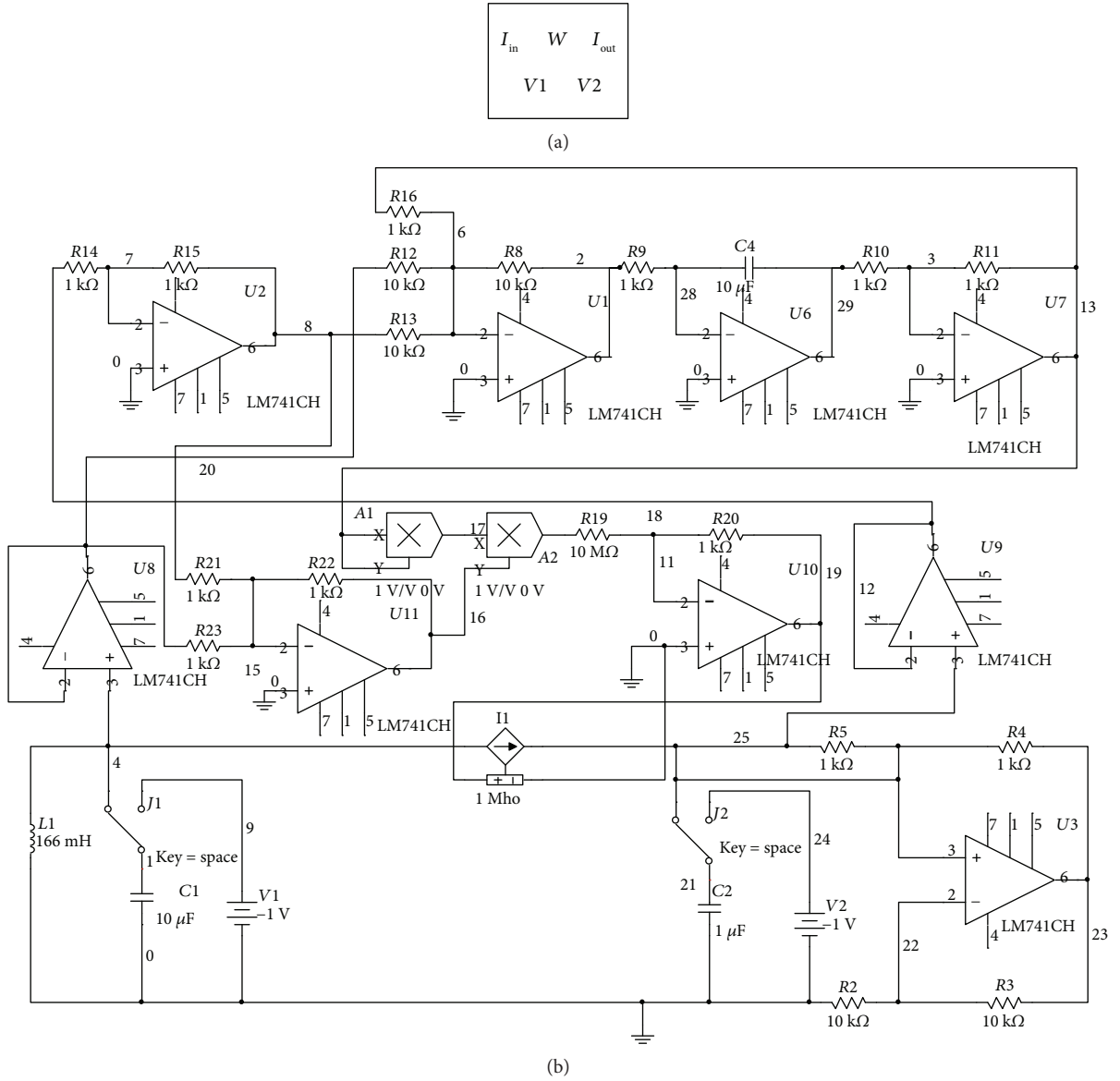


FIGURE 11: The memristor and its internal circuit. (a) The memristor. (b) Its internal circuit.

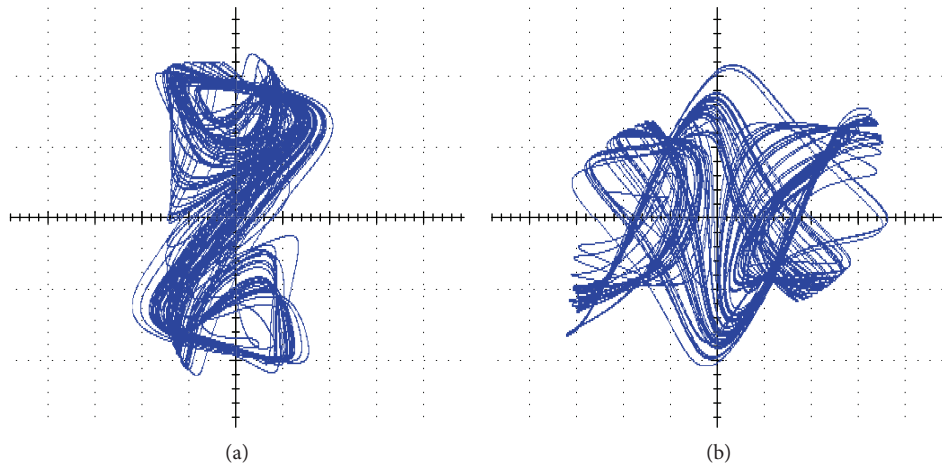


FIGURE 12: Circuit implementation of the double-scroll hyperchaotic system. (a) (y, w) plane. (b) (x, y) plane.

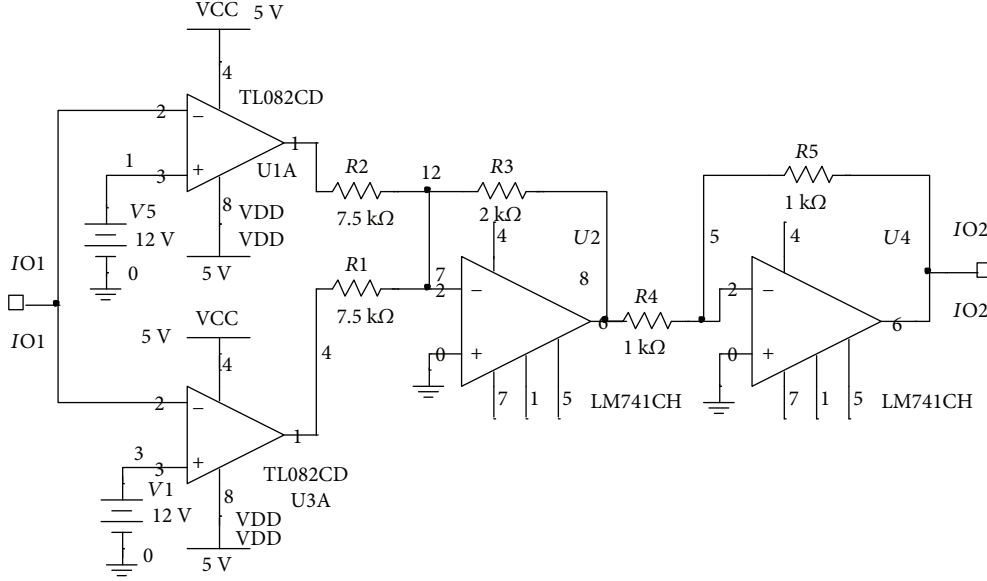


FIGURE 13: Step function circuit.

$$\begin{aligned}
 \dot{x}_1 &= a[f(w_1)(y_1 - x_1 - h(y_1)) + g(x_1)], \\
 \dot{y}_1 &= f(w_1)(x_1 - y_1 + h(y_1)) + z_1, \\
 \dot{z}_1 &= -b(y_1 - h(y_1)), \\
 \dot{w}_1 &= y_1 - x_1 - h(y_1) - cw_1,
 \end{aligned} \tag{21}$$

where $f(w_1) = dw_1^2$, $g(x_1) = 0.9x_1$, a , b , c , and d are system parameters, $a = 10$, $b = 60$, $c = 10$, and $d = 0.1$, and initial values $x_1(0) = 1$ and $y_1(0) = z_1(0) = w_1(0) = 0$.

And the response system is

$$\begin{aligned}
 \dot{x}_2 &= a[f(w_2)(y_2 - x_2 - h(y_2)) + g(x_2)] + u_1, \\
 \dot{y}_2 &= f(w_2)(x_2 - y_2 + h(y_2)) + z_2 + u_2, \\
 \dot{z}_2 &= -b(y_2 - h(y_2)) + u_3, \\
 \dot{w}_2 &= y_2 - x_2 - h(y_2) - cw_2 + u_4,
 \end{aligned} \tag{22}$$

where $f(w_2) = dw_2^2$, $g(x_2) = 0.9x_2$, a , b , c , and d are system parameters, $a = 10$, $b = 60$, $c = 10$, and $d = 0.1$, and initial values $x_2(0) = 1$ and $y_2(0) = z_2(0) = w_2(0) = 0$.

The state error is defined as

$$e = P - \epsilon Q, \tag{23}$$

where ϵ is diagonal matrix, $P = [x_1, y_1, z_1, w_1]^T$, and $Q = [x_2, y_2, z_2, w_2]^T$. $\epsilon = \text{diag}\{\epsilon_1, \epsilon_2, \epsilon_3, \epsilon_4\}$ is scaling function matrix (if $\epsilon = \text{diag}\{1, 1, 1, 1\}$, $\epsilon = \text{diag}\{-1, -1, -1, -1\}$, $\epsilon = \text{diag}\{\alpha, \alpha, \alpha, \alpha\}$ (α is a constant), and $\epsilon = \text{diag}\{\alpha_1, \alpha_2, \alpha_3, \alpha_4\}$, respectively, then the synchronization is called as complete synchronization, antisynchronization, projective synchronization, and modified projective synchronization). In this paper, we choose $\epsilon = \text{diag}\{-1, -1, -1, -1\}$, that is to say, the synchronization type is antisynchronization.

The synchronization controller of the response system is designed as

$$\begin{aligned}
 u_1 &= -w_2^2(y_2 - x_2 - h(y_2)) - w_1^2(y_1 - x_1 - h(y_1)) \\
 &\quad - 9x_2 - 9x_1 - \mu_1 e_1, \\
 u_2 &= -0.1w_2^2(x_2 - y_2 + h(y_2)) - z_2 \\
 &\quad - 0.1w_1^2(x_1 - y_1 + h(y_1)) - z_1 - \mu_2 e_2, \\
 u_3 &= 60(y_2 - h(y_2)) + 60(y_1 - h(y_1)) - \mu_3 e_3, \\
 u_4 &= -y_2 + x_2 + h(y_2) + 10w_4 - y_1 + x_1 \\
 &\quad + h(y_1) + 10w_1 - \mu_4 e_4.
 \end{aligned} \tag{24}$$

According to the systems (21), (22), (23), and controller (24), we could obtain the final expression of the error system as

$$\begin{aligned}
 \dot{e}_1 &= -\mu_1 e_1, \\
 \dot{e}_2 &= -\mu_2 e_2, \\
 \dot{e}_3 &= -\mu_3 e_3, \\
 \dot{e}_4 &= -\mu_4 e_4.
 \end{aligned} \tag{25}$$

Let $\mu_1 = 2$, $\mu_2 = 9$, $\mu_3 = 7$, and $\mu_4 = 4$, it is obvious that all roots of the error system have negative real parts. When $t \rightarrow \infty$, the error system (25) converge to 0 and therefore the synchronization between the drive system and the response system is realized.

Next, we illustrate the validity of the proposed controller by MATLAB 2010a. Selecting initial values $x_1(0) = 3$, $y_1(0) = 0$, $z_1(0) = 0$, $w_1(0) = 0$, $x_2(0) = 3$, $y_2(0) = 1$, $z_2(0) = 2$, and $w_2(0) = 2$, we could get those of the error system as $e_1(0) = 6$, $e_2(0) = 1$, $e_3(0) = 2$, and $e_4(0) = 2$. Keeping the system parameters, the initial values, the scale factors, and synchronization controllers unchanged, simulation results are illustrated in Figure 16. One can see that the error dynamic system is stable asymptotically by using the designed controllers, which implies that the drive system and the response system could achieve synchronization well.

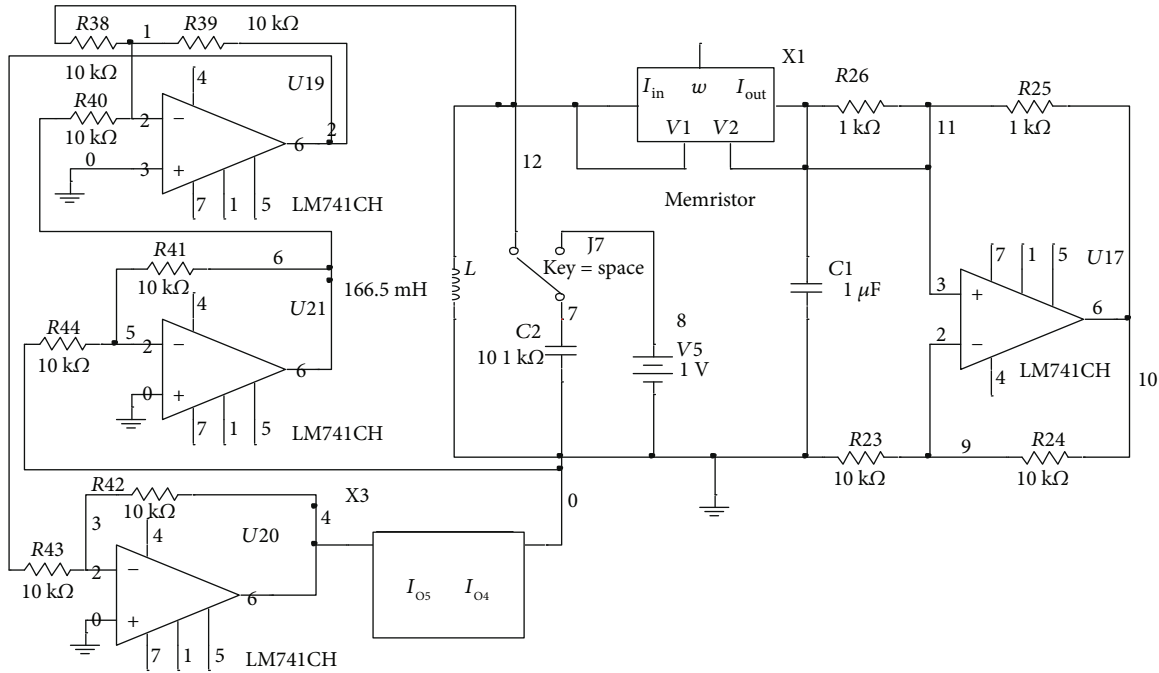


FIGURE 14: Circuit diagram of the multiscroll hyperchaotic system.

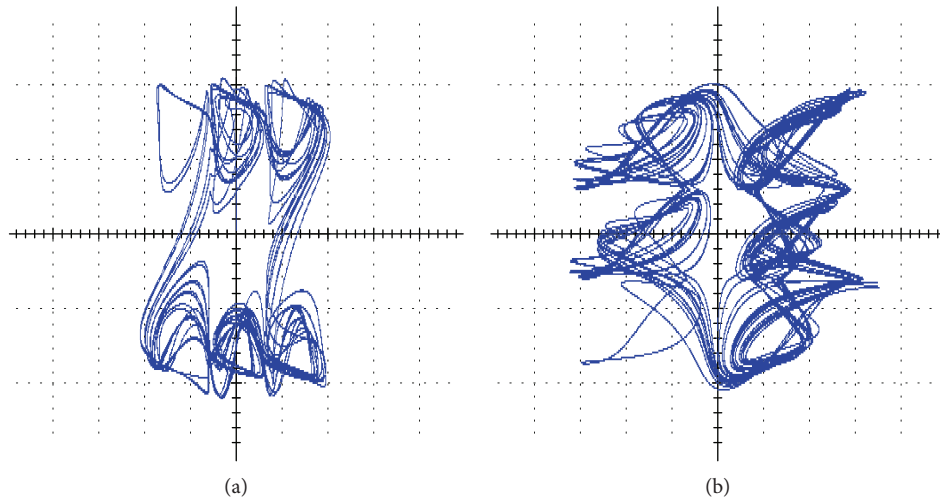


FIGURE 15: Circuit implementation of the multiscroll hyperchaotic system. (a) (y, w) plane. (b) (x, y) plane.

4.2. Drive-Response Circuit Synchronization of the Switching Systems. Drive-response synchronous circuit of the multi-scroll hyperchaotic system is demonstrated in Figure 17.

The $x_1 - T$ and $y_1 - T$ waveforms of the drive system and the $x_2 - T$ and $y_2 - T$ waveforms of the response system are, respectively, shown in Figures 18(a) and 18(b). The $x_1 - x_2$ waveform at the time of synchronization is shown in Figure 19. From the simulation results, we could see that voltage signal waveforms of the drive and response system are exactly the same, and the synchronous phase diagram of the corresponding state is a straight line through the origin point with 45 degrees, indicating that the corresponding state variables in the two circuits achieve a good synchronization. When it is applied to the secure communication,

the synchronization method is simple and the circuit implementation is convenient.

The drive-response synchronous circuit of the double-scroll hyperchaotic system is similar to that of the multiscroll one and will be omitted here.

4.3. Application to Secure Communication. In the circuit implementation, the double-scroll and multiscroll circuits are encapsulated, respectively, so as to simplify the circuit structure.

4.3.1. Description of Encryption and Decryption Algorithm. In this subsection, the synchronization circuit above is applied to secure communications. A voice signal $m(t) =$

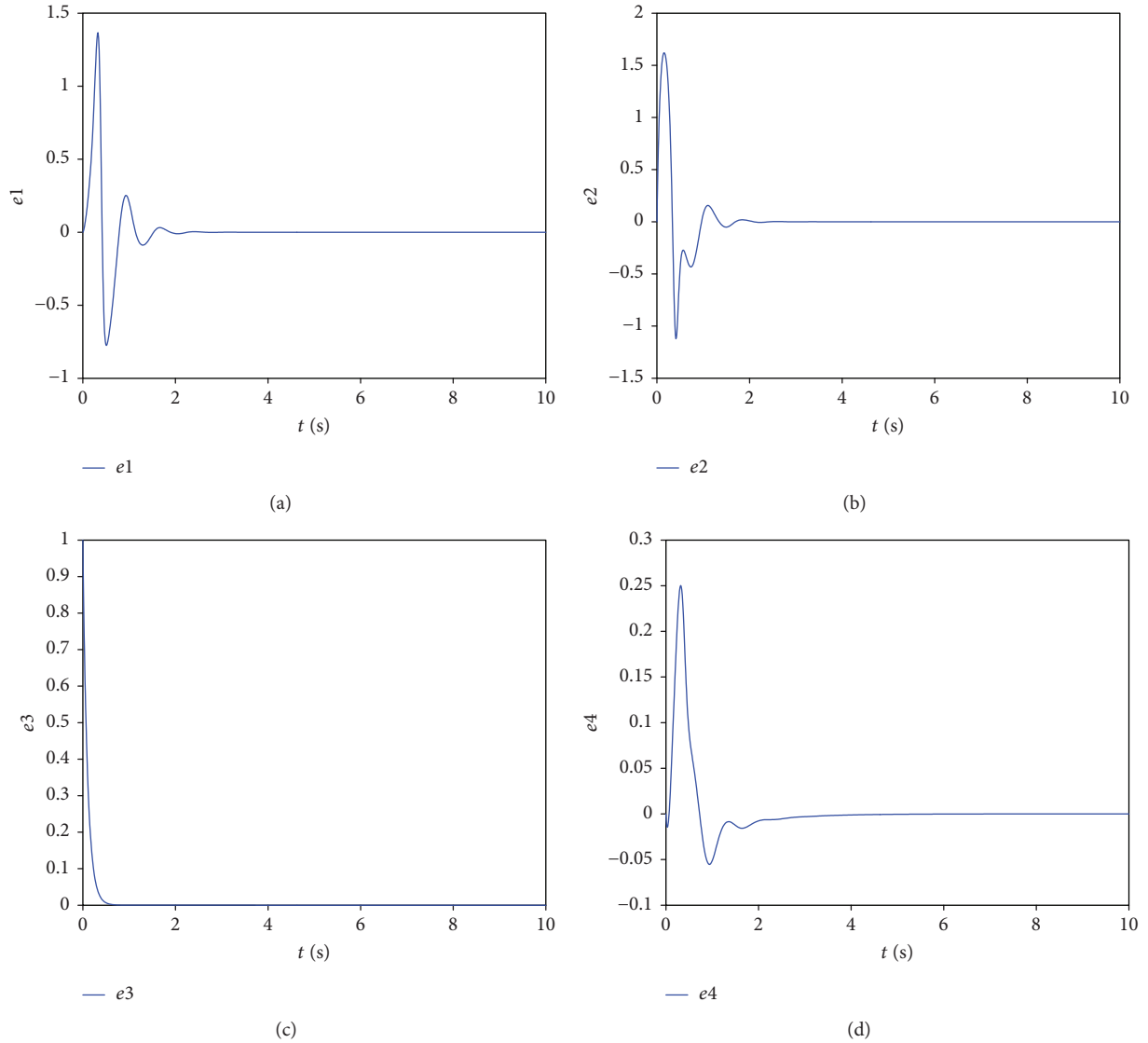


FIGURE 16: The state trajectories of the error system. (a) State trajectories of e_1 . (b) State trajectories of e_2 . (c) State trajectories of e_3 . (d) State trajectories of e_4 .

$0.5(0.1 \sin t + 1)$ carrying the message to be transmitted could be masked by the chaotic sequence $x_1(t)$, which is a key sequence from the double-scroll and multiscroll hyperchaotic system. And

$$x_1 = \begin{cases} x_{1d}, & 2n\pi \leq t \leq \frac{2n\pi + \pi}{2}, \\ x_{1m}, & 2n\pi + \frac{3\pi}{2} \leq t < (2n+1)\pi, \end{cases} \quad (26)$$

$n = 0, 1, 2, \dots$

The chaotic synchronous circuit given above could be applied to extract the message at the receiver. Some strategies could be used to make the actual transmitted signal $s(t)$ as broadband as possible, that is, to make its detection through spectral techniques difficult. In general, three strategies are proposed in chaotic secure communications [28]. One is signal masking, where $s(t) = x_1(t) + \alpha m(t)$; the second is

modulation, $s(t) = x_1(t) + m(t)$; the third is a combination of masking and modulation, $s(t) = x_1(t) + \alpha m(t)$. Here, chaotic masking is used to encryption. The transmitted signal is $s(t) = x_1(t) + \alpha m(t)$ and injected into the transmitter and, simultaneously, transmitted to the receiver. By the above synchronous circuit, a chaotic receiver is then derived to recover the voice signal at the receiving end, that is,

$$\begin{aligned} m(t) &= \frac{1}{\alpha} \lim_{t \rightarrow \infty} (x_2(t) + s(t)) \\ &= \frac{1}{\alpha} \lim_{t \rightarrow \infty} (x_2(t) + x_1(t) + \alpha m(t)) = m(t). \end{aligned} \quad (27)$$

The switching encryption circuit is shown in Figure 20. System 1 and system 2 represent the double-scroll and multiscroll hyperchaotic circuit, respectively. When the voice signal is a rising waveform, switch S1 connects to k1, and switch S2 connects to k3. At this time, x_{1d} is used as the key

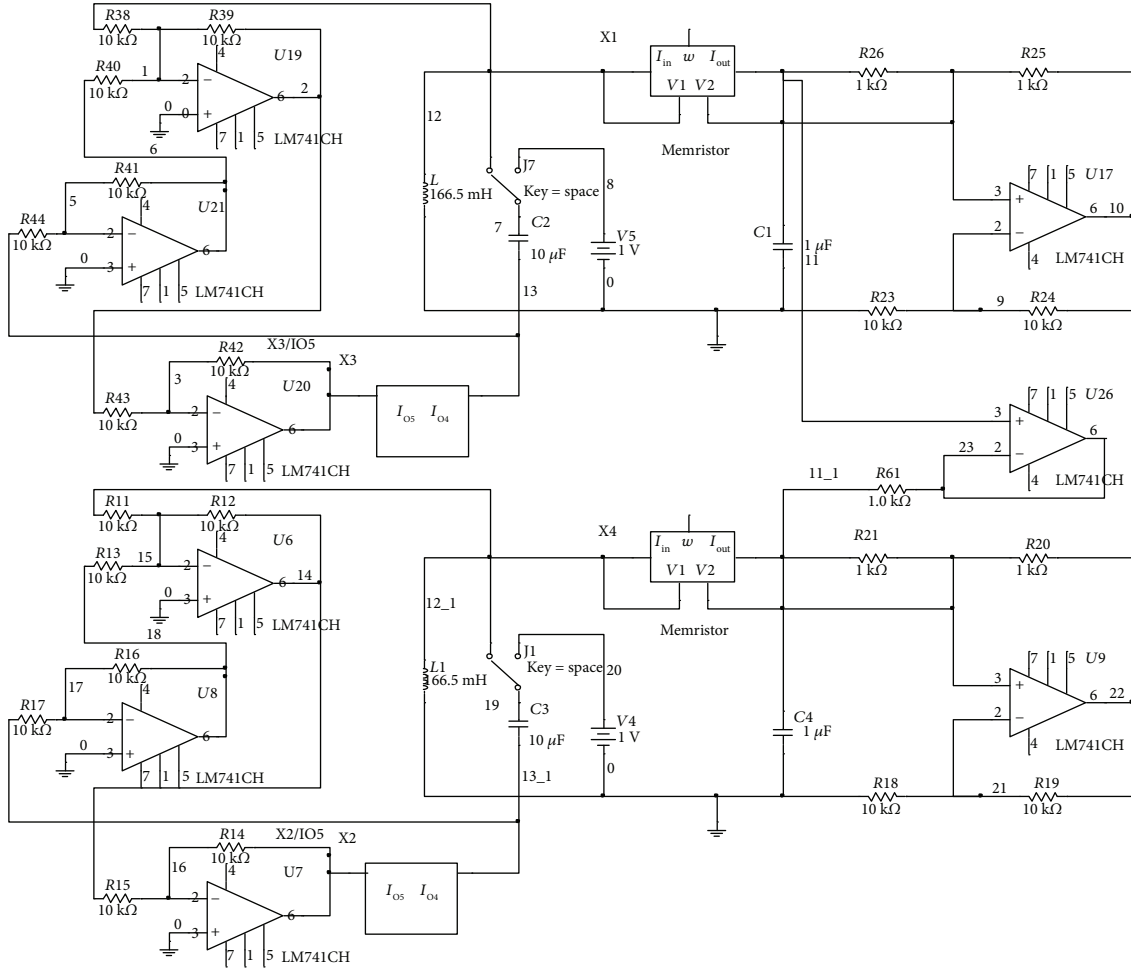
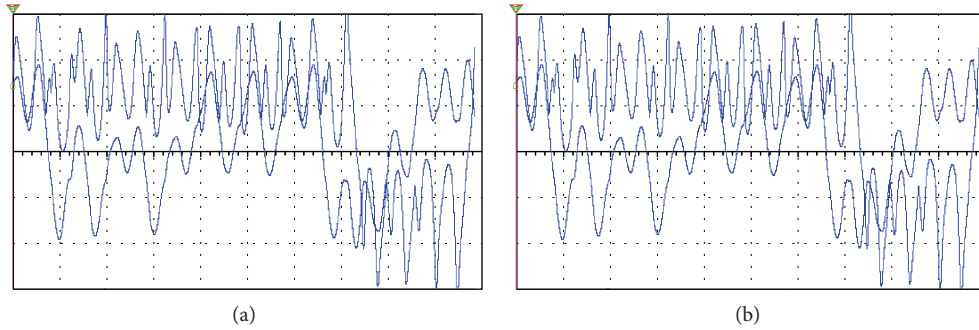
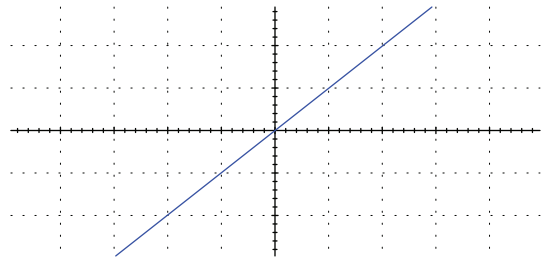


FIGURE 17: Drive-response synchronous circuit of the multiscroll hyperchaotic system.

FIGURE 18: The $x_1 - T$ and $y_1 - T$ waveforms and the $x_2 - T$ and $y_2 - T$ waveforms.

sequence in the encryption, that is to say, the double-scroll hyperchaotic system works. When the voice signal is a falling waveform, switch S1 connects to k_2 , and switch S2 connects to k_4 . At this point, x_{1m} is used to encrypt the voice signal, and the multiscroll hyperchaotic system does. With the voice waveform changes, the connection mode of the switch S1 and switch S2 is different. Finally, the switching between the double-scroll and the multiscroll hyperchaotic system is realized. In the decryption process, the chaotic signal generated by the response system is used to decrypt the signal. The

FIGURE 19: The $x_1 - x_2$ waveform at the time of synchronization.

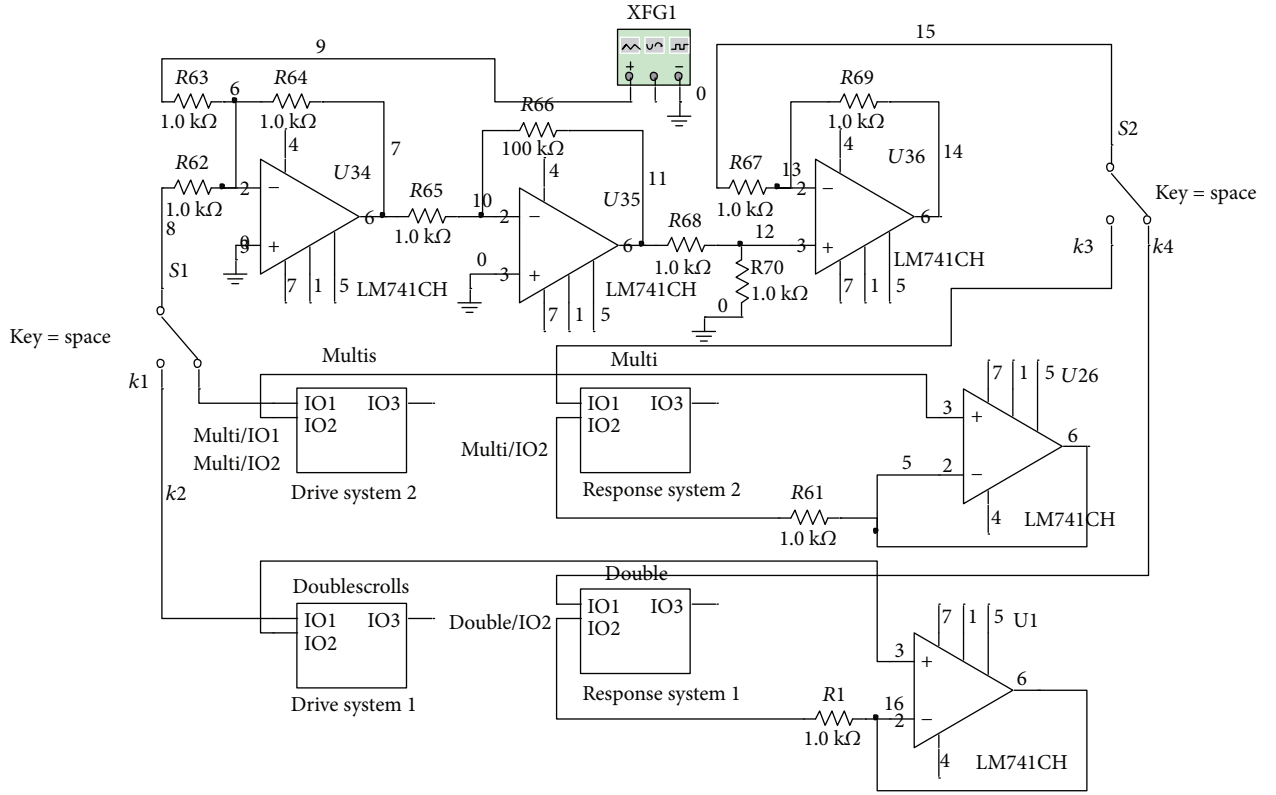


FIGURE 20: The switching encryption circuit.

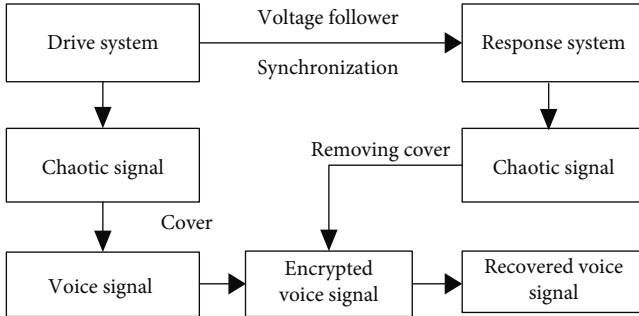


FIGURE 21: Encryption and decryption flow chart.

schematic diagram is shown in Figure 21. The key sequence generated by the drive system is used to cover the voice signal and that generated by the response system works in removing the cover of the encrypted signal.

Results of encryption and decryption are displayed in Figure 22. We can know that the voice signal is completely covered by the chaotic signal, and the original shape could not be seen at all after the voice signal and the chaotic signal generated by the driving system is superimposed. The cracker could not get any information of the voice signal from the channel [29–30]. It has proved that the switching encryption method has pretty good privacy.

Moreover, the decrypted voice signal and the original voice signal are identical, indicating that the original signal could be recovered well by the chaotic signal generated by the response system. This proves the effectiveness and reliability of the encryption method.

4.3.2. Security Analyses

(1) *Key Space Analysis.* The size of key space is the total number of different keys used in the encryption process. The key space should be large enough to resist attacks. In the encryption scheme, thirteen key parameters are used, which are $x(0)$, $y(0)$, $z(0)$, and $w(0)$ from the double-scroll hyperchaotic system, $\dot{x}(0)$, $\dot{y}(0)$, $\dot{z}(0)$, and $\dot{w}(0)$ from the multiscroll hyperchaotic system, scaling function matrix $\epsilon = \text{diag}\{-1, 1, -1, -1\}$, synchronization controller u , and system parameters a , b , c , and d . If the precision is chosen as 10^{-14} , the total key space is $(10^{14})^{14}$, which is obviously larger than that in [31].

(2) *Key Sensitivity Analysis.* In order to test the sensitivity of the encryption algorithm, key parameter $x(0) = 1$ is changed to $x(0) = 1 + 10^{-4}$ and others unchanged in the decryption, the result is shown in Figure 23. We could see that the encryption scheme in the paper is so sensitive to key parameters that a small change can lead to a completely different result.

(3) *Encryption Speed.* For a good encryption algorithm, running speed is an important reference aspect. MATLAB 2014a is used to run the program that realizes the proposed algorithm in a personal computer with a Pentium 4 CPU 3.0 GHz, 4.0 GB RAM, 500 GB hard disk, and Microsoft Windows 7 operating system. The encryption algorithm in the paper is compared with that in [32] and [33]; results between different algorithms are shown in Table 1. We could see that the speed of our encryption algorithm is much faster.

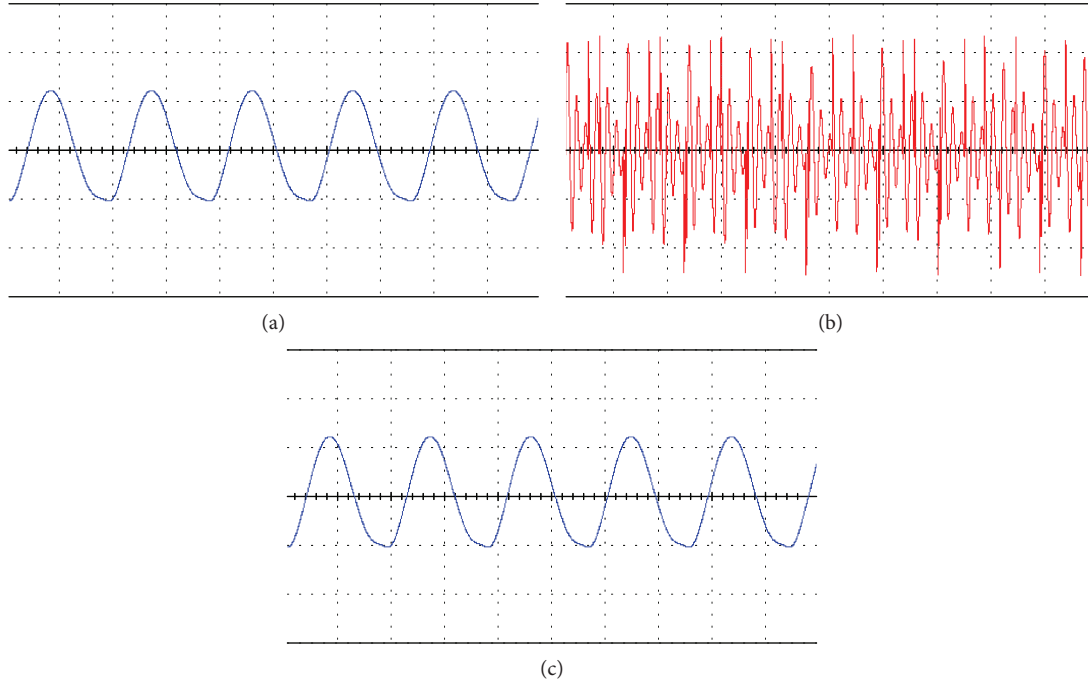


FIGURE 22: Encrypted and decrypted waveforms. (a) Original voice signal. (b) Encrypted voice signal. (c) Decrypted voice signal.

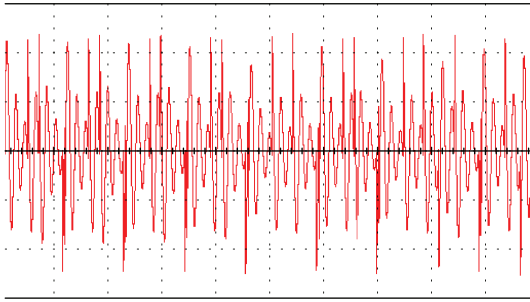


FIGURE 23: Wrong decryption result.

TABLE 1: Comparison of encryption speed between different algorithms.

Algorithms	Encryption speed (MB/s)
Algorithm of [32]	4.80
Algorithm of [33]	6.21
The proposed algorithm	7.91

5. Conclusions

In this paper, a new switching scroll hyperchaotic system was proposed, which consisted of the double-scroll and multi-scroll hyperchaotic system. Based on a memristor device, the double-scroll hyperchaotic system was taken as an example to analyse the dynamic properties, such as Lyapunov exponents, bifurcation diagram, dissipation and equilibrium points, and stability. Furthermore, circuit implementation of the system was introduced in detail and the results are consistent with those of numerical simulations. At last, the

switching scroll hyperchaotic system was successfully applied to voice encryption and showed its effectiveness.

Data Availability

The data used to support the findings of this study are available from the corresponding author upon request.

Conflicts of Interest

The authors declare that they have no conflicts of interest.

Acknowledgments

The work was supported by the National Natural Science Foundation of China (no. 31700644), Postdoctoral Science Foundation of China (nos. 2015M582122 and 2016T90644), Key Research and Development Project of Shandong Province (nos. 2016ZDJS02A07 and 2017GNC12105), the Agricultural Machinery Research and Development Project of Shandong Province (2018YF004).

References

- [1] X. Shi, S. Duan, L. Wang, T. Huang, and C. Li, "A novel memristive electronic synapse-based Hermite chaotic neural network with application in cryptography," *Neurocomputing*, vol. 166, pp. 487–495, 2015.
- [2] J. Yang, L. Wang, Y. Wang, and T. Guo, "A novel memristive hopfield neural Network with application in associative memory," *Neurocomputing*, vol. 227, pp. 142–148, 2017.
- [3] L. Wang, X. Wang, S. Duan, and H. Li, "A spintronic memristor bridge synapse circuit and the application in memristive

- cellular automata,” *Neurocomputing*, vol. 167, pp. 346–351, 2015.
- [4] S. Zhu, L. Wang, and S. Duan, “Memristive pulse coupled neural network with applications in medical image processing,” *Neurocomputing*, vol. 227, pp. 149–157, 2017.
 - [5] J. Gao, P. Zhu, A. Alsaedi, F. E. Alsaadi, and T. Hayat, “A new switching control for finite-time synchronization of memristor-based recurrent neural networks,” *Neural Networks*, vol. 86, pp. 1–9, 2017.
 - [6] A. Abdurahman, H. Jiang, and Z. Teng, “Exponential lag synchronization for memristor-based neural networks with mixed time delays via hybrid switching control,” *Journal of the Franklin Institute*, vol. 353, no. 13, pp. 2859–2880, 2016.
 - [7] A. Abdurahman and H. Jiang, “New results on exponential synchronization of memristor-based neural networks with discontinuous neuron activations,” *Neural Networks*, vol. 84, pp. 161–171, 2016.
 - [8] J. Gao, P. Zhu, W. Xiong, J. Cao, and L. Zhang, “Asymptotic synchronization for stochastic memristor-based neural networks with noise disturbance,” *Journal of the Franklin Institute*, vol. 353, no. 13, pp. 3271–3289, 2016.
 - [9] P. Jiang, Z. Zeng, and J. Chen, “On the periodic dynamics of memristor-based neural networks with leakage and time-varying delays,” *Neurocomputing*, vol. 219, pp. 163–173, 2017.
 - [10] T. D. Dongale, K. V. Khot, S. S. Mali et al., “Development of Ag/ZnO/FTO thin film memristor using aqueous chemical route,” *Materials Science in Semiconductor Processing*, vol. 40, pp. 523–526, 2015.
 - [11] Z. Guo, S. Yang, and J. Wang, “Global synchronization of memristive neural networks subject to random disturbances via distributed pinning control,” *Neural Networks*, vol. 84, pp. 67–79, 2016.
 - [12] S. Ding, Z. Wang, J. Wang, and H. Zhang, “ H_∞ state estimation for memristive neural networks with time-varying delays: the discrete-time case,” *Neural Networks*, vol. 84, pp. 47–56, 2016.
 - [13] V.-T. Pham, S. Vaidyanathan, C. K. Volos, S. Jafari, N. V. Kuznetsov, and T. M. Hoang, “A novel memristive time-delay chaotic system without equilibrium points,” *The European Physical Journal Special Topics*, vol. 225, pp. 127–136, 2016.
 - [14] S. Song, X. Song, and I. T. Balsera, “Adaptive projective synchronization for fractional-order T-S fuzzy neural networks with time-delay and uncertain parameters,” *Optik*, vol. 129, pp. 140–152, 2017.
 - [15] Y. Ma, Y. Li, and X. Jiang, “Simulation and circuit implementation of 12-scroll chaotic system,” *Chaos, Solitons and Fractals*, vol. 75, pp. 127–133, 2015.
 - [16] Z. Chen, G. Wen, H. Zhou, and J. Chen, “Generation of grid multi-scroll chaotic attractors via hyperbolic tangent function series,” *Optik*, vol. 130, pp. 594–600, 2017.
 - [17] L. Chen, W. Pan, R. Wu, K. Wang, and Y. He, “Generation and circuit implementation of fractional-order multi-scroll attractors,” *Chaos, Solitons and Fractals*, vol. 85, pp. 22–31, 2016.
 - [18] M. García-Martínez, L. J. Ontañón-García, E. Campos-Cantón, and S. Čelikovský, “Hyperchaotic encryption based on multi-scroll piecewise linear systems,” *Applied Mathematics and Computation*, vol. 270, pp. 413–424, 2015.
 - [19] H. Liu, A. Kadir, and Y. Li, “Audio encryption scheme by confusion and diffusion based on multi-scroll chaotic system and one-time keys,” *Optik*, vol. 127, no. 19, pp. 7431–7438, 2016.
 - [20] B. S. T. Alkahtani, “Chua’s circuit model with Atangana-Baleanu derivative with fractional order,” *Chaos, Solitons and Fractals*, vol. 89, pp. 547–551, 2016.
 - [21] L. Chua, “Memristor-the missing circuit element,” *IEEE Transactions on Circuit Theory*, vol. 18, no. 5, pp. 507–519, 1971.
 - [22] D. B. Strukov, G. S. Snider, D. R. Stewart, and R. Stanley Williams, “The missing memristor found,” *Nature*, vol. 453, no. 7191, pp. 80–83, 2008.
 - [23] S. Wen, Z. Zeng, and T. Huang, “Adaptive synchronization of memristor-based Chua’s circuits,” *Physics Letters A*, vol. 376, no. 44, pp. 2775–2780, 2012.
 - [24] P. Liu and S. Liu, “Anti-synchronization between different chaotic complex systems,” *Physica Scripta*, vol. 83, no. 6, article 065066, 2011.
 - [25] D. Cafagna and G. Grassi, “New 3D-scroll attractors in hyperchaotic Chua’s circuits forming a ring,” *International Journal of Bifurcation and Chaos*, vol. 13, no. 10, pp. 2889–2903, 2003.
 - [26] L. Chua, M. Komuro, and T. Matsumoto, “The double scroll family,” *IEEE Transactions on Circuits and Systems*, vol. 33, no. 11, pp. 1072–1118, 1986.
 - [27] Y. Wang and X. Liao, “Stability analysis of multimode oscillations in three coupled memristor-based circuits,” *AEU-International Journal of Electronics and Communications*, vol. 70, no. 12, pp. 1569–1579, 2016.
 - [28] B. Mensour and A. Longtin, “Synchronization of delay-differential equations with application to private communication,” *Physics Letters A*, vol. 244, no. 1–3, pp. 59–70, 1998.
 - [29] L. Wang, H. Song, and P. Liu, “A novel hybrid color image encryption algorithm using two complex chaotic systems,” *Optics and Lasers in Engineering*, vol. 77, pp. 118–125, 2016.
 - [30] X. Li, L. Wang, Y. Yan, and P. Liu, “An improvement color image encryption algorithm based on DNA operations and real and complex chaotic systems,” *Optik*, vol. 127, no. 5, pp. 2558–2565, 2016.
 - [31] Z. Wang, X. Huang, Y. X. Li, and X. N. Song, “A new image encryption algorithm based on the fractional-order hyperchaotic Lorenz system,” *Chinese Physics B*, vol. 22, no. 1, article 010504, 2013.
 - [32] X. Wu, Y. Li, and J. Kurths, “A new color image encryption scheme using CML and a fractional-order chaotic system,” *PLoS One*, vol. 10, no. 3, article e0119660, 2015.
 - [33] M. Ahmad, U. Shamsi, and I. R. Khan, “An enhanced image encryption algorithm using fractional chaotic systems,” *Procedia Computer Science*, vol. 57, pp. 852–859, 2015.

Research Article

Investigation of Cortical Signal Propagation and the Resulting Spatiotemporal Patterns in Memristor-Based Neuronal Network

Ke Ding ^{1,2}, Zahra Rostami,³ Sajad Jafari,³ and Boshra Hatef ⁴

¹School of Information Technology, Jiangxi University of Finance and Economics, Nanchang 330013, China

²Jiangxi E-Commerce High Level Engineering Technology Research Centre, Jiangxi University of Finance and Economics, Nanchang 330013, China

³Biomedical Engineering Department, Amirkabir University of Technology, Tehran 15875-4413, Iran

⁴Neuroscience Research Center, Baqiyatallah University of Medical Sciences, Tehran, Iran

Correspondence should be addressed to Boshra Hatef; boshrahatef@gmail.com

Received 27 December 2017; Revised 8 March 2018; Accepted 28 March 2018; Published 27 June 2018

Academic Editor: Daniela Paolotti

Copyright © 2018 Ke Ding et al. This is an open access article distributed under the Creative Commons Attribution License, which permits unrestricted use, distribution, and reproduction in any medium, provided the original work is properly cited.

Complexity is the undeniable part of the natural systems providing them with unique and wonderful capabilities. Memristor is known to be a fundamental block to generate complex behaviors. It also is reported to be able to emulate synaptic long-term plasticity as well as short-term plasticity. Synaptic plasticity is one of the important foundations of learning and memory as the high-order functional properties of the brain. In this study, it is shown that memristive neuronal network can represent plasticity phenomena observed in biological cortical synapses. A network of neuronal units as a two-dimensional excitable tissue is designed with 3-neuron Hopfield neuronal model for the local dynamics of each unit. The results show that the lattice supports spatiotemporal pattern formation without supervision. It is found that memristor-type coupling is more noticeable against resistor-type coupling, while determining the excitable tissue switch over different complex behaviors. The stability of the resulting spatiotemporal patterns against noise is studied as well. Finally, the bifurcation analysis is carried out for variation of memristor effect. Our study reveals that the spatiotemporal electrical activity of the tissue concurs with the bifurcation analysis. It is shown that the memristor coupling intensities, by which the system undergoes periodic behavior, prevent the tissue from holding wave propagation. Besides, the chaotic behavior in bifurcation diagram corresponds to turbulent spatiotemporal behavior of the tissue. Moreover, we found that the excitable media are very sensitive to noise impact when the neurons are set close to their bifurcation point, so that the respective spatiotemporal pattern is not stable.

1. Introduction

The brain is composed of an extremely large number of neurons [1], as the basic and also complex adaptive blocks of the brain system [2, 3]. Neuronal information transference is possible via propagation of the electrical and chemical signals in neuronal network [4, 5]. Indeed, fluctuation of the membrane potential of the neurons has a specific pattern in both time domain and space domain within the information processing [6]. These fluctuations actually bring a functional coherence and interplay between different parts, so that the related controlling behaviors are possible [7]. It is confirmed

that emergence of a particular spatiotemporal pattern is in direct relationship with the intrinsic properties of the system [6, 8, 9]. Metabolically, generation and transference of the information and the related signals are costly [4, 10]. However, the way that the brain is wired has made it a nature-made computer with high level of efficiency in computation and cognition [4]. Although the human brain is not very quick at handling complex calculations, it beats a traditional computer system when it comes to energy efficiency [11]. Therefore, many efforts have been made to build up a hardware structure and a software design or even employ a mathematical model to study the brain system [12, 13], regarding some functional

properties or physical effects [14]. There can be considered some factors responsible for energy efficiency of neuronal network including mechanisms of action potential propagation, synaptic neurotransmitters, and other factors that are studied in more detail in [4]. In this regard, it is interesting to investigate the emerged spatiotemporal patterns accompanied by the complex dynamics [8]. The recent studies on neural network and emulator circuit implementations [13–15] have led to the fourth circuit element called memristor [16] in addition to resistor, capacitor, and inductor [15, 17, 18]. Memristor (contraction of memory and resistor) is a two-terminal circuit element with nonlinear characteristics and high performance [19]. It has attracted much attention in biological models, adaptive filters, or integrated circuits [20] due to multistability phenomenon in coexisting attractors with chaotic demonstrations [21]. For the application of biological models, it can mimic how neurons in a network change their behavior when they are activated. Actually, its respond at each moment does not rely only on the signals it is receiving at that exact moment but is influenced by its own recent activity, too.

Many studies prove that biological behaviors are the outcome of collective activities of the neurons in neural network [22]. Indeed, the brain activities are not determined by each individual neuron, separately, but the intrinsic coherence coming from collective activities and patterns of maintenance or destruction of the local synchronization between the agents [23, 24]. As a result, it is not only about the components and their fluctuation pattern, individually, but also about the connections among them. In other words, neuronal information is carried by evolutionary spatiotemporal patterns indicating a powerful, efficient, and purposeful functional connectivity. Besides, the connection strength determines the specific spatial patterns in the network, as well [24]. Actually, what seems to have the most significant and delicate influence over the ultimate performance of the system is the interactions between the components, both quantitatively and qualitatively. Thus, we need to know the spatiotemporal distribution of the brain cells membrane potential and the pattern of propagated waves in the two-dimensional space focusing on the connections [8]. However, obviously, association of a large number of unites within nonlinear connections and interactions makes it so hard to grasp some of the concepts and deal with the related topics. Therefore, some simplifications with acceptable range of reductions are needed [25]. Regardless of these reductions in what is actually happening in the real neuronal network, this procedure can help us understand the related complicated occurrence, to some extent. In this study, the main idea is to notice the neurons at the level of population and consider a group of correlated neurons within more realistic interconnections and communication tools.

The point at which neurons are able to communicate with each other is called synapse [3], which bridges the neurons in the neuronal network [26]. In fact, transmission of the electrical signal in neuronal system can take place through synapses. It is also found that learning and memory are the two significant brain abilities attributed to synapses and their functional properties [3]. From a perspective, learning and

memory are interrelated with each other. Memory is the internal mental recorded information, while learning is the ability of modifying the information stored in the memory based on the new inputs. More precisely, it also can be said that learning is the first step of memory since the sensory system sends information to the brain. Synaptic plasticity is postulated to be one of the important foundations of learning and memory [27]. Furthermore, plasticity is reported to be responsible for certain abilities like rapid response to threat stimuli and localization of the sound source [28]. The invention of memristor has made it possible to realize some complex activities which were impeded by lack of an appropriate device to model synaptic plasticity. The focus of this study is to demonstrate the capability of memristive neuronal network to represent some complex behaviors and large-scale plasticity which is also well described via experimental observations in the prefrontal cortex [29], visual cortex [30], and neocortex [31].

Real cortical tissue has a laminar structure [32]. Indeed, neurons of cerebral cortex are arranged in characteristic layers [3]. Primarily, presence or absence of neuronal cell bodies specifies the layers of cerebral cortex. This laminar structure of the cortex plays a significant role in organizing the inputs and outputs of the brain [3]. In fact, different inputs need to be processed in different ways while the outputs arise from different cortical regions. Accordingly, the laminar structure of cerebral cortex helps providing required circumstances. Considering distribution of the cortical electrical activities, related spatiotemporal patterns arise from the interface between the levels of activities of neurons in the surfaces. With given explanations, in this study, we simplify the case to a two-dimensional network of neuronal models, expressing an excitable cortical tissue to investigate the resulting pattern of the wave propagation in the surface.

In order to study the factors affecting wave propagation, it is interesting to figure out what a memristor-type synaptic connection exactly does, not only for one limited agent but also for large number of neuronal units and how much it affects the spatial distribution of the cell membrane potential and leads to wave propagation via the complex demonstrations. Actually, the answer of these questions may also reflect the influence of memory and learning process in a neuronal network through the emerged patterns. In other words, we examine different plasticity levels for the synaptic connections by means of different memristor contributions. On the other hand, by noticing differential equation models, which are used in this study, the initial states of the variables of a system refer to the result of their past dynamics. Therefore, we choose a different initial condition for a local area of the network indicating the different input sensory signals that have been applied to that specific area in the past. After that, we investigate the effect of memristor-type synapse against resistor-type synapse on the pattern formation in the network. Plus, we also expand our computations to noise considerations in some separated snapshots, because noise plays an important role in dynamical response of oscillatory systems.

The results show that different spatiotemporal patterns take place in the excitable tissue without supervision. As is

clear through the snapshots, the overall pattern is mostly determined by memristor-type coupling. In accordance with some reports on the role of synaptic plasticity in some important high-order cortical activities, our results confirm that synaptic plasticity makes the tissue capable of representing different complex demonstrations. In fact, the increase and decrease of the memristor effect greatly changes the ultimate appearance of the tissue, which, in turn, actually resulted from the pattern of electrical activity of each neuron interacting with the neighbor neurons in the whole tissue. Moreover, the resulting patterns are found to be robust against noise for all the cases except for $k = 0.9$, in which some concentric circular patterns are formed in the two-dimensional space. For further study, we sought to realize whether it is possible to find a meaningful relationship between the qualitative properties of the coupled neurons and the spatiotemporal demonstrations from a two-dimensional lattice. Therefore, the bifurcation analysis is carried out for different intensities of memristor-type coupling. It is revealed that the spatiotemporal electrical activity of the tissue concurs with the bifurcation analysis. We show the memristor coupling intensities by which the system undergoes periodic behavior and prevents the tissue from holding wave propagation. In addition, the chaotic-like behavior in bifurcation diagram corresponds to turbulent spatiotemporal behavior of the tissue. Moreover, it is found that the excitable media is very sensitive to noise impact when the neurons are set close to their bifurcation point, so that the respective spatiotemporal pattern is not stable.

The rest of the paper is organized as follows.

In the next section, the mathematical model is introduced with description of its variables and parameters. After that, in the third section, our numerical method is explained and the results are displayed. The computational analysis for variation of k and D can be found in Section 3.1. Sections 3.2 and 3.3 include the noise and the bifurcation analysis, respectively. Finally, the fourth section concludes our study.

2. Model and Description

There are a number of mathematical neural models capable of representing complex dynamic behaviors. These models introduced for a large number of neurons have properties that benefit investigations on biological neuronal network. Usually, in these models, it is assumed that the presynaptic firing rate determines the synaptic input current [33]. Hopfield neural model is defined as a graded response model [34]. This model has been successful in representing different dynamical behaviors including chaotic behaviors [35, 36] having to do with nonlinear demonstrations of the brain performance.

Neurons have a selective response to a compact range of parameters. In our study, the idea is to provide a compact range of connections and interactions in a neuronal network. For this purpose, we designed a square array of neuronal units with nearest neighbor connections. Each unit has a topology with hyperbolic-type memristor-based connection. A hyperbolic-type Hopfield neural network is considered for each agent. In this 3-neuron Hopfield neural network, one of the connection weights is defined as a memristive-type

weight. The Hopfield equation for the i -th neuron is described as follows:

$$C_i \frac{dx_i}{dt} = -\frac{x_i}{R_i} + \sum_{j=1}^N w_{ij} \tanh(x_j) + I_i, \quad (1)$$

where variable x denotes the voltage across the capacitor C , R stands for membrane resistance between the inside and outside of the neuron, I is an input bias current, $\tanh(x_j)$ is the neuron activation function for voltage input from the j -th neuron, and w_{ij} is synaptic weight that illustrates the strength of connections between i -th and j -th neurons. In our work, the proposed Hopfield network is achieved by replacing resistive connection with hyperbolic-type memristor, which is discussed in detail in [35]. The set of parameters are $N = 3$, $C_i = 1$, $R_i = 1$ ($i = (1 : 3)$). The weight matrix is considered as

$$W = \begin{bmatrix} w_{11} & w_{12} & w_{13} \\ w_{21} & w_{22} & w_{23} \\ w_{31} & w_{32} & w_{33} \end{bmatrix} = \begin{bmatrix} -1.4 & 1.2 & -7 \\ 1.1 & 0 & 2.8 \\ kw & -2 & 4 \end{bmatrix}, \quad (2)$$

where w is the synaptic weight connecting the first and the third neurons with the proportion of k . The parameter k is a constant indicating the strength of hyperbolic-type memristor-type coupling.

The differential equations describing the desired memristor-type neuronal unit can be expressed as follows:

$$\begin{aligned} \dot{x}_1 &= -x_1 - 1.4 \tanh(x_1) + 1.2 \tanh(x_2) - 7 \tanh(x_3) \\ \dot{x}_2 &= -x_2 + 1.1 \tanh(x_1) + 2.8 \tanh(x_3) \\ \dot{x}_3 &= -x_3 + kw \tanh(x_1) - 2 \tanh(x_2) + 4 \tanh(x_3) \\ \dot{x}_4 &= -x_4 + \tanh(x_1) \\ w &= a - b \tanh(x_4). \end{aligned} \quad (3)$$

After that, we develop the case to a large array network of neuronal units within coupling intensities. Therefore, the equations for the square array network are represented as follows:

$$\begin{aligned} \dot{x}_{1mn} &= -x_{1mn} - 1.4 \tanh(x_{1mn}) + 1.2 \tanh(x_{2mn}) - 7 \\ &\quad \cdot \tanh(x_{3mn}), \\ \dot{x}_{2mn} &= -x_{2mn} + 1.1 \tanh(x_{1mn}) + 2.8 \tanh(x_{3mn}), \\ \dot{x}_{3mn} &= -x_{3mn} + kw_{mn} \tanh(x_{1mn}) - 2 \tanh(x_{2mn}) + 4 \\ &\quad \cdot \tanh(x_{3mn}) + D \\ &\quad \cdot \tanh(x_{3_{m-1n}} + x_{3_{m+1n}} + x_{3_{mn-1}} + x_{3_{mn+1}} - 4x_{3mn}), \\ \dot{x}_{4mn} &= -x_{4mn} + \tanh(x_{1mn}), \\ w_{mn} &= a - b \tanh(x_{4mn}), \end{aligned} \quad (4)$$

where the subscript mn denotes the position of each neuronal unit in the two-dimensional square array network. D is the

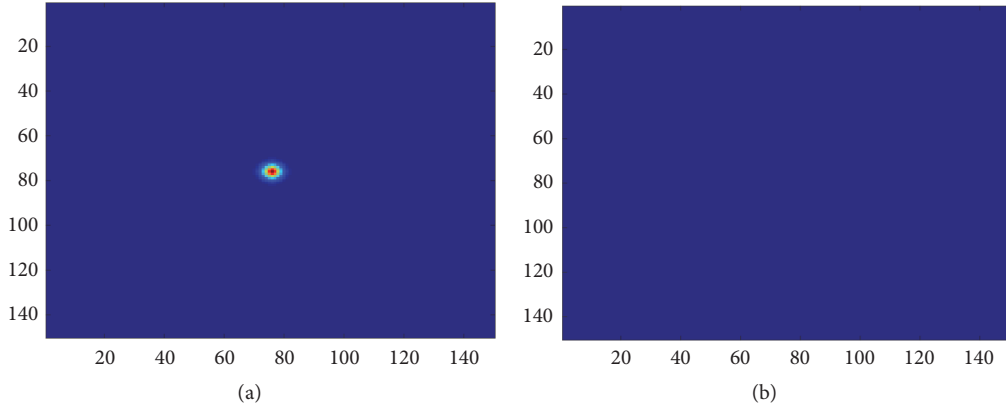


FIGURE 1: The snapshots of spatial distribution of membrane potential with color scale for neurons in the square array network for $k = 0$ and $D = 1$ at (a) $t = 2$ time units and (b) $t = 6$ time units.

resistor-type coupling intensity. $a = 1$ and $b = 0.01$ are constant. The reader will pay attention that the parameter D denotes the resistor-type coupling strength in this study while parameter k shows the memristor-type coupling strength.

3. Numerical Results and Discussions

In our study, we design a square array network consisting of 150×150 neuronal units. Our numerical results are calculated by Runge-Kutta 4th-order method with the time step $h = 0.01$ under no flux boundary. The initial states of the network except the small central area, which is observable in the following images, are set as $(x_1, x_2, x_3, x_4) = (0, 0.1, 0, 0)$. In addition, the initial condition of the central local area is $(x_1, x_2, x_3, x_4) = (0, -0.1, 0, 0)$.

3.1. Computational Analysis for Variation of k and D . Considering (2), there are two types of coupling between neurons in the whole network, namely, the memristor-type coupling and the resistor-type coupling. We pick different levels of memristor-type coupling by adjusting parameter k , and then we consider two levels of resistor-type coupling intensity by adjusting parameter D , in each case of k adjustments.

It seems that neurons need to have an appropriate level of memristor effect to be capable of responding to the received stimulus in a desired pattern leading to wave propagation. Otherwise, the generated circular wave (in the central area of the network) will not be developed. Even though a propagated wave can travel a further distance by strengthening the resistive coupling intensity between the agents (which is adjustable by parameter D), still the lack of wave propagation remains and the ultimate general pattern does not change. Moreover, the excitable media are able to switch over different spatial behaviors by varying the memristive coupling strength. Hence, from this point of view, memristor-type coupling is more noticeable against resistor-type coupling. To put it more clearly, the distribution of membrane potential in the two-dimensional excitable media is shown in colored levels. In some cases, the central local area is maintained for a few seconds or continues to grow

under a particular pattern, while in others the continuity of the central part is very short.

Firstly, Figure 1 shows the result in two snapshots when there is no effect of memristor in the network ($k = 0$). Moreover, the neuronal units are connected to each other with the coupling intensity of $D = 1$. As it is observable, there is no propagation in this case and the generated signals find no path to travel the tissue. In fact, the generated wave front dies right at the beginning of its existence. Besides, there is no sign of propagation even when we choose a higher resistor-type coupling intensity by $D = 5$ under no memory effect by $k = 0$ (Figure 2). Here the only difference that can be seen between the results in Figures 1 and 2 is in the increased radius of the initiated wave front in Figure 2 in comparison with Figure 1. In this case, the central concentrated energy does not flow to the rest of the neurons and vanishes right at the beginning of its existence.

For the next step, we provide the tissue a nonzero memory effect with $k = 0.5$ under resistor coupling strength of $D = 1$ and $D = 5$ displayed in Figures 3 and 4, respectively. In this case, the membrane potential of the central local area finds permission to flow beyond the central part but not too far. The propagated wave is shown in four snapshots for this case. As it is observable, in this case, the wave front disappears not right at the beginning but after a limited time before getting too wide (see Figure 3). Moreover, increasing the resistor-type coupling intensity from $D = 1$ to $D = 5$ only brings the time-limited propagated wave a greater radius and does not prevent it from disappearing (see Figure 4).

After that, on the way of increasing memory properties, leading to more synaptic plasticity, we set $k = 0.7$ (Figures 5 and 6). Interestingly, this slight increase from $k = 0.5$ to $k = 0.7$ in the level of memory effects brings out significantly different dynamics from the tissue. In fact, it makes the tissue represent a very distinctive pattern for the distribution of membrane potential in its two-dimensional space. The spatial fluctuations become so turbulent and great number of very small rotating seeds can be seen. These countless rotating seeds result in such turbulent appearance as is clear through the depicted snapshots in Figures 5 and 6. We investigate

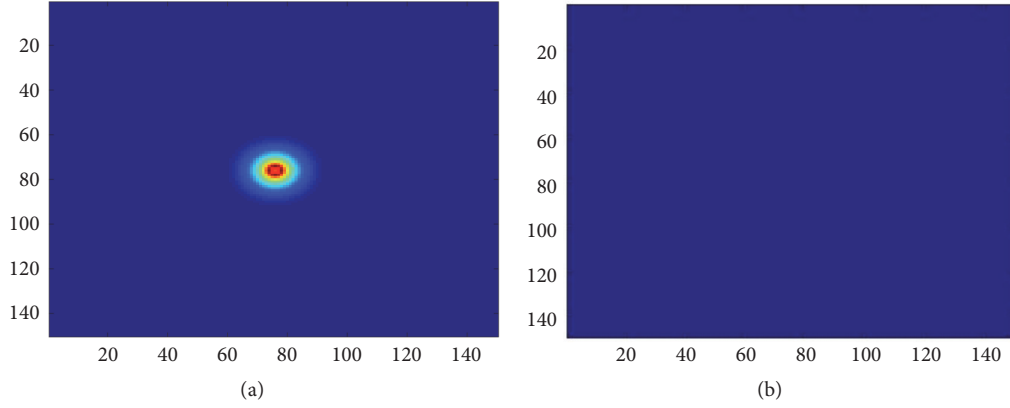


FIGURE 2: The snapshots of spatial distribution of membrane potential with color scale for neurons in the square array network for $k = 0$ and $D = 5$ at (a) $t = 2$ time units and (b) $t = 6$ time units.

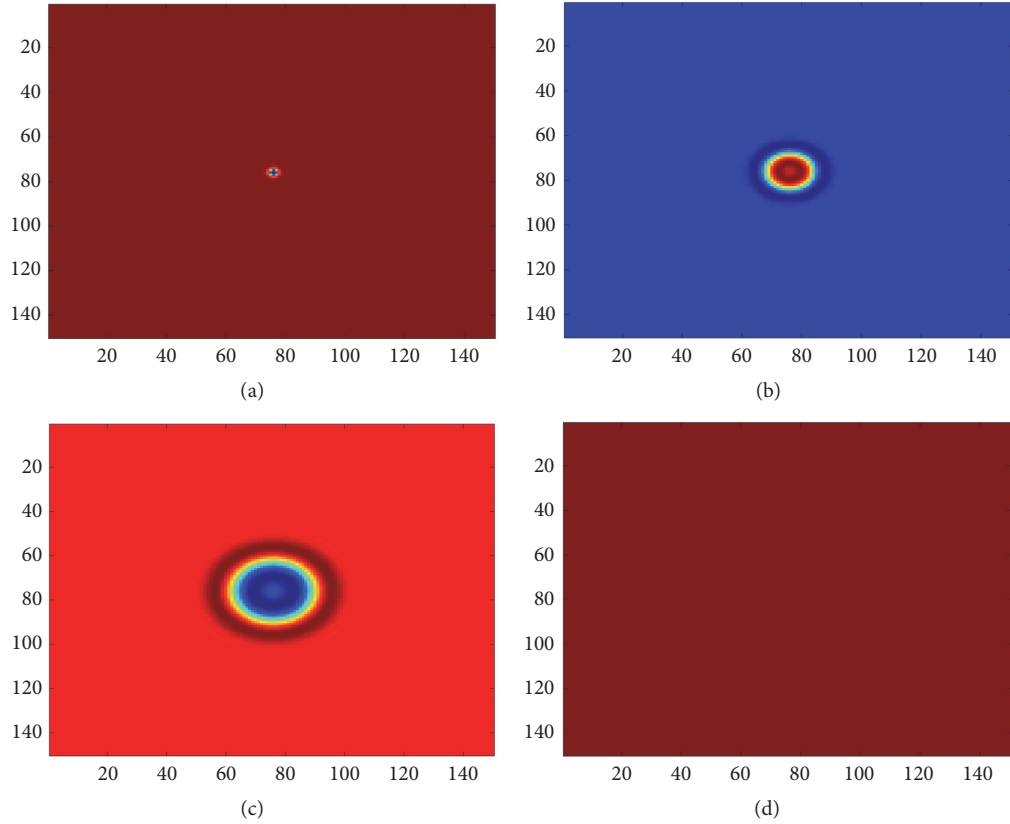


FIGURE 3: The snapshots of spatial distribution of membrane potential with color scale for neurons in the square array network for $k = 0.5$ and $D = 1$ at (a) $t = 2$ time units, (b) $t = 20$ time units, (c) $t = 100$ time units, and (d) $t = 200$ time units.

this level of memory effects with two resistance coupling intensities by $D = 1$ and $D = 5$ and the resulting snapshots are displayed in Figures 5 and 6, respectively. As before, greater amounts of parameter D cause the radius of the turbulent propagating wave increase, so that a more extensive area is covered in the snapshots of the same moments.

Furthermore, we examine a slightly further increase in the level of memory effects by applying $k = 0.8$ in two modes of $D = 1$ and $D = 5$. The resulting spatiotemporal patterns

are shown in Figures 7 and 8, respectively. As it is observable, in this case, the regular symmetrical deformations are surrounded by a growing circular wave front. As soon as the circular wave front touches the boundaries, it starts getting into some deformations, too. Eventually, the mixture of the resulting deformations covers the entire tissue and makes it represent a completely different appearance (Figure 7(d)).

Considering all the above, we set a higher level of memristor-type coupling by $K = 0.9$, in order to see whether

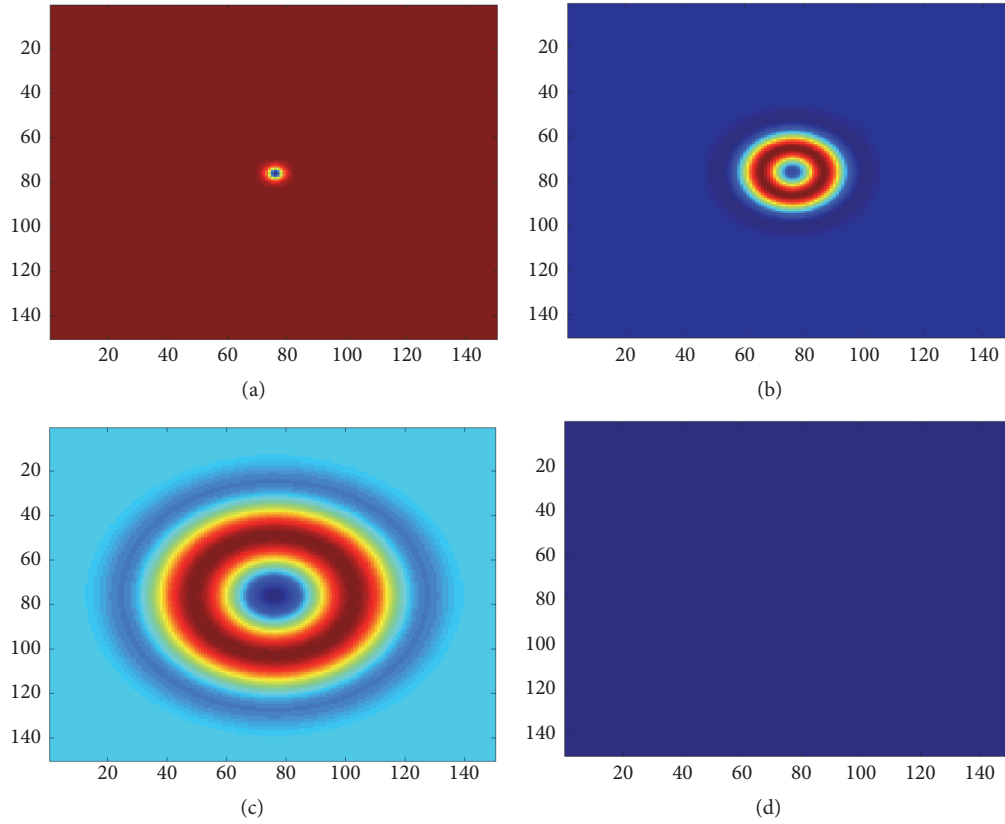


FIGURE 4: The snapshots of spatial distribution of membrane potential with color scale for neurons in the square array network for $k = 0.5$ and $D = 5$ at (a) $t = 2$ time units, (b) $t = 20$ time units, (c) $t = 100$ time units, and (d) $t = 200$ time units.

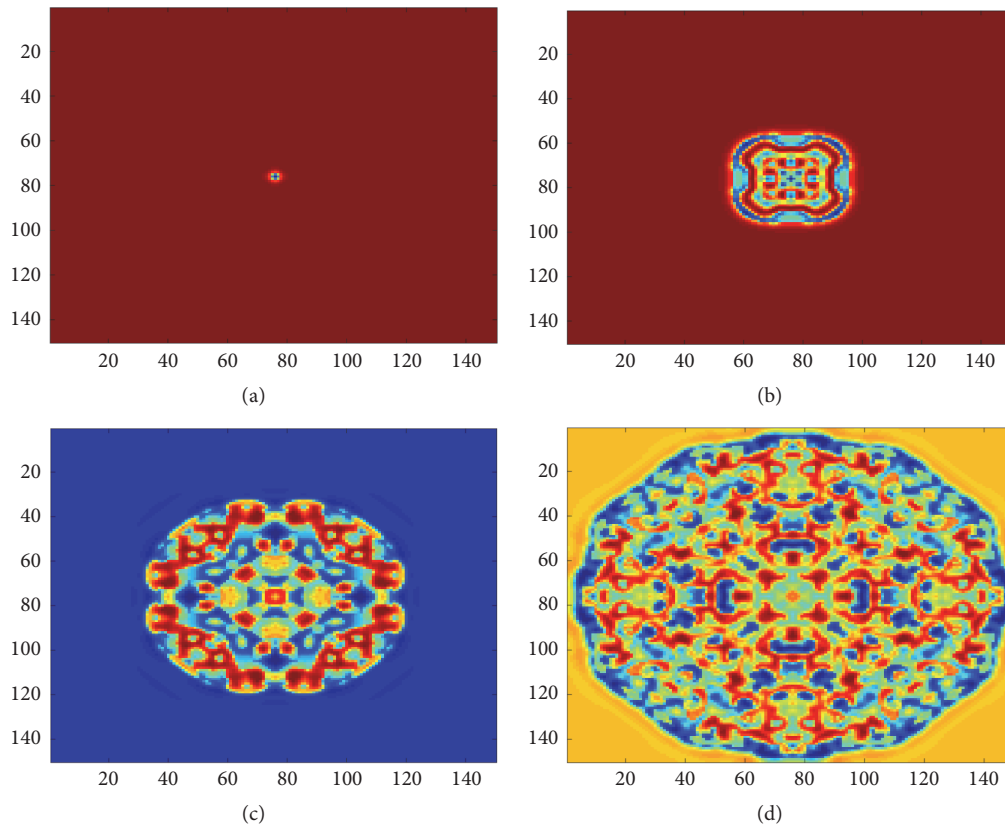


FIGURE 5: The snapshots of spatial distribution of membrane potential with color scale for neurons in the square array network for $k = 0.7$ and $D = 1$ at (a) $t = 2$ time units, (b) $t = 75$ time units, (c) $t = 170$ time units, and (d) $t = 300$ time units.

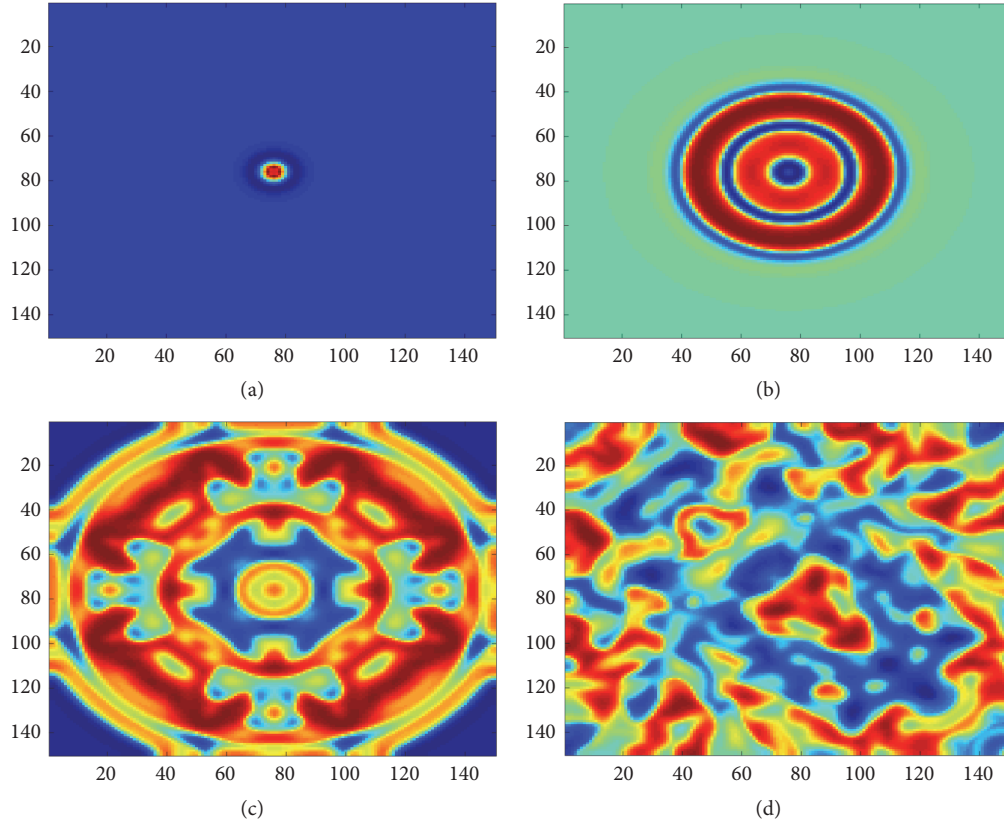


FIGURE 6: The snapshots of spatial distribution of membrane potential with color scale for neurons in the square array network for $k = 0.7$ and $D = 5$ at (a) $t = 2$ time units, (b) $t = 75$ time units, (c) $t = 135$ time units, and (d) $t = 300$ time units.

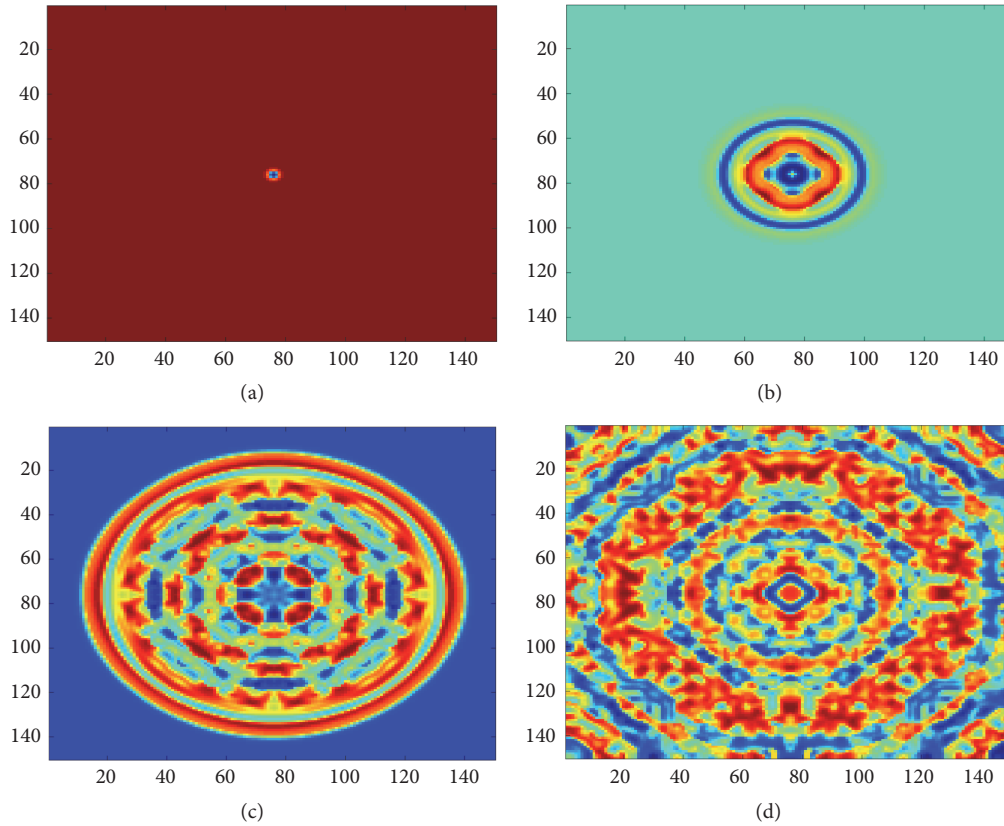


FIGURE 7: The snapshots of spatial distribution of membrane potential with color scale for neurons in the square array network for $k = 0.8$ and $D = 1$ at (a) $t = 2$ time units, (b) $t = 75$ time units, (c) $t = 170$ time units, and (d) $t = 300$ time units.

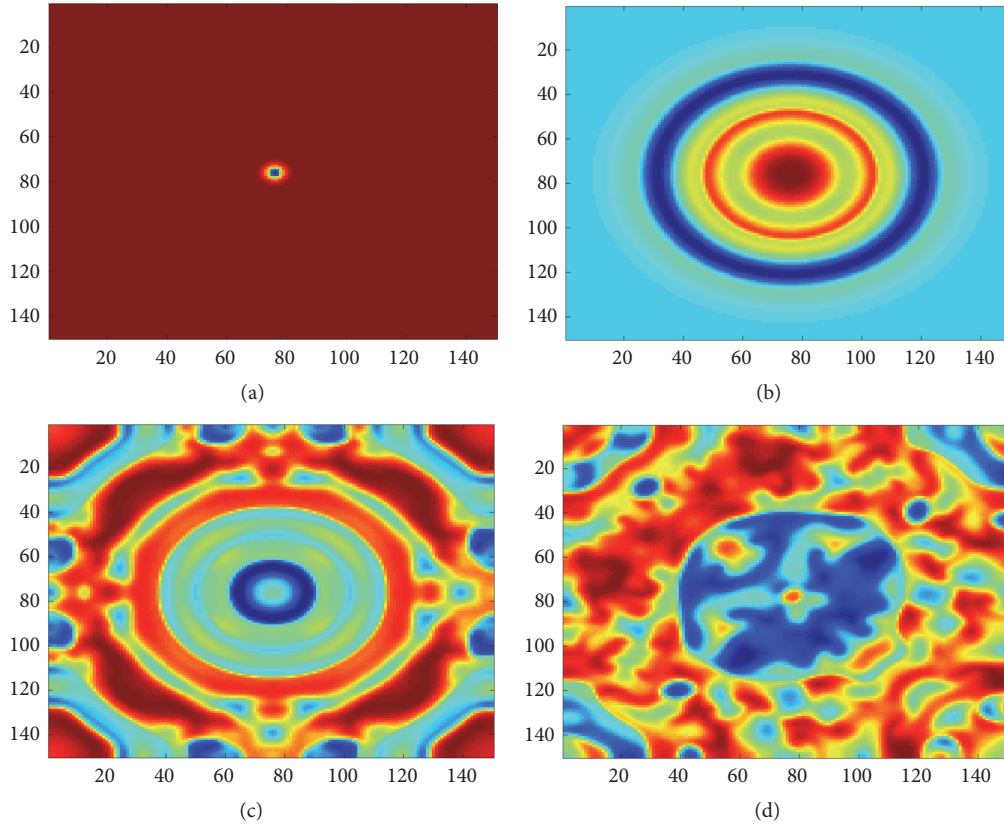


FIGURE 8: The snapshots of spatial distribution of membrane potential with color scale for neurons in the square array network for $k = 0.8$ and $D = 5$ at (a) $t = 2$ time units, (b) $t = 75$ time units, (c) $t = 135$ time units, and (d) $t = 300$ time units.

the resulting turbulent pattern continues to grow by more strengthening the memristor-type coupling in the network. The results are represented for $D = 1$ and $D = 5$ in Figures 9 and 10, respectively.

As is visible in the displayed results in Figures 9 and 10, the spatial pattern takes a completely different appearance when we pick the strength of memristor-type coupling beyond a certain threshold. Besides, there is no sign of any small rotating seeds either. In this case, with this set of parameters, the central local area does not vanish and there exist a set of concentric circles. Unlike the previous cases, these arising circular wave fronts keep their overall curvature during the whole time span. Moreover, these circular wave fronts take a larger radius and find more expansion when the resistor-type coupling is increased from $D = 1$ to $D = 5$ (Figure 10). As a result, this level of memristor effect causes a recognizable change in the resulting spatiotemporal behavior. Even though more synaptic plasticity is provided in this case, the turbulent spatial pattern changes into a circular discipline with no deformation.

For further investigation, we put the memory influence of the excitable tissue in a higher level by setting $k = 1$ with $D = 1$ and $D = 5$ in Figures 11 and 12, respectively. Interestingly, neither partial deformation nor circular pattern is observable in this case. Besides, the ultimate wave front stops to grow after reaching a certain length of the radius.

Moreover, by further increase of the memory level by $k = 1.5$, the propagated wave subsides and finally disappears. For this level of k , the snapshots in Figures 13 and 14 show the results for $D = 1$ and $D = 5$, respectively.

3.2. Noise Effect. In this part, we expand our computational analysis to investigate stability of the emerged patterns under the noise effect. For this purpose, the Gaussian white noise $\xi(t)$ is added to the initial conditions, which were defined in the first paragraph of Section 3. The statistical properties of Gaussian white noise are defined by [37]

$$\langle \xi(t) \xi(t') \rangle = 2G\delta(t - t'), \quad (5)$$

where G is noise intensity and $\delta(*)$ is Dirac- δ function. Two levels of noise intensities are applied to the whole tissue by $G = 0.01$ and $G = 0.1$.

The results show that the spatial pattern totality is not influenced by the noise effect for $k = 0$, $k = 0.5$, $k = 0.7$, $k = 0.8$, $k = 1$, and $k = 1.5$, so that the ultimate spatial pattern does not change significantly for these cases. These results are depicted in Figures 15–18, 20 and 21. However, as illustrated in Figure 19, in the case $k = 0.9$, a remarkable change is made in the network fluctuations pattern due to the noise effects. It seems that this level of memristor-type coupling makes the tissue sensitive to noise and makes it represent a

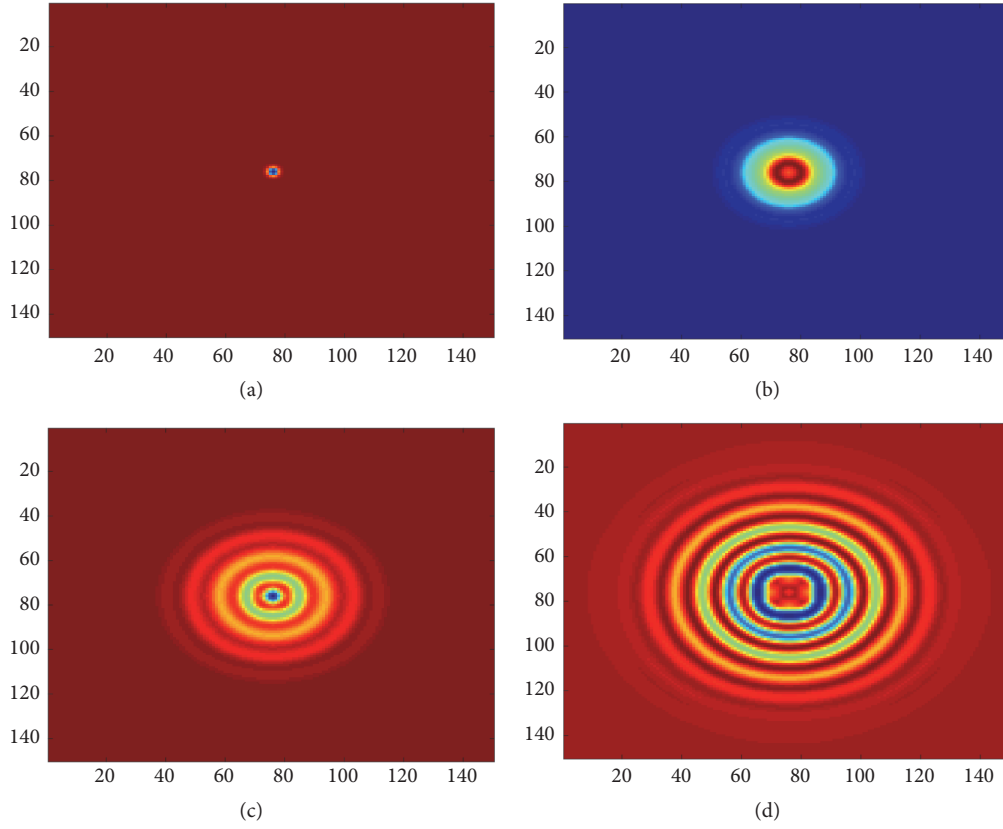


FIGURE 9: The snapshots of spatial distribution of membrane potential with color scale for neurons in the square array network for $k = 0.9$ and $D = 1$ at (a) $t = 2$ time units, (b) $t = 75$ time units, (c) $t = 170$ time units, and (d) $t = 300$ time units.

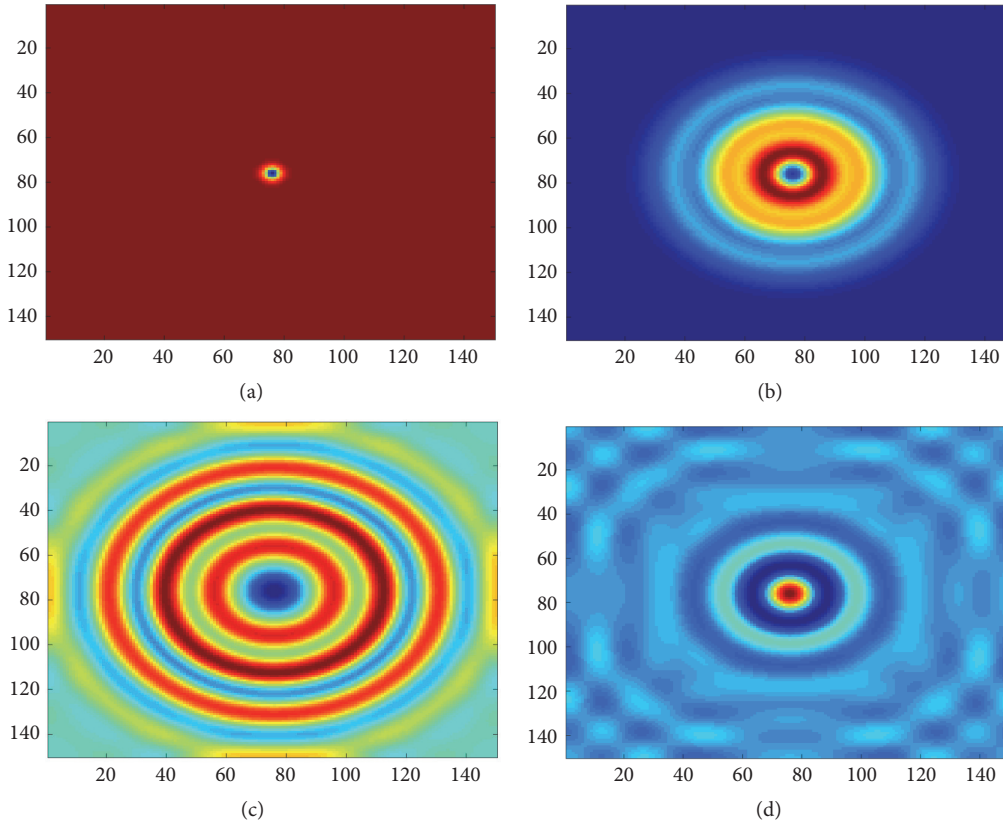


FIGURE 10: The snapshots of spatial distribution of membrane potential with color scale for neurons in the square array network for $k = 0.9$ and $D = 5$ at (a) $t = 2$ time units, (b) $t = 75$ time units, (c) $t = 135$ time units, and (d) $t = 300$ time units.

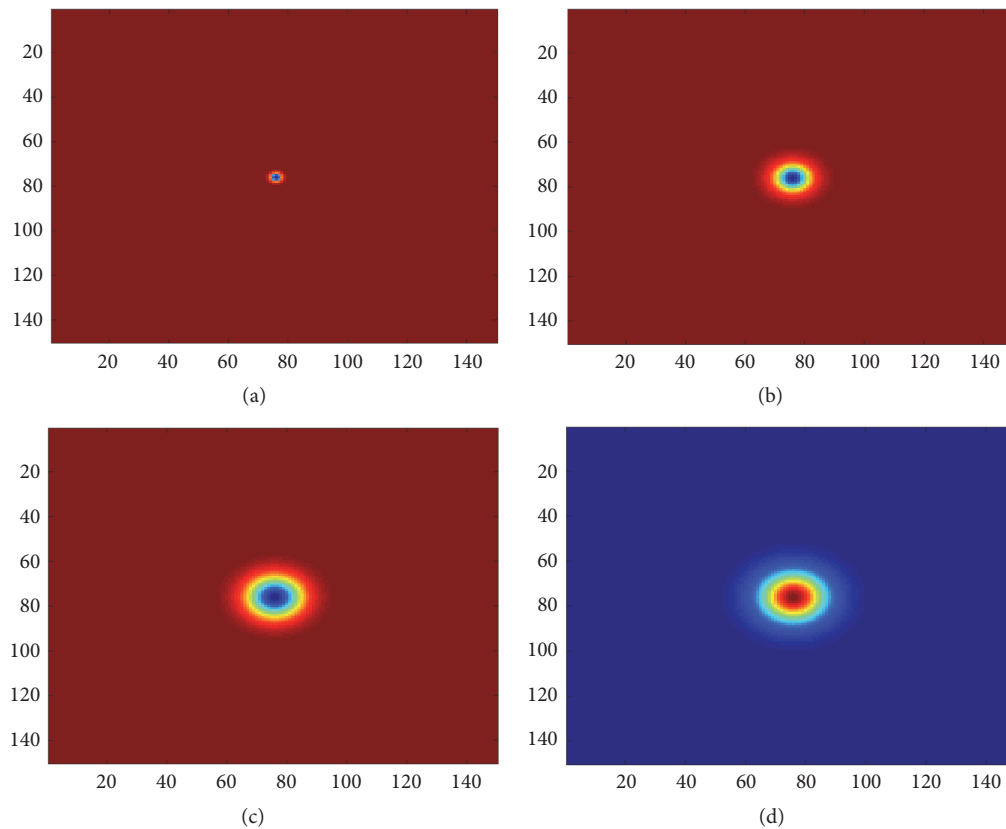


FIGURE 11: The snapshots of spatial distribution of membrane potential with color scale for neurons in the square array network for $k = 1$ and $D = 1$ at (a) $t = 2$ time units, (b) $t = 75$ time units, (c) $t = 170$ time units, and (d) $t = 300$ time units.

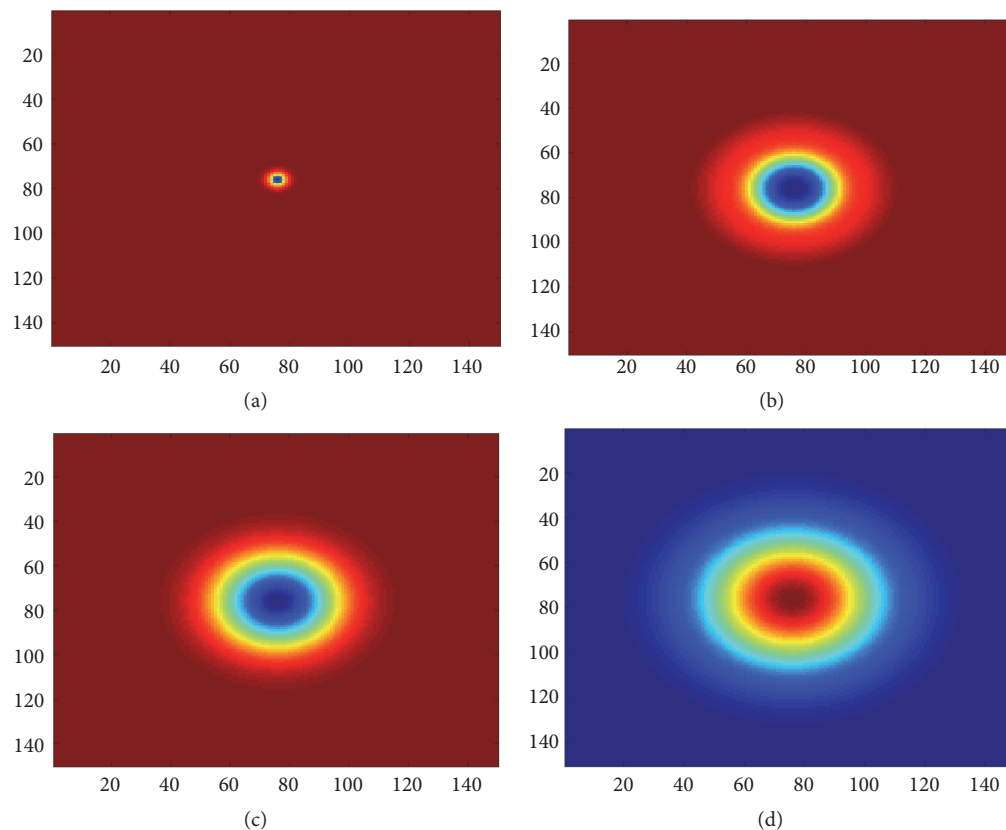


FIGURE 12: The snapshots of spatial distribution of membrane potential with color scale for neurons in the square array network for $k = 1$ and $D = 5$ at (a) $t = 2$ time units, (b) $t = 75$ time units, (c) $t = 135$ time units, and (d) $t = 300$ time units.

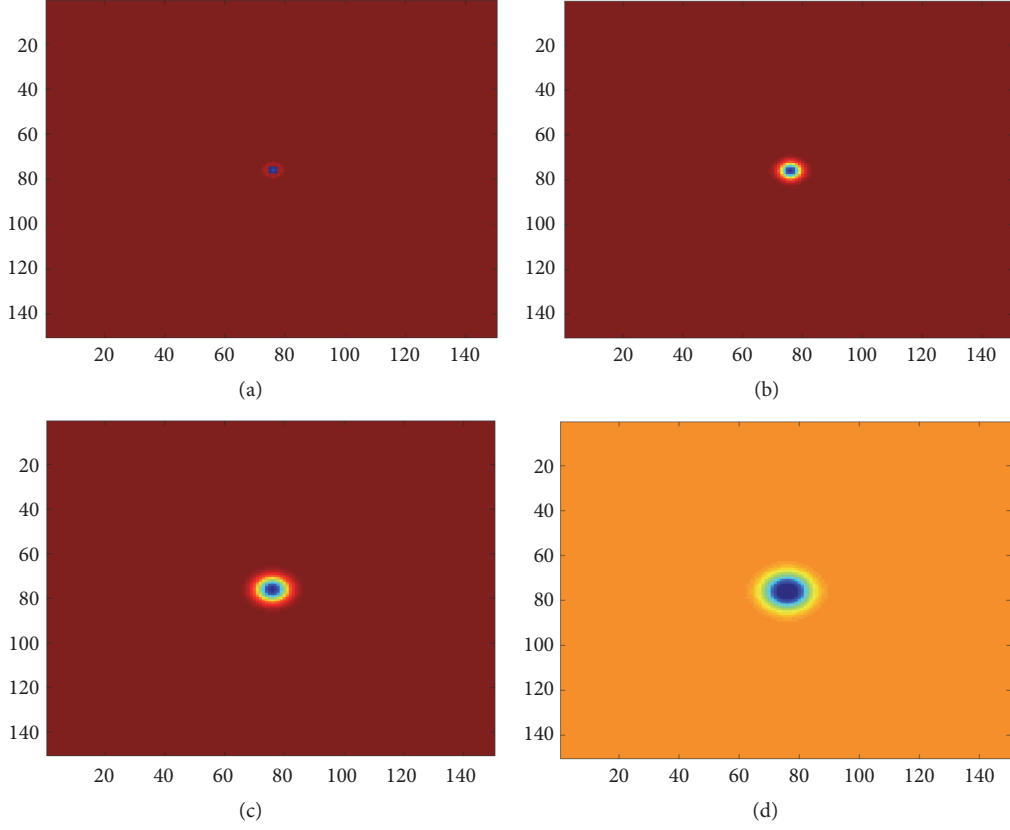


FIGURE 13: The snapshots of spatial distribution of membrane potential with color scale for neurons in the square array network for $k = 1.5$ and $D = 1$ at (a) $t = 2$ time units, (b) $t = 75$ time units, (c) $t = 170$ time units, and (d) $t = 300$ time units.

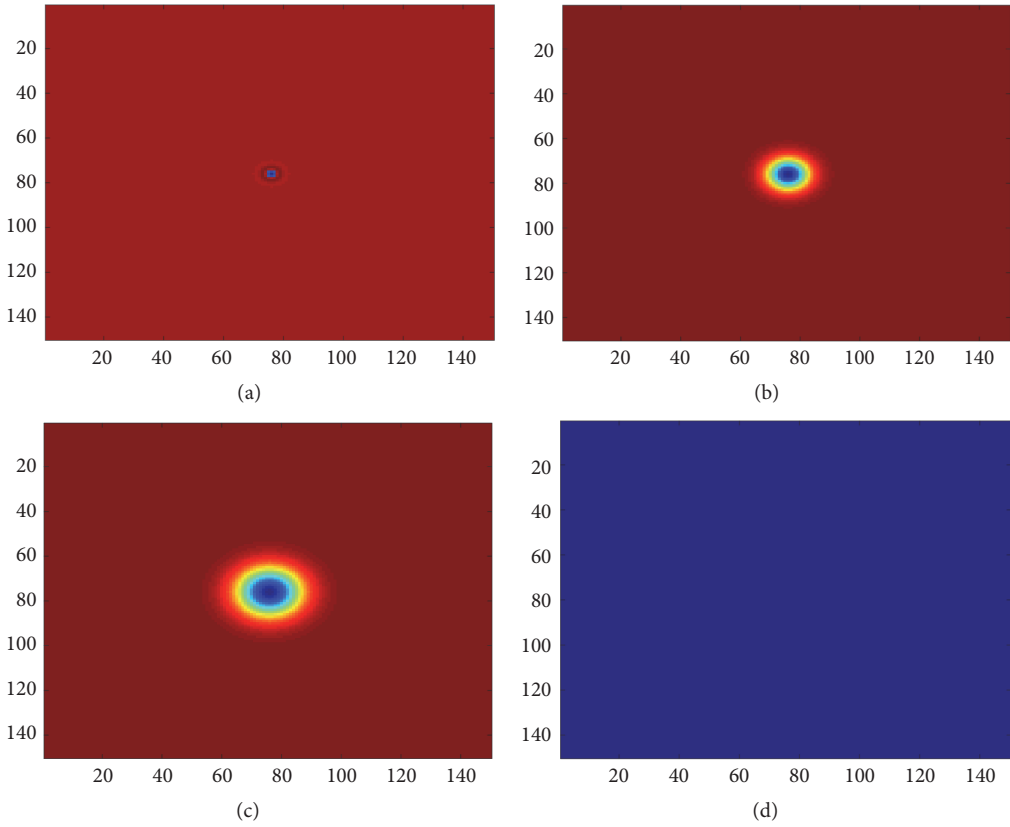


FIGURE 14: The snapshots of spatial distribution of membrane potential with color scale for neurons in the square array network for $k = 1.5$ and $D = 5$ at (a) $t = 2$ time units, (b) $t = 75$ time units, (c) $t = 135$ time units, and (d) $t = 300$ time units.

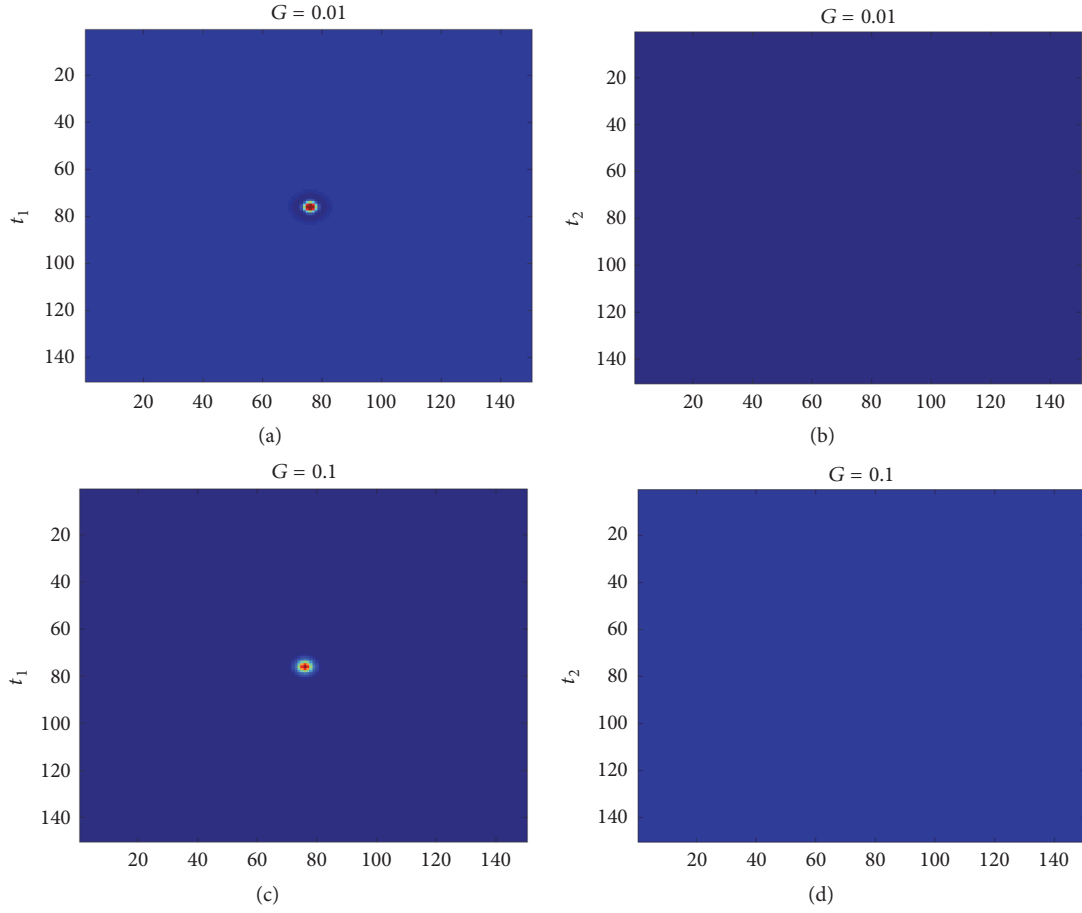


FIGURE 15: The snapshots of spatial distribution of membrane potential with color scale for neurons in the square array network for $k = 0$ and $D = 1$ at $t_1 = 2$ time units and $t_2 = 6$ time units. ((a), (b)) $G = 0.01$ and ((c), (d)) $G = 0.1$.

different collective behavior. Noticing the results before noise considerations, the coupling $k = 0.9$ was the only case with continuity of the central local area accompanied by sustained circular patterns. Our examination shows that, in opposition to the other memristor-type coupling levels, in this level the spatial representation is not robust against noise. Therefore, as is clear through the snapshots in Figure 19 the circular wave fronts change into some symmetrical deformations by increasing the noise intensity (see Figure 19(l)). In other words, the results reveal that the contribution of memristive effects denoting the synaptic plasticity determines the robustness of the excitable media against noise.

3.3. Numerical Results of Bifurcation Analysis. Knowing that the dynamic behavior of a system can be revealed from its bifurcation analysis, in this subsection, the bifurcation analysis is carried out by setting different memristor-type couplings for a system of two coupled neuronal units. In this way, a qualitative analysis of the role of parameter k is available. We set $D = 1$. The numerical result can be found in Figure 22.

In Figure 22, it is shown that the system can switch over completely different dynamical behaviors under variation of memristor-type coupling. In accordance with the results

represented in Sections 3.1 and 3.2, the whole diagram confirms that the system starts with periodic behavior, in which no propagation took place and then goes through some complicated behaviors, in which the two-dimensional lattice demonstrated wave propagation within multiple tiny rotating spiral seeds, and finally again it arrives at periodic dynamics, in which no propagation occurred.

In this paper, it was reported in Section 3.1 that the coupling intensity of $k = 0$, $k = 0.5$, $k = 1$, and $k = 1.5$ prevents the tissue from supporting wave propagation. Corresponding to these results, Figure 22 shows that the system undergoes periodic behavior by these mentioned memristor coupling intensities. Further, the chaotic behavior for $k = 0.7$ and $k = 0.8$ in Figure 22 concurs with the results in Figures 5 and 7, respectively, in which a turbulent electrical demonstration arose out of the respective memristor-type coupling intensities. Besides, in the previous subsections, the coupling intensity $k = 0.9$ was reported to be the only case significantly affected by the noise perturbation. In accordance with that, here our bifurcation analysis explains instability of the system in $k = 0.9$. Actually, the stability of the spatiotemporal pattern against noise is reduced when the neurons are set very close to their bifurcation point, which

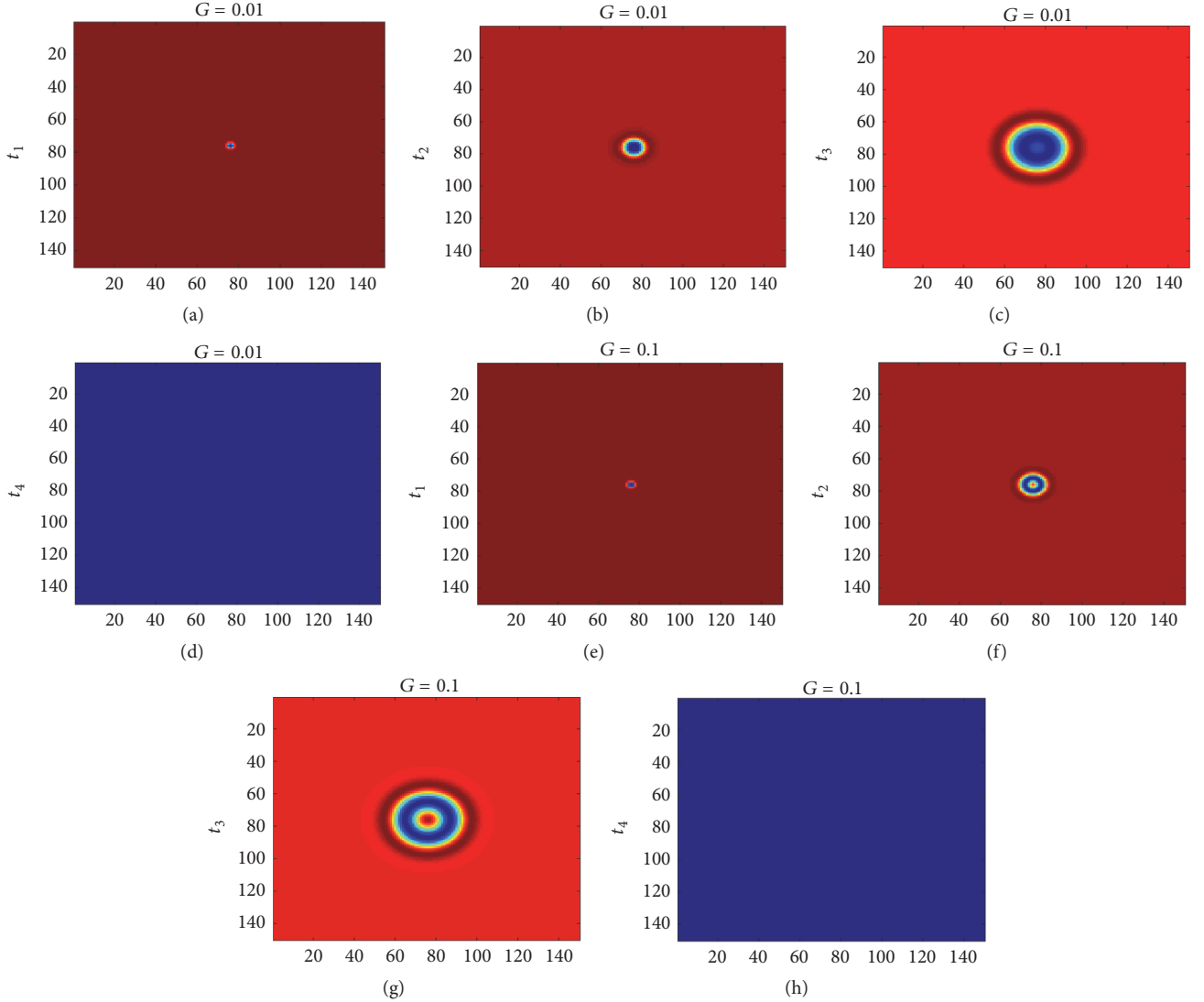


FIGURE 16: The snapshots of spatial distribution of membrane potential with color scale for neurons in the square array network for $k = 0.5$ and $D = 1$ at $t_1 = 2$ time units, $t_2 = 75$ time units, $t_3 = 170$ time units, and $t_4 = 300$ time units. ((a)–(d)) $G = 0.01$ and ((e)–(h)) $G = 0.1$.

is $k = 0.9$ (see Figure 23). At this point, the excitable media is very sensitive to perturbation. Thus, the media undergoes completely different dynamics in $k = 0.9$ by the noise impact.

4. Conclusion

In this study, the synaptic plasticity by means of memristor was investigated and the potential spatiotemporal patterns were detected. We showed that the memristive neuronal network is capable of representing plasticity phenomenon observed in biological cortical synapses. Excitable media were modeled by a network of 150×150 neuronal units with nearest neighbor connections containing memristor-type coupling. The 3-neuron Hopfield neuronal model was defined for the local dynamics of each unit. The tissue model was postulated to be capable of representing different dynamic behaviors mostly determined by the memristive properties. Our study showed that the level of memristive

effect plays a determinative role for the tissue to support wave propagation and also switch over different complex spatial demonstrations. In fact, the changes of dynamic law that govern the neurons within their connections were brought out from increasing or decreasing the memristor-type coupling strength. Although the resulting propagated waves could be expanded by greater amounts of resistor-type coupling, the total spatial pattern of the neurons did not change under the variation of resistor-type coupling. Further, we expanded our computations to investigate the stability of the resulting complex patterns against noise. It was revealed that all the spatial patterns were robust against noise impact except one case, in which the primary circular patterns changed into symmetrical deformations after the noise impact.

Finally, for further study, we sought to discover whether it is possible to find a meaningful relationship between the qualitative properties of the coupled neurons and the spatiotemporal demonstrations from a two-dimensional lattice.

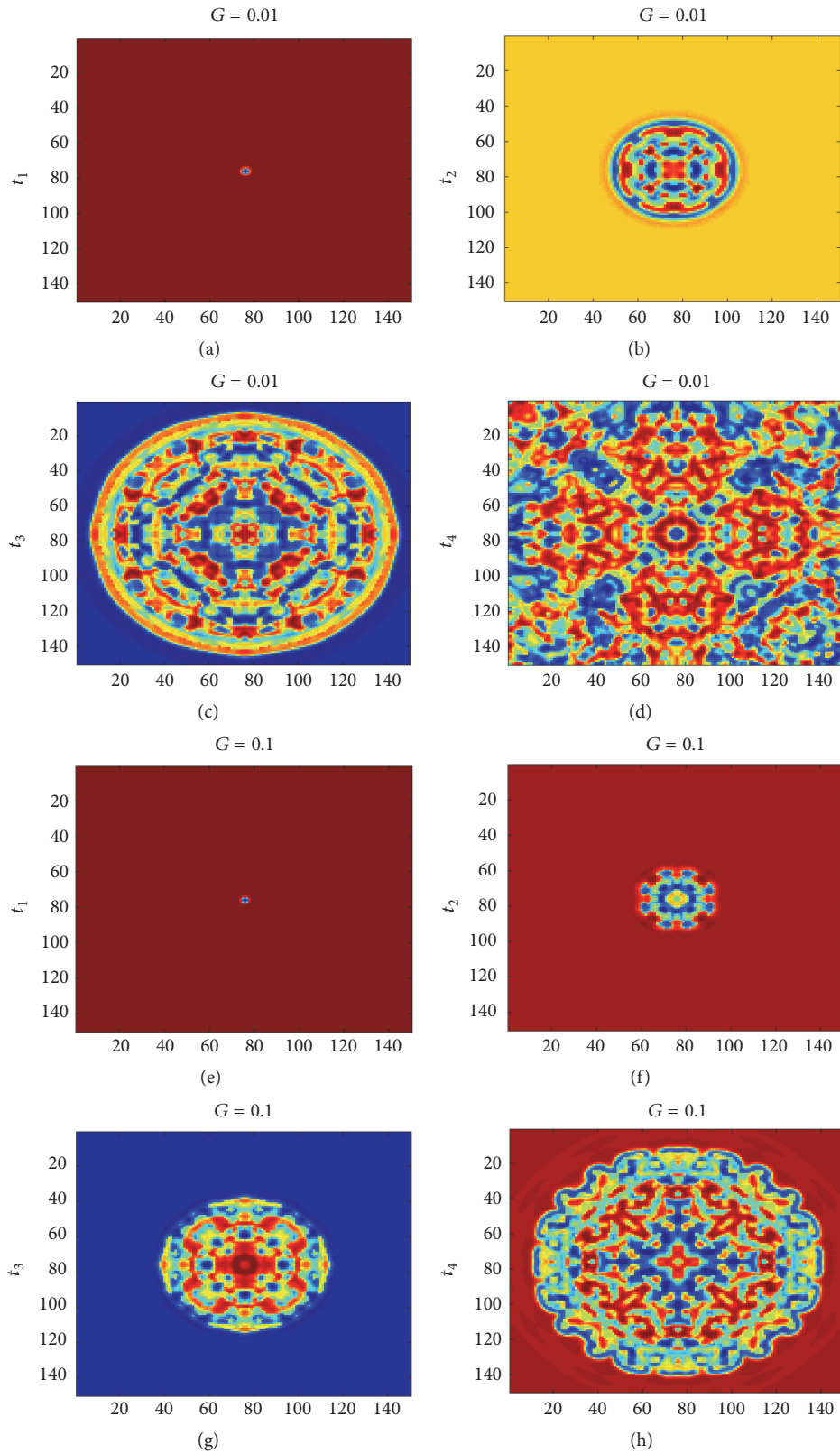


FIGURE 17: The snapshots of spatial distribution of membrane potential with color scale for neurons in the square array network for $k = 0.7$ and $D = 1$ at $t_1 = 2$ time units, $t_2 = 75$ time units, $t_3 = 170$ time units, and $t_4 = 300$ time units. ((a)–(d)) $G = 0.01$ and ((e)–(h)) $G = 0.1$.

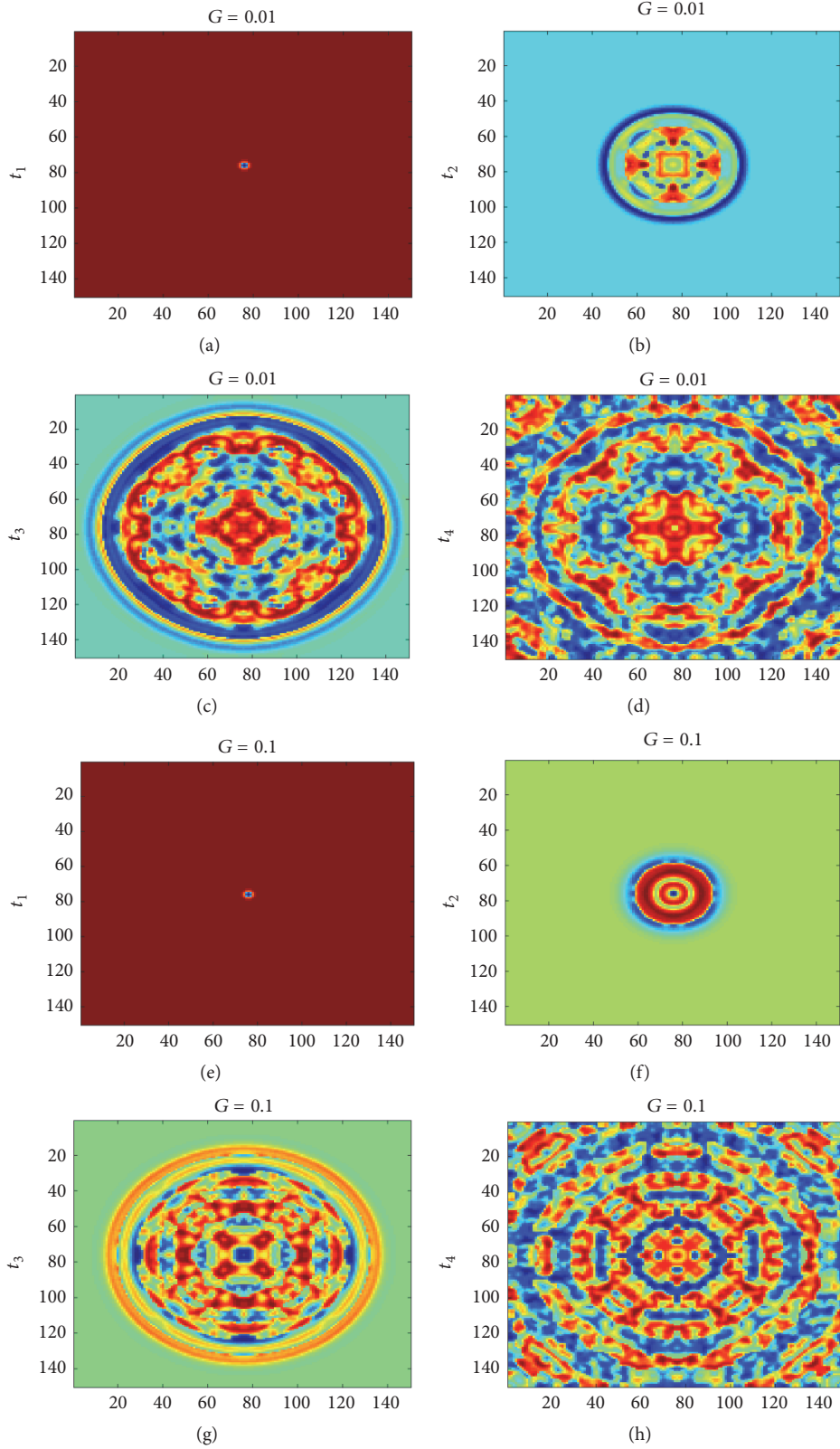


FIGURE 18: The snapshots of spatial distribution of membrane potential with color scale for neurons in the square array network for $k = 0.8$ and $D = 1$ at $t_1 = 2$ time units, $t_2 = 75$ time units, $t_3 = 170$ time units, and $t_4 = 300$ time units. ((a)–(d)) $G = 0.01$ and ((e)–(h)) $G = 0.1$.

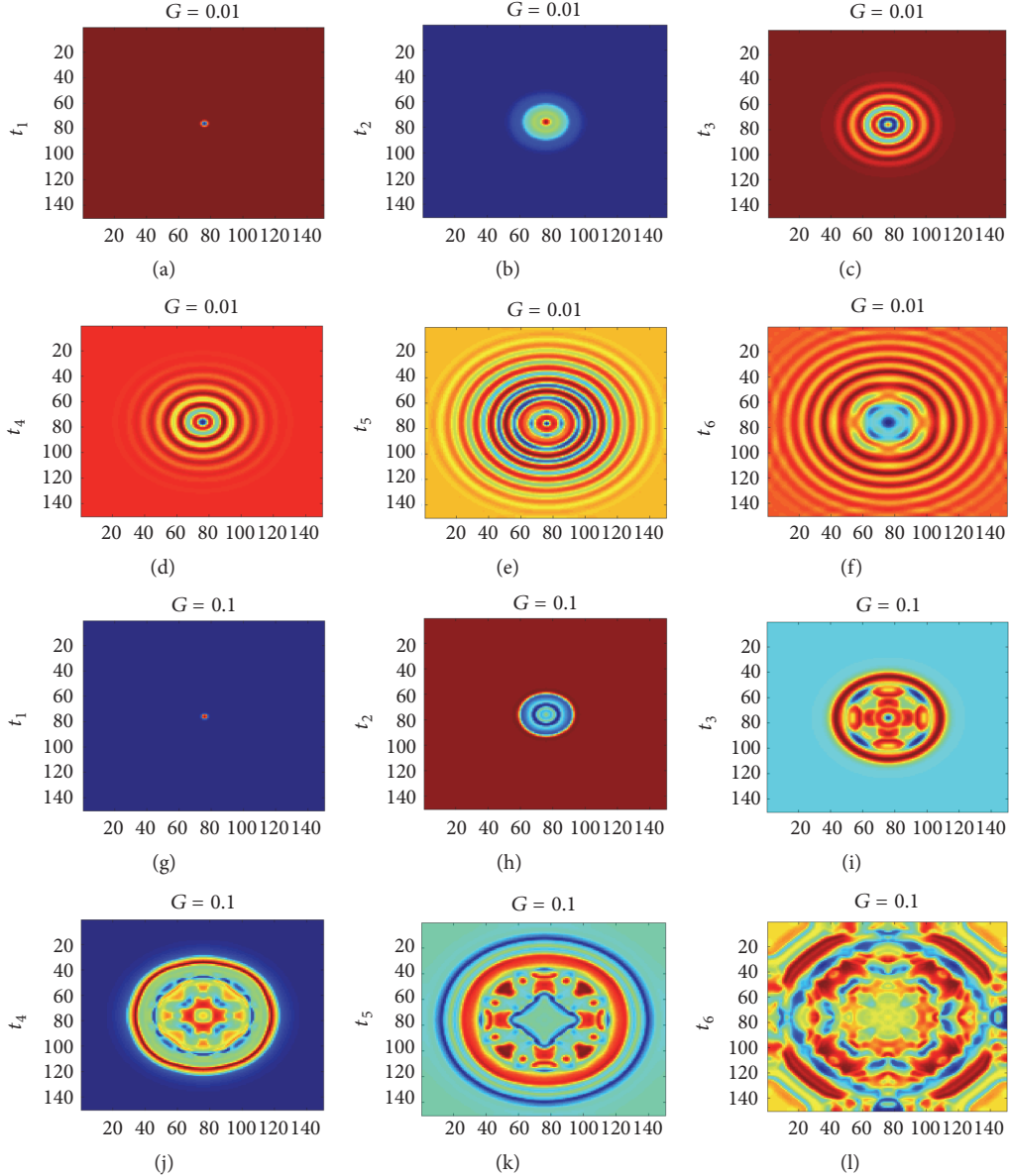


FIGURE 19: The snapshots of spatial distribution of membrane potential with color scale for neurons in the square array network for $k = 0.9$ and $D = 1$ at $t_1 = 2$ time units, $t_2 = 75$ time units, $t_3 = 170$ time units, $t_4 = 300$ time units, $t_5 = 450$ time units, and $t_6 = 600$ time units. ((a)–(f)) $G = 0.01$ and ((g)–(i)) $G = 0.1$.

Therefore, first the bifurcation analysis was carried out for different intensities of memristor-type coupling to see the possible mutual influence of the coupled neurons under memristive effects, and then the results were compared to our two-dimensional analysis. Our study revealed that the spatiotemporal patterns of electrical activity of the tissue concur with the bifurcation analysis. It was shown that the memristor coupling intensities, by which the system undergoes periodic behavior, prevent the tissue from holding wave propagation. In addition, the chaotic-like behavior in bifurcation diagram concurs with the turbulent spatiotemporal electrical activity of the tissue. Moreover, we showed that the excitable media is very sensitive to noise impact when the neurons are set close

to their bifurcation point, so that the spatiotemporal pattern is not stable.

Conflicts of Interest

The authors declare no conflicts of interest.

Acknowledgments

This paper is partially supported by the National Natural Science Foundation of China under Grant 61561023, the Key Project of Youth Science Fund of Jiangxi China under Grant 20133ACB21009, the Project of Science and Technology

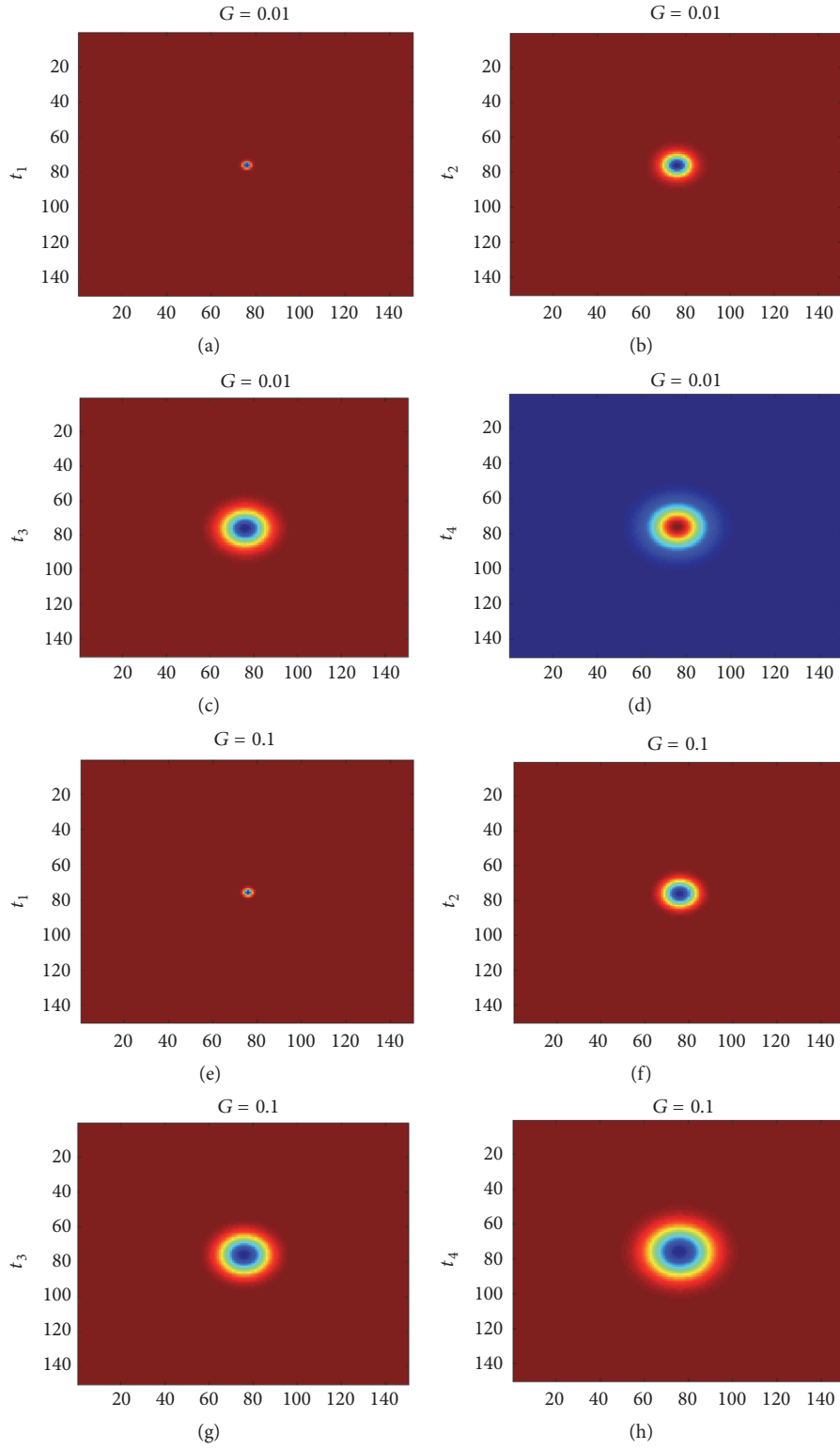


FIGURE 20: The snapshots of spatial distribution of membrane potential with color scale for neurons in the square array network for $k = 1$ and $D = 1$ at $t_1 = 2$ time units, $t_2 = 75$ time units, $t_3 = 170$ time units, and $t_4 = 300$ time units. ((a)–(d)) $G = 0.01$ and ((e)–(h)) $G = 0.1$.

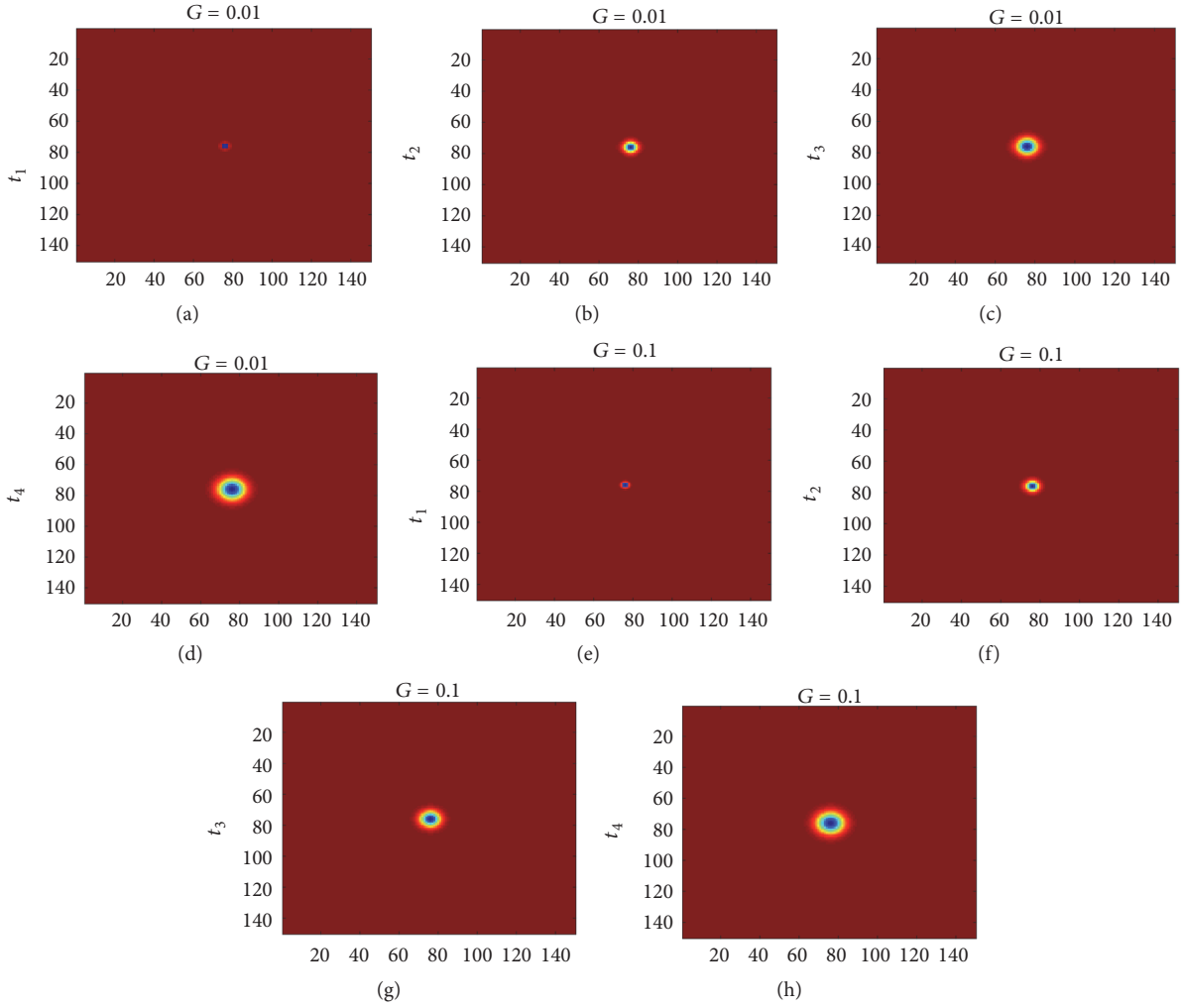


FIGURE 21: The snapshots of spatial distribution of membrane potential with color scale for neurons in the square array network for $k = 1.5$ and $D = 1$ at $t_1 = 2$ time units, $t_2 = 75$ time units, $t_3 = 170$ time units, and $t_4 = 300$ time units. ((a)–(d)) $G = 0.01$ and ((e)–(h)) $G = 0.1$.

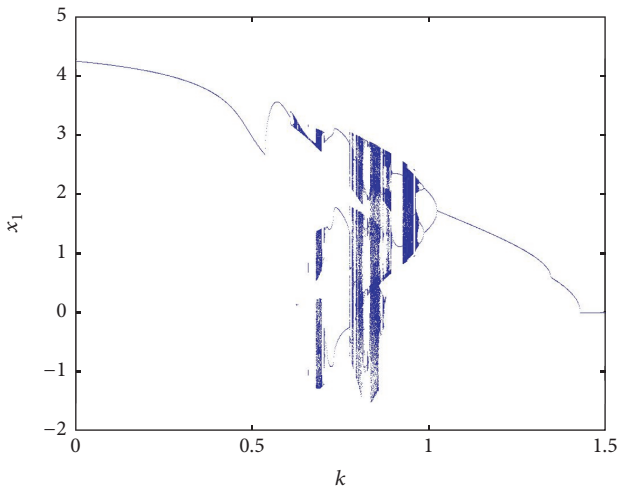


FIGURE 22: Bifurcation diagram of two coupled neurons for different memristor-type coupling intensities ($k = 0$ to $k = 1.5$), while $D = 1$ and other parameters are at their nominal values.

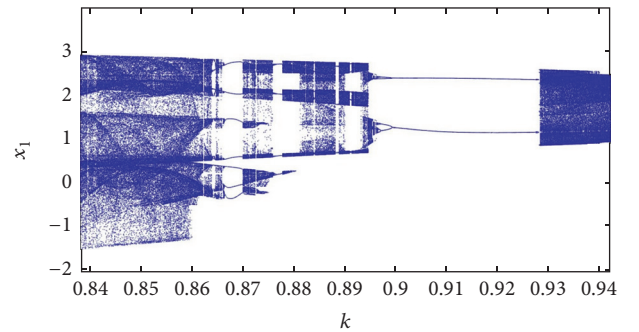


FIGURE 23: Bifurcation diagram of two coupled neurons for different memristor-type coupling intensities ($k = 0.84$ to $k = 0.94$), while $D = 1$ and other parameters are at their nominal values.

Fund of Jiangxi Education Department of China under Grant GJJ160429, and the Project of Jiangxi E-Commerce High Level Engineering Technology Research Centre. Sajad Jafari

was supported by Iran National Science Foundation (no. 96000815).



References

- [1] J. Ma, F. Wu, and C. Wang, "Synchronization behaviors of coupled neurons under electromagnetic radiation," *International Journal of Modern Physics B*, vol. 31, no. 2, Article ID 1650251, 14 pages, 2017.
- [2] S. Guo, J. Tang, J. Ma, and C. Wang, "Autaptic modulation of electrical activity in a network of neuron-coupled astrocyte," *Complexity*, vol. 2017, Article ID 4631602, 13 pages, 2017.
- [3] E. R. Kandel, *Principles of Neural Science*, vol. 4, McGraw-hill, New York, NY, USA, 2000.
- [4] L. Yu and Y. Yu, "Energy-efficient neural information processing in individual neurons and neuronal networks," *Journal of Neuroscience Research*, vol. 95, no. 11, pp. 2253–2266, 2017.
- [5] E. A. Boroujeni and H. R. Momeni, "Non-fragile nonlinear fractional order observer design for a class of nonlinear fractional order systems," *Signal Processing*, vol. 92, no. 10, pp. 2365–2370, 2012.
- [6] T. Kapitaniak, "Generating strange nonchaotic trajectories," *Physical Review E: Statistical, Nonlinear, and Soft Matter Physics*, vol. 47, no. 2, pp. 1408–1410, 1993.
- [7] L. Yu, M. De Mazancourt, A. Hess et al., "Functional connectivity and information flow of the respiratory neural network in chronic obstructive pulmonary disease," *Human Brain Mapping*, vol. 37, no. 8, pp. 2736–2754, 2016.
- [8] C. Wang, M. Lv, A. Alsaedi, and J. Ma, "Synchronization stability and pattern selection in a memristive neuronal network," *Chaos: An Interdisciplinary Journal of Nonlinear Science*, vol. 27, no. 11, Article ID 113108, 2017.
- [9] J. Ma, H. Qin, X. Song, and R. Chu, "Pattern selection in neuronal network driven by electric autapses with diversity in time delays," *International Journal of Modern Physics B*, vol. 29, no. 1, Article ID 1450239, 2015.
- [10] L. Yu and L. Liu, "Optimal size of stochastic Hodgkin-Huxley neuronal systems for maximal energy efficiency in coding pulse signals," *Physical Review E: Statistical, Nonlinear, and Soft Matter Physics*, vol. 89, no. 3, Article ID 032725, 2014.
- [11] Y. Babacan and F. Kaçar, "Memristor emulator with spike-timing-dependent-plasticity," *AEÜ - International Journal of Electronics and Communications*, vol. 73, pp. 16–22, 2017.
- [12] H. Kim, M. P. Sah, C. Yang, T. Roska, and L. O. Chua, "Neural synaptic weighting with a pulse-based memristor circuit," *IEEE Transactions on Circuits and Systems I: Regular Papers*, vol. 59, no. 1, pp. 148–158, 2012.
- [13] S. P. Adhikari, C. Yang, H. Kim, and L. O. Chua, "Memristor bridge synapse-based neural network and its learning," *IEEE Transactions on Neural Networks and Learning Systems*, vol. 23, no. 9, pp. 1426–1435, 2012.
- [14] E. Tlelo-Cuautle, L. G. de la Fraga, V.-T. Pham, C. Volos, S. Safari, and A. D. J. Quintas-Valles, "Dynamics, FPGA realization and application of a chaotic system with an infinite number of equilibrium points," *Nonlinear Dynamics*, vol. 89, no. 2, pp. 1129–1139, 2017.
- [15] V. T. Pham, S. Jafari, S. Vaidyanathan, C. Volos, and X. Wang, "A novel memristive neural network with hidden attractors and its circuitry implementation," *Science China Technological Sciences*, vol. 59, no. 3, pp. 358–363, 2016.
- [16] D. B. Strukov, G. S. Snider, D. R. Stewart, and R. S. Williams, "The missing memristor found," *Nature*, vol. 453, pp. 80–83, 2008.
- [17] L. O. Chua, "Memristor—the missing circuit element," *IEEE Transactions on Circuit Theory*, vol. 18, no. 5, pp. 507–519, 1971.
- [18] L. O. Chua and S. M. Kang, "Memristive devices and systems," *Proceedings of the IEEE*, vol. 64, no. 2, pp. 209–223, 1976.
- [19] Y. Babacan and F. Kaçar, "Floating memristor emulator with subthreshold region," *Analog Integrated Circuits and Signal Processing*, vol. 90, no. 2, pp. 471–475, 2017.
- [20] C. K. Volos, A. Akgul, V.-T. Pham, and M. S. Baptista, "Antimonotonicity, crisis and multiple attractors in a simple memristive circuit," *Journal of Circuits, Systems and Computers*, vol. 27, no. 2, Article ID 1850026, 2018.
- [21] H. Bao, N. Wang, B. Bao, M. Chen, P. Jin, and G. Wang, "Initial condition-dependent dynamics and transient period in memristor-based hypogenetic jerk system with four line equilibria," *Communications in Nonlinear Science and Numerical Simulation*, vol. 57, pp. 264–275, 2018.
- [22] J. Ma, Y. Xu, C. Wang, and W. Jin, "Pattern selection and self-organization induced by random boundary initial values in a neuronal network," *Physica A: Statistical Mechanics and its Applications*, vol. 461, pp. 586–594, 2016.
- [23] J. Ma, L. Mi, P. Zhou, Y. Xu, and T. Hayat, "Phase synchronization between two neurons induced by coupling of electromagnetic field," *Applied Mathematics and Computation*, vol. 307, pp. 321–328, 2017.
- [24] G.-Y. Zhang, J. Ma, L.-C. Yu, and Y. Chen, "Synchronization of spiral waves in a two-layer coupled inhomogeneous excitable system," *Chinese Physics B*, vol. 17, no. 11, pp. 4107–4113, 2008.
- [25] F. Wu, C. Wang, W. Jin, and J. Ma, "Dynamical responses in a new neuron model subjected to electromagnetic induction and phase noise," *Physica A: Statistical Mechanics and Its Applications*, vol. 469, pp. 81–88, 2017.
- [26] Y. Babacan, F. Kaçar, and K. Gürkan, "A spiking and bursting neuron circuit based on memristor," *Neurocomputing*, vol. 203, pp. 86–91, 2016.
- [27] J. G. Howland and Y. T. Wang, "Synaptic plasticity in learning and memory: stress effects in the hippocampus," *Progress in Brain Research*, vol. 169, pp. 145–158, 2008.
- [28] K. D. Cantley, R. C. Ivans, A. Subramaniam, and E. M. Vogel, "Spatio-temporal pattern recognition in neural circuits with memory-transistor-driven memristive synapses," in *Proceedings of the 2017 International Joint Conference on Neural Networks, IJCNN 2017*, pp. 4633–4640, USA, May 2017.
- [29] T. Rinaldi, C. Perrodin, and H. Markram, "Hyper-connectivity and hyper-plasticity in the medial prefrontal cortex in the valproic acid animal model of autism," *Frontiers in Neural Circuits*, vol. 2, Article ID 4, 2008.
- [30] J. A. Varela, K. Sen, J. Gibson, J. Fost, L. F. Abbott, and S. B. Nelson, "A quantitative description of short-term plasticity at excitatory synapses in layer 2/3 of rat primary visual cortex," *The Journal of Neuroscience*, vol. 17, no. 20, pp. 7926–7940, 1997.
- [31] J.-V. Le Bé and H. Markram, "Spontaneous and evoked synaptic rewiring in the neonatal neocortex," *Proceedings of the National Academy of Sciences of the United States of America*, vol. 103, no. 35, pp. 13214–13219, 2006.
- [32] M. S. El Naschie and T. Kapitaniak, "Soliton chaos models for mechanical and biological elastic chains," *Physics Letters A*, vol. 147, no. 5–6, pp. 275–281, 1990.

- [33] S. Brezetskyi, D. Dudkowski, and T. Kapitaniak, “Rare and hidden attractors in Van der Pol-Duffing oscillators,” *The European Physical Journal Special Topics*, vol. 224, no. 8, pp. 1459–1467, 2015.
- [34] J. J. Hopfield, “Neurons with graded response have collective computational properties like those of two-state neurons,” *Proceedings of the National Academy of Sciences of the United States of America*, vol. 81, no. 10, pp. 3088–3092, 1984.
- [35] B. Bao, H. Qian, Q. Xu, M. Chen, J. Wang, and Y. Yu, “Coexisting behaviors of asymmetric attractors in hyperbolic-type memristor based hopfield neural network,” *Frontiers in Computational Neuroscience*, vol. 11, no. 81, pp. 1–14, 2017.
- [36] B. Bao, H. Qian, J. Wang et al., “Numerical analyses and experimental validations of coexisting multiple attractors in Hopfield neural network,” *Nonlinear Dynamics*, vol. 90, no. 4, pp. 2359–2369, 2017.
- [37] Y. Wang and J. Ma, “Bursting behavior in degenerate optical parametric oscillator under noise,” *Optik—International Journal for Light and Electron Optics*, vol. 139, pp. 231–238, 2017.

Research Article

Fractional-Order Memristor Emulator Circuits

C. Sánchez-López ¹, **V. H. Carbajal-Gómez** ¹,
M. A. Carrasco-Aguilar¹ and **I. Carro-Pérez**²

¹UATx, Mexico

²ITESM, Mexico

Correspondence should be addressed to C. Sánchez-López; carlsanmx@yahoo.com.mx

Received 16 March 2018; Revised 24 April 2018; Accepted 24 April 2018; Published 28 May 2018

Academic Editor: Viet-Thanh Pham

Copyright © 2018 C. Sánchez-López et al. This is an open access article distributed under the Creative Commons Attribution License, which permits unrestricted use, distribution, and reproduction in any medium, provided the original work is properly cited.

This brief leads the synthesis of fractional-order memristor (FOM) emulator circuits. To do so, a novel fractional-order integrator (FOI) topology based on current-feedback operational amplifier and integer-order capacitors is proposed. Then, the FOI is substituting the integer-order integrator inside flux- or charge-controlled memristor emulator circuits previously reported in the literature and in both versions: floating and grounded. This demonstrates that FOM emulator circuits can also be configured at incremental or decremental mode and the main fingerprints of an integer-order memristor are also holding up for FOMs. Theoretical results are validated through HSPICE simulations and the synthesized FOM emulator circuits can easily be reproducible. Moreover, the FOM emulator circuits can be used for improving future applications such as cellular neural networks, modulators, sensors, chaotic systems, relaxation oscillators, nonvolatile memory devices, and programmable analog circuits.

1. Introduction

Resistors, inductors, capacitors, and memristors are basic network elements and the real behavior of each of them is time-varying and nonlinear [1–3]. For the last three cases, the real behavior of each element has always been modeled from integer-order differential equations. However, it is well known that this kind of modeling is only a narrow subset of fractional calculus, which is a generalization of arbitrary order differentiation and integration, and this last approach can be used to better model the description of natural phenomena [4–8]. In this context, fractional calculus is beginning to be used for describing the behavior of memristive elements and systems, i.e., memristors, memcapacitors, meminductors, and any combination of them. Particularly, few studies have been realized on fractional-order memristors (FOM). Thus, [9] analyzes the FOM state equation behavior when a step signal is applied and demonstrates that by controlling fractional parameters associated with the FOM, the saturation time of the resistance can be controlled. In [10], fractional calculus is used to generalize the memristor and higher-order elements, although without any physical meaning. From a mathematical point of view,

[11] reports the memfractance concept and according to the fractional-order, it shows the interpolated characteristics between different memristive elements. In [12], the relationship between fracmemristance and fractance is discussed. By combining capacitors together with memristors, net-grid-type structures were also described to approximate the capacitive and inductive fracmemristor. In [13], the no ideal fractional interaction between flux and charge of a memristor is described. However, a piecewise nonlinear model of the memristor is considered and as a consequence, the fractional-order dynamic system is approached but again without any deep physical understanding. More recently, [14] reports the use of Valsa-algorithm for approximating a fractional-order capacitor. Afterwards, this element is substituting the integer-order capacitor into a memristor emulator circuit, obtaining the FOM behavior. However, the main disadvantage of [14] is that not only large RC-circuits are obtained, but the numerical value of each resistive and capacitive element is not commercially available and hence, parallel-series networks must again be used. Despite the FOM concept has been mathematically studied and ideal numerical results were shown, neither physical solid-state device nor emulator circuit has been developed until today. In this scope, this paper addresses

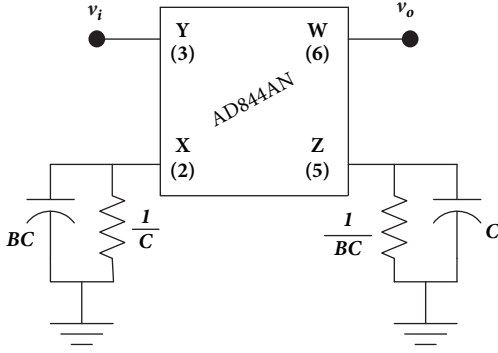


FIGURE 1: FOI circuit synthesis based on CFOA.

the synthesis of FOM emulator circuits from integer-order memristor emulator circuits previously reported in the literature [15–18]. The rest of the paper is organized as follows. In Section 2, a novel fractional-order integrator (FOI) topology based on current-feedback operational amplifier (CFOA) and integer-order capacitors is discussed. In Section 3, the FOI previously designed is replacing the integer-order integrator (IOI) inside flux- or charge-controlled memristor emulator circuits, at their floating and grounded versions, and the FOMs can also be configured for operating at incremental or decremental mode [2]. Section 4 shows HSPICE simulation results, showing that the fingerprints of an integer-order memristor are holding up for their fractional versions. Finally, some conclusions are summarized in Section 5.

2. Fractional-Order Integrator

A challenge at fractional calculus is the building or in best of cases, the approximation of fractances [19, 20]. In this sense, several mathematical approximations were researched and by its quickly convergence, continuous fractional expansion approach is the most adequate. Thus, the first-order approximation of an FOI is given by

$$\frac{1}{s^\alpha} \approx \frac{(1-\alpha)s + (1+\alpha)}{(1+\alpha)s + (1-\alpha)} = \frac{Bs + 1}{B + s}, \quad (1)$$

$$B = \frac{1-\alpha}{1+\alpha} \quad \forall 0 < \alpha < 1,$$

where α is the fractional-order. It is important to mention that high-order fractance approximations can also be obtained; however, the synthesis of them leads to complex and bulky circuits [21, 22]. A simple circuit able to synthesize (1) is given in Figure 1, whose transfer function is

$$\frac{v_o(s)}{v_i(s)} = A_{v1}A_{v2}A_i \frac{Bs + 1}{B + s} \approx \frac{1}{s^\alpha}, \quad (2)$$

where $A_{v1,2} \approx 0.98$ and $A_i \approx 0.98$ are the voltage and current gains of the voltage and current followers associated with X-Y, W-Z, and Z-X terminals of the CFOA, respectively. To design the FOI, we propose the following design guide:

- (1) Given α , use (1) to compute B .

- (2) Choose $C = 0.1 \text{ mF}$ and evaluate $R = C^{-1} = 10 \text{ k}\Omega$.
- (3) Using the numerical value of B obtained in the first step, evaluate BC and $R_f = (BC)^{-1}$ of Figure 1. Resistances with noncommercial values are adjusted with precision potentiometers and capacitances with series and parallel connections.
- (4) Frequency denormalization is done for $C^{\text{new}} = C/kf$, where kf is the denormalization constant.

Following these steps and from (1), we assume $\alpha = 0.99, 0.75, 0.50, 0.25, 1 \text{ m}$, and as a consequence $B = 5 \text{ m}, 0.14, 0.33, 0.60, 0.99$; $V_{dd} = \pm 10 \text{ V}$, $v_i(t) = A_m \sin(\omega t)$, where $A_m = 2 \text{ V}$ is the amplitude of the voltage signal source, $\omega = 2\pi f$, $f = 20 \text{ kHz}$, and $kf = 50 \text{ k}$. According to the third and fourth steps, $BC/kf = 10 \text{ pF}, 0.28 \text{ nF}, 0.66 \text{ nF}, 1.2 \text{ nF}, 2 \text{ nF}$, $R_f = (BC)^{-1} = 2 \text{ M}\Omega, 70 \text{ k}\Omega, 30 \text{ k}\Omega, 16.6 \text{ k}\Omega, 10 \text{ k}\Omega$, and $C/f = 2 \text{ nF}$. To make a fair comparison, an IOI is obtained of Figure 1 by removing $(BC)^{-1}$ and BC . In this way, Figures 2(a)–2(e) illustrate the transient behavior of the FOI for each α described above and one can observe that for $\alpha = 0.99$ (Figure 2(a)), the behavior of the FOI approximates to IOI, whereas for $\alpha = 1 \text{ m}$, $B \approx 1$ and hence, Figure 1 becomes a voltage follower, as described in (2) and depicted in Figure 2(e) [23]. Note that, for all graphics, HSPICE results are in agreement with experimental results. Moreover, from point of view of root locus analysis, the zero and pole of (2) are moved when α varies. This is a serious disadvantage, since C should quickly be discharged when R_f is low. To mitigate this problem, the pole is set up and fixed for $\alpha = 0.99$ and the FOI behavior is plotted when the zero is varied. Figures 2(a)–2(e) show that this assumption can still model the behavior of FOI with a low error level. Nevertheless, when $\alpha = 1 \text{ m}$, the error increases and the pole is not placed on the zero. Hence, Figure 1 becomes again a voltage follower, but with a light phase shifting, as depicted in Figure 2(e). For convenience, the magnitude and phase response in the frequency domain of Figure 1 for the three cases (IOI, FOI, and FOI with R_f fixed) and when α varies are illustrated in Figure 3. In the former figure, one can observe that the magnitude response has slope $-20\alpha \text{ dB/dec}$ which decreases when α also decreases. Notice that when $\alpha = 0.99$, the magnitude response of the three cases is superimposed and with 49.42 dB at DC. Afterwards, when α is monotonically decreased, the magnitude and slope of the second and third case are modified. Thus, for $\alpha = 0.75$, the magnitude at DC of the second case is 16.45 dB and from 3 kHz , this is superimposed with the magnitude of the first case. Later, when α takes the aforementioned values and from 20 kHz , the frequency responses of the second and third cases are similar, as shown in Figure 3(a), confirming the previous analysis [20]. Note that, at low-frequency, the magnitude of the FOI varies for the different values of α , whereas the magnitude at DC of the third case remains at 49.42 dB . Moreover, Figure 3(b) shows the phase response given by $\theta = -90^\circ\alpha$ or $\theta = -\pi\alpha/2 \text{ rad}$. Similarly as above, when $\alpha = 0.99$ the phase response for all cases is superimposed at -90° . This behavior is modified for second and third cases, and when α takes different values. Therefore, for FOI, one can observe in Figure 3(b) that the phase becomes zero when $\alpha = 1 \text{ m}$,

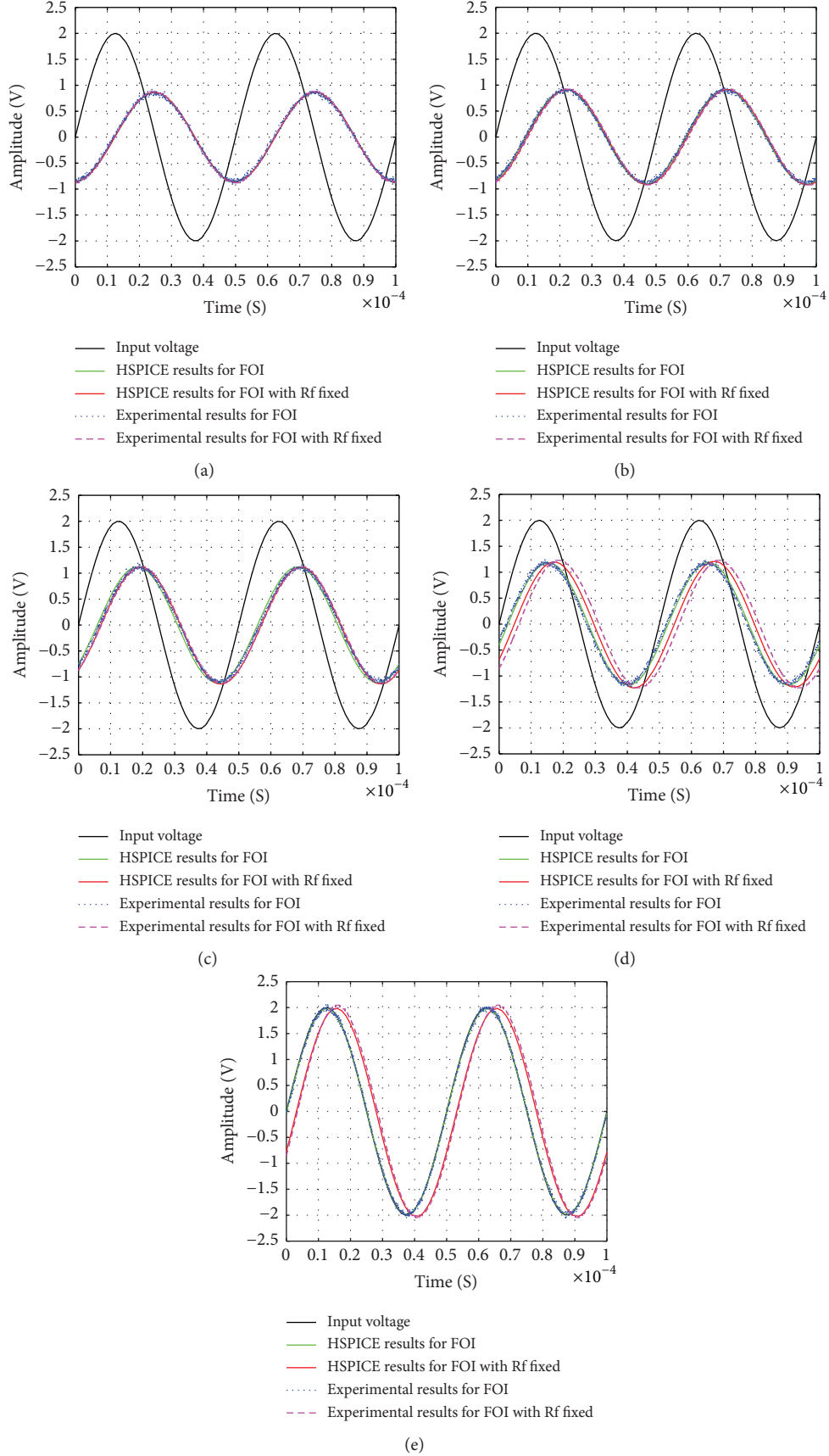


FIGURE 2: Transient responses of IOI, FOI, and FOI with R_f fixed when (a) $\alpha = 0.99$, (b) $\alpha = 0.75$, (c) $\alpha = 0.5$, (d) $\alpha = 0.25$, and (e) $\alpha = 1$ m, all operating to $f = 20$ kHz.

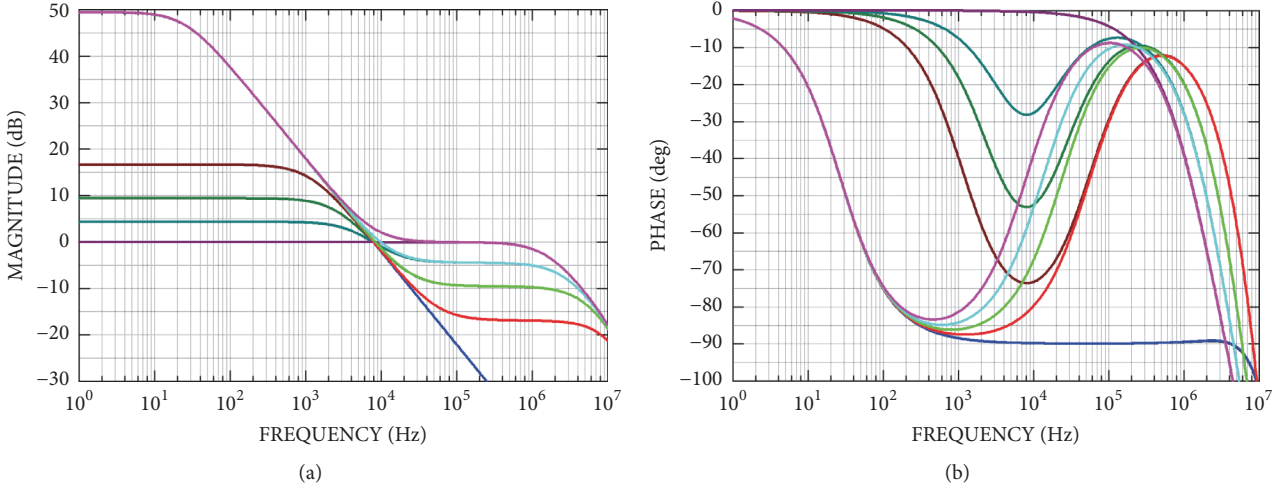


FIGURE 3: Behavior of IOI (black line), FOI for: $\alpha = 0.99$ (blue line), $\alpha = 0.75$ (red line), $\alpha = 0.5$ (green line), $\alpha = 0.25$ (cyan line), and $\alpha = 1$ m (magenta line); and FOI with R_f fixed for $\alpha = 0.99$ (light blue line), $\alpha = 0.75$ (light red line), $\alpha = 0.5$ (light green line), $\alpha = 0.25$ (light cyan line), and $\alpha = 1$ m (light magenta line): (a) magnitude response and (b) phase response.

TABLE 1: Numerical values of the phase and magnitude response of IOI, FOI, and FOI with R_f fixed for $\alpha \in (0, 1)$ and $f = 20$ kHz.

α	Phase (Deg)				Magnitude (dB)			
	IOI	FOI	FOI with R_f fixed	Difference	IOI	FOI	FOI with R_f fixed	Difference
0.99	-89.92	-89.91	-89.91	0	-8.25	-8.25	-8.25	0
0.75	-	-66.71	-69.89	3.18	-	-7.71	-7.70	-0.01
0.5	-	-42.27	-49.66	7.19	-	-5.93	-5.85	-0.08
0.25	-	-20.31	-33.44	13.13	-	-3.19	-2.96	-0.23
1 m	-	-0.88	-22.09	21.21	-	0.072	0.541	0.469

whereas a level of error is glimpsed for FOI with R_f fixed. From these graphics, we can claim that the proposed topology is stable until 1 MHz, approximately [24]. Table 1 gives the numerical value of the magnitude and phase response for $f = 20$ kHz and different α . It is important to mention that, for any design where $\alpha > 1$ is required, the FOI must be connected in cascade with q integer-order integrators, such that $\hat{\alpha} = \alpha - q$. For instance, let us suppose $\alpha = 4.35$; then $q = 4$ and $\hat{\alpha} = 4.35 - 4 = 0.35$.

3. Fractional-Order Memristor Synthesis

In [15], a flux-controlled floating memristor emulator circuit which uses four positive second-generation current conveyors (CCII+s) and one analog multiplier was reported. According to Figure 1 in [15], the topology has an IOI circuit well defined and its memristance equation given by (9) in [15] is also of integer-order. To obtain an FOM from integer-order memristor, the integrator circuit of the latter must be replaced by FOI circuit, as shown in Figure 4(a). Following the analysis given in [15, 25], the behavioral model is deduced as

$$\frac{v_m(t)}{i_m(t)} = R_1 \pm \frac{R_4}{10R_2} \left(R_1 - \frac{V_V}{i_m(t)} \right) {}_a J_t^\alpha v_m(t) - \frac{V_H}{i_m(t)}, \quad (3)$$

where V_H and V_V are DC voltage sources to control horizontally and vertically the offset of the dependent-frequency

pinched hysteresis loop on the voltage-current plane, respectively [25], and ${}_a J_t^\alpha$ denotes the fractional-order integral operator of

- (i) Riemann-Liouville and Caputo fractional integral

$${}_a J_t^\alpha v_m(t) = \frac{1}{\Gamma(\alpha)} \int_a^t \frac{v_m(\tau)}{(t-\tau)^{1-\alpha}} d\tau, \quad (4)$$

- (ii) or Grunwald-Letnikov fractional integral

$${}_a J_t^\alpha v_m(t) = \lim_{h \rightarrow 0} h^\alpha \sum_{p=0}^{(t-a)/h} \frac{\Gamma(\alpha+p)}{p! \Gamma(\alpha)} v_m(t-ph), \quad (5)$$

where for both fractional integrals, a and t are the lower and upper limits of integration.

Defining the fractional-order flux $\phi_m^\alpha(t) = {}_a J_t^\alpha v_m(t)$, (3) can be rewritten as

$$\begin{aligned} \frac{v_m(t)}{i_m(t)} &= R_1 \pm \frac{R_4}{10R_2} \left(R_1 - \frac{V_V}{i_m(t)} \right) \phi_m^\alpha(t) - \frac{V_H}{i_m(t)} \\ &= M(\phi_m^\alpha(t)), \end{aligned} \quad (6)$$

where $M(\phi_m^\alpha(t))$ is the flux-controlled fracmemristance and can be controlled by applying a voltage or current signal

TABLE 2: Component list of Figure 4(a), Figure 1 in [15], Figure 4(b), and Figure 5 in [18], assuming $C = 0.1 \text{ mF}$, $kf = 50 \text{ e3}$, $\alpha \approx 1$, and $f = 20 \text{ kHz}$.

Element	Figure 4(a)		Figure 1 in [15]		Figure 4(b)		Figure 5 in [18]		Tolerance
	Inc.	Dec.	Inc.	Dec.	Inc.	Dec.	Inc.	Dec.	
V_H	-37 mV	-75 mV	-40 mV	-70 mV	-49 mV		-50 mV		
V_V	36 mV	76 mV	39 mV	85 mV	-50 mV		-93 mV	-95 mV	
A_m				2 V					
$\pm V_{dd}$				$\pm 10 \text{ V}$					
R_1		10 k Ω					9 k Ω		
R_2	1 k Ω		10 k Ω				11.5 k Ω		
R_3	-		2.4 k Ω		-		9.5 k Ω		$\pm 5\%$
R_4		10 k Ω			-		-		
C^{-1}	10 k Ω		-		10 k Ω		-		
$(BC)^{-1}$	2 M Ω		-		2 M Ω		-		
BC/kf	10 pF		-		10 pF		-		
C/kf	2 nF		-		2 nF		-		$\pm 20\%$
$C_z = C/kf$	-		2 nF		-		2 nF		

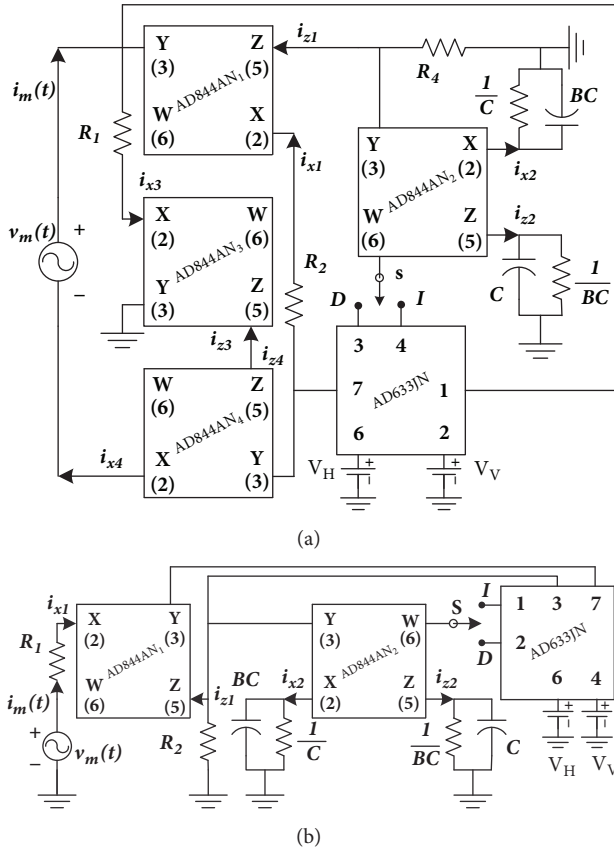


FIGURE 4: (a) Flux-controlled floating fracmemristor and (b) charge-controlled grounded fracmemristor.

across the memristor, as depicted in Figure 4(a). Moreover, charge-controlled memristor emulator circuits have also been reported in the literature. According to Figure 5 in [18], the emulator circuit has also an IOI circuit and if it is

exchanged with Figure 1, then a fractional-order charge-controlled grounded memristor emulator circuit is obtained, as shown in Figure 4(b). Hence, following the analysis given in [18, 25], one obtains

$$\frac{v_m(t)}{i_m(t)} = R_1 \pm \frac{R_2}{10} \left(R_2 + \frac{V_V}{i_m(t)} \right) {}_a J_t^\alpha i_m(t) + \frac{V_H}{i_m(t)} \quad (7)$$

and the fractional-order charge becomes $q_m^\alpha(t) = {}_a J_t^\alpha i_m(t)$. Hence, (7) can be written as

$$\begin{aligned} \frac{v_m(t)}{i_m(t)} &= R_1 \pm \frac{R_2}{10} \left(R_2 + \frac{V_V}{i_m(t)} \right) q_m^\alpha(t) + \frac{V_H}{i_m(t)} \\ &= M(q_m^\alpha(t)), \end{aligned} \quad (8)$$

where $M(q_m^\alpha(t))$ is the charge-controlled fracmemristance. Regarding Figure 4, the **S** switch is used for selecting the kind of fracmemristor, where **I** denotes the incremental topology and **D** denotes the decremental topology. Note that if $V_H = V_V = 0$ and $\alpha = 1$, then (6) and (8) are reduced to their original versions given in [15, 18].

4. Numerical Simulations

Once the behavioral model for each floating and grounded fracmemristor at its incremental and decremental version has been deduced, numerical simulations can be realized. Henceforth, numerical results of the incremental topologies will be shown below in the left-side and for the decremental topologies will be shown in the right-side. On the one hand, to design the integer-order floating memristor working at incremental and decremental mode, the design guideline reported in [15] was used. Table 2 gives the numerical value of each element of Figure 4(a) and Figure 1 reported in [15], with $v_m(t) = A_m \sin(\omega t)$. On the other hand, since it is not possible to deduce, by now, an analytical model to make a frequency analysis [15], each design variable of the fracmemristor was varied in order to adjust the frequency-dependent pinched

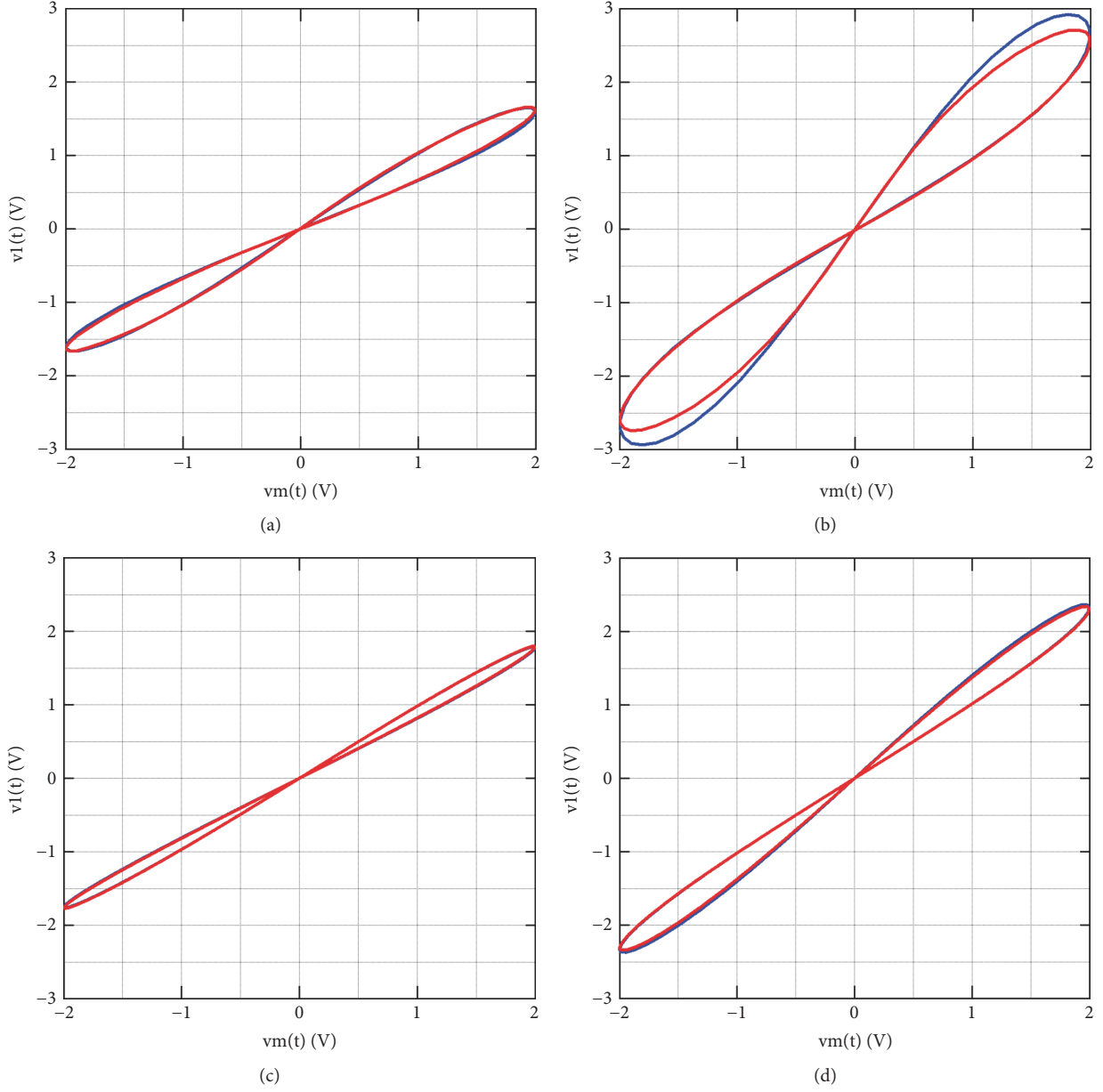


FIGURE 5: Comparing the frequency-dependent pinched hysteresis loops of the flux-controlled floating memristor (blue line) and fracmemristor (red line): (a) incremental mode, (b) decremental mode, and for the charge-controlled grounded memristor (blue line) and fracmemristor (red line): (c) incremental mode and (d) decremental mode.

hysteresis loop behavior with its integer version. In this way, Figures 5(a) and 5(b) show the pinched hysteresis loops of the flux-controlled floating memristor and fracmemristor at each operation mode and one can observe a good agreement among the graphics for the incremental case. However, a slight variation is glimpsed for the decremental case and could be due to the nonlinearities of the analog multiplier. A similar analysis is done for Figure 4(b) at its integer-order version and Figure 5 taken from [18]. Table 2 also gives the numerical value of each element used in numerical simulations. Thus, Figures 5(c) and 5(d) depict the behavior of each pinched hysteresis loop at each operation mode. For Figure 5(c), one can observe that both hysteresis loops

are almost the same and hence, Figure 4(b) becomes an integer-order memristor [18]. Moreover, when the **S**-switch is connected to **D**-terminal and **I**-terminal is grounded, Figure 4(b) is now configured at decremental mode and Figure 5(d) illustrates the hysteresis loops. On this last figure, one can observe a good agreement among them. Therefore, the behavior of Figure 4(b) becomes also an integer-order memristor. Comparing all graphics of Figure 5, we note that, for each case, the area of each lobe of the latter figures is less than the area of each lobe of the former. Nonetheless, the hysteresis loops of Figures 5(c) and 5(d) can be widened by adjusting the numerical value of R_1 or R_2 . However, this will have a negative impact, since the hysteresis loops should

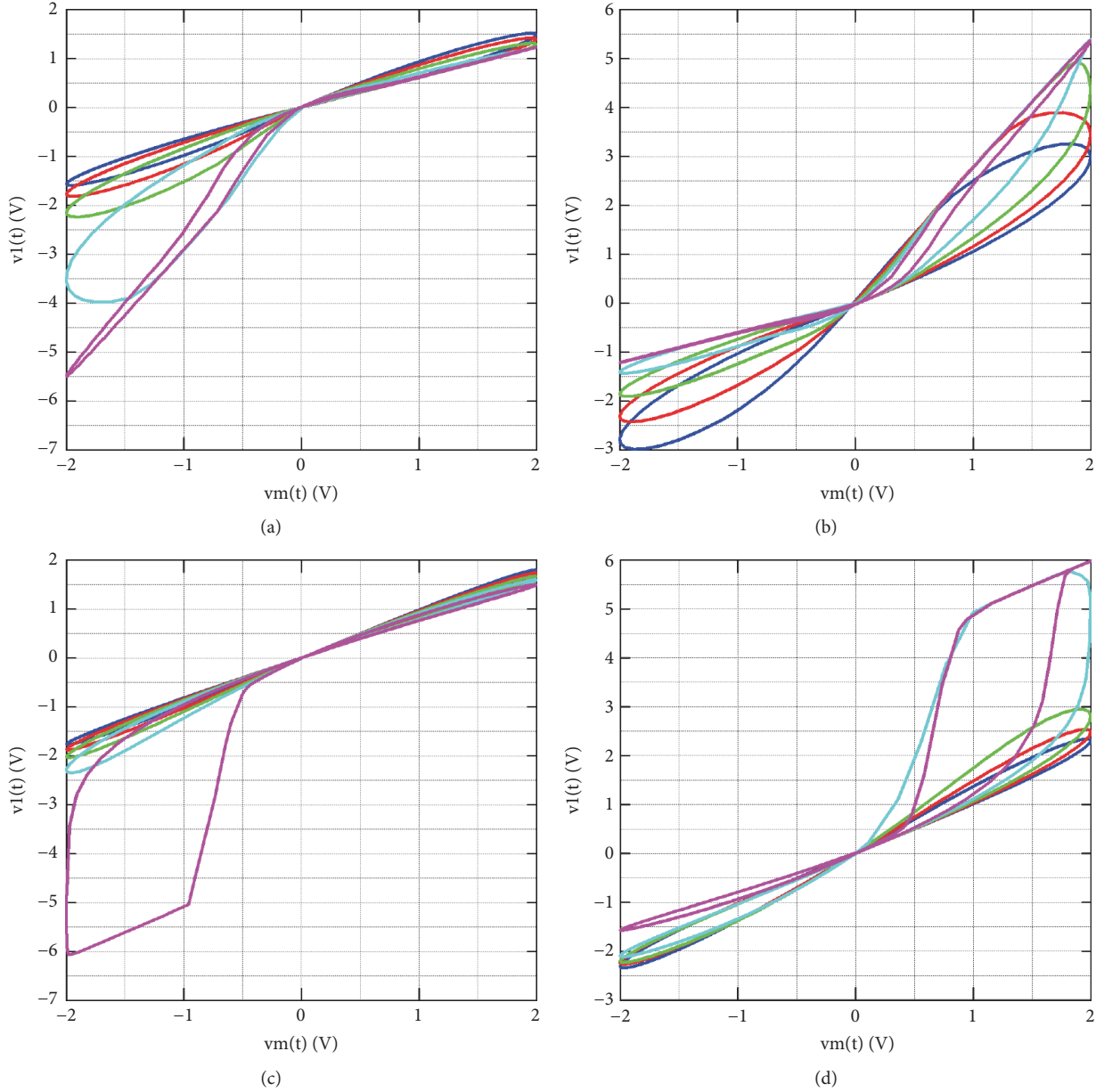


FIGURE 6: Fractional-order frequency-dependent pinched hysteresis loops of the floating fracmemristor operating at (a) incremental mode and (b) decremental mode. For the grounded fracmemristor operating at (c) incremental mode and (d) decremental mode. For all cases: $\alpha = 0.99$ (light blue line), $\alpha = 0.75$ (light red line), $\alpha = 0.5$ (light green line), $\alpha = 0.25$ (light cyan line), and $\alpha = 1$ m (light magenta line).

be lost with a small variation of α . It is worth noting that, unlike [15, 18], the behavior of each frequency-dependent pinched hysteresis loop and at each operation mode has been improved, achieving that, after the offset compensation, all they are operating to 20 kHz and the lobe area of each hysteresis loop becomes relatively equal, obtaining frequency-dependent pinched hysteresis loops almost symmetrical. Furthermore, the real behavior of Figures 4(a) and 4(b) in their integer-order versions was experimentally verified in [15, 18] and Figure 5 shows similar behaviors.

Once obtained the hysteresis loops of the floating and grounded fracmemristor in both operation modes and for $\alpha = 0.99$, we can now reduce α in order to obtain the

behavior of each fractional-order frequency-dependent pinched hysteresis loop. Figure 6(a) shows the hysteresis loops of Figure 4(a) at incremental mode and for five numerical values of α , whereas Figure 6(b) illustrates the fractional hysteresis loops of Figure 4(a) at decremental mode. In both figures, note that, when $\alpha = 1$ m, the hysteresis loops are seriously deformed and as a consequence, the emulator circuits do not work. This behavior is due to that the FOI becomes a voltage follower, as shown in Figure 2(e) (light green line). Moreover, Figures 6(c) and 6(d) show the fractional hysteresis loops of Figure 4(b) configured at incremental and decremental mode, respectively. On these last figures, we note that when α takes different values, the

TABLE 3: Component list of Figure 1 when α varies, assuming $C = 0.1$ mF and $kf = 50$ e3.

Element	$\alpha = 0.99$	$\alpha = 0.75$	$\alpha = 0.5$	$\alpha = 0.25$	$\alpha = 1$ m
C^{-1}			10 k Ω		
$R_f = (BC)^{-1}$			2 M Ω		
BC/kf	10 pF	0.28 nF	0.66 nF	1.2 nF	2 nF
C/kf			2 nF		

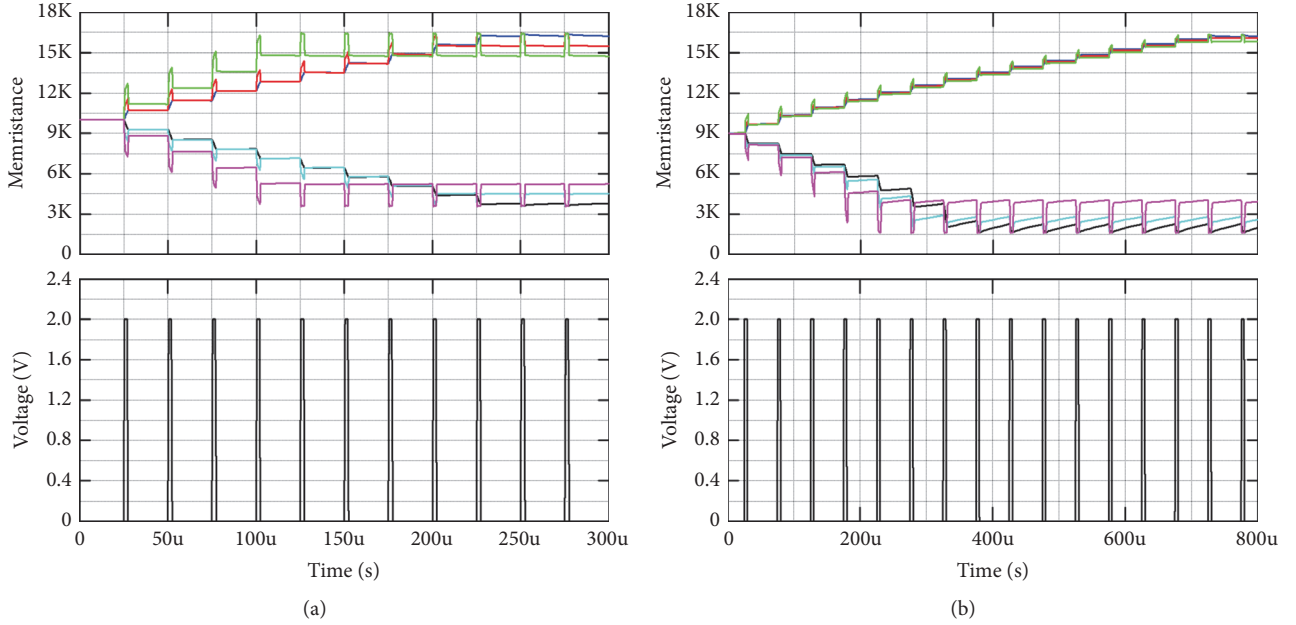


FIGURE 7: Incremental and decremental fracmemristance variation when a pulse train (bottom graphics) is applied to (a) Figure 4(a) and (b) Figure 4(b). For the incremental case: $\alpha = 0.99$ (light blue line), $\alpha = 0.75$ (light red line), and $\alpha = 0.5$ (light green line). For the decremental case: $\alpha = 0.99$ (black line), $\alpha = 0.75$ (light cyan line), and $\alpha = 0.5$ (light magenta line).

range of variation of the hysteresis loops is shorter than Figures 6(a) and 6(b). Similarly as above, when $\alpha = 1$ m, the emulator circuit does not work. For all graphics of Figures 5 and 6, $v_1(t) = i_m(t)R_1$ was used to indirectly plot $i_m(t)$. At this point, our results indicate that, by selecting adequately the numerical value of each element of Figures 4(a) and 4(b) for a particular operating frequency, both emulator circuits are able to generate fractional hysteresis loops. Table 3 gives the numerical value of each element of Figure 1 for different values of α . However, comparing the linear time-varying parts of (6) and (8) we note that the former has four design variables and the latter only two, limiting the performance range of the emulator circuit when α varies and as a consequence, Figure 4(a) has better performance, as shown in Figure 6. It is worth stressing that our results are confirming the theory given in [10]. Besides the fractional pinched hysteresis loops, other fingerprint of the fracmemristor is when the pinched hysteresis loop shrinks when increasing the excitation frequency and although herein is not shown, each fracmemristor behaves as a time-invariant resistor. Moreover, it is interesting to research other fingerprints related to the fracmemristance, which is the nonvolatility of its fracmemristance. This means that once the fracmemristance is programmed, its last value must be *frozen* during a long time and when the input

signal is not applied. Therefore, for Figure 4(a) configured at incremental and decremental mode, a pulse train with 2 V of amplitude, 1.36 μ s of pulse width, and 25 μ s of period is applied and as illustrated in Figure 7(a) (top graphics), one obtains the incremental fracmemristance change for $\alpha = 0.99$ (light blue line), $\alpha = 0.75$ (light red line), and $\alpha = 0.5$ (light green line), whereas the decremental fracmemristance changes for the same values of α are also obtained and given by black line, light cyan line, and light magenta line, respectively. A similar analysis is done for Figure 4(b) also configured at incremental and decremental mode but with a pulse train of 2 V of amplitude, 4 μ s of pulse width, and 50 μ s of period. In this way, Figure 7(b) (top graphics) shows the incremental and decremental fracmemristance change for the same values of α and labeled with the same kind of lines described before. Note that, for all graphics, during nonpulse period the fracmemristance is nonvolatile and its variation is negligible. However, an overshoot signal is glimpsed for all fracmemristances and it is due to the behavior of the FOI. Nonetheless, after of the overshoot, each fracmemristance for each α is held up. Furthermore, when α is near to 1, not only the fracmemristances are similar to the memristances and hence, the maximum (17 k Ω for Figure 7(a) and 16 k Ω for Figure 7(b)) and minimum (4 k Ω for Figure 7(a) and 1.64 k Ω for Figure 7(b)) fracmemristance are obtained, but the range

of variation of the former should monotonically be reduced when α decreases and as a consequence, the maximum and minimum fracmemristance are also reduced, as shown in Figure 7. It is worth stressing that the proposed synthesis methodology is only applicable for those integer-order memristor topologies where the IOI circuit is clearly defined, and when it is replaced by FOI circuit, the resulting emulator circuit behavior, in general, is lightly modified.

5. Conclusions

A synthesis methodology for obtaining the behavior of FOM emulator circuits from integer-order memristor emulator circuits at their versions floating and grounded and operating at incremental and decremental mode has been described. Basically, the methodology consists of exchanging the IOI circuit clearly defined in the integer-order memristor emulator circuit by an FOI circuit, so that not only an FOM is obtained, but also the synthesized topology is not drastically modified with respect to its original topology. In each fractional topology, a mechanism of offset compensation in order to push or pull the crossing point of the hysteresis loops towards the origin was used [25] and as a consequence, both fracmemristors are able to operate at high-frequency. However, it is important to mention that, at high-frequency, not only parasitic elements associated with the active devices affect the performance of the emulators, but also the parasitic elements associated with the breadboard or printed circuit board. Therefore, there is a limit on the operating frequency of the emulators, as has already been reported in [16, 17, 26]. It has numerically been demonstrated that the fractional-order frequency-dependent pinched hysteresis loops are reduced when α decreases, but each hysteresis loop becomes a straight line whether the operating frequency of the signal source also increases. Furthermore, nonvolatility tests were also shown and one can observe in Figure 7 that the range of variation of each incremental and decremental fracmemristance is reduced when α decreases. Finally, it is worth remarking that to the best knowledge of the authors, solid-state FOMs have not been still fabricated and therefore, not only the use of emulator circuits is necessary for researching and improving future real applications [27, 28], but also FOM emulator circuits have not been reported in the literature, until today.

Data Availability

Experimental and simulation data along with source files can be obtained through a letter sent to first author, explaining their intended use.

Conflicts of Interest

The authors declare that they have no conflicts of interest.

Acknowledgments

This work was supported in part by the Proyecto Apoyado por el Fondo Sectorial de Investigación para la Educación of the National Council for Science and Technology (CONACYT),

Mexico, under Grant 222843; in part by the Universidad Autónoma de Tlaxcala (UATx), Tlaxcala de Xicohtencatl, TL, Mexico, under Grant CACyPI-UATx-2017; and in part by the Program to Strengthen Quality in Educational Institutions, under Grant C/PFCE-2016-29MSU0013Y-07-23.

References

- [1] J. Vlach and K. Singhal, *Computer Methods for Circuit Analysis and Design*, Kluwer, Norwell, MA, USA, 1981.
- [2] A. Adamatzky and L. Chua, Eds., *Memristor Networks*, Springer, Switzerland, 2014.
- [3] R. Tetzlaff, *Memristors and Memristive Systems*, Springer, New York, NY, USA, 2014.
- [4] K. B. Oldham and J. Spanier, *The Fractional Calculus: Theory and Applications of Differentiation and Integration to Arbitrary Order*, Academic Press, New York, NY, USA, 1974.
- [5] R. Hilfer, *Applications of Fractional Calculus in Physics*, World Scientific, Singapore, 2001.
- [6] R. Caponetto, G. Dongola, L. Fortuna, and I. Petras, *Fractional Order Systems: Modeling and Control Applications*, World Scientific Publishing, 2010.
- [7] I. Petras, *Fractional-Order Nonlinear Systems: Modeling, Analysis and Simulation*, Springer, Berlin, Germany, 2011.
- [8] F. Padula and A. Visioli, *Advances in Robust Fractional Control*, Springer, New York, NY, USA, 2014.
- [9] M. E. Fouda and A. G. Radwan, "On the fractional-order memristor model," *Journal of Fractional Calculus and Applications*, vol. 4, no. 1, pp. 1–7, 2013.
- [10] J. Tenreiro Machado, "Fractional generalization of memristor and higher order elements," *Communications in Nonlinear Science and Numerical Simulation*, vol. 18, no. 2, pp. 264–275, 2013.
- [11] M.-S. Abdelouahab, R. Lozi, and L. Chua, "Memfractance: A Mathematical Paradigm for Circuit Elements with Memory," *International Journal of Bifurcation and Chaos*, vol. 24, no. 9, Article ID 1430023-1, 2014.
- [12] Y.-F. Pu and X. Yuan, "Fracmemristor: fractional-order memristor," *IEEE Access*, vol. 4, pp. 1872–1888, 2016.
- [13] F. Z. Wang, L. Shi, H. Wu, N. Helian, and L. O. Chua, "Fractional memristor," *Applied Physics Letters*, vol. 111, no. 24, Article ID 243502, 2017.
- [14] S. H. Rashad, E. M. Hamed, M. E. Fouda, A. M. AbdelAty, L. A. Said, and A. G. Radwan, "On the analysis of current-controlled fractional-order memristor emulator," in *Proceedings of the 2017 6th International Conference on Modern Circuits and Systems Technologies (MOCAST)*, pp. 1–4, Thessaloniki, Greece, May 2017.
- [15] C. Sánchez-López, J. Mendoza-López, M. A. Carrasco-Aguilar, and C. Muñoz-Montero, "A floating analog memristor emulator circuit," *IEEE Transactions on Circuits and Systems II: Express Briefs*, vol. 61, no. 5, pp. 309–313, 2014.
- [16] C. Sánchez-López, M. A. Carrasco-Aguilar, and C. Muñoz-Montero, "A 16 Hz-160 kHz memristor emulator circuit," *International Journal of Electronics and Communications*, vol. 61, no. 5, pp. 1–12, 2015.
- [17] C. Sánchez-López and L. E. Aguila-Cuapio, "A 860 kHz grounded memristor emulator circuit," *AEÜ - International Journal of Electronics and Communications*, vol. 73, pp. 23–33, 2017.
- [18] A. S. Elwakil, M. E. Fouda, and A. G. Radwan, "A simple model of double-loop hysteresis behavior in memristive elements,"

- IEEE Transactions on Circuits and Systems II: Express Briefs*, vol. 60, no. 8, pp. 487–491, 2013.
- [19] A. Charef, “Analogue realisation of fractional-order integrator, differentiator and fractional PID μ controller,” *IEE Proceedings—Control Theory and Applications*, vol. 153, no. 6, pp. 714–720, 2006.
 - [20] D. Goyal and P. Varshney, “CCII and RC fractance based fractional order current integrator,” *Microelectronics Journal*, vol. 65, pp. 1–10, 2017.
 - [21] C. Muñoz-Montero, L. V. García-Jiménez, L. A. Sánchez-Gaspariano et al., “New alternatives for analog implementation of fractional-order integrators, differentiators and PID controllers based on integer-order integrators,” *Nonlinear Dynamics*, vol. 90, no. 1, pp. 241–256, 2017.
 - [22] C. Muñoz-Montero, L. A. Sánchez-Gaspariano, C. Sánchez-López et al., “On the electronic realizations of fractional-order phase-lead-lag compensators with OpAmps and FPAAAs,” in *Fractional order control and synchronization of chaotic systems*, A. Azar, S. Vaidyanathan, and A. Ouannas, Eds., vol. 688 of *Stud. Comput. Intell.*, pp. 131–164, Springer, Cham, Switzerland, 2017.
 - [23] J. C. Trigeassou, N. Maamri, J. Sabatier, and A. Oustaloup, “Transients of fractional-order integrator and derivatives,” *Signal, Image and Video Processing*, vol. 6, no. 3, pp. 359–372, 2012.
 - [24] A. G. Radwan, A. M. Soliman, A. S. Elwakil, and A. Sedeek, “On the stability of linear systems with fractional-order elements,” *Chaos, Solitons & Fractals*, vol. 40, no. 5, pp. 2317–2328, 2009.
 - [25] C. Sánchez-López, M. A. Carrasco-Aguilar, and F. E. Morales-López, “Offset reduction on memristor emulator circuits,” in *Proceedings of the IEEE International Conference on Electronics, Circuits, and Systems*, vol. 1, pp. 296–299, December 2015.
 - [26] Sánchez-López, “A 1.7 MHz Chua’s circuit using VMs and CF+s,” *Revista Mexicana de Física*, vol. 58, no. 1, pp. 86–93, 2012.
 - [27] I. Carro-Pérez, H. Gonzalez-Hernandez, and C. Sanchez-Lopez, “High-frequency memristive synapses,” in *Proceedings of the 2017 IEEE 8th Latin American Symposium on Circuits & Systems (LASCAS)*, pp. 1–4, Bariloche, Argentina, February 2017.
 - [28] I. Carro-Pérez, C. Sánchez-López, and H. G. González-Hernández, “Experimental verification of a memristive neural network,” *Nonlinear Dynamics*, pp. 1–18, 2018.

Research Article

Memristor-Based Canonical Chua's Circuit: Extreme Multistability in Voltage-Current Domain and Its Controllability in Flux-Charge Domain

Han Bao, Tao Jiang, Kaibin Chu, Mo Chen, Quan Xu, and Bocheng Bao 

School of Information Science and Engineering, Changzhou University, Changzhou 213164, China

Correspondence should be addressed to Bocheng Bao; mervinbao@126.com

Received 16 December 2017; Accepted 17 January 2018; Published 25 March 2018

Academic Editor: Viet-Thanh Pham

Copyright © 2018 Han Bao et al. This is an open access article distributed under the Creative Commons Attribution License, which permits unrestricted use, distribution, and reproduction in any medium, provided the original work is properly cited.

This paper investigates extreme multistability and its controllability for an ideal voltage-controlled memristor emulator-based canonical Chua's circuit. With the voltage-current model, the initial condition-dependent extreme multistability is explored through analyzing the stability distribution of line equilibrium point and then the coexisting infinitely many attractors are numerically uncovered in such a memristive circuit by the attraction basin and phase portraits. Furthermore, based on the accurate constitutive relation of the memristor emulator, a set of incremental flux-charge describing equations for the memristor-based canonical Chua's circuit are formulated and a dimensionality reduction model is thus established. As a result, the initial condition-dependent dynamics in the voltage-current domain is converted into the system parameter-associated dynamics in the flux-charge domain, which is confirmed by numerical simulations and circuit simulations. Therefore, a controllable strategy for extreme multistability can be expediently implemented, which is greatly significant for seeking chaos-based engineering applications of multistable memristive circuits.

1. Introduction

Initial condition-dependent extreme multistability, first encountered in several coupled nonlinear dynamical systems [1–3], is a coexisting phenomenon of infinitely many attractors for a given set of system parameters. More recently, due to the existence of infinitely many equilibrium points, for example, line equilibrium point or plane equilibrium point, this special dynamical phenomenon of extreme multistability is naturally exhibited in a class of ideal flux/voltage-controlled memristor-based chaotic circuits/systems [4–9], thereby leading to the emergence of infinitely many disconnected attractors.

Extreme multistability is a fantastic kind of multistability, which makes a nonlinear dynamical circuit or system supply great flexibility for its potential uses in chaos-based engineering applications [10–12], but also raises new challenges for its control of the existing multiple stable states [11–14]. Generally, multistability is confirmed in hardware experiments

by randomly switching on and off experimental circuit supplies [9, 15–21] or by MATLAB numerical or PSPICE/PSIM circuit simulations [4–8, 22–28]. Consequently, to direct the nonlinear dynamical circuit or system to a desired oscillating mode, an effective control approach should be proposed [12]. To this end, this paper takes an ideal voltage-controlled memristor emulator-based canonical Chua's circuit as an example; a controllable strategy for extreme multistability is achieved through converting the initial condition-dependent dynamics in the voltage-current domain into the system parameter-associated dynamics in the flux-charge domain [29, 30].

Besides, for a memristor-based circuit or system with line equilibrium point or plane equilibrium point, its stability at the equilibrium point is very difficult to be determined due to the existence of one or two zero eigenvalues [5–9], which results in the fact that the coexisting infinitely many attractors' behaviors can not be precisely interpreted from the stabilities of the nonzero eigenvalues. As a matter of fact,

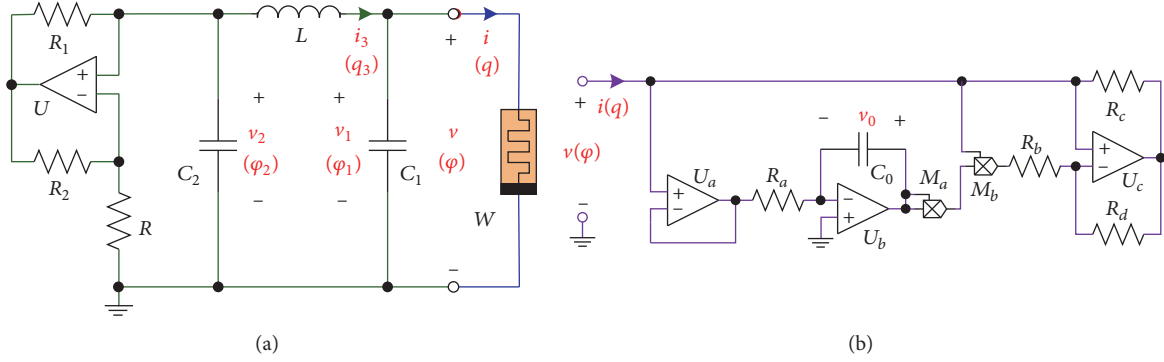


FIGURE 1: Memristor-based canonical Chua's circuit. (a) Circuit schematic with simple topology. (b) Ideal voltage-controlled memristor emulator implemented with discrete components.

the memristor initial condition and other initial conditions all have dynamical effects on the memristor-based circuit or system [8, 9]. However, the dynamical effects are implied, which can not be explicitly expressed in the voltage-current domain. How about the memristor-based circuit or system in the flux-charge domain?

Flux-charge analysis method was first postulated as a tool of dimensionality reduction [31–36], in which the initial conditions of the memristor-based circuit or system are not precisely formulated, thereby leading to the absence of the initial condition-dependent dynamical behaviors [34–36]. In the last two years, a new flux-charge analysis method is reported in [29, 30], which judiciously utilizes the incremental flux and charge to substitute the conventional flux and charge and efficaciously solves the issue of the original flux-charge analysis method. Accordingly, based on the voltage-current relation, an accurate flux-charge relation of the ideal voltage-controlled memristor emulator is established. With the accurate constitutive relation, an incremental flux-charge model for the memristor-based canonical Chua's circuit is constructed, upon which all the initial conditions in the voltage-current model can be explicitly formulated by the system parameters in the flux-charge model and the multiple stable states can be consequently controlled by changing the initial condition-related system parameters.

The rest of the paper is structured as follows. In Section 2, an ideal voltage-controlled memristor emulator-based canonical Chua's circuit is presented. With the voltage-current model, the initial condition-dependent extreme multistability is explored and then the coexisting infinitely many attractors are numerically uncovered. In Section 3, based on the accurate constitutive relation of the memristor emulator, a set of incremental flux-charge equations for the memristor-based canonical Chua's circuit are formulated and a dimensionality reduction model is thus established, upon which the feasibility of the flux-charge analysis method is verified by MATLAB numerical simulations. In Section 4, an equivalent circuit of the incremental flux-charge model is designed and circuit simulations for the initial condition-dependent behaviors are executed, from which the controllability of extreme multistability is physically confirmed. The conclusions are drawn in the last section.

TABLE 1: Circuit parameters of memristor-based canonical Chua's circuit.

Parameters	Significations	Values
C_0	Capacitance	1 nF
C_1	Capacitance	4.7 nF
C_2	Capacitance	33 nF
L_1	Inductor	30 mH
g	Total gain	0.2 V^{-2}
R_a	Resistance	4 k Ω
R_b	Resistance	1.5 k Ω
R_c, R_d	Resistance	2 k Ω
R	Resistance	1.5 k Ω
R_1, R_2	Resistance	2 k Ω

2. Extreme Multistability in the Voltage-Current Domain

Based on a canonical Chua's circuit and an ideal voltage-controlled memristor emulator, a new memristor-based canonical Chua's circuit is constructed, as shown in Figure 1(a), which is simple and physically realizable. The ideal voltage-controlled memristor emulator is equivalently implemented with an electronic circuit via op-amp integrators and analog multipliers [5, 6, 34], as shown in Figure 1(b). In our next work, the considered circuit parameters remained unchanged and are listed in Table 1, where g is the total gain of two multipliers M_a and M_b .

2.1. Conventional Voltage-Current Model. For the ideal voltage-controlled memristor emulator in Figure 1(b), the relationships of the input voltage v , the input current i , and the voltage v_0 of the capacitor C_0 can be mathematically described in the voltage-current domain as

$$C_0 \frac{dv_0}{dt} = -\frac{1}{R_a} v, \quad (1)$$

$$i = W(v_0) v = -\frac{1}{R_b} (1 - g v_0^2) v.$$

Thus, for the state variables of v_0 , v_1 , v_2 , and i_3 in Figure 1, the describing circuit equations are easily given in the voltage-current domain as

$$\begin{aligned} C_0 \frac{dv_0}{dt} &= -\frac{1}{R_a} v_1, \\ C_1 \frac{dv_1}{dt} &= \frac{1}{R_b} (1 - g v_0^2) v_1 + i_3, \\ C_2 \frac{dv_2}{dt} &= \frac{v_2}{R} - i_3, \\ L \frac{di_3}{dt} &= v_2 - v_1, \end{aligned} \quad (2)$$

where $v = v_1$.

Introduce four new state variables and scale the circuit parameters as

$$\begin{aligned} x_1 &= v_0, \\ x_2 &= v_1, \\ x_3 &= v_2, \\ x_4 &= R i_3, \\ \tau &= \frac{t}{RC_2}, \\ R_b &= R, \\ a &= \frac{RC_2}{R_a C_0}, \\ b &= \frac{C_2}{C_1}, \\ c &= \frac{R^2 C_2}{L}. \end{aligned} \quad (3)$$

Model (2) can be reexpressed as

$$\begin{aligned} \dot{x}_1 &= -a x_2, \\ \dot{x}_2 &= b (1 - g x_1^2) x_2 + b x_4, \\ \dot{x}_3 &= x_3 - x_4, \\ \dot{x}_4 &= c (x_3 - x_2), \end{aligned} \quad (4)$$

which indicates that there are only four parameters in the normalized system model.

With the circuit parameters in Table 1, the normalized parameters for model (4) are obtained by (3) as

$$\begin{aligned} a &= 12.375, \\ b &= 7.0213, \\ c &= 2.475, \\ g &= 0.2. \end{aligned} \quad (5)$$

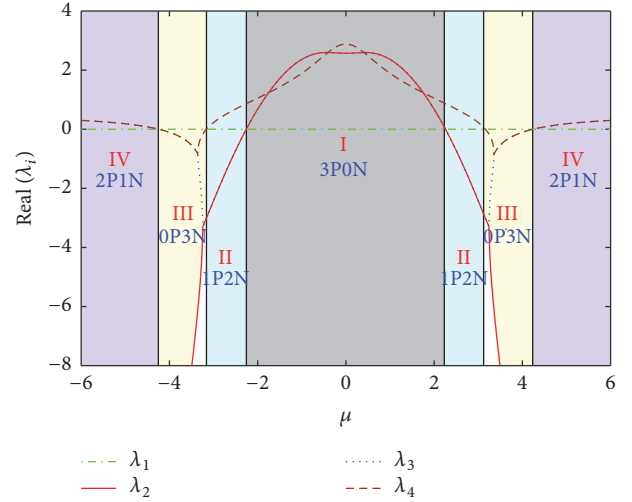


FIGURE 2: Stability distributions classified by the real parts of three nonzero eigenvalues of the line equilibrium point P in the region of $-6 \leq \mu \leq 6$, where $i = 1, 2, 3, 4$.

In the following works, the memristor-based canonical Chua's circuit modeled by (4) and the typical system parameters given by (5) are utilized.

2.2. Stability Distribution of Line Equilibrium Point. Similar to the memristive Chua's circuit containing an ideal voltage-controlled memristor emulator [5, 6], the memristor-based canonical Chua's circuit has a line equilibrium point, which is expressed by

$$P = \{(x_1, x_2, x_3, x_4) \mid x_2 = x_3 = x_4 = 0, x_1 = \mu\}, \quad (6)$$

where the constant μ is uncertain.

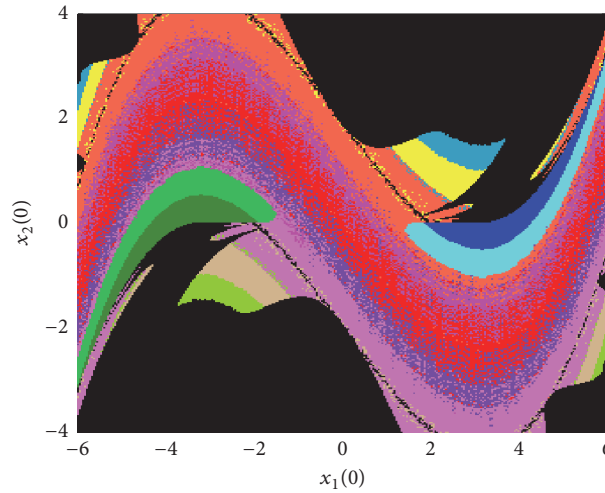
At the line equilibrium point P , the Jacobian matrix is given as

$$J_P = \begin{bmatrix} 0 & -a & 0 & 0 \\ 0 & b(1 - g\mu^2) & 0 & b \\ 0 & 0 & 1 & -1 \\ 0 & -c & c & 0 \end{bmatrix}. \quad (7)$$

For the Jacobian matrix given in (7), the normalized parameters determined in (5), and the constant μ that increased in the region $[-6, 6]$, four eigenvalues with a zero root, a real root, and a pair of conjugated complex roots can be calculated by MATLAB numerical simulations. The real parts of these four eigenvalues are drawn in Figure 2, which can be used to classify the stability distributions. It can be seen from Figure 2 that the sign of the real parts of three nonzero eigenvalues varies with the increase of μ , leading to the occurrence of three kinds of unstable regions marked with I, II, and IV and a kind of stable region marked with III. Additionally, it can also be observed that the stability distributions of the nonzero eigenvalues in the negative region of μ are symmetrical to those in the positive region of μ .

TABLE 2: Nonzero eigenvalues and attractor types for different memristor initial conditions.

$x_1(0)$	Nonzero eigenvalues	Stability regions	Attractor types
0	$2.8804, 2.5704 \pm j2.3364$ (Unstable node-foci)	Region I: 3P0N	Double-scroll chaotic attractor
2	$1.0514, 0.6765 \pm j4.4019$ (Unstable node-foci)	Region I: 3P0N	Infinite
2.4	$0.7591, -0.4132 \pm j4.3865$ (Unstable saddle-foci)	Region II: 1P2N	Chaotic spiral attractor
3.2	$-3.1446 \pm j1.4734, -0.0692$ (Stable node-foci)	Region III: 0P3N	Stable point attractor
4.3	$0.0203 \pm j1.2808, -17.9841$ (Unstable saddle-foci)	Region VI: 2P1N	Stable point attractor
4.5	$0.0800 \pm j1.3134, -20.5750$ (Unstable saddle-foci)	Region VI: 2P1N	Limit cycle with period 1
4.8	$0.1486 \pm j1.3483, -24.6301$ (Unstable saddle-foci)	Region VI: 2P1N	Asymmetric double-scroll chaotic attractor

FIGURE 3: Attraction basin in the $x_1(0)$ - $x_2(0)$ plane, where $a = 12.375$, $b = 7.0213$, $c = 2.475$, $g = 0.2$, and $x_3(0) = x_4(0) = 0$.

Due to the existence of the zero eigenvalue, the stability of the memristor-based canonical Chua's circuit can not be simply determined by the three nonzero eigenvalues of the line equilibrium point. The following numerical simulations demonstrate that the zero eigenvalue also has influence on the dynamics of the circuit under some circuit parameters [6–9].

The initial conditions for numerical simulations of the coexisting attractors' behaviors are taken as $[x_1(0), 10^{-9}, 0, 0]$; that is, only the memristor initial condition $x(0)$ is variable. For some different values of the memristor initial condition $x_1(0)$, nonzero eigenvalues, stability regions given in Figure 2, and the related attractor types numerically solved by (4) are summarized in Table 2. It is demonstrated that, for the different values of $x_1(0)$ located in different stability regions, there exist various attractor types with different topologies or different periodicities or different locations. Consequently, coexisting infinitely many attractors' behavior

or extreme multistability occurs in the memristor-based canonical Chua's circuit.

2.3. Coexisting Infinitely Many Attractors. With reference to the stability distributions in Figure 2 and the initial condition-dependent attractor types in Table 2, the proposed memristor-based canonical Chua's circuit has various stable states under different initial conditions; that is, its long-term behavior closely relies on the initial conditions therefore leading to the emergence of coexisting infinitely many attractors.

For the normalized parameters in (5) and the initial conditions of $x_3(0) = 0$ and $x_4(0) = 0$, the attraction basin in the plane of the initial conditions of $x_1(0)$ and $x_2(0)$ is depicted in Figure 3. It should be illustrated that many more diverse attractor types for different initial conditions can be certainly observed in the memristor-based canonical Chua's circuit; however, for visual effects, only fourteen kinds

TABLE 3: Different color regions and the corresponding attractor types.

Colors	Coexisting attractor types	Examples in Figure 4
Blue and forest green	Right- and left-point attractors	Figure 4(a)
Cyan and lime green	Right- and left-period-1 limit cycles with small size	Figure 4(b)
Cadet blue and lawn green	Left- and right-period-1 limit cycles with large size	Figure 4(c)
Tan and yellow	Left- and right-multi-period limit cycles	Figure 4(d)
Orchid and coral	Left- and right-chaotic spiral attractors	Figure 4(e)
Medium slate blue and fuchsia	Left- and right-half-baked double-scroll chaotic attractors	Figure 4(f)
Red	Standard double-scroll chaotic attractor	Figure 4(g)
Black	Unbounded orbit	Figure 4(h)

of color areas are classified by the basin of attraction in the $x_1(0)$ - $x_2(0)$ plane, among which the largest black area represents the unbounded zone.

Corresponding to different color areas, different types of coexisting attractors are listed in Table 3. Spontaneously, for the initial conditions in the different color areas of the attraction basin, the phase portraits of typical coexisting attractors are obtained, as shown in Figure 4, where for the sake of observations two point attractors in Figure 4(a) are marked by two five-pointed stars. Of course, these generated coexisting attractors intersect the neighborhood of the line equilibrium point, implying that the initials-dependent dynamical system (4) [37] always oscillates in self-excited states, rather than hidden states [38–40].

It should be mentioned that just like the ideal flux/voltage-controlled memristor-based chaotic circuits [4–9], the proposed memristor-based canonical Chua's circuit has a line equilibrium point with complicated stability distributions already depicted in Figures 2–4, whereas most of conventionally nonlinear dynamical systems with no equilibrium point [10], with only several determined equilibrium points [15–21], or with curves of equilibrium points [41–43] have relatively simple stability distributions with some divivable nonlinear dynamical behaviors.

3. Controllability of Extreme Multistability in the Flux-Charge Domain

Due to the existence of the line equilibrium point, the memristor-based canonical Chua's circuit can exhibit the special phenomenon of extreme multistability under different initial conditions. For seeking the potential uses of the multistable memristive circuit in chaos-based engineering applications [10–12], an effective control method should be applied to direct the memristive circuit to the desired oscillation mode [12]. For this purpose, an incremental flux-charge model is newly constructed, in which the initial condition-dependent dynamics in the voltage-current domain is converted into the system parameter-associated dynamics in the flux-charge domain.

3.1. Newly Constructed Incremental Flux-Charge Model. The accurate constitutive relation of the ideal voltage-controlled memristor emulator in Figure 1(b) should be firstly

established in the flux-charge domain. Define $q(t; 0)$ and $\varphi(t; 0)$ as the incremental charge and incremental flux of the ideal memristor emulator, respectively. According to (1), the incremental charge within the time interval $[0, t]$ is deduced as

$$\begin{aligned}
 q(t; 0) &= \int_0^t i \, d\tau = \int_0^t -\frac{1}{R_b} (1 - g v_0^2) v_1 \, d\xi \\
 &= \frac{1}{R_b} \int_0^t (1 - g v_0^2) R_a C_0 \, dv_0 \\
 &= \frac{1}{\kappa R_b} [v_0(t) - v_0(0)] - \frac{g}{3\kappa R_b} [v_0^3(t) - v_0^3(0)] \quad (8) \\
 &= \frac{g\kappa^2}{3R_b} [\varphi(t; 0)]^3 - \frac{g\kappa}{R_b} v_0(0) [\varphi(t; 0)]^2 \\
 &\quad + \frac{1}{R_b} [g v_0^2(0) - 1] \varphi(t; 0),
 \end{aligned}$$

where $\kappa = 1/(R_a C_0)$, $v_0(0)$ stands for the memristor initial state, and the memristor inner state variable $v_0(t) = -\kappa\varphi(t; 0) + v_0(0)$. Thus, the initial state $v_0(0)$ can be explicitly represented in the flux-charge domain.

Suppose that $\varphi_1(t; 0)$, $\varphi_2(t; 0)$, and $q_3(t; 0)$ are the incremental fluxes of the capacitors C_1 and C_2 and the incremental charge of the inductor L , respectively, and set $v_1(0)$, $v_2(0)$, and $i_3(0)$ as the initial voltages of the capacitors C_1 and C_2 and the initial current of the inductor L , respectively. While connecting the power supply at $t = 0$, the incremental flux-charge model of the memristor-based canonical Chua's circuit can be yielded by integrating (2) from 0 to t .

Integrating the second, third, and fourth equations of (2) from 0 to t gives

$$\begin{aligned}
 C_1 [v_1(t) - v_1(0)] &= -q(t; 0) + q_3(t; 0), \\
 C_2 [v_2(t) - v_2(0)] &= \frac{1}{R} \varphi_2(t; 0) - q_3(t; 0), \quad (9) \\
 L [i_3(t) - i_3(0)] &= \varphi_2(t; 0) - \varphi_1(t; 0).
 \end{aligned}$$

Consider the fact that the fluxes $\varphi_1(t)$ and $\varphi_2(t)$ of the capacitors C_1 and C_2 and the charge $q_3(t)$ of the inductor L can be expressed as

$$\varphi_1(t) = \int_{-\infty}^t v_1(\xi) \, d\xi = \varphi_1(t; 0) + K_1,$$

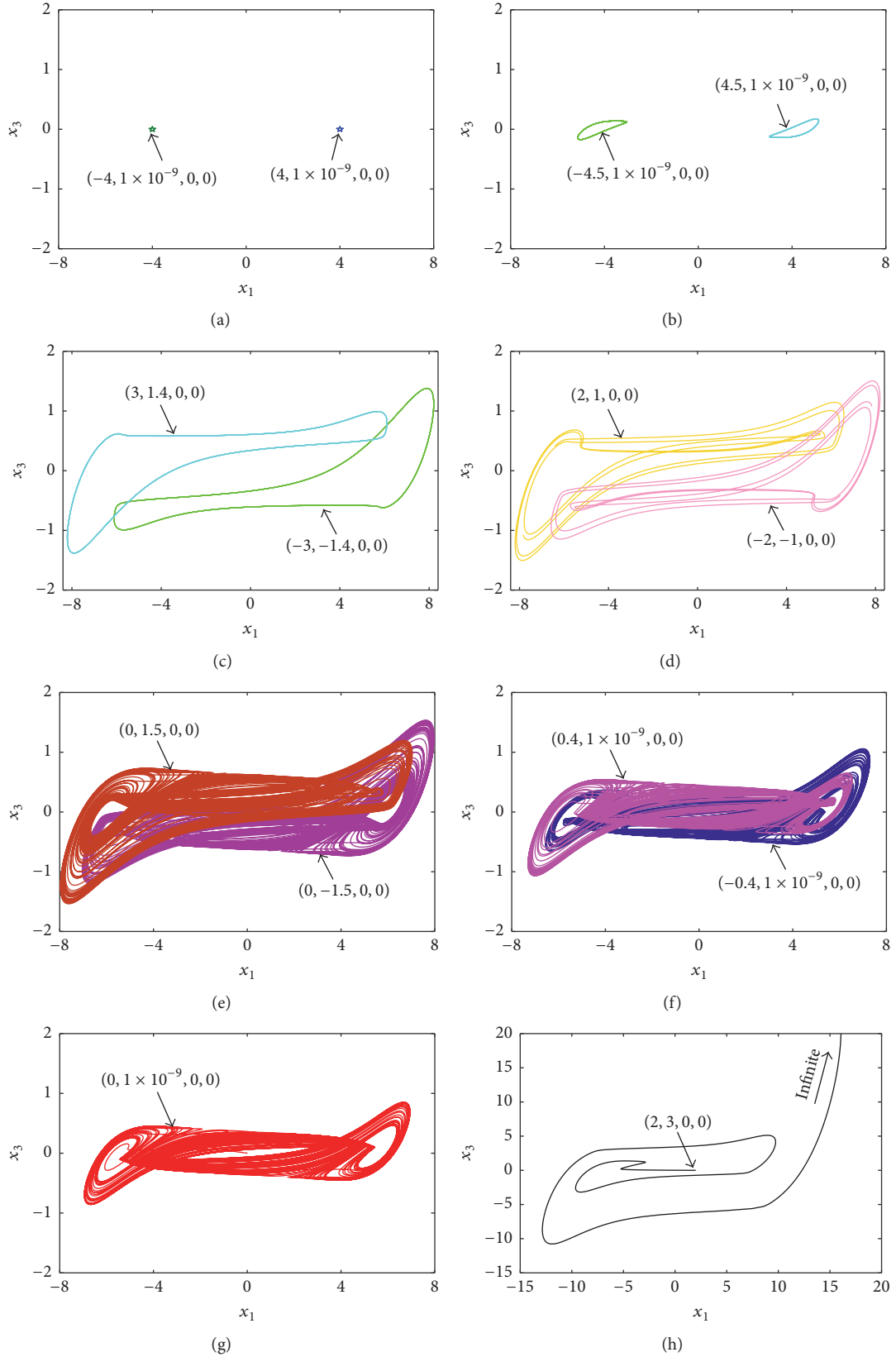


FIGURE 4: Phase portraits of coexisting infinitely many attractors in the x_1 - x_3 plane for different values of $x_1(0)$ and $x_2(0)$. (a) Right- and left-point attractors. (b) Right- and left-period-1 limit cycles with small size. (c) Left- and right-period-1 limit cycles with large size. (d) Left- and right-multiperiod limit cycles. (e) Left- and right-chaotic spiral attractors. (f) Left- and right-half-baked double-scroll chaotic attractors. (g) Standard double-scroll chaotic attractor. (h) Unbounded orbit.

$$\begin{aligned}\varphi_2(t) &= \int_{-\infty}^t v_2(\xi) d\xi = \varphi_2(t; 0) + K_2, \\ q_3(t) &= \int_{-\infty}^t i_3(\xi) d\xi = q_3(t; 0) + K_3,\end{aligned}\quad (10)$$

respectively, where $K_1 = \int_{-\infty}^0 v_1(\xi) d\xi$, $K_2 = \int_{-\infty}^0 v_2(\xi) d\xi$, and $K_3 = \int_{-\infty}^0 i_3(\xi) d\xi$ represent three arbitrary real constants. Therefore, the state variables $v_1(t)$, $v_2(t)$, and $i_3(t)$ in the voltage-current domain can be signified as

$$\begin{aligned}v_1(t) &= \frac{d\varphi_1(t)}{dt} = \frac{d\varphi_1(t; 0)}{dt}, \\ v_2(t) &= \frac{d\varphi_2(t)}{dt} = \frac{d\varphi_2(t; 0)}{dt}, \\ i_3(t) &= \frac{dq_3(t)}{dt} = \frac{dq_3(t; 0)}{dt}.\end{aligned}\quad (11)$$

Substituting (11) into (9), the circuit equations of Figure 1 can be thereby modeled in the flux-charge domain as

$$\begin{aligned}C_1 \frac{d\varphi_1(t; 0)}{dt} &= -q(t; 0) + q_3(t; 0) + C_1 v_1(0), \\ C_2 \frac{d\varphi_2(t; 0)}{dt} &= \frac{1}{R} \varphi_2(t; 0) - q_3(t; 0) + C_2 v_2(0), \\ L \frac{dq_3(t; 0)}{dt} &= \varphi_2(t; 0) - \varphi_1(t; 0) + Li_3(0).\end{aligned}\quad (12)$$

Equation (12) is the incremental flux-charge model of the proposed memristor-based canonical Chua's circuit.

Analogously, introduce three new state variables and scale the circuit parameters as

$$\begin{aligned}y_1 &= \frac{\varphi_1(t; 0)}{RC_2}, \\ y_2 &= \frac{\varphi_2(t; 0)}{RC_2}, \\ y_3 &= \frac{q_3(t; 0)}{C_2}, \\ \tau &= \frac{t}{RC_2}, \\ R_b &= R, \\ a &= \frac{RC_2}{R_a C_0}, \\ b &= \frac{C_2}{C_1}, \\ c &= \frac{R^2 C_2}{L}, \\ \eta &= v_0(0), \\ \eta_1 &= v_1(0),\end{aligned}$$

$$\eta_2 = v_2(0),$$

$$\eta_3 = Ri_3(0).$$

(13)

Model (12) can be rewritten as

$$\begin{aligned}\dot{y}_1 &= -bF(y_1) + by_3 + \eta_1, \\ \dot{y}_2 &= y_2 - y_3 + \eta_2, \\ \dot{y}_3 &= c(y_2 - y_1) + \eta_3,\end{aligned}\quad (14)$$

where the normalized memristor constitutive relation is turned as $F(y_1) = (1/3)ga^2y_1^3 - ga\eta y_1^2 + (g\eta^2 - 1)y_1$.

It should be emphasized that the initial conditions of (14) are ensured as $y_1(0) = y_2(0) = y_3(0) = 0$. The memristor inner parameter η denotes the initial capacitor voltage of the memristor emulator in the voltage-current domain, and the system parameters η_1 , η_2 , and η_3 reflect the three initial voltages of the canonical Chua's circuit in the voltage-current domain.

For the circuit parameters given in Table 1, the normalized parameters a , b , c , and g in (14) are the same as those given in (5). With these determined parameters, the initial conditions-dependent extreme multistability in the memristor-based canonical Chua's circuit can be effectively controlled by adjusting the system parameters η , η_1 , η_2 , and η_3 .

3.2. System Parameter-Related Stability Distribution. For the normalized model (14), the equilibrium points are obviously obtained as

$$E = \left(\bar{y}_1, \bar{y}_1 - \frac{1}{c}\eta_3, \bar{y}_1 + \eta_2 - \frac{1}{c}\eta_3 \right), \quad (15)$$

in which \bar{y}_1 can be numerically solved by

$$\begin{aligned}\bar{y}_1^3 - \frac{3\eta}{a}\bar{y}_1^2 + \frac{3}{ga^2}(g\eta^2 - 2)\bar{y}_1 \\ - \frac{3c\eta_1 + 3bc\eta_2 - 3b\eta_3}{ga^2bc} = 0.\end{aligned}\quad (16)$$

Define P and Q to be

$$\begin{aligned}P &= \frac{3}{ga^2}(g\eta^2 - 2) - \frac{3\eta^2}{a^2} = -\frac{6}{ga^2}, \\ Q &= \frac{\eta^3}{a^3} - \frac{6\eta}{ga^3} - \frac{3c\eta_1 + 3bc\eta_2 - 3b\eta_3}{ga^2bc}.\end{aligned}\quad (17)$$

According to the classical Cardan discriminant $\Delta = (Q/2)^2 + (P/3)^3$, when $\Delta < 0$, there are three real roots in (16), which can be given as

$$\bar{y}_{1,1} = \sqrt[3]{-\frac{Q}{2} + \sqrt{\Delta}} + \sqrt[3]{-\frac{Q}{2} - \sqrt{\Delta}} + \frac{\eta}{a},$$

$$\begin{aligned}
\bar{y}_{1,2} &= -\frac{1-j\sqrt{3}}{2} \sqrt[3]{-\frac{Q}{2} + \sqrt{\Delta}} - \frac{1+j\sqrt{3}}{2} \sqrt[3]{-\frac{Q}{2} - \sqrt{\Delta}} \\
&\quad + \frac{\eta}{a}, \\
\bar{y}_{1,3} &= -\frac{1+j\sqrt{3}}{2} \sqrt[3]{-\frac{Q}{2} + \sqrt{\Delta}} - \frac{1-j\sqrt{3}}{2} \sqrt[3]{-\frac{Q}{2} - \sqrt{\Delta}} \\
&\quad + \frac{\eta}{a},
\end{aligned} \tag{18}$$

indicating that the model (14) has three equilibrium points.

The Jacobian matrix at equilibrium point E is deduced as

$$\mathbf{J}_E = \begin{bmatrix} -bF'(\bar{y}_1) & 0 & b \\ 0 & 1 & -1 \\ -c & c & 0 \end{bmatrix}, \tag{19}$$

where $F'(\bar{y}_1) = ga^2\bar{y}_1^2 - 2ga\eta\bar{y}_1 + g\eta^2 - 1$. Consequently, three eigenvalues of the model (14) at E are yielded by solving the following characteristic polynomial:

$$P(\lambda) = \det(\mathbf{I}\lambda - \mathbf{J}) = \lambda^3 + p_1\lambda^2 + p_2\lambda + p_3 = 0, \tag{20}$$

in which $p_1 = bF'(\bar{y}_1) - 1$, $p_2 = -bF'(\bar{y}_1) + bc + c$, and $p_3 = bcF'(\bar{y}_1) - bc$.

Based on (15)–(20), it can be known that the line equilibrium point described by (6) in the voltage-current domain is converted into several determined equilibrium points represented by (15) in the flux-charge domain, whose locations and stabilities are decided by the initial condition-related system parameters η , η_1 , η_2 , and η_3 . Therefore, the extreme multistability in the voltage-current domain can readily be controlled by the system parameters in the flux-charge domain.

Take $\eta_1 = \eta_2 = \eta_3 = 0$ as an example. When the normalized system parameters a , b , c , and g for the model (14) are fixed as given in (5) and the relationship of $-2\sqrt{10} \leq \eta \leq 2\sqrt{10}$ is satisfied, three equilibrium points consisting of one zero equilibrium point and two nonzero equilibrium points are solved from (16) as

$$\begin{aligned}
E_0 &= (0, 0, 0) \\
E_{\pm} &= \left(\frac{12\eta \pm \rho}{99}, \frac{12\eta \pm \rho}{99}, \frac{12\eta \pm \rho}{99} \right),
\end{aligned} \tag{21}$$

where $\rho = 4\sqrt{120 - 3\eta^2}$, which means that the nonzero equilibrium points depended on the initial condition η of the memristor emulator.

For the zero equilibrium point E_0 , there exist $F'(\bar{y}_1) = g\eta^2 - 1$. In this way, the Jacobian matrix of (19) with the increase of η is identical with the Jacobian submatrix obtained from (7) by deleting row 1 and column 1 with the increase of μ . As a consequence, the Jacobian matrix of (19) has three eigenvalues; their stability distributions are the same as those of the nonzero eigenvalues of the Jacobian matrix

of (7). Whereas for two nonzero equilibrium points E_{\pm} , the complicated stability distributions can be numerically found as the memristor initial condition η is tuned.

3.3. Controllability of Extreme Multistability. With model (14), it is demonstrated that the initial condition-dependent extreme multistability in the memristor-based canonical Chua's circuit is transformed into the system parameter-associated dynamics, therefore leading to the controllability of extreme multistability through directly adjusting the system parameters.

The normalized system parameters a , b , c , and g are given in (5) and the initial conditions for (14) are ensured as $y_1(0) = y_2(0) = y_3(0) = 0$. Referring to the initial conditions in Figure 4, $\eta_2 = 0$ and $\eta_3 = 0$ in (14) remained unchanged, whereas η and η_1 are assigned as some different values in the regions $[-6, 6]$ and $[-4, 4]$, respectively. For different locations of the parameter space constructed by η and η_1 , various types of disconnected attractors are numerically simulated, as shown in Figure 5, where for the sake of observations two point attractors overlapped together in Figure 5(a) are marked by two five-pointed stars and two limit cycles in Figure 5(b) are marked with bold lines. Obviously, the dynamical behaviors featured by Figure 5 are consistent with those featured by Figure 4, ignoring the computational errors in MATLAB simulation [44], which verify the feasibility of the incremental flux-charge model of the memristor-based canonical Chua's circuit.

4. Controlling Multiple Stable States in Physical Circuit

With model (14), the equivalent circuit using analog multipliers and op-amps linked with resistors and/or capacitors [7, 8, 45] can be handily designed, as shown in Figure 6, which is composed of the linear calculating circuit with three integrating channels and the memristor constitutive relation circuit. In Figure 6, v_1 , v_2 , and v_3 represent three state variables of the capacitor voltages, respectively, and RC stands for the time constant of the integrators.

According to the fundamental theory of circuit, the circuit state equations of Figure 6 are expressed as

$$\begin{aligned}
RC \frac{dv_1}{dt} &= -\frac{RF(v_1)}{R_b} + \frac{Rv_3}{R_b} + \eta_1, \\
RC \frac{dv_2}{dt} &= v_2 - v_3 + \eta_2, \\
RC \frac{dv_3}{dt} &= \frac{R(v_2 - v_1)}{R_c} + \eta_3,
\end{aligned} \tag{22}$$

where $F(v_1) = Rv_1^3/R_1 - R\eta v_1^2/R_2 + R\eta^2 v_1/R_3 - v_1$. Thus, the circuit parameters can be chosen as $R_b = R/b$, $R_c = R/c$, $R_1 = 3R/(ga^2)$, $R_2 = R/(ga)$, and $R_3 = R/g$.

The op-amps OP07CP and multipliers AD633JNZ with ± 15 V power supplies are utilized. The integrating time constant is selected as $RC = 10 \text{ k}\Omega \times 10 \text{ nF} = 100 \mu\text{s}$. Thus, for the system parameters given in (5), the circuit parameters in

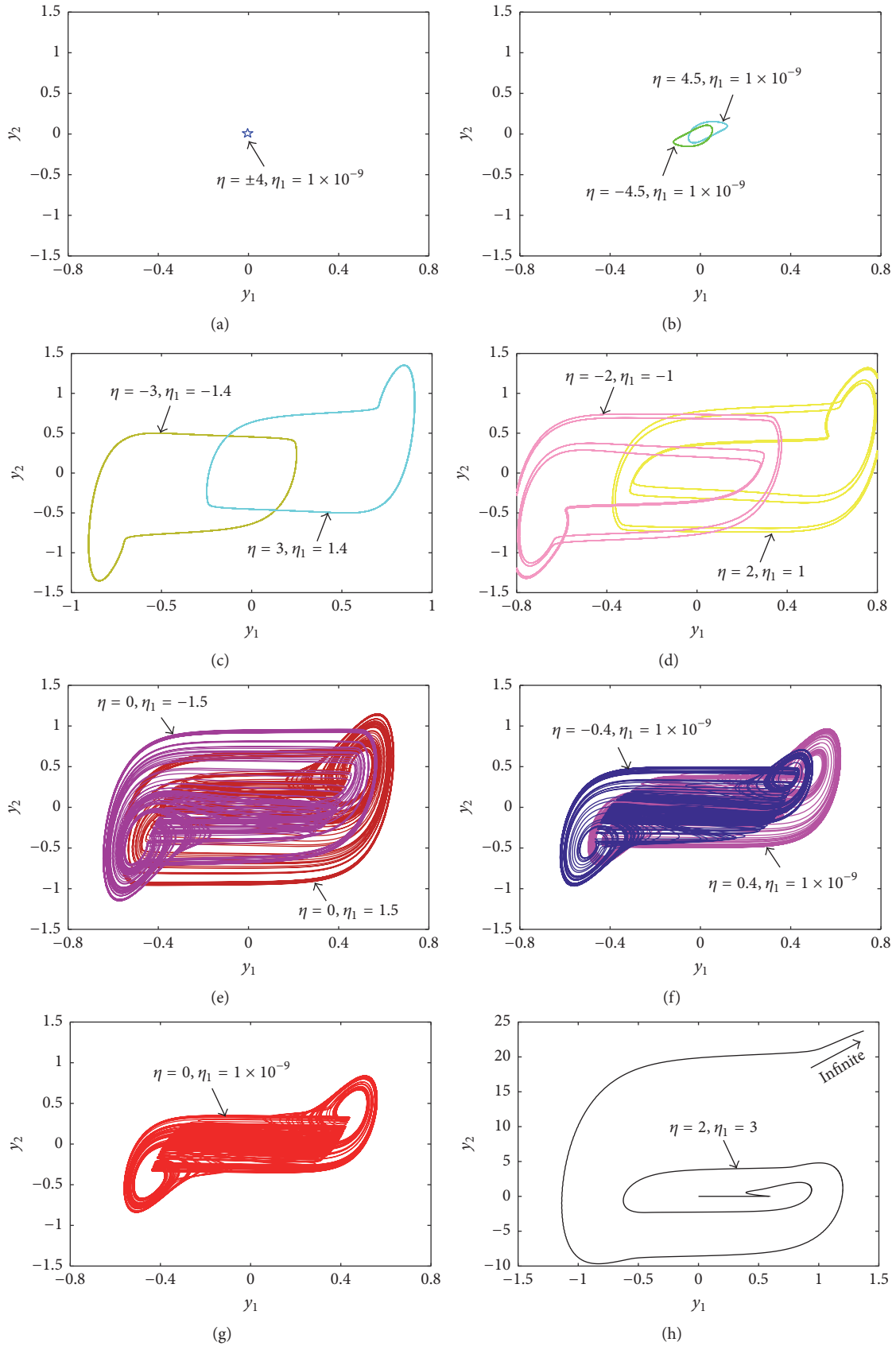


FIGURE 5: Phase portraits of various types of attractors distributed in different locations of the parameter space of η and η_1 . (a) Two point attractors. (b) Right- and left-period-1 limit cycles with small size. (c) Right- and left-period-1 limit cycles with large size. (d) Right- and left-multiperiod limit cycles. (e) Right- and left-chaotic spiral attractors. (f) Right- and left-half-baked double-scroll chaotic attractors. (g) Standard double-scroll chaotic attractor. (h) Unbounded orbit.

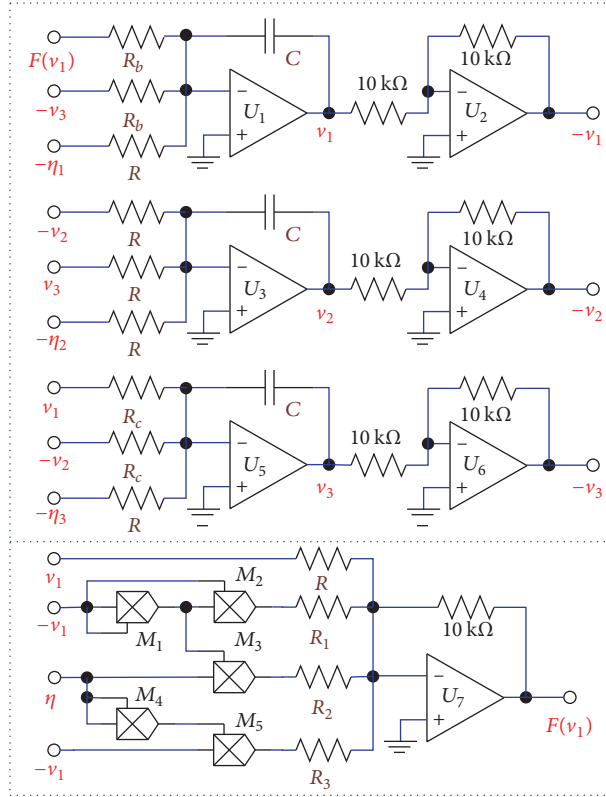


FIGURE 6: Equivalent circuit of model (14) for controlling multistable states; the upper dashed box is the linear calculating circuit and the lower dashed box is the memristor constitutive relation circuit.

Figure 6 are calculated as $R_b = 1.4242\text{ k}\Omega$, $R_c = 4.0404\text{ k}\Omega$, $R_1 = 0.9795\text{ k}\Omega$, $R_2 = 4.0404\text{ k}\Omega$, and $R_3 = 50\text{ k}\Omega$. Additionally, the gains of the multipliers in Figure 6 are all fixed as 1 and the values of η_2 and η_3 are maintained as 0.

To better present the control effect of the multistable states generated from the equivalent circuit in Figure 6, the NI Multisim 12.0 simulation and circuit design software is utilized, in which the default initial values of three capacitors are assigned as 0. For several different values of η and η_1 , the Multisim intercepted phase portraits are displayed, as shown in Figure 7. Note that the initial value of $1 \times 10^{-9}\text{ V}$ can be achieved by a slightly induced voltage in the equivalent circuit, so the value of η_1 is set as 0. Comparing the results of Figure 7 with those of Figure 5, it is concluded that the circuit simulations agree with the numerical simulations, further confirming the feasibility of the controllable strategy for extreme multistability.

5. Conclusion

By replacing Chua's diode in the canonical Chua's circuit with an ideal voltage-controlled memristor emulator, a memristor-based canonical Chua's circuit is presented in this paper. Because of the existence of a line equilibrium point, the initial condition-dependent extreme multistability easily emerged in such a memristive circuit, resulting in the coexistence of infinitely many attractors. To implement the controllability

of the extreme multistability, an incremental flux-charge model for the memristive circuit is formulated through deriving the accurate constitutive relation of the memristor emulator. Thus, the initial condition-dependent dynamics in the voltage-current domain is converted into the system parameter-associated dynamics in the flux-charge domain, that is, the implicit expression of the initial conditions in the voltage-current domain can be transformed into the explicit representation of the system parameters in the flux-charge model, leading to the fact that the multiple steady states emerging in the memristive circuit can be consequently controlled by changing the initial condition-related system parameters. The feasibility of the controllable strategy for extreme multistability is confirmed by numerical simulations and circuit simulations, which is greatly significant for seeking the potential uses of the multistable memristive circuits in chaos-based engineering applications.

Conflicts of Interest

The authors declare that they have no conflicts of interest.

Acknowledgments

This work was supported by the National Natural Science Foundations of China under Grants nos. 51777016, 61601062,

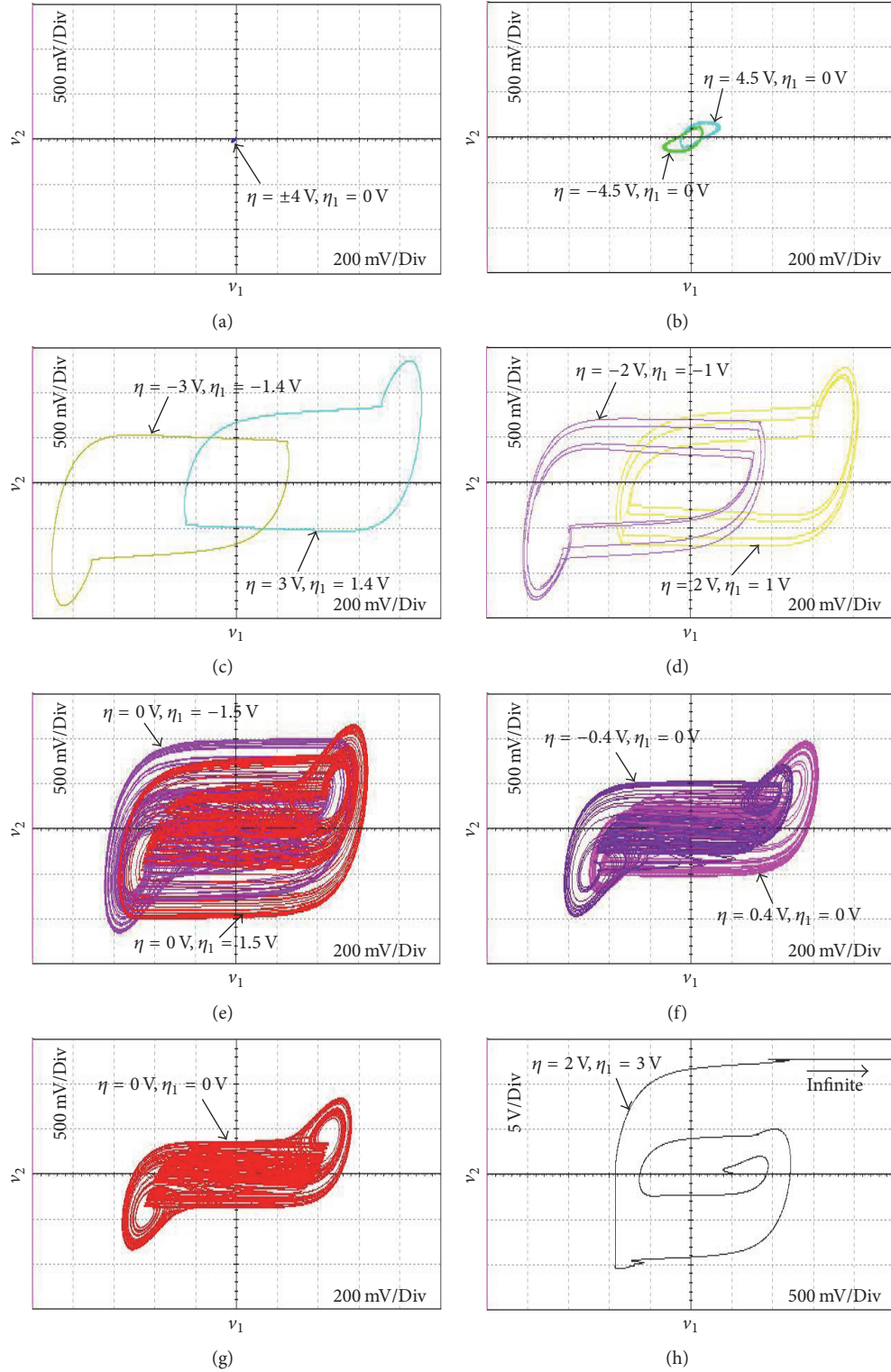


FIGURE 7: Multisim intercepted phase portraits of various types of attractors for different values of η and η_1 . (a) Two point attractors. (b) Right- and left-period-1 limit cycles with small size. (c) Right- and left-period-1 limit cycles with large size. (d) Right- and left-multiperiod limit cycles. (e) Right- and left-chaotic spiral attractors. (f) Right- and left-half-baked double-scroll chaotic attractors. (g) Standard double-scroll chaotic attractor. (h) Unbounded orbit.

51607013, and 11602035 and the Natural Science Foundations of Jiangsu Province, China, under Grant no. BK20160282.

References

- [1] C. N. Ngonghala, U. Feudel, and K. Showalter, "Extreme multistability in a chemical model system," *Physical Review E: Statistical, Nonlinear, and Soft Matter Physics*, vol. 83, no. 5, Article ID 056206, 2011.
- [2] M. S. Patel, U. Patel, A. Sen et al., "Experimental observation of extreme multistability in an electronic system of two coupled Rössler oscillators," *Physical Review E: Statistical, Nonlinear, and Soft Matter Physics*, vol. 89, no. 2, Article ID 022918, 2014.
- [3] C. Hens, S. K. Dana, and U. Feudel, "Extreme multistability: Attractor manipulation and robustness," *Chaos: An Interdisciplinary Journal of Nonlinear Science*, vol. 25, no. 5, Article ID 053112, 2015.
- [4] F. Yuan, G. Wang, P. Jin, X. Wang, and G. Ma, "Chaos in a Meminductor-Based Circuit," *International Journal of Bifurcation and Chaos*, vol. 26, no. 8, Article ID 1650130, 2016.
- [5] B.-C. Bao, Q. Xu, H. Bao, and M. Chen, "Extreme multistability in a memristive circuit," *IEEE Electronics Letters*, vol. 52, no. 12, pp. 1008–1010, 2016.
- [6] B. Bao, T. Jiang, Q. Xu, M. Chen, H. Wu, and Y. Hu, "Coexisting infinitely many attractors in active band-pass filter-based memristive circuit," *Nonlinear Dynamics*, vol. 86, no. 3, pp. 1711–1723, 2016.
- [7] B. C. Bao, H. Bao, N. Wang, M. Chen, and Q. Xu, "Hidden extreme multistability in memristive hyperchaotic system," *Chaos, Solitons & Fractals*, vol. 94, pp. 102–111, 2017.
- [8] H. Bao, N. Wang, B. Bao, M. Chen, P. Jin, and G. Wang, "Initial condition-dependent dynamics and transient period in memristor-based hypogenetic jerk system with four line equilibria," *Communications in Nonlinear Science and Numerical Simulation*, vol. 57, pp. 264–275, 2018.
- [9] B. Bao, T. Jiang, G. Wang, P. Jin, H. Bao, and M. Chen, "Two-memristor-based Chua's hyperchaotic circuit with plane equilibrium and its extreme multistability," *Nonlinear Dynamics*, pp. 1–15, 2017.
- [10] Z. Wang, A. Akgul, V.-T. Pham, and S. Jafari, "Chaos-based application of a novel no-equilibrium chaotic system with coexisting attractors," *Nonlinear Dynamics*, vol. 89, no. 3, pp. 1877–1887, 2017.
- [11] S. Morfu, B. Nofiele, and P. Marquié, "On the use of multistability for image processing," *Physics Letters A*, vol. 367, no. 3, pp. 192–198, 2007.
- [12] A. N. Pisarchik and U. Feudel, "Control of multistability," *Physics Reports*, vol. 540, no. 4, pp. 167–218, 2014.
- [13] P. R. Sharma, M. D. Shirmali, A. Prasad, N. V. Kuznetsov, and G. A. Leonov, "Control of multistability in hidden attractors," *The European Physical Journal Special Topics*, vol. 224, no. 8, pp. 1485–1491, 2015.
- [14] D. Dudkowski, A. Prasad, and T. Kapitaniak, "Perpetual Points: New Tool for Localization of Coexisting Attractors in Dynamical Systems," *International Journal of Bifurcation and Chaos*, vol. 27, no. 4, Article ID 1750063, 2017.
- [15] Z. T. Njitacke, J. Kengne, H. B. Fotsin, A. N. Negou, and D. Tchiotso, "Coexistence of multiple attractors and crisis route to chaos in a novel memristive diode bridge-based Jerk circuit," *Chaos, Solitons & Fractals*, vol. 91, pp. 180–197, 2016.
- [16] J. Kengne, Z. N. Tabekoueng, V. K. Tamba, and A. N. Negou, "Periodicity, chaos, and multiple attractors in a memristor-based Shinriki's circuit," *Chaos: An Interdisciplinary Journal of Nonlinear Science*, vol. 25, no. 10, Article ID 103126, 2015.
- [17] J. Kengne, Z. T. Njitacke, and H. B. Fotsin, "Dynamical analysis of a simple autonomous jerk system with multiple attractors," *Nonlinear Dynamics*, 2015.
- [18] B. C. Bao, Q. D. Li, N. Wang, and Q. Xu, "Multistability in Chua's circuit with two stable node-foci," *Chaos: An Interdisciplinary Journal of Nonlinear Science*, vol. 26, no. 4, Article ID 043111, 2016.
- [19] M. Chen, Q. Xu, Y. Lin, and B. Bao, "Multistability induced by two symmetric stable node-foci in modified canonical Chua's circuit," *Nonlinear Dynamics*, vol. 87, no. 2, pp. 789–802, 2017.
- [20] J. Kengne, A. N. Negou, and D. Tchiotso, "Antimonotonicity, chaos and multiple attractors in a novel autonomous memristor-based jerk circuit," *Nonlinear Dynamics*, vol. 88, no. 4, pp. 2589–2608, 2017.
- [21] B. Bao, H. Qian, Q. Xu, M. Chen, J. Wang, and Y. Yu, "Coexisting behaviors of asymmetric attractors in hyperbolic-type memristor based hopfield neural network," *Frontiers in Computational Neuroscience*, vol. 11, no. 81, pp. 1–14, 2017.
- [22] J. C. Sprott, S. Jafari, A. J. M. Khalaf, and T. Kapitaniak, "Megastability: Coexistence of a countable infinity of nested attractors in a periodically-forced oscillator with spatially-periodic damping," *The European Physical Journal Special Topics*, vol. 226, no. 9, pp. 1979–1985, 2017.
- [23] E. B. Ngouonkadi, H. B. Fotsin, P. Louodop Fotso, V. Kamdoun Tamba, and H. A. Cerdeira, "Bifurcations and multistability in the extended Hindmarsh-Rose neuronal oscillator," *Chaos, Solitons & Fractals*, vol. 85, pp. 151–163, 2016.
- [24] C. Li and J. C. Sprott, "Multistability in the lorenz system: A broken butterfly," *International Journal of Bifurcation and Chaos*, vol. 24, no. 10, Article ID 1450131, 2014.
- [25] Q. Xu, Y. Lin, B. Bao, and M. Chen, "Multiple attractors in a non-ideal active voltage-controlled memristor based Chua's circuit," *Chaos, Solitons & Fractals*, vol. 83, pp. 186–200, 2016.
- [26] O. S. Ojoniyi and A. N. Njah, "A 5D hyperchaotic Sprott B system with coexisting hidden attractors," *Chaos, Solitons & Fractals*, vol. 87, pp. 172–181, 2016.
- [27] G. Huang and J. Cao, "Multistability of neural networks with discontinuous activation function," *Communications in Nonlinear Science and Numerical Simulation*, vol. 13, no. 10, pp. 2279–2289, 2008.
- [28] T. Malashchenko, A. Shilnikov, and G. Cymbalyuk, "Six types of multistability in a Neuronal model based on slow calcium current," *PLoS ONE*, vol. 6, no. 7, Article ID e21782, 2011.
- [29] F. Corinto and M. Forti, "Memristor circuits: flux—charge analysis method," *IEEE Transactions on Circuits and Systems I: Regular Papers*, vol. 63, no. 11, pp. 1997–2009, 2016.
- [30] F. Corinto and M. Forti, "Memristor Circuits: Bifurcations without Parameters," *IEEE Transactions on Circuits and Systems I: Regular Papers*, vol. 64, no. 6, pp. 1540–1551, 2017.
- [31] B.-C. Bao, "Reply: Comment on 'Is memristor a dynamic element?'," *IEEE Electronics Letters*, vol. 50, no. 19, pp. 1344–1345, 2014.
- [32] M. Itoh and L. O. Chua, "Duality of memristor circuits," *International Journal of Bifurcation and Chaos*, vol. 23, no. 1, Article ID 1330001, 2013.
- [33] F. Z. Wang, "A triangular periodic table of elementary circuit elements," *IEEE Transactions on Circuits and Systems I: Regular Papers*, vol. 60, no. 3, pp. 616–623, 2013.

- [34] B. Bao, F. Hu, Z. Liu, and J. Xu, "Mapping equivalent approach to analysis and realization of memristor-based dynamical circuit," *Chinese Physics B*, vol. 23, no. 7, Article ID 070503, 2014.
- [35] A. L. Fitch, D. Yu, H. H. C. Iu, and V. Sreeram, "Hyperchaos in a memristor-based modified canonical Chua's circuit," *International Journal of Bifurcation and Chaos*, vol. 22, no. 6, Article ID 1250133, 2012.
- [36] F. Yuan, G. Wang, and X. Wang, "Chaotic oscillator containing memcapacitor and meminductor and its dimensionality reduction analysis," *Chaos: An Interdisciplinary Journal of Nonlinear Science*, vol. 27, no. 3, Article ID 033103, 2017.
- [37] J. Ma, F. Wu, G. Ren, and J. Tang, "A class of initials-dependent dynamical systems," *Applied Mathematics and Computation*, vol. 298, pp. 65–76, 2017.
- [38] G. A. Leonov, N. V. Kuznetsov, and T. N. Mokaev, "Hidden attractor and homoclinic orbit in Lorenz-like system describing convective fluid motion in rotating cavity," *Communications in Nonlinear Science and Numerical Simulation*, vol. 28, no. 1-3, pp. 166–174, 2015.
- [39] V. T. Pham, S. Vaidyanathan, C. K. Volos, and S. Jafari, "Hidden attractors in a chaotic system with an exponential nonlinear term," *The European Physical Journal Special Topics*, vol. 224, no. 8, Article ID A1507, pp. 1507–1517, 2015.
- [40] D. Dudkowski, S. Jafari, T. Kapitaniak, N. V. Kuznetsov, G. A. Leonov, and A. Prasad, "Hidden attractors in dynamical systems," *Physics Reports*, vol. 637, pp. 1–50, 2016.
- [41] S. Jafari, J. C. Sprott, V.-T. Pham, C. Volos, and C. Li, "Simple chaotic 3D flows with surfaces of equilibria," *Nonlinear Dynamics*, vol. 86, no. 2, pp. 1349–1358, 2016.
- [42] V.-T. Pham, S. Jafari, C. Volos, A. Giakoumis, S. Vaidyanathan, and T. Kapitaniak, "A chaotic system with equilibria located on the rounded square loop and its circuit implementation," *IEEE Transactions on Circuits and Systems II: Express Briefs*, vol. 63, no. 9, pp. 878–882, 2016.
- [43] V.-T. Pham, S. Jafari, X. Wang, and J. Ma, "A chaotic system with different shapes of equilibria," *International Journal of Bifurcation and Chaos*, vol. 26, no. 4, Article ID 1650069, 2016.
- [44] N. V. Kuznetsov, G. A. Leonov, M. V. Yuldashev, and R. V. Yuldashev, "Hidden attractors in dynamical models of phase-locked loop circuits: limitations of simulation in MATLAB and SPICE," *Communications in Nonlinear Science and Numerical Simulation*, vol. 51, pp. 39–49, 2017.
- [45] Q. Li, S. Hu, S. Tang, and G. Zeng, "Hyperchaos and horseshoe in a 4D memristive system with a line of equilibria and its implementation," *International Journal of Circuit Theory and Applications*, vol. 42, no. 11, pp. 1172–1188, 2014.

Research Article

Three-Dimensional Memristive Hindmarsh–Rose Neuron Model with Hidden Coexisting Asymmetric Behaviors

Bocheng Bao , Aihuang Hu, Han Bao, Quan Xu, Mo Chen, and Huagan Wu 

School of Information Science and Engineering, Changzhou University, Changzhou 213164, China

Correspondence should be addressed to Bocheng Bao; mervinbao@126.com

Received 27 December 2017; Accepted 24 January 2018; Published 28 February 2018

Academic Editor: Viet-Thanh Pham

Copyright © 2018 Bocheng Bao et al. This is an open access article distributed under the Creative Commons Attribution License, which permits unrestricted use, distribution, and reproduction in any medium, provided the original work is properly cited.

Since the electrical activities of neurons are closely related to complex electrophysiological environment in neuronal system, a novel three-dimensional memristive Hindmarsh–Rose (HR) neuron model is presented in this paper to describe complex dynamics of neuronal activities with electromagnetic induction. The proposed memristive HR neuron model has no equilibrium point but can show hidden dynamical behaviors of coexisting asymmetric attractors, which has not been reported in the previous references for the HR neuron model. Mathematical model based numerical simulations for hidden coexisting asymmetric attractors are performed by bifurcation analyses, phase portraits, attraction basins, and dynamical maps, which just demonstrate the occurrence of complex dynamical behaviors of electrical activities in neuron with electromagnetic induction. Additionally, circuit breadboard based experimental results well confirm the numerical simulations.

1. Introduction

In the past three decades, numerous simplified neuron models had been fantastically extended from the classical Hodgkin–Huxley model [1] to reconstruct the main dynamical characteristics of neuronal electrical activities [2–8], among which the two- and three-dimensional Hindmarsh–Rose (HR) neuron models are effective and available for dynamical analysis in electrical activities of biological neurons [9, 10]. In the last few years, a wide variety of the HR neuron models, such as original three-dimensional HR models [10–16], extended or nonlinear feedback coupled HR models [17–20], time delayed HR models [20–22], fractional-order HR models [23, 24], and memristor based HR models under electromagnetic radiations [9, 25–27], have been proposed and further studied by bifurcation analysis methods for understanding the dynamics of electrical activities among neurons [8]. For this reason, bifurcation analysis theory plays an essential role in describing mode transitions between spiking and bursting in the neuronal electrical activities [9–27].

Inspired by the constructing approach of the three-dimensional HR neuron model [3, 24], a novel three-dimensional memristive HR neuron model is presented in

this paper, which could be used to better describe complex dynamical characteristics of neuronal electrical activities with electromagnetic induction or further exhibit some undiscovered complex dynamical behaviors in neuronal electrical activities. Interestingly, our proposed memristive HR neuron model has no equilibrium point, which can be classified as a particular dynamical system with hidden oscillating patterns [28–31]. Furthermore, coexisting asymmetric attractors' behavior can also be observed in such memristive HR neuron model as well, indicating the emergence of bistability dynamics, which has been found in some specified neuron models [32–35]. However, the phenomenon of hidden coexisting asymmetric attractors has not been previously reported for the HR neuron model.

This paper is organized as follows. In Section 2, based on the brief reviews on the HR neuron model, a three-dimensional memristive HR neuron model is presented, upon which hidden coexisting asymmetric attractors are numerically revealed by phase portraits and time series and its bistability dynamics are confirmed by the attraction basins related to the initial values. In Section 3, hidden coexisting asymmetric attractors' behaviors are demonstrated by bifurcation diagrams, Lyapunov exponents, and dynamical maps, from which numerous types of coexisting asymmetric

attractors are easily observed. In addition, a physical implementation circuit is fabricated and breadboard experiments are carried out to confirm the hidden coexisting asymmetric attractors in Section 4. The conclusions are summarized in Section 5.

2. Three-Dimensional Memristive HR Neuron Model

2.1. Brief Reviews on the HR Neuron Model. Through simplifying the classical Hodgkin–Huxley model [1], the two-dimensional Hindmarsh–Rose (HR) neuron model was proposed by Hindmarsh and Rose [2] in 1982, which is described by two first-order ordinary differential equations as

$$\begin{aligned}\dot{x} &= y - ax^3 + bx^2 + I \\ \dot{y} &= c - dx^2 - y,\end{aligned}\quad (1)$$

in which two variables x and y are the membrane potential and recovery variable (also called spiking variable), respectively, and a term I is the externally applied current. The parameters a, b, c , and d are four positive constants, which are often assumed as $a = 1, b = 3, c = 1$, and $d = 5$, respectively [2, 11–14].

To permit numerous dynamical behaviors, for example, chaotic dynamics, for the membrane potential, an extra third equation was introduced by Hindmarsh and Rose [3] in 1984 to improve the two-dimensional neuron model (1), which is expressed by three first-order ordinary differential equations as

$$\begin{aligned}\dot{x} &= y - ax^3 + bx^2 + I - z \\ \dot{y} &= c - dx^2 - y \\ \dot{z} &= r(s(x - x_1) - z),\end{aligned}\quad (2)$$

where the variable z is the bursting variable and the constant x_1 is the resting potential of the model. The newly added parameters r and s are two positive constants but r is very small. Thus, a new variable z , a slowly evolving current, is coupled into the first equation of the two-dimensional model (1) to tune the externally applied current I . If the three-dimensional neuron model (2) is in its firing state, the value of z increases [24].

2.2. Constructed Memristive HR Neuron Model. Motivated by the above constructing approach of the model (2), a three-dimensional memristive HR neuron model with electromagnetic induction effect is proposed through introducing a flux-controlled ideal memristor into the first equation of the model (1), which can be mathematically modeled by

$$\begin{aligned}\dot{x} &= y - ax^3 + bx^2 + I + k\phi x \\ \dot{y} &= c - dx^2 - y \\ \dot{\phi} &= x,\end{aligned}\quad (3)$$

where the new variable ϕ is the magnetic flux indicating the time integral of the membrane potential x . The newly adding term $k\phi x$ represents the externally applied electromagnetic induction and k is the strength of the electromagnetic induction.

It is important to stress that the introduced memristor in (3) is ideal and flux-controlled. According to the definitions of ideal memristor by state-dependent Ohm's laws between the terminal voltage v and terminal current i [36, 37], a flux-controlled ideal memristor W is thereby given as

$$\begin{aligned}i &= W(\phi) v, \\ \dot{\phi} &= v,\end{aligned}\quad (4)$$

where the memductance $W(\phi)$ can be interpreted as the flux-dependent rate of change of charge. Therefore, the memductance $W(\phi)$ utilized in (3) can be written by

$$W(\phi) = k\phi, \quad (5)$$

in which the coefficient k is positive.

To exhibit three characteristic fingerprints of pinched hysteresis loop of the memristor modeled by (4) and (5) [38], a sinusoidal voltage source $v = A \sin(2\pi F\tau)$ is connected at the input terminals of the memristor, where A and F are the amplitude and frequency, respectively. Let $k = 1$. When $A = 4$ is maintained unchanged and F is assigned as 0.1, 0.2, and 0.5, respectively, the $v - i$ plots are shown in Figure 1(a), while when $F = 0.1$ is fixed and A is determined as 3, 4, and 5, respectively, the $v - i$ plots are shown in Figure 1(b). It is seen from Figure 1 that the $v - i$ plots are the hysteresis loops pinched at the origin. The hysteresis loop is pinched regardless of the stimulus amplitudes but shrinks into a linear function at infinite frequency and its lobe area decreases with increasing the frequency. The numerical results in Figure 1 indicate that the memristor modeled by (4) can behave three fingerprints for distinguishing memristors [38].

In the next work, the three-dimensional memristive HR neuron model given in (3) is considered. It should be remarked that the adjustable parameters of interest are I and k , and their regions are correspondent to the first quadrant of the parameter space ($I > 0$ and $k > 0$). For any uncertain parameter I , the existence of any equilibrium point is not allowed in the three-dimensional memristive HR neuron model, neither stable nor unstable. Only if the applied current $I = -1$ will the model show an equilibrium point, which is not in the considered parameter region. This case is often encountered in various kinds of nonlinear dynamical systems that are known to generate the specified hidden attractors [28–31].

2.3. Coexisting Asymmetric Attractors. When the original parameters are selected as $a = 1, b = 3, c = 1$, and $d = 5$, respectively [2], an example for model (3) with $I = 1$ and $k = 0.9$ is given as shown in Figure 2, where the orbits marked by the red and blue colors emerge from the initial values $(0, 0, -2)$ and $(0, 0, 2)$, respectively. In Figure 2(a), the phase portraits in the $x - \phi$ plane display the bistability phenomenon of hidden coexisting asymmetric

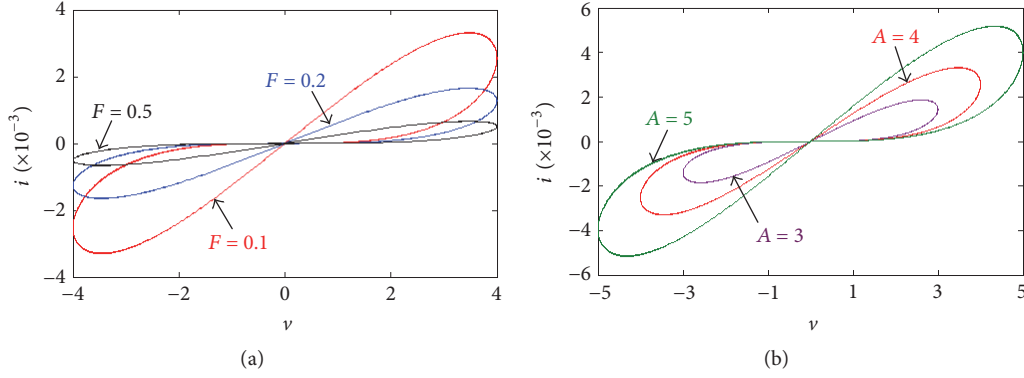


FIGURE 1: Pinched hysteresis loops of the flux-controlled ideal memristor. (a) $A = 4$ with $F = 0.1, 0.2$, and 0.5 . (b) $F = 0.1$ with $A = 3, 4$, and 5 .

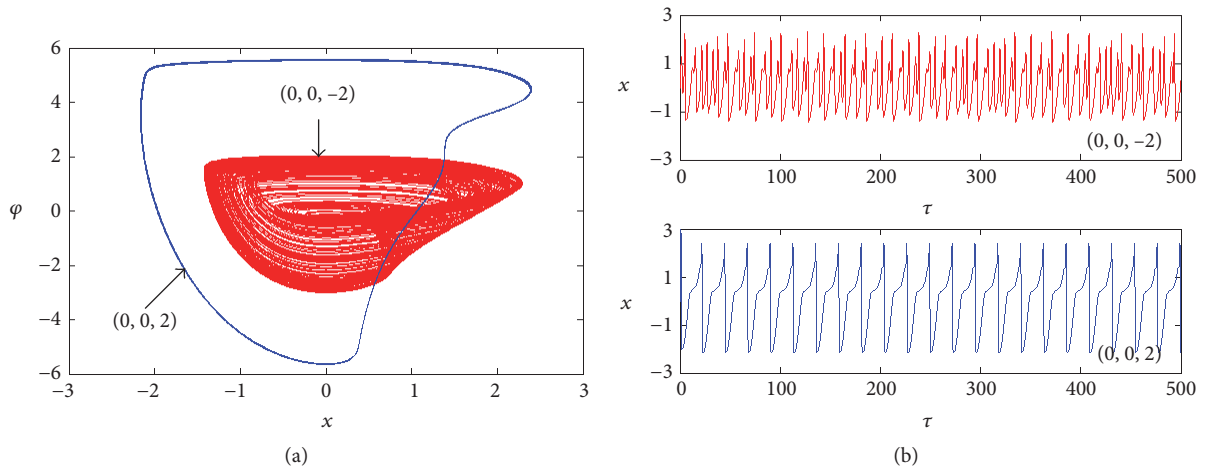


FIGURE 2: Hidden coexisting asymmetric attractors emerged from the initial values $(0, 0, -2)$ and $(0, 0, 2)$. (a) Phase portraits in the x - φ plane. (b) Time series of the variable x .

attractors consisting of chaotic attractor and limit cycle in the memristive HR neuron model, whereas in Figure 2(b), the time series of the membrane potential x demonstrate the coexistence of chaotic and periodic spikes in the memristive HR neuron model as well. Correspondingly, three Lyapunov exponents for the initial values $(0, 0, -2)$ are 0.0782 , 0 , and -3.0684 , respectively, while those for $(0, 0, 2)$ are 0 , -0.2717 , and -2.8556 , respectively. Remark that Wolf et al.'s method [39] with MATLAB ODE113 algorithm is here used to calculate three Lyapunov exponents.

For the coexisting asymmetric attractors shown in Figure 2(a), the corresponding attraction basins in the $x(0)$ - $\varphi(0)$ and $x(0)$ - $\gamma(0)$ planes of the initial values are drawn in Figures 3(a) and 3(b), where the attraction basins for chaotic attractors and periodic limit cycles are colored in the fuchsia and cyan regions, respectively. The results effectively indicate the emergence of bistability phenomenon in the memristive HR neuron model.

Particularly, the emerging coexisting asymmetric attractors do not associate with any equilibrium point, indicating that the memristive HR neuron model always operates in hidden oscillating patterns [28–31]. Additionally, it is

interesting to note that, just like the self-excited coexisting asymmetric attractors in hyperbolic-type memristor based Hopfield neural network [32], such hidden coexisting asymmetric attractors in the memristive HR neuron model are induced by electromagnetic induction also, which illustrates the occurrence of complex dynamical behaviors of electrical activities in neuron with electromagnetic induction.

3. Hidden Coexisting Asymmetric Attractors' Behavior

When the applied current I and electromagnetic induction strength k are considered as two bifurcation parameters, hidden coexisting asymmetric behaviors of the memristive HR neuron model are numerically studied by MATLAB ODE45 algorithm under two sets of the initial values $(0, 0, -2)$ and $(0, 0, 2)$.

3.1. Bifurcation Behaviors with Increasing k . Figure 4 gives the bifurcation diagrams of x and the first two Lyapunov exponents as $I = 1$ and $k = 0.5 \sim 1.4$, where in Figure 4(a) the orbits marked by the red and blue colors emerge from

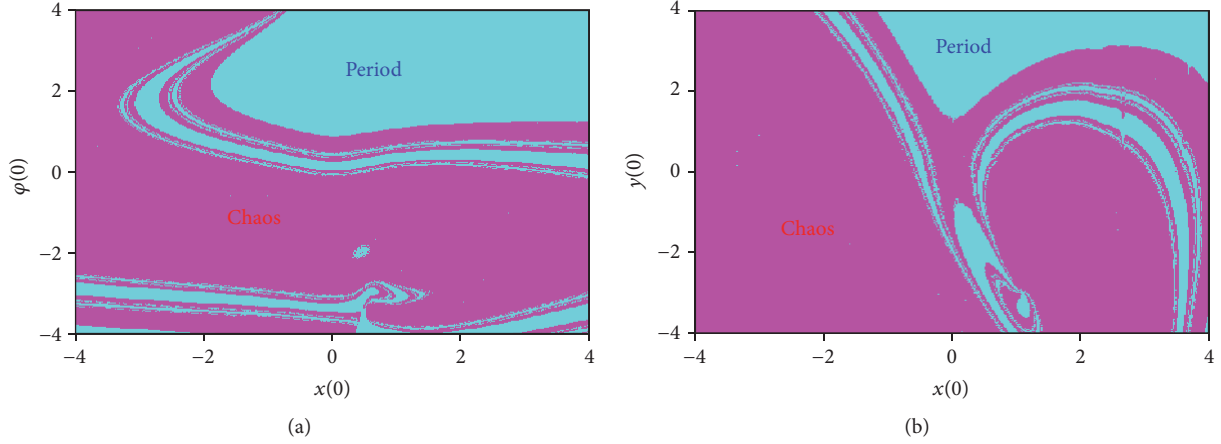


FIGURE 3: Attraction basins in two different planes for $I = 1$ and $k = 0.9$, indicating the emergence of bistability phenomenon. (a) The $x(0)$ - $\varphi(0)$ plane with $y(0) = 0$. (b) The $x(0)$ - $y(0)$ plane with $\varphi(0) = 0$.

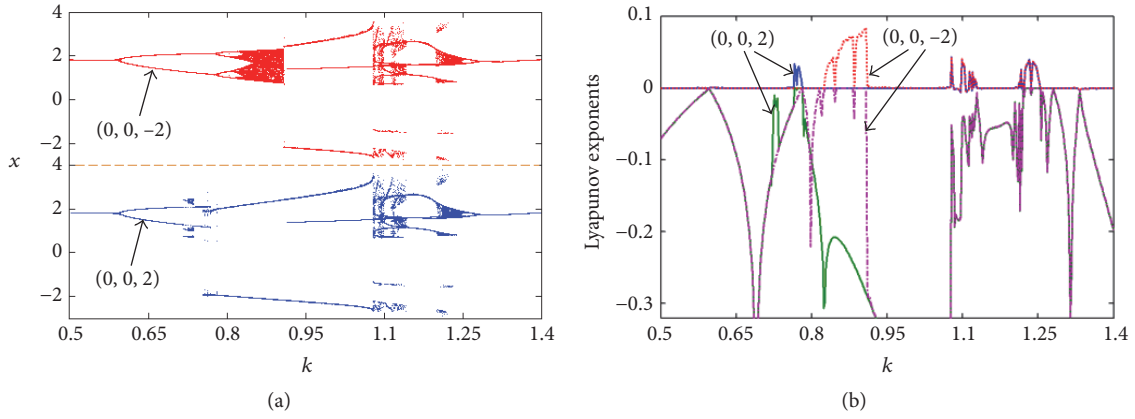


FIGURE 4: For the initial values $(0, 0, -2)$ and $(0, 0, 2)$, hidden coexisting asymmetric behaviors with $I = 1$ and $k = 0.5 \sim 1.4$. (a) Bifurcation diagrams of x . (b) First two Lyapunov exponents.

the initial values $(0, 0, -2)$ and $(0, 0, 2)$, respectively, and in Figure 4(b) the Lyapunov exponents marked by the red and fuchsia colors correspond to the initial values $(0, 0, -2)$ and those marked by blue and green colors correspond to $(0, 0, 2)$. It can be seen from Figure 4 that complex dynamics appear in the memristive HR neuron model, in which chaotic attractors with different topologies, limit cycles with different periodicities, period-doubling bifurcation routes, tangent bifurcation routes, crisis scenarios, coexisting bifurcation modes, and so on can be found. Therefore, the electromagnetic induction by the introduced memristor induces numerous complex dynamics for the membrane potential x , especially including hidden coexisting asymmetric behaviors.

The concerned coexisting behaviors of asymmetric attractors mainly locate in two parameter regions $[0.718, 0.736]$ and $[0.754, 0.909]$, in which some different types of hidden coexisting asymmetric attractors occur. When $I = 1$ and $k = 0.735$ and 0.81 , respectively, the phase portraits in the x - φ plane for the other two types of hidden coexisting asymmetric attractors are depicted in Figure 5. In detail, Figure 5(a) exhibits the coexistence of hidden chaotic

attractor and hidden limit cycle, and Figure 5(b) displays the coexistence of two hidden limit cycles with different periodicities.

3.2. Bifurcation Behaviors with Increasing I . Figure 6 demonstrates the bifurcation diagrams of x and the first two Lyapunov exponents as $I = 0 \sim 2.4$ and $k = 0.9$, where the initial values for different colored orbits in Figure 6(a) and different colored Lyapunov exponents in Figure 6(b) are consistent with those used in Figures 4(a) and 4(b). In the same way, it can be observed from Figure 6 that complex dynamics are coined in the memristive HR neuron model, reflecting the dynamical effect of the externally applied current I in neurons.

The parameter region $[0.98, 1.65]$ has the benefit for the coexisting behaviors of asymmetric attractors, in which several different types of hidden coexisting asymmetric attractors can be clearly found. When $k = 0.9$ is fixed and I is set to 1.15 and to 1.62 , respectively, the phase portraits in the x - φ plane for the two types of hidden coexisting asymmetric attractors are plotted in Figure 7, where in Figure 7(a) the

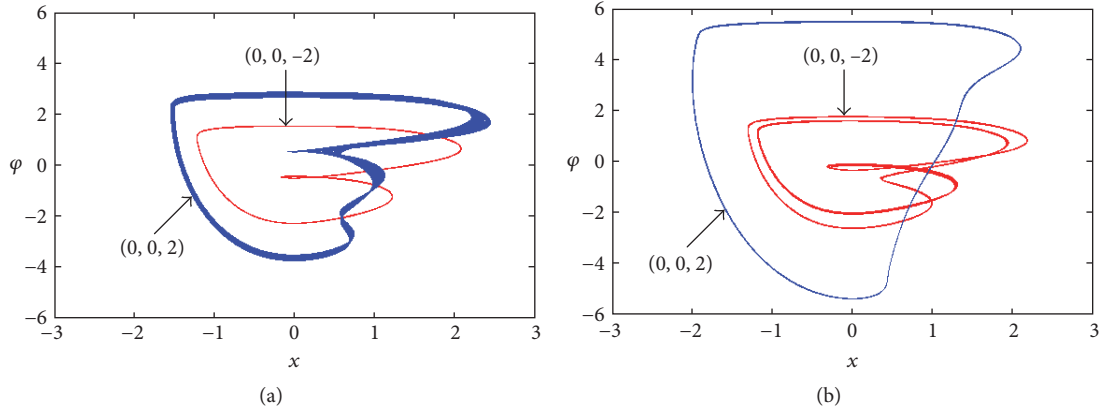


FIGURE 5: Phase portraits in the x - φ plane for the other two types of hidden coexisting asymmetric attractors. (a) $I = 1$ and $k = 0.735$. (b) $I = 1$ and $k = 0.81$.

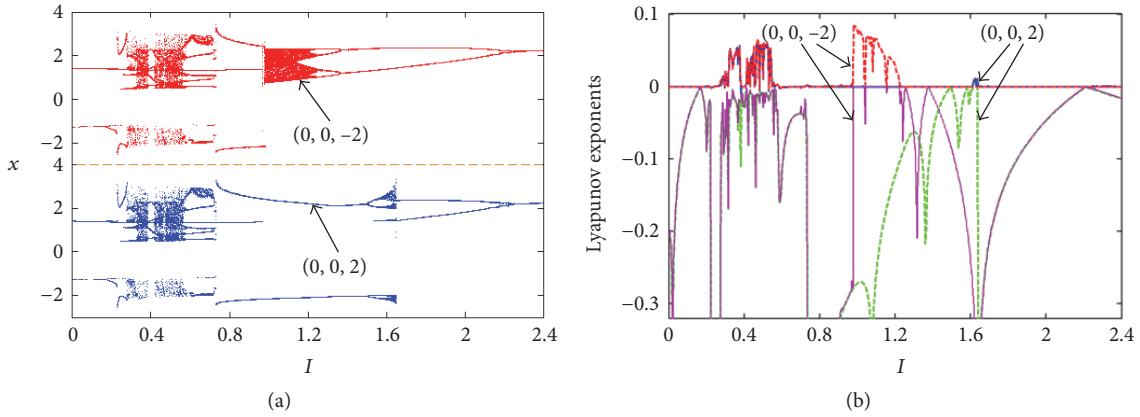


FIGURE 6: For the initial values $(0, 0, -2)$ and $(0, 0, 2)$, hidden coexisting asymmetric behaviors with $I = 0 \sim 2.4$ and $k = 0.9$. (a) Bifurcation diagrams of x . (b) First two Lyapunov exponents.

coexistence of hidden chaotic attractor and hidden period 1 limit cycle is displayed, and in Figure 7(b) the coexistence of hidden period 2 limit cycle and hidden chaotic attractor with large size is presented.

3.3. Coexisting Asymmetric Behaviors in the Parameter Space. For intuitively manifesting the coexisting behaviors of asymmetric attractors in the memristive HR neuron model, dynamical maps depicted by the largest Lyapunov exponent under two sets of the initial values are numerically plotted in the k - I parameter space [40], as shown in Figures 8(a) and 8(b), where the luminous yellow, red, and black colored regions stand for the chaotic, periodic, and divergent behaviors, respectively. Figure 8 indicates how dynamical evolution in the electromagnetic induction strength k and applied current I affects the coexisting behaviors under different initial values being considered. When the two parameters k and I are evolved, some chaotic regions are embedded in the periodic regions; however, different chaotic regions appear on the parameter spaces of Figures 8(a) and 8(b), which are caused by the coexisting asymmetric attractors' behaviors under different initial values. The numerical results in Figure 8 illustrate that the dynamical behaviors depicted

by the largest Lyapunov exponent based dynamical maps are well agreed with those revealed by the bifurcation behaviors in Figures 4 and 6.

It should be remarkable for the dynamical maps in Figure 8 that the chaotic attractors in different locations of the chaotic region have different topologies and the limit cycles in different locations of the periodic region have different periodicities. Specifically, except for several types of coexisting asymmetric behaviors shown in Figures 2, 5, and 7, another type of coexisting asymmetric behaviors of chaotic attractor and divergent orbit can also be uncovered, which means that another form of bistability exists in the memristive HR neuron model.

4. Circuit Design and Breadboard Experiments

4.1. Physical Circuit Designs and Parameter Selections. The flux-controlled ideal memristor W characterized by (4) and (5) and its constructing three-dimensional memristive HR neuron model expressed by (3) can be physically realized by using an electronic circuit via analog multipliers and operational amplifiers connected with resistors and/or capacitors [41–43], as drawn in Figures 9(a) and 9(b), respectively. Of

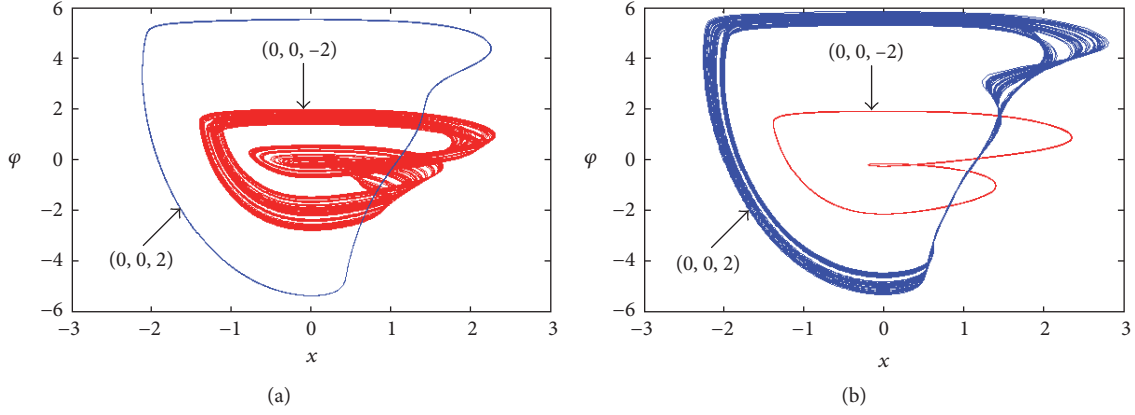


FIGURE 7: Phase portraits in the x - φ plane for the other two types of hidden coexisting asymmetric attractors. (a) $I = 1.15$ and $k = 0.9$. (b) $I = 1.62$ and $k = 0.9$.

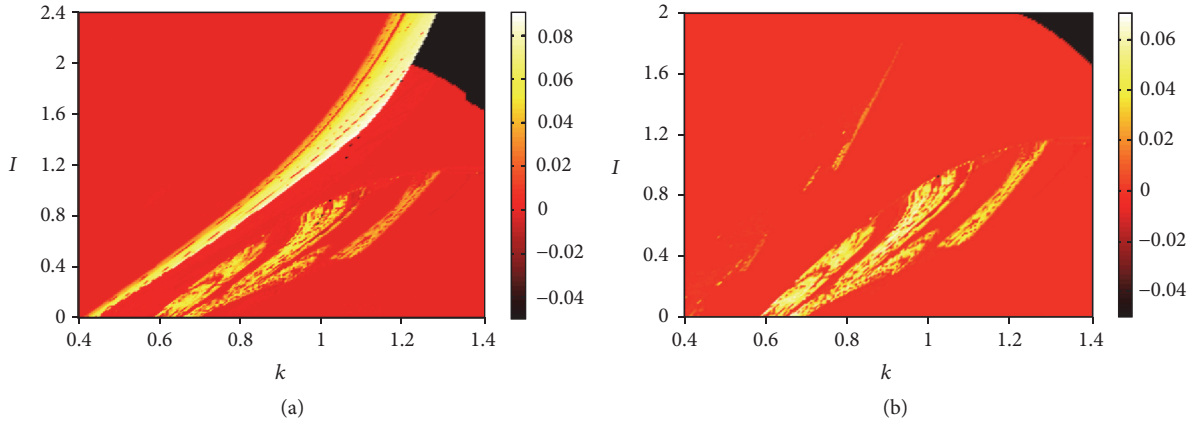


FIGURE 8: In the k - I parameter space, dynamical maps depicted by the largest Lyapunov exponent under different initial values. (a) Dynamical map for the initial values $(0, 0, -2)$. (b) Dynamical map for the initial values $(0, 0, 2)$.

course, this three-dimensional memristive HR neuron model also can be digitally implemented in field-programmable gate arrays (FPGA) as well [44, 45].

The implementation circuit of the flux-controlled ideal memristor in Figure 9(a) contains an integrator with time constant RC , an inverter, a multiplier M_0 , and a resistor R_k . For the input voltage v and output current i , the mathematical model for the memristor emulator can be easily given as

$$i = W(v_\varphi) v = \frac{g_0}{R_k C} v_\varphi v = \frac{1}{RC} \cdot k v_\varphi v \quad (6)$$

$$\dot{v}_\varphi = \frac{1}{RC} \cdot v,$$

where v_φ is the inner variable of the memristor emulator and g_0 is the gain of the multipliers M_0 , $k = g_0 R / R_k$, and $W(v_\varphi) = k v_\varphi / RC$.

The main circuit of the memristive HR neuron model in Figure 9(b) has two integrating channels for implementing the first and second equations of (3). According to Kirchhoff's

circuit laws and electrical properties of the circuit components, the circuit equations of Figure 9(b) are written as

$$RC \frac{dv_x}{dt} = \frac{R}{R_2} v_y - \frac{g_1 g_2 R}{R_4} v_x^3 + \frac{g_2 R}{R_3} v_x^2 + \frac{R}{R_1} V_I + \frac{g_0 R}{R_k} v_\varphi v_x \quad (7)$$

$$RC \frac{dv_y}{dt} = \frac{R}{R_6} V_{y0} - \frac{g_3 R}{R_5} v_x^2 - \frac{R}{R_7} v_y$$

$$RC \frac{dv_\varphi}{dt} = v_x,$$

where v_x and v_y are two circuit variables, V_I and V_{y0} are two applied voltages, and g_1 , g_2 , and g_3 are the gains of the multipliers M_1 , M_2 , and M_3 , respectively.

Considering that the dynamic amplitude of the recovery variable y in the numerical simulations exceeds the linear operation ranges of operational amplifier and multiplier, the following linear transformation

$$(v_x, v_y, v_\varphi) \rightarrow (v_x, 2.5v_y, v_\varphi) \quad (8)$$

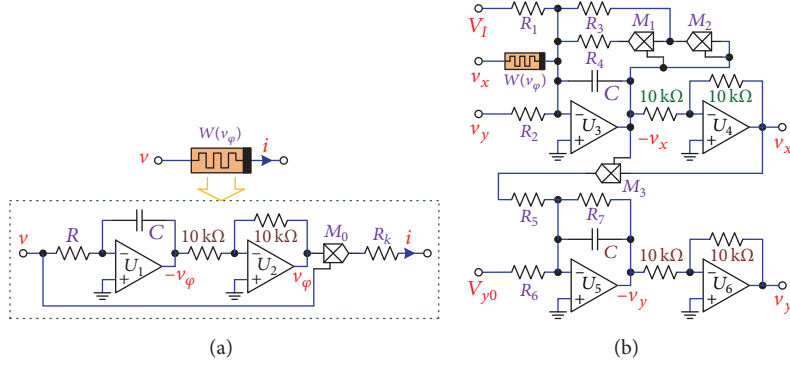


FIGURE 9: Physical electronic circuit implementation for the memristive HR neuron model. (a) Implementation circuit of the flux-controlled ideal memristor. (b) Main circuit of the memristive HR neuron model.

should be utilized to reduce the dynamic voltage amplitude of v_y in the circuit equations of the memristive HR neuron model. Thus, by comparing (8) with (3), there yields

$$\begin{aligned}
 R_1 &= \frac{R}{I}, \\
 R_k &= \frac{g_0 R}{k}, \\
 R_2 &= \frac{R}{2.5}, \\
 R_3 &= \frac{g_2 R}{3}, \\
 R_4 &= g_1 g_2 R, \\
 R_5 &= \frac{g_3 R}{2}, \\
 R_6 &= 2.5R, \\
 R_7 &= R.
 \end{aligned} \tag{9}$$

Let the time constant $RC = 10 \text{ k}\Omega \times 33 \text{ nF} = 330 \mu\text{s}$; that is, $R = 10 \text{ k}\Omega$ and $C = 33 \text{ nF}$ and the multiplier gains $g_0 = g_1 = 0.1$ and $g_2 = g_3 = 1$. According to (9), the circuit parameters for the breadboard experiments of the memristive HR neuron model can be calculated, as listed in Table 1.

4.2. Results Captured from Breadboard Experiments. According to the circuit diagrams in Figure 9 and circuit parameters in Table 1, a hardware circuit using commercially discrete components can be welded on a breadboard. The operational amplifiers AD711JN and analog multipliers AD633JN supplied by $\pm 15 \text{ V}$ voltage modules are chosen. The DC voltages V_I and V_{y0} are provided by Tektronix PWS 2326 DC Power Supply and the experimental results are measured by Tektronix TDS 3054C Digital Phosphor Oscilloscope. The photograph of the connectedly experimental prototype for the memristive HR neuron model is displayed in Figure 10.

For experimentally measuring the pinched hysteresis loops of the memristor emulator given in Figure 9(a),

TABLE 1: Circuit parameters of the memristive HR neuron model for breadboard experiments.

Parameters	Significations	Values
R, R_7	Resistance	$10 \text{ k}\Omega$
R_1	Resistance	$10 \text{ k}\Omega$ (adjustable)
R_k	Resistance	$1.11 \text{ k}\Omega$ (adjustable)
R_2	Resistance	$4 \text{ k}\Omega$
R_3	Resistance	$3.3 \text{ k}\Omega$
R_4	Resistance	$1 \text{ k}\Omega$
R_5	Resistance	$5 \text{ k}\Omega$
R_6	Resistance	$25 \text{ k}\Omega$
C	Capacitance	33 nF
V_I, V_{y0}	DC voltage	1 V
g_0, g_1	Multiplier gain	0.1
g_2, g_3	Multiplier gain	1

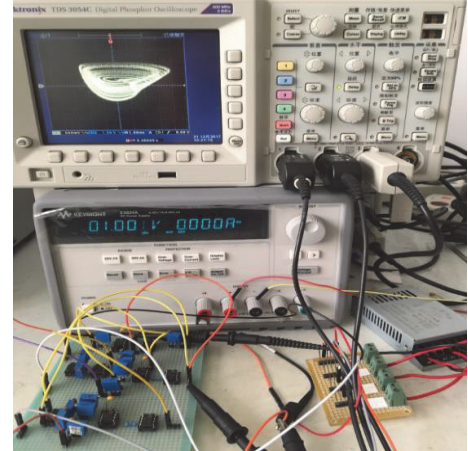


FIGURE 10: Photograph of the experimental breadboard and typical chaotic attractor captured by the digital oscilloscope.

a sinusoidal voltage source $v = A \sin(2\pi ft)$ generated by Tektronix AFG 3102C Function Generator is linked to the input terminals of the memristor emulator, where the physical frequency is calculated by $f = F/RC$. For $k = 1$, the adjustable

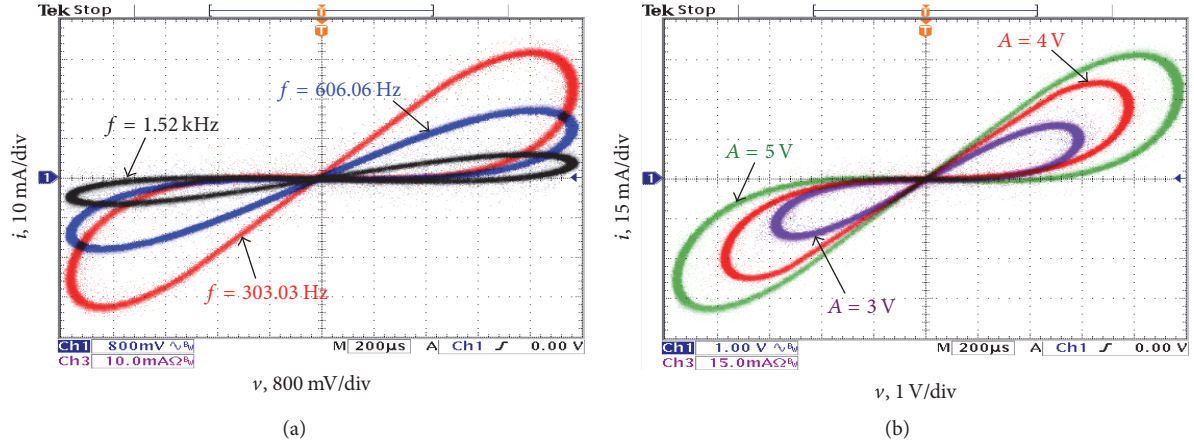


FIGURE 11: Experimentally measured pinched hysteresis loops of the memristor emulator. (a) $A = 4$ V with different frequencies. (b) $f = 303.03$ Hz with different amplitudes.

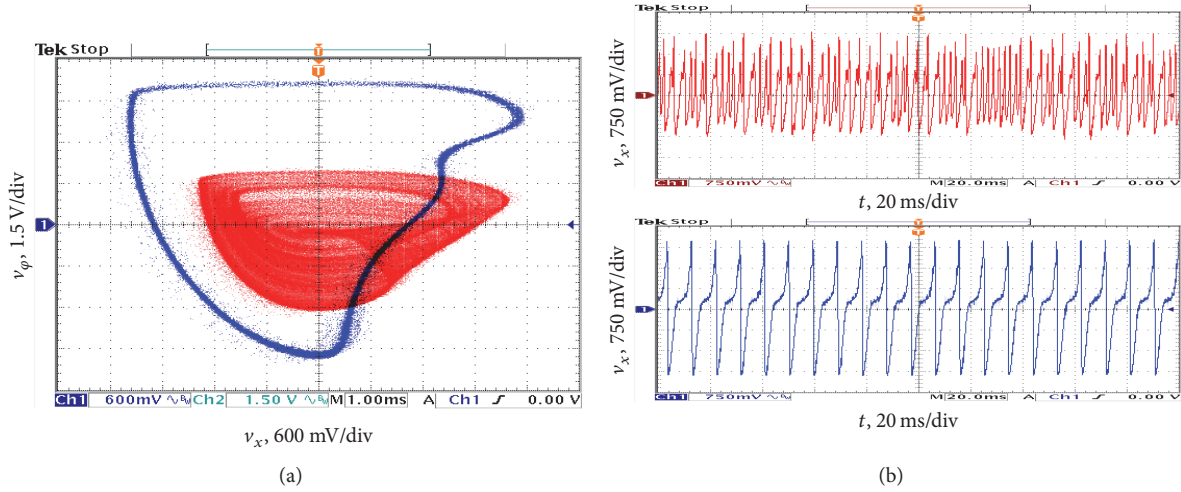


FIGURE 12: Experimentally measured hidden coexisting asymmetric attractors while repeatedly switching on and off the experimental power supply. (a) Phase portraits in the v_x - v_ϕ plane. (b) Time series of the variable v_x .

resistance $R_k = 10$ k Ω . When the amplitudes and frequencies of the sinusoidal voltage source used during numerical simulations in Figure 1 are employed, the pinched hysteresis loops for the corresponding amplitudes and frequencies are captured, as shown in Figures 11(a) and 11(b), respectively, which experimentally validate the characteristic fingerprints of the memristor emulator. It should be addressed that for better observing the experimental results, all the output currents sensed by the current probe are magnified by ten times.

The circuit parameters listed in Table 1 are used and the different initial voltages of three capacitors are randomly sensed by repeatedly switching on and off the experimental power supply [46]. For the typical circuit parameters in Table 1, two adjustable circuit parameters of R_1 and R_k correspond to the adjustable model parameters of $I = 1$ and $k = 0.9$. Corresponding to Figure 2, the phase portraits in the v_x - v_ϕ plane and time series of the variable v_x that emerged from different initial voltages are experimentally

obtained, as shown in Figure 12. The experimental results indicate that hidden coexisting asymmetric attractors also can be measured from the breadboard experiments of the memristive HR neuron model as well.

When the applied current $I = 1$, that is, the resistance R_1 is fixed as 10 k Ω and the resistance R_k is set to 1.36 k Ω and to 1.23 k Ω , respectively, the phase portraits in the v_x - v_ϕ plane are captured, as shown in Figures 13(a) and 13(b). Furthermore, when the electromagnetic induction strength $k = 0.9$, that is, $R_k = 1.11$ k Ω and R_1 is set to 8.70 k Ω and to 6.17 k Ω , respectively, the phase portraits in the v_x - v_ϕ plane are captured, as shown in Figures 13(c) and 13(d). Ignoring some tiny differences between numerical simulations and breadboard experiments due to the computational errors and parasitic circuit parameters, the experimental results are almost the same as the numerical simulations, which imply that the coexisting asymmetric attractors' behaviors that emerged from the memristive HR neuron model can be validated experimentally.

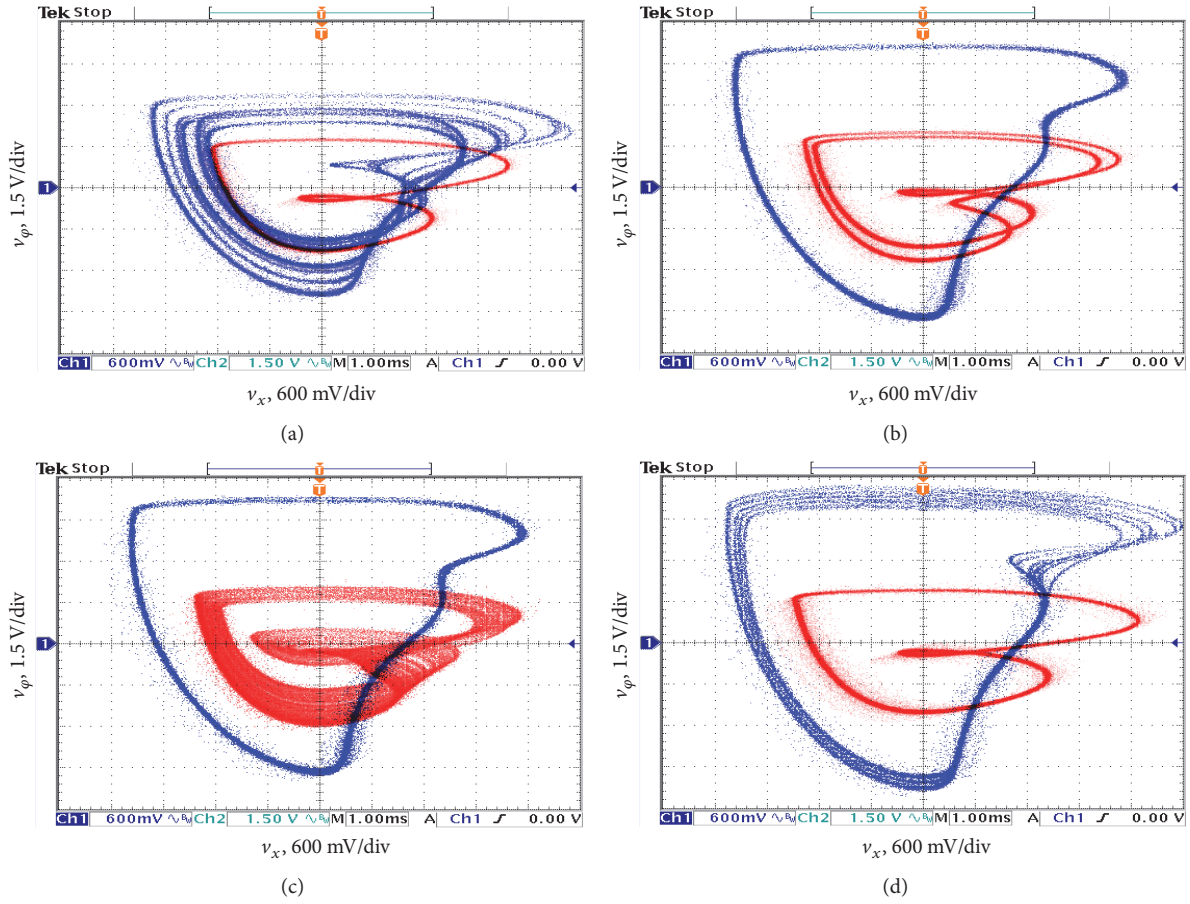


FIGURE 13: Experimentally measured phase portraits in the v_x - v_ϕ plane for hidden coexisting asymmetric attractors under different circuit parameters. (a) $R_1 = 10 \text{ k}\Omega$ and $R_k = 1.36 \text{ k}\Omega$. (b) $R_1 = 10 \text{ k}\Omega$ and $R_k = 1.23 \text{ k}\Omega$. (c) $R_1 = 8.70 \text{ k}\Omega$ and $R_k = 1.11 \text{ k}\Omega$. (d) $R_1 = 6.17 \text{ k}\Omega$ and $R_k = 1.11 \text{ k}\Omega$.

5. Conclusions

This paper presents a novel three-dimensional memristive HR neuron model to describe complex dynamics of neuronal activities with electromagnetic induction. The most prominent feature of this neuron model is that it does not contain any equilibrium point but can exhibit hidden coexisting behaviors of asymmetric attractors. Through executing bifurcation analyses, phase portraits, attraction basins, and dynamical maps, hidden coexisting asymmetric attractors are uncovered from the mathematical model and verified from the corresponding breadboard experiments. Thus, the proposed memristive HR neuron model can imitate the complex dynamical behaviors of electrical activities in neuron with electromagnetic induction. Further investigations will be performed in our future works.

Conflicts of Interest

The authors declare that they have no conflicts of interest.

Acknowledgments

This work was supported by the grants from the National Natural Science Foundations of China under Grant nos.

51777016, 51607013, 11602035, and 61601062 and the Natural Science Foundations of Jiangsu Province, China, under Grant no. BK20160282.

References

- [1] A. L. Hodgkin and A. F. Huxley, "A quantitative description of membrane current and its application to conduction and excitation in nerve.," *The Journal of Physiology*, vol. 117, no. 4, pp. 500–544, 1952.
- [2] J. L. Hindmarsh and R. M. Rose, "A model of the nerve impulse using two first-order differential equations," *Nature*, vol. 296, no. 5853, pp. 162–164, 1982.
- [3] J. L. Hindmarsh and R. M. Rose, "A model of neuronal bursting using three coupled first order differential equations," *Proceedings of the Royal Society of London B: Biological Sciences*, vol. 221, no. 1222, pp. 87–102, 1984.
- [4] C. R. Laing and C. C. Chow, "A spiking neuron model for binocular rivalry," *Journal of Computational Neuroscience*, vol. 12, no. 1, pp. 39–53, 2002.
- [5] K. Tsumoto, H. Kitajima, T. Yoshinaga, K. Aihara, and H. Kawakami, "Bifurcations in Morris-Lecar neuron model," *Neurocomputing*, vol. 69, no. 4–6, pp. 293–316, 2006.
- [6] H. Gu and B. Pan, "A four-dimensional neuronal model to describe the complex nonlinear dynamics observed in the firing

- patterns of a sciatic nerve chronic constriction injury model," *Nonlinear Dynamics*, vol. 81, no. 4, pp. 2107–2126, 2015.
- [7] F. Wu, C. Wang, and Y. Xu, "Model of electrical activity in cardiac tissue under electromagnetic induction," *Scientific Reports*, vol. 6, article 28, 2016.
 - [8] J. Ma and J. Tang, "A review for dynamics in neuron and neuronal network," *Nonlinear Dynamics*, vol. 89, no. 3, pp. 1569–1578, 2017.
 - [9] M. Ge, Y. Jia, Y. Xu, and L. Yang, "Mode transition in electrical activities of neuron driven by high and low frequency stimulus in the presence of electromagnetic induction and radiation," *Nonlinear Dynamics*, vol. 91, no. 1, pp. 515–523, 2018.
 - [10] M. Storace, D. Linaro, and E. de Lange, "The Hindmarsh-Rose neuron model: bifurcation analysis and piecewise-linear approximations," *Chaos: An Interdisciplinary Journal of Nonlinear Science*, vol. 18, no. 3, Article ID 033128, 2008.
 - [11] G. Innocenti, A. Morelli, R. Genesio, and A. Torcini, "Dynamical phases of the Hindmarsh-Rose neuronal model: studies of the transition from bursting to spiking chaos," *Chaos: An Interdisciplinary Journal of Nonlinear Science*, vol. 17, no. 4, Article ID 043128, 2007.
 - [12] J. M. González-Miranda, "Complex bifurcation structures in the Hindmarsh-Rose neuron model," *International Journal of Bifurcation and Chaos*, vol. 17, no. 9, pp. 3071–3083, 2007.
 - [13] J. M. González-Miranda, "Observation of a continuous interior crisis in the Hindmarsh-Rose neuron model," *Chaos: An Interdisciplinary Journal of Nonlinear Science*, vol. 13, no. 3, pp. 845–852, 2003.
 - [14] G. Innocenti and R. Genesio, "On the dynamics of chaotic spiking-bursting transition in the Hindmarsh-Rose neuron," *Chaos: An Interdisciplinary Journal of Nonlinear Science*, vol. 19, no. 2, Article ID 023124, 2009.
 - [15] T. Wei, B. Ou, J. Li et al., "Transcriptional profiling of rice early response to *Magnaporthe oryzae* identified OsWRKYs as important regulators in rice blast resistance," *PLoS ONE*, vol. 8, no. 3, Article ID e59720, 2013.
 - [16] S. R. D. Djeundam, R. Yamapi, T. C. Kofane, and M. A. Azizalaoui, "Deterministic and stochastic bifurcations in the Hindmarsh-Rose neuronal model," *Chaos: An Interdisciplinary Journal of Nonlinear Science*, vol. 23, no. 3, Article ID 033125, 2013.
 - [17] E. B. Ngouonkadi, H. B. Fotsin, P. Louodop Fotso, V. Kamdoun Tamba, and H. A. Cerdeira, "Bifurcations and multistability in the extended Hindmarsh-Rose neuronal oscillator," *Chaos, Solitons & Fractals*, vol. 85, pp. 151–163, 2016.
 - [18] K. Wu, T. Luo, H. Lu, and Y. Wang, "Bifurcation study of neuron firing activity of the modified Hindmarsh-Rose model," *Neural Computing and Applications*, vol. 27, no. 3, pp. 739–747, 2016.
 - [19] S. K. Thottil and R. P. Ignatius, "Nonlinear feedback coupling in Hindmarsh-Rose neurons," *Nonlinear Dynamics*, vol. 87, no. 3, pp. 1879–1899, 2017.
 - [20] H. Wang, Y. Zheng, and Q. Lu, "Stability and bifurcation analysis in the coupled HR neurons with delayed synaptic connection," *Nonlinear Dynamics*, vol. 88, no. 3, pp. 2091–2100, 2017.
 - [21] S. Lakshmanan, C. P. Lim, S. Nahavandi, M. Prakash, and P. Balasubramaniam, "Dynamical analysis of the Hindmarsh-Rose neuron with time delays," *IEEE Transactions on Neural Networks and Learning Systems*, vol. 28, no. 8, pp. 1953–1958, 2017.
 - [22] H. Wang, Q. Wang, and Y. Zheng, "Bifurcation analysis for Hindmarsh-Rose neuronal model with time-delayed feedback control and application to chaos control," *Science China Technological Sciences*, vol. 57, no. 5, pp. 872–878, 2014.
 - [23] D. Jun, Z. Guang-Jun, X. Yong, Y. Hong, and W. Jue, "Dynamic behavior analysis of fractional-order Hindmarsh-Rose neuronal model," *Cognitive Neurodynamics*, vol. 8, no. 2, pp. 167–175, 2014.
 - [24] E. Kaslik, "Analysis of two- and three-dimensional fractional-order Hindmarsh-Rose type neuronal models," *Fractional Calculus and Applied Analysis*, vol. 20, no. 3, pp. 623–645, 2017.
 - [25] M. Lv, C. Wang, G. Ren, J. Ma, and X. Song, "Model of electrical activity in a neuron under magnetic flow effect," *Nonlinear Dynamics*, vol. 85, no. 3, pp. 1479–1490, 2016.
 - [26] M. Lv and J. Ma, "Multiple modes of electrical activities in a new neuron model under electromagnetic radiation," *Neurocomputing*, vol. 205, pp. 375–381, 2016.
 - [27] L. Lu, Y. Jia, W. Liu, and L. Yang, "Mixed stimulus-induced mode selection in neural activity driven by high and low frequency current under electromagnetic radiation," *Complexity*, vol. 2017, Article ID 7628537, pp. 1–11, 2017.
 - [28] S. Jafari, J. C. Sprott, and S. M. R. H. Golpayegani, "Elementary quadratic chaotic flows with no equilibria," *Physics Letters A*, vol. 377, no. 9, pp. 699–702, 2013.
 - [29] V.-T. Pham, C. Volos, S. Jafari, Z. Wei, and X. Wang, "Constructing a novel no-equilibrium chaotic system," *International Journal of Bifurcation and Chaos*, vol. 24, no. 5, Article ID 1450073, 2014.
 - [30] F. R. Tahir, S. Jafari, V.-T. Pham, C. Volos, and X. Wang, "A novel no-equilibrium chaotic system with multiwing butterfly attractors," *International Journal of Bifurcation and Chaos*, vol. 25, no. 4, Article ID 1550056, 2015.
 - [31] A. P. Kuznetsov, S. P. Kuznetsov, E. Mosekilde, and N. V. Stankevich, "Co-existing hidden attractors in a radio-physical oscillator system," *Journal of Physics A: Mathematical and Theoretical*, vol. 48, no. 12, Article ID 125101, 2015.
 - [32] B. Bao, H. Qian, Q. Xu, M. Chen, J. Wang, and Y. Yu, "Coexisting behaviors of asymmetric attractors in hyperbolic-type memristor based hopfield neural network," *Frontiers in Computational Neuroscience*, vol. 11, article 81, 2017.
 - [33] A. Shilnikov, R. L. Calabrese, and G. Cymbalyuk, "Mechanism of bistability: tonic spiking and bursting in a neuron model," *Physical Review E: Statistical, Nonlinear, and Soft Matter Physics*, vol. 71, no. 2, Article ID 056214, 2005.
 - [34] B. Bao, H. Qian, J. Wang et al., "Numerical analyses and experimental validations of coexisting multiple attractors in Hopfield neural network," *Nonlinear Dynamics*, vol. 90, no. 4, pp. 2359–2369, 2017.
 - [35] T. Malashchenko, A. Shilnikov, and G. Cymbalyuk, "Six types of multistability in a Neuronal model based on slow calcium current," *PLoS ONE*, vol. 6, no. 7, Article ID e21782, 2011.
 - [36] L. Chua, "Resistance switching memories are memristors," *Applied Physics A: Materials Science & Processing*, vol. 102, no. 4, pp. 765–783, 2011.
 - [37] L. O. Chua, "The fourth element," *Proceedings of the IEEE*, vol. 100, no. 6, pp. 1920–1927, 2012.
 - [38] S. P. Adhikari, M. P. Sah, H. Kim, and L. O. Chua, "Three fingerprints of memristor," *IEEE Transactions on Circuits and Systems II: Express Briefs*, vol. 60, no. 11, pp. 3008–3021, 2013.
 - [39] A. Wolf, J. B. Swift, and H. L. a. Swinney, "Determining Lyapunov exponents from a time series," *Physica D: Nonlinear Phenomena*, vol. 16, no. 3, pp. 285–317, 1985.

- [40] P. C. Rech, "Period-adding and spiral organization of the periodicity in a Hopfield neural network," *International Journal of Machine Learning and Cybernetics*, vol. 6, no. 1, 2013.
- [41] H. Bao, N. Wang, B. Bao, M. Chen, P. Jin, and G. Wang, "Initial condition-dependent dynamics and transient period in memristor-based hypogenetic jerk system with four line equilibria," *Communications in Nonlinear Science and Numerical Simulation*, vol. 57, pp. 264–275, 2018.
- [42] B. C. Bao, H. Bao, N. Wang, M. Chen, and Q. Xu, "Hidden extreme multistability in memristive hyperchaotic system," *Chaos, Solitons & Fractals*, vol. 94, pp. 102–111, 2017.
- [43] K. Rajagopal, A. Akgul, S. Jafari, and B. Aricioglu, "A chaotic memcapacitor oscillator with two unstable equilibriums and its fractional form with engineering applications," *Nonlinear Dynamics*, vol. 91, no. 2, pp. 957–974, 2018.
- [44] K. Rajagopal, L. Guessas, A. Karthikeyan, A. Srinivasan, and G. Adam, "Fractional order memristor no equilibrium chaotic system with its adaptive sliding mode synchronization and genetically optimized fractional order PID synchronization," *Complexity*, vol. 2017, Article ID 1892618, pp. 1–19, 2017.
- [45] K. Rajagopal, A. Karthikeyan, and A. K. Srinivasan, "FPGA implementation of novel fractional-order chaotic systems with two equilibriums and no equilibrium and its adaptive sliding mode synchronization," *Nonlinear Dynamics*, vol. 87, no. 4, pp. 2281–2304, 2017.
- [46] B. Bao, T. Jiang, G. Wang, P. Jin, H. Bao, and M. Chen, "Two-memristor-based Chua's hyperchaotic circuit with plane equilibrium and its extreme multistability," *Nonlinear Dynamics*, vol. 89, no. 2, pp. 1157–1171, 2017.